Micromachined Ultrasonic Transducers for 3-D Imaging

Christiansen, Thomas Lehrmann

Publication date:
2015

Document Version
Publisher's PDF, also known as Version of record

PhD Thesis

Micromachined Ultrasonic Transducers for 3-D Imaging

Thomas Lehrmann Christiansen

Supervised by: Prof. Erik Vilain Thomsen, PhD, and Prof. Jørgen Arendt Jensen, PhD, Dr. Techn.

Technical University of Denmark
Kgs. Lyngby, Denmark 2015

Cover image: A photo of a wafer being processed in the cleanroom. The wafer contains the first generation of transducer arrays developed during this project. Photo by Jesper Scheel.

Technical University of Denmark
Department of Micro- and Nanotechnology
Ørsteds Plads 345E
2800 Kgs. Lyngby
DENMARK
Tel: (+45) 4525 5700
Fax: (+45) 4588 7762
Web: www.nanotech.dtu.dk
E-mail: info@nanotech.dtu.dk
Author e-mail: thomas_lehrmann@me.com

Contents

Summary

Real-time ultrasound imaging is a widely used technique in medical diagnostics. Recently, ultrasound systems offering real-time imaging in 3-D has emerged. However, the high complexity of the transducer probes and the considerable increase in data to be processed compared to conventional 2-D ultrasound imaging results in expensive systems, which limits the more wide-spread use and clinical development of volumetric ultrasound.

The main goal of this thesis is to demonstrate new transducer technologies that can achieve real-time volumetric ultrasound imaging without the complexity and cost of state-of-the-art 3-D ultrasound systems. The focus is on row-column addressed transducer arrays. This previously sparsely investigated addressing scheme offers a highly reduced number of transducer elements, resulting in reduced transducer manufacturing costs and data processing. To produce such transducer arrays, capacitive micromachined ultrasonic transducer (CMUT) technology is chosen for this project. Properties such as high bandwidth and high design flexibility makes this an attractive transducer technology, which is under continuous development in the research community.

A theoretical treatment of CMUTs is presented, including investigations of the anisotropic plate behaviour and modal radiation patterns of such devices. Several new CMUT fabrication approaches are developed and investigated in terms of oxide quality and surface protrusions, culminating in a simple four-mask process capable of producing 62+62-element row-column addressed CMUT arrays with negligible charging issues. The arrays include an integrated apodization, which reduces the ghost echoes produced by the edge waves in such arrays by $15.8\,\mathrm{dB}$. The acoustical cross-talk is measured on fabricated arrays, showing a $24\,\mathrm{dB}$ reduction in cross-talk compared to 1-D arrays for 2-D imaging. Volumetric imaging is successfully demonstrated using a beamformer specifically developed for row-column addressed arrays. Furthermore, a technique for estimating flow velocities in all three dimensions is presented.

Based on the developed techniques, a complete hand-held $3\,\mathrm{MHz}$ $\lambda/2$-pitch ultrasound probe for volumetric imaging with 62+62 elements and in-handle electronics is produced and used on a commercial bk3000 scanner from BK Medical. The scanner is made for conventional 2-D ultrasound imaging, proving that the developed technology enables real-time volumetric ultrasound imaging with a total system cost and complexity equivalent to that of 2-D ultrasound imaging systems.

Resumé

(Summary in Danish)

Ultralydsbilleddannelse er hyppigt brugt i medicinsk diagnostik, og i de senere år er ultralydssystemer, der muliggør 3-D billeddannelse i realtid, blevet tilgængelige. Imidlertid er sådanne systemer forbundet med store økonomiske omkostninger grundet kompleksiteten af de anvendte transducere samt den markant øgede datamængde sammenlignet med systemer til konventionel 2-D billeddannelse. Dette begrænser en mere udbredt brug af 3-D ultralyd og hæmmer udviklingen af nye kliniske applikationer.

Hovedformålet med denne afhandling er at demonstrere nye transducerteknologier, der tillader realtids ultralydsbilleddannelse i 3-D uden kompleksiteten og omkostningerne ved moderne 3-D ultralydssystemer. Fokus er på den hidtil sparsomt undersøgte række-søjle adressering, som muliggør en betydelig reduktion i fremstillingsomkostninger og dataprocessering grundet et lavere antal transducerelementer. Dette projekt benytter sig desuden af såkaldt kapacitiv mikrofremstillet ultralydstransducer (CMUT) -teknologi til fremstilling af transducerne. Egenskaber såsom stor båndbredde og betydelig designfleksibilitet gør dette til en attraktiv transducerteknologi, som er under stadig udvikling i forskningsmiljøet.

Denne afhandling indeholder som det første en teoretisk analyse af CMUT'er, herunder en analyse af den anisotrope pladeopførsel og strålingskarakteristikken. Desuden er adskillige nye CMUT-fremstillingsmetoder udviklet og undersøgt i forbindelse med oxidkvalitet og overfladefremspring, og dette har resulteret i udviklingen af en simpel fire-maske proces, hvormed 62+62-element række-søjle adresserede CMUT transducere uden opladningsproblemer kan produceres. Transducerne har en integreret apodisering, som reducerer de uønskede ekkoer genereret af kantbølger fra række-søjle adresserede transducere med $15.8\,\mathrm{dB}$. Den akustiske krydstale i de fremstillede transducere er målt til at være reduceret med $24\,\mathrm{dB}$ sammenlignet med konventionelle 1-D transducere til 2-D billeddannelse. 3-D billeddannelse er også demonstreret ved brug af en fokuseringsalgoritme udviklet specifikt til række-søjle adresserede transducere. Desuden præsenteres en teknik hvormed hastighedskomposanterne i alle tre rumlige dimensioner kan bestemmes.

Baseret på de udviklede teknikker fremstilles en komplet, håndholdt $3\,\mathrm{MHz}$ $\lambda/2$-pitch ultralydsprobe til 3-D billeddannelse. Den indeholder 62+62 elementer og integreret elektronik, og er designet til brug med en kommerciel bk3000 skanner fra BK Medical. Skanneren er oprindeligt udviklet til konventionel 2-D skanning, hvilket viser, at den ud-

viklede transducerteknologi muliggør realtids 3-D ultralydsbilleddannelse med en samlet systemomkostning og kompleksitet, som er sammenlignelig med et 2-D ultralydssystem.

Preface

This PhD thesis has been submitted to the Department of Micro- and Nanotechnology at the Technical University of Denmark in partial fulfillment of the requirements for acquiring the PhD degree. The research providing the foundation for the thesis has been conducted over a period of two years and ten months from September 1st, 2012, to June 23rd, 2015. It has been carried out partly at the Department of Micro- and Nanotechnology (DTU Nanotech) and partly at the Center for Fast Ultrasound Imaging (CFU), Department of Electrical Engineering, both located at the Technical University of Denmark (DTU). It has been supervised by Prof. Erik Vilain Thomsen, PhD, and co-supervised by Prof. Jørgen Arendt Jensen, PhD, Dr. Techn.

When the project started in the summer of 2012, Prof. Erik Vilain Thomsen had recently started a collaboration with Prof. Jørgen Arendt Jensen with the goal of developing next-generation technology for medical ultrasound diagnostics using so-called capacitive micromachined ultrasonic transducers, or "CMUTs". Initially, my time on the project was spent on establishing a knowledge basis enabling further research in this transducer technology, which was relatively unexplored at DTU at the time. This involved understanding and expanding the theory behind CMUTs, and to investigate cleanroom processes with which they could be fabricated.

I then started a collaboration with Morten Fischer Rasmussen, a PhD student in Prof. Jørgen Arendt Jensen's group working on advanced beamforming techniques for 3-D ultrasound imaging. This shaped the remainder of my project period, where the focus has been on developing 2-D CMUT arrays for 3-D ultrasound imaging. I have strived to involve myself in most aspects of the process; from theoretical models and acoustic design over microfabrication to new imaging techniques and the development of prototype CMUT probes for use with commercial ultrasound scanners. All of this in close collaboration with my colleagues at DTU and the industrial partners at BK Medical ApS in Herlev and Sound Technology Inc in State College, PA, USA.

During the project period, I have had the pleasure of co-supervising a total of 24 engineering students in four master's projects, two bachelor's projects, and eight smaller student projects. All of these have had part in shaping the final outcome of this thesis, and have given me invaluable inputs and experiences. I had the opportunity of meeting fellow researchers at conferences in Dresden (Germany), Side (Turkey), Prague (Czech

Republic), and Chicago (USA). In addition to this, I had the priveledge of spending a two-month external stay in October and November of 2014 as a visiting researcher in the Khuri-Yakub Ultrasonics Group at Stanford University, CA, USA.

The project was funded by DTU Nanotech and grant 82-2012-4 from the Danish National Advanced Technology Foundation.

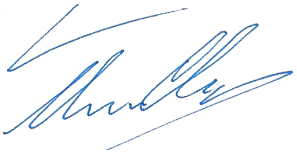

Thomas Lehrmann Christiansen
Copenhagen, June 2015

Acknowledgements

First and foremost, my sincerest gratitude goes to my supervisor, Prof. Erik Vilain Thomsen, and my co-supervisor, Prof. Jørgen Arendt Jensen. Thank you for letting me participate in this exciting research project and for giving me such freedom to explore new ideas. You have both been a source of inspiration to me and have provided me with the best possible working environment and support. Because of this, the last three years have become exactly the PhD project I had hoped for.

My warmest regards goes to all of my colleagues at DTU Nanotech and at CFU. Thank you for being inspiring and helpful; and most of all, thank you for being such good friends. You have made my last three years a joy, and I am surely going to miss being around you. A very special thank you goes to my former office mate Mette Funding la Cour for always providing a great atmosphere to the "CMUT office", and to Morten Fischer Rasmussen for being such a big part in making this project as exciting as it turned out to be.

I would also like to thank my collaboration partners at DTU Danchip, BK Medical, and Sound Technology, in particular Jan Bagge, Lars Moesner, and Chris Beers. You have been an invaluable resource of knowledge and assistance, and this project would not have been possible without your help. Thank you to all the students that I have supervised; you have been a vital part of my project and have greatly contributed to its success. A special thanks goes to Prof. B. T. Khuri-Yakub from Stanford University for letting me join his research group for two months in 2014, and to the Ministry of Higher Education and Science for the EliteForsk grant that financed the stay.

Last, but definitely not least, a huge thanks goes to my family. First and foremost to you, Signe, for always supporting me, for always being my notion of home. Being with you is my greatest privilege of all.

Abbreviations

1-D	One-Dimensional
2-D	Two-Dimensional
3-D	Three-Dimensional
4-D	Real-time three-dimensional
AC	Alternating Current
AFM	Atomic Force Microscopy
BHF	Buffered HydroFluoric acid
BOX	Buried OXide
CCB	Chip Carrier Board
CMUT	Capacitive Micromachined Ultrasonic Transducer
CT	Computed Tomography
DC	Direct Current
DI	De-Ionized
DTU	Danmarks Tekniske Universitet (Technical University of Denmark)
$f_{\#}$	f-number, equal to the focal length divided by the aperture diameter
FEA	Finite Element Analysis
FWHM	Full Width at Half Maximum
IAC	Infinite Array of Cells
KOH	Potassium Hydroxide
LOCOS	LOCal Oxidation of Silicon
LPCVD	Low-Pressure Chemical-Vapor Deposition
LSF	Line Spread Function
MEMS	Micro Electro Mechanical Systems
MOS	Metal-Oxide-Semiconductor
MRI	Magnetic Resonance Imaging
PCB	Printed Circuit Board
RF	Radio Frequency
PSF	Point Spread Function
RIE	Reactive Ion Etching
RMS	Root Mean Square
RTV	Room Temperature Vulcanization

SARUS	Synthetic Aperture Real-time Ultrasound System
SC	Single Cell
SEM	Scanning Electron Microscopy
SNR	Signal to Noise Ratio
SOI	Silicon-On-Insulator
ToF	Time of Flight
TO	Transverse Oscillation
UV	Ultra Violet

CHAPTER 1

Introduction

1.1 3-D Ultrasound Imaging

For decades, ultrasound imaging has been an important diagnostic tool in the clinic. It is used in numerous branches of medicine, from cardiology over obstetrics to urology. The vast majority of ultrasound scanner systems today are used for 2-D imaging, i.e. imaging in planes. Recently, however, more advanced ultrasound systems capable of performing real-time 3-D (4-D) imaging has emerged. Although competing 3-D imaging modalities such as CT and MRI have detail resolutions that ultrasound inherently cannot compete with, the combination of patient safety, cost-effectiveness, portability, and real-time imaging ability makes ultrasound the preferred choice in many clinical situations.

Volumetric imaging has several advantages over conventional 2-D ultrasound imaging. The location and orientation of 2-D images are determined by the transducer probe, rendering some views inaccessible due to patient anatomy or position. With 3-D imaging, any view angle is available from the acquired volume data. This capability is equally valuable for therapeutic procedures requiring follow-up studies that depend on the ability to aquire a view that has the same orientation and position as a previous examination. Furthermore, diagnostic and therapeutic decisions often require accurate estimates of e.g. organ, cyst, or tumour volumes. 3-D imaging can provide this without relying on the assumptions and operator-dependent skills involved in such estimations using 2-D scans.

Conventional 2-D ultrasound images are created using probes containing 1-D transducer arrays. Such arrays consist of a large number of individual transducer elements, typically 128 or 192, mounted side-by-side as shown in Fig. 1.1. Each element is connected to a channel on the ultrasound scanner containing both a transmitting and a receiving circuit. Thereby, sound can be emitted or received with any phase delay profile, allowing electronic focusing and steering of the beam along the azimuth direction as illustrated in Fig. 1.1. To avoid the interference of grating lobes arising from the periodicity of the array, the element inter-distance – or "pitch" – is kept less than the wavelength of the ultrasound. In linear and convex arrays, where beam steering is not employed, the pitch is usually equal to the wavelength (λ-pitch), whereas phased arrays uses a $\lambda/2$-pitch configuration to allow beam steering in up to a 90° sector angle (Jensen 1996, p. 38). An acoustical lens creates a fixed focus in the elevation direction, defining the thickness of the plane being imaged. The axial resolution is proportional to the wavelength of the ultrasound. This is also true for the lateral resolution at the focus (the full-width at half-maximum, FWHM), which is proportional to $\lambda f_{\#}$ (Szabo 2014, p. 172). Here,

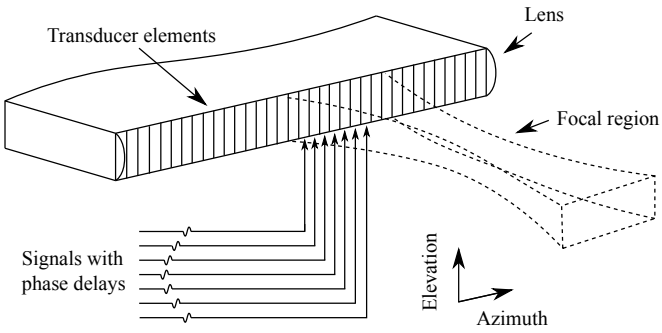

Figure 1.1: Illustration of the principle behind a 1-D transducer array used for 2-D ultrasound imaging. The transducer elements are placed side-by-side and are each connected to a channel on the ultrasound scanner. By adjusting the phase delay on each channel, the emitted and received sound can be focused and steered in the azimuth dimension. A lens ensures a fixed focus in the elevation dimension.

the f-number, $f_{\#}$, is defined by the focal depth divided by the aperture (array) width. However, as the wavelength decreases, the frequency increases, leading to higher attenuation in the tissue which attenuates ultrasound with roughly $1\,\mathrm{dB}/(\mathrm{MHz}\cdot\mathrm{cm})$ (Jensen 1996, p. 23). There is therefore a trade-off between resolution and penetration depth, so depending on the application, the frequency of ultrasound transducers is typically found in the interval $1\,\mathrm{MHz}$-$15\,\mathrm{MHz}$ (Szabo 2014, p. 26). The corresponding wavelength is between $1.5\,\mathrm{mm}$ and $100\,\mu\mathrm{m}$, which defines the width of the elements in the array due to the pitch requirement. At the same time, the array aperture must be kept large to maintain a good lateral resolution, and this is the reason for the significant number of elements employed in modern 1-D arrays.

There are three main ways in which 3-D ultrasound imaging can be performed using hand-held probes: With free-hand scanning, mechanical probes, or 2-D array transducers (Karadayi, Managuli, and Kim 2009). The first two are based on 1-D transducer arrays. In free-hand scanning, the operator uses a 1-D array to acquire multiple 2-D images at arbitrary positions and angles controlled by the operator. A sensing system tracks the movement of the transducer, and the 2-D images are then post-processed to produce a volumetric image of the scanned region. While this approach offers a relatively low-cost and flexible solution, image quality suffers from position inaccuracies and irregular scanning due to the hand-held manipulation. The latter also inhibits real-time imaging in this modality. A method to better control and track the position of the 1-D transducer array is to mechanically move it in a precise and predefined way. This is the principle of mechanical probes, in which the 1-D transducer array is mounted on a mechanical stage inside the probe. Servo or stepper motors are then used to control and track the movement of the transducer array. Fig. 1.2(a) shows an example of a mechanical probe,

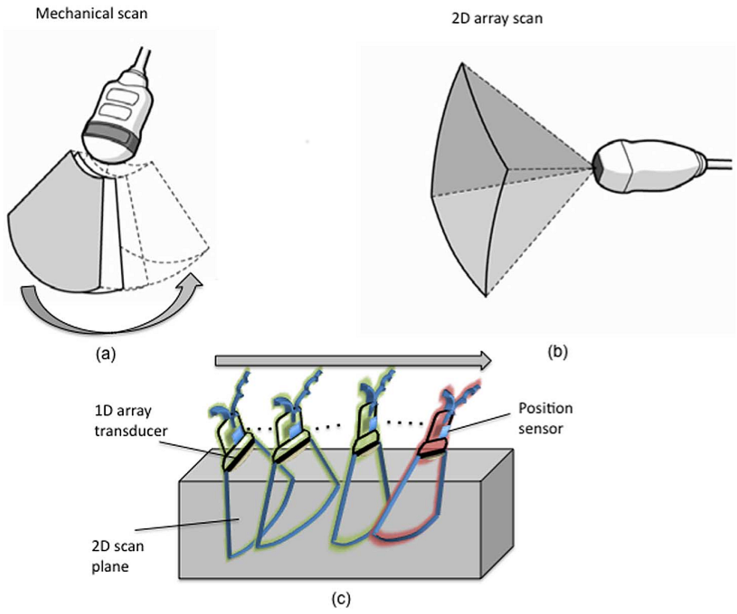

Figure 1.2: Illustration of three ways in which 3-D ultrasound imaging can be performed. Figure (a) shows a mechanical probe, in which a 1-D array is "wobbled" back and forth in a controlled manner to enable imaging of a volume. Figure (c) shows a more crude method in which a conventional 1-D array is translated manually over the region of interest, and the 2-D slices are then postprocessed to yield a 3-D image. Figure (b) shows a 2-D matrix array. The organization of the transducer elements in a rectangular grid allows for beam steering in both lateral directions, enabling the illustrated pyramidal scan. From (Karadayi, Managuli, and Kim 2009).

where the transducer array is "wobbled" back and forth in a fan-like arc. Alternatively, the transducer array can be rotated around an axis or translated linearly. It is apparent that this technique relies on the accuracy of the mechanical positioning stage. The tracking error naturally increases with the displacement frequency due to the larger accelerations involved in changing the direction of the array, and therefore such probes are usually limited to producing images with frame rates below 10 Hz (Roh 2014).

To obtain true high quality, real-time 3-D images (i.e. at a frame rate of more than approximately 20 Hz), 2-D matrix arrays have been employed. Such arrays were first introduced in the early 1990's by researchers at Duke University (Ramm, Smith, and Pavy 1991; Smith, Pavy, and Ramm 1991). By arranging the transducer elements in a rectangular grid, it is possible to steer the ultrasond beam in both the azimuth and elevation directions and thereby acquire data from a volume. In principle, the concept is

Figure 1.3: Picture of a fully wired $3.5\,\mathrm{MHz}$ 32×32 matrix array produced by Vermon S.A. (Tours, France). Even this modest size array has a cable size which excludes it from any practical clinical use.

simple, but in practice, it presents a formidable technical challenge. To obtain the same resolution as in 2-D imaging, the number of elements along each lateral dimension must be equal to that of a 1-D array. Yet, even a small 1-D array with 128 elements would translate into $128 \times 128 = 16384$ elements in a 2-D matrix array. From a transducer fabrication viewpoint, such a large number of elements poses a significant challenge in element yield and in providing electrical connections to each element. Also, the small size of the elements results in lowered capacitance and hence increased electrical impedance mismatch between the element and the cable connecting it to the ultrasound scanner, calling for preamplifiers and matching circuits in the probe handle (Karadayi, Managuli, and Kim 2009). Even so, the sheer number of wires results in an impractically large cable from the transducer. Fig. 1.3 shows a picture of a fully wired 32×32 matrix array produced by Vermon S.A., Tours, France. It is clear that even this size array has a cable size which excludes it from any practical clinical use.

The beamforming process carried out by the scanner presents its own issues. The time needed to perform a sufficient number of transmit/receive events scales with the number of elements, and so does the amount of data that must be collected and processed. In practice, 2-D matrix arrays and their associated beamforming techniques must therefore be subjected to certain constraints to allow for real-time imaging. The issue of achieving sufficient frame rates was addressed by von Ramm et al. (Ramm, Smith, and Pavy 1991) using a parallel beamforming approach. Instead of emitting tightly focused ultrasound beams, broader beams are emitted in this approach to enable full insonification of the whole volume of interest with much fewer transmit events. Multiple parallel beams are then beamformed in receive along each insonified region. This enables real-time imaging at the expense of lower resolution and the introduction of image artefacts due to the

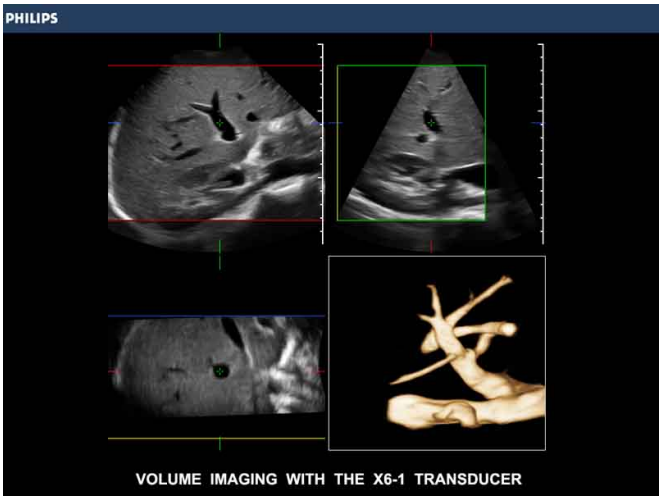

Figure 1.4: Cross-sectional and 3-D images of the liver veins produced with the state-of-the-art, fully sampled X6-1 PureWave xMATRIX Array with 9212 elements from Phillips (Eindhoven, Holland). From (Phillips 2015).

multiple scan line formation.

The issue of reducing channel count whilst maintaining the size of the array aperture was in the earlier versions of 2-D matrix arrays addressed by introducing sparse arrays, in which only a subset of the elements are active at the same time. Amongst these are Vernier arrays, random arrays, and Mills cross arrays, presenting each their benefits and drawbacks (Austeng and Holm 2002; Brunke and Lockwood 1997; Davidsen, Jensen, and Smith 1994; Karaman et al. 2009; Yen, Steinberg, and Smith 2000). However, all of them suffer from reduced signal-to-noise ratio (SNR) and introduce higher sidelobes and/or grating lobes. More recently, fully sampled arrays with reduced channel count have become available by splitting the beamforming in two stages: Fine delays and summation between elements in close proximity is carried out by electronics placed inside the transducer probe, and much fewer signals are then funnelled out to the ultrasound scanner, which performs the final beamforming. An example of such a state-of-the-art fully sampled matrix transducer is the X6-1 PureWave xMATRIX Array from Phillips (Eindhoven, Holland), with 9212 elements. An example of imaging of the liver veins with this transducer is given in Fig. 1.4 (Phillips 2015).

Despite the recent advances in real-time 3-D ultrasound imaging, the ultrasound systems supporting such imaging modalities are highly advanced and rely on cutting edge software, hardware, and manufacturing technology. This results in expensive equipment, impairing the low-cost advantage of ultrasound and thus limiting its more widespread use.

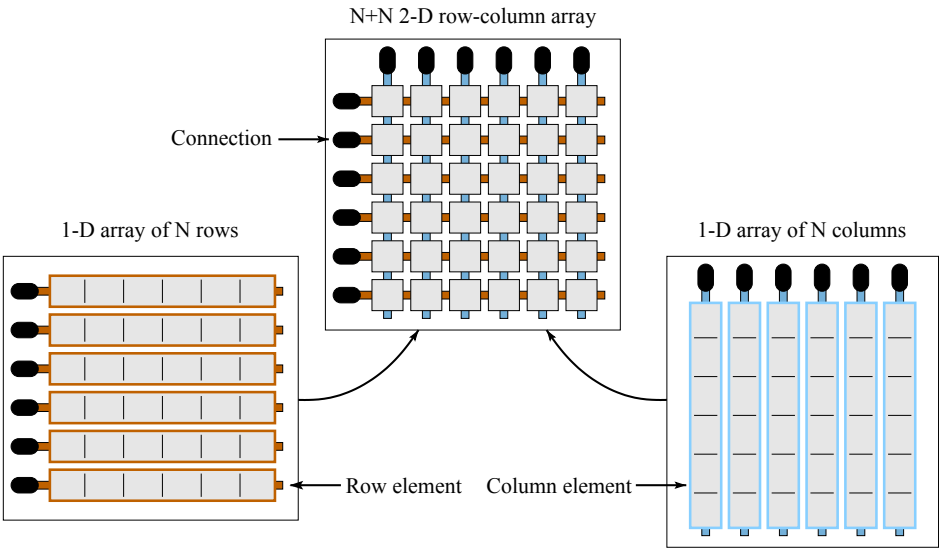

Figure 1.5: The row-column addressing scheme. By addressing the 2-D array by its row- and column indices, two 1-D arrays oriented orthogonal to one another are effectively produced. The number of connections needed to address an $N \times N$ array thereby becomes $2N$, as opposed to the N^2 connections required in a fully addressed matrix array. Modified from (Rasmussen and Jensen 2013).

Moreover, the thermal budget starts to become a consideration for modern probes with integrated electronics due to the constraints on transducer probe heating dictated by the standards for medical equipment (Sampson et al. 2013).

Recently, an alternative to matrix arrays have been suggested. These are so-called row-column addressed 2-D arrays, which were first proposed in 2003 by Morton and Lockwood (Morton and Lockwood 2003). Here, the 2-D array is addressed via its row- and column indices, effectively producing two 1-D arrays oriented orthogonal to one another as shown in Fig. 1.5. The number of connections needed to address an $N \times N$ array thereby becomes $2N$, as opposed to the N^2 connections required in a fully addressed matrix array. For example, the number of connections for a 128×128 array is consequently reduced from 16384 to 256. This significant reduction decreases the complexity of 2-D arrays for real-time 3-D imaging considerably. However, row-column addressed transducer arrays have only been sparsely investigated in the literature, and further research is needed to assess the possibilities and drawbacks associated with transducer arrays using this addressing scheme.

1.2 Capacitive Micromachined Ultrasonic Transducers (CMUTs)

A central part of the ultrasound scanning system is the ultrasound transducer. It is responsible of converting the electrical signals from the scanner to sound waves, which are send into the patient. The sound echoes from the tissue are then received by the transducer and converted into electrical signals that can be manipulated by the scanner to create the ultrasound image.

Since ultrasound imaging emerged in the middle of the 20th century, and before that in sonar, the dominant transducer technology has been piezoelectric transducers (Szabo 2014). These are based on crystals or ceramics with the property that they are able to deform when a voltage is applied across them. Conversely, when the piezoelectric material is deformed, a voltage difference is created on the opposing faces of the crystal. In the wake of the fabrication techniques developed in the semiconductor industry and later the MEMS industry, an alternative to piezoelectric ultrasound transducers emerged in the mid-1990's (Haller and Khuri-Yakub 1994, 1996; Schindel et al. 1995). These were coined capacitive micromachined ultrasonic transducers or CMUTs, and they rely on a capacitive actuation mechanism rather than piezoelectricity. As opposed to piezoelectric transducers, which are made using conventional mechanical processes, such transducers are made using cleanroom fabrication techniques, with which structures in the order of microns can routinely be made. The work presented in this thesis is based on CMUT technology, partly because of the design flexibility of CMUTs, and partly to explore the possibilities of this still evolving technology.

A cross-section of a typical CMUT is seen in Fig. 1.6. It consists of a fixed bottom substrate over which a thin deformable plate is suspended. Both are usually made from electrically conducting, highly doped silicon, or contains a conducting metal electrode, and they are separated by an insulating material (drawn blue in Fig. 1.6). The insulator is in most cases either silicon dioxide or silicon nitride. The central part of the CMUT contains a gap, which is typically evacuated to create a vacuum. An insulating layer is placed in the bottom of the vacuum gap to prevent the top plate and the bottom substrate to come into electrical contact.

The top plate and the bottom substrate constitute the top- and bottom electrodes in a capacitor, which is charged if an external voltage supply is connected. During transmit, as seen in the left illustration of Fig. 1.6, the opposing sign of the charges on the two electrodes induces an attractive force between the electrodes, resulting in deformation of the top plate. If the frequency of the voltage signal is in the ultrasound range (1-20 MHz for medical ultrasound), an ultrasound pressure wave is generated at the surface of the top plate. In receive mode, shown to the right in Fig. 1.6, a pressure wave impinges on the surface of the CMUT and a voltage or current is generated depending on the electrical readout circuit. Usually, the CMUT is biased with a DC voltage in both transmit- and receive mode to improve the efficiency of the transducer as described in further detail in Chapter 2.

The individual CMUT can in principle have any shape, but in this thesis, only circular

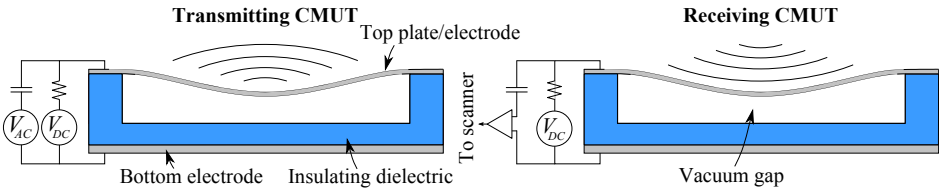

Figure 1.6: Cross-sectional illustration of a typical CMUT in transmit mode (left) and receive mode (right). It contains a fixed bottom substrate and a deformable top plate suspended over a vacuum gap. The bottom substrate and the top plate are conducting and form two electrodes separated by an insulating dielectric. An insulator is also placed in the bottom of the vacuum cavity to prevent electrical contact between the bottom substrate and the top plate.

and square CMUTs are considered. Rectangular CMUTs have shown to be undesirable due to the reduced frequency separation of plate modes leading to loss in output pressure (Wong et al. 2008). The size of the CMUT is dictated by the desired frequency of the ultrasound as covered in Chapter 2, and typical dimensions are in the order of $\sim 1\,\mu\mathrm{m}$ for the plate thickness and $\sim 60\,\mu\mathrm{m}$ for the plate diameter/side length. In order to achieve high enough field strengths with realistic voltages, the separation between the bottom substrate and the top plate needs to be in the sub-micron range.

As described in Section 1.1, the width of the elements in a transducer array is dictated by the wavelength of the ultrasound, and the width is roughly equal to a whole or one half wavelength. Since the size of the individual CMUT is typically considerably smaller than the wavelength, each element in a CMUT array consists of a multitude of individual CMUTs, from hereon referred to as CMUT "cells". Fig. 1.7 shows an example of a transducer array where each element is composed of a large number of square CMUT cells. Each CMUT cell within an element shares the same top- and bottom electrode to allow simultaneous actuation of the whole element.

1.3 Motivation and Objective

The primary aim of the work presented in this thesis is to investigate and demonstrate new transducer technologies and designs, which enable real-time 3-D ultrasound imaging without the complexity of state-of-the-art 2-D matrix probes. The focus will be on developing row-column addressed 2-D arrays and exploring their advantages and shortcomings for use in real-time volumetric ultrasound imaging. The ultrasound transducer is the central focus in this work, and CMUT technology will be used as a platform. A major part of the thesis is therefore concerned with advancing the knowledge on this technology and developing both the theoretical understanding and the processes needed to fabricate such transducers. The final goal is to demonstrate a functioning row-column addressed CMUT

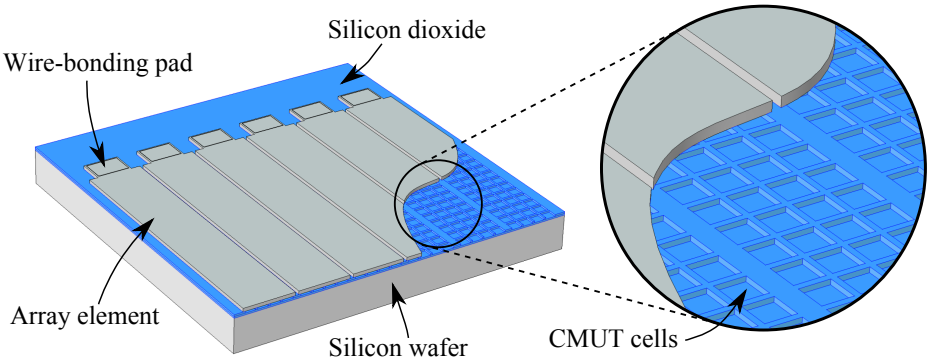

Figure 1.7: Illustration showing the components of a simple 1-D linear CMUT array. The substrate is a conductive silicon wafer, which acts as a common bottom electrode. A few micron thin silicon plate rests on top of an insulating oxide containing the CMUT cells. The silicon plate is structured to define the individual elements. The wire-bonding pad is used to interface the array to external electronics and cables. Only a cut-out of the array is shown, and the top plate is locally removed to visualize the CMUT cells.

transducer probe that can be connected to a commercial ultrasound scanner and produce real-time volumetric ultrasound images.

1.4 Publications in the Thesis

This thesis is based on the 14 publications and two patents listed below, covering three main subjects: Transducer theory, microfabrication, and row-column addressed arrays. In the printed version of the thesis, the publications are included as a separate appendix collection. The publication letter refers to the appendix name containing the corresponding paper.

Transducer Theory

Three conference papers and two journal papers cover theoretical aspects of CMUTs, focusing on the behaviour of anisotropic circular and square CMUT plates, the radiation pattern of circular CMUTs, and the transmit pressure and receive sensitivity of such transducers.

Paper A

M. F. la Cour, **T. L. Christiansen**, J. A. Jensen, and E. V. Thomsen.
"Modelling of CMUTs with Anisotropic Plates".
Published in: *Proceedings of IEEE Ultrason. Symp.*, pp. 588-591 (2012).

Paper B

M. F. la Cour, **T. L. Christiansen**, C. Dahl-Petersen, K. Reck, O. Hansen, J. A. Jensen, and E. V. Thomsen.
"Modeling and Measurements of CMUTs with Square Anisotropic Plates".
Published in: *Proceedings of IEEE Ultrason. Symp.*, pp. 2187-2190 (2013).

Paper C

T. L. Christiansen, O. Hansen, J. A. Jensen, and E. V. Thomsen.
"Modal radiation patterns of baffled circular plates and membranes".
Published in: *J. Acoust. Soc. Am.*, Vol. 135, No. 5, pp. 2523-2533 (2014).

Paper D

A. Lei, S. E. Diederichsen, M. F. la Cour, M. B. Stuart, **T. L. Christiansen**, J. A. Jensen, and E. V. Thomsen.
"Dimensional Scaling for Optimized CMUT Operations".
Published in: *Proceedings of IEEE Ultrason. Symp.*, pp. 2595-2598 (2014).

Paper E

M. F. la Cour, **T. L. Christiansen**, J. A. Jensen, and E. V. Thomsen.
"Electrostatic and Small-Signal Analysis of CMUTs with Circular and Square Anisotropic Plates".
Accepted for: *IEEE Trans. Ultrason., Ferroelec., Freq. Contr.* (May, 2015).

Microfabrication

A conference paper and a journal paper cover the protrusions generated during oxidation of structured silicon dioxide and their implications on the bonding quality during CMUT fabrication.

Paper F

T. L. Christiansen, O. Hansen, M. D. Johnsen, J. N. Lohse, J. A. Jensen, and E. V. Thomsen.
"Void–Free Direct Bonding of CMUT Arrays with Single Crystalline Plates and Pull–In Insulation".
Published in: *Proceedings of IEEE Ultrason. Symp.* pp. 1737-1740 (2013).

Paper G

T. L. Christiansen, O. Hansen, J. A. Jensen, and E. V. Thomsen.
"Thermal Oxidation of Structured Silicon Dioxide".
Published in: *ECS J. Solid State Sc.*, Vol. 3, No. 5, pp. N63-N68 (2014).

Row-column addressed 2-D arrays

Four conference papers and three journal papers on row-column addressed arrays are included. The first describes a structure that can be used to overcome problems with

oxide quality. The following three are concerned with the development of an integrated apodization which solves the problem of edge waves and resulting ghost echoes. A paper addresses the cross-talk in row-column addressed arrays, and two conference abstracts describe the development of a 3-D velocity estimator for row-column addressed arrays and a fully functioning row-column probe for use on a commercial scanner, respectively.

Paper H

T. L. Christiansen, C. Dahl-Petersen, J. A. Jensen, and E. V. Thomsen.
"2-D Row-Column CMUT Arrays with an Open-Grid Support Structure".
Published in: *Proceedings of IEEE Ultrason. Symp.*, pp. 1712-1715 (2013).

Paper I

T. L. Christiansen, M. F. Rasmussen, J. A. Jensen and E. V. Thomsen.
"Row-Column Addressed 2-D CMUT Arrays with Integrated Apodization".
Published in: *Proceedings of IEEE Ultrason. Symp.*, pp. 600-603 (2014)

Paper J

M. F. Rasmussen, **T. L. Christiansen**, E. V. Thomsen, and J. A. Jensen.
"3-D Imaging using Row-Column Addressed Arrays with Integrated Apodization – Part I: Apodization Design and Line-element Beamforming".
Published in: *IEEE Trans. Ultrason., Ferroelec., Freq. Contr.*, Vol. 62, No. 5, pp. 947-958 (2015).

Paper K

T. L. Christiansen, M. F. Rasmussen, J. P. Bagge, L. N. Moesner, J. A. Jensen, and E. V. Thomsen.
"3-D Imaging using Row-Column Addressed Arrays with Integrated Apodization – Part II: Transducer Fabrication and Experimental Results".
Published in: *IEEE Trans. Ultrason., Ferroelec., Freq. Contr.*, Vol. 62, No. 5, pp. 959-971 (2015).

Paper L

T. L. Christiansen, J. A. Jensen, and E. V. Thomsen.
"Acoustical cross-talk in row-column addressed 2-D transducer arrays for ultrasound imaging".
Submitted to: *J. Acoust. Soc. Am.* (2015).

Paper M

S. Holbek, **T. L. Christiansen**, M. F. Rasmussen, M. B. Stuart, E. V. Thomsen, and J. A. Jensen.
"3-D Vector Flow Estimation with Row-Column Addressed Arrays".
Accepted for: *IEEE Ultrason. Symp.* (2015).

Paper N

T. L. Christiansen, M. Engholm, C. Beers, M. Berkheimer, L. N. Moesner, J. P. Bagge, M. B. Stuart, A. Lei, S. E. Diederichsen, J. A. Jensen, and E. V. Thomsen.
"A Row-Column Addressed CMUT Probe with Integrated Electronics for Volumetric Imaging".
Accepted for: *IEEE Ultrason. Symp.* (2015).

Patents

Two patent applications were filed. The first describes integrated apodization in ultrasonic transducer arrays and the second covers methods for 3-D flow estimation using row-column addressed arrays.

Patent A

T. L. Christiansen, M. F. Rasmussen, E. V. Thomsen, and J. A. Jensen.
"Ultrasound Imaging Transducer Array with Integrated Apodization".
Filed on December 19, 2013, Number PCT/IB2013/002838.

Patent B

T. L. Christiansen, S. Holbek, M. F. Rasmussen, E. V. Thomsen, and J. A. Jensen.
"3-D Flow Estimation using Row-Column Addressed Transducer Arrays".
Filed on January 19, 2015, US application no. 14/599,857.

1.5 Thesis Outline

In this work, the capacitive micromachined ultrasonic transducer (CMUT) technology is used as a platform. Chapter 2 of the thesis will focus on understanding and optimizing these transducers by reviewing and advancing the theoretical knowledge on the subject. The basic transduction mechanism is explained and the static and dynamic behavior is investigated. Subsequently, the CMUT dimensions leading to the best performance is analyzed, and the chapter ends with a derivation of the sound radiation from a single CMUT.

Chapter 3 covers the optimization of the imaging performance of row-column addressed arrays. After a brief literature review, the basic principle behind such arrays is described and the advantages and disadvantages of row-column addressed arrays compared to full 2-D matrix arrays are discussed. In particular, the issue of edge waves leading to ghost echoes is investigated in detail. A solution is presented in the form of an integrated apodization, and experimental results are given to confirm its effect. Finally, it is shown how row-column addressed arrays can also be used to estimate velocities in a volume, yielding the velocity components in all three dimensions.

In Chapter 4, the focus is shifted towards the microfabrication techniques required to produce CMUT arrays, the main focus being on row-column addressed 2-D CMUT arrays. The chapter introduces the prevalent methods for fabricating CMUTs and presents new solutions to problems with surface protrusions in conjunction with wafer bonding. Several iterations of processes capable of producing both 1-D arrays and 2-D row-column addressed arrays are presented. The chapter demonstrates the incremental improvements of each process developed during the project, from an initially non-functioning process with low oxide insulation quality and poor device performance to the final process capable of producing high-performance and reliable 2-D row-column CMUT arrays with a simple and fast process based on a LOCOS (LOCal Oxidation of Silicon) technique.

Chapter 5 presents characterization results from fabricated transducers as well as a description of the test setup used. The transducer performance is assessed both electrically through impedance measurements and acoustically through hydrophone- and pulse-echo measurements. Key parameters for the individual elements are given, and the resolution of the array when used for volumetric imaging is assessed. In addition to this, issues regarding charging and acoustical cross-talk in the arrays are investigated.

Chapter 6 describes the development of a row-column probe. The mechanical design, packaging, electronics, and interface to the scanner are covered, and imaging with the probe is demonstrated. The probe is the first example of a hand-held row-column addressed transducer probe capable of real-time 3-D ultrasound imaging on a commercial ultrasound scanner, without the complexity of state-of-the-art matrix probes.

The thesis is concluded in Chapter 7, where suggestions for future research are also provided.

The intention with the chapters is to provide relevant background information and key results from the project. Detailed process descriptions and lithography mask layouts for selected cleanroom fabrication processes developed in the project are given in the appendix. To improve the flow of the text, some details from the papers listed in Section 1.4 have been left out. All papers are provided in the appendix, and the reader is referred to these for further in-depth details. In addition to the papers, the appendix includes all patent applications filed during the project. Note that in the printed version of the thesis, the papers and patent applications are provided as a separate publication appendix.

CHAPTER 2

Transducer Theory

The core of the ultrasound scanning system is the ultrasound transducer. In order to be able to optimize the transducer behaviour, it is essential to have an in-depth understanding of the mechanisms behind it. In the subsequent sections, the behavior of the CMUT is analyzed in detail from a theoretical perspective. First, energy considerations are used to derive the governing equations of the CMUT followed by an investigation of the static behavior based on the papers A, B, and E. Then, linearization is used to describe the dynamics and subsequently determine the optimal dimensioning of the CMUT using results from Paper D. Finally, the acoustic radiation of a circular CMUT is presented based on Paper C.

2.1 Lumping and System Equations

The following describes how energy considerations can be used to derive the governing equations of the CMUT. It is partly based on the papers A, B, and E. The derivation employs a single important approximation to reduce the complexity of the equations: Let $w(x, y, t)$ be the actual deflection of the plate at the Cartesian coordinates (x, y) at time t. It is then assumed that

$$w(x, y, t) = w_0 \tilde{w}(x, y) \ , \tag{2.1}$$

where w_0 is the center deflection of the plate with an implicit time dependency and $\tilde{w}(x, y)$ is the deflection shape normalized to this center deflection. Fig. 2.1 shows a cross-section of a CMUT along with the annotation used. In reality, the electric field in the CMUT for a given applied voltage varies with position due to the deflection shape, and the shape will thus be dependent on the center deflection. Also, higher modes of the plate might be excited, which changes the deflection shape. However, the distortion created by the varying electric field can be shown to be negligible, and in most practical situations, the frequencies used will only excite the first mode shape of the plate. Therefore, the approximation in Eq. (2.1) is generally a good assumption.

Assuming a loss-less system, the total energy stored in the transducer can be characterized by four terms:

$$U_{\text{t,m}} = U_{\text{s}} + U_{\text{kin}} - U_{\text{e}} - U_{\text{p}} \ . \tag{2.2}$$

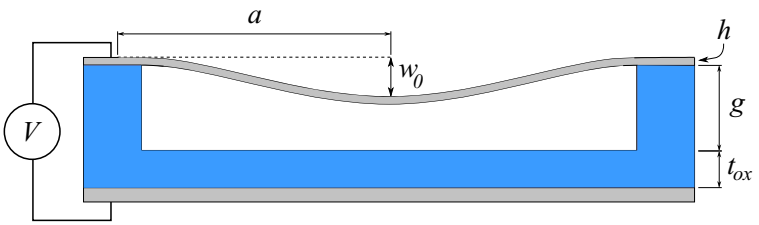

Figure 2.1: Cross-sectional illustration of a typical CMUT along with the annotation used. It contains a fixed bottom substrate and a deformable top plate (here assumed circular or square) with thickness h and radius/half side-length a suspended over a vacuum gap of height g. The bottom substrate and the top plate are conducting and are separated by an insulator. An insulator of thickness t_{ox} is also placed in the bottom of the vacuum cavity to prevent electrical contact between the bottom substrate and the top plate. The center deflection is denoted w_0.

The two first terms are contributed by the internal energy of the plate, which is comprised of the potential energy or strain energy, U_s, as well as the kinetic energy, U_kin, due to the plate inertia. U_e is the electrical energy stored in the capacitor formed by the top electrode and the bottom electrode. It is subtracted since this energy originates from work done *on* the system by the voltage V. The same argument goes for U_p, which is the work done on the system by the external pressure, p. All of the four energy terms are evaluated in the following.

The strain energy of a thin silicon plate where plane stress can be assumed is given by

$$U_\mathrm{s} = \frac{1}{2}\iiint_\Omega (\sigma_1\epsilon_1 + \sigma_2\epsilon_2 + \sigma_6\epsilon_6)\,\mathrm{d}x\,\mathrm{d}y\,\mathrm{d}z\ , \tag{2.3}$$

where the integral runs over the whole volume Ω of the plate in a Cartesian coordinate system. The strains are defined by

$$\epsilon_1 = -z\frac{\partial^2 w(x,y,t)}{\partial x^2}\ ,\ \epsilon_2 = -z\frac{\partial^2 w(x,y,t)}{\partial y^2}\ ,\ \epsilon_6 = -2z\frac{\partial^2 w(x,y,t)}{\partial x \partial y}\ , \tag{2.4}$$

and the stresses σ_1, σ_2, and σ_6 are found from the strains and the stiffness matrix, see Paper E. Due to the assumption in Eq. (2.1), the integral in Eq. (2.3) reduces to a constant k_0 times w_0^2 and the strain energy can be written as

$$U_\mathrm{s} = \frac{1}{2}k_0 w_0^2\ . \tag{2.5}$$

The kinetic energy of the plate is found by integrating the kinetic energy of each infinitesimal point of the plate, such that

$$U_{\text{kin}} = \frac{1}{2}\iiint_{\Omega} \rho \left(\frac{\partial}{\partial t} w(x,y,t)\right)^2 \mathrm{d}x\,\mathrm{d}y\,\mathrm{d}z \ . \tag{2.6}$$

Here, ρ is the mass density of the plate. Once again, the integral over the volume of the plate becomes a constant m_0 times the second time derivative of w_0^2 due to the assumption in Eq. (2.1). The kinetic energy can thus be written

$$U_{\text{kin}} = \frac{1}{2} m_0 \left(\frac{\partial w_0}{\partial t}\right)^2 \ . \tag{2.7}$$

Note that although the plate is a distributed mechanical system, the two spatial dependencies x and y has effectively been removed in Eqs. (2.5) and (2.7). The equations actually describe the energy of a discrete mass-spring system with mass m_0 and spring constant k_0. Thus, by use of the assumption in Eq. (2.1), the plate has been "lumped" into a discrete mass-spring system, which describes the deflection at the center of the plate, w_0. Note that this lumping is not unique; any parameter describing the deflection, e.g. the average deflection, could have been used (Köymen et al. 2012). The description of the system will be consistent as long as the same lumped parameter is used throughout the analysis.

The electrical energy stored in the capacitor made up by the top- and bottom electrodes is given by

$$U_{\text{e}} = \frac{1}{2} V^2 C(w_0) \ , \tag{2.8}$$

where V is the applied voltage and the capacitance is given by

$$C(w_0) = \iint_S \frac{\epsilon_0}{g_{\text{eff}} - w(x,y,t)} \mathrm{d}x\,\mathrm{d}y = \iint_S \frac{\epsilon_0}{g_{\text{eff}} - w_0 \tilde{w}(x,y)} \mathrm{d}x\,\mathrm{d}y \ . \tag{2.9}$$

Here, S is the surface of the plate and g_{eff} is the effective vacuum gap height at zero deflection, i.e. the height the gap would have if it contained only vacuum. Usually, there will be a dielectric insulator inside the gap with relative permittivity ϵ_r. If the thickness of the insulator is t_{ox} and the height of the actual vacuum gap is g, the effective vacuum gap becomes

$$g_{\text{eff}} = g + \frac{t_{\text{ox}}}{\epsilon_r} \ . \tag{2.10}$$

The work performed on the CMUT by the external pressure is

$$U_{\text{p}} = \iint_S p w(x,y,t) \mathrm{d}x\,\mathrm{d}y = p w_0 \iint_S \tilde{w}(x,y) \mathrm{d}x\,\mathrm{d}y \ , \tag{2.11}$$

which is equivalent to the work done by a pressure p on a flat piston of surface area $A_0 = \iint_S \tilde{w}(x,y)\mathrm{d}x\,\mathrm{d}y$. Inserting into (2.11) yields

$$U_{\mathrm{p}} = pw_0A_0 \ . \tag{2.12}$$

Combining Eqs. (2.2), (2.5), (2.7), (2.8), and (2.12) gives an expression for the total stored energy in the CMUT:

$$U_{\mathrm{t,m}} = \frac{1}{2}k_0w_0^2 + \frac{1}{2}m_0\left(\frac{\partial w_0}{\partial t}\right)^2 - \frac{1}{2}V^2C(w_0) - pw_0A_0 \ . \tag{2.13}$$

The stored energy is seen to be a function of three dependent variables, one for each of the three domains of the transducer: V (electrical), w_0 (mechanical), and p (acoustical). All three dependent variables have time t as the independent variable. The stored energy in the electrical and acoustical domains are found by adjusting the signs to account for the change in the definition of work and internal energy:

$$U_{\mathrm{t,e}} = -\frac{1}{2}k_0w_0^2 - \frac{1}{2}m_0\left(\frac{\partial w_0}{\partial t}\right)^2 + \frac{1}{2}V^2C(w_0) - pw_0A_0 \tag{2.14}$$

$$U_{\mathrm{t,a}} = -\frac{1}{2}k_0w_0^2 - \frac{1}{2}m_0\left(\frac{\partial w_0}{\partial t}\right)^2 - \frac{1}{2}V^2C(w_0) + pw_0A_0 \ . \tag{2.15}$$

From Eqs. (2.13), (2.14), and (2.15) it is possible to derive one governing equation for each of the three domains. This is achieved by differentiating the stored energy in each domain with respect to its corresponding variable, yielding the charge Q (electrical), force F (mechanical), and volume displacement W (acoustical):

$$Q = \frac{\partial U_{\mathrm{t,e}}}{\partial V} = VC(w_0) \tag{2.16}$$

$$F = \frac{\partial U_{\mathrm{t,m}}}{\partial w_0} = k_0w_0 + m_0\frac{\partial^2 w_0}{\partial t^2} - \frac{1}{2}V^2\frac{\partial}{\partial w_0}C(w_0) - pA_0 \tag{2.17}$$

$$W = \frac{\partial U_{\mathrm{t,a}}}{\partial p} = w_0A_0 \ . \tag{2.18}$$

Equations (2.16)-(2.18) provide a non-linear description of the transducer behavior, which is valid for any transducer geometry where Eq. (2.1) is a good approximation.

2.2 Statics: Stable Position and Pull-in

Although the CMUT is operated as a dynamic device, a static analysis provides relevant insight into the behavior of the CMUT. Recall that both the applied voltage V and pressure p have static terms in the form of a DC bias voltage and a constant ambient pressure in the medium relative to the vacuum in the CMUT cavity. Thus, a static analysis is needed to investigate their influences on the CMUT.

The force on the CMUT plate in the static case is equal to Eq. (2.17) without the second term:

$$F_{\mathrm{s}} = k_0 w_0 - \frac{1}{2} V^2 \frac{\partial}{\partial w_0} C(w_0) - p A_0 \ . \tag{2.19}$$

The equation for the stable position is found by setting the resulting force to zero, yielding

$$k_0 w_0 = \frac{1}{2} V^2 \frac{\partial}{\partial w_0} C(w_0) + p A_0 \ . \tag{2.20}$$

The effective spring constant of the lumped system can be found by differentiating the total force in Eq. (2.19) with respect to the center deflection:

$$k_{\mathrm{eff}} = k_0 - \frac{1}{2} V^2 \frac{\partial^2}{\partial w_0^2} C(w_0) \ . \tag{2.21}$$

Note that the effective spring constant contains two terms: The first is the spring constant of the isolated lumped mechanical system, while the second term is from the electric field. For zero voltage, the effective spring constant is equal to k_0. As the voltage increases, the effective spring constant of the system is reduced. This known as the "spring softening" effect. At a critical voltage, the "pull-in" voltage, the effective spring constant becomes zero. This voltage is given by

$$V_{\mathrm{PI}} = \sqrt{\frac{2k_0}{\frac{\partial^2}{\partial w_0^2} C(w_{\mathrm{PI}})}} \ . \tag{2.22}$$

Beyond this point, the effective spring constant becomes negative and the plate is pulled down to the bottom electrode. Inserting the pull-in voltage in Eq. (2.20) yields an equation for the corresponding pull-in deflection w_{PI}:

$$k_0 w_{\mathrm{PI}} = \frac{k_0 \frac{\partial}{\partial w_0} C(w_{\mathrm{PI}})}{\frac{\partial^2}{\partial w_0^2} C(w_{\mathrm{PI}})} + p A_0 \ . \tag{2.23}$$

Paper E presents detailed analytical and numerical calculations of the parameters derived above. For convenience, Table 2.1 lists the appropriate values for a CMUT with either circular or square plates made from highly doped (001) silicon aligned to the $\langle 110 \rangle$ direction. This is the configuration that applies to the CMUTs fabricated in this project. Note that the capacitance, pull-in voltage and pull-in deflection are all evaluated at zero pressure. Paper E presents simple scaling factors that can adjust these parameters in accordance to the actual pressure in the medium.

2.3 Dynamics: Equivalent Circuit Representation

The previous sections introduced the governing equations of the CMUT and used them to derive the static behavior. In this section, the dynamic behavior of the CMUT is

Table 2.1: Static transducer parameters for highly doped (001) silicon plates aligned to the $\langle 110 \rangle$ direction. a is the radius/half side-length, h is the plate thickness, g_{eff} is the effective gap height, w_0 is the center deflection of the plate, and ϵ_0 is the vacuum permittivity. The capacitance, pull-in voltage and pull-in deflection are evaluated at zero pressure. Derived partly from Paper E.

	Circular	Square
Lumped mass m_0	$\frac{\pi}{3}\rho h a^2$	$1.215\rho h a^2$
Lumped spring const. k_0	$858.8\,\text{GPa} \cdot \frac{h^3}{a^2}$	$771.3\,\text{GPa} \cdot \frac{h^3}{a^2}$
Lumped surface area A_0	$\frac{1}{3}\pi a^2$	$1.215a^2$
Capacitance $C(w_0)$	$\frac{\epsilon_0 \pi a^2}{g_{\text{eff}}} \sqrt{\frac{g_{\text{eff}}}{w_0}} \arctan\sqrt{\frac{w_0}{g_{\text{eff}}}}$	$\frac{\epsilon_0 4a^2}{g_{\text{eff}}} \frac{1}{1-0.296\frac{w_0}{g_{\text{eff}}}-0.136\left(\frac{w_0}{g_{\text{eff}}}\right)^2}$
Pull-in voltage V_{PI}	$\sqrt{300.52\,\text{GPa} \cdot \frac{h^3 g_{\text{eff}}^3}{\epsilon_0 a^4}}$	$\sqrt{284.52\,\text{GPa} \cdot \frac{h^3 g_{\text{eff}}^3}{\epsilon_0 a^4}}$
Pull-in deflection w_{PI}	$0.463 g_{\text{eff}}$	$0.466 g_{\text{eff}}$

analyzed. The goal is to find the equivalent two-port linear element describing the CMUT. As illustrated in Fig. 2.2, such an element converts an input voltage V (current i) into a pressure p (volume flow $\dot{W}$), or vice versa, and the tools available for analyzing linear systems can be directly applied to it. However, as was seen in the previous sections, a CMUT is an inherently non-linear device. Therefore, it is assumed in the following that only small signals are applied. For a receiving CMUT, this is a reasonable assumption, since the pressures received in ultrasound imaging, and consequently the associated plate deflection, are relatively small. On the contrary, a transmitting CMUT will experience large deflections and generate high pressures. Non-linear effects can therefore not be neglected in this case if accurate results are required. Still, the small-signal model can provide valuable insight into the basic scaling mechanisms and behavior of the CMUT.

Using the small-signal assumption, Eqs. (2.16)-(2.18) may be linearized around an operating point $(V_{\text{op}}, w_{\text{op}}, p_{\text{op}})$ by differentiating with respect to each of the variables while the other two are kept constant. This linearization can be expressed in matrix form as

$$\begin{bmatrix} \partial Q \\ \partial F \\ \partial W \end{bmatrix} = \mathbf{A} \begin{bmatrix} \partial V \\ \partial w_0 \\ \partial p \end{bmatrix}, \tag{2.24}$$

with

$$\mathbf{A} = \begin{bmatrix} \frac{\partial Q}{\partial V} & \frac{\partial Q}{\partial w_0} & \frac{\partial Q}{\partial p} \\ \frac{\partial F}{\partial V} & \frac{\partial F}{\partial w_0} & \frac{\partial F}{\partial p} \\ \frac{\partial W}{\partial V} & \frac{\partial W}{\partial w_0} & \frac{\partial W}{\partial p} \end{bmatrix} = \begin{bmatrix} C(w_{\text{op}}) & V_{\text{op}} \frac{\partial}{\partial w_0} C(w_{\text{op}}) & 0 \\ -V_{\text{op}} \frac{\partial}{\partial w_0} C(w_{\text{op}}) & k_{\text{eff}} + m_0 \frac{\partial^2}{\partial t^2} & -A_0 \\ 0 & A_0 & 0 \end{bmatrix}. \tag{2.25}$$

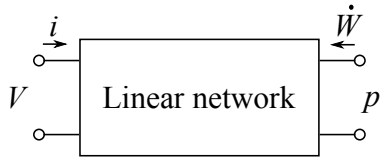

Figure 2.2: A two-port linear element conceptually representing the dynamics of the transducer. The linear network inside the two-port element converts voltage V to pressure p and, equivalently, current i to volume flow $\dot{W}$.

Since the dynamics of the system are of interest, it is more convenient to use the time derivatives of Q, w_0, and W, which are denoted $\dot{Q} = i$, $\dot{w}_0 = v$, and $\dot{W}$. Rewriting yields

$$\begin{bmatrix} \int \partial i \mathrm{d}t \\ \partial F \\ \int \partial \dot{W} \mathrm{d}t \end{bmatrix} = \mathbf{A} \begin{bmatrix} \partial V \\ \int \partial v \mathrm{d}t \\ \partial p \end{bmatrix} . \tag{2.26}$$

Furthermore, the analysis is simplified by transforming to the frequency domain by a Laplace transform of the linear system in Eq. (2.26):

$$\begin{bmatrix} \partial i/s \\ \partial F \\ \partial \dot{W}/s \end{bmatrix} = \mathfrak{L}\{\mathbf{A}\} \begin{bmatrix} \partial V \\ \partial v/s \\ \partial p \end{bmatrix} \Leftrightarrow \begin{bmatrix} \partial i \\ \partial F \\ \partial \dot{W} \end{bmatrix} = \mathbf{B} \begin{bmatrix} \partial V \\ \partial v \\ \partial p \end{bmatrix} , \tag{2.27}$$

with

$$\mathbf{B} = \begin{bmatrix} sC(w_{\mathrm{op}}) & V_{\mathrm{op}} \frac{\partial}{\partial w_0} C(w_{\mathrm{op}}) & 0 \\ -V_{\mathrm{op}} \frac{\partial}{\partial w_0} C(w_{\mathrm{op}}) & k_{\mathrm{eff}}/s + sm_0 & -A_0 \\ 0 & A_0 & 0 \end{bmatrix} , \tag{2.28}$$

where $s = j\omega$ is the complex angular frequency with j being the imaginary unit and ω the real angular frequency. From the construction of the matrix elements, it is seen that the first element in the diagonal describes the current i as a function of voltage V when the velocity and pressure are kept constant. This is equal to the inverse electrical impedance for a blocked mechanical system, $1/Z_{\mathrm{e,b}}$. The second diagonal element relates force F and velocity v for constant voltage and pressure and it is thus the mechanical impedance, $Z_{\mathrm{m,s}}$, for a short circuited electrical system and vacuum in the acoustical system (such that neither voltage nor pressure can be built up). The two first off-diagonal elements relate force F and voltage V as well as the current i and velocity v. They thus describe the coupling Γ_{em} between the mechanical and electrical domains. The last two off-diagonal elements relate force F and pressure p as well as volume flow $\dot{W}$ and velocity v. These

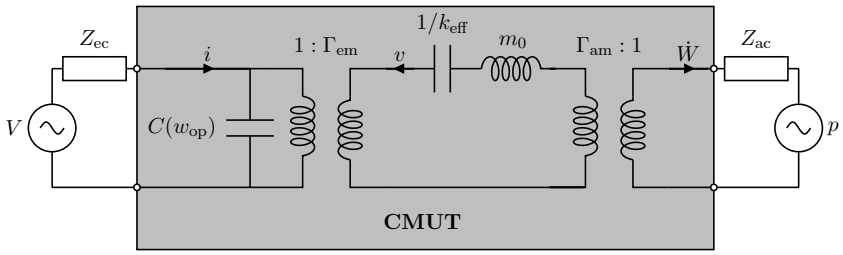

Figure 2.3: Equivalent circuit representation of the CMUT and the external circuits. The transducer itself is represented by the circuit in the grey box, while the external electrical and acoustical circuits are represented by their respective Thévenin equivalents.

are therefore the coupling terms between the mechanical and acoustical domains, Γ_{am}. Inserting in Eq. (2.28) yields

$$\mathbf{B} = \begin{bmatrix} 1/Z_{\text{e,b}} & \Gamma_{\text{em}} & 0 \\ -\Gamma_{\text{em}} & Z_{\text{m,s}} & -\Gamma_{\text{am}} \\ 0 & \Gamma_{\text{am}} & 0 \end{bmatrix}, \tag{2.29}$$

Note that there is no acoustical impedance, since the transducer only interfaces to the acoustical domain, it does not include it. The transducer also interfaces to the electrical domain, but it includes a capacitive element, hence the electrical impedance. There is no direct coupling between the electrical and acoustical domains, since any interaction is done through the mechanical domain of the plate.

The linear system described by Eqs. (2.27) and (2.29) has the same behavior as the electrical circuit shown in Fig. 2.3, or equivalently, the circuit in Fig. 2.3 is described by Eqs. (2.27) and (2.29). Fig. 2.3 is therefore the two-port linear element represented by the "black box" in Fig. 2.2. The resemblance between Eqs. (2.27) and (2.29) and Fig. 2.3 is in fact general for lumped linear acoustical, mechanical, and electrical systems (among others) due to the similarity of the governing equations. This has the advantage that any lumped linear system including several energy domains, as per definition is the case with any transducer, can be represented by an equivalent electrical circuit. All the tools available for analyzing electrical circuits can then be directly applied.

In practice, one may analyze the transducer behavior by measuring the electrical impedance using an impedance analyzer. If the impedance is measured in a low-impedance medium such as air or ideally vacuum, the acoustical terminals in Fig. 2.3 will be shorted, and the circuit seen by the impedance analyzer will correspond to that shown in Fig. 2.4(a). In the shown circuit, a resistor has been added to represent mechanical losses in the transducer. The components in Fig. 2.4(a) are derived from the components in Fig. 2.3, and are given by

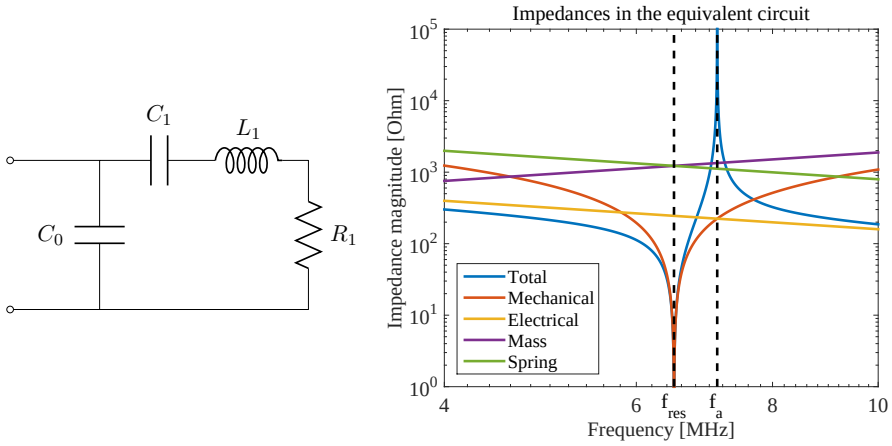

Figure 2.4: (a) Reduced version of the circuit shown in Fig. 2.3 as seen from the electrical terminal when the transducer is operating in a low impedance medium such as air or ideally vacuum. A resistor has been added to account for mechanical losses. (b) Logarithmic plot of the impedances in the circuit in (a). The component values are $C_0 = 100\,\mathrm{pF}$, $C_1 = 20\,\mathrm{pF}$, $L_1 = 30\,\mu\mathrm{H}$, and $R_1 = 0\,\Omega$.

$$C_0 = C(w_{\mathrm{op}}) \tag{2.30}$$

$$C_1 = \frac{\Gamma_{\mathrm{em}}^2}{k_{\mathrm{eff}}} \tag{2.31}$$

$$L_1 = \frac{m_0}{\Gamma_{\mathrm{em}}^2} \tag{2.32}$$

$$R_1 = \frac{b}{\Gamma_{\mathrm{em}}^2}\,, \tag{2.33}$$

where b is the mechanical damping. The absolute impedance of the circuit has been plotted in Fig. 2.4(b) for an ideal system with no losses (i.e. $R_1 = 0\,\Omega$). The impedance magnitude of each element has been plotted along with the mechanical impedance and the total impedance magnitudes.

Two frequencies stand out: The first is the frequency at which the impedance of the mass and the spring in the mechanical domain becomes equal, which is identical to the mechanical resonance frequency, $f_{\mathrm{res}} = \omega_{\mathrm{res}}/(2\pi)$, occasionally referred to as the series resonance. Here, the total impedance of the system reaches a minimum; in the ideal case with no damping, the impedance becomes zero because the two impedances are of

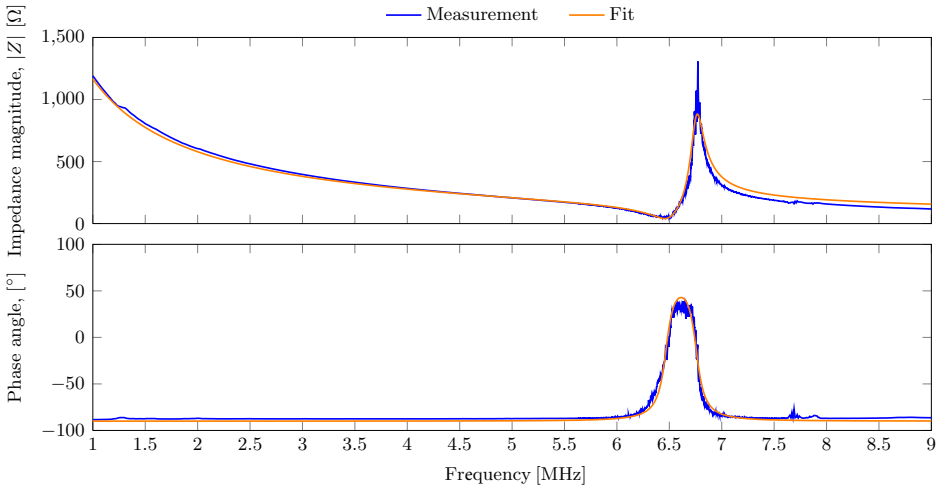

Figure 2.5: Measured impedance magnitude and phase of a CMUT fabricated using Process C described in Section 4.6. A fit has been made to the measurement assuming a circuit as shown in Fig. 2.4(a).

equal magnitude and $180°$ phase-shifted. The second special frequency is that where the magnitude of the mechanical impedance equals that of the electrical impedance. The two impedances are $180°$ phase-shifted and connected in parallel, so the total impedance becomes infinite. This is known as the anti-resonance frequency, or the parallel resonance with reference to the electrical circuit.

In Fig. 2.5, an impedance measurement is shown. It was performed on a CMUT fabricated using Process C described in Section 4.6 at a DC bias voltage of $190\,\mathrm{V}$. The plot shows both the impedance magnitude (top) and the phase (bottom). The latter is $-90°$ as expected for a capacitor, except around the resonance and anti-resonance frequency where it crosses $0°$ because the phase shifts cancel out as explained in the paragraph above. A fit has been made to the measurement by finding suiting values of the components in Fig. 2.4(a) using an iterative fitting routine. Fig. 2.6 shows the fitted component values as a function of the applied DC bias voltage, which was varied from $0\,\mathrm{V}$ to $250\,\mathrm{V}$ in steps of $0.5\,\mathrm{V}$. The electrical capacitance, C_0, is seen to increase slightly with DC bias due to the CMUT plates being pulled towards the bottom electrode, thus decreasing the gap and hence increasing the capacitance. The mechanical stiffness, mass, and damping are not directly affected by the DC bias voltage, but when translated to the electrical domain, they are dominated by the electromechanical turns ratio Γ_{em} as shown in Eqs. (2.31), (2.32), and (2.33). The electromechanical turns ratio Γ_{em} is the proportionality factor between voltage and force or, equivalently, current and velocity. It is repeated here for convenience:

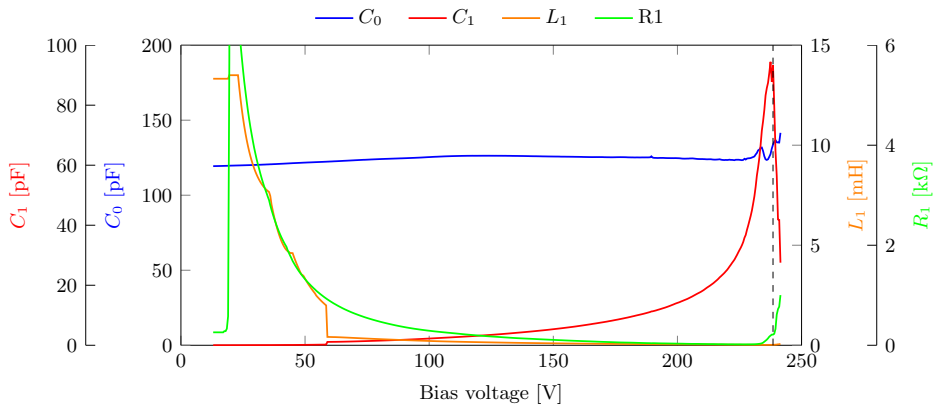

Figure 2.6: Component values of a CMUT fabricated fabricated using Process C described in Section 4.6 as a function of applied DC bias voltage. The component names refer to the components in Fig. 2.4(a). The values were extracted by fitting the impedance of the model in Fig. 2.4(a) to the measured impedance as exemplified in Fig. 2.5.

$$\Gamma_{\text{em}} = V_{\text{op}} \frac{\partial}{\partial w_0} C(w_{\text{op}}) \ . \tag{2.34}$$

The derivative of the capacitance increases with w_{op}. Thus, as the bias voltage is increased, the turns ratio also increases. The mechanical capacitance C_1 therefore expectedly increases with DC bias while the opposite is true for L_1 and R_1. At the voltage marked with a dashed line, the CMUT enters pull-in, and the values abruptly change since the mechanical response moves out of the probed frequency range. Recalling that the lumped spring constant of the CMUT is inversely proportional to the measured mechanical capacitance C_1, the rapid increase in C_1 close to the pull-in voltage is evidence of the spring-softening effect. The small kinks seen in the curves are due to the fitting routine, which becomes less efficient at low DC bias voltages due to a weak mechanical response, and at voltages close to the unstable pull-in point.

2.4 Electromechanical Coupling Coefficient

An important figure of merit for the transducer is the coupling coefficient, traditionally denoted k^2. It is a measure of the transducer's ability to convert electrical energy into mechanical energy or vice versa and is defined as the stored mechanical energy relative to the total stored energy in the transducer:

$$k^2 = \frac{E_{\text{m}}}{E_{\text{total}}} = \frac{1}{1 + E_{\text{e}}/E_{\text{m}}} \ . \tag{2.35}$$

For a dynamic system, it is more convenient to consider the power. The isolated transducer behavior is examined by shorting the acoustic terminal in Fig. 2.3. In practice, this corresponds to operating the transducer in vacuum. The coupling coefficient then becomes

$$k^2 = \frac{1}{1 + P_\mathrm{e}/P_\mathrm{m}} = \frac{1}{1 + Z_\mathrm{m,s}/(\Gamma_\mathrm{em}^2 Z_\mathrm{e,b})} \,. \tag{2.36}$$

From Eq. (2.36) it is seen that in order to maximize the coupling coefficient, $Z_\mathrm{m,s}$ should be decreased while $Z_\mathrm{e,b}$ and Γ_em should be increased.

As described in the previous section, the electromechanical turns ratio Γ_em is the proportionality factor between voltage and force or, equivalently, current and velocity. It is thus intuitively obvious that this factor should be increased to maximize the power transfer between the electrical and mechanical domains. As discussed in the previous section, the turns ratio increases with increasing DC bias voltage. Thus, the operating voltage should be as close as possible to the pull-in voltage V_PI. This is the primary motivation for applying a DC bias voltage when operating a CMUT, the secondary being suppression of second harmonics arising from the force's square dependency on the voltage as seen in Eq. (2.17). It is not practical to be right at the pull-in voltage, since even a small AC excitation could make the plate cross the pull-in point and collapse. Therefore, the DC bias voltage is as a rule of thumb kept around $80\,\%$ of pull-in, if the CMUT is to be operated in the conventional mode, to allow for an AC excitation and fabricational inaccuracies. Several authors have investigated the possibilities in using the CMUT in pull-in mode (Bayram, Hæggström, et al. 2003; Huang et al. 2003; Oralkan et al. 2006; Park, Oralkan, and Khuri-Yakub 2011; Yaralioglu, Bayram, and Khuri-Yakub 2006). Studies have shown that it offers the potential of improved performance and decreased cross-coupling effects (Bayram, Kupnik, Yaralioglu, Oralkan, Ergun, et al. 2007; Bayram, Kupnik, Yaralioglu, Oralkan, Lin, et al. 2005; Jin et al. 2001), but it also suffers from increased charging issues (Park, Kupnik, et al. 2010; Zhang et al. 2010). For this reason, only the conventional operating mode with $V_\mathrm{op} < V_\mathrm{PI}$ is considered here. Note that any parasitic capacitance in the system will decrease the change in total capacitance of the system at a given operating point w_op, which from Eq. (2.34) is shown to decrease the turns ratio and hence the coupling coefficient. It is therefore imperative to keep the parasitic capacitance at a minimum.

As stated above, the electrical impedance of the CMUT should be increased to increase the coupling coefficient. This makes intuitively sense, as a low electrical impedance will act as a short preventing some of the current to enter the mechanical part of the circuit in Fig. 2.4(a). The electrical impedance of the CMUT is the impedance of the capacitor, and it is increased by decreasing the capacitance of the device itself. Therefore, ideally the area of either the top or bottom electrode should be made as small as possible to increase the coupling coefficient of the transducer. However, by decreasing the capacitance, the pull-in voltage is increased since a smaller electrode results in a smaller total force on the plate for a given voltage. This presents a practical limit to how small the electrode can be made: It was shown above that the optimal operating condition is achieved by setting the

DC bias voltage as close as practically possible to the pull-in voltage. As the electrode is made smaller, larger operating voltages are therefore required, which is undesirable, both from a patient safety perspective, but also from a device perspective, where the breakdown voltage of the insulating dielectrics defines the maximum allowed operating voltage. The exact scaling of the pull-in voltage as a function of electrode size may be found by numerically solving Eq. (2.22) for varying electrode sizes. Yaralioglu et al. did this via finite element modeling for a circular CMUT by solving for the pull-in voltage for a range of electrode radii (Yaralioglu, Ergun, et al. 2003). Here, it was concluded that the increase in pull-in voltage was negligible for electrodes down to $\sim 50\,\%$ of the plate radius. In qualitative terms, the part of the electrode plate near the rim is thus not contributing significantly to the deflection of the plate, but acts mainly as a parasitic capacitance. However, this is usually a secondary parasitic compared to the parasitics originating from outside of the individual CMUT cells in the form of cabling and external electronics. Note that, in principle, one could cancel out the internal capacitance of the CMUT by using an external compensation circuit. This is, however, not a desirable approach, since it would only be effective in a certain frequency range, thus leading to a decrease in the bandwidth and thereby the resolution of the ultrasound image (Yaralioglu, Ergun, et al. 2003).

In the case of shorted acoustical terminals in Fig. 2.3 (corresponding to operation in vacuum), the mechanical impedance reaches a minimum at the resonance frequency of the plate as discussed in the previous section. In the case of no mechanical damping or losses, it becomes zero at the resonance frequency, which is then found as

$$Z_{\mathrm{m,s}} = 0 \Leftrightarrow \omega_{\mathrm{res}} = \sqrt{\frac{k_{\mathrm{eff}}}{m_0}} \propto \frac{h}{a^2}\,. \tag{2.37}$$

The proportionality to the dimensions of the CMUT plate suggests that these should be adjusted according to the desired operating frequency of the transducer in order to increase the coupling coefficient. The interaction with the medium makes this dependency more complex, and is covered in detail in the following sections. If mechanical losses are present, a resistor can be inserted in the mechanical circuit in Fig. 2.3, such as shown in Fig. 2.4(a), and the mechanical impedance becomes equal to this resistance at resonance. Note that for $k_{\mathrm{eff}} = k_0$, the resonance frequency given by Eq. (2.37) corresponds to the first natural frequency of the plate, where the whole plate is vibrating in phase as described by the static deflection profile.[1] Higher order modes are not captured and would require a new lumped model for each mode as e.g. described in (Rønnekleiv 2008). However, the first mode is mainly of interest since it produces the best coupling due to its in-phase vibration. Note also that the spring softening effect originating from the DC bias voltage will decrease the resonance frequency of the plate for increasing bias voltages.

[1] In fact, the static deflection shape is not exactly identical to the mode shape as covered in Paper C, and the resonance frequency given by Eq. (2.37) is thus in this case only approximately correct.

The frequency at which $Z_{\mathrm{m,s}}$ is minimum is therefore dependent on the applied DC bias voltage.

In practice, the coupling coefficient may be found by measuring the impedance of the transducer in a low impedance medium such as air or ideally vacuum. As explained in the previous section, such a measurement will reveal the resonance and anti-resonance frequency of the transducer, which may be used to calculate the coupling coefficient. The relationship has been shown for piezo-electric transducers in e.g. (Berlincourt, Curran, and Jaffe 1964), but it is repeated here for a generic lumped system where it is assumed that losses are negligible.

At the anti-resonance, ω_{a}, the total impedance is infinite, or equivalently, the admittance is zero. Thus,

$$Z_{\mathrm{m,s}} + \Gamma_{\mathrm{em}}^2 Z_{\mathrm{e,b}} = 0 \Leftrightarrow \frac{k_{\mathrm{eff}}}{i\omega_{\mathrm{a}}} + i\omega_{\mathrm{a}} m_0 = -\frac{\Gamma_{\mathrm{em}}^2}{i\omega_{\mathrm{a}} C} \,. \tag{2.38}$$

Using Eq. (2.37), the above expression may be rewritten to

$$\frac{\omega_{\mathrm{a}}^2}{\omega_{\mathrm{res}}^2} - 1 = \frac{\Gamma_{\mathrm{em}}^2}{k_{\mathrm{eff}} C} \Leftrightarrow 1 - \frac{\omega_{\mathrm{res}}^2}{\omega_{\mathrm{a}}^2} = \frac{1}{1 + k_{\mathrm{eff}} C / \Gamma_{\mathrm{em}}^2} \,. \tag{2.39}$$

The expression after the last equality sign is equal to the definition of the coupling coefficient k^2 given in Eq. (2.36) in the special case where the operating frequency is zero. In this case, Eq. (2.36) is identical to the original definition given by Eq. (2.35). Therefore, a measure of the coupling coefficient may be found from the resonance and anti-resonance frequency:

$$k^2 = 1 - \frac{\omega_{\mathrm{res}}^2}{\omega_{\mathrm{a}}^2} = 1 - \frac{f_{\mathrm{res}}^2}{f_{\mathrm{a}}^2} \,. \tag{2.40}$$

From the analysis of the coupling coefficient presented above, it is clear that a DC bias voltage as close as possible to the pull-in voltage should be applied. Also, parasitic capacitances should be avoided, and the performance may be further increased by reducing the internal capacitance of the CMUT through reduction of either the top or bottom electrode size at the expense of higher pull-in voltages. Finally, the CMUT should be dimensioned such that its center frequency fits the desired operating frequency. The term center frequency is used, since the interaction with the acoustic medium will shift the optimal frequency away from the resonance frequency of the CMUT plate. This interaction with the acoustic medium will be covered in the following.

2.5 Interaction with the Acoustic Medium

When the CMUT is interfacing a medium other than vacuum, which is the case for medical imaging, the acoustic terminal will contain an acoustic impedance as shown in Fig. 2.3.

While the impedances of the external electrical circuit as well as the internal impedances of the CMUT are variable and available for optimization, the acoustical impedance is given by the medium and is thus fixed. This impedance, also known as the radiation impedance, is in general complex. It contains a real part describing the damping of the plate movement induced by the medium, and it contains an imaginary part, which describes how energy is being stored in the medium and delivered back to the transducer. In the limiting case of very short wavelengths compared to the size of the CMUT, the acoustic impedance is equal to the characteristic impedance of the medium per effective area of the CMUT. Here, the characteristic impedance is given by

$$Z_{\mathrm{c}} = \rho_{\mathrm{m}} c \,, \tag{2.41}$$

where ρ_m is the mass density of the medium and c is the speed of sound in the medium. In medical imaging, the medium is the human tissue, which on average has acoustical properties close to water with $\rho_{\mathrm{m}} \simeq 1000\,\mathrm{kg/m^3}$ and $c \simeq 1500\,\mathrm{m/s}$ (Jensen 1996, p. 15). The characteristic acoustic impedance is thus equal to $Z_{\mathrm{c}} = 1.5\,\mathrm{MRayl}$. In the short wavelength limit, the acoustic impedance is purely real and independent of frequency and CMUT dimensions. However, an array element in an ultrasound transducer is always below one wavelength in width to avoid grating lobes, implying that the size of the CMUT cell has sub-wavelength dimensions. In this case, the acoustic impedance becomes complex, which affects the optimum frequency at which the CMUT should be operated due to the shift in center frequency created by the moving mass of the medium. Greenspan presented an analytic solution to the radiation impedance of a single circular plate clamped at its edges (Greenspan 1979), and the solution has been plotted in Fig. 2.7. The impedance has been normalized to the characteristic impedance of the medium divided by the effective area A_0.

It is seen that for high values of ka, where $k = 2\pi/\lambda$ with λ being the wavelength, the solution indeed approaches the characteristic impedance given in Eq. (2.41). The point $ka = \pi$, corresponding to $a = \lambda/2$, has been highlighted, since this is the maximum value of ka that is relevant for CMUTs used in arrays in which the element width must be less than λ. Both the real and imaginary part of the acoustic impedance varies considerably in the region in which $ka \leq \pi$. Hence, the medium's impact on the CMUT behavior is highly dependent on the size and operating frequency of the CMUT.

The impedance shown in Fig. 2.7 is, however, insufficient for analyzing the optimal transducer behavior. Aside from the fact that the case for square plates has not been solved analytically, more significantly the effect of mutual impedances between CMUT cells in an array cannot be represented by a simple analytic expression. Numerical methods must therefore be employed to solve the problem and predict the optimal operating conditions of the array. Oguz et al. have presented a method involving numerically solving an $N \times N$ mutual impedance matrix describing the total acoustic impedance for an array with N CMUT cells (Oguz, Atalar, and Köymen 2013). It is dependent on the specific layout of the transducer array, the operating frequency, the positions of the CMUT cells, the

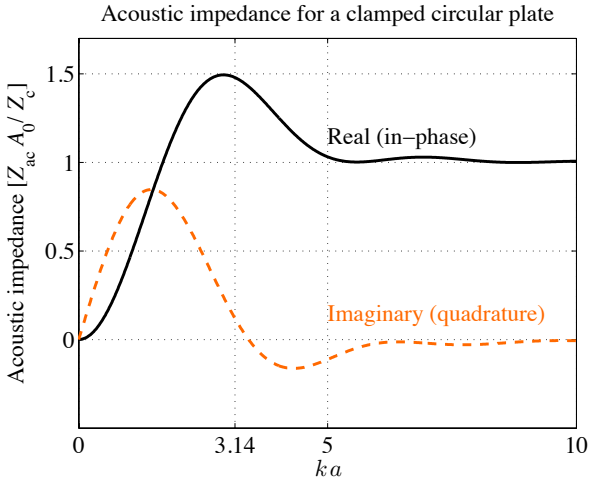

Figure 2.7: Acoustic impedance of a circular clamped plate as a function of wavenumber times radius ka (Greenspan 1979). The impedance has been normalized to the characteristic impedance of the medium divided by the effective area A_0. $ka = \pi$ corresponding to $a = \lambda/2$, where λ is the wavelength, has been highlighted since CMUTs with diameters larger than one wavelength are not relevant for transducer arrays where the pitch should be less than λ.

CMUT dimensions, and the operating voltages. The following section seeks to simplify the analysis in order to find general scaling guidelines for the optimal CMUT dimensions. This is done by employing finite element analysis (FEA) of a single CMUT and an infinite array of CMUTs based on Paper D. The actual behavior will be somewhere between these two solutions, and the analysis thus only reveals the general scaling trends.

2.6 Transducer Optimization

In terms of imaging performance, the transducer's two most critical figures of merit are the sensitivity and the emitted pressure. High sensitivity allows smaller signals to be detected and higher pressures means stronger echoes are produced. Both contribute to increasing the signal-to-noise ratio (SNR) and optimization of these parameters is therefore central to the imaging performance. In transmit, the maximum output pressure, and not the pressure per volt, is the most interesting parameter since the maximum voltage is limited by the pull-in voltage. Hence, a CMUT with high output pressure per input voltage might not be able to emit high pressures if the maximum applicable voltage is low. As opposed to this, the sensitivity in voltage per input pressure is the most relevant parameter, since this, combined with the noise floor of the system, defines the lowest possible pressure that can

be detected.

A secondary parameter defining the imaging performance is the bandwidth of the transducer: Large bandwidth means short ring-down time and thereby higher resolution. However, bandwidth, and hence resolution, is of secondary concern if the sensitivity and emitted pressure do not provide a sufficiently high dynamic range. Therefore, the two latter will be the primary focus in the following.

The CMUT essentially contains three dimensional parameters that are freely adjustable. These are the plate radius/half side-length a, the plate thickness h, and the effective gap height g_{eff}. The plate dimensions are linked through the center frequency, which is dictated by the desired imaging frequency. Thus, there are in reality two degrees of freedom in the design of the individual CMUT cell: Either plate thickness or radius/side-length, and gap height.

In Paper D, these two degrees of freedom are varied in a FEA model to investigate the effect on the emitted pressure and the receive sensitivity. The model uses a square CMUT with an initial set of a, h, and g_{eff} (the latter is in this model equal to g since the gap only contains vacuum). Mechanical losses are introduced to give the plate a quality factor of 100, corresponding to typical measured values from fabricated CMUTs. It then calculates the pull-in voltage and sets the applied DC and AC voltages to $80\,\%$ and $50\,\%$ of this, respectively. These voltages are chosen as they have proven to be practical in experimental setups. The frequency of the maximum emitted pressure is found, and the side length is adjusted in a feedback-loop until this frequency is $5\,\mathrm{MHz}$. The procedure is repeated for varying gap heights and plate thicknesses. Two different models are set up: one for a single CMUT cell (SC) and one for an infinite 2-D array of CMUT cells with an interspacing of $5\,\mu\mathrm{m}$ (IAC). In both models, the CMUT(s) is/are interfaced by an infinite medium of water and placed in an infinite rigid baffle. The two models represent two extremes and illustrate the cells' mutual effect on each other. An actual CMUT transducer array will be somewhere in between these extremes, and this analysis is therefore only meant to reveal the general scaling trends.

In Fig. 2.8(a) (top), the plate side-length is plotted as a function of plate thickness for a fixed immersion frequency of $5\,\mathrm{MHz}$. The wave-length at $5\,\mathrm{MHz}$ is $300\,\mu\mathrm{m}$, and the side-length thus varies between $\lambda/10$ and λ, or equivalently $ka = \pi/10$ and $ka = \pi$. The corresponding center frequency is plotted in Fig. 2.8(a) (bottom). The frequency in immersion, i.e. in a water-like medium, is constant at $5\,\mathrm{MHz}$ due to the model requirements. However, the center frequency in vacuum, i.e. the resonance frequency of the plate, is seen to deviate considerably from the $5\,\mathrm{MHz}$ to maintain a constant center frequency in immersion. The difference in interaction with the medium for the two cell configurations is seen in Fig. 2.8(b), where the calculated acoustical impedance is given for both configurations. With a real part close to the characteristic impedance of the medium and a small imaginary part (X), the impedance for IAC is close to that of a plane wave. The smaller imaginary part for IAC compared to SC (see bottom plot in Fig. 2.8(b)) is what mainly causes the difference in frequency shift from vacuum to immersion between the two configurations in Fig. 2.8(a). Comparing Fig. 2.8(a) and

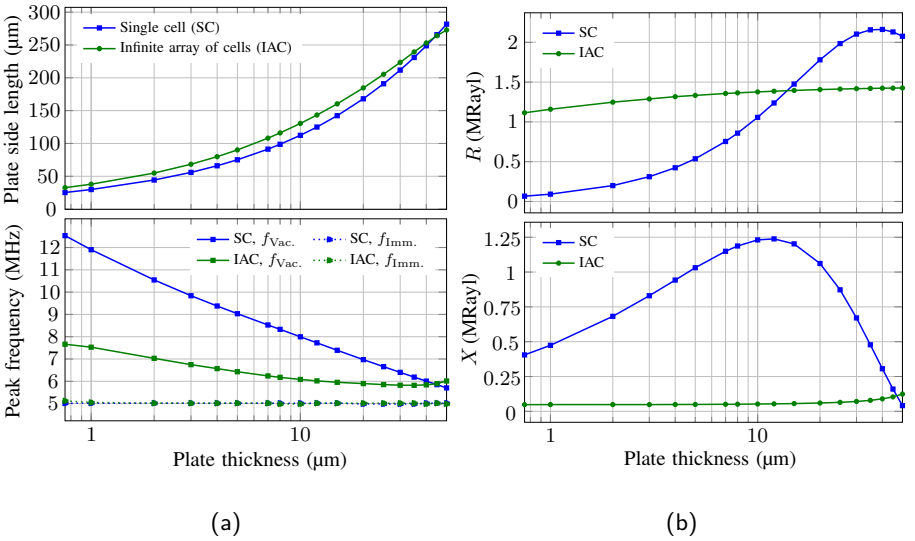

Figure 2.8: (a) Top: Plot of the plate side length as a function of plate thickness required to maintain a constant immersion frequency of $5\,\mathrm{MHz}$ for the two cell configurations single cell (SC) and infinite array of cells (IAC). Bottom: Corresponding resonance frequencies in vacuum and immersion for the plates plotted in the top figure. (b) Real (top) and imaginary (bottom) parts of the acoustic impedance for the plates plotted in figure a. From Paper D.

Fig. 2.8(b), the frequency shift is identical in the two configurations at the plate thickness yielding identical imaginary impedance magnitudes.

The full dimensional FEA scaling study is seen in Fig. 2.9(a), where the extracted peak surface pressure and peak receive sensitivity are plotted as function of plate thickness for three different gap heights. The sensitivity is evaluated as the voltage generated by the CMUT with a fixed charge on the electrodes for a given homogeneous surface pressure. The pressure scaling in Fig. 2.9(a) (top) shows similar tendency for both SC and IAC with increasing pressure for thicker plates and larger gap height. This scaling follows intuition as thicker plates with larger area equals higher mass and more inertia. Increasing the gap height means one can apply a higher voltage and thereby increase the potential energy of the system. The dimensional scaling of the receive sensitivity is seen in Fig. 2.9(a) (bottom). The sensitivity for both SC and IAC is as expected improved for increasing gap height due to higher applicable voltages and hence increased charge on the electrodes. For SC, the sensitivity is increasing for decreasing plate thickness. This is expected, since a lower thickness means less mass and therefore lower mechanical impedance. The decreasing sensitivity tendency levels off for thick plates due the maximum in real

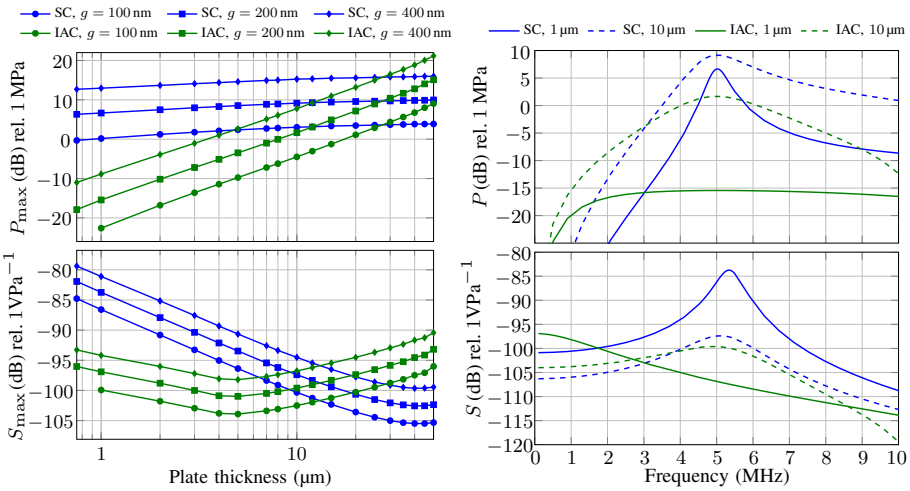

(a) (b)

Figure 2.9: (a) Maximum output pressure (top) and sensitivity (bottom) as a function of plate thickness for a fixed immersion frequency of $5\,\mathrm{MHz}$ plotted for three different gap heights g. (b) Corresponding normalized pulse-echo sensitivity. From Paper D.

impedance for SC seen in Fig. 2.8(b). For IAC, the sensitivity is also decreasing with thickness until a thickness of $\sim 5\,\mu\mathrm{m}$ where it begins to increase. The turning point corresponds to the thickness where the mechanical impedance reaches the critical value that changes the CMUT from under-damped to over-damped. This is seen from Fig. 2.9(b), where the simulated frequency response is shown for the plate thicknesses $1\,\mu\mathrm{m}$ (solid line) and $10\,\mu\mathrm{m}$ (dashed line) for both the SC (blue) and IAC (green) configuration. The $1\,\mu\mathrm{m}$ thick plate in the IAC configuration is seen to exhibit an over-damped behavior with no resonance. The maximum in the transmit pressure at $5\,\mathrm{MHz}$ is not an actual resonance, but a result of the drop in pressure at lower frequencies, since the pressure must approach zero for zero frequency as a consequence to the infinite medium. As opposed to this, a resonance is visible for the $10\,\mu\mathrm{m}$ thick plate, increasing the sensitivity at that particular frequency. In Fig. 2.9(a), the thickness where the SC and IAC receive scaling lines with the same gap height intersect corresponds to the thickness where the real impedances of SC and IAC intersect in Fig. 2.8(b).

From the above discussion it is evident that for a CMUT with voltage readout, both the maximum transmit pressure and sensitivity is improved by increasing the gap size to increase the separation between the electrodes. This increases the applicable voltage and

the gap should thus be increased as much as the voltage rating of the system (insulators, external electronics, etc.) allows. This conclusion is unambiguous for the two investigated simulation setup. However, the conclusion regarding the optimal size of the CMUT plate is different in the two scenarios: For the single CMUT cell, larger plates improves transmit pressure but decreases the sensitivity. For the infinite array of cells, the latter follows a different trend. Here, sensitivity decreases for larger plate sizes until a certain size (roughly at a thickness of $5\,\mu\mathrm{m}$), at which the sensitivity increases with increasing plate sizes due to a shift from over-damped to under-damped behavior.

2.7 Sound Radiation

In terms of imaging and beamforming, it is relevant to know how the CMUT radiates sound. This can be evaluated using the *radiation pattern*, which describes the relative pressure far from the transducer as a function of angle. For simplicity, the following analysis considers circular CMUTs, offering an analytic solution to the problem. It is based on Paper C, which presents a general derivation of the radiation pattern of a plate or membrane subjected to an external excitation force valid for any mode of the membrane and the plate with arbitrary boundary conditions. Only the case of a homogeneously excited clamped plate, corresponding to the CMUTs developed in this thesis, is covered here. Additional boundary conditions and excitations are investigated in Paper C.

The equation of motion of a stress-free plate resembling that of a CMUT with a silicon plate is

$$\rho_p h \frac{\partial^2}{\partial t^2} w + \nabla^2 D \nabla^2 w = p_{\text{ext}} \ , \tag{2.42}$$

where w is the plate deflection normal to the plane of the CMUT surface and ρ_p is the mass density of the plate of thickness h and flexural rigidity $D = Eh^3/[12(1-\nu^2)]$. Here, E and ν are the Young's modulus and Poisson's ratio of the plate material, respectively. Note that the first term in Eq. (2.42) accounts for the inertial effects; in the absence of this term, the equation describes the static case. The pressure on the CMUT p_{ext} is assumed to be a purely external pressure, corresponding to the case where the surface pressure generated by the radiator itself is negligible compared to the pressure exerted on the CMUT by external forces. In this case, the system is fully described by its eigenmodes, which for the plate are given by the solution to the homogeneous equivalent of Eq. (2.42), i.e. for $p_{\text{ext}} = 0$. Any external pressure function can then be included by using the eigenmodes derived in the following as a basis.

Using polar coordinates, it is assumed that the solutions to the equation of motion can be written as time harmonic, separable product functions of the form

$$w(\varrho, \phi, t) = F(\varrho) G(\phi) e^{\mathrm{i}\omega t} \ . \tag{2.43}$$

Here, $F(\varrho)$ and $G(\phi)$ are solutions to the resulting set of ordinary differential equations, where ϱ and ϕ are the radial and angular coordinates, respectively. In the time dependent

part, i=$\sqrt{-1}$ is the imaginary unit, ω the angular frequency, and t the time variable. Using this approach, the time independent mode functions of a plate with radius a are given by (Wah 1962)

$$w_{nm}(\varrho,\phi) = A_{nm}\left[J_n(K_{nm}\frac{\varrho}{a}) + B_{nm}I_n(K_{nm}\frac{\varrho}{a})\right] \times \cos[n(\phi+\phi_0)] \ , \qquad (2.44)$$

where $J_n(z)$ denotes the Bessel function of the first kind, order n, and $I_n(z)$ denotes the modified Bessel function of the first kind, order n. A_{nm} and B_{nm} are modal constants corresponding to the integer mode numbers n and m. The values of B_{nm} are, together with the values of K_{nm}, dictated by the boundary conditions, while the modal amplitude constants, A_{nm}, are found as the expansion coefficients corresponding to the excitation pressure p_{ext}. The phase term ϕ_0 is the angular misalignment of the observation point and the mode pattern.

In the case where the plate is clamped around its circumference at $\varrho = a$, the displacement and slope at the edge is zero. Thus, the displacement given by Eq. (2.44) and its derivative with respect to the radial coordinate ϱ must disappear at $\varrho = a$, resulting in the equations

$$J_n(K_{nm}) + B_{nm}I_n(K_{nm}) = 0 \ , \qquad (2.45)$$

and

$$[nJ_n(K_{nm}) - K_{nm}J_{n+1}(K_{nm})] + B_{nm}[nI_n(K_{nm}) + K_{nm}I_{n+1}(K_{nm})] = 0 \ . \qquad (2.46)$$

From Eq. (2.45), it is seen that the modal constant B_{nm} is

$$B_{nm} = -\frac{J_n(K_{nm})}{I_n(K_{nm})} \ , \qquad (2.47)$$

such that the resulting mode functions for the clamped plate becomes

$$w_{nm}(\varrho,\phi) = A_{nm}\left[J_n(K_{nm}\frac{\varrho}{a}) - \frac{J_n(K_{nm})}{I_n(K_{nm})}I_n(K_{nm}\frac{\varrho}{a})\right] \times \cos[n(\phi+\phi_0)] \ , \qquad (2.48)$$

From Eqs. (2.45) and (2.46), it is seen that the wavenumbers K_{nm} are solutions to the transcendental equation

$$\frac{J_{n+1}(K_{nm})}{I_{n+1}(K_{nm})} + \frac{J_n(K_{nm})}{I_n(K_{nm})} = 0 \ . \qquad (2.49)$$

Now that the eigenmodes of the plate has been derived, the next step is to find the pressure field generated by these modes. The following derivations are carried out using the velocity potential, Φ, defined through the relation $\mathbf{u} = \nabla\Phi$, where $\mathbf{u}$ is the velocity

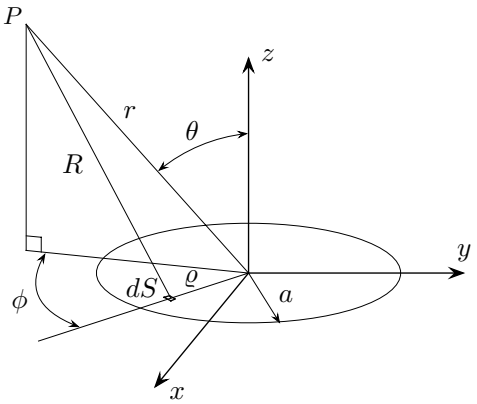

Figure 2.10: An illustration of the variables used to determine the velocity potential in the point P originating from a circular source of radius a. From Paper C.

vector. The pressure is readily found from the velocity potential as $p = \rho_a \partial\Phi/\partial t$, where ρ_a is the mass density of the acoustic medium, and the velocity is found from the definition of the velocity potential (Morse and Ingard 1968, pp. 307-387).

The steady-state velocity potential at any point in the half-space above a radiator in an infinite rigid baffle is given by Rayleigh's integral (Rayleigh 1896, p. 109)

$$\Phi = \frac{1}{2\pi} e^{\mathrm{i}\omega t} \int_S u(\varrho, \phi) \frac{e^{-\mathrm{i}kR}}{R} \,\mathrm{d}S \;, \tag{2.50}$$

where $k = \omega/c$ is the wavenumber with the speed of sound given by c, and $\mathrm{d}S$ denotes a differential area element. $u(\varrho, \phi)$ is the velocity in polar coordinates of the radiator with radius a. From Fig. 2.10, it is seen that the distance R to the observation point P from a point located on the radiator at (ϱ, ϕ) is given by $R^2 = \varrho^2 + r^2 - 2\varrho r \sin\theta\cos\phi$, where r is the distance to the observation point P from the center of the radiator, θ is the azimuthal angle, and ϕ is the polar angle. In the far field, $r \gg a \geq \varrho$, so that $R \simeq r - \varrho \sin\theta\cos\phi$. In this limit, the velocity potential therefore becomes

$$\Phi \simeq \frac{1}{2\pi r} e^{\mathrm{i}k(ct-r)} \int_S u(\varrho, \phi) e^{\mathrm{i}k\varrho \sin\theta\cos\phi} \,\mathrm{d}S \;, \tag{2.51}$$

where the time-independent velocity eigenmodes are given by

$$u(\varrho, \phi) = \mathrm{i}\omega w(\varrho, \phi) \;. \tag{2.52}$$

In the case of a clamped plate, the mode functions are given by Eq. (2.48). The velocity mode functions are then found by inserting this expression into Eq. (2.52), and the far field velocity potential given by Eq. (2.51) thus becomes

$$\Phi_{nm} = \frac{\mathrm{i}e^{\mathrm{i}k(ct-r)}}{2\pi r} A_{nm}\omega 2\pi a^2 R_{nm}(\eta,\phi_0)\ , \tag{2.53}$$

with $\eta = ka\sin\theta$ and

$$R_{nm}(\eta,\phi_0) = \frac{\mathrm{i}^n\cos(n\phi_0)}{K_{nm}^4 - \eta^4}\left\{\alpha_{nm}J_{n-1}(\eta)\eta - [\gamma_{nm} + \delta_{nm}\eta^2]J_n(\eta)\right\}\ . \tag{2.54}$$

The constants α_{nm}, γ_{nm}, and δ_{nm} in Eq. (2.54) are given by

$$\alpha_{nm} = 2K_{nm}^2 J_n(K_{nm})\ , \tag{2.55a}$$

$$\gamma_{nm} = K_{nm}^3[J_{n-1}(K_{nm}) + \frac{J_n(K_{nm})}{I_n(K_{nm})}I_{n-1}(K_{nm})]\,, \tag{2.55b}$$

$$\delta_{nm} = K_{nm}[J_{n-1}(K_{nm}) - \frac{J_n(K_{nm})}{I_n(K_{nm})}I_{n-1}(K_{nm})]\,. \tag{2.55c}$$

The factor in front of $R_{nm}(\eta,\phi_0)$ in Eq. (2.53) is identical to the velocity potential of a monopole of strength $\omega A_{nm}2\pi a^2$ in an infinite rigid baffle. The magnitude of $R_{nm}(\eta,\phi_0)$ therefore expresses the relative signal strength as a function of the wavelength compared to the CMUT dimensions and the angles θ and ϕ_0. $\|R_{nm}(\eta,\phi_0)\|$ is thereby the radiation pattern for any mode of the plate.

To find the radiation pattern for a given excitation of the clamped plate, the modal amplitude constants A_{nm} must be found. This may be accomplished by representing the actual plate displacement as an infinite series of eigenfunctions:

$$G = \sum_{n=0}^{\infty}\sum_{m=0}^{\infty} A_{nm}\tilde{w}_{nm}(\varrho,\phi)\ , \tag{2.56}$$

where $\tilde{w}_{nm}(\varrho,\phi)$ are the eigenfunctions given by Eq. (2.48) normalized by division with the modal amplitude constants A_{nm}. Assuming that the excitation p_{ext} is a homogeneous pressure (be it electrostatic or pressure in the medium), the modal amplitude constants can be found as described in Paper C. Thus, inserting Eq. (2.56) in Eq. (2.42), multiplying with the complex conjugate of the eigenfunctions, integrating over the area of the plate, and exploiting the orthogonality of the eigenfunctions yields

$$A_{nm} = \frac{\int_0^a\int_0^{2\pi}\tilde{w}_{nm}(\varrho,\phi)\tilde{w}_{nm}^*(\varrho,\phi)\varrho\,\mathrm{d}\varrho\,\mathrm{d}\phi}{\{\rho_p h(\omega_{nm}^2 - \omega^2) + \mathrm{i}\omega b\}\|\tilde{w}_{nm}(\varrho,\phi)\|^2}\ . \tag{2.57}$$

Here, ω_{nm} is the resonance frequency of the corresponding mode, b is the mechanical damping of the plate, and $\|\tilde{w}_{nm}(\varrho,\phi)\|^2$ is the norm square given by

$$\|\tilde{w}_{nm}(\varrho,\phi)\|^2 = \int_0^a\int_0^{2\pi}\tilde{w}_{nm}(\varrho,\phi)\tilde{w}_{nm}^*(\varrho,\phi)\varrho\,\mathrm{d}\varrho\,\mathrm{d}\phi\ . \tag{2.58}$$

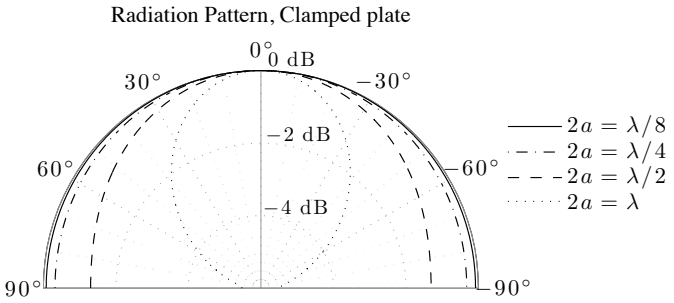

Figure 2.11: The radiation pattern of a clamped circular plate with homogeneous excitation, representing a typical CMUT. The four patterns correspond to four plate diameters $2a$ in fractions of the wavelength.

The integration over ϕ implies that the modal amplitude constants for all modes with $n \neq 0$, corresponding to the non-axisymmetric modes, become zero. Thus, only the axisymmetric modes of the plate $w_{0m}(\varrho)$ are excited, and the radiation pattern becomes

$$R_{0m}(\eta) = \frac{1}{\eta^4 - K_{0m}^4}\left\{\alpha_{0m} J_1(\eta)\eta + [\gamma_{0m} + \delta_{0m}\eta^2]J_0(\eta)\right\}. \tag{2.59}$$

As described in Section 2.6, the operating frequency of the CMUT will in practice be below the resonance frequency of the first mode of the plate due to the interaction with the medium. Therefore, it is reasonable to assume that only the contribution from the first mode is significant such that the radiation pattern becomes that given in Eq. (2.59) with $m = 0$. In Fig. 2.11, the radiation pattern for this mode has been plotted as a function of θ for selected plate sizes in units of the wavelength in the range relevant for CMUTs, i.e. for $2a \leq \lambda$. Note that the sound radiation is to a good approximation equal in all directions for $2a \leq \lambda/2$. Even for $2a = \lambda$, the signal varies less than $-6\,\mathrm{dB}$. It is therefore reasonable to assume that in the far field, i.e. at distances much greater than the size of the CMUT, the CMUT emits nearly spherical waves. Since the individual CMUT is less than one wavelength in size, any point of interest in the imaged volume will in practice always meet the far field condition. In simulations and derivations of the sound field from a transducer array, it can therefore generally be assumed that the elements are made up of point sources.

2.8 Chapter Summary

In this chapter, a theoretical treatment of the CMUT was presented. The static and small-signal dynamic behavior was derived using energy considerations and an assumption of

a constant deflection shape of the deformable plate of the CMUT, allowing for lumping and linearization of the system. The derivation was performed using anisotropic theory to describe the deflection of the plate having either circular or square geometry based on Papers A, B, and E.

From the static analysis, the pull-in voltage was determined. The small-signal dynamic behavior was described using an equivalent circuit model from which the coupling coefficient of the transducer was derived. From this, it was shown that the transducer should be operated as close as possible to the pull-in voltage, and that the electrical capacitance of the transducer should be kept at a minimum. Also, a method for experimentally extracting the coupling coefficient was devised.

A FEA model including interaction with the acoustic medium was used to investigate the optimal scaling parameters for a square CMUT based on Paper F. Two scenarios were investigated, representing two extremes: That of a single isolated CMUT cell and that of an infinite 2-D array of CMUT cells. It was shown that the mutual impedance from neighboring cells has a significant impact on the behavior of the CMUT. The following was found to be true for both configurations: For a fixed center frequency in immersion, CMUTs with thick plates produce the highest transmit pressure. Also, the separation between the top- and bottom electrodes should be made as large as the voltage rating of the system allows to produce the highest transmit pressures. A larger separation also increases the sensitivity for a voltage readout. However, the two scenarios disagreed for the optimal plate size in terms of sensitivity. In the single cell scenario, the smaller plates produced higher sensitivities, whereas this trend shifted for the infinite array scenario with decreasing sensitivities for increasing plate sizes until a critical point after which the sensitivity increased again. This was explained by the plate behavior going from over-damped to under-damped at the plate size defining this point.

Finally, the far field sound radiation of a CMUT was analyzed based on results from Paper C. Using a circular clamped plate to represent the CMUT, is was shown analytically that a CMUT used in an ultrasound transducer array will radiate sound similarly to that of a point source for all practical imaging purposes.

CHAPTER 3

Row-Column Addressed Arrays

In this chapter, the imaging principle behind row-column addressed 2-D arrays is described in detail. After a brief literature review, an estimate of row-column addressed arrays' performance relative to fully addressed 2-D arrays is given. Then, the beamforming required to produce volumetric images is developed based on the findings in Paper J. It is subsequently shown that the long elements in row-column addressed arrays produce edge effects that lead to ghost echoes in the final beamformed image. A solution is proposed in the form of integrated apodization, which is demonstrated both theoretically and experimentally to mitigate the edge wave problem as covered in Papers I and J. An optimized apodization layout is developed that efficiently damps the edge waves without affecting the imaging performance of the array. The technique is demonstrated by simulations and experimentally based on Papers J and K as well as Patent A. The last part of the chapter describes how row-column addressed arrays can be used to estimate velocities in a volume. This technique, which is also described in Paper M and Patent B, can be used to estimate all three components of the velocity vector in all points of a volume. From this, key parameters such as the volume flow rate in a blood vessel can be calculated.

3.1 Literature Review

The concept of volumetric imaging using row-column addressing as applied in this work was first introduced by Morton and Lockwood in 2003 (Morton and Lockwood 2003), and later expanded by Demoré et al. (Démoré et al. 2009). Different techniques to improve the resolution, sensitivity, or frame rate of row-column addressed arrays were explored theoretically by Daher et al. (Daher and Yen 2004, 2006) and Yen (Yen 2013) using synthetic aperture techniques and spatial matched filters. Recently, Rasmussen and Jensen used a fully addressed 32×32 array in a measurement study to compare the imaging performance of a fully addressed array to that of a row-column addressed array (Rasmussen and Jensen 2013a). For the same number of channels used, the row-column addressed array exhibited superior detail resolution compared to the fully addressed array.

Several groups have presented realizations of row-column addressed arrays. Yen's group have demonstrated imaging with several versions of row-column addressed piezo-arrays, starting in 2006 where Seo and Yen (Seo and Yen 2006) presented the first experimental demonstration of a row-column addressed array. The $64 + 64$ elements used

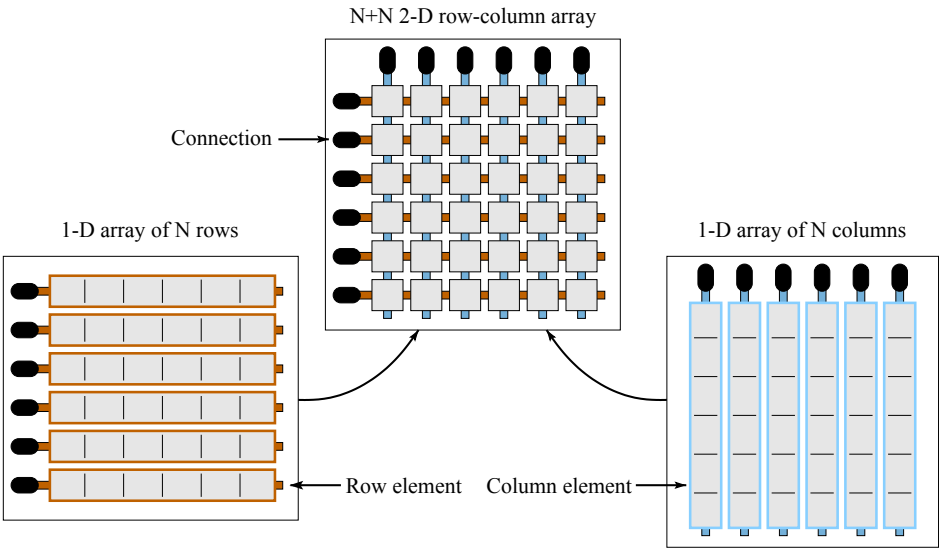

Figure 3.1: The row-column addressing scheme. By addressing the 2-D array by its row- and column indices, two 1-D arrays oriented orthogonal to one another are effectively produced. The number of connections needed to address an $N \times N$ array thereby becomes $2N$, as opposed to the N^2 connections required in a fully addressed matrix array. Modified from (Rasmussen and Jensen 2013b).

in this array was later surpassed by a $256 + 256$ element array (Seo and Yen 2007, 2008, 2009) by the same authors. More recently, Chen et al. (Y. Chen, Nguyen, and Yen 2011) and Yen et al. (Yen et al. 2009) have introduced piezo-arrays manufactured with a dual layer structure to simplify the fabrication process. Zemp et al. (Zemp, Zheng, and Zhang 2011) and Sampaleanu et al. (Sampaleanu et al. 2014) have performed feasibility studies and recently photoacoustic imaging (Chee et al. 2014) using CMUTs. Additionally, the group of Yeow have demonstrated both characterization (Logan, Wong, and Yeow 2009) and imaging using a $16 + 16$ element (A. I. H. Chen et al. 2011) and a $32 + 32$ element (Lawrence et al. 2014; Logan, Wong, A. I. H. Chen, et al. 2011) row-column addressed CMUT array.

3.2 Imaging Principle and Estimated Performance

A row-column addressed array is a 2-D array which is addressed via its row- and column indices. Effectively, this creates two 1-D arrays oriented orthogonal to one another as shown in Fig. 3.1. Each of the two 1-D arrays can electronically focus in one lateral dimension when delays are applied to the elements in the array. The imaging principle is

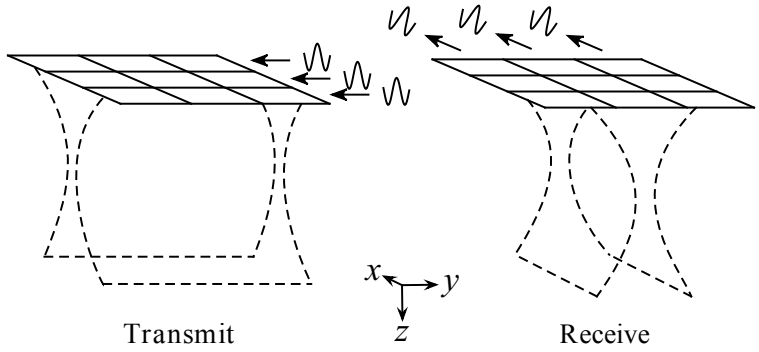

Figure 3.2: The imaging principle of a row-column addressed array. One of the 1-D arrays (left) is used as a transmit array, which can focus in the x- and z-directions. The sound echoes from this insonified region of the volume is then received by the orthogonal 1-D array (right), which can focus in the y- and z-directions. By translating the foci of the two arrays, the entire volume can be imaged. From Patent A.

shown in Fig. 3.2. One of the 1-D arrays is used to transmit ultrasound into the object of interest. In the illustrated example, the transmit array is able to focus the beam in the x- and z-directions, whilst no electronic transmit focusing can be performed in the y-direction. As a result, the emitted ultrasound is focused along a line parallel to the y-direction. By adjusting the delays on the transmit elements, this focal line may be translated to any position in the xz-plane. The orthogonal 1-D array then receives the echoes scattered from the insonified region of the volume. By applying delays, the received signals may be focused in a line normal to any position in the yz-plane. The combination of the two orthogonal line-foci of the transmit- and receive array produces a point focus in the volume. By translating this focus throughout the volume, a 3-D image may be formed.

To produce real-time images, the frame rate should be above roughly $20\,\mathrm{Hz}$ corresponding to one frame every $50\,\mathrm{ms}$. Assuming an imaging depth of $15\,\mathrm{cm}$ and a speed of sound of $1540\,\mathrm{m/s}$, the round-trip time of a pulse-echo event is

$$t = \frac{2 \cdot 0.15\,\mathrm{m}}{1540\,\mathrm{m/s}} \simeq 0.2\,\mathrm{ms}\ . \tag{3.1}$$

Thus, up to a total of 250 pulse-echo events may be used to produce one image frame. If e.g. single element emission synthetic aperture imaging is used, where the transmit aperture is synthesized by emitting with one transmit element at a time and receiving with all receive elements for each emission (Jensen, Nikolov, et al. 2006), the transmit array may then have 250 elements. If the receive array has the same number of elements, which would be the case for a square array, the total number of elements is 500 in a $250 + 250$ configuration. A channel count of this magnitude was demonstrated experimentally by

Seo and Yen (Seo and Yen 2007, 2008, 2009), who successfully produced images with a $256+256$ row-column addressed piezo-array. A 2-D matrix array of equal size would have 65536 elements; over a factor of 7 more than the current state-of-the-art X6-1 PureWave xMATRIX probe from Phillips having 9212 elements (Phillips 2015). This demonstrates the potential of having very large row-column addressed 2-D arrays with low channel count and real-time capability.

A larger array means improved lateral resolution, which can be derived using the Fresnel approximation (Szabo 2014, pp. 172,189). This states that in the far field of the transducer array, and at the focal distance of a focused transducer, the pressure field may be described by the Fourier transform of the transducer aperture. A finite array of transducer elements has an aperture A described by a simple rect function along one lateral dimension. The Fourier transform of a rect function is the sinc function, which therefore describes the pressure field in that dimension. Consider the transmitting array to the left in Fig. 3.2. Denoting the size of this array along the x-dimension L_x, the position along the array x ($x = 0$ being the center of the array), the wavelength of the ultrasound λ, and the mass density of the medium ρ_a, the pressure field at the depth z becomes (Szabo 2014, p. 172)

$$p_{x,\text{one-way}} = \mathfrak{F}[A] = \frac{L_x\sqrt{\rho_a}}{\sqrt{\lambda z}}\,\text{sinc}\left(\frac{L_x x}{\lambda z}\right), \tag{3.2}$$

where $\mathfrak{F}$ denotes the Fourier transform. It is assumed here that z is either at the focus of the transducer or in the far field. The FWHM of the sinc function is

$$\text{FWHM}_{\text{one-way}} = \frac{1.208 z\lambda}{L_x} = 1.208\lambda f_{\#}\,. \tag{3.3}$$

This shows that the lateral detail resolution for a given wavelength and depth scales with the array size. The subscript "one-way" is to emphasize that the FWHM is for focusing of only the transmit aperture (or only the receive aperture due to acoustic reciprocity). A row-column addressed array can only perform one-way focusing in each lateral dimension if conventional delay-and-sum beamforming is used, and its detail resolution is therefore defined by Eq. (3.3). As opposed to this, a 2-D matrix array can focus both in transmit and in receive. The resulting pulse-echo field is proportional to the Fourier transform of the convoluted transmit- and receive apertures (Karaman et al. 2009). If the same aperture is used for transmitting and receiving, the pulse-echo field along one dimension thereby becomes

$$p_{x,\text{two-way}} \propto \mathfrak{F}[A * A] = \mathfrak{F}[A]\mathfrak{F}[A] = (\mathfrak{F}[A])^2\,. \tag{3.4}$$

The FWHM using two-way focusing is

$$\text{FWHM}_{\text{two-way}} = \frac{0.886 z\lambda}{L_x} = 0.886\lambda f_{\#}\,. \tag{3.5}$$

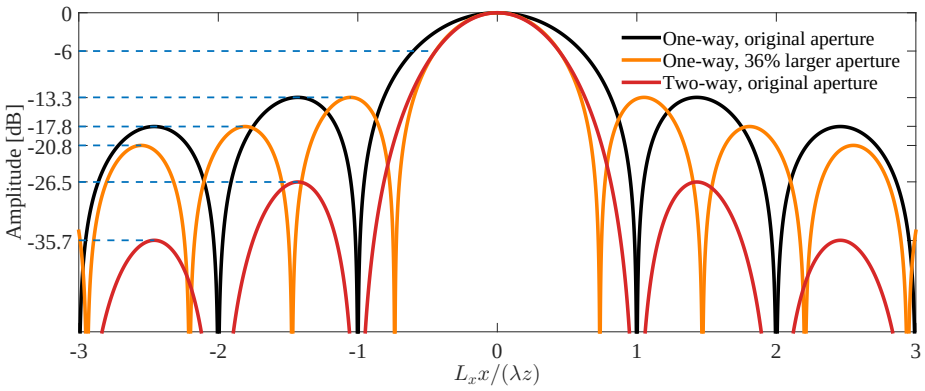

Figure 3.3: Plot of the resulting field at the focal distance or in the far field originating from a one-way focused array (black), a one-way focused array with $36\,\%$ larger aperture side-length (orange), and a two-way focused array (red). The two former are plotted using a normalized Eq. (3.2), while the latter uses Eq. (3.4).

The ratio between the resolution using one-way focusing and the resolution two-way focusing is therefore

$$\frac{\text{FWHM}_{\text{one-way}}}{\text{FWHM}_{\text{two-way}}} = \frac{1.208\lambda f_{\#}}{0.886\lambda f_{\#}} \simeq 1.36\ . \tag{3.6}$$

Thus, for the same aperture size, the FWHM of a row-column addressed array is $36\,\%$ larger than the FWHM of a two-way focused 2-D array. Based on the FWHM, the detail resolution for the two types of arrays will consequently be equal if the side-length of the row-column addressed array is increased by $36\,\%$ relative to the fully addressed 2-D array. This is in contrast to the factor of 2 increase requirement claimed in the literature (Démoré et al. 2009). In Fig. 3.3, the resulting field from the one-way focused array (black), the two-way focused array (red), and the one-way focused array with a $36\,\%$ larger side-length (orange) is plotted. It is seen that the FWHM of the two latter are indeed identical.

The ratio between the number of elements in a row-column addressed array and a fully addressed 2-D matrix array with equal detail resolution is from the above derivation found to be

$$\frac{\text{Elements in 2-D array}}{\text{Elements in row-column array}} = \frac{N^2}{1.36 \cdot 2 \cdot N} = \frac{N}{2.72}\ . \tag{3.7}$$

Any $N + N$ channel row-column addressed array with $N \geq 3$ will thus achieve a better detail resolution than a fully addressed 2-D array with the same total number of channels.

However, changing the aperture size will only affect the argument in the sinc function in Eq. (3.2), not the shape of the function. Hence, the normalized amplitudes remain unchanged and so do the side-lobe levels relative to the main lobe level. This is seen in Fig. 3.3, where the two one-way focused arrays have side-lobe levels of equal magnitude. As a consequence of the squaring of the Fourier transform of the apertures given in Eq. (3.4), the amplitudes of the side-lobes are halved by a factor of two in dB when two-way focusing is performed. One measure of contrast is the side-lobe level (Szabo 2014, p. 230). Therefore, a fully addressed 2-D array will have superior contrast performance relative to a row-column addressed array.

Note that the above calculations are only strictly valid for a continuous wave emission at a single frequency (Szabo 2014, p. 171), and as such they should only be seen as estimates of the imaging performance. Also, the estimates are made using an un-apodized aperture, and does therefore not take into account the effects of applying different apodization functions. In addition to this, parameters such as signal-to-noise ratio and emitted intensity should be included in a complete comparison of the two types of arrays.

3.3 Beamforming

When an image is generated, the scattering strength of an individual point in the image is evaluated by first calculating the time of flight from the transmitting element(s) to the point and back to the respective receive elements. All received signals are then summed at the calculated time instances, yielding the scattering strength for that point in the image. By repeating the calculation for each point in the volume, a 3-D image is formed, if desired using multiple transmit/receive sequences with different transmit foci. This beamforming approach is termed delay-and-sum beamforming.

Conventional delay-and-sum beamformers usually assume the geometry of the sound sources and receivers to be points emitting spherical waves. However, the emitted wavefront of an element in a row-column addressed array has the shape of a cylinder surface: it is a plane wave in the plane aligned along the element and a circle arc in the plane orthogonal to the element. Assuming the geometry of the elements to be points is therefore a poor approximation leading to errors in the time-of-flight calculation. A better approximation assumes the elements to be line segments, and the elements are therefore explicitly referred to as "line-elements" in the following. When an array of line-elements is focused, the geometry of the focal zone is also a line segment. Calculating the distances between the line-elements and a given point should therefore be calculated as the distance between a line segment and a point. This is the topic of the following, which is based on the derivation in Paper J.

The vectors $\mathbf{fp}$ and $\mathbf{pr}_n$, seen in Fig. 3.4, connect the point $\mathbf{p}$ to the closest point on respectively the focal line $\mathbf{f}$ and the receiving element $\mathbf{r}_n$. $\mathbf{sf}$ is the vector from the source element $\mathbf{s}$ to the focal line $\mathbf{f}$. Since the source elements and the focal line are parallel,

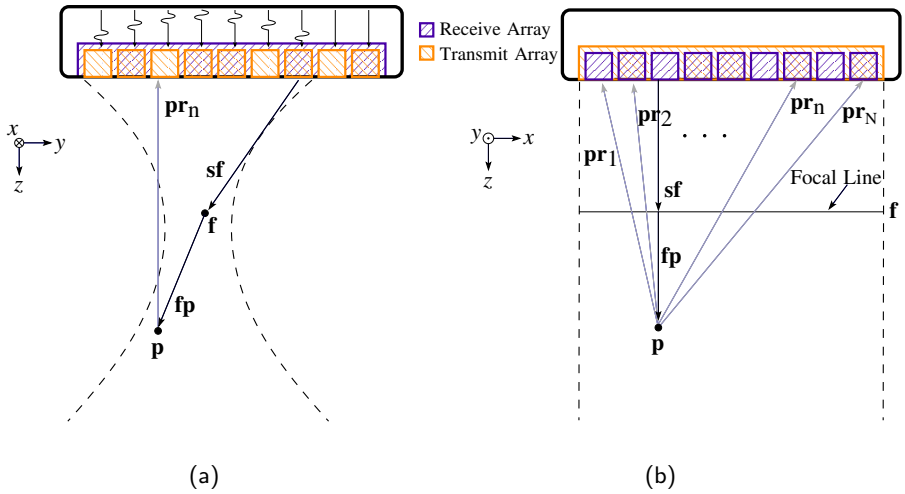

Figure 3.4: Time of flight (ToF) illustration of a focused emission. The vector $\mathbf{sf}$ connects the first source line-element that is excited with the focal line $\mathbf{f}$. $\mathbf{fp}$ is the vector from the nearest point on the focal line to the point being beamformed ($\mathbf{p}$), and $\mathbf{pr}_n$ is the vector from $\mathbf{p}$ to the nearest point on the receive line-element $\mathbf{r}_n$. In (a) the setup is sliced orthogonal to the transmitting line-elements and parallel with the receiving line elements. In (b) the setup is sliced parallel with the transmitting line-elements and orthogonal to the receiving line elements. In (a) the focal zone $\mathbf{f}$ looks like a focal point, but in (b) it is seen to be a focal line. From Paper J.

determining the distance between them can be solved in the z-y plane. The time of flight of a wavefront is given by the shortest distance from the source $\mathbf{s}$ through the focal line $\mathbf{f}$ to the point being focused $\mathbf{p}$ and back to the receiving element $\mathbf{r}_n$, divided by the speed of sound. Using the notation from Fig. 3.4, this can be written as:

$$\mathrm{ToF}_m(\mathbf{p}, n) = \frac{\|\mathbf{sf}\| \pm \|\mathbf{fp}\| + \|\mathbf{pr}_n\|}{c}, \tag{3.8}$$

where c is the speed of sound in the medium, n is an index from 1 to the number of receive elements N, and m is the emission index. Only one value of ToF_m is calculated per emission. If the point being focused is closer to the transducer array than the focal line, then the case of $-\|\mathbf{fp}\|$ is used, otherwise $+\|\mathbf{fp}\|$ is used.

To determine $\|\mathbf{fp}\|$ and $\|\mathbf{pr}_n\|$, the distance between a point and line must be calculated. The line segment from point $\mathbf{a}$ to point $\mathbf{b}$ is termed $\mathbf{ab}$. This is illustrated in Fig. 3.5. The projection of the point $\mathbf{p}$ onto the line $\mathbf{ab}$ is termed l and is determined by the usual equation for projection. l is positive if the projected point is located on the same side of $\mathbf{a}$

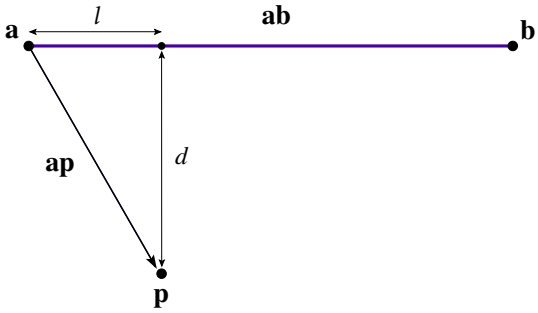

Figure 3.5: Projection of the point $\mathbf{p}$ onto the line segment $\mathbf{ab}$. l is the distance from $\mathbf{a}$ to the projected point and d is the shortest distance from $\mathbf{p}$ to $\mathbf{ab}$. From Paper J.

as $\mathbf{b}$, and negative if it is located on the other side. By normalizing l with the length of the line segment, $\hat{l}$ takes the values $[0, 1]$ when the projected point is located between $\mathbf{a}$ and $\mathbf{b}$:

$$\hat{l} = \frac{l}{\|\mathbf{ab}\|} = \frac{\mathbf{ap} \cdot \mathbf{ab}}{\|\mathbf{ab}\|^2} \,. \tag{3.9}$$

When the projection of $\mathbf{p}$ onto the line lies between $\mathbf{a}$ and $\mathbf{b}$, i.e. when $\hat{l} \in [0, 1]$, the standard formula for the distance between a line and a point can be used:

$$d = \frac{\|\mathbf{ab} \times \mathbf{ap}\|}{\|\mathbf{ab}\|} \,. \tag{3.10}$$

When $\hat{l} \notin [0, 1]$, the shortest distance from the line segment to the point is the distance from the closest end of the line segment ($\mathbf{a}$ or $\mathbf{b}$) to the point ($\mathbf{p}$). The following therefore determines the minimum distance between the point $\mathbf{p}$ and the line segment $\mathbf{ab}$:

$$d(\mathbf{ab}, \mathbf{p}) = \begin{cases} \dfrac{\|\mathbf{ab} \times \mathbf{ap}\|}{\|\mathbf{ab}\|} & \text{if } 0 \leq \hat{l} \leq 1 \\ \|\mathbf{ap}\| & \text{if } \hat{l} < 0 \\ \|\mathbf{bp}\| & \text{if } \hat{l} > 1 \,. \end{cases} \tag{3.11}$$

Using Eq. (3.11), the distances $\|\mathbf{fp}\|$ and $\|\mathbf{pr}_n\|$ can now be determined as

$$\|\mathbf{fp}\| = d(\mathbf{f}, \mathbf{p}) \quad \text{and} \quad \|\mathbf{pr}_n\| = d(\mathbf{r}_n, \mathbf{p}) \,. \tag{3.12}$$

By inserting Eq. (3.12) into Eq. (3.8), we arrive at

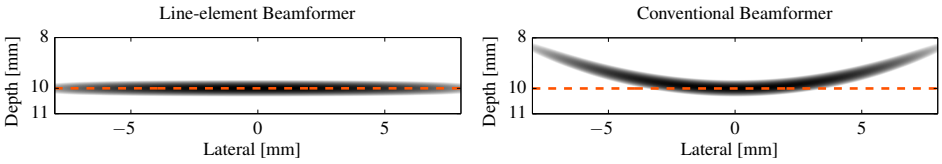

Figure 3.6: B-mode images of a wire phantom beamformed with the proposed line-element beamformer (a) and with a conventional beamformer (b). The dashed lines indicate the location of the wire phantom. The B-mode images are shown with a dynamic range of 40 dB. When using a conventional beamformer, the B-mode image is seen to be geometrically distorted. From Paper J.

$$\mathrm{ToF}_m(\mathbf{p}, n) = \frac{\left\|\mathbf{s}_{zy} - \mathbf{f}_{zy}\right\|}{c} + \frac{d(\mathbf{r}_n, \mathbf{p}) \pm d(\mathbf{f}, \mathbf{p})}{c} \,, \tag{3.13}$$

where $\mathbf{s}_{zy}$ and $\mathbf{f}_{zy}$ are the coordinates in the z-y plane of $\mathbf{s}$ and $\mathbf{f}$, respectively. The focused signal at point $\mathbf{p}$ is calculated by summing all receive signals at the time instances given by Eq. (3.13):

$$s_m(\mathbf{p}) = \sum_{n=1}^{N} a_{\mathrm{elec}}(n)\, y_{m,n}(\mathrm{ToF}_m(\mathbf{p}, n)) \,, \tag{3.14}$$

where N is the number of receive elements, $a_{\mathrm{elec}}(n)$ is the electronic receive apodization, and $y_{m,n}(t)$ is the measured signal from emission m on the receive element n at time t.

In Fig. 3.6, the importance of using a line-element beamformer is shown. In both figures, a wire phantom consisting of point scatterers located at 10 mm depth at the center of the transducer array is imaged. The transducer parameters and simulation setup are given in Paper J. In Fig. 3.6(a), the line-element beamformer has been used, resulting in a reproduction of the wire with no geometrical distortions. In Fig. 3.6(b), conventional beamforming assuming point sources/receivers located at the center of the elements has been used. In this case, the geometrical distortion of the wire due to the error in the time-of-flight calculation is apparent, clearly demonstrating the need to take the non-infinitesimal size of the sources/receivers into consideration.

It should be noted that while the assumption of cylindrical waves utilized above is valid in general for row-column addressed arrays, the amplitude of the wave front is only homogeneous in the near field of the element relative to its length direction. In the far field of the element, natural focusing occurs, corresponding to the height of the cylindrical wave being focused. In this case, objects in the center of the image will be over-pronounced. The transition to the far field occurs at $z_t \simeq L_x^2/(\pi\lambda)$, where L_x is the

element length and λ is the wavelength (Szabo 2014, p. 176). For example, for an element length of $2\,\mathrm{cm}$ operating at $3\,\mathrm{MHz}$, the transition occurs at a depth of $z_t = 25\,\mathrm{cm}$. Thus, for realistic element sizes, imaging is performed in the element's near field (in the length direction), where the focusing effect is negligible.

3.4 Edge Effects

Row column addressed arrays are quite different acoustically from fully addressed arrays. Due to the row-column addressing, each element may have a length that is hundreds of times longer than the lengths of the square elements used in a fully addressed array. The long length of the elements results in prominent edge effects. This section investigates how the elements of a row-column addressed array behave and what can be done to decrease the edge effects. The behavior of the elements is first investigated by analyzing their spatial impulse response as presented in Paper J.

The origin of the edge waves can be analyzed by the linear theory of wave propagation. The pressure at a given point $\mathbf{p}$ at the time t has in the literature (Pierce 1989) been shown to be

$$p(\mathbf{p}, t) = \rho_0 \frac{\partial}{\partial t} v(t) * h(\mathbf{p}, t) \tag{3.15a}$$

$$= \rho_0 \, v(t) * \frac{\partial}{\partial t} h(\mathbf{p}, t) \, , \tag{3.15b}$$

where $*$ denotes temporal convolution, ρ_0 is the density of the medium, v is the velocity normal to the transducer surface, and h is the spatial impulse response. It is noted that v is the convolution of the aperture excitation signal and the electro-mechanical impulse response of the aperture. The spatial impulse response $h(\mathbf{p}, t)$ is the observed sound field at the point $\mathbf{p}$ when the aperture is excited by a Dirac delta function. The Huygens-Fresnel principle states that the field originating from a sound radiating surface can be calculated by considering all points on the surface as the source of an expanding spherical wave. The field at any point in space is then constructed by superposition of these spherical waves. The acoustic reciprocity theorem states that if the sound source and the sound receiver are interchanged, the received signal remains unchanged. In other words, the spatial impulse response can be determined by letting the point $\mathbf{p}$ be the source of a spherical wavefront and then integrate the wave's intersection with the aperture. This integral is termed the Rayleigh integral (Harris 1981a; Stepanishen 1971).

The intersection of the spherical wave and the plane of the aperture makes a circle arc. The spatial impulse response at a certain time t is thereby determined by the length of the arc that intersects the aperture. The radius of the expanding sphere is $R = ct$, where t is time and c is the speed of sound. Determining the arc intersection is reduced to a two-dimensional problem by projecting the point $\mathbf{p}$ on to the transducer plane. Without

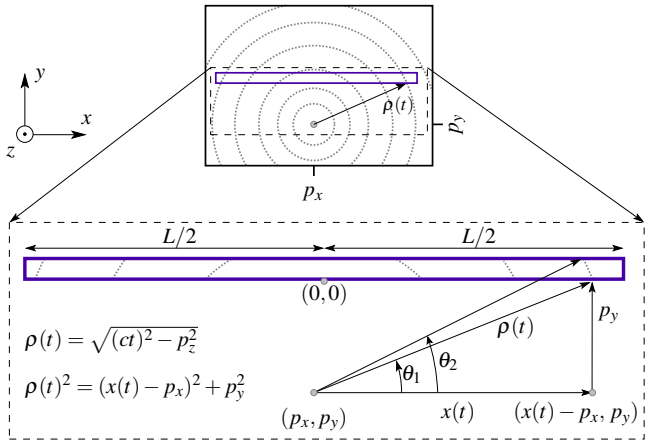

Figure 3.7: Spatial impulse response of long thin line-elements. At the top a large aperture is shown with integration paths marked with gray dashed lines. The integration paths are used in Eq. (3.16) to determine the spatial impulse response. Within the large aperture a thin line-element is illustrated. At the bottom, a zoom on the line-element is shown. The expression in Eq. (3.19) approximates the integration paths with vertical lines. The thinner the line-element is, the better the approximation. From Paper J.

loss of generality, the aperture is assumed flat. In the following, a normal right-handed coordinate system consisting of x, y, and z coordinates is used. The aperture plane is spanned by the x- and y-axes and the z-axis is orthogonal to the aperture plane. If the coordinate of $\mathbf{p}$ is (p_x, p_y, p_z), then the projection of $\mathbf{p}$ onto the $x\,y$-plane is (p_x, p_y, 0). The radius of the circle created by the intersection between the aperture and the expanding spherical wave is $\varrho(t) = \sqrt{(ct)^2 - p_z^2}$ and the center of the circle is located at (p_x, p_y). The line integral along this expanding arc is the Rayleigh integral in polar coordinates. This is the case shown in the aperture at the top of Fig. 3.7. The integration is performed along the gray dashed lines. Several authors (Harris 1981b; Stepanishen 1981; J. N. Tjøtta and S. Tjøtta 1982) have determined the solution to the Rayleigh integral in polar coordinates of an apodized aperture to be:

$$h(\mathbf{p}, t) = \begin{cases} \dfrac{c}{2\pi} \displaystyle\int_{\theta_1(t)}^{\theta_2(t)} a(\varrho(t), \theta)\, \mathrm{d}\theta\ , & \text{if } t \geq \dfrac{p_z}{c} \\ 0\ , & \text{else}\ , \end{cases} \tag{3.16}$$

where a is the apodization function of the aperture in polar coordinates with origin at the projection of $\mathbf{p}$ onto the aperture plane. a is equal to 0 when evaluated outside of the

aperture surface. If the apodization function is constant along the integration paths, (3.16) becomes

$$h(\mathbf{p},t) = \begin{cases} \frac{c}{2\pi}(\theta_2(t) - \theta_1(t))\, a_\varrho(\varrho(t)) \,, & \text{if } t \geq \frac{p_z}{c} \\ 0 \,, & \text{else .} \end{cases} \tag{3.17}$$

In the following, the aperture is assumed to be a long, thin, and rectangular line-element. The x, y -coordinates are chosen such that the x-axis is oriented along the length of the line-element and the origin is placed at the center of the line-element length. This is illustrated in Fig. 3.7.

At the top of Fig. 3.7, a large aperture is shown where the full integral along the dashed lines must be carried out to find the spatial impulse response. Within the large aperture, a line-element is shown. A zoom on the line-element is shown at the bottom of the figure. By approximating the integration paths on the line-element by a vertical line, the apodization function $a_\varrho(\varrho)$ from Eq. (3.17) changes dependent variable from the radius ϱ to the position x, representing the position along the line-element: $a_x(x(t))$. The thinner the line-element is, the better is the approximation. From the triangle at the bottom right in Fig. 3.7, the x-variable as a function of time is determined to:

$$x(t) = p_x \pm \sqrt{\varrho(t)^2 - p_y^2} \tag{3.18a}$$

$$= p_x \pm \sqrt{(ct)^2 - p_z^2 - p_y^2} \,. \tag{3.18b}$$

The spatial impulse response then approximately becomes:

$$h(\mathbf{p},t) \approx \begin{cases} \frac{c}{2\pi}(\theta_2(t) - \theta_1(t))\, a_x(x(t)) \,, & \text{if } t \geq t_1 \\ 0 \,, & \text{else ,} \end{cases} \tag{3.19}$$

where $t_1 = \sqrt{p_y^2 + p_z^2}/c$ is the earliest time at which the spherical wave arrives at the aperture. For a long thin line-element, the angular element width $(\theta_2(t) - \theta_1(t))$ changes much slower than the apodization function at the edges of the line-element, i.e.

$$\frac{\frac{\mathrm{d}}{\mathrm{d}t}(\theta_2(t) - \theta_1(t))}{2\pi} \ll \frac{\mathrm{d}}{\mathrm{d}t}\, a_x(x(t)) \,. \tag{3.20}$$

By inserting Eq. (3.19) into Eq. (3.15b), and using Eq. (3.20), the pressure field is seen to be proportional to

$$p(\mathbf{p},t) \propto \begin{cases} v(t) * \frac{\mathrm{d}}{\mathrm{d}t} a_x(x(t)) \,, & \text{if } t \geq t_1 \\ 0 \,, & \text{else .} \end{cases} \tag{3.21}$$

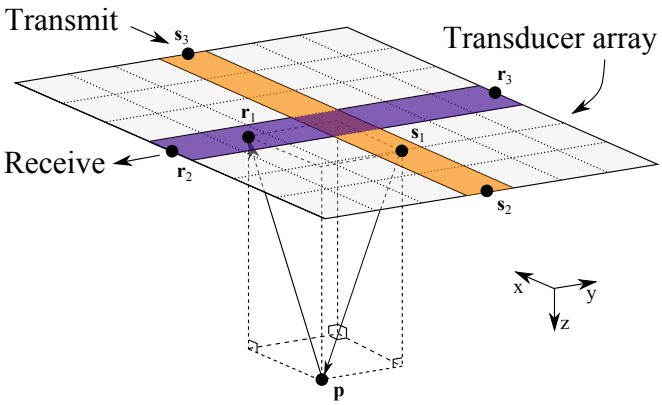

Figure 3.8: Illustration of a pulse-echo simulation setup with one line-element transmitting and one line-element receiving. A scatterer is located at the point $\mathbf{p}$, $\mathbf{s}_1$ is the closest point on the transmit element to $\mathbf{p}$, and $\mathbf{r}_1$ is the closest point on the receive element to $\mathbf{p}$. $\mathbf{s}_2$, $\mathbf{s}_3$ and $\mathbf{r}_2$, $\mathbf{r}_3$ are the edges of the transmit and receive line-elements, respectively. From Paper J.

Consider now the transmitting element of the row-column addressed array shown in Fig. 3.8. Using the acoustic reciprocity, the pressure in point $\mathbf{p}$ can be found by assuming that $\mathbf{p}$ emits a spherical wavefront that is received by the transmitting line-element. The wavefront reaches the closest point on the transmit line-element ($\mathbf{s}_1$) at time $t = t_1$. At $t = t_2$ the wavefront first reaches the closest edge at $\mathbf{s}_2$, and at $t = t_3$ the wavefront reaches the furthest edge of the line-element at $\mathbf{s}_3$. The apodization of a single line-element is usually constant or only slowly varying over the entire element surface. Since the apodization function evaluates to zero outside of the element area, there is a discontinuity at the element edges at $\mathbf{s}_2$ and $\mathbf{s}_3$. The derivative of the aperture function is therefore approximately zero everywhere except at the discontinuities at $\mathbf{s}_1$, $\mathbf{s}_2$, and $\mathbf{s}_3$, where it is the Dirac delta function, δ:

$$\frac{\mathrm{d}}{\mathrm{d}t} a_x(x(t)) \approx \delta(t - t_1) - \delta(t - t_2) - \delta(t - t_3) \tag{3.22}$$

By inserting Eq. (3.22) into Eq. (3.21), it is seen that the spatial transmit impulse response contains three individual responses. As a result, a single transmit pulse develops three wavefronts that passes the point $\mathbf{p}$. When a scatterer is located at $\mathbf{p}$, there are therefore three reflected waves returning to the line-element. Using the same argumentation, the spatial receive impulse response contains also three responses, meaning each wavefront is measured three times. The pulse-echo spatial impulse response is the convolution of the transmit and receive impulse responses and therefore contains up to nine responses. Referring to Fig. 3.8, the three wavefronts appears to originate from $\mathbf{s}_1$, $\mathbf{s}_2$ and $\mathbf{s}_3$. The receive line-element behaves as if it measures at the three discrete points $\mathbf{r}_1$, $\mathbf{r}_2$ and $\mathbf{r}_3$.

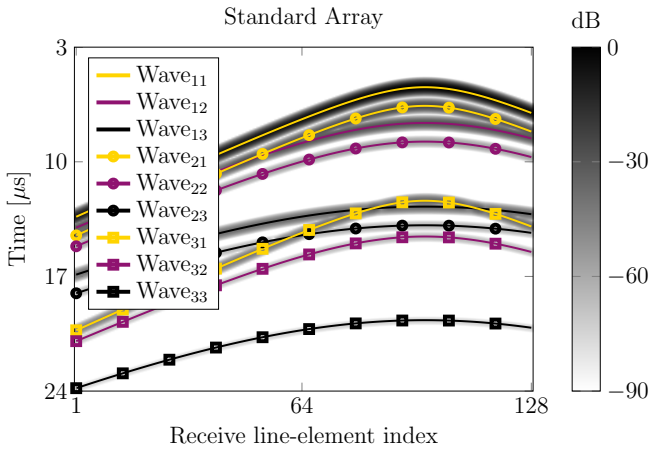

Figure 3.9: Nine echoes are received from a single line-element emission reflected by a scatter located at $(x, y, z) = (5, 4, 3)$ mm. The gray-scale image is the envelope of the received signals and the overlaid lines are predicted time-of-flights. The predicted time-of-flight is calculated using Eq. (3.23). That nine echoes are received exactly at the times predicted verifies the assumption that each line-element behaves as three discrete elements as illustrated in Fig. 3.8. The amplitude of the four most powerful ghost echoes is in this case approximately -40 dB and for the four weakest ghost echoes approximately -70 dB. From Paper J.

This analysis considered two out of four edges. The two long edges will also give rise to a response, but for elements with a width in the order of a wavelength, the two extra responses will merge with the $\mathbf{s}_1/\mathbf{r}_1$ response and are therefore negligible.

That nine echoes are measured from a single scatterer can be tested by a single line-element pulse-echo simulation. Fig. 3.9 shows the signals received by a $128+128$ element row-column addressed array from a single scatter located at the point $\mathbf{p} = (5, 4, 3)$ mm, when exciting the center line-element with a two-cycle sinusoidal 5 MHz pulse. Further details are found in Paper J. As expected, nine echoes are received. Overlaid on the gray level receive echoes are the expected echo arrival time combinations of the three sources and the three receive points of Fig. 3.8. The echo arrival time, i.e. the time-of-flight (ToF), is calculated as

$$\text{ToF}(\mathbf{p}, n, i) = \frac{\|\mathbf{p} - \mathbf{s}_n\| + \|\mathbf{r}_i - \mathbf{p}\|}{c}, \tag{3.23}$$

where both n and i are indexes between 1 and 3. The wavefronts are named wave_{ni}, where n indicates the $\mathbf{s}$-index and i indicates the $\mathbf{r}$-index. It is seen that the arrival time at each receive line-element of all received echoes are perfectly predicted, and the location assumption of the transmitter and receiver of each wavefront, shown in Fig. 3.8, must therefore be correct.

It is only the first echo, wave_{11}, that can be used for imaging, as the amplitudes of the other ghost echoes are too weak. The amplitude of the most powerful ghost echo is approximately 40 dB lower than the amplitude of the main echo. Even though the ghost echoes cannot be used for imaging, they still degrade the image quality, since they will result in multiple points in the image for each scatterer present. It is seen from Eq. (3.21) that to reduce the edge waves, and thereby the ghost echoes, the derivative of the apodization function must be kept as small as possible. The apodization function therefore has to converge to zero when approaching the line-element edges. This cannot be achieved by the usual electronic apodization, since this does not change the line-element apodization value along the length of it. Instead, the apodization must be integrated into the transducer array itself, which is the subject of the following section.

3.5 Integrated Apodization

In practice, there are several ways of integrating an apodization into the transducer elements, and a number of these are covered in Patent A and in (Joyce and Lockwood 2012). In this work, it has been exploited that the transducer elements of a CMUT consist of many individual CMUT cells as covered in the previous chapters. Since the output pressure and sensitivity of the element scales with the number of cells, a fixed apodization can be applied by varying the number of cells in the element.

3.5.1 Hann Apodization

In Paper I, the effect of such an integrated apodization was measured experimentally using a fabricated CMUT array. The fabrication details are covered in the paper and in Chapter 4. In the study, two $32 + 32$ row-column addressed CMUT arrays were produced; one without integrated apodization and one with integrated apodization. The mask layout of the two transducer arrays are depicted in Fig. 3.10. The complete mask set is given in the appendix (Mask Set A).

In the array with no integrated apodization (Fig. 3.10(a)), circular CMUT cells are densely distributed over the array, with 3 cells along the width of the elements and 96 cells along their length. Each section of the array, where a row and a column intersect, can accommodate a maximum of 9 CMUT cells. For the array with integrated apodization (Fig. 3.10(b)), the number of cells in this square section is varied according to a circularly symmetric Hann function. Such an apodization have in simulations been shown to be very effective at suppressing the ghost echoes (Démoré et al. 2009; Rasmussen and Jensen 2013b). This effectively alters the active area and consequently the intensity of the emitted/received signal, gradually decreasing it towards the edges of the array to suppress the edge waves.

The field emitted from each array was measured by scanning a hydrophone over the center of the array at a depth of $5.3\,\text{mm}$ while actuating the whole array simultaneously. In practice, the elements were shorted so this could be achieved using a single channel

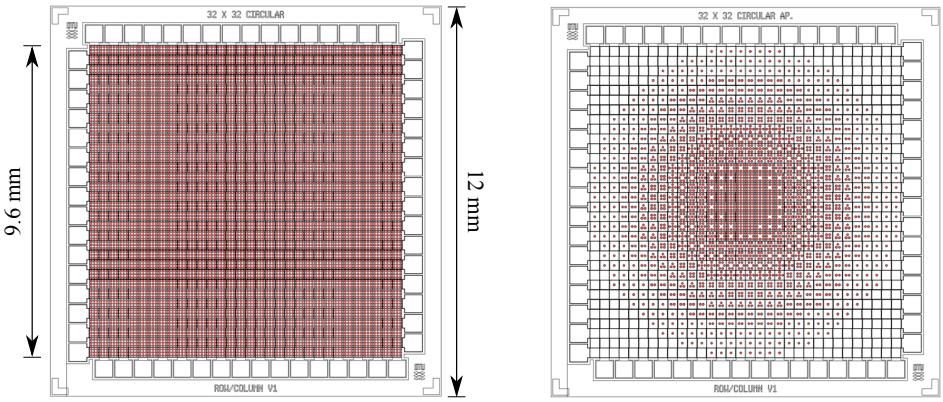

(a) (b)

Figure 3.10: Mask layout of the row-column addressed $32 + 32$ CMUT transducers without integrated apodization (a) and with integrated apodization (b). The red circles indicate the individual CMUT cells, which are densely packed in the non-apodized configuration, while the number of cells follows a circular symmetric Hann function in the apodized layout. From Paper I.

from an amplifier, see further details in Paper I. Simulations emulating this setup was performed in Field II (Jensen 1996c; Jensen and Svendsen 1992). The measured and simulated emitted fields generated by the two arrays are shown in Fig. 3.11. The result for the array without integrated apodization is shown in Fig. 3.11(a) and Fig. 3.11(c) (simulation and measurement, respectively), while the result for the array with integrated apodization is shown in Fig. 3.11(b) and Fig. 3.11(d). The main wave arrives after $3.6\,\mu\mathrm{s}$, corresponding to a distance of $5.3\,\mathrm{mm}$. In addition to this, a spherical wave is emitted from the edges of the array. The arrival time of the wave front is the distance travelled divided by the speed of sound. The arrival time of the edge wave at the position of the hydrophone is then

$$t_{\text{edge}} = \sqrt{d^2 + x^2}/c\,, \tag{3.24}$$

where d is the perpendicular distance from the point being measured and the transducer surface, x is the lateral distance of the point being measured from the edge of the array, and c is the speed of sound. The predicted arrival time of an edge wave originating from the array aperture edge at $-4.8\,\mathrm{mm}$ has been plotted with a dashed line in both the simulated and measured fields for the array without integrated apodization in Fig. 3.11(a) and Fig. 3.11(c), respectively. It is seen that the edge wave is accurately predicted, thereby confirming its origin.

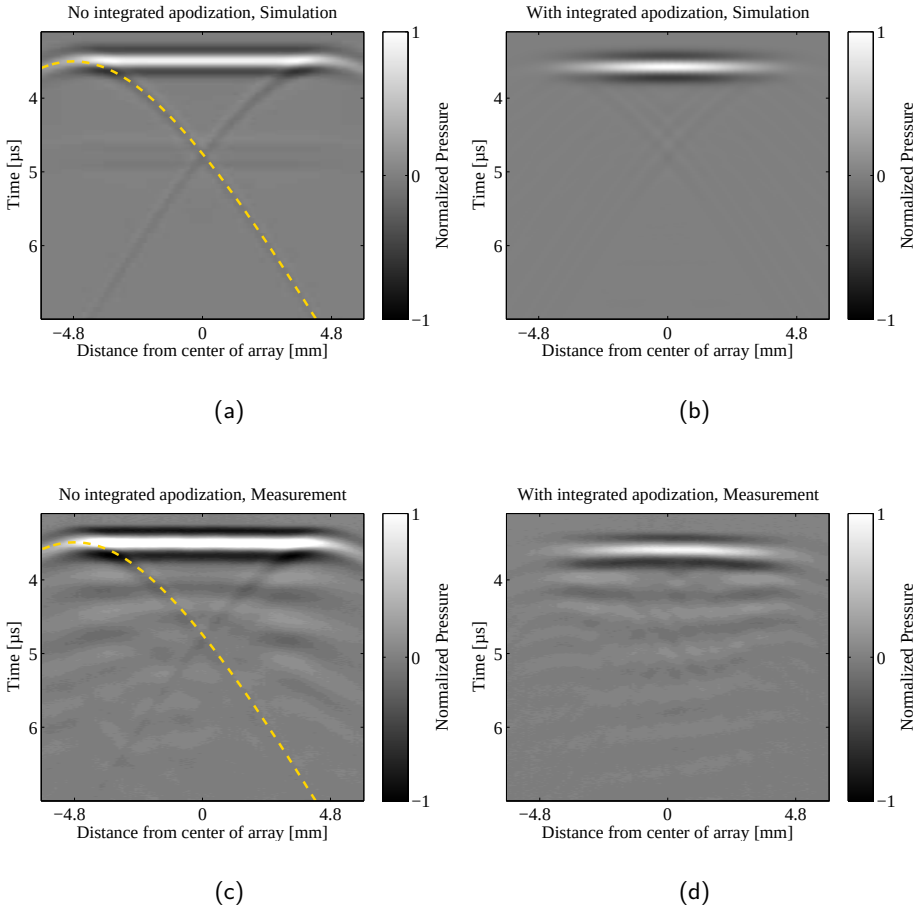

Figure 3.11: Simulated (a and b) and measured (c and d) pressure field along a line through the center of the array at a depth of $5.3\,\mathrm{mm}$. a and c show the result for the array without integrated apodization, and b and d show the result with integrated Hann apodization. The pressure has been normalized to the maximum pressure of the measurement with no integrated apodization. The extend of the array aperture (from $-4.8\,\mathrm{mm}$ to $4.8\,\mathrm{mm}$) is marked. Two edge waves are clearly visible for the non-apodized array, and the dashed line show the analytically calculated expected arrival time of the edge wave originating at $-4.8\,\mathrm{mm}$. The ripples in the experimental results are due to transducer ringing, and these are therefore not reproduced in the simulations. From Paper I.

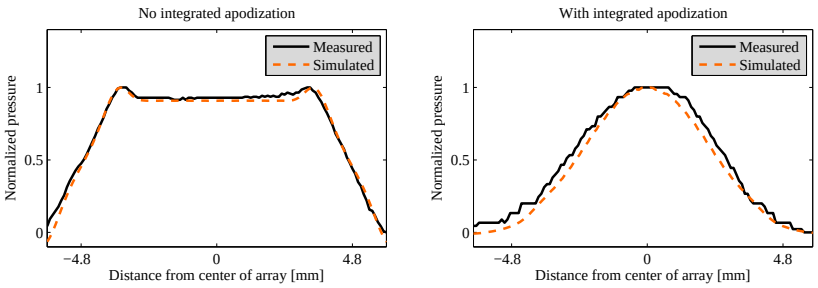

(a) (b)

Figure 3.12: Measured and simulated pressure at a distance of $5.3\,\mathrm{mm}$ from the transducer surface at time $3.6\,\mu\mathrm{s}$. The pressure is measured along a line through the center of the array. The extend of the array aperture (from $-4.8\,\mathrm{mm}$ to $4.8\,\mathrm{mm}$) is marked. The pressure has been normalized to the maximum pressure to allow comparison of the profile of the emitted field over the array. From Paper I.

For the array with integrated apodization (Fig. 3.11(b) and Fig. 3.11(d)), the two edge waves are seen to be significantly damped. The damping in terms of edge wave energy can be quantified by summing the squared pressure values along the curve given by (3.24) for both arrays. This yields a reduction of edge wave energy of $13.0\,\mathrm{dB}$ ($95\,\%$) for the simulation and $8.4\,\mathrm{dB}$ ($85\,\%$) for the measurement. The deviance between the simulation and measurement may be contributed to the transducer ringing present in the measurements due to the lack of a backing material. This will add to the calculated edge wave energy in both cases and thereby reduce the energy ratio.

In Fig. 3.12(a) and Fig. 3.12(b), the amplitude of the measured and simulated pressure field is shown for the two arrays. The amplitude is extracted at the arrival of the main wave at time $3.6\,\mu\mathrm{s}$, and it thereby corresponds to a horizontal cross-section of the plots in Fig. 3.11. The profiles of the simulated and measured amplitudes are seen to be comparable for both of the arrays. The correspondence is especially relevant for the array with integrated apodization, since it demonstrates that the emitted field, and thereby the apodization, can be accurately predicted.

From the study, it is seen that the Hann apodization indeed suppresses the edge waves. However, the energy emitted from such an array is significantly reduced at all points except from the center of the array as seen in Fig. 3.12(b). Therefore, the only location where this apodization function allows the row-column addressed array to perform well is straight down at the center of the array. Even if the array angles the transmit beam to the sides, like a phased array transducer, the echoes returning to the transducer surface will be significantly attenuated because they will hit the apodized part of the transducer first.

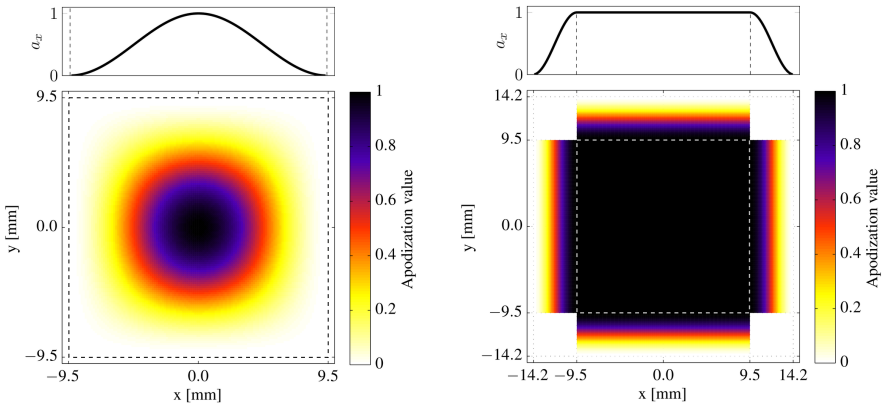

Figure 3.13: The two types of apodization investigated in Paper J: Hann apodization (a) and the new apodization layout where a roll-off region is added to the ends of the line-elements (b). The top graph shows the apodization of a single line-element as a function of the position along the line-element. The bottom figure shows the apodization of the full transducer array. The dashed lines mark the edge of the line-elements and the row-column addressed array. The size of the area within the dashed lines is identical in both figures.

3.5.2 A New Apodization Layout

To investigate alternative apodizations without these limitations, a simulation study was performed in Paper J. Here, two types of apodizations were investigated. The first of these was the circularly symmetric Hann apodization as shown in shown in Fig. 3.13(a), where the top graph shows the apodization of a single line-element. This apodization is identical to the one presented in the previous section, and is included for reference. Note that since the row and column line-elements are overlapping, so are their apodization functions. At each position on the transducer surface, two apodization functions are overlapping, one from a row element and one from a column element. The effective apodization is the multiplication of the two apodization functions. The vertical line-elements close to the edges are multiplied by values close to zero by the horizontal apodization function. Similarly, the horizontal line-elements at the edges are multiplied by values close to zero by the vertical apodization function.

An alternative to the overlapping apodizations is to not apodize the central part of the transducer surface, but instead adding a roll-off region on both sides of all line-elements as shown in Fig. 3.13(b). This roll-off region is used for the apodization function to

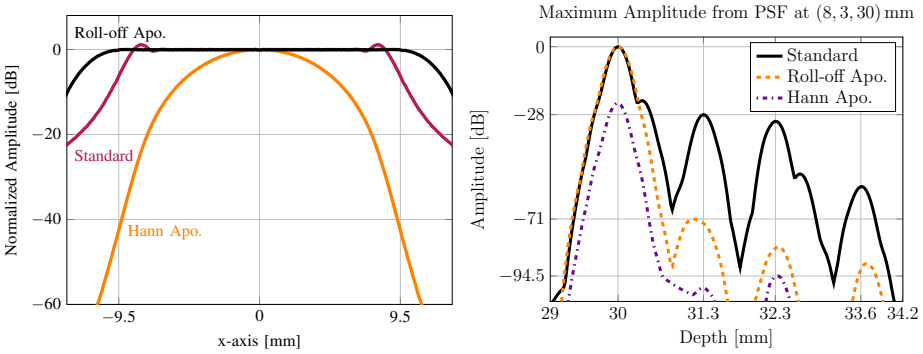

Figure 3.14: (a) Maximum received echo intensity from a single scatter at a depth of $10\,\mathrm{mm}$ for varying lateral position. The received signal acquired with an integrated Hann apodized array is seen to decrease fast already from the center of the array. The signal received with the standard array without any apodization decreases just before the edge of the array, and the roll-off apodized array maintains the same signal strength until the edge of the array. (b) Maximum intensity of the PSFs at $(x,y,z) = (8,3,30)\,\mathrm{mm}$ as a function of depth. The Hann apodized array is added for comparison. Both the roll-off apodized array and the Hann apodized array greatly suppresses the ghost echoes, but the maximum intensity of the main response of the Hann apodized array is $24\,\mathrm{dB}$ lower compared to the two other arrays. Both figures are from Paper J.

converge smoothly to zero. This way, the central region of the aperture surface has a uniform apodization value of 1, and there is no overlapping of the apodization functions where these are less than 1. At the same time, the discontinuities at the edges have been removed. If the added roll-off region is short, then the derivative of the aperture function will be high, and if the roll-off region is wide, the derivative will be low. From Eq. (3.21), it then follows that a wider roll-off region is better at suppressing the edge waves. Each line-element thereby becomes longer, but there are the same number of row- and column-elements in the array. In practice, however, there is an upper limit on the edge apodization width since a very large footprint results in difficulties getting a good acoustical contact between the aperture and the human body. This trade-off is investigated in detail in Paper J, in which an apodization width of 16 wavelengths was found to be a good compromise.

In Fig. 3.14(a), the simulated maximum received main echo as a function of scatterer position is shown. This expresses the array sensitivity as a function of position. The scatterer is placed directly in front of the transmitting line-element at a depth of $10\,\mathrm{mm}$.

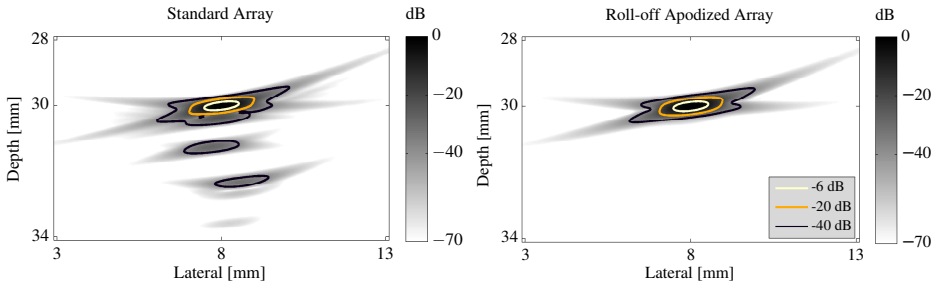

(a) (b)

Figure 3.15: PSF at $(x,y,z) = (8,3,30)\,\mathrm{mm}$. The PSF of a standard non-apodized transducer array is shown in (a) and the PSF of a transducer array with integrated roll-off apodization is shown in (b). The main response of the PSFs are practically identical, but the ghost echoes of the roll-off apodized array are greatly suppressed compared to the non-apodized standard array. Both figures are from Paper J.

The center line-element of the array emits a two-cycled pulse and the received echoes are measured on all receive line-elements. The received signal is envelope detected and the maximum value is plotted against the scatterer position. Consistent with the measurement in Fig. 3.12(b), the Hann apodized array is seen to loose sensitivity very fast. At the edge of the array, the returned main echo is $40\,\mathrm{dB}$ weaker than in the center of the array. On a standard array without the integrated apodization, the Fresnel-diffraction of a sharp edge is evident close to the aperture edges at $\pm 9.5\,\mathrm{mm}$ (Naik 2010, p.145). This effect is also seen in the measurement in Fig. 3.12(a). The edge apodized array has a constant sensitivity over the entire central aperture.

In Fig. 3.15, the PSF at $(x,y,z) = (8,3,30)\,\mathrm{mm}$, where 9 echoes are measured, is shown for both the standard and roll-off apodized array. The point scatterer is deliberately offset from the center of the array to demonstrate the effect of the apodization at a point that exposes the difference between the apodization layouts. Because several of the ghost echoes arrive with a very short time interval, only 5 of the 8 ghost responses can be distinguished. The main response of the two arrays are almost identical, but the ghost echoes of the roll-off apodized array are greatly suppressed compared to the non-apodized standard array. The maximum intensity of the PSFs in Fig. 3.15 is seen in Fig. 3.14(b) as a function of depth. The corresponding values for the Hann-apodized array has been added for comparison. The ghost responses seen on the PSF from the standard array are greatly attenuated by both the Hann-apodized array and the roll-off apodized array. The maximum ghost echo is attenuated by $43\,\mathrm{dB}$ for the roll-off apodized array and by $66.5\,\mathrm{dB}$ for the Hann apodized array. On the other hand, the main response of the Hann apodized array is

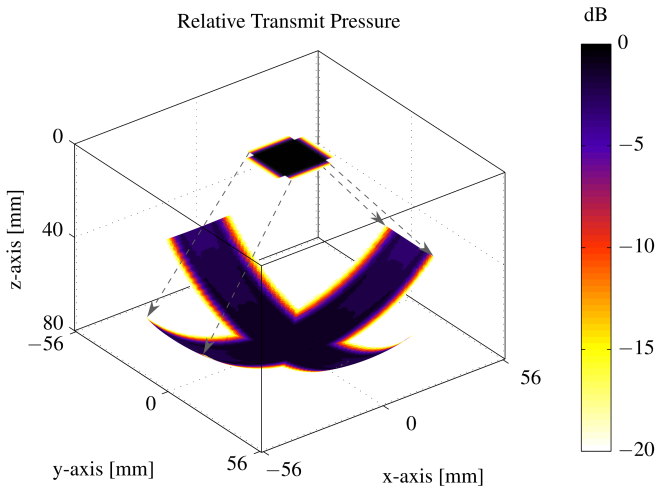

Figure 3.16: Peak pressure distribution of a phased row-column addressed array. The transmit array of the row-column addressed array is used as a normal 1-D phased array from 2-D ultrasound imaging. Each voxel representing the pressure is located within the focal line. 200 emissions are used for simulating the figure and all 128 elements are excited during each emission. Each emission focuses at a different focal angle, but the focal distance is kept constant. For the pressure field to attain the cross shape shown in the figure, the transmit and receive arrays are interchanged after 100 emissions. From Paper J.

seen to be attenuated by $24\,\mathrm{dB}$, which clearly demonstrates the problem with the Hann apodization. Taking the main response damping into consideration, the maximum ghost echo damping of the Hann apodized array becomes $42.5\,\mathrm{dB}$. As opposed to this, the roll-off apodized array has preserved the amplitude of the main response. Adding roll-off regions to row-column addressed arrays is therefore proposed as the standard solution, and it is included in Patent A.

The above analysis changes if the scatterer is not located below the array, but rather to the side of it. Because of the apodization, negligible energy is emitted to the side of the array. However, the vertical and horizontal arrays of the row-column addressed 2-D array can each steer the transmit beam in one direction. In Fig. 3.16, the relative peak pressure is shown when steering the transmit beam to the sides. For the phased array transmit beam, all 128 elements were focused at a distance of $80\,\mathrm{mm}$. The transmit beam was varied by $\pm 45°$ and each voxel in the figure is placed on the focal line for a given emission. 200 emissions were used to create Fig. 3.16, which is realistic for real-time imaging as covered in Section 3.2. When the horizontal array is used as a transmit array, it can steer the transmit angle within in the z-x plane, and at the same time the vertical array is receiving. When the sequence has completed, the two arrays switch function, and now

the vertical array is used as a transmit array. This leads to the energy being distributed as a cross, as seen in Fig. 3.16. Row-column addressed arrays are therefore also well suited for cross-plane imaging. Full pyramid volume imaging can be achieved by defocusing the emitted energy using a curved array or an acoustic lens (Démoré et al. 2009; Morton and Lockwood 2003). When the transmit beam is steered to the side, the echoes arrive at the edge of the receive array first. To measure this signal, the roll-off region of the receive line-elements must be disabled in that direction. For CMUTs, this can conveniently be achieved by simply removing the DC bias from the roll-off region. As covered in Chapter 2, the electro-mechanical coupling efficiency of CMUTs is highly dependent on the DC bias, and removing the DC bias should therefore make the contribution from the apodized regions of the array negligible.

3.5.3 Imaging Experiments

The new apodization layout was tested in practice by fabricating a CMUT array presented in detail in Paper K. The mask layout of this is seen in Fig. 3.17, and the complete mask set is found in the appendix as Mask Set B. It consists of 62 row elements, 62 column elements, and four apodization regions, each supplied with a DC bias. To the right in Fig. 3.17, a zoom-in on one apodized element end is shown. As seen, it consists of a collection of CMUT cells (red squares), the number of which is reduced towards the outer edge according to the findings presented in the previous section. The central part of the array, i.e. excluding the apodized element ends, is densely populated with CMUT cells and is thus not apodized in any way. In this part of the array, each element contains four square CMUT cells along the width of the element.

As covered in Paper K, the array was connected to the experimental Synthetic Aperture Real-time Ultrasound System (SARUS) (Jensen, Holten-Lund, et al. 2013) via electronics that allowed all elements of the array to both transmit and receive. The transducer array was submerged in vegetable oil, and a $0.3\,\mathrm{mm}$ diameter steel wire was placed a depth of $2.3\,\mathrm{cm}$. The wire was imaged by emitting with one row at a time and receiving with all columns for each emission. An image of the wire was then reconstructed with the beamformer presented in Section 3.3 using synthetically constructed transmit foci from the single element emissions. This way, both transmit and receive focus could be obtained in every point of the image.

Two imaging sequences were run: One with the apodization enabled, and one with the apodization disabled. In practice, the disabling of the apodization was achieved by modifying the DC bias supply on the front-end electronics, such that the DC bias voltage seen by the apodized regions of the array became zero. Using the argument from the previous section, the electro-mechanical coupling efficiency of CMUTs is highly dependent on the DC bias as covered in Chapter 2, and removing the DC bias should therefore make the contribution from the apodized regions of the array negligible. The effect was confirmed in practice by emitting only with the apodized part of the array with and without DC bias. The recorded signal with no DC bias was $18\,\mathrm{dB}$ lower than the

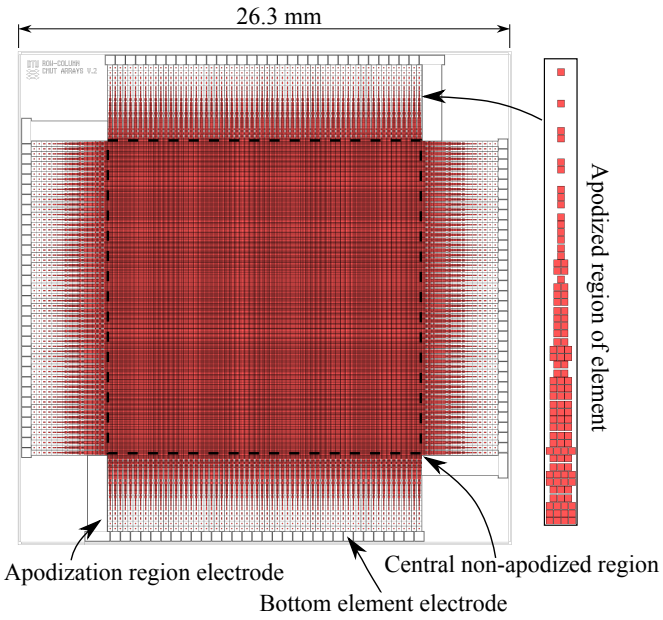

Figure 3.17: Array mask layout. The red squares are the individual CMUT cells, which are densely populated in the central region of the array shown within the dashed line. A zoom-in on the apodized region of one element is seen in the right part of the figure. The layout is covered by Patent A. The figure is from Paper K.

signal with DC bias, showing that the apodization was considerably suppressed in the no-bias configuration.

The result of the two measurements is seen in Fig. 3.18(a) (apodization disabled) and Fig. 3.18(b) (apodization enabled). Both figures show a cross-section of the wire beamformed with 800×800 points and displayed with a dynamic range of 40 dB. This thereby is a measure of the line spread function (LSF) of the array, i.e. the array's ability to resolve a line source. In Fig. 3.18(a), where the integrated apodization is disabled, a ghost echo is clearly visible below the main echo. The maximum amplitude of this ghost echo is -22.6 dB relative to the maximum amplitude of the main echo. The lateral and axial full-with-at-half-maximum (FWHM), i.e. the -6 dB resolution, are 1.79 mm and 0.71 mm, respectively.

Fig. 3.18(b) shows the result with the integrated apodization enabled, and here the ghost echo is not visible within the 40 dB dynamic range. The amplitude of the signal the same distance from the main echo as the ghost echo in Fig. 3.18(a) is -38 dB relative to the maximum amplitude of the main echo. Thus, the apodization has reduced the amplitude of the ghost echo by 15.8 dB. The lateral and axial FWHM are here 1.91 mm

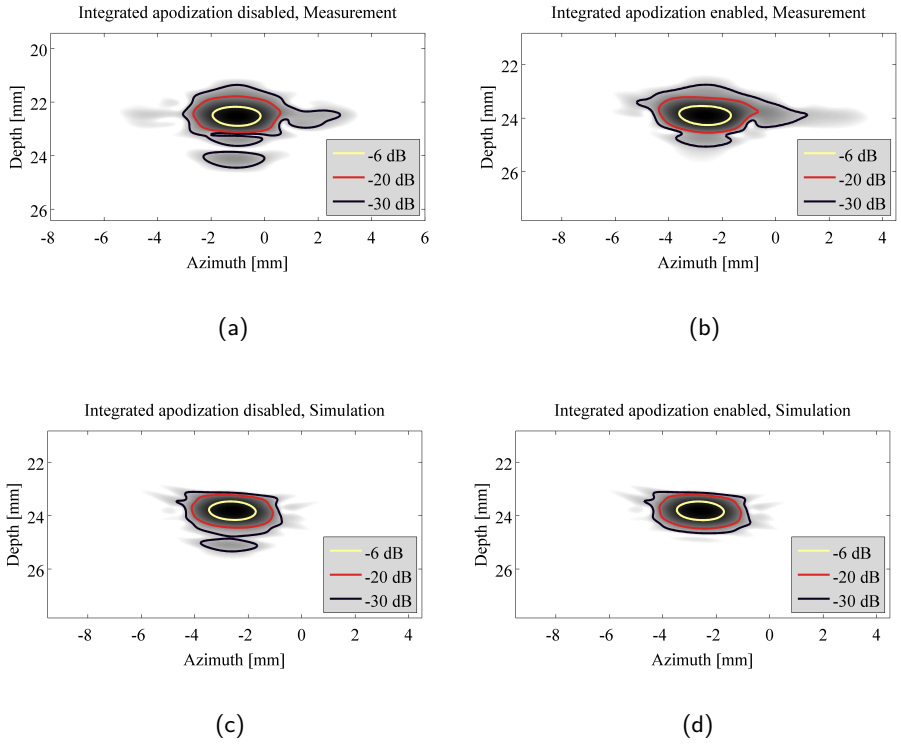

Figure 3.18: Measured (a and b) and simulated (c and d) line spread function at a depth of 2.3 cm using dynamic range of 40 dB. (a) and (c) show the result with the integrated apodization disabled, while (b) and (d) show the result with the integrated apodization enabled. The line spread function was acquired using a line of point scatterers in the simulation, while a 0.3 mm diameter steel wire was used for the measurements. The image was beamformed using full synthetic aperture imaging with 62 single element emissions and data received by 62 receive elements for each emission. The azimuth zero-point is positioned at the center of the array. The figures are from Paper K.

and 0.71 mm, respectively. The axial FWHM is therefore unchanged, while the lateral FWHM is 12 % larger for the apodized measurement. However, this can be attributed to the wire being placed 1 mm further from the center of the array in the apodized measurement due to alignment imperfections. The signal-to-noise ratio (SNR) in the beamformed image was calculated using the method presented in Eq. (9) in (Rasmussen and Jensen 2014), yielding a SNR of 46.9 dB.

For comparison, the LSF was simulated in Field II (Jensen 1996c; Jensen and Svendsen

Table 3.1: Line spread function metrics (From Paper K).

Parameter	Measurement	Simulation	Unit
Lateral FWHM, no apodization	1.79	1.74	mm
Lateral FWHM, with apodization	1.91	1.76	mm
Axial FWHM, no apodization	0.71	0.69	mm
Axial FWHM, with apodization	0.71	0.69	mm
Ghost echo damping	15.8	18.9	dB

1992) using a row-column addressed transducer array closely emulating the real transducer array used for the measurements. The exact same imaging sequence and beamforming technique as in the measurements were used in the simulation. Further details are given in Paper K. The result of the simulation is seen in Fig. 3.18(c) (without integrated apodization) and Fig. 3.18(d) (with integrated apodization). The lateral and axial FWHM of the LSF for the simulated array without integrated apodization are 1.74 mm and 0.69 mm, respectively. The corresponding metrics for the LSF of the simulated array with integrated apodization are 1.76 mm and 0.69 mm. Note that, as opposed to the measurements, the wire phantom is placed in exactly the same position in the two simulations (corresponding to the position of the wire during the measurement with the integrated apodization enabled). Therefore, both the axial and lateral FWHM are practically unchanged between the two. The ghost echo is clearly visible in the simulation of the array without integrated apodization (Fig. 3.18(c)), while the integrated apodization is seen to reduce it significantly (Fig. 3.18(d)). The damping of the ghost echo in the simulations is 18.9 dB; a comparison between the experimental and simulated results is seen in Table 3.1. Note that the measured ghost echo damping is 3.1 dB lower than the simulated. This can be attributed to the fact that the response from the simulated wire is not identical to the response from the physical wire.

3.6 3-D Flow Estimation

Using ultrasound, it is possible to detect the velocity of moving objects (Jensen 1996b). Velocity estimates are of considerable clinical importance, as it provides non-invasive means of monitoring e.g. the blood flow conditions in a patient. It is often used to detect anomalies in the flow which could be an indication of stenosis. In this section, it is shown that row-column addressed arrays can be used to estimate the velocity of objects moving in arbitrary directions within a volume, which has so far only been demonstrated with fully addressed arrays with a much higher channel count (Pihl and Jensen 2014; Pihl, Stuart, et al. 2014). The technique presented in this section is based on Paper M and Patent B.

A commonly used technique for estimating velocities using 1-D transducer arrays is so-called color flow mapping. Here, ultrasound pulses are sent into the tissue at a certain

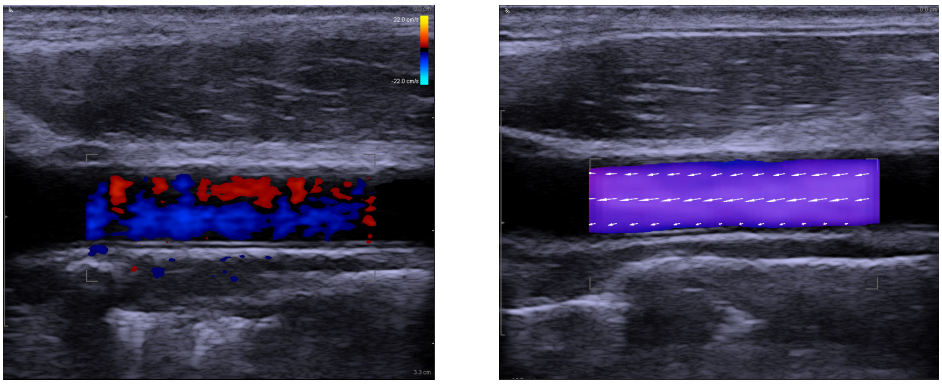

(a) (b)

Figure 3.19: (a) Blood velocity estimation in a vessel oriented perpendicular to the transducer using color flow mapping. The estimator cannot measure the velocity and displays the flow as moving either left or right or as not moving at all (blue, red, and black colors, respectively). (b) The same situation, but this time using vector flow imaging incorporating transverse oscillation. The estimation of the direction and magnitude of the flow is now unambiguous. From (BK Medical 2015).

pulse repetition frequency. Each pulse will result in echoes recorded by the transducer, and if the tissue is moving away from or towards the transducer, there will be a shift between consecutive echoes. From this shift, the velocity of the moving object(s) along the ultrasound beam can be found. Details on the different velocity estimation algorithms are found in (Jensen 1996b). The main issue with this technique is that only the velocity along the ultrasound beam, the axial velocity, is measured. Hence, if the blood vessel is oriented at an angle relative to the ultrasound beam, the blood velocity along the vessel can only be found by compensating for this angle, which must be measured by the operator. In the case where the vessel is oriented perpendicular to the ultrasound beam, no velocities can be measured as exemplified by Fig. 3.19(a).

A solution to this problem is the so-called transverse oscillation (TO) technique introduced by Jensen and colleagues (Jensen 1996a, 2000; Jensen and Munk 1998; Udesen and Jensen 2006). In the TO method, an oscillation oriented transverse to that of the ultrasound beam is introduced in the ultrasound field. By introducing this transverse oscillation, objects moving in the lateral direction will cause a change in the received signal, which can be used to estimate their velocity in this direction. The transversely oscillating field is generated by applying the same transmit beam as used in conventional axial velocity estimation and adjusting the apodization of the receive aperture in such a

way that the whole aperture resembles two point sources. Two point sources separated in space will give rise to a field in which an interference pattern is present, which creates the transverse oscillation. Using the Fraunhofer approximation, the relation between the lateral spatial wavelength λ_x and the apodization function is

$$\lambda_x = \frac{2\lambda_z z_0}{d} \,, \tag{3.25}$$

where d is the distance between the two peaks in the apodization function, z_0 is depth, and λ_z is the axial wavelength (Udesen and Jensen 2006). In axial velocity estimation, a Hilbert transform is performed to yield two 90° phase shifted signals; the in-phase signal and the quadrature signal. This enables the direction of the flow to be determined. To achieve this in the lateral direction as well, two receive beams are beamformed as shown in Fig. 3.20(a). They are steered so that the transverse distance between the beams is $\lambda_x/4$, which corresponds to a 90° phase shift in space. From the relation in Eq. (3.25), it is clear that the steering angle must be

$$\theta = \arctan\left(\frac{\lambda_z}{2d}\right) \,. \tag{3.26}$$

In Fig. 3.20(b), the two fields generated by steering the beams and applying the receive apodization resembling two point sources is shown (Jensen and Munk 1998).

From the above, it follows that by emitting ultrasound in one direction and receiving along the same direction, the axial velocity can be estimated. From the two receive beams steered by $\lambda_x/4$, estimation of the transverse velocity can be performed. The technique therefore yields two components of the velocity vector, which can be used to estimate any direction of a velocity in a plane. The velocity field can be visualized using vector arrows, which is therefore often referred to as vector flow imaging. This technique is today available on commercial BK Medical scanners, and an example is shown in Fig. 3.19(b) (BK Medical 2015).

Having the velocities in a plane is, however, insufficient if e.g. the volume flow is to be found. In this case, the cross-sectional dimensions of the vessel must first be measured, and by rotating the transducer 90°, the peak velocity of the blood flow can be found as in e.g. Fig. 3.19(b). Using a geometrical assumption for the cross-sectional shape of the vessel, the volume flow can be estimated. However, even finding the peak velocity in a vessel can be challenging, since it relies on the operator's ability to position the scan plane directly in the middle of the vessel, where the velocity is highest. To remedy this, the technique has therefore been expanded to be used with fully addressed 2-D transducer arrays (Pihl and Jensen 2014; Pihl, Stuart, et al. 2014). This enables estimation of all three velocity components in a volume, providing operator-independent and assumption-free calculation of e.g. volume flow rates. However, this technique suffers from the requirement of a fully addressed 2-D transducer array. As described in Paper M, Patent B and in the following, row-column addressed arrays can, however, also provide

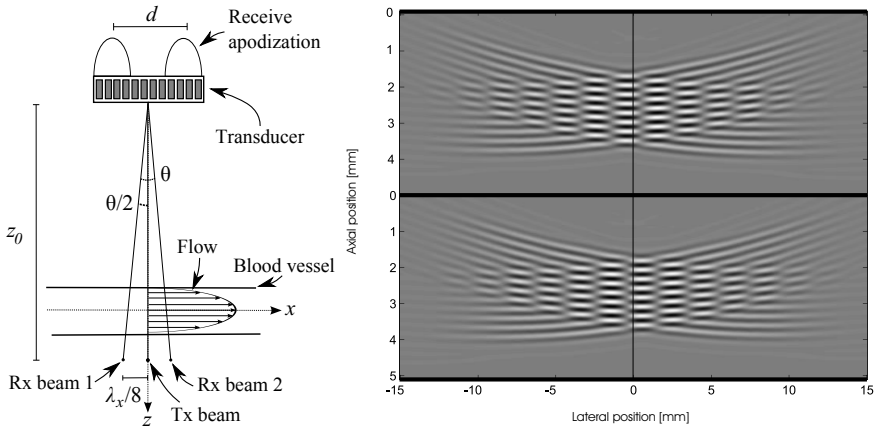

Figure 3.20: (a) Illustration of the receive apodization employed to generate the transversely oscillating field and the two receive beams used for the in-phase and quadrature signals. (b) The two resulting transversely oscillating fields generated. From (Jensen and Munk 1998).

estimation of all three velocity components in a volume using a fraction of the channels of a fully addressed 2-D array.

Since a row-column addressed array is made up of two orthogonal 1-D arrays, the TO technique can be applied just like for a conventional 1-D array. In Fig. 3.21, the concept is illustrated. First, transmit focusing is performed in the x-dimension using one of the 1-D arrays, e.g. the rows (top left in Fig. 3.21). The transverse oscillation field is then synthesized in the y-direction using the orthogonal 1-D array (hence the columns) as seen in the bottom left of Fig. 3.21. This allows estimation of the y-component of the velocity vector. The axial (z) component may be estimated as well using a conventional axial velocity estimator, i.e. by receiving without the TO apodization. Note that the setup is acoustically identical to a conventional 1-D array with an elevation lens in transmit: The transmitting rows create a line focus equivalent to that created by a 1-D array with an elevation lens emitting a plane wave. The receiving columns then produce the TO field, allowing 2-D velocity estimation in a plane. By shifting the transmit focus of the rows, the plane can be shifted in the x-direction (referring to Fig. 3.21), whereby the axial (z) and one lateral (y) component of the velocity can be mapped out in the whole volume.

The lateral component in the x-direction can be obtained by flipping the transmit-receive sequence as shown to the right in Fig. 3.21. Now, the rows are used to synthesize the TO field in the x-direction, whereby the x-component of the velocity vector can be

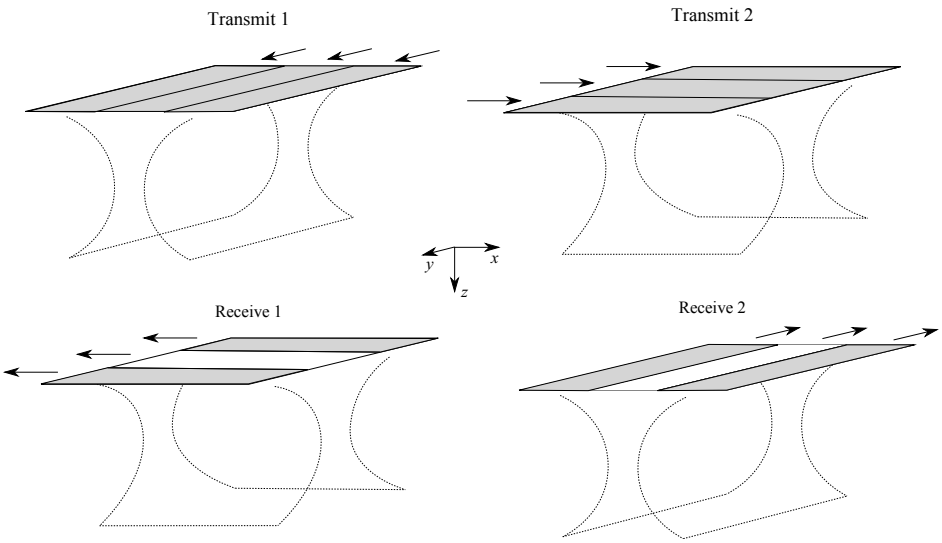

Figure 3.21: Illustration showing the principle of 3-D velocity estimation using row-column addressed arrays. Two sequences are used: First, transmit focusing is performed in the x-dimension, and the transverse oscillation field is synthesized in the y-direction. This allows estimation of the y-component of the velocity vector. Afterwards, the transmit/receive-sequence is flipped to allow estimation of the x-component of the velocity vector. The grey shaded areas are added to conceptually illustrate the apodization. From Patent B.

estimated in the plane defined by the transmit focus. Again, by shifting the transmit focus of the columns, this plane can be translated throughout the volume.

In Fig. 3.22, an example of an actual implementation of the above described scheme is shown. The figure is from Paper M and shows the estimated velocities in a cross-section of a simulated cylindrical blood vessel with a parabolic flow having a peak velocity of $1\,\mathrm{m/s}$. The vessel has a diameter of $12\,\mathrm{mm}$ and is located at a depth of $3\,\mathrm{cm}$ oriented parallel to the transducer surface. The simulation setup is seen in Fig. 3.23. From the above discussion, it is clear that this setup constitutes the most challenging situation from a velocity estimation perspective: The blood is flowing at 90° relative to the ultrasound beam, which necessitates the use of Transverse Oscillation. Also, the flow in the vessel is out of the plane being imaged. This view would be impossible without estimation of all three components of the velocity vector, which requires a 2-D transducer array. In the simulation, the array is a $3\,\mathrm{MHz}$, $64 + 64$ row-column addressed array with $\lambda/2$-pitch closely resembling the array used for the measurements in Section 3.5.3.

Using Field II (Jensen 1996c; Jensen and Svendsen 1992), the velocities were estimated by emitting along 11 evenly distributed lines in the plane perpendicular to the vessel. The lines were steered from -12° to 12° with an inter-spacing of 2.4°. One

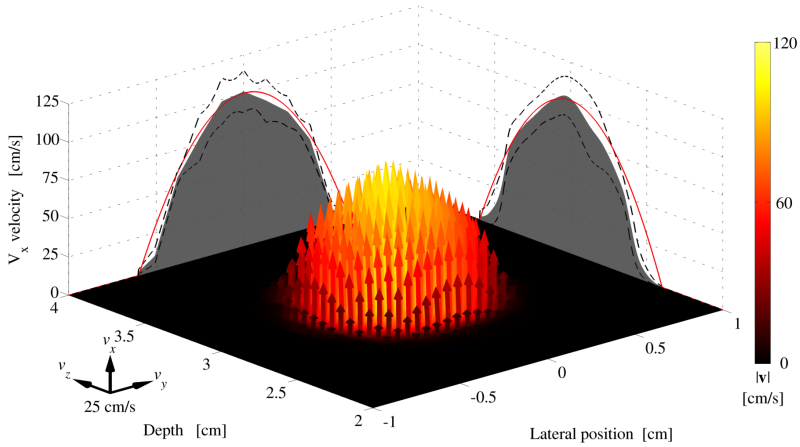

Figure 3.22: Estimated velocities from the cross-section of a simulated $1.2\,\mathrm{cm}$ diameter cylindrical blood-vessel positioned at a depth of $3\,\mathrm{cm}$. The setup is seen in Fig. 3.23. The arrows show the estimated mean from 10 frames, and the velocity profile along a line through the center of the vessel in both the y- and z-directions is projected on the side-walls of the plot. The grey area shows the mean velocity, the two dashed lines the standard deviation and the red line the true velocity. From Paper M.

frame was made by first performing 2×32 focused emissions along the first line, with alternating emissions using all rows, respectively all columns. When the rows were emitting, the columns were receiving and vice versa. The received data allowed estimation of the two lateral components of the velocity vector. For this purpose, two apodization peaks separated by $d = 9.7\,\mathrm{mm}$ was used, and the angle between the two receive beams for in-phase and quadrature signals were consequently $\theta = 1.48°$ in accordance with Eq. (3.26). The axial component of the velocity vector may be estimated using received data from either the rows or columns. In this case, the received data from the columns were used. This procedure was repeated for each of the 11 lines, after which the whole sequence was repeated a total of 10 times to produce 10 frames.

The arrows in Fig. 3.22 show the mean of these 10 frames. The velocity profile along a line through the center of the vessel in both the y- and z-directions is projected on the side-walls of the plot. The grey area shows the mean velocity, the two dashed lines the standard deviation and the red line the true velocity. It is seen that the estimator is able to predict the velocity with a bias of $-8.6\,\%$ for the x-direction, $-0.6\,\%$ for the y-direction, and $-0.1\,\%$ for the z-direction. The maximum velocity in the vessel was estimated to be $1.02\,\mathrm{m/s}$, which is $2\,\%$ higher than the actual peak velocity.

These results show that it is indeed possible to use row-column addressed arrays

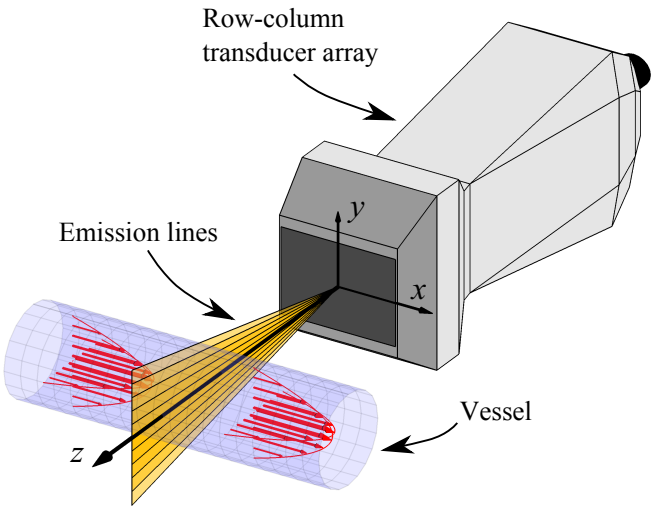

Figure 3.23: Simulation setup used for evaluating the velocity estimator. The emisson lines are the lines along which beamforming is performed for the axial velocity estimation. The two lateral velocity estimates are found using pairs of beamformed lines on either side of the shown lines in each lateral direction separated by $\lambda_x/4$ as shown in Fig. 3.20(a). The estimated velocity is shown in Fig. 3.22. From Paper M.

for estimating 3-D velocities. The view seen in Fig. 3.22 would be highly relevant for clinical examinations, as it allows for direct measurement of the volume flow through a blood vessel independent of the operator and transducer angle. It is stressed that such a view has only previously been demonstrated with a fully addressed 2-D transducer with $1024/128 = 8$ times the number of channels used in this example (Pihl and Jensen 2014; Pihl, Stuart, et al. 2014).

3.7 Chapter Summary

This chapter described the concept of row-column addressed arrays, and presented an analysis and optimization of their imaging performance. After a brief literature review, the imaging principle behind row-column addressed 2-D arrays was described including an estimate of the resolution and contrast obtainable with such arrays relative to fully addressed 2-D arrays. Then, the beamforming required to produce volumetric images was developed based on the findings in Paper J. Subsequently, it was shown that the long elements in row-column addressed arrays produce edge effects that lead to ghost echoes in the final beamformed image. A solution was proposed in the form of integrated apodization, which was demonstrated both theoretically and experimentally to mitigate

the edge wave problem as covered in Papers I and J. An optimized apodization layout was developed that efficiently damps the edge waves without affecting the imaging performance of the array. The technique was demonstrated both by simulations and experimentally based on Papers J and K as well as Patent A. The last part of the chapter described how row-column addressed arrays can be used to estimate velocities in a volume as covered by Patent B. A simulated example from Paper M incorporating a blood vessel phantom was used to demonstrate the performance of the technique, proving that it is indeed able to estimate all three components of the velocity vector and thereby estimate key parameters such as the volume flow.

CHAPTER 4

Microfabrication

In this chapter, the microfabrication of CMUT arrays is described. A brief review of the two prevalent fabrication methods found in the literature is given, followed by an account of the few reported attempts to produce row-column addressed CMUT arrays. Two critical aspects of CMUT microfabrication, oxide quality and oxide protrusions, are discussed in detail, partly based on Paper G. The fabrication approach presented in Paper F is introduced as an effective solution to the problem of oxide protrusions. This approach is then incorporated in a new process for fabricating row-column addressed 2-D CMUT arrays. Although such arrays are successfully produced, the process is shown to have certain drawbacks that could potentially compromise the device reliability. Consequently, a modified process based on LOCOS oxidation is introduced, effectively eliminating the limitations of the previous process. The chapter is concluded with a discussion of issues with production yield experienced during fabrication. The source of the limited yield is identified and a solution to the problem is proposed.

4.1 Available Methods

In the literature, two prevalent methods of fabricating CMUTs have been demonstrated: Sacrificial release and wafer bonding. Sacrificial release was applied in the demonstration of the first micromachined CMUTs (Haller and Khuri-Yakub 1994, 1996), and has since been used in numerous realizations of both 1-D arrays (Jin, Oralkan, et al. 2001; Oralkan, Ergun, Johnson, et al. 2002; Oralkan, Jin, Degertekin, et al. 1999; Oralkan, Jin, Kaviani, et al. 2000; Savoia, Caliano, and Pappalardo 2012), 2-D arrays (Oralkan, Ergun, Cheng, et al. 2003), and annular ring arrays for catheter use (Demirci et al. 2004; Nikoozadeh et al. 2009; Yeh et al. 2006). As the name suggests, this process uses sacrificial layers of thin-films to create the CMUT cavities. Fig. 4.1 shows an example of such a process in one of its more simple forms (Jin, Ladabaum, and Khuri-Yakub 1998). Here, a silicon wafer is used as the starting substrate (a). It is highly doped to make it electrically conductive, so that the silicon substrate can be used as a common bottom electrode for all elements in the array. A thin layer of low-pressure chemical-vapor deposition (LPCVD) nitride (Si_3N_4) is then deposited as an etch stop in the sacrificial etch step performed later (b). A layer of amorphous silicon is then deposited (c) and patterned using lithography and dry etching (d). This layer is the sacrificial layer that will form the CMUT cavities after removal. Other materials such as silicon dioxide (Jin, Ladabaum, and Khuri-Yakub 1998) or chromium (Savoia, Caliano, and Pappalardo 2012) may also be used as sacrificial

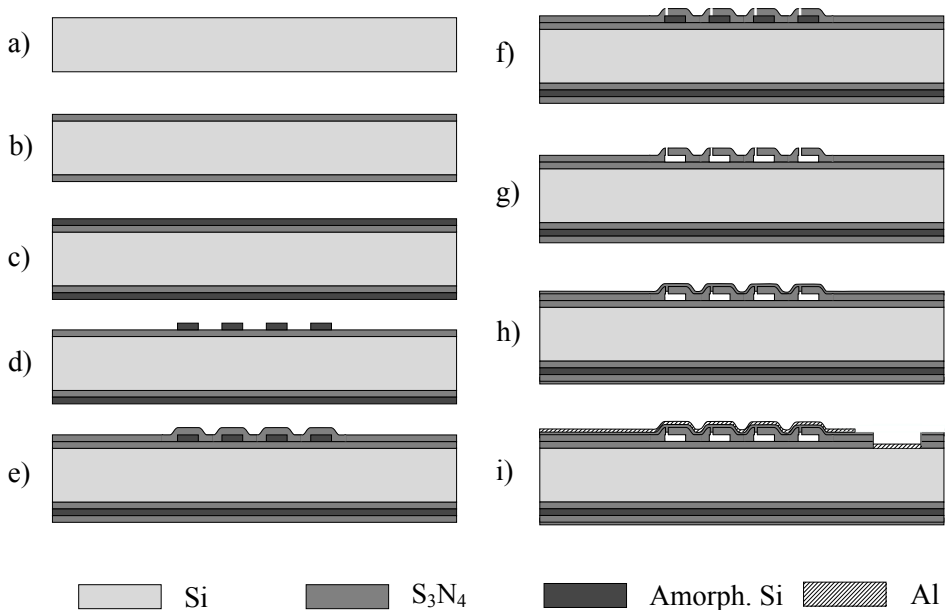

Figure 4.1: A simple process flow illustrating the sacrificial release technique commonly used for fabricating CMUTs. a) Higly doped silicon wafer, b) first nitride deposition, c) amorphous silicon deposition, d) patterning, e) second nitride deposition, f) etch via holes, g) sacrificial etch, h) vacuum sealing with third nitride deposition, i) open to substrate, metallize, and pattern metal.

layers. Next, a second layer of LPCVD nitride is deposited (e) and small holes are etched through the nitride layer (f) to allow for removal of the sacrificial silicon layer in potassium hydroxide (KOH), which selectively etches the silicon (g). Finally, the etch holes are sealed with a nitride deposition (h), and after opening to the bottom substrate, aluminium is sputtered and patterned to produce the top electrodes and contacts (i).

There are, however, some drawbacks with the sacrificial release method. Amongst these are high residual stresses in the thin-films, sticktion of larger membranes during sacrificial release due to capillary forces, and loss of active area due to etch channels (Ergun et al. 2005; Khuri-Yakub and Oralkan 2011). As a consequence, an alternative fabrication method was introduced in 2003 by Huang and colleagues (Huang et al. 2003). This technique is based on wafer or fusion bonding, a well-known technique used for joining two silicon wafers in a strong covalent bond. In Fig. 4.2, a commonly used process is shown (Huang et al. 2003). As in the sacrificial release method, a highly doped silicon wafer is used as a starting point (a). The wafer is thermally oxidized (b), and the oxide is patterned through a lithography mask using either wet or dry etching of the oxide (c).

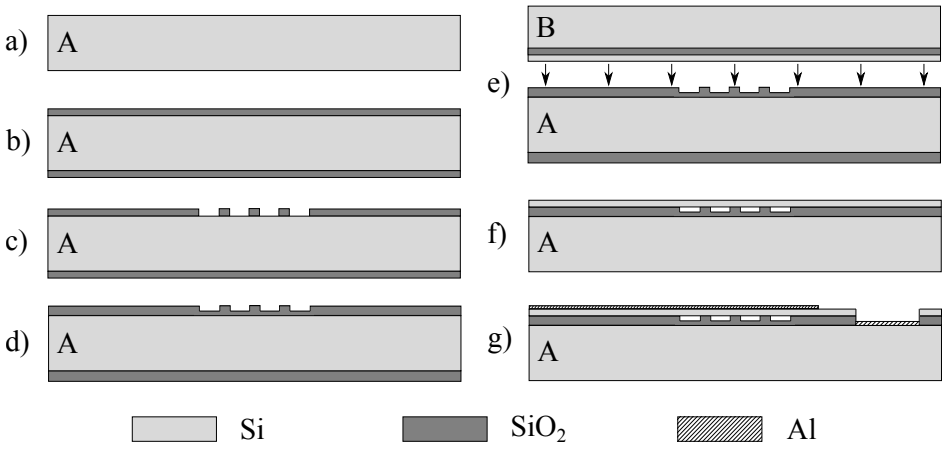

Figure 4.2: A simple process flow illustrating the wafer bonding technique commonly used for fabricating CMUTs. a) Higly doped silicon wafer, b) first thermal oxidation, c) patterning, d) second thermal oxidation for insulation oxide, e) wafer bonding, f) handle and oxide removal, g) open to substrate, metallize, and pattern metal. The two wafers are labeled A and B, respectively, where B is an SOI wafer.

This forms the CMUT cavities, and a second thermal oxidation is subsequently performed to produce an insulating oxide in the bottom of the cavities (d). An insulating oxide is needed to avoid electrical shorting of the top-and bottom electrodes in case of pull-in. As covered in Section 4.2, fabrication trials in this project have also shown that significant leak currents are allowed to run along the cavity side-wall in the absence of an insulation oxide.

The next step is then to bond a second wafer onto the first, thereby sealing off the cavities (e). The bonding is usually performed in an evacuated chamber to produce vacuum sealed cavities. Vacuum sealed cavities eliminates impurities that may cause device failure, and improves the performance by removing squeeze-film damping. The second wafer is a silicon-on-insulator (SOI) wafer composed of a thick ($\sim 500\,\mu\mathrm{m}$) silicon handle layer and thin silicon device layer with a buried oxide (BOX) layer in between, both being in the order of $1\,\mu\mathrm{m}$ in thickness. By removing the handle layer and BOX layer, e.g. using two consecutive etches, the thin device layer is left suspended over the cavities forming the top plate of the CMUT (f). The term plate and not membrane is deliberately used, since the silicon plate is ideally stress-free, which creates a plate-like behaviour. This is opposed to the membrane-like behaviour of e.g. a silicon nitride membrane with residual stress made using a sacrificial release process. The device layer may be highly doped in which case the CMUT plate is conductive and acts as a top electrode. However, the plate is usually metallized simultaneously with the subsequent contact metallization

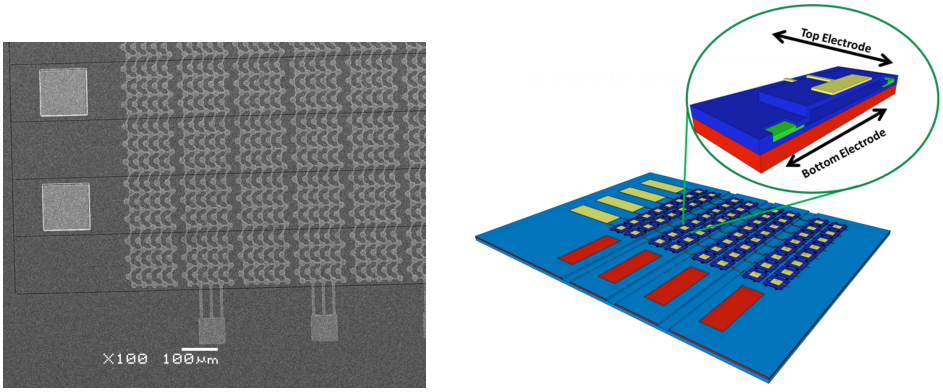

(a) (b)

Figure 4.3: The two types of 2-D row-column addressed CMUT arrays presented in the literature by the group of Yeow (a) and the group of Zemp (b), respectively (Logan, Wong, and Yeow 2009; Zemp, Zheng, and Zhang 2011).

to compensate for the non-negligible electrical resistance of the thin silicon plate (g).

There are a number of advantages associated with the fusion bonding technique compared to the sacrificial release method. First, the limitations on CMUT size and cavity gap height posed by the sacrificial release method are much less pronounced in the wafer bonding approach, in which cavities with large aspect ratios are achievable. This combined with the fact that the cavity and plate are defined on two different wafers allows for increased design flexibility. Furthermore, the number of process steps is generally reduced compared to sacrificial release methods, which is beneficial for both production costs and production yield (Ergun et al. 2005; Huang et al. 2003). Finally, the plate material can be made of single-crystalline silicon with well-defined mechanical properties, which increases the predictability of the device behaviour. For these reasons, the wafer bonding approach has been used in several more recent publications in the literature (Huang et al. 2003; Kupnik et al. 2010; Park and Khuri-Yakub 2012; Park, Lee, Kupnik, and Khuri-Yakub 2011; Park, Lee, Kupnik, Oralkan, et al. 2008; Zhuang et al. 2009), and is also chosen as the basis for the work presented in this thesis.

There have only been two attempts to fabricate 2-D row-column addressed CMUT arrays. The first was presented in 2009, where the group of Yeow demonstrated the fabrication of a $32 + 32$ row-column addressed array made using nitride-nitride bonding (Logan, Wong, and Yeow 2009). Identical arrays have subsequently been used for experimental investigations (Chen, Wong, Logan, et al. 2011; Chen, Wong, and Yeow 2014; Logan, Wong, Chen, et al. 2011; Wong et al. 2014). The fabrication approach

uses a silicon wafer as a substrate on which a thermal oxide is grown. On top of this, doped LPCVD polysilicon is deposited, chemically-mechanically polished, and patterned to form the bottom electrodes. A layer of LPCVD nitride is deposited on the bottom electrodes, and the CMUT cavities are etched into the nitride. A second wafer covered with a layer of nitride is bonded onto the structured wafer, which leaves a thin nitride membrane suspended over the cavities after etching away the top wafer. Contact holes are opened to the bottom electrodes and an aluminium layer is evaporated onto the nitride membrane and patterned to form contacts and top electrodes oriented orthogonal to the bottom electrodes. A micrograph of the device is seen in Fig. 4.3(a).

The second attempt was presented by the group of Zemp, who used a slight modification of a sacrificial release method (Zemp, Zheng, and Zhang 2011). Arrays made using this approach have also been used for experimental investigations (Chee et al. 2014; Sampaleanu et al. 2014). In this technique, bottom electrodes are made by patterning an SOI wafer. This wafer is then used as the substrate wafer for the sacrificial release process, which is similar to the one presented above in Fig. 4.1. An illustration of the structure is shown in Fig. 4.3(b).

In the following, the development of several new fabrication processes are presented, both for 1-D CMUT arrays and in particular for 2-D row-column addressed CMUT arrays. All are based on the wafer bonding method, and all use thermal silicon dioxide as the insulating material between the top- and bottom electrodes. As a consequence, the two most critical parameters are the mechanical quality of the wafer bonding and the electrically insulating properties of the oxide. These two subjects are therefore covered in the two following sections before the full fabrication processes are presented.

4.2 Oxide Quality

In Chapter 2, it was found that the pull-in voltage of the CMUT should be as high as possible to produce the highest output pressure and the highest sensitivity (for a voltage readout). The definition of "as high as possible" depends on two factors: How high voltages the external electronics can supply and comply with and how high voltages the CMUT itself can withstand. With regard to the latter, the insulator separating the top- and bottom electrodes is the limiting factor. In case of a fusion bonded CMUT, the insulating material is silicon dioxide, which can withstand electric fields up to 0.5-1 $\mathrm{V/nm}$ before the insulating properties break down (May and Sze 2004, p. 53). This is only true for high-quality dry oxides with few impurities. A typical CMUT, such as the one presented in Paper K, has a total oxide thickness of roughly $700\,\mathrm{nm}$, and an insulation oxide thickness of $300\,\mathrm{nm}$. As described in Paper K, the pull-in voltage of the device is $100\,\mathrm{V}$, such that the electric field seen by the insulation oxide in the event of pull-in will be $0.33\,\mathrm{V/nm}$. This example illustrates that high quality oxides are essential if the CMUT is to function without the risk of oxide breakdown.

For this reason, considerable time was spent in the beginning of the project on testing

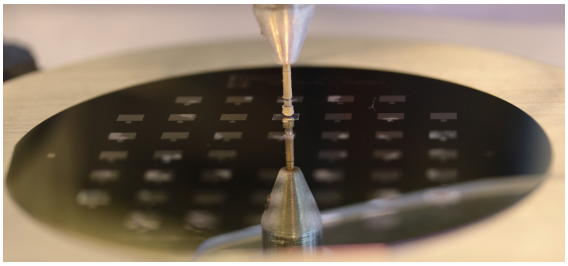

Figure 4.4: Setup used to test the quality of the thermal oxide grown in the furnaces.

the quality of the oxides grown in the furnaces at the Danchip cleanroom. Initially, tests were made on fabricated CMUTs, which showed very high leakage currents even at a few volts. The source of this leakage current turned out to originate from within the CMUT cavities, which did not have insulation oxides in the bottom of the cavities in the very first prototype iterations. It thus became clear that an insulation oxide is essential, and any oxide quality test should be performed on a simple metal-oxide-semiconductor (MOS) structure, in which the metal is structured to ensure that no surface currents may flow between the two electrodes.

Fig. 4.4 shows an image of the setup developed to test the oxides: A $100\,\mathrm{nm}$ thick thermal oxide is grown on a highly doped silicon wafer, and a layer of $200\,\mathrm{nm}$ aluminium is deposited through a shadow mask to define 44 pads of equal size. Then, the oxide on the back of the wafer is stripped in hydrofluoric acid with the front protected by photoresist. In the test setup, the wafer is put on a grounded chuck, and a probe needle is placed on the metal pads as seen in Fig. 4.4. The voltage is then ramped up and the current monitored to identify the breakdown voltage of the oxide. The breakdown voltage was initially found to be in the order of 0.1-$0.6\,\mathrm{V/nm}$, varying considerably from test to test. As the tested oxides had experienced a minimum of processing, it was concluded that the source of the poor oxide quality was contaminated oxide furnaces. After replacing the quartz tubes in the furnaces, the oxide quality was significantly improved, yielding breakdown voltages in the range 0.7-$1\,\mathrm{V/nm}$. An example of a set of measurements on a test wafer with high quality oxide made after the furnace tube replacements is seen in Fig. 4.5. For low voltages, only the noise floor of the measurement setup is seen. At higher voltages, the Fowler-Nordheim tunnelling current characteristic of high quality oxides is observed (Lenzlinger and Snow 1969). Finally, the breakdown of the oxide occurs, which is seen as an abrupt increase in current up to the compliance of the measurement equipment.

Initially, the oxide quality was so poor that a row-column fabrication process was developed which did not use the grown oxides as insulating material. Rather, all potentials were supported by the BOX layers. The process, which is presented in Paper H, involved a number of complex processing steps, and it was therefore abandoned quickly after the oxide quality issue had been resolved.

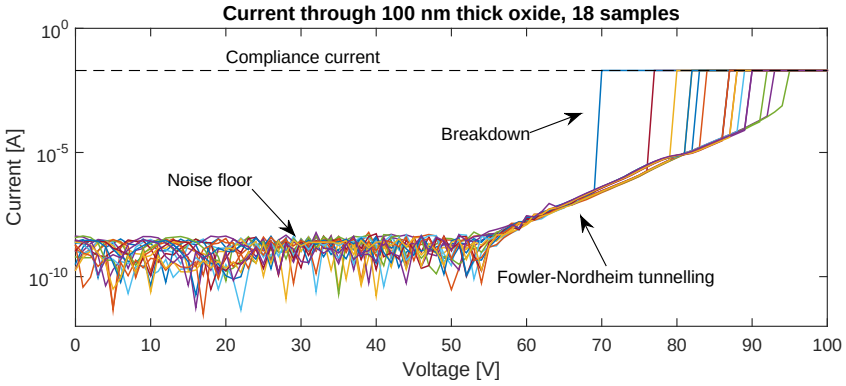

Figure 4.5: Example of a set of 18 measurements performed on a single test wafer with $100\,\mathrm{nm}$ dry oxide. The compliance current is set by the measurement equipment. Note the tunnelling currents before breakdown, which are expected in high quality oxides.

4.3 Protrusions

Using fusion bonding for fabricating CMUTs demands extreme cleanliness and very low surface roughness of the wafers. When the two wafers are joined, an initial bond is established even at room temperature due to van der Waals interactions and hydrogen bonds. A subsequent annealing step at high temperature promotes the creation of strong covalent bonds, which fuses the two wafers. A prerequisite for the bonds to form, however, is that the RMS surface roughness is in the order of $0.5\,\mathrm{nm}$ (Plössl and Kräuter 1999). Commercially available silicon wafers have a surface roughness in the order of Ångstrøms, so this requirement is in general met for unprocessed wafers. However, processing of the wafer may introduce increased surface roughness or protruding structures that inhibit the wafer bonding.

The latter is an issue for the commonly used approach originally introduced by Huang and colleagues (Huang et al. 2003). During the second oxidation step that forms the insulating oxide in the bottom of the CMUT cavities (see Fig. 4.2(d)), 2-D oxidation effects will lift the cavity edges, creating protrusions at the surface. Fig. 4.6 shows a close-up of the CMUT cavity near the cavity edge after the second oxidation. The structure has been simulated using Athena 5.20.0.R (Silvaco Inc., Santa Clara, CA, USA). The first oxide acts as a partial diffusion mask during the second oxidation, resulting in a slower oxide growth at the masking oxide than in the cavity, in which the oxide has been removed during the etching step (Fig. 4.2(c)). There will be a transition region in the vicinity of the cavity edge, where the oxide mask is lifted as seen in Fig. 4.6. Depending on the protrusion height h, this protruding oxide may prevent successful bonding. A thorough investigation of the mechanism behind the protrusion formation and the parameters that

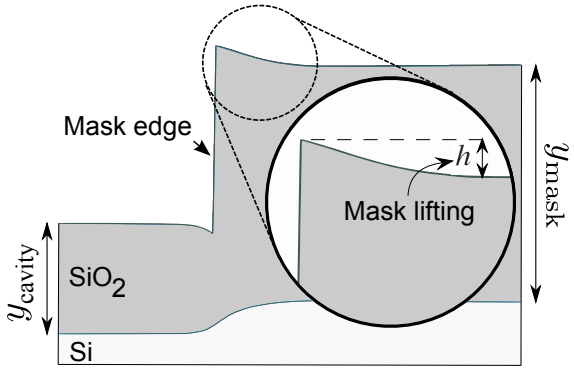

Figure 4.6: Simulated oxide geometry in the vicinity of the CMUT cavity edge showing the lifting of the oxide after the second thermal oxidation. From Paper G.

influence the protrusion height was therefore presented in Paper G. In the following, the main findings of this paper are given.

4.3.1 Oxidation Model

The oxide growth in the vicinity of an oxide step such as that formed by the CMUT cavities can be modeled under the assumption that the oxidation rate is diffusion limited. In the oxide film, the continuity equation governs the transport of the oxidant. For realistic diffusion times $t > y_{\text{ox}}^2/(4D)$, where y_{ox} is the thickness of the oxide and D is the diffusivity, the diffusion will be almost stationary, such that the time derivative of the oxidant concentration C becomes

$$\frac{\partial C}{\partial t} = D\nabla^2 C \simeq 0 \,, \tag{4.1}$$

where ∇^2 denotes the Laplace operator. Hence, the oxide growth rate can be expressed directly as a function of the flux density normal to the silicon/oxide interface, J,

$$\frac{ds}{dt} = \frac{J}{N} \,, \tag{4.2}$$

where s is the oxide thickness at time t at the silicon/oxide interface, and N is the number of oxidizer molecules incorporated per unit volume of the oxide. Thus, if the normal incident flux density at the interface can be found, the oxide thickness can be calculated by a time integration of Eq. (4.2).

This can be achieved by use of conformal mapping, covered in detail in Paper G, with which the flux- and concentration distribution in the structured oxide can be calculated. As an example, Fig. 4.7 shows the iso-concentration and iso-flux contour lines of an oxide

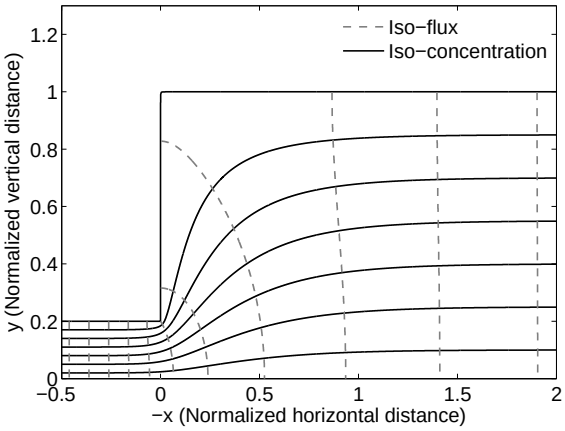

Figure 4.7: Iso-concentration and iso-flux lines in an oxide step geometry calculated using the conformal mapping approach. The distances are normalized to the thickness of the mask oxide (to the right of the step). From Paper G.

step with a thickness ratio of $y_{\text{mask}}/y_{\text{cavity}} = 5$, where y_{cavity} is the thickness of the oxide grown in the cavities and y_{mask} is the thickness of the oxide mask. The definition of these thicknesses are shown in Fig. 4.6. The flux density at the step, J_0, is in the derivation in Paper G shown to be proportional to the flux density in the cavity oxide, J_{cavity},

$$J_0 \simeq 0.83 J_{\text{cavity}} \ . \tag{4.3}$$

The ratio of the oxide grown at the step to the oxide thickness grown in the cavity far from the step, β, thus becomes a constant, since

$$\beta = \frac{\int_0^{t_0} J_0(t)/N dt}{\int_0^{t_0} J_{\text{cavity}}(t)/N dt} = 0.83 \frac{\int_0^{t_0} J_{\text{cavity}}(t)/N dt}{\int_0^{t_0} J_{\text{cavity}}(t)/N dt} = 0.83 \ . \tag{4.4}$$

The lifting of the mask at the mask edge at time t, denoted h in Fig. 4.6, may then simply be expressed as

$$h(t) = 0.56\{\beta y_{\text{cavity}}(t) - [y_{\text{mask}}(t) - y_{\text{mask}}(0)]\} \ , \tag{4.5}$$

where the factor of 0.56 accounts for the volume expansion by a factor of 2.2 of the growing oxide compared to the consumed silicon (May and Sze 2004, p. 43).

It is seen from Eq. (4.5) that the mask lifting becomes a function only of the oxide thicknesses far from the step, which may be found using Deal and Grove's model (Deal and Grove 1965). This states that the thickness of the growing oxide at time t is

$$y_{\text{ox}} = \sqrt{\frac{A^2}{4} + B(t+\tau)} - \frac{A}{2} \ , \tag{4.6}$$

where τ is the time shift induced by an already existing oxide. The constants A and B are found via the parabolic and linear rate constants, B and B/A, given by

$$B = B_0 \exp\left(-\frac{E_{a,B}}{k_B T}\right) , \tag{4.7}$$

$$\frac{B}{A} = \frac{B_0}{A_0} \exp\left(-\frac{E_{a,B/A}}{k_B T}\right) , \tag{4.8}$$

where k_B is Boltzmann's constant, T is the absolute temperature, $E_{a,B}$ and $E_{a,B/A}$ are activation energies, and B_0 and B_0/A_0 are the parabolic and linear rate constants in the infinite temperature limit. The relevant values are given in Paper G. The partial pressure, P, of the oxidant during the oxidation influences the parabolic and linear rate constants, such that for a reference pressure of $P_0 = 1$ atm, the pressure dependency is given by

$$\frac{B}{A}(P) = \frac{B}{A}\frac{P}{P_0} , \tag{4.9}$$

$$B(P) = B\frac{P}{P_0} . \tag{4.10}$$

4.3.2 Parameter Dependency

From Eq. (4.5), the mask lifting's dependency on processing parameters can be deduced. Both the initial mask oxide thickness, $y_{\text{mask}}(0)$, and the final thickness of the oxide grown in the cavity, y_{cavity}, is assumed fixed. Thus, the only variable is the final mask oxide thickness, with thicker mask oxides yielding smaller mask lifting. The thickness of the oxide can be described by Eq. (4.6). In the limit of large values of $t + \tau$, where the oxidation time t is dictated by the desired thickness of the oxide in the cavities, and τ is dictated by the initial mask oxide thickness, Eq. (4.6) reduces to

$$y_{\text{ox}} \simeq \sqrt{B(t+\tau)} \, , t + \tau \gg 0 . \tag{4.11}$$

The final oxide mask thickness therefore becomes

$$y_{\text{mask}} = \sqrt{y_{\text{cavity}}[y_{\text{cavity}} + A] + y_{\text{mask}}(0)[y_{\text{mask}}(0) + A]} . \tag{4.12}$$

If both y_{cavity} and $y_{\text{mask}}(0)$ are constants, the mask lifting depends only on the constant A, which relates to the oxidant diffusivity D and surface reaction rate k as $A = 2D/k$ (Deal and Grove 1965). In Fig. 4.8, A has been plotted for both dry and wet oxidations in the relevant temperature range. It is seen that A decreases for increasing temperatures, and thus the final mask oxide thickness will decrease for increasing temperatures. From Eq. (4.5), it is seen that this results in an increased mask lifting. This is true for both wet and dry oxidations. However, A decreases more rapidly for increasing temperatures for wet oxidations, indicating that the mask lifting will depend more strongly on temperature

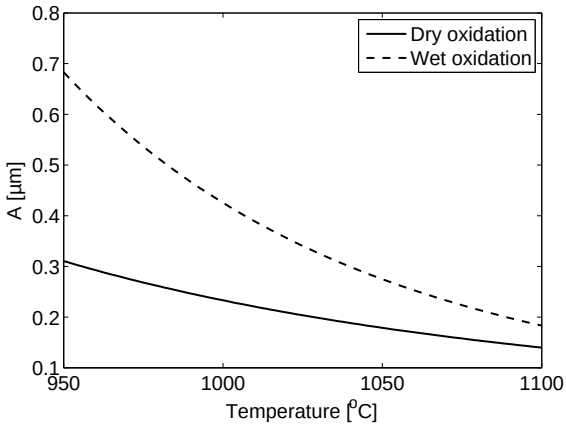

Figure 4.8: Plot of the constant A as a function of temperature for both dry and wet oxidations. From Paper G.

for wet oxidations compared to dry oxidations. In addition to this, A will, for a given temperature, be larger for wet oxidations than for dry oxidations, yielding a larger mask lifting for dry oxidations.

In order to experimentally investigate the processing parameter dependency, a total of 12 samples were fabricated. All samples had an initial oxide mask thickness of 357 nm, in which cavities were etched using either reactive ion etching (RIE) or buffered hydrofluoric acid (BHF). The two different etches were used to test the effect of having either an anisotropic etch (RIE), yielding an approximately right-angle step, or an isotropic etch (BHF) resulting in a more sloped and rounded cavity edge. For both types of etches, a second oxidation was performed. The second oxidation was carried out at different oxidation temperatures from 950 °C to 1100 °C for both wet and dry oxidations. The oxidation times for the respective oxidation temperatures were chosen such that a final thickness of roughly 200 nm was achieved in the cavities. Silicon dummy wafers were included in each oxidation, allowing the actual oxide thickness to be measured, the values of which are listed in Paper G. A total of six oxidations were carried out, each containing two samples; one with RIE etched cavities and one with BHF etched cavities. No wet oxidations were performed at 1050 °C and 1100 °C, as the required oxidation time to reach 200 nm is impractically short (< 15 minutes), potentially resulting in a less well-defined and homogeneous oxide. Further details on the sample preparation is given in Paper G.

The protrusions were then measured using atomic force microscopy (AFM), and the measured profiles were compared to simulated profiles, the details of which is found in Paper G. Fig. 4.9 shows the measured and simulated profiles of the oxide mask in the vicinity of the mask edge after the second oxidation. Each plot shows the result for a

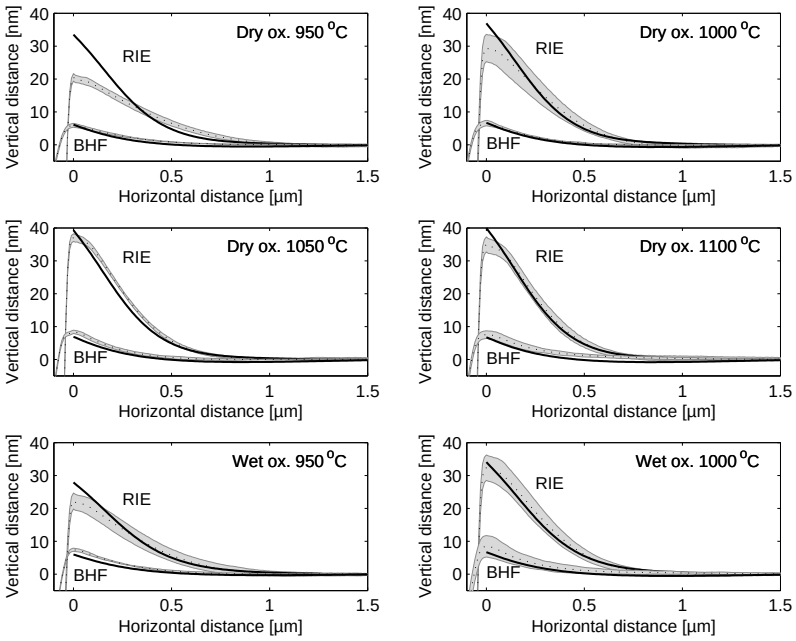

Figure 4.9: Simulated and measured profiles of the mask surface in the vicinity of the cavity edge. The dotted lines indicate the mean of the measurements while the shaded area shows ± 2 standard deviations. The solid black lines show the simulated profiles. From Paper G.

given temperature at either dry or wet oxidation. Furthermore, the results from both RIE and BHF etched oxide masks are given in each plot. In Fig. 4.10, the simulated and measured mask lifting at the cavity edge has been extracted for each of the six oxidation temperatures and -types. The figure has been divided into four sections, equivalent to the four combinations of wet and dry oxidations, RIE and BHF mask etchings. Furthermore, for the RIE etched masks, the analytical prediction given by Eq. (4.5) has been plotted along with the measured and simulated values. Only the RIE etched mask has been compared to the analytical prediction, since the assumption of a right-angle edge is poor for an isotropically BHF etched cavity.

It is seen that the analytical prediction in general overestimates both the measured and the simulated mask lifting. The deviation from the measured values is expected, since the simulated values also overestimate these. The reason for the deviation between the analytical and the simulated values can be explained by the fact that the conformal mapping, on which the theory is based, assumes a right angle oxide step and a flat oxide-silicon interface at all times, which is of course a simplifying assumption. Furthermore,

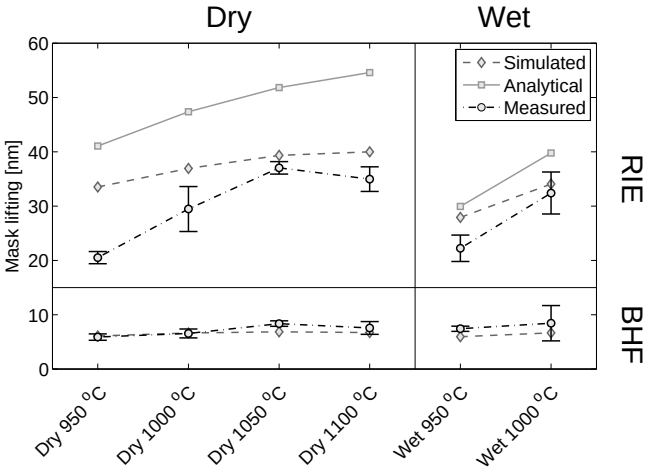

Figure 4.10: Mask lifting at the cavity edge as a function of oxidation temperature and type for oxide mask etched by either RIE or BHF. Both measured, simulated and analytically estimated values are given. From Paper G.

the simulated profile considers the top surface of the oxide mask, while the conformal mapping only considers the oxide grown at the silicon/oxide interface, i.e. below the mask. Thus, the geometrical deformation of the oxide mask created during growth is not captured by the theory.

Despite the mentioned discrepancies, both the simulated and the analytically estimated values of the mask lifting successfully capture the qualitative parameter dependency. As was predicted by Eq. (4.5), and confirmed by both simulations and measurements, the mask lifting increases with oxidation temperature. Note, however, that the temperature dependency seen in Fig. 4.10 is slightly misleading, since the final oxide thickness outside the mask is not exactly the same for all oxidations. Rather, it increases slightly with temperature (see Paper G), leading to an exaggerated temperature dependency.

The analytical estimate and the simulated values both predict that, for equal temperatures, the wet oxidations should yield smaller mask liftings than dry oxidations. Furthermore, they both predict a more pronounced temperature dependency for wet oxidations compared to dry oxidations. However, the measurements do not show significantly different mask liftings for wet and dry oxidations at 950 °C and 1000 °C, respectively.

In general, the oxidation temperature and oxidation type are seen to have only a minor influence on the mask lifting. As opposed to this, the type of etch used for the oxide mask exhibits a much more pronounced influence. Both simulations and measurements demonstrate significantly smaller mask liftings for BHF etched masks compared to RIE etched masks. For all temperatures, the measured mask lifting is on average a factor of

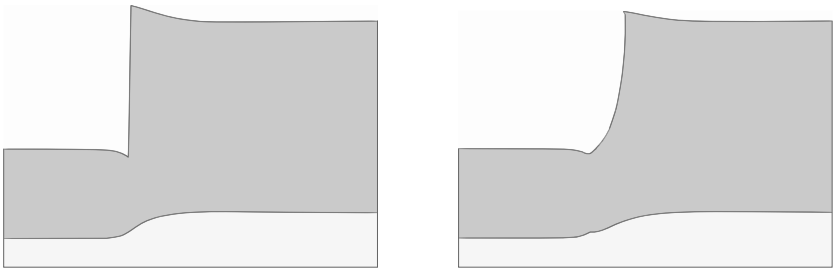

(a) (b)

Figure 4.11: Simulations of the oxide geometry in the vicinity of the CMUT cavity edge in the case of an anisotropically (a) and an isotropically etched cavity (b). Both simulations show the final geometry after the second oxidation.

four higher for the RIE etched masks compared to the BHF etched masks. This effect is to be expected, since the sloped mask edge created by the isotropic BHF etch impedes the oxidant diffusion from the side of the mask. This may be seen from Fig. 4.11, where the simulated structures are shown after the second oxidation. Fig. 4.11(a) shows the case for the anisotropically etched cavities, while Fig. 4.11(b) shows the isotropic case.

Regardless of the processing parameters, it is seen that the protrusion height by far exceeds the $0.5\,\mathrm{nm}$ required to achieve good fusion bonding. In practice, the protrusions must therefore be removed before bonding can take place. This has in previous examples from the literature been done by either performing chemical-mechanical polishing or by a masked etch, in which the oxide is removed in the vicinity of the cavity etches, thereby removing the protrusions (Yoon et al. 2011). While this enables the bonding to take place, it also introduces additional processing steps, which is undesirable in terms of production cost and yield. Alternatively, a third approach could be to make a timed etch during the cavity etch (Fig. 4.2(c)), such that an insulating oxide is left in the bottom of the cavities. This would make the second oxidation superfluous, and thereby no protrusions would be created. However, timed etches are in general to be avoided, as they are difficult to control. Achieving a homogeneous result over an entire wafer is also very challenging and consequently the characteristics of the CMUTs would vary between and within arrays.

4.4 A New Process

As a solution to the protrusion problem, a new process was proposed in Paper F. In Fig. 4.12(a), the conventional process with a double oxidation is shown, illustrating the problem of protrusions. In Fig. 4.12(b), the proposed process is shown. Rather than

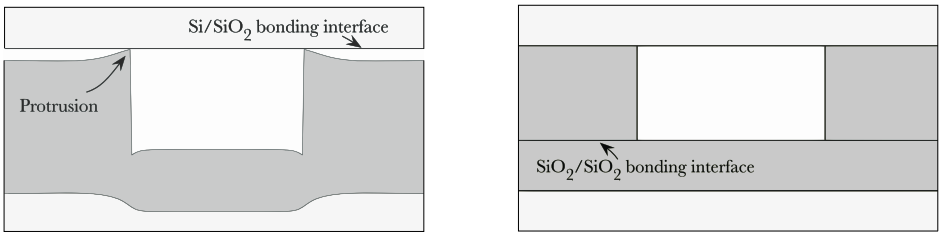

Figure 4.12: (a) The conventional wafer bonding process with a double oxidation resulting in protrusions that inhibit good bonding. (b) The proposed process in which the oxide with cavities and the insulation oxide is placed on two different wafers, thereby avoiding the protrusions. From Paper F.

performing a double oxidation, one oxidation is performed on each of the two wafers to be bonded. The cavities are then etched into one of the oxides and the oxide on the second wafer acts as the insulating oxide. By etching the cavities in the top SOI wafer (wafer B in Fig. 4.2), the resulting structure becomes identical to the one created by the conventional process with a single-crystalline silicon plate and insulation oxide in the bottom of the cavity.

To demonstrate the difference in bonding quality for the two processes, two wafers were made using each their process, both utilizing the cavity mask from Mask Set A. The processing was stopped just after the handle removal step corresponding to Fig. 4.2(f). Further details on the processing is given in Paper F. The result of the fabrication is seen in Fig. 4.13, showing one half of each of the two wafers. The color variation is due to variations in BOX layer thickness after the handle removal. It is evident from the figure that the thin silicon layer has broken off the arrays in the double oxidation approach due to the protrusions, demonstrating that additional processing is indeed needed in order to remove the protrusions and achieve good bonding. The array yield on this wafer was consequently only $7\,\%$. As opposed to this, the proposed process produced void-free bonding with an array yield of $100\,\%$. It is stressed that this is achieved without introducing further processing steps, and that the resulting structure is unaltered compared to the conventional process. For this reason, this process has been used as the base-line process at DTU for the fabrication of 1-D CMUT arrays. The detailed process parameters for this 1-D array process is given in the appendix as Process A.

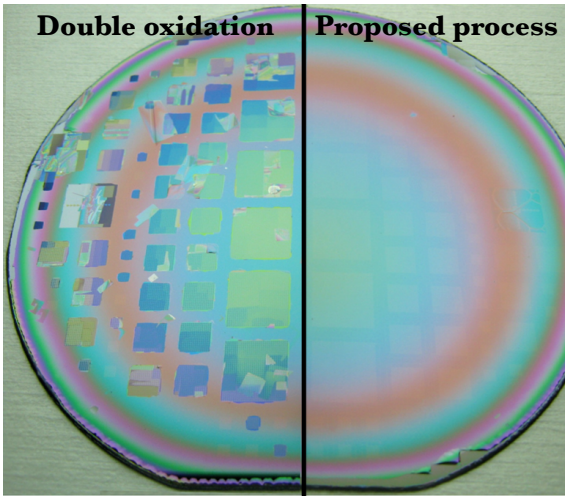

Figure 4.13: A split-screen view of the result of the array fabrication using the double oxidation process (left) and the proposed process (right), showing poor and excellent bonding results, respectively. The color variation is due to variations in BOX layer thickness after the handle removal. From Paper F.

4.5 Adaptation to Row-Column Arrays (Process B)

For the fabrication of 2-D row-column addressed arrays, the proposed process described in the previous section requires some modification as explained in the following. The process developed for such arrays is illustrated in Fig. 4.14; the detailed process parameters are listed in the appendix as Process B. As in the process proposed by Zemp and colleagues (Zemp, Zheng, and Zhang 2011), an SOI wafer is used as the starting substrate. The device layer is highly doped and has a thickness of $20\,\mu\mathrm{m}$. Following a dry thermal oxidation (Fig. 4.14(a)), a lithography step is performed to define the CMUT cavities, which are etched in a RIE etch (b). After stripping the photoresist, the bottom electrodes are then defined in the device layer using a second masked etch, in which both the oxide and the silicon device layer are etched using RIE (c). The thickness of the SOI device layer and its doping level is chosen such that the conductivity in the bottom electrode is sufficient for device operation. The handle layer only acts as a mechanical support, and the doping level is kept low to minimize the electrical conductivity and hence the capacitive coupling between elements via the handle substrate. Fig. 4.15(a) shows an optical micrograph taken after step c of a small $6 + 6$ element array made using Mask Set A. The yellow BOX layer of the wafer is seen between the vertically oriented bottom electrodes. The red circles are the CMUT cells, which have been etched into the thermally grown oxide. The bonding pads to the left and right of the array are isolated, and only act as mechanical

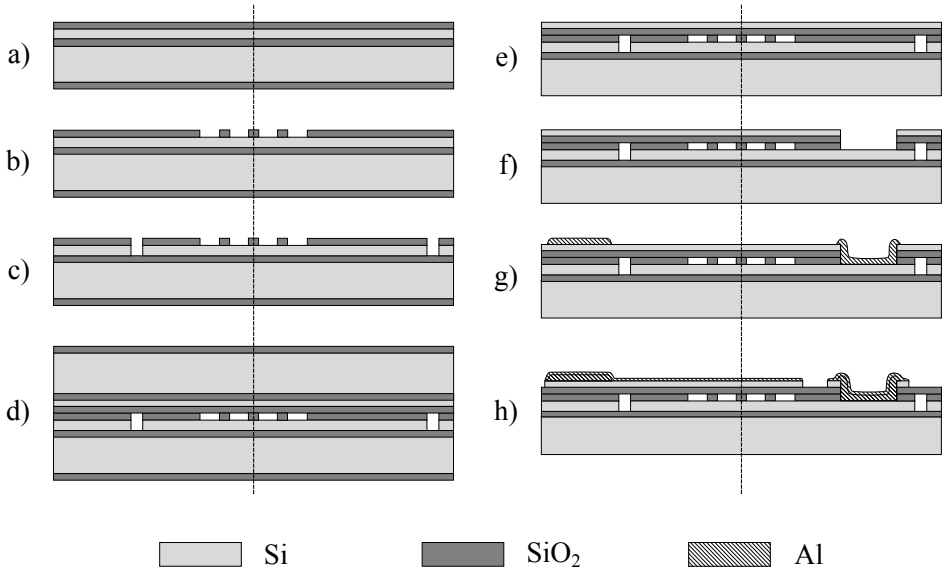

Figure 4.14: Process flow showing the first row-column process (in this thesis called Process B). The dashed line separates the layer composition comprising the top electrodes (to the left of the line) and the bottom electrodes (to the right of the line). The steps are: a) oxidation, b) cavity etch, c) bottom electrode etch, d) wafer bonding, e) handle etch, f) etch access to bottom electrodes, g) deposit and etch wire-bonding pads, and h) deposit and etch top electrodes. A total of five lithography masks are used (in steps b, c, f, g, and h). From Paper K.

support of the subsequently fabricated top electrode bonding pads.

Following the fabrication of the bottom wafer, a second SOI wafer with a highly doped $2\,\mu\mathrm{m}$ device layer is dry oxidized. Both SOI wafers are cleaned using a standard RCA cleaning procedure (Kern 1990) and bonded together in vacuum (0.01 mbar) using fusion bonding and a subsequent annealing step at 1100 °C (d). The oxide layer covering both wafers is removed in BHF, after which the handle layer and BOX layer of the top SOI wafer are etched using both RIE and BHF, respectively (e).

A third lithography step followed by selective RIE in first the silicon layer and subsequently the oxide layer is used to define openings to the bottom electrodes (f). The thin device layer is partly transparent in the visible spectrum, and alignment to the bottom wafer alignment marks can therefore be performed. Fig. 4.14(g) shows the wire-bonding pads, which are made by depositing a 800 nm aluminium layer on the entire wafer using electron beam evaporation. This is followed by a lithography step and a selective wet aluminium etch in $50\,^{\circ}\mathrm{C}$ phosphoric acid diluted in water (2:1). The top electrodes are then finally defined by a step similar to the previous, but this time with a 200 nm

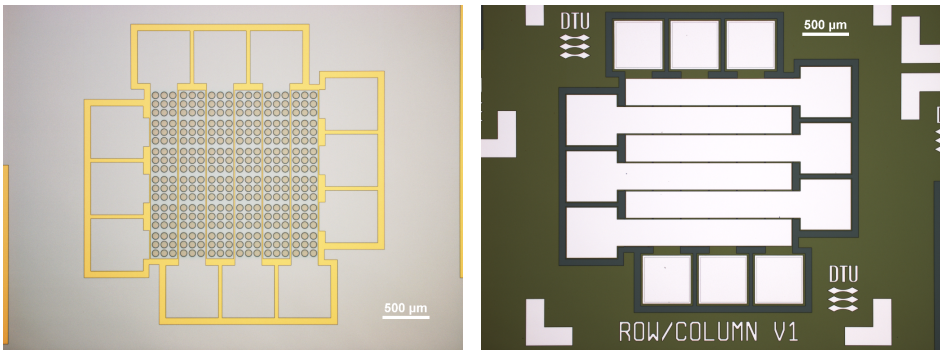

(a) (b)

Figure 4.15: Optical micrographs of a $6+6$ element row-column array made using Mask Set A in two different stages of the fabrication process. (a) shows the array at step c in Fig. 4.14, while (b) shows the completed array at step h in Fig. 4.14.

aluminium deposition. Before removing the photoresist, the exposed silicon layer is etched using deep RIE to isolate the individual top electrodes, thereby concluding the fabrication process (h). The advantage of the two consecutive aluminium deposition/etch steps is that thick contact pads can be made to facilitate wire-bonding, while at the same time avoiding a thick layer of aluminium on the CMUT plate, which would impact its performance. Fig. 4.15(b) shows the array from Fig. 4.15(a) after the fabrication of the array has been completed. The horizontally oriented top electrodes are now visible, and the color of the oxide has changed due to an increased thickness resulting from the bonding of the two wafers having each their oxide.

Note that this process uses five lithography steps, and, wherever possible, the same lithography step is used for multiple etches. The process is designed such that no critical lithography steps must be made on a heavily structured surface, which would have a negative impact on the lithography quality. For example, the bottom electrode etch is performed as the last step on the bottom wafer, and the bonding pads are defined before the top electrodes such that the structuring of the top plate is performed as the final step. Also, all etches use stop-layers that are highly selective to the respective etches, thereby omitting the need for timed etches. Any front-to-back or wafer-to-wafer alignment is avoided to improve the robustness of the process. In order to achieve this, the bonding process proposed in the previous section is flipped such that the cavities are defined on the same wafer as the bottom electrodes. If the cavities were made on the top SOI wafer, the two wafers would need alignment during bonding due to the presence of the bottom electrodes. The price for avoiding alignment during bonding is that the insulation oxide is

placed on the plate of the CMUT, which counteracts the benefit of having a pure silicon plate with highly predictable mechanical behaviour.

4.6 Second Row-Column Process: LOCOS (Process C)

Process B described in the previous section was successfully used to produce row-column addressed arrays. It was used for fabricating arrays with both Mask Set A and Mask Set B, and arrays produced with this process was used for the experimental data presented in the Papers I, K, and L. However, the process has some disadvantages: First, the insulation oxide is placed on the top plate of the CMUT, which makes the mechanical behaviour of the plate less predictable than if it were a single-crystalline silicon plate. As covered later in Section 4.7, problems with low fabrication yield due to stress problems and consequent plate rupture was also originally thought to be caused by this oxide. As explained in Section 4.7, this was, however later dismissed as the cause. A second and more obvious issue with the process is that the side-walls of the bottom electrodes are left exposed. This lack of electrical insulation renders arrays made with this process vulnerable to shorts between top- and bottom electrodes, which are only separated by the oxide that is suspended over the trenches made during the bottom electrode patterning.

For this reason, a second process was developed, which is shown in Fig. 4.16. The detailed processes parameters are given in the appendix as Process C. Inspired by the work of Park and colleagues (Park, Lee, Kupnik, and Khuri-Yakub 2011; Park, Lee, Kupnik, Oralkan, et al. 2008), this process incorporates local oxidation of silicon (LOCOS) to produce the CMUT cavities. The local oxidation is achieved by patterning a layer of nitride on top of the oxide. As seen in Fig. 4.16, this is done by first growing a thermal oxide, on top of which a layer of nitride and a layer of polysilicon is deposited (a). The polysilicon is then patterned using lithography and etched with RIE (b). The polysilicon is also stripped from the back side of the wafer, after which the nitride is wet etched in $180\,^{\circ}\mathrm{C}$ phosphoric acid (c). After stripping the polysilicon mask, a second lithography step is used to define the bottom electrodes, which are etched out using two consecutive RIE etches in the oxide and the silicon device layer, respectively (d). The device layer thicknesses of the SOI wafers are identical to those used in the process described in Section 4.5. A second thermal oxidation, the LOCOS oxidation, is then performed (e). The nitride prevents the diffusion of oxygen, such that additional oxide is only grown in the regions not covered by nitride. Therefore, a thick oxide is grown around the cavities defined by the patterned nitride. Importantly, also the side-walls of the bottom electrodes are oxidized in this process.

After completing the fabrication of the bottom wafer, the process is very similar to Process B described in Section 4.5. A second SOI wafer with a highly doped $2\,\mu\mathrm{m}$ device layer is bonded to the bottom wafer after RCA cleaning of both wafers (f). Note that, as opposed to the process in Section 4.5, the top wafer is not oxidized, since the insulation oxide is now located on the bottom wafer. The handle layer and BOX layer

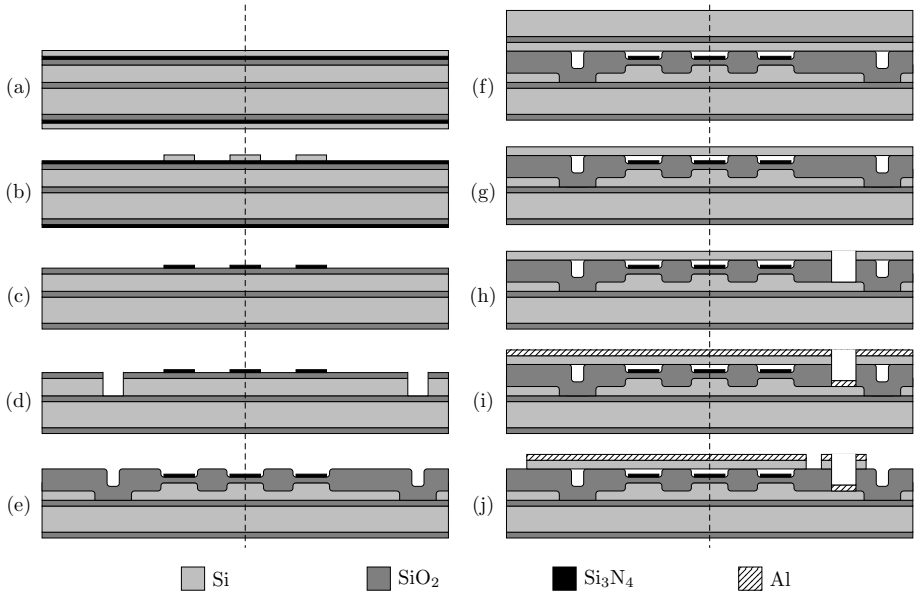

Figure 4.16: Process flow showing the second row-column process incorporating LOCOS oxidation (Process C). The dashed line separates the layer composition comprising the top electrodes (to the left of the line) and the bottom electrodes (to the right of the line). The steps are: a) oxidation, nitride deposition, and polysilicon deposition, b) cavity patterning in polysilicon, c) nitride etch and polysilicon strip, d) bottom electrode etch e) LOCOS oxidation, f) wafer bonding, g) handle etch, h) etch access to bottom electrodes, i) deposit titanium/aluminium, and j) etch top electrodes. A total of four lithography masks are used (in steps b, d, h, and j).

of the top SOI wafer are then etched using both RIE and BHF, respectively (g), after which contact openings to the bottom electrodes are defined using lithography and RIE of first the silicon layer and subsequently the oxide layer (h). Following this, $400\,\mathrm{nm}$ aluminium is deposited on the top side of the wafer (i). The layer is thicker than the layer used in Process B, since no contact pads are defined in Process C. This simplification of the process was made possible after concluding that $400\,\mathrm{nm}$ aluminium is sufficient for achieving good wire-bonding. Therefore, the same metal layer may be used for both bonding pads and top electrodes. As a further alteration from Process B, a $10\,\mathrm{nm}$ layer of titanium was deposited before the aluminium as an adhesion layer. This was done after experiencing problems with insufficient adhesion of the aluminium to the silicon, which caused some wire-bonds in mounted arrays to detach. Due to the Ti/Al layer, the selective aluminium wet etch used in Process B could not be used. Instead, the metal was etched

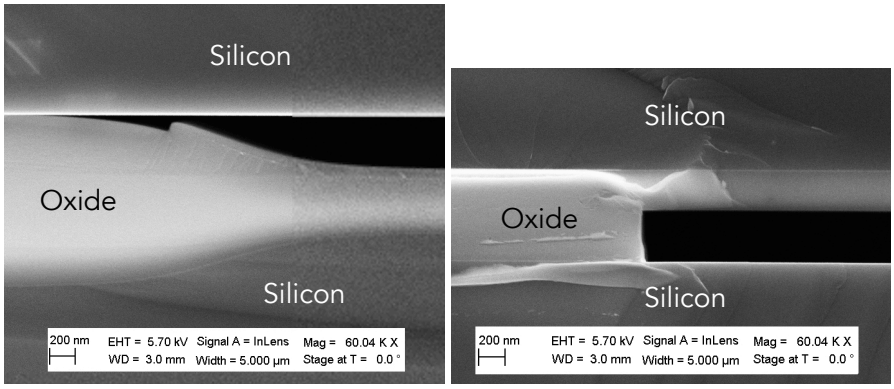

(a) (b)

Figure 4.17: SEM image of the cavity edge from Process C (a) and Process B (b). A thicker post oxide is a result of the LOCOS process and the insulation oxide have been moved from the bottom of the plate to the top of the bottom electrode.

using RIE as described in the appendix under Process C. The original argument for using the wet aluminium etch was the good selectivity towards silicon, such that the CMUT plate would not be etched during the contact pad etch (Fig. 4.14(g)). With the omission of the contact pad etch in the LOCOS process, over-etching is not an issue, since the underlying silicon layer is to be etched anyway in the subsequent silicon RIE etch of the top electrodes (Fig. 4.16(j)).

Process C uses a total of four masks, the insulation oxide is placed in the bottom of the CMUT cavities, and the side-walls of the bottom electrodes are completely electrically insulated by the LOCOS oxide. Fig. 4.17 shows a scanning electron micrograph (SEM) of two cleaved devices showing the region around the cavity edge for both Process C (a) and Process B (b). The nitride acting as a diffusion blocking layer is visible on top of the insulation oxide in Fig. 4.17(a). The region around the edge of the bottom electrode is depicted in Fig. 4.18. It is seen that Process C (a) has produced completely insulated side-walls as opposed to Process B (b), in which the bare silicon is exposed. The scallops visible in both images originate from the deep RIE with alternating etch- and passivation cycles used to etch out the bottom electrodes. In addition to the above mentioned advantages, Process C also has a number of advantages with respect to the device performance in terms of higher breakdown voltages and reduced parasitic capacitances due to the thick LOCOS oxide, as well as decreased charging issues. These subjects will be presented in further detail in Chapter 5.

The two regions shown in Figs. 4.17 and 4.18 were investigated in detail though

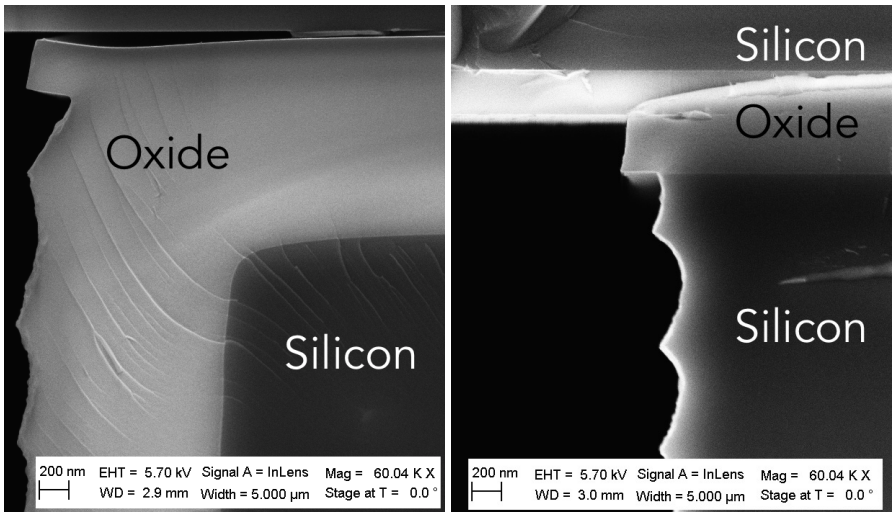

(a) (b)

Figure 4.18: SEM image of the cavity edge from Process C using LOCOS (a) and Process B (b). The bottom electrode of Process C is insulated with an oxide unlike that produced with Process B.

simulations during the development of Process C, since 2-D oxidation effects at the bottom electrode edge and lifting of the nitride layer at the cavity edge might generate protrusions that would inhibit fusion bonding. The processing parameters given in the appendix under Process C are therefore carefully chosen to yield a structure that is suitable for bonding. A detailed description of the optimization of the process is found in (Engholm 2015). Due to a slightly changed bonding region caused by the smooth transitions in the LOCOS oxide evident from Figs. 4.17 and 4.18, the mask layout were altered accordingly to produce the desired CMUT cavity sizes and to provide sufficient bonding area. Mask Set C in the appendix shows the mask set used for the LOCOS processing (Process C) of arrays equivalent to those processed with Process B and Mask Set B.

4.7 Yield Issues

For both of the processes presented in Sections 4.5 and 4.6, the array yield was limited due to broken top plates on some of the arrays. An example of this is shown in Fig. 4.19, which shows two $62 + 62$ row-column addressed arrays made using Mask Set B. Note that the plate is ruptured along lines which seemingly follows a circular pattern revolving

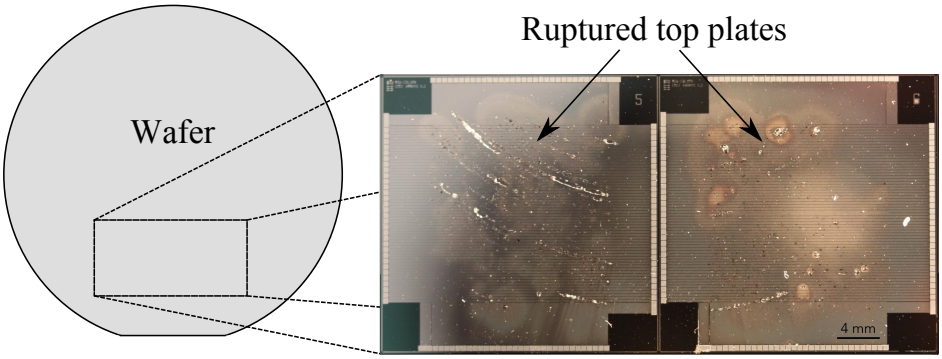

Figure 4.19: Photo of two $62 + 62$ arrays on a wafer after completed processing using Mask Set B. Note the striped patterns across the arrays, which appear to follow a circular path revolving around the center of the wafer. In these regions, the top plate has broken off the arrays.

around the center of the wafer. This type of defect, in some cases with the entire top plate broken off, was seen on many arrays, rendering the affected arrays useless. The defect typically occurred right after the handle removal (corresponding to Fig. 4.14(e) and Fig. 4.16(g)), and occasionally it deteriorated slightly during the following processing steps.

These defects were only seen in the 2-D row-column processes, and not in the 1-D array process described in Process A, with which wafers having $100\,\%$ array yield was routinely produced. Initially, the reason was thought to be stress in the oxide on the top plate produced by the process described in Section 4.5. However, the problem was later observed in the LOCOS process as well, in which the top plate is oxide-free. Therefore, the oxide on the plate was dismissed as the cause.

Apart from the above, only two factors distinguishes the 2-D processes from the 1-D process: The use of an SOI wafer for the bottom substrate and the patterning of bottom electrodes in this. To identify the source of the low yield, the 2-D LOCOS process was made in three versions:

1. A version made using Process C shown in Fig. 4.16.
2. A version in which no bottom electrodes were defined, i.e. step d in Fig. 4.16 was omitted.
3. A version in which no bottom electrodes were defined and where the bottom wafer was a standard silicon wafer.

The two first versions both had problems with top plates rupturing after the handle etch. Thus, the patterning of the bottom electrodes had no apparent effect on the yield. As

opposed to this, the last version produced a $100\,\%$ array yield, strongly indicating that the bottom SOI wafer was the source of the problem. The circular pattern produced by the defects as seen in Fig. 4.19 further suggested that the stress causing the plate rupture was radially oriented and that it was a wafer-scale stress rather that a local stress. Such a stress could originate from a curved wafer, and the wafer bow throughout the process was therefore investigated in detail.

An SOI wafer will usually have a wafer bow due to the compressive stress in the BOX. This will make the wafer convex seen from the side with the device layer, since the BOX is closest to this surface. However, the exact curvature depends on the way the SOI wafer is produced, which may introduce further stresses. Fig. 4.20(a) shows an illustration of a wafer suffering from wafer bow. One measure of the amount of wafer bow is to measure the total deflection of the wafer as shown in the figure. On a standard $10\,\mathrm{cm}$ silicon wafer, this measure typically yields a wafer bow below $10\,\mu\mathrm{m}$. In the following, a positive wafer bow is defined as a convex wafer seen from the device layer, i.e. if the device layer of the wafer is assumed to be located on the top side of the wafer illustrated in Fig. 4.20(a), this wafer will have a positive bow.

The wafer bow was measured using a stylus profilometer for selected process steps for the LOCOS process shown in Fig. 4.16 on page 94, and the result is given in Fig. 4.20(b). The letters in Fig. 4.20(b) refer to the letter of the respective process step in Fig. 4.16. The wafer bow measured in step (a) is identical to the original wafer bow of the SOI wafer, since both sides of the wafer have had the same layer deposited. Notice the significant positive curvature due to the compressive stress of the BOX. When the bottom electrodes are etched out, the wafer bow increases due to a reduction of the effective stiffness of the device layer situated on top of the BOX. A slight reduction in wafer bow is subsequently seen after the LOCOS oxidation. Overall, however, the wafer bow is in the same order of magnitude for the three first columns in Fig. 4.20(b). Then, after the bonding step, a large decrease in wafer bow is observed. This is because the stiffness of the second SOI wafer counteracts the bow of the bottom SOI wafer, effectively increasing the second moment of inertia of the wafer stack. Furthermore, the top SOI wafer has a positive bow, so when this wafer is bonded upside down to the bottom wafer, the two bows counteract each other. When the handle of the top wafer is etched away, there is nothing to counteract the stresses in the bottom wafer, and the result is once again a large positive wafer bow as seen in the fifth column in Fig. 4.20(b). The measurement was taken before the removal of the top SOI BOX, which explains the higher bow compared to the processed bottom wafer just before bonding shown in column three.

The device layer of the top wafer is forced to adhere to the bow of the bottom wafer, which induces stresses in the top plate that is suspended over the CMUT cavities. This was believed to be the most probable cause of the broken top plates shown in Fig. 4.19. No broken top plates were seen when producing 1-D arrays where the bottom wafer is a standard wafer with very little wafer bow. To mimic the latter successful configuration, a standard wafer was fusion bonded onto the back of the bottom SOI wafer. In practice, the stack of three wafers (the top SOI wafer, the structured bottom wafer, and the support

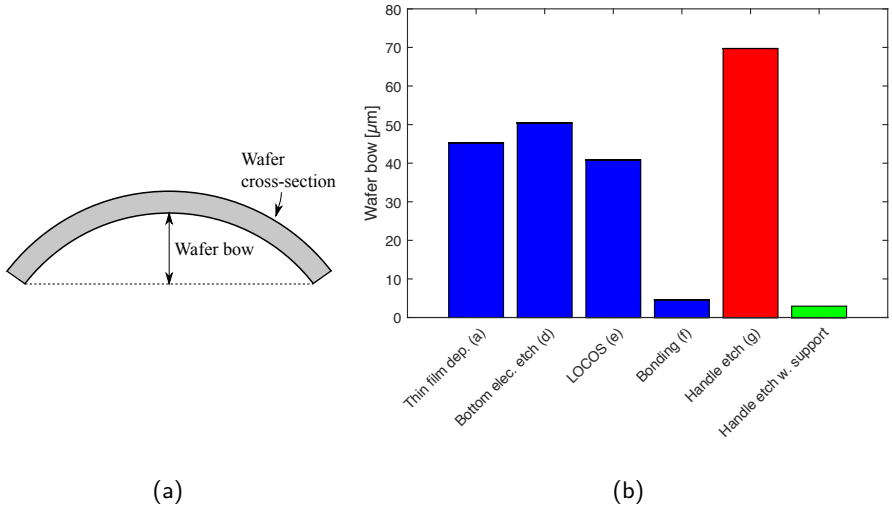

Figure 4.20: (a) Illustration of the measure used to quantify the bow of a wafer. (b) Wafer bow measured as a function of process step. The letters refer to the process in Fig. 4.16. The last two columns correspond to the two situations where the handle is etched with no support (red), and with a support wafer bonded to the back of the bottom wafer (green).

wafer) was bonded simultaneously and thus annealed at the same time. The purpose of the support wafer was to prevent the bottom wafer from bending during removal of the handle of the top wafer. As seen in the last column of Fig. 4.20(b), this indeed had the desired effect, resulting in a wafer bow similar to that measured right after fusion bonding of the two SOI wafers. This resolved the problem and no broken top plates were observed when applying the support.

Alternatively, the curvature of the wafer could be compensated for by applying carefully selected thin films to the back side of the wafer. The advantage of using the support wafer is that this technique is less sensitive to the individual wafer bow of each wafer. If compensating layers are used, the layers must be adjusted according to the bow of each wafer, which varied both between and within batches received from the SOI wafer vendor. However, the support wafer increases the final thickness of the array, which might result in substrate resonances being positioned in the frequency band of the transducer as discussed in Section 5.6. Such effects might be remedied by thinning down the array after processing is completed.

4.8 Chapter Summary

This chapter described the microfabrication of CMUT arrays. A brief review of the two prevalent fabrication methods found in the literature was given, followed by an account of the few reported attempts to produce row-column addressed CMUT arrays. Two critical aspects of CMUT microfabrication, oxide quality and oxide protrusions, were discussed in detail, partly based on Paper G. The fabrication approach presented in Paper F was introduced as an effective solution to the problem of oxide protrusions. This approach was then incorporated in a new process (Process B) for fabricating row-column addressed 2-D CMUT arrays. Process B was shown to have certain drawbacks such as exposed bottom electrodes and oxide on the CMUT plates that could potentially compromise the device reliability. Therefore, a modified process (Process C) based on LOCOS oxidation was introduced, effectively eliminating the limitations of the previous process. Process C also provides a thicker insulation oxide, which is beneficial in terms of oxide breakdown voltage and parasitic capacitance. Finally, it was shown that wafer bow results in a limited fabrication yield due stress and consequently fractured CMUT plates. A effective solution to this was demonstrated, in which a support wafer was bonded to the wafer stack before etching free the CMUT plates to compensate for the wafer bow.

CHAPTER 5

Transducer Characterization

In this chapter, the measured performance of the final layout of 2-D row-column addressed CMUT arrays developed in this project is presented. These arrays were fabricated using either Mask Set B or C, corresponding to the fabrication processes described in Sections 4.5 and 4.6, respectively. The array layout consists of 62 rows and 62 columns designed for a nominal 3 MHz operating frequency and a $\lambda/2$-pitch. Furthermore, the layout incorporates the developed apodization described in Sections 3.5.2 and 3.5.3. The first part of the chapter reviews the array design in detail to provide a basis for understanding the subsequent characterization. Then, the mounting of the array and the interconnect electronics used to perform the measurements are presented. Following this, electrical characterization results of arrays made using Process B are given based on Paper K. These are used to determine the pull-in of the array, the resonance frequency, and the capacitance, which reveals capacitive coupling of the bottom electrodes to the substrate. In several arrays made using Process B, issues of charging are observed, which leads to a decrease in coupling coefficient over time. It is shown that this issue is not present in arrays made using Process C, which shows stable performance over 20 hours of testing.

In the last part of the chapter, acoustical characterization results are presented based on Paper K. The emitted pressure, sensitivity, insertion loss, bandwidth, center frequency, and impulse response is evaluated over an entire array. It is also experimentally demonstrated that volumetric images can be produced with the array. Then, the acoustical cross-talk in the array is investigated based on results from Paper L. It is shown that the orthogonal orientation of transmitting and receiving elements leads to a significant decrease in acoustical cross-talk compared to that seen in 1-D CMUT arrays.

5.1 Array Overview

The final array layout was designed such that the apodization presented in Sections 3.5.2 and 3.5.3 could be incorporated. Furthermore, to obtain a high fill-factor, the geometry of the CMUT cells were designed to be square, and the operating frequency was adjusted such that the cells could be closely fitted in the width of a $\lambda/2$–pitch array element. These considerations resulted in a CMUT cell with a plate thickness of $1.7\,\mu\mathrm{m}$, and a square side length of $60\,\mu\mathrm{m}$, designed for a center frequency in immersion of $2.74\,\mathrm{MHz}$. The corresponding element pitch for this frequency was $270\,\mu\mathrm{m}$. The distance between the individual cells as well as the kerf was set to $5\,\mu\mathrm{m}$ to provide adequate bonding area

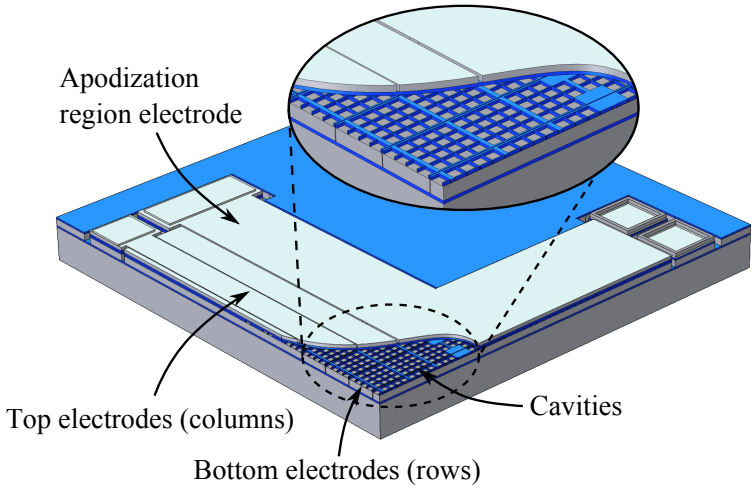

Figure 5.1: 3-D illustration of the CMUT row-column addressed transducer array showing a detail of the upper right corner of the array seen in Fig. 3.17 on page 64. A section of the top electrodes have been removed to reveal the underlying CMUT cavities. Oxide is blue, silicon is dark gray, and aluminum is light gray. Dimensions are not to scale. From Paper K.

during the fabrication. For the LOCOS fabrication process (Process C), these distances were altered slightly in the mask set to comply with the LOCOS oxide geometry as seen in Mask Set C. All dimensions used for the fabrication process described in Section 4.5 (Process B) can be seen in Paper K.

A 3-D drawing of the corner portion of the array is given in Fig. 5.1, showing the composition of the array as it looks when fabricated using Process B. It consists of 62 row elements, 62 column elements, and four apodization region electrodes. The apodization region electrodes provide DC bias to the integrated apodization, which is located at both ends of the row- and column elements. The apodization is seen in Fig. 3.17 on page 64, showing the layout of the CMUT cells. The argumentation for this layout is provided in Sections 3.5.2 and 3.5.3.

5.2 Interconnect Electronics

In order to test the prototype arrays, interconnect electronics were developed together with engineers from BK Medical. This consisted of a printed circuit board (PCB) on which the array was mounted as shown in Fig. 5.2. This PCB was used solely as a chip carrier board (CCB), allowing for easy replacement of arrays in the electronics PCB described later. The array was mounted using a non-conductive epoxy, and aluminium wire-bonds were made from the array to gold bonding pads on the CCB, after which they were coated

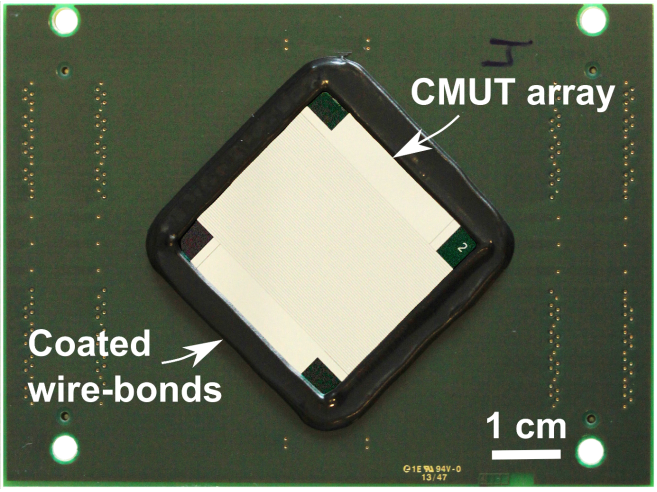

Figure 5.2: The row-column addressed CMUT array mounted and wirebonded on the carrier board. Two connectors are located on the back side of the carrier board (the vias to the connectors can be seen to the left and right in the picture). The CMUT array is rotated 45° clockwise to ensure that the length of each trace to the connector pins is equal. The top electrodes can be seen going from the top left to the bottom right of the array. From Paper K.

using glob-top. Each of these bonding pads were electrically connected to a pin in one of two FX11 connectors located on the back of the CCB. The vias to the connectors can be seen to the left and right in Fig. 5.2. The traces going from the array to the connectors were all made the same length to ensure equal capacitance/inductance. To facilitate this, the array was rotated 45° with respect to the connectors as seen in Fig. 5.2.

The two FX11 connectors were designed to fit into two counterparts located on a second PCB. This PCB contained the electronics required to interface the array to the ultrasound scanner system. An schematic illustration of the electronics is seen in Fig. 5.3. Each element on the transducer array is supplied with a DC bias voltage through a $1\,\mathrm{M}\Omega$ resistor (R), which acts as a low-pass filter in conjunction with the CMUT. Furthermore, the resistors ensure that the DC voltage can be maintained in the event of a short circuit of a top- and bottom electrode within the CMUT array, or any other DC short of the row- or column signals. The DC bias is split up such that half of the voltage is applied to the top electrodes (columns), while the reverse polarity is applied to the bottom electrodes (rows). This ensures that the electronics should only be rated for half of the DC bias voltage.

A $10\,\mathrm{nF}$ capacitor (C) provides high-pass filtering of the AC signals going either to the CMUT element as transmit pulses or from the element to the receivers of the ultrasound scanner system. The signal is led through a MAX4805A pre-amplifier (Maxim Integrated,

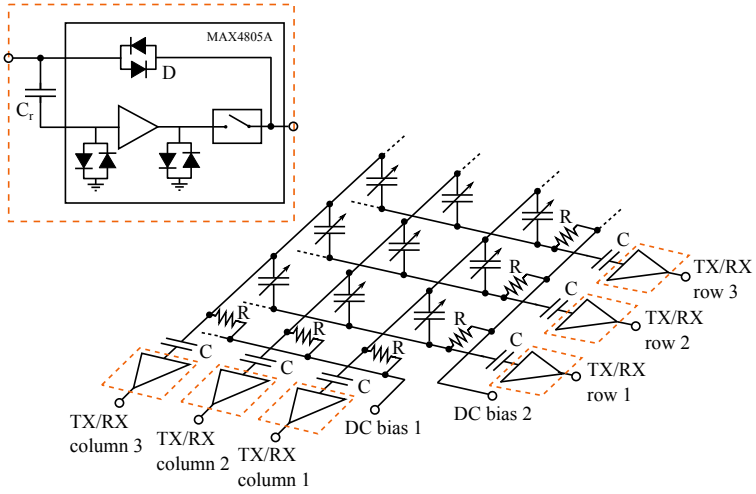

Figure 5.3: Sketch of the front end electronics showing three row channels and column channels, respectively. The variable capacitors denote the CMUTs contained in the elements. Every column channel has contact via the CMUTs to all row channels and vice versa. The DC biases are low pass filtered through a $1\,\mathrm{M}\Omega$ resistor (R) in conjunction with the CMUT, while the AC signal to and from the CMUT via the MAX4805A pre-amplifier is high-pass filtered using a 10 nF capacitor (C) together with the resistor R before going to the transmitters/receivers. The inset shows a detail of the MAX4805A circuit. From Paper K.

San Jose, CA, USA) , which amplifies the received signals nominally $8.7\,\mathrm{dB}$ before they are sent via a cable to the scanner system. Note that if a transmit pulse is sent on a column channel, all the row channels will provide a ground path for the AC signal. This will be established through the rows' capacitor (C), then through the transmit-path diodes (D) inside the MAX4805A (see inset in Fig. 5.3) and finally to the transmit amplifier output of the row channels of the scanner system. It is therefore mandatory that the row channels of the scanner are in the low impedance transmit mode to establish this ground-reference. No ground is accessible through the receive path due to the high impedance of the $47\,\mathrm{pF}$ capacitor, C_r. During reception, the AC voltage generated by the CMUT element is low enough so that the diode pair (D) in the transmit path does not provide a path to ground. Therefore, all row channels and column channels will receive and amplify the received signal.

Note that all elements in the array, including the four apodization region electrodes, are connected to a channel on the scanner via the interconnect electronics. Although no signals are transmitted nor received on the apodization region electrodes, this setup was chosen to allow for easy DC biasing of the apodized regions.

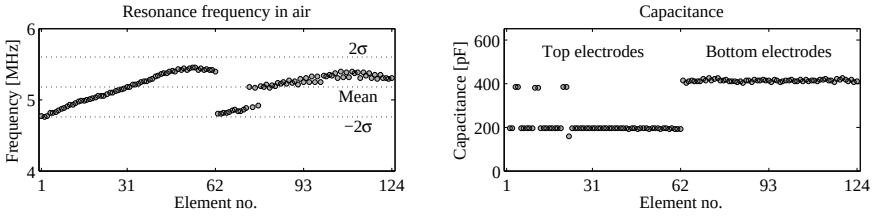

(a) (b)

Figure 5.4: Resonance frequency in air (a) and capacitance evaluated at 40 Hz (b) vs. element number. The resonance frequency is shown with mean and two standard deviations (2σ). Element 1-62 are top electrode elements and element 63-124 are bottom electrode elements. The elements 4-5, 11-12, and 21-22 are pair-wise shorted due to fabrication errors, hence the altered capacitance. From Paper K.

5.3 Electrical Characterization

In order to characterize the transducer without the influence of an acoustic medium and the interconnect electronics, a series of electrical tests were performed directly on the CCB using an Agilent 4294A impedance analyzer (Hewlett-Packard, Palo Alto, CA, USA). Each element of the array was accessed via the pins of the connectors on the CCB using an Agilent 42941A probe (Hewlett-Packard, Palo Alto, CA, USA). When measuring on individual columns, all rows were electrically shorted using a custom-built connector to enable measurement of a whole column at the time. The reverse was true when measuring on individual rows. In all measurements, a 500 mV excitation voltage was used on top of a DC bias of 40 V, which was applied to the array using the built-in DC bias of the impedance analyzer. These values were chosen to acquire adequate signal from the array to locate the resonance peak, whilst at the same time ensuring negligible frequency shift of the resonance peak due to the spring softening effect.

For every element, a set of three impedance sweeps were performed: one spanning the whole range of the impedance analyzer from 40 Hz to 110 MHz, a second from 1 MHz to 20 MHz, and a final in an interval of ± 1 MHz from the detected resonance frequency of the element. From this, the capacitance and resonance frequency in air of each individual element were found. The capacitance was determined at the lowest measured frequency (40 Hz), and the resonance frequency was found as the local minimum in impedance magnitude in the vicinity of the resonance.

The resonance frequency in air and capacitance of each element are shown in Fig. 5.4. Mean and standard deviation over the whole array is given in Table 5.1. The capacitance is seen to be very homogeneous for both the rows and columns with a standard deviation

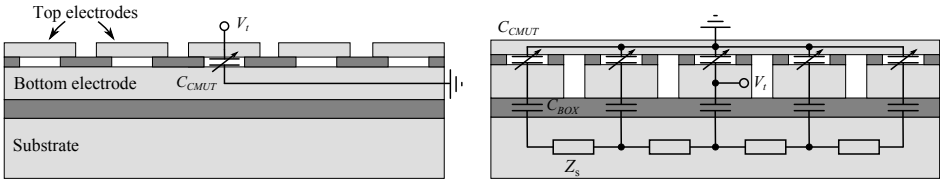

Figure 5.5: Illustration of the electrical circuit seen by the impedance analyzer when probing a top electrode (a) and a bottom electrode (b), respectively. The figures show a cross-section, such that the top electrodes are oriented perpendicular to the cut in (a) while the array is rotated 90° in (b).

of $1.2\,\%$ and $0.5\,\%$, respectively. This is a consequence of the lateral accuracy of the cleanroom processing, which uses UV photolithography for defining the lateral dimensions of the array. The apodization region electrodes have a much higher capacitance than the elements, and their capacitances have therefore only been listed in Table 5.1 to better visualize the capacitance of the elements in Fig. 5.4(b). This higher capacitance is a consequence of the large area of the apodization region electrodes as can be seen in Fig. 5.1. Note also that the column elements 4-5, 11-12, and 21-22 are pair-wise shorted. This is due to fabrication errors in the final aluminium and silicon etch shown in Fig. 4.14(h) on page 91. Any particle covering the element kerf on the mask during the lithography step prior to these etches will result in contact between two top electrodes (columns). This is especially critical for row-column addressed arrays, where the size of the elements results in a extensive total kerf length. The kerf is only $5\,\mu\mathrm{m}$, so any particle larger than this will result in a short circuit, which was seen to affect these three different locations of the array.

Note that the rows (bottom electrodes) have a higher capacitance than the columns (top electrodes). This is due to capacitive coupling to the substrate of the bottom SOI wafer. When a top electrode is probed, all bottom electrodes are grounded. As seen in Fig. 5.5(a), only the capacitance from the top electrode to the grounded bottom electrodes, denoted C_{CMUT}, is seen in this configuration. The situation when a bottom electrode is probed is illustrated in 5.5(b). In this case, the substrate will appear grounded since the signal may follow a path through the substrate and couple to ground via the neighboring bottom electrodes as shown in the figure. Although the substrate has a non-negligible impedance Z_s, the parallel coupling of the bottom electrodes results in a relatively low-impedance path to ground. Therefore, the capacitance measured when probing a bottom electrode will have a contribution from both C_{CMUT} and C_{BOX}.

The resonance frequency in air given in Fig. 5.4(a) is seen to vary slightly more than

Table 5.1: Transducer impedance characterization parameters

Parameter	Mean value	Std.	Unit
Resonance frequency in air	5.18	0.21	MHz
Element capacitance (top)	194	1	pF
Element capacitance (bottom)	413	5	pF
Apo. reg. electrode capacitance (top)	2677	105	pF
Apo. reg. electrode capacitance (bottom)	4308	14	pF
Pull-in voltage	100	3	V

the capacitance, the standard deviation being 4 %. This is a consequence of the thickness variation of the device layer of the SOI wafer, which is used to define the top electrode that acts as the top vibrating plate of the individual CMUT cells. This thickness is harder to control precisely, as the SOI wafer was ordered from external wafer suppliers, who promised a thickness tolerance of 300 nm. Since the resonance frequency in air scales linearly with the thickness as shown in Eq. (2.37) on page 27, the observed frequency variation is well within this tolerance limit. Note that the resonance frequency in air is far from the intended center frequency of the array of 2.74 MHz. This is a predictable and well-known effect, as the acoustical loading of air is much lower than the loading from a liquid medium. The resonances reported here therefore only serves as a measure of the functionality and homogeneity of the array.

Finally, the pull-in voltage was measured to determine the operating voltage of the array. To avoid charging of the array elements during pull-in (Huang et al. 2005), the pull-in voltage was measured on test-elements made on the same wafer as the array. The pull-in voltage was found by performing impedance sweeps whilst increasing the DC bias voltage sequentially using a Keithley 2400 sourcemeter (Keithley Instruments Inc., Cleveland, OH, USA). The pull-in voltage was then identified as the point where the resonance peak in the impedance measurement was abruptly shifted to a higher frequency due to the collapse of the plates. This was done on a total of five test elements, yielding a pull-in voltage of 100 ± 3 V as reported in Table 5.1. It was chosen to operate the array with a DC bias voltage of 80 % of the pull-in voltage and an AC amplitude of 50 % of the pull-in voltage. Thus, for all subsequently described measurements with this array, the DC bias voltage was set to 80 V (± 40 V on the two bias supplies), and the AC amplitude to 50 V.

5.4 Acoustical Characterization

The acoustical characterization of the transducer array was performed using the interconnect electronics described in Section 5.2. The CCB with the array was mounted on the electronics PCB and placed in a water-proof box. The box was closed with an aluminium

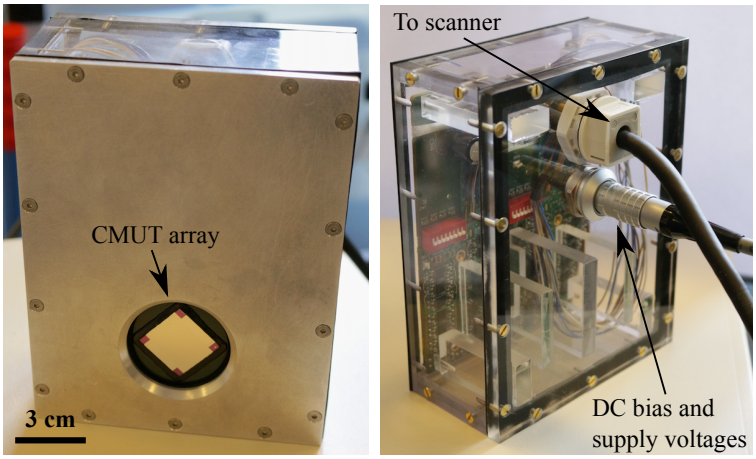

Figure 5.6: Images of the water-proof box in which the array and electronics were mounted during the acoustical measurements. The left image shows the font side with the exposed array, and the right image shows the back where the cables and electronics PCB are visible.

lid with an opening through which the array was exposed. The setup is depicted in Fig. 5.6.

All acoustical measurements were performed in rapeseed oil to provide electrical insulation of the exposed electrodes on the array. The speed of sound in the oil was measured to be $1480\,\mathrm{m/s}$, and the damping 0.3 dB/MHz·cm, which is in agreement with previously reported values for vegetable oil (Oralkan et al. 2002). The DC bias voltage was in all measurements set to $80\,\mathrm{V}$ ($80\,\%$ of pull-in), while the amplitude of the AC signal was set to 50 V ($50\,\%$ of pull-in). The DC bias was provided through a TOE8842 dual DC power supply (Toellner Electronic Instrumente GmbH, Herdecke, Germany) set to ± 40 V, and the AC signals were generated using the experimental ultrasound system SARUS (Jensen et al. 2013), which was also used to record all received signals. The system was set to sample at $70\,\mathrm{MHz}$ and to record signals down to a depth of $4\,\mathrm{cm}$.

First, a reference measurement was made using a $2.5\,\mathrm{MHz}$ sinusoidal excitation with 2 and 4 cycles, respectively. Here, each individual element was excited one at a time in a tank of oil with no immediate reflecting structures. For each excitation, the signals received by all elements were recorded. This served the dual purpose of determining the cross-talk of the array (covered in detail in Section 5.6) and providing a noise frame reference, that was subtracted from all subsequent measurements.

A second setup was established to determine the pulse-echo impulse response of each element. A plane reflector (a $4.1\,\mathrm{cm}$ thick PVC plastic material) was positioned $2.5\,\mathrm{cm}$ away from and parallel to the transducer surface. Then, 20 realizations of random Gaussian noise was transmitted on one element at a time and received on the transmitting

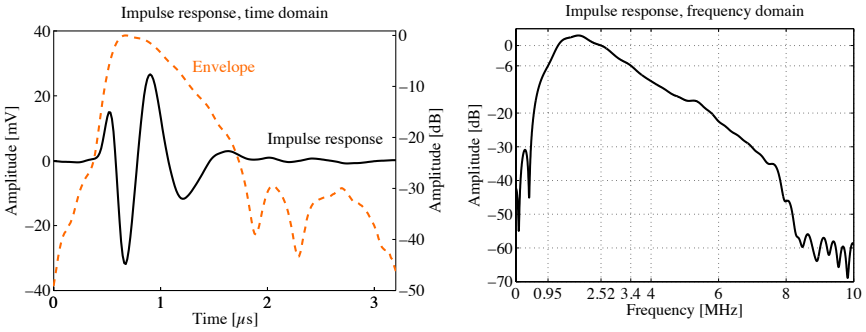

(a) (b)

Figure 5.7: (a) Pulse-echo impulse response from the center bottom electrode element (no. 96). The solid line (left axis) shows the measured voltage signal and the dashed line (right axis) shows the envelope of the measured signal given in dB. (b) Frequency domain of the impulse response. The center frequency ($2.52\,\mathrm{MHz}$) and the $-6\,\mathrm{dB}$ bandwidth relative to the center frequency ($0.95\,\mathrm{MHz}$ to $3.4\,\mathrm{MHz}$) have been indicated. From Paper K.

element. The recorded signal was cross-correlated with the excitation signal for each of the 20 realizations, and the 20 results were averaged to yield the pulse-echo impulse response of the respective element (Schroeder 1979). The higher the number of realizations, the closer one gets to a true white signal, so the number of realizations is a compromise between acquisition/processing time and accuracy. In Fig. 5.7(a), the impulse response of element no. 96 (the center row element) is shown, in this case using 600 realizations of the Gaussian noise. The corresponding spectrum is shown in Fig. 5.7(b). Note that the deduced impulse response describes the impulse response of the whole system consisting of transducer, front-end electronics, as well as receivers and transmit amplifiers in the SARUS system. It thereby characterizes the impulse response of the actual imaging setup, which may explain the drop in the spectrum amplitude for higher frequencies.

From the spectrum of the impulse response, the center frequency and bandwidth for each element can be found. The center frequency, f_c, was determined by summing all frequencies from 0 to half the sampling frequency, f_s, weighted by the spectrum amplitude for each frequency, S, and dividing by the sum of the spectrum amplitudes:

$$f_c = \sum_{i=0}^{N/2} \left[S(if_s/N) \cdot if_s/N \right] \Big/ \sum_{i=0}^{N/2} S(if_s/N) \; . \tag{5.1}$$

This yielded a center frequency in immersion of $2.77 \pm 0.26\,\mathrm{MHz}$. Since the pitch of the array was $270\,\mu\mathrm{m}$, see Section 5.1, the pitch in units of the wavelength is thereby

Table 5.2: Transducer acoustical characterization parameters

Parameter	Mean	Std.	Unit
Center frequency in immersion	2.77	0.26	MHz
-6 dB fractional bandwidth	102	10	%
Transmit pressure peak-to-peak	590	73	kPa
Sensitivity at 2.5 MHz	0.299	0.090	$\mu V/Pa$
Insertion loss	-53.7	3.6	dB
Nearest neighbour crosstalk level	-23.9	3.7	dB
Transmit to receive elements crosstalk level	-40.2	3.5	dB

0.51, which is very close to the desired pitch of $\lambda/2$. The relative $-6\,\mathrm{dB}$ bandwidth was determined as the distance in frequency between the $-6\,\mathrm{dB}$ points in the spectrum relative to the center frequency of the element, yielding a relative bandwidth of 102 ± 10 %. The $-6\,\mathrm{dB}$ bandwidth is illustrated for element no. 96 in Fig. 5.7(b). Fig. 5.7(a) also shows the envelope of the impulse response in decibels, computed as the log-compressed absolute values of the analytic signal. The $-20\,\mathrm{dB}$ and $-40\,\mathrm{dB}$ pulse duration for this element are $1.23\,\mu\mathrm{s}$ and $3.06\,\mu\mathrm{s}$, respectively, corresponding to 3.1 and 7.7 periods at its center frequency of $2.52\,\mathrm{MHz}$.

A third setup was established to determine the transmit pressure of the elements. A HGL-0400 hydrophone connected to a AC-2010 pre-amplifier (Onda Corporation, CA, USA) was placed $7\,\mathrm{mm}$ from the transducer surface and scanned over each element using the positioner of the intensity measurement system AIMS-3 (Onda Corporation, CA, USA), while transmitting a $2.5\,\mathrm{MHz}$, 4-cycle sinusoidal signal on the element being measured. The recorded pressure at $7\,\mathrm{mm}$ was then compensated to find the pressure at the transducer surface. The compensation was found by a simulation in COMSOL Multiphysics 4.4 (COMSOL AB, Stockholm, Sweden). Here, an element with the same dimensions as the physical elements in the array was set to emit a continuous $2.5\,\mathrm{MHz}$ pressure wave, and the pressure magnitude at a distance of $7\,\mathrm{mm}$ from the element relative to the pressure magnitude at the element surface was found and used as the compensation factor (9.6). The resulting surface pressure emitted by the elements is seen in Table 5.2 to be 590 ± 73 kPa.

Subsequently, the pulse-echo signal from each element against a plane reflector (a $4.1\,\mathrm{cm}$ thick PVC plastic material) set at a distance of $7\,\mathrm{mm}$ from and parallel to the transducer surface was measured. Once again, a $2.5\,\mathrm{MHz}$ 4-cycle sinusoidal excitation pulse was used. The pressure received by the element was deduced by using the pressure measured with the hydrophone setup at a distance of $7\,\mathrm{mm}$ from the transducer surface and compensating for the pressure drop from $7\,\mathrm{mm}$ to $14\,\mathrm{mm}$ (the return trip to the transducer surface) by using the COMSOL Multiphysics simulation described above. This yielded a factor of 0.7, which was used to compensate for the pressure drop. Thereby, the sensitivity of each element could be found by dividing the received voltage signal with the

incident pressure (0.7 times the measured pressure). The value of $0.299 \pm 0.090\ \mu\mathrm{V/Pa}$ listed in Table 5.2 is the signal generated by the transducer itself, i.e. the signal has been reduced to account for the nominal $8.7\,\mathrm{dB}$ voltage gain supplied by the pre-amplifiers.

The insertion loss of a transducer is defined as the round-trip loss of signal power, i.e. it is the ratio of the power of the received signal to the power of the transmitted signal (Szabo 2014, p. 136). This can be found by normalizing the voltage received by an element after a pulse-echo event to the transmit voltage used to excite the element. A log-compression of this ratio using the $20\log_{10}$ convention yields the insertion loss in dB. To exclude the loss in the oil, the received voltage from the pulse-echo measurements against the plane reflector is compensated for the loss in pressure in the oil during the round trip to the plane reflector as described in the paragraph above. It is assumed that the plane reflector is ideal, so any deviance from this will lead to an over-estimation of the insertion loss. Also, the insertion loss should only be a measure of the transducer itself, so the voltage gain supplied by the pre-amplifiers have been removed in the calculations. In Table 5.2, the average insertion loss and standard deviation for all elements in the array are listed.

5.5 Volumetric Imaging

For the imaging experiments, a wire phantom consisting of a steel wire with a diameter of $0.3\,\mathrm{mm}$ was used. It was positioned $23\,\mathrm{mm}$ away from the transducer array surface and oriented approximately parallel to the rows of the array, but with a $5°$–$10°$ angle with respect to the transducer array surface due to alignment inaccuracies. Both the transducer array and the wire phantom was positioned in electrically insulating rapeseed oil as with the measurements described in the previous section. In the following, the azimuth direction is defined as being parallel to the column elements, while the elevation direction is parallel to the row elements.

To image the 3-D volume, synthetic transmit focusing with single element emissions was used. The rows were used as transmitters and the columns as receivers. Each row element was excited with a 2-cycle sinusoidal signal, one row element at a time. The acoustical pressure was for each emission recorded on all 62 receive elements. From each measured data set, the entire 3-D volume was beamformed using the beamformer described in Section 3.3, creating one low resolution image. By summation of each beamformed low resolution image, the final 3-D volume was created. A Hann apodization function was used both in transmit and in receive. The pulse repetition frequency was $20\,\mathrm{Hz}$, the sampling rate was $70\,\mathrm{MHz}$, and data were recorded until a depth of $4\,\mathrm{cm}$ was reached. As with the previous measurements, a $50\,\mathrm{V}$ excitation amplitude and a $80\,\mathrm{V}$ DC bias was used.

In Fig. 5.8, a 3-D rendered image of the wire is shown. Note that the signal from the wire dies out as it crosses the borders of the array. This is partly because the transmitting elements are oriented parallel to the wire, partly because the regions of the wire located

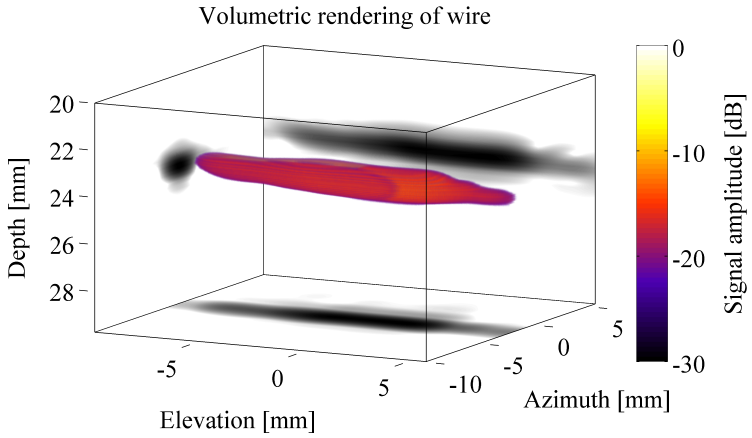

Figure 5.8: 3-D beamformed image of a wire shown at a dynamic range of $30\,\mathrm{dB}$. The beamformed image has been projected to the side-walls of the plot in all three dimensions using the same dynamic range. The azimuth and elevation zero-point is positioned at the center of the array. From Paper K.

outside the array is reflecting the received sound away from the array. The first issue could be addressed by using a phased array technique as proposed in Section 3.5.2, while the second issue is related to the nature of the wire used, and will not be seen for a structure behaving like a collection of point scatterers. The latter effect also implies that the front of the emitted single-element plane wave is parallel to the element surface once emitted, but the smooth wire reflects the wave as a mirror in the direction along the wire. Since the wire is not parallel to the transducer array surface, more energy is received at one end of the transducer array than the other. This is seen in Fig. 5.8, where the beamformed wire is not symmetric around zero in the elevation direction.

Cross-sections of the wire are shown in Fig. 3.18 on page 65, both with and without the integrated apodization enabled. From these, the resolution was extracted and given in Table 3.1 on page 66.

5.6 Cross-talk

The acoustical cross-talk of the array may be investigated using the data acquired during the reference measurement described in Section 5.4. This is the subject of the current section, which presents the findings in Paper L.

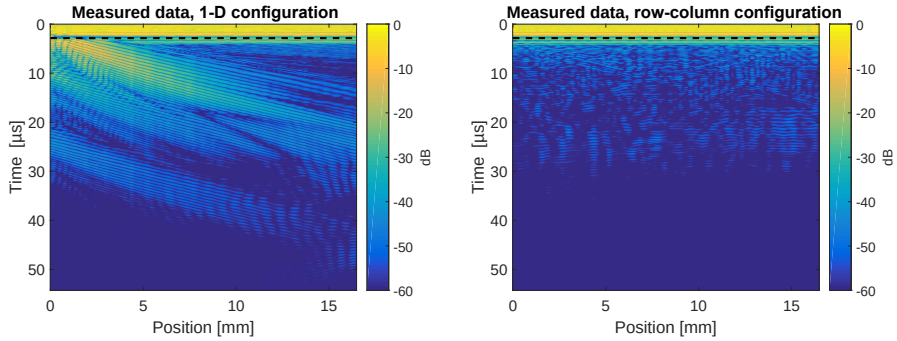

(a) (b)

Figure 5.9: Data acquired using the two setups shown in Fig. 5.10. Time zero corresponds to the onset of the transmit pulse. The black dashed line indicates the end of the transmit pulse, and only data after this time has been included in the cross-talk analysis. Both plots have been normalized to the same value. From Paper L.

5.6.1 Measured Data

In the reference measurement, one element is set to emit sound into a large tank of oil. Since there are no nearby reflecting structures, all received signals are due to cross-talk in the array. The data in Fig. 5.9(a) is generated by transmitting on the outer-most row element (not the apodization element), and receiving data on all 62 rows. The left illustration in Fig. 5.10 shows this setup. Fig. 5.9(b) is generated by transmitting on the outer-most column element (not the apodization element), and again receiving data on all 62 rows as shown in the right illustration in Fig. 5.10. The columns correspond to top elements in the array, and the rows to bottom elements. Figure 5.9 shows the envelope of the recorded signals, which have been found using a Hilbert transform and a subsequent log-compression. Time zero corresponds to the onset of the trigger in the SARUS system, and the position along the array is shown on the abscissa with one element for each $270\,\mu\mathrm{m}$.

There are two main types of cross-talk in a transducer array: Electrical cross-talk due to capacitive and inductive coupling, and acoustical cross-talk due to vibrations being transmitted to neighboring elements. The electrical cross-talk happens much faster than the acoustical cross-talk, since the latter is limited by the relatively slow speed of sound. In Fig. 5.9, a strong signal is seen simultaneously on all channels just after time zero. This is due to the transmit pulse being sent to the first column element. This high-voltage signal couples capacitively/inductively to the other elements either via the transducer or the external electronics. The coupled signals are then amplified by the pre-amplifiers

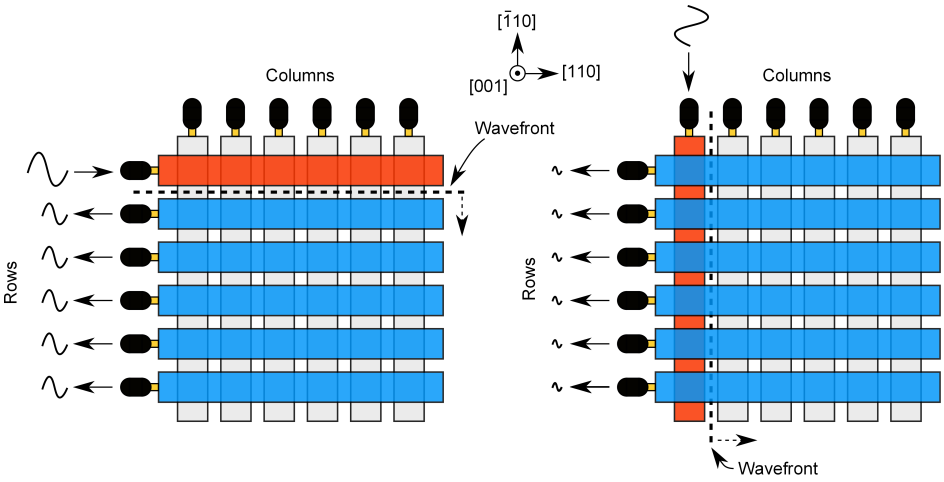

Figure 5.10: Illustration of the two setups used for measuring the cross-talk. In the case to the left, one row (red) is actuated, and the received signal on all rows (blue) are recorded. This corresponds to a 1-D array configuration. In the case to the right, one column is actuated, and the signals from the rows are recorded. This corresponds to the row-column configuration. The wavefront generated by the actuated element is shown with a black dashed line. The size of the sine-symbols graphically illustrates the magnitude of the signals. The crystallographic directions of the silicon substrate are shown in the top. From Paper L.

and sent to the scanner. In the following analysis, this cross-talk is disregarded by only including data after the transmit pulse has ended as indicated by a black dashed line in Fig. 5.9. In this way, the acoustical cross-talk of the array may be analyzed separately (any electrical cross-talk actuating the neighboring elements will produce acoustical signals, which are therefore also included). The acoustical cross-talk is more severe than the electrical cross-talk for the beamformed image due to the slow decay of the former; as seen in Fig. 5.9(a), the cross-talk signals are visible in almost the whole time-span of the data, which corresponds to an imaging depth of $4\,\mathrm{cm}$.

The nearest neighbor cross-talk for every element was found by repeating the measurement shown in Fig. 5.9 with a new element emitting for each data acquisition. The signal from the nearest neighbor next in line to the emitting element was then extracted. To provide a relative measure, the signal was normalized to the transmit voltage after the latter was corrected for the insertion loss of the emitting element. The insertion loss is reported in Table 5.2. This correction corresponds to a normalization of the neighbor's signal to the signal that the emitting element would have received if the transmitted pulse was reflected right at the transducer surface and subsequently received by the emitting element. Thus, it yields the relative acoustical coupling from one element to its neighbor. This calculation resulted in a nearest neighbor cross-talk of -23.9 ± 3.7 dB as seen

in Table 5.2, which is consistent with values reported in the literature for 1-D CMUT arrays (Bayram, Kupnik, Yaralioglu, Oralkan, Ergun, et al. 2007; Jin et al. 2001). This is expected, as the setup is essentially identical to that of a 1-D array. For this reason, the setup is dubbed the 1-D configuration in the following.

During imaging with row-column addressed arrays, either the rows or columns are used as transmitters and the orthogonal elements as receivers as covered in Chapter 3. In the measurement shown in Fig. 5.9(b), a column is emitting, and consequently the received data from the rows will be used for the beamforming. It is therefore denoted the row-column configuration in the following. It is readily seen that the cross-talk seems less pronounced in this data set in Fig. 5.9(b) compared to the data from the 1-D configuration in Fig. 5.9(a). To provide a measure of the cross-talk from the emitting element to the orthogonal elements, which are receivers in the row-column configuration, the average of the maximum signal received on each receiving element is used. Repeating the emission sequence for each of the columns and recording on all rows for each emission yields a mean cross-talk of $-40.2\,\mathrm{dB}$ with a standard deviation of $3.5\,\mathrm{dB}$ as listed in Table 5.2.

This cross-talk is much lower than that seen in 1-D CMUT arrays (Bayram, Kupnik, Yaralioglu, Oralkan, Ergun, et al. 2007; Jin et al. 2001). Recalling that the nearest-neighbor cross-talk in the row-column addressed array was similar to the values reported for 1-D CMUT arrays, the explanation for the decrease is likely to be found in the orthogonal orientation of transmitting and receiving elements in the row-column configuration. The idea is illustrated in Fig. 5.10. In the left figure, it is shown that the wave front of the acoustical wave generated by the emitting element will impinge parallel to each of the other rows. Thus, the whole element surface vibrates in phase, generating a strong received signal on the rows. The case for the row-column configuration is seen in Fig. 5.10 (right). Here, the wave front from an emitting column element is oriented perpendicular to the receiving rows. As the element is much longer than the wavelength of the acoustical wave, the signals generated at the actuated parts of the element will average out due to the symmetry of the wave, and ideally no signal is received. The discussion related to the analysis of the edge waves provided in Section 3.4 is analogous. In practice, however, the finite length of the elements and the reflections and mode conversions of the waves will contribute with some net cross-talk as observed in the experiment.

5.6.2 Dispersion Relations

The acoustical cross-talk in a CMUT array is in general comprised of substrate waves, interface waves, and longitudinal waves in the medium (Bayram, Kupnik, Yaralioglu, Oralkan, Ergun, et al. 2007; Eccardt, Lohfink, and Garssen 2005; Jin et al. 2001). While the first two are dispersive waves, the latter are traveling non-dispersively at the speed of sound c in the medium. The following gives a brief presentation of the dispersion relation for the substrate waves and the interface waves.

The substrate of the CMUT is made from a silicon wafer, and the waves travelling in this may be described by Lamb wave theory. Assuming an idealized case in which the

substrate is an isolated silicon plate of thickness d having infinite lateral extent, a pair of characteristic equations describe the dispersion relation of the Lamb waves (Lamb 1917):

$$\frac{\tan(\beta d/2)}{\tan(\alpha d/2)} = -\frac{4\alpha\beta k^2}{(k^2-\beta^2)^2} \tag{5.2}$$

$$\frac{\tan(\beta d/2)}{\tan(\alpha d/2)} = -\frac{(k^2-\beta^2)^2}{4\alpha\beta k^2} \ . \tag{5.3}$$

Here,

$$\alpha^2 = \frac{\omega^2}{c_L^2} - k^2 \tag{5.4}$$

and

$$\beta^2 = \frac{\omega^2}{c_T^2} - k^2 \ , \tag{5.5}$$

where ω is the angular frequency, and k is the wave number. c_L and c_T are the longitudinal and shear wave velocities, respectively. The substrate of the array is made from a (001) silicon wafer having cubic symmetry along its principal axes with stiffness coefficients $c_{11} = 165.64\,\mathrm{GPa}$, $c_{12} = 63.94\,\mathrm{GPa}$, and $c_{44} = 79.51\,\mathrm{GPa}$ (Hall 1967). The transducer array is aligned to the wafer flat such that a Lamb wave propagating away from the emitting element travels in the $\langle 110\rangle$-directions, see Fig. 5.10. It follows that (Miller and Musgrave 1956)

$$c_L = \sqrt{\frac{c_{11}+c_{12}+2c_{44}}{2\rho}} = 9132\,\mathrm{m/s} \tag{5.6}$$

$$c_T = \sqrt{\frac{c_{44}}{\rho}} = 5842\,\mathrm{m/s} \ , \tag{5.7}$$

where $\rho = 2330\,\mathrm{kg/m^3}$ is the mass density of silicon.

Equation (5.2) describes the symmetric modes, S_n, whereas Eq. (5.3) describes the antisymmetric modes, A_n. The zeroth-order modes exist for all frequencies and have been observed in several studies of 1-D CMUT arrays (Bayram, Kupnik, Yaralioglu, Oralkan, Ergun, et al. 2007; Bayram, Kupnik, Yaralioglu, Oralkan, Lin, et al. 2005; Jin et al. 2001). The higher-order modes have lower cut-off frequencies at $f_c = nc_L/(2d)$ and $f_c = nc_T/(2d)$. At these frequencies, the plate resonates with infinite phase velocity and zero group velocity. Ladabaum *et al.* observed significant substrate ringing at the frequencies corresponding to longitudinal-wave resonances along the thickness of the substrate, and demonstrated that these resonances could be moved out of the transducer frequency spectrum by thinning the substrate (Ladabaum et al. 2000).

In addition to substrate waves and waves in the medium, evanescent waves may propagate next to the interface between the transducer and the medium. Previous studies

have shown that such waves are the most significant contribution to acoustical cross-talk in 1-D CMUT arrays (Bayram, Kupnik, Yaralioglu, Oralkan, Ergun, et al. 2007; Bayram, Kupnik, Yaralioglu, Oralkan, Lin, et al. 2005; Jin et al. 2001). Eccardt *et al.* have provided a simple description of the dispersion relation of these waves in CMUT arrays based on the assumption of a semi-infinite homogeneous fluid interfaced by a semi-infinite solid with a given surface stiffness per area and mass per area (Eccardt, Lohfink, and Garssen 2005). In this framework, the pressure wave propagating in the fluid at the interface is described by

$$p = \exp(-\gamma z + jkx - j\omega t) \,, \tag{5.8}$$

with $\gamma > 0$ being the decay constant in the z-direction perpendicular to the surface. Denoting the speed of sound in the medium c, the wave number along the surface is given by the relation $k^2 = \gamma^2 + \omega^2/c^2$, which is found by inserting the expression for the pressure in the time-dependent wave equation for the medium, $\partial^2 p/\partial t^2 = c^2 \nabla^2 p$. The impedance of the surface wave is given by

$$Z_w = \frac{j\omega\rho_m}{\gamma} \,, \tag{5.9}$$

where j is the imaginary unit and ρ_m is the mass density of the medium (Eccardt, Lohfink, and Garssen 2005). A surface with a homogeneous stiffness per area s and mass per area m will have an acoustic impedance given by

$$Z_i = \frac{s}{j\omega} + j\omega m \,. \tag{5.10}$$

The wave travels along this surface when $Z_w = Z_i$, and thus

$$\gamma = \frac{j\omega\rho_m}{Z_i} \,. \tag{5.11}$$

It therefore follows that the phase velocity of the surface wave is

$$c_{\text{phase}} = \frac{\omega}{k} = \frac{c}{\sqrt{1 - \left(\frac{\rho_m c}{Z_i}\right)^2}} \,, \tag{5.12}$$

from which the dispersion relation $k = \omega/c_{\text{phase}}$ is readily found. Note that for an infinitely stiff surface, the interface wave propagates non-dispersively at $c_{\text{phase}} = c$.

5.6.3 Frequency Domain Analysis

In order to further analyze the cross-talk, a 2-D Fourier transform can be performed on the data (Alleyne and Cawley 1991). This generates the reciprocal space representation of the data, i.e. a frequency-wavenumber representation, which offers means of identifying

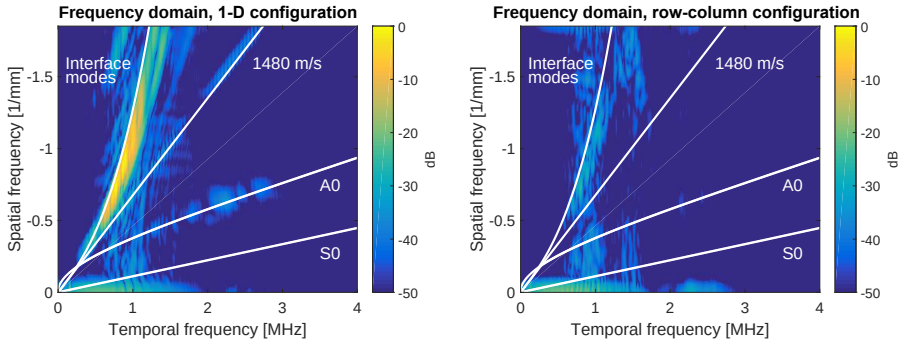

(a) (b)

Figure 5.11: 2-D Fourier transforms of the data shown in Fig. 5.9. The data has been multiplied with a Hann-window in both the spatial and temporal dimension before the Fourier transform. The theoretically calculated dispersion curves for the interface modes, the waves in the medium, and the substrate Lamb waves are shown as white solid lines. Both plots are normalized to the maximum value in the 1-D configuration. From Paper L.

the types of crosstalk by revealing the dispersion of the waves. The data shown in Fig. 5.9 (excluding data before the dashed black line) is multiplied by a Hann-window in both dimensions to suppress side-lobes. The resulting plots in the frequency domain are shown in Fig. 5.11. The maximum spatial frequency corresponds to one-half of the reciprocal pitch of the transducer array (the Nyquist frequency). The maximum temporal frequency is set to $4\,\mathrm{MHz}$, since no data is within the dynamic range of the plot above this frequency. The dispersion curves for the interface waves, substrate waves, and longitudinal waves in the medium have been plotted as well using the theory presented in the previous section. Calculation of the Lamb wave dispersion curves was done using the array substrate thickness of $520\,\mu\mathrm{m}$. Only the zeroth-order modes are visible in the shown frequency range. The dispersion curve for the interface waves was calculated assuming that the whole transducer surface is covered by CMUT cells (i.e. neglecting the $5\,\mu\mathrm{m}$ wide anchoring area between the cells). The surface stiffness per area is then found as the stiffness of a single cell divided by its effective area. For the square cells in the array, these are given in Table 2.1 on page 20. The mass per area of the surface is simply $m = \rho h$.

Note that both substrate waves, interface waves, and waves in the medium are clearly observed for the 1-D configuration (Fig. 5.11(a)). The plot has been normalized to the amplitude of the interface waves, which are by far the most dominating. The non-dispersive waves in the medium are located at or more than $36\,\mathrm{dB}$ below the interface waves, while the number is $34\,\mathrm{dB}$ for the A_0 Lamb wave. The S_0 Lamb wave is not

visible within the displayed dynamic range. The substrate waves and the waves in the medium are most visible in the frequency range defined by the $-6\,\mathrm{dB}$ bandwidth of the transducer, which has its limits at $0.95\,\mathrm{MHz}$ and $3.4\,\mathrm{MHz}$, respectively, see Fig. 5.7(b) on page 109.

Note that all types of waves are accurately predicted by the theory. The dispersion curve for the interface modes would follow the non-dispersive line at $1480\,\mathrm{m/s}$ for an infinitely stiff transducer surface (Eccardt, Lohfink, and Garssen 2005). Since the actual surface is comprised of small areas of solid silicon in addition to the CMUT cells, the calculated dispersion curve expectedly borders the lower part of the interface modes' spectrum.

For the row-column configuration (Fig. 5.11(b)), the cross-talk is seen to be reduced by more than $24\,\mathrm{dB}$. The plot is normalized to the $0\,\mathrm{dB}$-value for the 1-D configuration to illustrate the reduction.

5.7 Charging

Transducers made using Process B described in Section 4.5 were seen to exhibit a polarity- and time dependent charging phenomenon resulting in a decrease of the transducer coupling coefficient. An example of this is seen from the blue curve in Fig. 5.12 showing the coupling coefficient of a transducer test element measured over a time-span of 20 hours. During the first 10 hours, a positive DC bias potential is applied to the top electrode while the bottom electrode is grounded. The DC bias is set to roughly $80\,\%$ of the pull-in voltage of the CMUT test element ($120\,\mathrm{V}$ for this particular element). After five minutes with a DC bias of $0\,\mathrm{V}$, the polarity is switched to produce a negative potential of $-120\,\mathrm{V}$ on the top electrode. An impedance sweep is performed every 12 seconds in a fixed frequency range around the transducer resonance frequency ($4\,\mathrm{MHz}$-$8\,\mathrm{MHz}$). For each impedance sweep, the minimum impedance (the resonance frequency) and the maximum impedance (the anti-resonance frequency) is extracted in order to calculate the coupling coefficient based on Eq. (2.40) on page 28.

It is seen that for the positive polarity, the coupling coefficient is unstable during the first couple of hours after which it stabilizes for the remaining eight hours. When the DC bias is switched off, the mechanical response vanishes in the impedance measurement, and the coupling coefficient is hence zero. When the negative DC bias is applied, the coupling coefficient deteriorates with a characteristic decay time of $15\,\mathrm{min}$. Hereafter, it remains on a low level for the rest of the measurement. This indicates that the effective DC bias and hence the electrostatic force on the CMUT is reduced, since this will reduce the coupling coefficient as discussed in Section 2.4. To confirm this hypothesis, the capacitance was measured in the two polarities as shown in Fig. 5.13. A reference measurement was first made at $0\,\mathrm{V}$, after which the capacitance was measured at both positive and negative polarity at $120\,\mathrm{V}$. A delay of $20\,\mathrm{s}$ was applied before each capacitance measurement to ensure that the DC bias had time to stabilize.

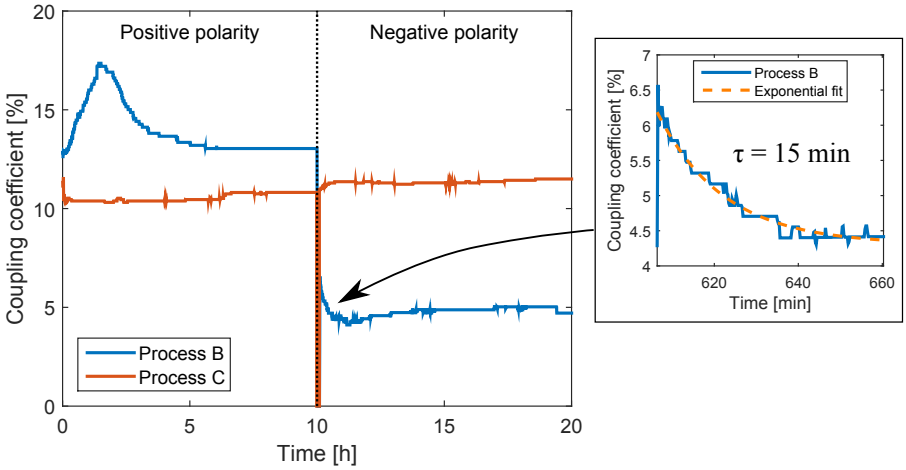

Figure 5.12: Charging of fabricated CMUTs investigated by measuring the coupling coefficient of the transducer. The measurement is performed for a total of 20 hours with the polarity of the applied DC bias switched after 10 hours. There is 5 minutes without DC bias between the two biased sections. The blue curve is measured on a CMUT element made using Process B, and the red curve on an identical element made using Process C. The inset shows a detail of the measurement and an exponential fit showing a characteristic decay time of $15\,\mathrm{min}$.

Each capacitance value in Fig. 5.13 has been normalized to the capacitance at $0\,\mathrm{V}$ DC bias. In the positive polarity, the capacitance expectedly increases by roughly $13\,\%$ due to the CMUT plates being pulled down by the electrostatic forces from the DC bias. As opposed to this, the capacitance is close to the unbiased capacitance in the negative polarity (less than $1\,\%$ difference). Thus, the electrostatic force seen by the CMUT plate is close to zero when the negative DC bias is applied. To confirm that the change in capacitance is not due to e.g. the formation of depletion layers in the silicon electrodes, an identical measurement was made on an element without cavities. As seen in Fig. 5.13, the capacitance of this element was unaffected by the DC polarity as expected. The test elements used for the measurements were equal in size to an array element, but designed to be easily probed. The layout may be seen in the appendix under Mask Set B.

In order for the electric field in the CMUT cavity to be reduced, charges within it must be screening the charges in the top- and bottom electrodes. A number of conclusions can be drawn regarding the nature of the charges: First, the polarity dependency was seen to depend on the orientation of the electric field relative to the oxide layer configuration in the CMUT. A cross-section of the CMUT used to perform the measurement resulting in the blue curve in Fig. 5.12 is illustrated in Fig. 5.14. Here, it is seen that the oxide is located on the top plate. As described in Section 4.4, the process used for 1-D arrays had

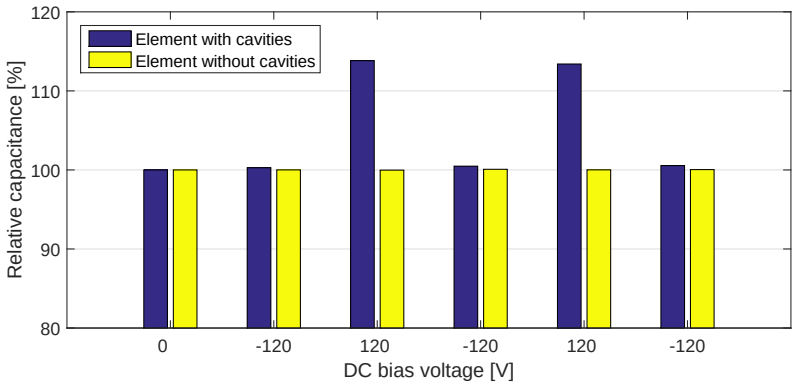

Figure 5.13: Measured capacitance as a function of DC bias voltage on a test element with cavities and an identical element without cavities. All capacitance values have been normalized to the capacitance at $0\,\mathrm{V}$ DC bias. The capacitance is unaffected by the bias for the element without cavities as expected. For the element with cavities, the capacitance increases for positive DC bias polarity due to the plates being pulled down by the electrostatic forces. This is not the case for negative bias polarity, showing that the field is screened by unwanted charges in this polarity.

the insulation oxide placed on the bottom electrode. If the silicon electrodes act as perfect conductors (i.e. no influence from depletion or inversion layers), then these two cavity structures are from an electrical viewpoint essentially flipped vertically, i.e. the situation for the 1-D CMUT cavities should be represented by the flipped version of Fig. 5.14. This would then require the polarity dependency to be flipped as well, such that the low response is observed with the *positive* DC bias potential on the top plate. This was indeed observed in practice.

Secondly, it was observed that CMUTs without insulation oxide could conduct large currents between the top- and bottom electrodes at even a few volts. The side-walls of the oxide in the CMUT cavity therefore has a significant conductivity. From the oxide quality tests performed (see Section 4.2), the oxide bulk itself is not likely to conduct currents. From these arguments, it seems most probable that the mobile charges are located in the vacuum gap, where they are able to move on the surfaces.

It should be noted that the number of charges needed to cancel out the electric field in the vacuum gap is relatively low. The element used for the measurements had an effective gap height of $\sim 400\,\mathrm{nm}$, so the charge per area built up by the $120\,\mathrm{V}$ DC bias used in the measurements is therefore

$$Q' = C'V = \frac{8.854\,\mathrm{pF/m}}{400\,\mathrm{nm}} \cdot 120\,\mathrm{V} = 2.7\,\mathrm{mC/m^2}\,, \tag{5.13}$$

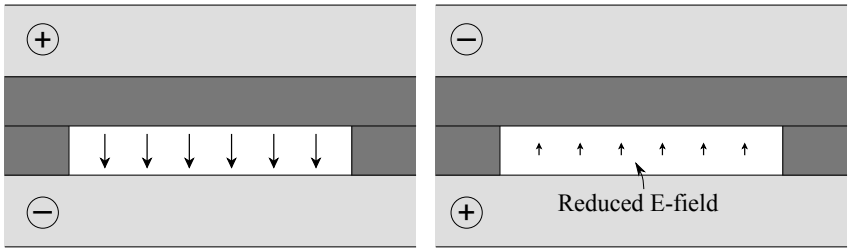

Figure 5.14: Illustration showing cross-section of the CMUT cavities used for measuring the blue curve in Fig. 5.12 in the two DC bias polarities. With the negative DC bias potential placed on the top electrode, the electric field is seen to be reduced due to unwanted charges between the two electrodes. In the illustration, silicon is light grey and silicon dioxide is dark grey.

yielding a number of charges per area of

$$n_{\text{charges}} = \frac{Q'}{e} = \frac{2.7\,\text{mC/m}^2}{1.602 \cdot 10^{-19}\text{C}} \simeq 1.7 \cdot 10^{12}\text{cm}^{-2}\,. \tag{5.14}$$

This number is roughly a factor of 1000 smaller than the number of bonds per area on the silicon dioxide or silicon surfaces in the vacuum gap (May and Sze 2004, p. 53). Thus, even a sparse monolayer of charges on the surfaces in the vacuum gap of the CMUT would be able to screen the electric field. This demonstrates how sensitive CMUTs are to even a small number of unwanted mobile charges, which emphasizes the need for strict material quality and contamination control if CMUTs are to achieve the performance stability required to replace the currently dominating piezoelectric technology.

The issue with mobile charges was not observed on arrays fabricated using Process C as exemplified by the red curve in Fig. 5.12. Apart from the fabrication method, the lateral dimensions of the element used for this measurement was identical to that used for measuring the blue curve. Due to slightly larger gaps in the CMUT cavity, the pull-in was higher for the element made using Process C, but in both cases, the DC bias was set to roughly $80\,\%$ of the respective pull-in voltages (i.e. $120\,\text{V}$ for the blue curve and $190\,\text{V}$ for the red curve). The pull-in voltage was measured on another element on the same wafer to avoid excessive charging of the devices. Thus, the voltage used might deviate from the desired $80\,\%$, and the magnitude of the coupling coefficient measured for the two different elements is not necessarily comparable. Rather, the point is to illustrate the performance stability of Process C compared to Process B.

For all arrays made using Process C, the performance was observed to be stable over time in both polarities. However, a fixed offset was seen between the polarities, with the negative polarity having slightly better coupling coefficient than the positive as seen in Fig. 5.12. This effect indicates fixed charges in the CMUT cavity, which screens the applied field in one polarity and enhances it in the reverse polarity. Note also that since

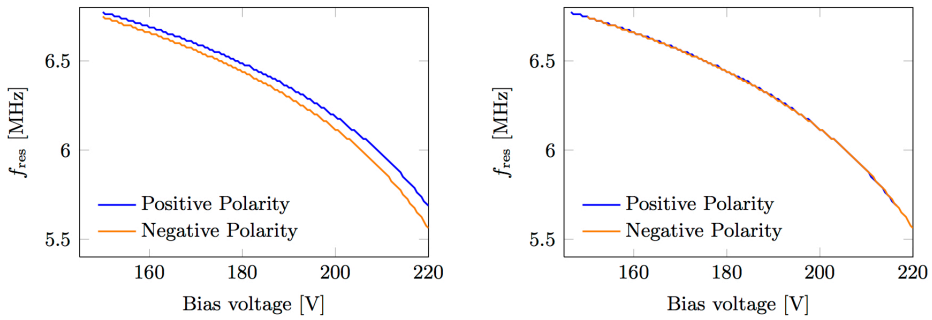

Figure 5.15: Resonance frequency of a device made using Process C as a function of increased DC bias in both polarities. The left figure shows the actual measurement, while the curve for the positive polarity has been shifted by $-3.5\,\mathrm{V}$ in the right figure. The similarity of the curves show that no mobile charges are present, but fixed charges are responsible for the shift in voltage.

the insulation oxide is placed on the bottom electrode in this process, the negative bias polarity produces the best coupling coefficients. This confirms the observations regarding the layer orientation commented on above.

The actual amount of fixed charge produced by Process C was measured by monitoring the resonance frequency of the device as a function of increased DC bias in both polarities. As seen in Fig. 5.15, the two resulting curves are identical in the two polarities except for an offset in voltage. The identical shape of the curves confirms that no mobile charges are present. A total of nine measurements on different test elements were performed, resulting in an offset voltage of -3.15 ± 0.59 V produced by the charges. The surface charge density needed to produce the offset voltage can be found similarly to the calculation above, yielding $1.5 \cdot 10^{10}\ \mathrm{cm}^{-2}$. Surface defects in this order of magnitude (equal to roughly 1 defect per 100,000 surface atoms) are expected for even high-quality annealed oxides (May and Sze 2004, p. 53). This therefore indicates that Process C produces CMUTs that represent the best that one can achieve in terms of charging control.

5.8 Chapter Summary

This chapter presented characterization results from row-column addressed 62+62 CMUT arrays made using the final layout presented in Chapter 3 and the fabrication processes presented in Chapter 4. The first part of the chapter reviewed the array design in detail after which the mounting of the array and the interconnect electronics used to perform the measurements were presented. Following this, electrical characterization results of arrays made using Process B were given based on Paper K. The pull-in, resonance frequency,

and capacitance was evaluated for all elements, which revealed capacitive coupling of the bottom electrodes to the substrate.

Acoustical characterization results were presented based on Paper K. The emitted pressure, sensitivity, insertion loss, bandwidth, center frequency, and impulse response were evaluated over an entire array. It was also experimentally demonstrated that volumetric images can be produced with the array. Following this, an investigation of the acoustical cross-talk in the array was presented based on results from Paper L. It was shown that the orthogonal orientation of transmitting and receiving elements leads to a significant decrease in acoustical cross-talk compared to that seen in 1-D CMUT arrays.

In several arrays made using Process B, issues of charging were observed, leading to a decrease in coupling coefficient over time and a significant difference in coupling coefficient for the two DC bias voltage polarities. It was shown that this issue is not present in arrays made using Process C, which shows a stable coupling coefficient over 20 hours of testing.

CHAPTER 6

Probe Development

This chapter presents the development of a row-column addressed CMUT probe for use on a commercial bk3000 ultrasound scanner from BK Medical. The array layout and fabrication technology presented in the previous chapters were used to produce the transducer, and custom buffer amplifier boards were designed to be placed in the handle in order to drive the cable to the scanner. The first section presents the design requirements to the transducer array and the interconnect electronics. The second section covers the assembly of the probe, where the transducer and electronics are electrically shielded and mounted in a 3-D printed probe handle featuring a protective lens coating on the transducer array. Finally, the probe performance is evaluated both in terms of element characteristics and imaging performance, where volumetric imaging with the probe is demonstrated on the SARUS experimental scanner. The complete volumetric beamforming algorithm had not yet been implemented on the bk3000 scanner at the end of this project, but the compatibility with the probe is demonstrated by real-time cross-plane images produced using the bk3000 scanner.

6.1 Probe Design

Aside from demonstrating the first ever produced row-column addressed probe for use on a commercial scanner, the main purpose of developing the probe was to demonstrate that volumetric imaging can be performed without the complexity of state-of-the-art matrix probes and their associated scanner systems. Ideally, one could envision a situation where the complexity and cost of real-time 3-D ultrasound imaging is reduced to that of conventional a 2-D ultrasound system. To show that this is in fact possible in practice, the probe was designed to be used on a bk3000 scanner from BK Medical Aps (Herlev, Denmark), which is made for conventional 2-D scanning. The scanner can supply an AC excitation voltage amplitude of up to 75 V, and has two built-in DC voltage supplies of ± 95 V. The latter may be used directly as DC bias for the CMUT transducer array if the two polarities are placed on the top- and bottom electrodes of the array similar to the approach described in Section 5.2. Also, the cable from the probe to the scanner is a coaxial cable used for 1-D transducer arrays. Therefore, the two most expensive parts of the scanner system – the cable and the scanner itself – are identical to that of a conventional 2-D ultrasound system. The only difference is the beamforming algorithm and the transducer array itself. The former, presented in Section 3.3, is a standard delay-

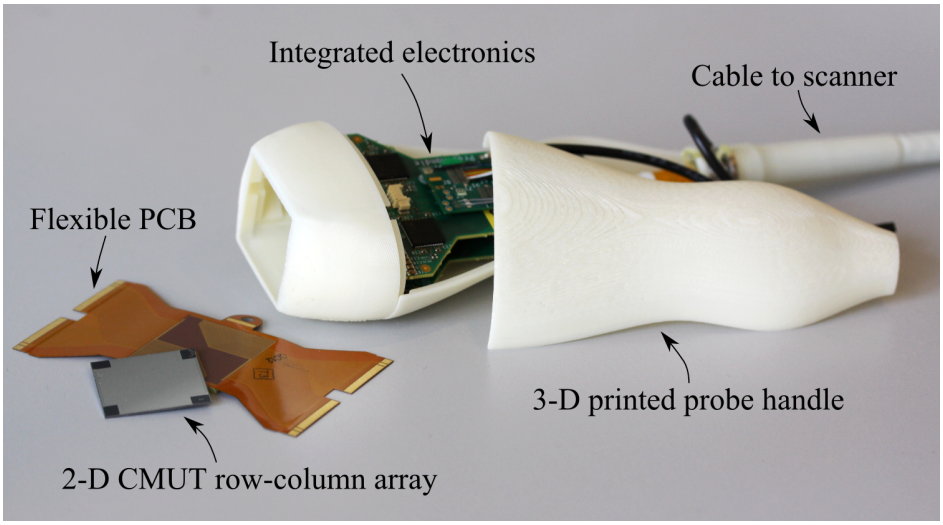

Figure 6.1: Image showing the main components of the probe: The CMUT array itself, the flexible PCB, and the amplifier PCBs which are all encapsulated in a 3-D printed probe handle. The amplifier PCBs drive the cable to the ultrasound scanner carrying the channel signals as well as voltage supplies for the electronics and the CMUT bias. The image does not show the shielding foil and the protective coating of the array surface.

and-sum beamformer, which therefore may readily be implemented on the scanner. The fabrication of the transducer array only uses one additional mask step compared to a 1-D transducer process as covered in Section 4.6. Therefore, the total system cost is comparable to a 2-D imaging system.

The main components of the probe are seen in Fig. 6.1. It consists of the CMUT array itself, which is mounted on a flexible PCB that connects to a set of rigid buffer amplifier PCBs. The buffer amplifiers drive the cable to the scanner, and the entire probe is encapsulated in a 3-D printed probe handle. Not shown in the image are the electrical shielding material and the coating of the transducer array.

In the previous chapters, a row-column addressed transducer layout with $62 + 62$ channels and four apodization region electrodes was developed and described in Chapter 3. An optimized fabrication process based on LOCOS processing was also developed and described in Chapter 4. The developed layout and fabrication technology was used for producing the CMUT array for the probe, which was designed to have a nominal center frequency of $3\,\mathrm{MHz}$. The desired pull-in voltage of the array was $240\,\mathrm{V}$, such that the $190\,\mathrm{V}$ DC bias supplied by the scanner would correspond to $80\,\%$ of the pull-in voltage. The maximum AC excitation that the scanner can deliver ($\pm 75\,\mathrm{V}$) thus corresponds to roughly $31\,\%$ of the pull-in voltage. The vertical dimensions of the CMUT used to achieve

Table 6.1: Vertical dimensions for the CMUT array (lateral given in Mask Set C).

Parameter	Value	Unit
Plate thickness	1.85	µm
Vacuum gap height	448	nm
Nitride thickness	56	nm
Insulation oxide thickness	410	nm
Post oxide thickness	1346	nm

this voltage specification are listed in table 6.1. The lateral dimensions are dictated by the mask layout, which is given in the appendix as Mask Set C.

The interconnect electronics made by the collaboration partners at BK Medical Aps (Herlev, Denmark) were almost identical to the electronics described in Section 5.2, except for a change in the suppliers of the pre-amplifiers and a significantly smaller foot-print of the PCBs to allow for mounting inside the probe handle. Two amplifier PCBs were used with each 64 channels of which two channels were reserved the apodization electrodes (the motivation for this setup is given in Section 5.2). The total size of the probe could have been reduced slightly by instead using four PCBs that addressed the channel connections on each of the four sides of the array. However, the approach with two PCBs was chosen for practical reasons, as it allowed the PCB setup to be used for probes with either 1-D arrays or row-column addressed arrays. The gain of the amplifiers was set to $0\,\mathrm{dB}$, so the amplifiers only functioned as high impedance buffer amplifiers improving the voltage readout of the CMUT elements.

6.2 Probe Assembly

The assembly of the probe was mainly carried out by the collaboration partners at Sound Technology, Inc. (State College, PA, USA). After completing the cleanroom fabrication, the CMUT array was mounted and glued onto the flexible PCB seen in Fig. 6.1, which contained a rigid support directly beneath the array. The wire-bonding used to connect the array elements to bonding pads on the flexible PCB was performed at DELTA Dansk Elektronik, Lys & Akustik (Hørsholm, Denmark). Traces on the flexible PCB led to two sets of connector pins, which could be connected to the two rigid amplifier PCBs. A glob-top dam was applied around the array as seen in Fig. 6.2(a). The glob-top dam was applied such that the height was higher than the wire-bonds, and with the corners left open. The former was done to ensure that the wire-bonds were not exposed to mechanical stresses when pressing the probe against an object, and the latter was done to ease the application of the coating seen in Fig. 6.2(b). Before the coating, the array surface was cleaned gently with acetone/IPA without any mechanical cleaning. The coating was performed using room temperature vulcanization (RTV) silicone (speed of sound: $1000\,\mathrm{m/s}$), which provided electrical insulation of the transducer surface and wire-bonds simultaneously.

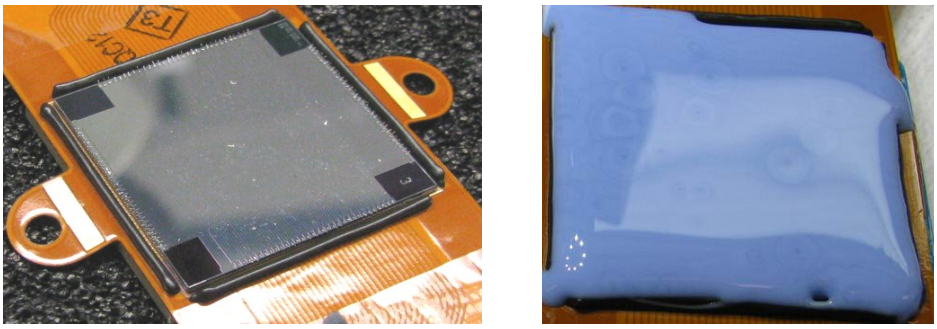

(a) (b)

Figure 6.2: (a) CMUT array mounted on and wire-bonded to the flexible PCB. Note the glob-top dam around the array with the corners left open. (b) RTV silicone being applied to the array after cleaning the array surface.

Coating the wire-bonds with RTV silicone proved to be a more robust approach than covering them with glob-top, since the latter technique occasionally resulted in detaching wire-bonds.

Before curing of the RTV silicone, an aluminized polymer foil ($12.5\,\mu\mathrm{m}$ polypropylene with a sub-micron thick aluminum layer) was applied and planarized using a piece of glass after which the array and flexible PCB was mounted in the nose-piece of the 3-D printed handle as seen in Fig. 6.3(a). The aluminum foil was applied to provide a grounded shielding layer on top of the array for both patient safety and electrical noise shielding. The aluminum layer thickness was chosen to provide a compromise between acoustical transparency and electrical shielding performance. Thicker shielding layers of copper were also tested, but these resulted in significant acoustical reflections from the foil.

Before assembling the probe electronics, the nose piece was completed by applying a second layer of RTV silicone on top of the shielding as seen in Fig. 6.3(b). The coating was applied to a final thickness of $1.5\,\mathrm{mm}$ and leveled such that no lensing effect occurred. Then, the connectors on the flex PCB protruding from the back of the assembled nose piece were connected to the two rigid amplifier PCBs, and the cable was attached to the latter as seen in Fig. 6.4(a). The cable carried both the 128 channels as well as supplies for the buffer amplifiers and DC bias for the CMUT array. The entire probe electronics were wrapped in a shielding foil, which was connected to the shielding foil applied to the array as seen in Fig. 6.4(b). This shield was then connected to the shield on the coaxial cable via the two black wires in Fig. 6.4(b), and connected to the ground reference of the scanner. This was done to ensure optimal electrical screening of the ultrasound probe.

Finally, the two 3-D printed parts constituting the handle of the probe were attached

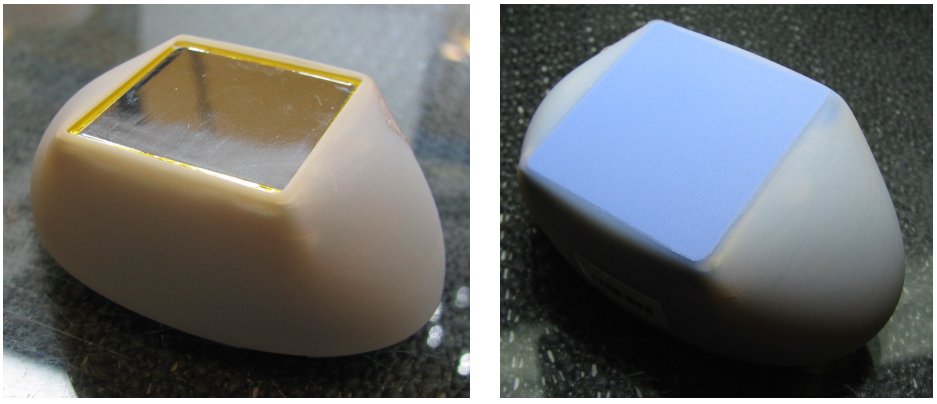

(a) (b)

Figure 6.3: (a) Nose piece before lensing showing the array covered with the aluminum shielding foil. (b) Completed nose piece after application of the lens, which is a flat coating made of RTV silicone.

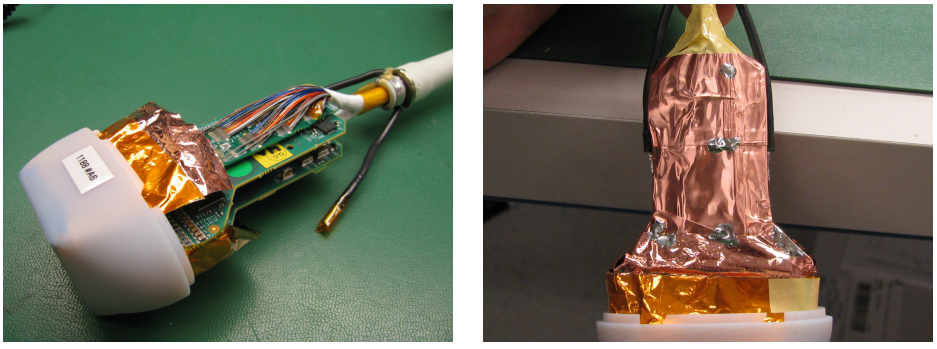

(a) (b)

Figure 6.4: (a) Nose piece with the amplifier boards and scanner cable connected. (b) Amplifier boards wrapped in shielding foil. The foil is soldered to the cable shield and the array shielding foil to provide an unbroken ground plane around all the electronics and array.

Figure 6.5: Image of the completed row-column probe with 62 row channels, 62 column channels and integrated apodization. The probe is designed to be used with a commercial bk3000 ultrasound scanner from BK Medical Aps (Herlev, Denmark).

to complete the row-column addressed CMUT probe. An image of the fully assembled probe is seen in Fig. 6.5.

6.3 Probe Characterization

After assembly, the probe was characterized acoustically. The pulse-echo impulse response of each element was measured at Sound Technology, Inc. (State College, PA, USA) using a XCDR II Pulse Echo Test System by emitting with one element at a time against a plane stainless steel reflector placed in DI water $25\,\mathrm{mm}$ from the face of the probe. Due to the available setup, the elements were actuated with a square pulse having an amplitude of $50\,\mathrm{V}$, and the elements were biased at $200\,\mathrm{VDC}$. The received signal was then de-convolved with the excitation pulse to yield the impulse response.

In Figs. 6.6(a) and 6.6(b), the average impulse response and its envelope are shown for the rows and columns, respectively. In this setup, the rows are the top electrodes of the CMUT array, while the columns are the bottom electrodes. This explains the lower pulse-echo response from the columns due to the substrate coupling discussed in

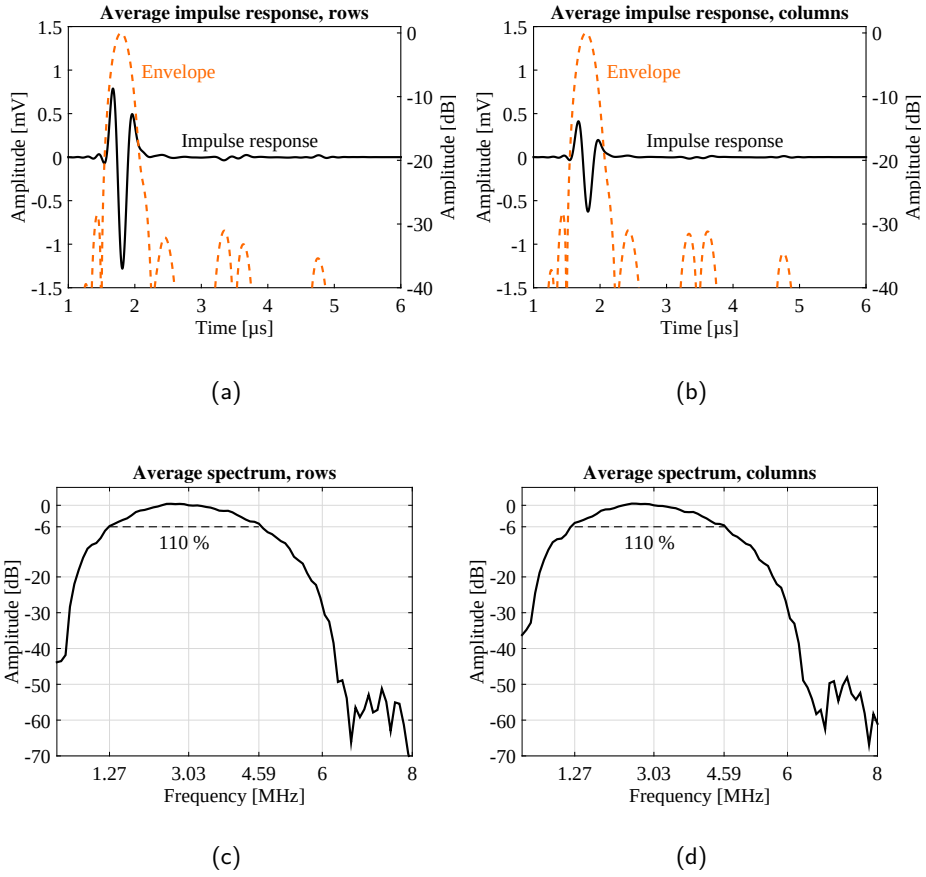

Figure 6.6: Average impulse response and normalized envelope of the rows (a) and columns (b) of the assembled probe. Note that the impulse response of the columns has an amplitude of roughly half that of the rows due to substrate coupling as discussed in Section 5.3. Also note the two lobes after the main lobe which are due to reflections from the shielding foil. The impulse response spectra are shown for the rows in (c) and for the columns in (d). The center frequency and $-6\,\mathrm{dB}$ fractional bandwidth are indicated in the plot.

Table 6.2: Probe characterization parameters.

Parameter	Mean	Std.	Unit
Rows			
Center frequency	3.03	0.13	MHz
$-6\,\mathrm{dB}$ fractional bandwidth	110	3	%
Peak-to-peak surface pressure	474	68	kPa
Sensitivity (rel. $1\,\mathrm{V}$)	-53.7	1.5	dB
Relative phase delay at $3\,\mathrm{MHz}$	0	5.2	Degree
Columns			
Center frequency	3.03	0.09	MHz
$-6\,\mathrm{dB}$ fractional bandwidth	110	4	%
Peak-to-peak surface pressure	425	60	kPa
Sensitivity (rel. $1\,\mathrm{V}$)	-59.7	0.7	dB
Relative phase delay at $3\,\mathrm{MHz}$	0	4.9	Degree

Section 5.3. Note the two extra lobes after the main lobe around $-30\,\mathrm{dB}$ starting at times $3.2\,\mu\mathrm{s}$ and $4.7\,\mu\mathrm{s}$. The time difference between the two is thus $1.5\,\mu\mathrm{s}$, which corresponds to the time difference between the main lobe and the first secondary lobe. This therefore suggests reflections within the probe. The speed of sound in the RTV silicone coating is $1000\,\mathrm{m/s}$, so the reflections indicate a reflecting structure at a distance of $0.7\,\mathrm{mm}$, which corresponds to the shielding foil covering the array.

In Figs. 6.6(c) and 6.6(d), the corresponding average spectra for the rows and columns are shown. The center frequency and $-6\,\mathrm{dB}$ fractional bandwidth relative to the center frequency are indicated in the plot, demonstrating an almost identical spectrum for the rows and the columns. The center frequency is calculated as described by Eq. (5.1) on page 109. Note that the spectrum is more ideal and Gaussian-like than the spectrum presented in Fig. 5.7(b) on page 109. This is possibly due to the use of dedicated characterization equipment for the probe as opposed to the SARUS experimental scanner that was used to produce Fig. 5.7(b). Table 6.2 presents statistics on the center frequency, fractional bandwidth, sensitivity, and relative phase delay between the elements, all extracted from the measured impulse response. The pulse-echo peak-to-peak sensitivity is reported in dB relative to $1\,\mathrm{V}$, and is valid for the specific setup used. The phase delay was found by extracting the time corresponding to the maximum in the impulse response envelope for each element, correcting for any linear slope due to misalignment between the transducer and plane reflector, and setting the mean to 0. Subsequently, the phase delay was calculated by dividing by the time it takes a $3\,\mathrm{MHz}$ wave to travel one full wavelength, and multiplying by $360°$.

A second setup was used to find the pressure emitted from the elements. A HGL-0400 hydrophone connected to a AC-2010 pre-amplifier (Onda Corporation, CA, USA) was placed $7\,\mathrm{mm}$ from the transducer surface and scanned over each element using the

positioner of the intensity measurement system AIMS-3 (Onda Corporation, CA, USA), while transmitting a $3\,\mathrm{MHz}$, 4-cycle sinusoidal signal on the element being measured. The voltages for which the probe was designed, i.e. an AC amplitude of $75\,\mathrm{V}$ and a DC bias of $190\,\mathrm{V}$, was used for the measurements. The recorded pressure at $7\,\mathrm{mm}$ was then compensated to find the pressure at the transducer surface. The compensation was found by a simulation in COMSOL Multiphysics 4.4 (COMSOL AB, Stockholm, Sweden). Here, an element with the same dimensions as the physical elements in the array was set to emit a continuous $3\,\mathrm{MHz}$ pressure wave, and the pressure magnitude at a distance of $7\,\mathrm{mm}$ from the element relative to the pressure magnitude at the element surface was found and used as the compensation factor (9.6). The resulting surface pressure emitted by the elements is seen in Table 6.2. It is interesting to note that there is no significant difference in the surface pressure emitted by the rows and columns. The $6\,\mathrm{dB}$ loss in pulse-echo sensitivity on the columns relative to the rows is therefore due to a loss during receive. This supports the discussion on capacitive substrate coupling in Section 5.3: If enough current can be supplied to maintain the voltage on the CMUT electrodes, the parasitic capacitance has no effect. During transmit, the amplifiers deliver enough current to achieve this. In receive, the CMUT itself generates the current, and the influence of the parasitic is thus seen.

6.4 Imaging Results

A set of volumetric imaging experiments were carried out using the probe. The SARUS experimental scanner (Jensen et al. 2013) was used for acquiring the data for volumetric imaging. The commercial bk3000 scanner was not used since the beamforming algorithm described in Section 3.3 had not been implemented at the time of the acquisition.

RF data was acquired down to a depth of $15\,\mathrm{cm}$ at a sampling frequency of $70\,\mathrm{MHz}$ using the voltages for which the probe was designed, i.e. $190\,\mathrm{V}$ DC bias and an AC amplitude of $75\,\mathrm{V}$ with a two-cycle excitation at $3\,\mathrm{MHz}$. A second DC voltage supply of $\pm 5\,\mathrm{V}$ was used to power the buffer amplifiers in the handle set to gain of $0\,\mathrm{dB}$. The DC voltage supplies were provided through a TOE8842 and a TOE8852 dual DC power supply (Toellner Electronic Instrumente GmbH, Herdecke, Germany), respectively. The RF data was acquired using single element emission with data being received on all elements for each emission. For the beamforming, only the data received by the 62 rows were used, while the transmit aperture was generated synthetically using the 62 columns. Thereby, ideal focusing could be performed in every point of the beamformed volume. A conservative pulse repetition frequency of $10\,\mathrm{Hz}$ was used to avoid any reverberations or potential probe heating in these preliminary tests. However, the use of 62 emissions to generate a volumetric image down to a depth of $15\,\mathrm{cm}$ sets a maximum volumetric frame rate of $1/(0.2\,\mathrm{ms} \cdot 62) \simeq 80\,\mathrm{Hz}$, where the round-trip time of a single pulse-echo event is given by Eq. (3.1) on page 43. Before beamforming, the RF data was high-pass and match filtered to remove low frequency noise from the scanner system.

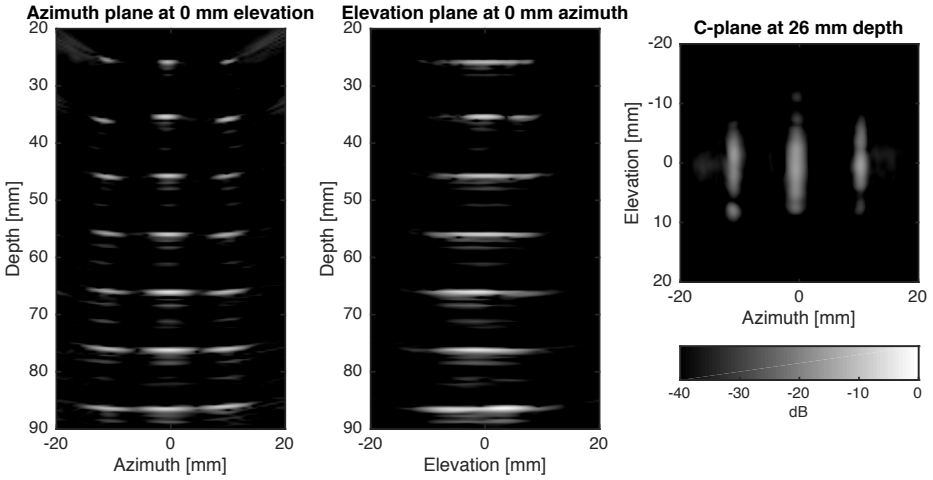

Figure 6.7: Volumetric imaging of a wire phantom using the developed probe. Three cross-planes (azimuth, elevation, and C-plane) are shown from a volume of $4\,\mathrm{cm} \times 4\,\mathrm{cm} \times 7\,\mathrm{cm}$ at a dynamic range of $40\,\mathrm{dB}$. The origin corresponds to the center of the transducer surface. Note the "ghost" wires, which are due to the extra reflections in the impulse response seen in Fig. 6.6.

Two different phantoms were imaged: The first contained a rectangular grid of $0.2\,\mathrm{mm}$ diameter wires with an inter-spacing of $1\,\mathrm{cm}$ submerged in DI water. This was used to evaluate the LSF for different spatial positions. The other phantom was a single $0.7\,\mathrm{mm}$ diameter wire-end submerged in DI water and oriented perpendicular to the transducer surface. It thereby mimicked a point target, allowing the PSF of the probe to be determined.

In Fig. 6.7, three cross-planes from the resulting volumetric image of the multi-wire phantom is shown at a dynamic range of $40\,\mathrm{dB}$. The origin corresponds to the center of the transducer surface. The azimuth plane is oriented perpendicular to the receiving rows and shows the cross-section of the wires. Note the two faint "ghost" wires underneath each wire. These are due to the reflections from the electric shielding foil inside the probe that are also visible in the impulse response seen in Fig. 6.6. Note also the grating lobe effect at the upper corners of the image near the transducer. This arises due to a synthetic steering of the beam in receive which exceeds that allowed by the array pitch of $270\,\mu\mathrm{m}$, corresponding to 0.54λ at $3\,\mathrm{MHz}$.

The elevation plane oriented perpendicular to the transmitting columns shows the full length of the wires with a rapid drop in signal near the array edge. As discussed in Section 5.5, this is partly due to the sound being emitted straight down from the array, and partly due to the nature of the wires, which reflect the sound away from the array

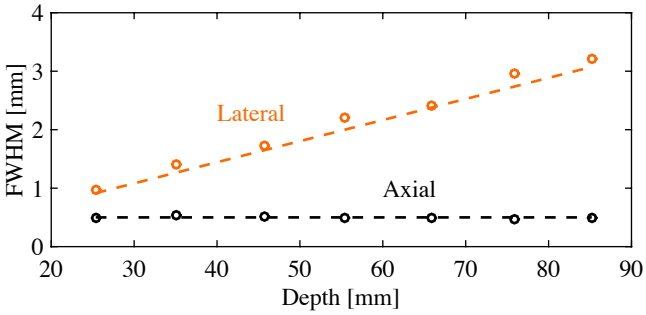

Figure 6.8: Axial and lateral FWHM as a function of depth extracted from the center column of wires shown in the azimuth cross-plane in Fig. 6.7. The points correspond to the measured FWHM and the dashed lines to the theoretical estimates. The latter are calculated by assuming a lateral FWHM given by Eq. (3.3) on page 44, and an axial FWHM equal to that of one wavelength at $3\,\mathrm{MHz}$ in water ($0.5\,\mathrm{mm}$).

when the impinging wave hits at an angle. The effect is also seen in the C-plane, where the azimuth direction is seen to provide a slightly larger field of view than the elevation direction due to the orientation of the wires.

In Fig. 6.8, both the axial and lateral FWHM has been extracted as a function of depth by using the center column of wires seen in the azimuth plane in Fig. 6.7. The resulting values for the seven wires have been given as circles in Fig. 6.8. Theoretically, the axial FWHM should be that of one wavelength at $3\,\mathrm{MHz}$ in water, which is $0.5\,\mathrm{mm}$. This value has been plotted with a black dashed line, showing excellent correspondence. The theoretical lateral FWHM in the focus is given by Eq. (3.3) on page 44. Due to the synthetic beamforming, all points in the volume are in focus, so that Eq. (3.3) should be able to predict the measured lateral FWHM. As seen by the orange dashed line, this is indeed the case.

Wires can only provide a measure of the LSF of the array. To get a measure of the true PSF, the second phantom consisting of a single wire-end was imaged using the same imaging sequence as described for the multi-wire phantom. The wire-end was pointing towards the array surface at a depth of $2.8\,\mathrm{cm}$ ($f_{\#} = 1.67$) such that it appeared as a point seen from the transducer array. A volumetric image was generated from the acquired data, and the exact location of the point determined. Then, an azimuth, elevation, and C-plane cross-section through the point was extracted, the result of which is shown in Fig. 6.9. The PSF is plotted at a dynamic range of $60\,\mathrm{dB}$ with contour lines at $-6\,\mathrm{dB}$ and $-30\,\mathrm{dB}$.

As expected, the PSF is seen to be symmetrical with a lateral FWHM of $1.86\,\mathrm{mm}$ in the azimuth direction and $1.83\,\mathrm{mm}$ in the elevation direction. These are slightly larger than the theory predicts (see Fig. 6.8), which is due to the $0.7\,\mathrm{mm}$ diameter of the physical point source. For both directions, the axial FWHM is $0.5\,\mathrm{mm}$, which is expected from

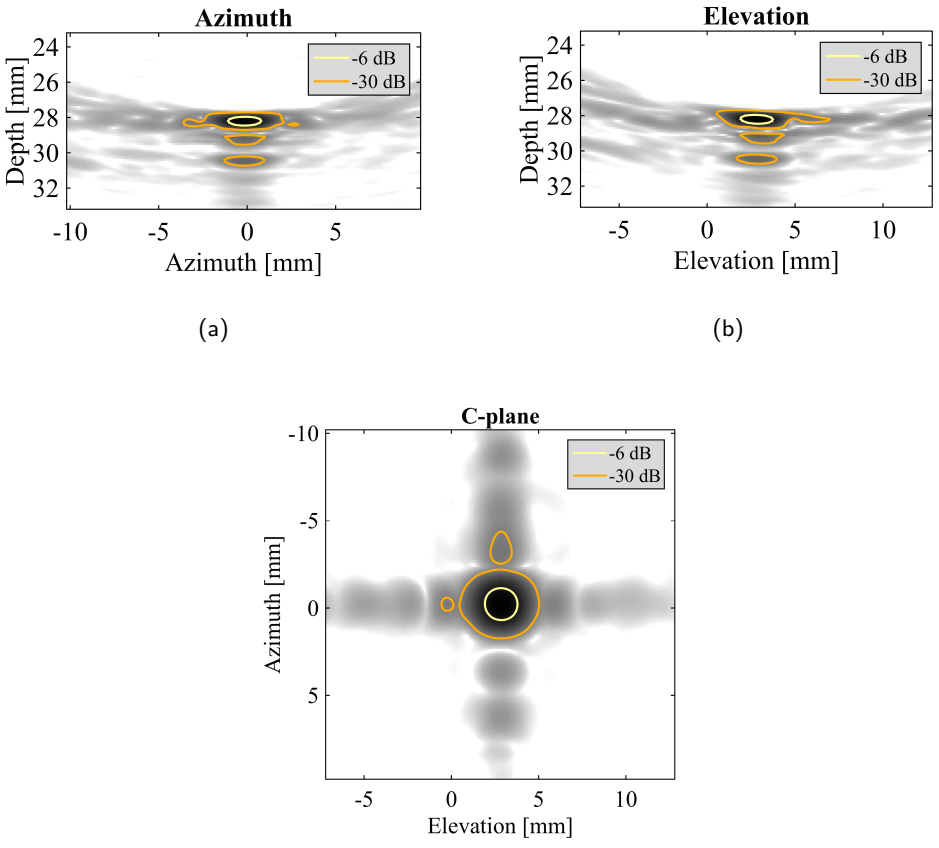

Figure 6.9: Volumetric image of a point target positioned at a depth of $2.8\,\mathrm{cm}$ ($f_{\#} = 1.67$). The dynamic range is $60\,\mathrm{dB}$ and contour lines are shown at $-6\,\mathrm{dB}$ and $-30\,\mathrm{dB}$. (a) Azimuth plane, (b) Elevation plane, (c) C-plane. Note the symmetry in the C-plane as expected. Note also the two extra "ghosts" in figure (a) and (b) within the $-30\,\mathrm{dB}$ contour line in the depth direction. These are due to the reflections from the shielding foil seen in the impulse response in Fig. 6.6.

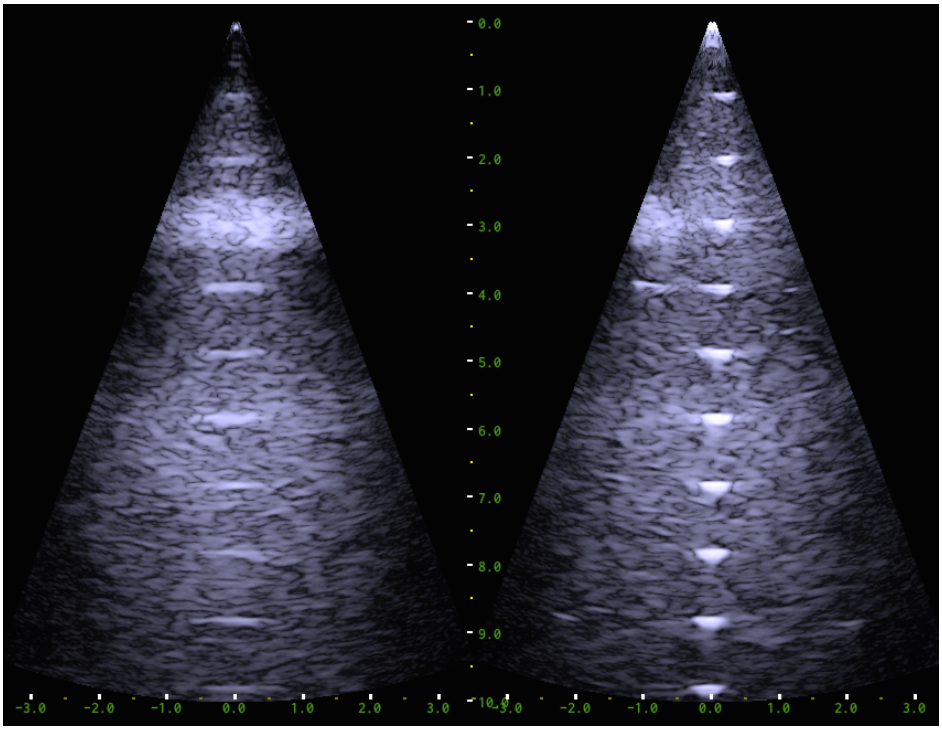

Figure 6.10: A snapshot of the real-time image display from the bk3000 scanner from BK Medical showing two cross-planes. The row-column addressed probe is here used as two decoupled 1-D phased arrays to demonstrate the probe's compatibility with the commercial scanner. The cross-planes show a set of wires in a tissue mimicking phantom down to a depth of $10\,\mathrm{cm}$ and a sector angle of 45°. Also, a hyperechoic cylinder is located at a depth of $3\,\mathrm{cm}$.

theory. Note the two extra "ghosts" in Figs. 6.9(a) and 6.9(b) within the $-30\,\mathrm{dB}$ contour line in the depth direction. These are due to the reflections from the shielding foil seen in the impulse response in Fig. 6.6.

A measure of the side-lobe energy may be found as the energy of the signal outside the $-6\,\mathrm{dB}$ contour line relative to that within it. This calculation leads to a value of $-40\,\mathrm{dB}$ for both lateral directions. Also, the SNR of the probe was found by acquiring data for 10 images and subtracting the mean of the 10 images from a single image to get the noise. The signal-to-noise ratio (SNR) in the beamformed image was then calculated using the method presented in Eq. (9) in (Rasmussen and Jensen 2014), yielding a SNR at the center of the point of $61.7\,\mathrm{dB}$.

As stated above, no volumetric images were produced using the bk3000 scanner

since the beamforming algorithm described in Section 3.3 had not yet been implemented. However, to prove the compatibility with the scanner, the bk3000 scanner was set to treat the probe as two decoupled 1-D phased arrays. This enabled real-time phased array imaging simultaneously in both the azimuth and elevation directions. All elements in each 1-D array was used as both transmitters and receivers, the transmit focus was set to a depth of $5\,\mathrm{cm}$, while dynamic receive focusing was employed. The transmit focus was steered in a sector angle of $45°$, and the probe was thus used as proposed in Fig. 3.16 on page 62.

A snapshot of the real-time image display from the scanner is shown in Fig. 6.10. The phased array images generated from the rows, respectively columns, are shown side-by-side. A tissue-mimicking phantom containing wires is imaged down to a depth of $10\,\mathrm{cm}$, the wires running parallel to the image plane in the left figure and perpendicular to the image plane in the right figure. Also, a hyperechoic cylinder is located at a depth of $3\,\mathrm{cm}$. The cylinder is seen across the whole left image, since it consists of point scatterers. As opposed to this, the wires reflect the sound away and are thus only seen in the center of the image.

Note that the images in Fig. 6.10 are not true cross-planes due to the lack of an elevation lens. Rather, eack plane is a sum of the signals received along the length of the elements. This is especially seen by looking at the hyperechoic cylinder, which is seen to coincide with the wires in the left image although it is located to the left of the wires in the right image. Therefore, Fig. 6.10 merely demonstrates the probe's compatibility with the scanner and real-time capability. For both volumetric images as well as cross-planes, be it phased array imaging or rectlinear imaging, the beamforming algorithm described in Section 3.3 must be implemented.

6.5 Chapter Summary

This chapter presented the development of the first ever demonstrated row-column addressed ultrasound probe. It was designed to be used with a commercial bk3000 scanner from BK Medical Aps (Herlev, Denmark). The scanner is made for conventional 2-D imaging, but due to the low channel count of the row-column addressed probe, the probe and scanner can be directly interfaced. The goal of this chapter was therefore to demonstrate that volumetric imaging with equipment in the price range of conventional 2-D imaging is possible. The transducer layout and fabrication technology presented in the previous chapters were used to produce an array that could be used with the voltages available on the scanner. A solution with a flexible mounting PCB and two rigid amplifier PCBs were used to mount the array and interface it to the scanner cable via buffer amplifiers. The array and electronics were electrically shielded with a metal foil, and the array was coated with a silicone coating before the entire probe was encapsulated in a 3-D printed handle. Each element was acoustically tested, and the volumetric imaging performance of the array was evaluated using the experimental SARUS scanner. The

compatibility with the bk3000 scanner was also demonstrated using the probe as two decoupled 1-D phased arrays, since the volumetric beamforming algorithm had not yet been implemented in the scanner at the time of this project's completion.

CHAPTER 7

Conclusion and Perspectives

This thesis has presented the results of the PhD project entitled Micromachined Ultrasonic Transducers for 3-D Imaging. The main goal of the project was to develop a transducer probe capable of real-time volumetric ultrasound imaging without the complexity of state-of-the-art matrix probes. To achieve this, row-column addressed arrays were investigated, since they offer a significant reduction in the number of transducer elements relative to matrix arrays. The capacitive micromachined ultrasonic transducer (CMUT) technology was chosen as a platform for the fabrication of the transducers due to the flexibility and possibilities of this technology.

In Chapter 2, a theoretical treatment of the CMUT was presented. The static and small-signal dynamic behavior was derived using energy considerations and an assumption of a constant deflection shape of the deformable plate of the CMUT, allowing for lumping and linearization of the system. The derivation was performed using anisotropic theory to describe the deflection of the plate having either circular or square geometry based on Papers A, B, and E. From the static analysis, the pull-in voltage was determined. The small-signal dynamic behavior was described using an equivalent circuit model from which the coupling coefficient of the transducer was derived. From this, it was shown that the transducer should be operated as close as possible to the pull-in voltage, and that the electrical capacitance of the transducer should be kept at a minimum. Also, a method for experimentally extracting the coupling coefficient was devised. A FEA model including interaction with the acoustic medium was used to investigate the optimal scaling parameters for a square CMUT based on Paper F. Two scenarios were investigated, representing two extremes: That of a single isolated CMUT cell and that of an infinite 2-D array of CMUT cells. It was shown that the mutual impedance from neighboring cells has a significant impact on the behavior of the CMUT. The following was found to be true for both configurations: For a fixed center frequency in immersion, CMUTs with thick plates produce the highest transmit pressure. Also, the separation between the top- and bottom electrodes should be made as large as the voltage rating of the system allows to produce the highest transmit pressures. A larger separation also increases the sensitivity for a voltage readout. However, the two scenarios disagreed for the optimal plate size in terms of sensitivity. In the single cell scenario, the smaller plates produced higher sensitivities, whereas this trend shifted for the infinite array scenario with decreasing sensitivities for increasing plate sizes until a critical point after which the sensitivity increased again. This was explained by the plate behavior going from over-damped to under-damped at the plate size defining this point. Finally, the far field sound radiation of a CMUT was analyzed

based on results from Paper C. Using a circular clamped plate to represent the CMUT, is was shown analytically that a CMUT used in an ultrasound transducer array will radiate sound similarly to that of a point source for all practical imaging purposes.

Chapter 3 described the concept of row-column addressed arrays and presented an analysis and optimization of their imaging performance. After a brief literature review, the imaging principle behind row-column addressed 2-D arrays was described including an estimate of the resolution and contrast obtainable with such arrays relative to fully addressed 2-D arrays. Then, the beamforming required to produce volumetric images was developed based on the findings in Paper J. Subsequently, it was shown that the long elements in row-column addressed arrays produce edge effects that lead to ghost echoes in the final beamformed image. A solution was proposed in the form of integrated apodization, which was demonstrated both theoretically and experimentally to mitigate the edge wave problem as covered in Papers I and J. An optimized apodization layout was developed that efficiently damps the edge waves without affecting the imaging performance of the array. The technique was demonstrated both by simulations and experimentally based on Papers J and K as well as Patent A. The last part of the chapter described how row-column addressed arrays can be used to estimate velocities in a volume as covered by Patent B. A simulated example from Paper M incorporating a blood vessel phantom was used to demonstrate the performance of the technique, proving that it is indeed able to estimate all three components of the velocity vector and thereby estimate key parameters such as the volume flow.

Chapter 4 described the microfabrication of CMUT arrays. A brief review of the two prevalent fabrication methods found in the literature was given, followed by an account of the few reported attempts to produce row-column addressed CMUT arrays. Two critical aspects of CMUT microfabrication, oxide quality and oxide protrusions, were discussed in detail, partly based on Paper G. The fabrication approach presented in Paper F was introduced as an effective solution to the problem of oxide protrusions. This approach was then incorporated in a new process (Process B) for fabricating row-column addressed 2-D CMUT arrays. Process B was shown to have certain drawbacks such as exposed bottom electrodes and oxide on the CMUT plates that could potentially compromise the device reliability. Therefore, a modified process (Process C) based on LOCOS oxidation was introduced, effectively eliminating the limitations of the previous process. Process C also provides a thicker insulation oxide, which is beneficial in terms of oxide breakdown voltage and parasitic capacitance. Finally, it was shown that wafer bow results in a limited fabrication yield due stress and consequently fractured CMUT plates. An effective solution to this was demonstrated, in which a support wafer was bonded to the wafer stack before etching free the CMUT plates to compensate for the wafer bow.

Chapter 5 presented characterization results from row-column addressed 62+62 CMUT arrays made using the final layout presented in Chapter 3 and the fabrication processes presented in Chapter 4. The first part of the chapter reviewed the array design in detail after which the mounting of the array and the interconnect electronics used to perform the measurements were presented. Following this, electrical characteriza-

tion results of arrays made using Process B were given based on Paper K. The pull-in, resonance frequency, and capacitance was evaluated for all elements, which revealed capacitive coupling of the bottom electrodes to the substrate. Acoustical characterization results were presented based on Paper K. The emitted pressure, sensitivity, insertion loss, bandwidth, center frequency, and impulse response were evaluated over an entire array. It was also experimentally demonstrated that volumetric images can be produced with the array. Following this, an investigation of the acoustical cross-talk in the array was presented based on results from Paper L. It was shown that the orthogonal orientation of transmitting and receiving elements leads to a significant decrease in acoustical cross-talk compared to that seen in 1-D CMUT arrays. In several arrays made using Process B, issues of charging were observed, leading to a decrease in coupling coefficient over time and a significant difference in coupling coefficient for the two DC bias voltage polarities. It was shown that this issue is not present in arrays made using Process C, which shows a stable coupling coefficient over 20 hours of testing.

The final chapter presented the development of the first ever demonstrated row-column addressed ultrasound probe. It was designed to be used with a commercial bk3000 scanner from BK Medical Aps (Herlev, Denmark). The scanner is made for conventional 2-D imaging, but due to the low channel count of the row-column addressed probe, the probe and scanner can be directly interfaced. The goal of this chapter was therefore to demonstrate that volumetric imaging with equipment in the price range of conventional 2-D imaging is possible. The transducer layout and fabrication technology presented in the previous chapters were used to produce an array that could be used with the voltages available on the scanner. A solution with a flexible mounting PCB and two rigid amplifier PCBs were used to mount the array and interface it to the scanner cable via buffer amplifiers. The array and electronics were electrically shielded with a metal foil, and the array was coated with a silicone coating before the entire probe was encapsulated in a 3-D printed handle. Each element was acoustically tested, and the volumetric imaging performance of the array was evaluated using the experimental SARUS scanner. The compatibility with the bk3000 scanner was also demonstrated using the probe as two decoupled 1-D phased arrays, since the volumetric beamforming algorithm had not yet been implemented in the scanner at the time of this project's completion.

The results of this PhD project have demonstrated the promising potentials of row-column addressed arrays. However, there are still a number of challenges that must be addressed in order for the technology to be a realistic alternative to the existing matrix probes. From an imaging perspective, it is a problem that only one-way focusing is possible in each dimension. However, there are a couple of strategies that might be employed to remedy this: One is to use an alternative beamforming approach, such as spatial match filtering. Preliminary results from colleagues at DTU Electrical Engineering have shown promising results, although the data processing requirements are much higher than for conventional delay-and-sum beamforming. Provided that only cross-plane imaging is of interest, another option could be to apply a focusing lens onto the array, which provides elevation focus in each dimension. The lens approach is also interesting

as a solution to the second major issue, namely that the row-column addressed arrays can only emit energy directly below the array and in a cross to the sides. For applications such as cardiac imaging, it is relevant to have a probe with a small foot-print capable of phased array imaging, such that the heart can be visualized through the ribs. True volumetric phased array imaging is possible with row-column addressed arrays, provided that the array is curved or a de-focusing lens is applied to spread the energy during transmit. An in-depth study of the possibilities in this approach is therefore highly relevant.

From a fabrication perspective, in this context CMUT fabrication, there are also a number of challenges left to address. Currently, the fabrication approach and array design produce significant parasitic capacitances, both due to substrate coupling and parasitic capacitances at the bonding areas. The latter might be addressed by optimizing the electrode layout and by increasing the oxide thickness outside the CMUT cells, while the former can be remedied by applying substrate bias to deplete the substrate for charge carriers, or by replacing the substrate with a non-conductive material. The thickness tolerances on the SOI wafers used to define the top plate of the CMUTs are also currently too poor to achieve highly predictable center frequencies and pull-in voltages. Thus, it is worth considering alternatives if a reliable and robust large-scale production becomes relevant.

From a packaging perspective, the manufactured probe can only be characterized as a preliminary prototype, and obviously there is therefore considerable room for improvement. For example, the current wire-bonding approach should be replaced with a more compact and robust process such as flip-chip bonding. The in-handle electronics may also be reduced in size by moving the passive electrical components responsible for filtering the DC and AC signals for each element (i.e. resistors and capacitors) to the silicon chip by integrating them in the cleanroom process.

This is only a small selection of the challenges involved in developing a commercially viable row-column addressed probe. However, the results so far demonstrate that the technology is a realistic alternative to state-of-the-art matrix probes, especially as a low-cost alternative. In a longer perspective, it is also highly interesting for wire-less 3-D scanning due to the reduced data processing requirement. Ultimately, these advantages might contribute to an increased use of real-time 3-D ultrasound imaging in medical diagnostics, and to the development of new clinical applications to the benefit of the patient.

Combined Bibliography

References from Chapter 1

Austeng, A. and S. Holm (2002). "Sparse 2-D arrays for 3-D phased array imaging - design methods". In: *IEEE Trans. Ultrason., Ferroelec., Freq. Contr.* 49.8, pp. 1073–1086 (cit. on p. 5).

Brunke, S. S. and G. R. Lockwood (1997). "Broad-bandwidth radiation patterns of sparse two-dimensional vernier arrays". In: *IEEE Trans. Ultrason., Ferroelec., Freq. Contr.* 44.5, pp. 1101–1109 (cit. on p. 5).

Davidsen, R. E., J. A. Jensen, and S. W. Smith (1994). "Two-Dimensional Random Arrays for Real Time Volumetric Imaging". In: *Ultrasonic Imaging* 16.3, pp. 143–163 (cit. on p. 5).

Haller, M. I. and B. T. Khuri-Yakub (1994). "A surface micromachined electrostatic ultrasonic air transducer". In: *Proc. IEEE Ultrason. Symp.* Vol. 2, pp. 1241–1244 (cit. on p. 7).

— (1996). "A surface micromachined electrostatic ultrasonic air transducer". In: *IEEE Trans. Ultrason., Ferroelec., Freq. Contr.* 43.1, pp. 1–6 (cit. on p. 7).

Jensen, J. A. (1996). *Estimation of Blood Velocities Using Ultrasound: A Signal Processing Approach*. New York: Cambridge University Press (cit. on pp. 1, 2).

Karadayi, K., R. Managuli, and Y. Kim (2009). "Three-Dimensional Ultrasound: From Acquisition to Visualization and From Algorithms to Systems". In: *IEEE Rev Biomed Eng* 2, pp. 23–39 (cit. on pp. 2–4).

Karaman, M., I. O. Wygant, O. Oralkan, and B. T. Khuri-Yakub (2009). "Minimally Redundant 2-D Array Designs for 3-D Medical Ultrasound Imaging". In: *IEEE Trans. Med. Imag.* 7, pp. 1051–1061 (cit. on p. 5).

Morton, C. E. and G. R. Lockwood (2003). "Theoretical assessment of a crossed electrode 2-D array for 3-D imaging". In: *Proc. IEEE Ultrason. Symp.* Pp. 968–971 (cit. on p. 6).

Phillips (2015). *http://www.healthcare.philips.com* (cit. on p. 5).

Ramm, O. T. von, S. W. Smith, and H. G. Pavy (1991). "High speed ultrasound volumetric imaging system – Part II: Parallel processing and image display". In: *IEEE Trans. Ultrason., Ferroelec., Freq. Contr.* 38, pp. 109–115 (cit. on pp. 3, 4).

Rasmussen, M. F. and J. A. Jensen (2013). "3D ultrasound imaging performance of a row-column addressed 2D array transducer: a simulation study". In: *Proc. SPIE Med. Imag.* 86750C, pp. 1–11 (cit. on p. 6).

Roh, Y. (2014). “Ultrasonic transducers for medical volumetric imaging”. In: *Jpn. J. Appl. Phys.* 53.07KA01, pp. 1–6 (cit. on p. 3).

Sampson, R., M. Yang, S. Wei, C. Chakrabarti, and T. F. Wenisch (2013). “Sonic Millip3De: A Massively Parallel 3D-Stacked Accelerator for 3D Ultrasound”. In: *IEEE 19th International Symposium on High Performance Computer Architecture*, pp. 318–329 (cit. on p. 6).

Schindel, D. W., D. A. Hutchins, L. Zou, and M. Sayer (1995). “The design and characterization of micromachined air-coupled capacitance transducers”. In: *IEEE Trans. Ultrason., Ferroelec., Freq. Contr.* 42.1, pp. 42–50 (cit. on p. 7).

Smith, S. W., H. G. Pavy, and O. T. von Ramm (1991). “High speed ultrasound volumetric imaging system – Part I: Transducer design and beam steering”. In: *IEEE Trans. Ultrason., Ferroelec., Freq. Contr.* 38, pp. 100–108 (cit. on p. 3).

Szabo, T. L. (2014). *Diagnostic ultrasound imaging: Inside out*. 2nd ed. Elsevier (Oxford, UK) (cit. on pp. 1, 2, 7).

Wong, S., M. Kupnik, X. Zhuang, D.-S. Lin, K. Butts-Pauly, and B. Khuri-yakub (2008). “Evaluation of wafer bonded CMUTs with rectangular membranes featuring high fill factor”. In: *IEEE Transactions on Ultrasonics, Ferroelectrics and Frequency Control* 55.9, pp. 2053–2065 (cit. on p. 8).

Yen, J. T., J. P. Steinberg, and S. W. Smith (2000). “Sparse 2-D array design for real time rectilinear volumetric imaging”. In: *IEEE Trans. Ultrason., Ferroelec., Freq. Contr.* 47.1, pp. 93–110 (cit. on p. 5).

References from Chapter 2

Bayram, B., E. Hæggström, G. G. Yaralioglu, and B. T. Khuri-Yakub (2003). “A new regime for operating capacitive micromachined ultrasonic transducers”. In: *IEEE Trans. Ultrason., Ferroelec., Freq. Contr.* 50.9, pp. 1184–1190 (cit. on p. 26).

Bayram, B., M. Kupnik, G. G. Yaralioglu, Ö. Oralkan, A. S. Ergun, D.-S. Lin, S. H. Wong, and B. T. Khuri-Yakub (2007). “Finite element modeling and experimental characterization of crosstalk in 1-D CMUT arrays”. In: *IEEE Trans. Ultrason., Ferroelec., Freq. Contr.* 54.2, pp. 418–430 (cit. on p. 26).

Bayram, B., M. Kupnik, G. G. Yaralioglu, Ö. Oralkan, D. Lin, X. Zhuang, A. S. Ergun, A. F. Sarioglu, S. H. Wong, and B. T. Khuri-Yakub (2005). “Characterization of cross-coupling in capacitive micromachined ultrasonic transducers”. In: *Proc. IEEE Ultrason. Symp.* Pp. 601–604 (cit. on p. 26).

Berlincourt, D., D. Curran, and H. Jaffe (1964). “Piezoelectric and Piezomagnetic Materials and Their Function in Transducers”. In: *Physical acoustics* 1, pp. 169–270 (cit. on p. 28).

Greenspan, M. (1979). “Piston radiator: some extensions of the theory”. In: *J. Acoust. Soc. Am.* 65.3, pp. 608–621 (cit. on pp. 29, 30).

Huang, Y., E. Hæggström, B. Bayram, X. Zhuang, A. S. Ergun, C. H. Cheng, and B. T. Khuri-Yakub (2003). "Collapsed Regime Operation of Capacitive Micromachined Ultrasonic Transducers based on Wafer-Bonding Technique". In: *Proc. IEEE Ultrason. Symp.* Pp. 1161–1164 (cit. on p. 26).

Jensen, J. A. (1996). *Estimation of Blood Velocities Using Ultrasound: A Signal Processing Approach*. New York: Cambridge University Press (cit. on p. 29).

Jin, X., Ö. Oralkan, F. L. Degertekin, and B. T. Khuri-Yakub (2001). "Characterization of One-Dimensional Capacitive Micromachined Ultrasonic Immersion Transducer Arrays". In: *IEEE Trans. Ultrason., Ferroelec., Freq. Contr.* 48.3, pp. 750–760 (cit. on p. 26).

Köymen, H., A. Atalar, E. Aydogdu, C. Kocabas, H. K. Oguz, S. Olcum, A. Ozgurluk, and A. Ünlügedik (2012). "An improved lumped element nonlinear circuit model for a circular CMUT cell". In: *IEEE Trans. Ultrason., Ferroelec., Freq. Contr.* 59.8, pp. 1791–1799 (cit. on p. 17).

Morse, P. M. and K. U. Ingard (1968). *Theoretical Acoustics*. New York: McGraw-Hill (cit. on p. 36).

Oguz, H. K., A. Atalar, and H. Köymen (2013). "Equivalent Circuit-Based Analysis of CMUT Cell Dynamics in Arrays". In: *IEEE Trans. Ultrason., Ferroelec., Freq. Contr.* 60.5, pp. 1016–1024 (cit. on p. 29).

Oralkan, Ö., B. Bayram, G. G. Yaralioglu, A. S. Ergun, M. Kupnik, D. T. Yeh, I. O. Wygant, and B. T. Khuri-Yakub (2006). "Experimental Characterization of Collapse-Mode CMUT Operation". In: *IEEE Trans. Ultrason., Ferroelec., Freq. Contr.* 53.8, pp. 1513–1523 (cit. on p. 26).

Park, K. K., M. Kupnik, H. J. Lee, Ö. Oralkan, and B. T. Khuri-Yakub (2010). "Zero-Bias Resonant Sensor with an Oxide-Nitride Layer as Charge Trap". In: *Proc. IEEE Sens.* Pp. 1024–1028 (cit. on p. 26).

Park, K. K., Ö. Oralkan, and B. T. Khuri-Yakub (2011). "Comparison of conventional and collapse-mode CMUT in 1-D array configuration". In: *Proc. IEEE Ultrason. Symp.* Pp. 1000–1003 (cit. on p. 26).

Rayleigh, J. W. S. (1896). *The theory of sound*. 2nd ed. Vol. II. London: MacMillian and Co., LTD (cit. on p. 36).

Rønnekleiv, A. (2008). "Fast and Accurate CMUT Modeling using Equivalent Circuits with Lumped Parameters". In: *Proc. IEEE Ultrason. Symp.* Pp. 496–499 (cit. on p. 27).

Wah, T. (1962). "Vibration of circular plates". In: *J. Acoust. Soc. Am.* 34, pp. 275–281 (cit. on p. 35).

Yaralioglu, G. G., B. Bayram, and B. T. Khuri-Yakub (2006). "Finite element analysis of CMUTs: Conventional vs. collapse operation modes". In: *Proc. IEEE Ultrason. Symp.* Pp. 586–589 (cit. on p. 26).

Yaralioglu, G. G., A. S. Ergun, B. Bayram, E. Hæggström, and B. T. Khuri-Yakub (2003). "Calculation and measurement of electromechanical coupling coefficient of capacitive micromachined ultrasonic transducers". In: *IEEE Trans. Ultrason., Ferroelec., Freq. Contr.* 50.4, pp. 449–456 (cit. on p. 27).

Zhang, P., G. Fitzpatrick, W. Moussa, and R. J. Zemp (2010). “CMUTs with Improved Electrical Safety and Minimal Dielectric Surface Charging”. In: *Proc. IEEE Ultrason. Symp.* Pp. 1881–1885 (cit. on p. 26).

References from Chapter 3

BK Medical (2015). *http://bkultrasound.com/bk-medical/VectorFlow* (cit. on pp. 67, 68).

Chee, R. K. W., A. Sampaleanu, D. Rishi, and R. J. Zemp (2014). “Top Orthogonal to Bottom Electrode (TOBE) 2-D CMUT Arrays for 3-D Photoacoustic Imaging”. In: *IEEE Trans. Ultrason., Ferroelec., Freq. Contr.* 61.8, pp. 1393–1395 (cit. on p. 42).

Chen, A. I. H., L. L. P. Wong, A. S. Logan, and J. T. W. Yeow (2011). “A CMUT-based real-time volumetric ultrasound imaging system with row-column addressing”. In: *Proc. IEEE Ultrason. Symp.* Pp. 1755–1758 (cit. on p. 42).

Chen, Y., M. Nguyen, and J. T. Yen (2011). “Real-time rectilinear volumetric acquisition with a 7.5 MHz dual-layer array transducer - Data acquisition and signal processing”. In: *Proc. IEEE Ultrason. Symp.* Pp. 1759–1761 (cit. on p. 42).

Daher, N. M. and J. T. Yen (2004). “Rectilinear 3-D ultrasound imaging using synthetic aperture techniques”. In: *Proc. IEEE Ultrason. Symp.* Vol. 2, pp. 1270–1273 (cit. on p. 41).

— (2006). “2-D Array for 3-D Ultrasound Imaging Using Synthetic Aperture Techniques”. In: *IEEE Trans. Ultrason., Ferroelec., Freq. Contr.* 53.5, pp. 912–924 (cit. on p. 41).

Démoré, C. E. M., A. Joyce, K. Wall, and G. Lockwood (2009). “Real-time volume imaging using a crossed electrode array”. In: *IEEE Trans. Ultrason., Ferroelec., Freq. Contr.* 56.6, pp. 1252–1261 (cit. on pp. 41, 45, 55, 63).

Harris, G. R. (1981a). “Review of transient field theory for a baffled planar piston”. In: *J. Acoust. Soc. Am.* 70, pp. 10–20 (cit. on p. 50).

— (1981b). “Transient field of a baffled planar piston having an arbitrary vibration amplitude distribution”. In: *J. Acoust. Soc. Am.* 70, pp. 186–204 (cit. on p. 51).

Jensen, J. A. (1996a). *Apparatus and method for determining movements and velocities of moving objects*. International patent PCT/DK97/00287 (cit. on p. 67).

— (1996b). *Estimation of Blood Velocities Using Ultrasound: A Signal Processing Approach*. New York: Cambridge University Press (cit. on pp. 66, 67).

— (1996c). “Field: A Program for Simulating Ultrasound Systems”. In: *Med. Biol. Eng. Comp.* 10th Nordic-Baltic Conference on Biomedical Imaging, Vol. 4, Supplement 1, Part 1, pp. 351–353 (cit. on pp. 56, 65, 70).

— (2000). *Estimation of vector velocity*. International patent PCT/DK00/00243 (cit. on p. 67).

Jensen, J. A., H. Holten-Lund, R. T. Nilsson, M. Hansen, U. D. Larsen, R. P. Domsten, B. G. Tomov, M. B. Stuart, S. I. Nikolov, M. J. Pihl, Y. Du, J. H. Rasmussen, and M. F.

Rasmussen (2013). “SARUS: A Synthetic Aperture Real-time Ultrasound System”. In: *IEEE Trans. Ultrason., Ferroelec., Freq. Contr.* 60.9, pp. 1838–1852 (cit. on p. 63).

Jensen, J. A. and P. Munk (1998). “A New Method for Estimation of Velocity Vectors”. In: *IEEE Trans. Ultrason., Ferroelec., Freq. Contr.* 45, pp. 837–851 (cit. on pp. 67–69).

Jensen, J. A., S. Nikolov, K. L. Gammelmark, and M. H. Pedersen (2006). “Synthetic Aperture Ultrasound Imaging”. In: *Ultrasonics* 44, e5–e15 (cit. on p. 43).

Jensen, J. A. and N. B. Svendsen (1992). “Calculation of Pressure Fields from Arbitrarily Shaped, Apodized, and Excited Ultrasound Transducers”. In: *IEEE Trans. Ultrason., Ferroelec., Freq. Contr.* 39, pp. 262–267 (cit. on pp. 56, 65, 70).

Joyce, A. W. and G. R. Lockwood (2012). “Variably Polarized Ceramic for Passive Aperture Apodization”. In: *Proc. IEEE Ultrason. Symp.* Pp. 1557–1559 (cit. on p. 55).

Karaman, M., I. O. Wygant, O. Oralkan, and B. T. Khuri-Yakub (2009). “Minimally Redundant 2-D Array Designs for 3-D Medical Ultrasound Imaging”. In: *IEEE Trans. Med. Imag.* 7, pp. 1051–1061 (cit. on p. 44).

Lawrence, W. L. P., A. I. H. Chen, Z. Li, A. S. Logan, and J. T. W. Yeow (2014). “A row-column addressed micromachined ultrasonic transducer array for surface scanning applications”. In: *Ultrasonics* 54.8, pp. 2072–2080 (cit. on p. 42).

Logan, A. S., L. L. P. Wong, A. I. H. Chen, and J. T. W. Yeow (2011). “A 32 x 32 element row-column addressed capacitive micromachined ultrasonic transducer”. In: *IEEE Trans. Ultrason., Ferroelec., Freq. Contr.* 58.6, pp. 1266–1271 (cit. on p. 42).

Logan, A. S., L. L. P. Wong, and J. T. W. Yeow (2009). “2-D CMUT wafer bonded imaging arrays with a row-column addressing scheme”. In: *Proc. IEEE Ultrason. Symp.* Pp. 984–987 (cit. on p. 42).

Morton, C. E. and G. R. Lockwood (2003). “Theoretical assessment of a crossed electrode 2-D array for 3-D imaging”. In: *Proc. IEEE Ultrason. Symp.* Pp. 968–971 (cit. on pp. 41, 63).

Naik, P. (2010). *Principles of Physics*. 4th ed. PHI (cit. on p. 61).

Phillips (2015). *http://www.healthcare.philips.com* (cit. on p. 44).

Pierce, A. D. (1989). *Acoustics, An Introduction to Physical Principles and Applications*. New York: Acoustical Society of America (cit. on p. 50).

Pihl, M. J. and J. A. Jensen (2014). “A Transverse Oscillation Approach for Estimation of Three-Dimensional Velocity Vectors. Part I: Concept and Simulation Study”. In: *IEEE Trans. Ultrason., Ferroelec., Freq. Contr.* 61, pp. 1599–1607 (cit. on pp. 66, 68, 72).

Pihl, M. J., M. B. Stuart, B. G. Tomov, M. F. Rasmussen, and J. A. Jensen (2014). “A Transverse Oscillation Approach for Estimation of Three-Dimensional Velocity Vectors. Part II: Experimental Validation”. In: *IEEE Trans. Ultrason., Ferroelec., Freq. Contr.* 51.10, pp. 1608–1618 (cit. on pp. 66, 68, 72).

Rasmussen, M. F. and J. A. Jensen (2013a). “3-D Ultrasound Imaging Performance of a Row-Column Addressed 2-D Array Transducer: A Measurement Study”. In: *Proc. IEEE Ultrason. Symp.* Pp. 1460–1463 (cit. on p. 41).

Rasmussen, M. F. and J. A. Jensen (2013b). “3D ultrasound imaging performance of a row-column addressed 2D array transducer: a simulation study”. In: *Proc. SPIE Med. Imag.* 86750C, pp. 1–11 (cit. on pp. 42, 55).

— (2014). “Comparison of 3-D Synthetic Aperture Phased Array Ultrasound Imaging with Parallel Beamforming”. In: *IEEE Trans. Ultrason., Ferroelec., Freq. Contr.* 61.10, pp. 1638–1650 (cit. on p. 65).

Sampaleanu, A., P. Zhang, A. Kshirsagar, W. Moussa, and R. Zemp (2014). “Top-orthogonal-to-bottom-electrode (TOBE) CMUT arrays for 3-D ultrasound imaging.” In: *IEEE Trans. Ultrason., Ferroelec., Freq. Contr.* 61.2, pp. 266–276 (cit. on p. 42).

Seo, C. H. and J. T. Yen (2006). “64 x 64 2-D array transducer with row-column addressing”. In: *Proc. IEEE Ultrason. Symp.* Vol. 1, pp. 74–77 (cit. on p. 41).

— (2007). “256 x 256 2-D array transducer with row-column addressing for 3-D imaging”. In: *Proc. IEEE Ultrason. Symp.* Pp. 2381–2384 (cit. on pp. 42, 44).

— (2008). “Recent results using a 256 x 256 2-D array transducer for 3-D Rectilinear Imaging”. In: *Proc. IEEE Ultrason. Symp.* Vol. 1-4, pp. 1146–1149 (cit. on pp. 42, 44).

— (2009). “A 256 x 256 2-D array transducer with row-column addressing for 3-D rectilinear imaging”. In: *IEEE Trans. Ultrason., Ferroelec., Freq. Contr.* 56.4, pp. 837–847 (cit. on pp. 42, 44).

Stepanishen, P. R. (1971). “Transient radiation from pistons in an infinite planar baffle”. In: *J. Acoust. Soc. Am.* 49, pp. 1629–1638 (cit. on p. 50).

— (1981). “Acoustic transients from planar axisymmetric vibrators using the impulse response approach”. In: *J. Acoust. Soc. Am.* 70, pp. 1176–1181 (cit. on p. 51).

Szabo, T. L. (2014). *Diagnostic ultrasound imaging: Inside out*. 2nd ed. Elsevier (Oxford, UK) (cit. on pp. 44, 46, 50).

Tjøtta, J. N. and S. Tjøtta (1982). “Nearfield and farfield of pulsed acoustic radiators”. In: *J. Acoust. Soc. Am.* 71, pp. 824–834 (cit. on p. 51).

Udesen, J. and J. A. Jensen (2006). “Investigation of Transverse Oscillation Method”. In: *IEEE Trans. Ultrason., Ferroelec., Freq. Contr.* 53, pp. 959–971 (cit. on pp. 67, 68).

Yen, J. T., C. H. Seo, S. I. Awad, and J. S. Jeong (2009). “A dual-layer transducer array for 3-D rectilinear imaging”. In: *IEEE Trans. Ultrason., Ferroelec., Freq. Contr.* 56.1, pp. 204–212 (cit. on p. 42).

Yen, J. T. (2013). “Beamforming of sound from two-dimensional arrays using spatial matched filters”. In: *J. Acoust. Soc. Am.* 134.5, pp. 3697–704 (cit. on p. 41).

Zemp, R. J., W. Zheng, and P. Zhang (2011). “Feasibility of Top-Orthogonal-to-Bottom Electrode (TOBE) 2D CMUT arrays for low-channel-count 3D imaging”. In: *Proc. IEEE Ultrason. Symp.* Pp. 498–502 (cit. on p. 42).

References from Chapter 4

Chee, R. K. W., A. Sampaleanu, D. Rishi, and R. J. Zemp (2014). "Top Orthogonal to Bottom Electrode (TOBE) 2-D CMUT Arrays for 3-D Photoacoustic Imaging". In: *IEEE Trans. Ultrason., Ferroelec., Freq. Contr.* 61.8, pp. 1393–1395 (cit. on p. 79).

Chen, A. I. H., L. L. P. Wong, A. S. Logan, and J. T. W. Yeow (2011). "A CMUT-based real-time volumetric ultrasound imaging system with row-column addressing". In: *Proc. IEEE Ultrason. Symp.* Pp. 1755–1758 (cit. on p. 78).

Chen, A. I. H., L. L. P. Wong, and J. T. W. Yeow (2014). "A CMUT-based Finger-mounted 3D Ultrasound Probe". In: *Proc. IEEE Ultrason. Symp.* Pp. 1603–1606 (cit. on p. 78).

Deal, B. E. and A. S. Grove (1965). "General Relationship for the Thermal Oxidation of Silicon". In: *J. Appl. Phys.* 36.12, pp. 3770–3778 (cit. on pp. 83, 84).

Demirci, U., A. S. Ergun, Ö. Oralkan, M. Karaman, and B. T. Khuri-Yakub (2004). "Forward-Viewing CMUT Arrays for Medical Imaging". In: *IEEE Trans. Ultrason., Ferroelec., Freq. Contr.* 51.7, pp. 887–895 (cit. on p. 75).

Engholm, M. (2015). "Capacitive Micromachined Ultrasonic Transducers for 3-D Medical Imaging using a LOCOS Based Process". MSc Thesis. Technical University of Denmark (cit. on p. 96).

Ergun, A. S., Y. Huang, X. Zhuang, Ö. Oralkan, G. G. Yaralioglu, and B. T. Khuri-Yakub (2005). "Capacitive Micromachined Ultrasonic Transducers: Fabrication Technology". In: *IEEE Trans. Ultrason., Ferroelec., Freq. Contr.* 52.12, pp. 2242–2258 (cit. on pp. 76, 78).

Haller, M. I. and B. T. Khuri-Yakub (1994). "A surface micromachined electrostatic ultrasonic air transducer". In: *Proc. IEEE Ultrason. Symp.* Vol. 2, pp. 1241–1244 (cit. on p. 75).

— (1996). "A surface micromachined electrostatic ultrasonic air transducer". In: *IEEE Trans. Ultrason., Ferroelec., Freq. Contr.* 43.1, pp. 1–6 (cit. on p. 75).

Huang, Y., A. S. Ergun, E. Hæggström, M. H. Badi, and B. T. Khuri-Yakub (2003). "Fabricating capacitive micromachined ultrasonic transducers with wafer-bonding technology". In: *J. Microelectromech. Syst* 12.2, pp. 128–137 (cit. on pp. 76, 78, 81).

Jin, X., I. Ladabaum, and B. T. Khuri-Yakub (1998). "The microfabrication of capacitive ultrasonic transducers". In: *J. Microelectromech. S.* 7.3, pp. 295–302 (cit. on p. 75).

Jin, X., Ö. Oralkan, F. L. Degertekin, and B. T. Khuri-Yakub (2001). "Characterization of One-Dimensional Capacitive Micromachined Ultrasonic Immersion Transducer Arrays". In: *IEEE Trans. Ultrason., Ferroelec., Freq. Contr.* 48.3, pp. 750–760 (cit. on p. 75).

Kern, W. (1990). "The Evolution of Silicon Wafer Cleaning Technology". In: *J. Electrochem. Soc.* 137.6, pp. 1887–1892 (cit. on p. 91).

Khuri-Yakub, B. T. and Ö. Oralkan (2011). "Capacitive micromachined ultrasonic transducers for medical imaging and therapy". In: *Journal of Micromechanics and Microengineering* 21.5, pp. 054004–054014 (cit. on p. 76).

Kupnik, M., S. Vaithilingam, K. Torashima, I. O. Wygant, and B. T. Khuri-Yakub (2010). "CMUT fabrication based on a thick buried oxide layer". In: *Proc. IEEE Ultrason. Symp.* Pp. 547–550 (cit. on p. 78).

Lenzlinger, M. and E. H. Snow (1969). "Fowler-Nordheim Tunneling into Thermally Grown SiO2". In: *J. Appl. Phys.* 40.1, pp. 278–283 (cit. on p. 80).

Logan, A. S., L. L. P. Wong, A. I. H. Chen, and J. T. W. Yeow (2011). "A 32 x 32 element row-column addressed capacitive micromachined ultrasonic transducer". In: *IEEE Trans. Ultrason., Ferroelec., Freq. Contr.* 58.6, pp. 1266–1271 (cit. on p. 78).

Logan, A. S., L. L. P. Wong, and J. T. W. Yeow (2009). "2-D CMUT wafer bonded imaging arrays with a row-column addressing scheme". In: *Proc. IEEE Ultrason. Symp.* Pp. 984–987 (cit. on p. 78).

May, G. S. and S. M. Sze (2004). *Fundamentals of semiconductor fabrication*. John Wiley and Sons, Inc. (cit. on pp. 79, 83).

Nikoozadeh, A., Ö. Oralkan, M. Gencel, J. W. Choe, D. N. Stephens, A. de la Rama, P. Chen, K. Thomenius, A. Dentinger, D. Wildes, K. Shivkumar, A. Mahajan, M. O'Donnell, D. Sahn, and B. T. Khuri-Yakub (2009). "Forward-Looking Volumetric Intracardiac Imaging Using a Fully Integrated CMUT Ring Array". In: *Proc. IEEE Ultrason. Symp.* Pp. 511–514 (cit. on p. 75).

Oralkan, Ö., A. S. Ergun, C.-H. Cheng, J. A. Johnson, M. Karaman, T. H. Lee, and B. T. Khuri-Yakub (2003). "Volumetric ultrasound imaging using 2-D CMUT arrays". In: *IEEE Trans. Ultrason., Ferroelec., Freq. Contr.* 50.11, pp. 1581–1594 (cit. on p. 75).

Oralkan, Ö., A. S. Ergun, J. A. Johnson, M. Karaman, U. Demirci, K. Kaviani, T. H. Lee, and B. T. Kuri-Yakub (2002). "Capacitive micromachined ultrasonic transducers: Next-generation arrays for acoustic imaging?" In: *IEEE Trans. Ultrason., Ferroelec., Freq. Contr.* 49, pp. 1596–1610 (cit. on p. 75).

Oralkan, Ö., X. Jin, F. L. Degertekin, and B. T. Khuri-Yakub (1999). "Simulation and experimental characterization of a 2-D capacitive micromachined ultrasonic transducer array element". In: *IEEE Trans. Ultrason., Ferroelec., Freq. Contr.* 46.6, pp. 1337–1340 (cit. on p. 75).

Oralkan, Ö., X. Jin, K. Kaviani, A. S. Ergun, F. L. Degertekin, M. Karaman, and B. T. Khuri-Yakub (2000). "Initial pulse-echo imaging results with one-dimensional capacitive micromachined ultrasonic transducer arrays". In: *Proc. IEEE Ultrason. Symp.* Vol. 1, pp. 959–962 (cit. on p. 75).

Park, K. K. and B. T. Khuri-Yakub (2012). "Dynamic response of an array of flexural plates in acoustic medium". In: *J. Acoust. Soc. Am.* 132.4, pp. 2292–2303 (cit. on p. 78).

Park, K. K., H. J. Lee, M. Kupnik, and B. T. Khuri-Yakub (2011). "Fabrication of Capacitive Micromachined Ultrasonic Transducers via Local Oxidation and Direct Wafer Bonding". In: *J. Microelectromech. S.* 20.1, pp. 95–103 (cit. on pp. 78, 93).

Park, K. K., H. J. Lee, M. Kupnik, Ö. Oralkan, and B. T. Khuri-Yakub (2008). "Fabricating capacitive micromachined ultrasonic transducers with direct wafer-bonding and locos

technology". In: *IEEE International Conference on Micro Electro Mechanical Systems*, pp. 339–342 (cit. on pp. 78, 93).

Plössl, A. and G. Kräuter (1999). "Wafer direct bonding: tailoring adhesion between brittle materials". In: *Materials Science and Engineering: R: Reports* 25.1-2, pp. 1–88 (cit. on p. 81).

Sampaleanu, A., P. Zhang, A. Kshirsagar, W. Moussa, and R. Zemp (2014). "Top-orthogonal-to-bottom-electrode (TOBE) CMUT arrays for 3-D ultrasound imaging." In: *IEEE Trans. Ultrason., Ferroelec., Freq. Contr.* 61.2, pp. 266–276 (cit. on p. 79).

Savoia, A. S., G. Caliano, and M. Pappalardo (2012). "A CMUT Probe for Medical Ultrasonography: From Microfabrication to System Integration". In: *IEEE Trans. Ultrason., Ferroelec., Freq. Contr.* 59.6, pp. 1127–1138 (cit. on p. 75).

Wong, L. L. P., A. Chen, Z. Li, A. Logan, and J. Yeow (2014). "A row-column addressed micromachined ultrasonic transducer array for surface scanning applications". In: *Ultrasonics* 54.8, pp. 2072–2080 (cit. on p. 78).

Yeh, D. T., Ö. Oralkan, I. O. Wygant, M. O'Donnell, and B. T. Khuri-yakub (2006). "3-D Ultrasound Imaging Using a Forward-Looking CMUT Ring Array for Intravascular/Intracardiac Applications". In: *IEEE Trans. Ultrason., Ferroelec., Freq. Contr.* 53.6, pp. 1202–1211 (cit. on p. 75).

Yoon, H.-S., M.-C. Ho, N. Apte, P. Cristman, S. Vaithilingam, M. Kupnik, K. Butts-Pauly, and B. T. Khuri-Yakub (2011). "Fabrication of CMUT Cells with Gold Center Mass for Higher Output Pressure". In: *AIP Conference Proceedings*, pp. 183–188 (cit. on p. 88).

Zemp, R. J., W. Zheng, and P. Zhang (2011). "Feasibility of Top-Orthogonal-to-Bottom Electrode (TOBE) 2D CMUT arrays for low-channel-count 3D imaging". In: *Proc. IEEE Ultrason. Symp.* Pp. 498–502 (cit. on pp. 78, 79, 90).

Zhuang, X., I. O. Wygant, D. S. Lin, M. Kupnik, O. Oralkan, and B. T. Khuri-Yakub (2009). "Wafer-bonded 2-D CMUT arrays incorporating through-wafer trench-isolated interconnects with a supporting frame". In: *IEEE Trans. Ultrason., Ferroelec., Freq. Contr.* 56.1, pp. 182–192 (cit. on p. 78).

References from Chapter 5

Alleyne, D. and P. Cawley (1991). "A two-dimensional Fourier transform method for the measurement of propagating multimode signals". In: *J. Acoust. Soc. Am.* 89.3, pp. 1159–1168 (cit. on p. 117).

Bayram, B., M. Kupnik, G. G. Yaralioglu, Ö. Oralkan, A. S. Ergun, D.-S. Lin, S. H. Wong, and B. T. Khuri-Yakub (2007). "Finite element modeling and experimental characterization of crosstalk in 1-D CMUT arrays". In: *IEEE Trans. Ultrason., Ferroelec., Freq. Contr.* 54.2, pp. 418–430 (cit. on pp. 115–117).

Bayram, B., M. Kupnik, G. G. Yaralioglu, Ö. Oralkan, D. Lin, X. Zhuang, A. S. Ergun, A. F. Sarioglu, S. H. Wong, and B. T. Khuri-Yakub (2005). "Characterization of

cross-coupling in capacitive micromachined ultrasonic transducers". In: *Proc. IEEE Ultrason. Symp.* Pp. 601–604 (cit. on pp. 116, 117).

Eccardt, P.-C., A. Lohfink, and H.-G. von Garssen (2005). "Analysis of Crosstalk between Fluid Coupled CMUT Membranes". In: *Proc. IEEE Ultrason. Symp.* Pp. 593–596 (cit. on pp. 115, 117, 119).

Hall, J. J. (1967). "Electronic Effects in the Elastic Constants of n-Type Silicon". In: *Phys. Rev.* 161.3, pp. 756–761 (cit. on p. 116).

Huang, Y. L., E. O. Hæggström, X. F. Zhuang, A. S. Ergun, and B. T. Khuri-Yakub (2005). "A solution to the charging problems in capacitive micromachined ultrasonic transducers". In: *IEEE Trans. Ultrason., Ferroelec., Freq. Contr.* 52.4, pp. 578–580 (cit. on p. 107).

Jensen, J. A., H. Holten-Lund, R. T. Nilsson, M. Hansen, U. D. Larsen, R. P. Domsten, B. G. Tomov, M. B. Stuart, S. I. Nikolov, M. J. Pihl, Y. Du, J. H. Rasmussen, and M. F. Rasmussen (2013). "SARUS: A Synthetic Aperture Real-time Ultrasound System". In: *IEEE Trans. Ultrason., Ferroelec., Freq. Contr.* 60.9, pp. 1838–1852 (cit. on p. 108).

Jin, X., Ö. Oralkan, F. L. Degertekin, and B. T. Khuri-Yakub (2001). "Characterization of One-Dimensional Capacitive Micromachined Ultrasonic Immersion Transducer Arrays". In: *IEEE Trans. Ultrason., Ferroelec., Freq. Contr.* 48.3, pp. 750–760 (cit. on pp. 115–117).

Ladabaum, I., P. Wagner, C. Zanelli, J. Mould, and G. Wojcik (2000). "Silicon Substrate Ringing in Microfabricated Ultrasonic Transducers". In: *Proc. IEEE Ultrason. Symp.* Pp. 943–946 (cit. on p. 116).

Lamb, H. (1917). "On Waves in an Elastic Plate". In: *Proc. Roy. Soc. (London), Ser. A* 93, pp. 114–128 (cit. on p. 116).

May, G. S. and S. M. Sze (2004). *Fundamentals of semiconductor fabrication*. John Wiley and Sons, Inc. (cit. on pp. 122, 123).

Miller, G. F. and M. J. P. Musgrave (1956). "On the Propagation of Elastic Waves in Aeolotropic Media. III. Media of Cubic Symmetry". In: *Proc. Roy. Soc. (London), Ser. A* 236, pp. 352–383 (cit. on p. 116).

Oralkan, Ö., A. S. Ergun, J. A. Johnson, M. Karaman, U. Demirci, K. Kaviani, T. H. Lee, and B. T. Kuri-Yakub (2002). "Capacitive micromachined ultrasonic transducers: Next-generation arrays for acoustic imaging?" In: *IEEE Trans. Ultrason., Ferroelec., Freq. Contr.* 49, pp. 1596–1610 (cit. on p. 108).

Schroeder, M. R. (1979). "Integrated-impulse method measuring sound decay without using impulses". In: *J. Acoust. Soc. Am.* 66.2, pp. 497–500 (cit. on p. 109).

Szabo, T. L. (2014). *Diagnostic ultrasound imaging: Inside out*. 2nd ed. Elsevier (Oxford, UK) (cit. on p. 111).

References from Chapter 6

Jensen, J. A., H. Holten-Lund, R. T. Nilsson, M. Hansen, U. D. Larsen, R. P. Domsten, B. G. Tomov, M. B. Stuart, S. I. Nikolov, M. J. Pihl, Y. Du, J. H. Rasmussen, and M. F. Rasmussen (2013). "SARUS: A Synthetic Aperture Real-time Ultrasound System". In: *IEEE Trans. Ultrason., Ferroelec., Freq. Contr.* 60.9, pp. 1838–1852 (cit. on p. 133).

Rasmussen, M. F. and J. A. Jensen (2014). "Comparison of 3-D Synthetic Aperture Phased Array Ultrasound Imaging with Parallel Beamforming". In: *IEEE Trans. Ultrason., Ferroelec., Freq. Contr.* 61.10, pp. 1638–1650 (cit. on p. 137).

Process Flows

PROCESS A

1-D SiO_2-SiO_2 Process

Used for: Fabrication of 1-D CMUT arrays.

Period used: January 2013 – current date.

Description: This process was developed in 2013 as a solution to the problem with protrusions arising from a double oxidation process, see paper F. It has since been used as the standard 1-D array process at DTU. Instead of oxidizing a wafer, etching cavities and oxidizing again to create the insulation oxide, the cavities are etched into an oxide grown on the SOI-wafer that is later to be bonded onto the first oxidized wafer. The resulting structure is the same as with the double oxidation, but no polishing or etching steps are needed to remove the protrusions. A difference is that this process utilizes a SiO_2-SiO_2 bonding. The process steps are illustrated below. It is described for use with mask set A, which includes an extra mask for alignment opening, but it can be used for other mask sets as well.

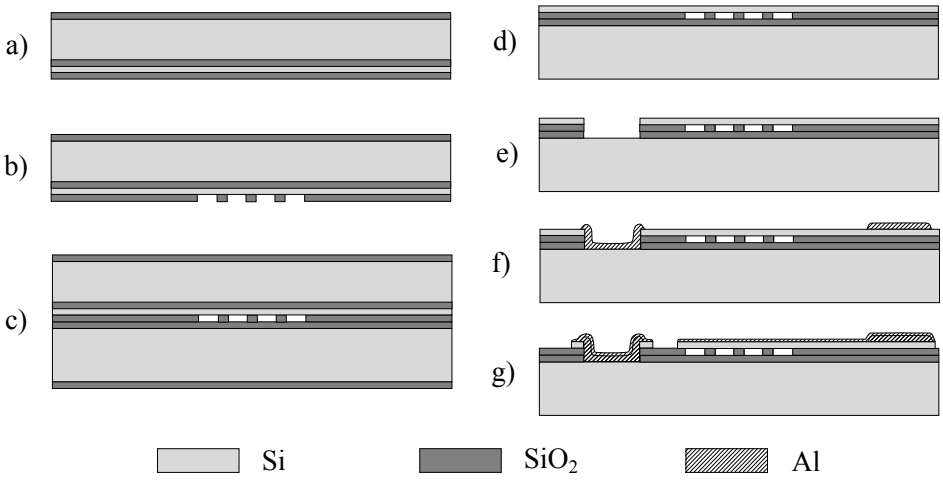

Step	Process	Equipment	Recipe	Comments
1	**RCA Cleaning**			
1.1	RCA1	RCA 1 bath	10 min	Prepare RCA 1 and RCA 2 before this step. Wash baths with water gun before adding new chemicals. Turn on heater for RCA 1 30 min before this step and turn on heater for RCA 2 when beginning this step.
1.2	Quickdump	Quickdump bath in front of RCA 1	3 min	
1.3	HF	5 % HF bath	30 s	
1.4	Rinse	Water bath in front of HF bath	20 s	
1.5	Bubble rinse	Bubbler in front of BHF bath	3 min	
1.6	RCA2	RCA 2 bath	10 min	
1.7	Quickdump	Quickdump bath in front of RCA 1	3 min	Turn off heater for RCA 1 and RCA 2
1.8	HF	5 % HF bath	30 s	
1.9	Rinse	Water bath in front of HF bath	20 s	
1.10	Rinse 2	Bubbler in front of BHF bath	5 min	
1.11	Spin dry	Spin dryer at RCA bench		
2	**Grow oxide (top wafer)**			**Figure a**
2.1	Thermal oxidation	Furnace: Boron drive-in	Recipe: dry1050, Time: 8h 35min, 20 min anneal	Expected thickness from logbook: 300 nm
2.2	Inspection	Filmtek	Measure oxide thickness, 5 points	Measured: 296$\pm$1.2 nm
3	**Grow oxide (bottom wafer)**			
3.1	Thermal oxidation	Furnace: Boron drive-in	Recipe: dry1100, Time: 8h 55min, 20 min anneal	Expected thickness from logbook: 400 nm
3.2	Inspection	Filmtek	Measure oxide thickness, 5 points	Measured: 413$\pm$2 nm

Step	Process	Equipment	Recipe	Comments
4	**Create CMUT cavities**			**Figure b**
4.1	Adhesion promotion	HMDS oven	Recipe 4	ca. 30 minutes
4.2	Spin on photoresist	SSE spinner	Recipe: 1,5um 4inch. Resist: AZ5214e. Baked for 90s@$90\,^{\circ}\mathrm{C}$	Or use manual spinner set to 4500 rpm (appr. 1.5 um). Heat on hot plate @ $90\,^{\circ}\mathrm{C}$ for 60 seconds. No alufoil on the hot plate!!
4.3	Exposure	KS Aligner	5 s @ 7 mW/cm2, hard contact	Mask: Cavities (e.g. page 187). Rotate aligner to zero and set both wheels to 10 before exposing.
4.4	Development	Developer bath	60 s in AZ351 developer	
4.5	Rinse/dry	Wet bench/Spin dryer	5 min. in DI water, spin dry	
4.6	Inspection	Optical microscope	Check for errors in lithography	Errors with MISSING resist are most severe!
4.7	Oxide etch	AOE	Recipe: m_res_ny, Time: 2 min.	Let AOE cool to 0-$1\,^{\circ}\mathrm{C}$ for roughly 20-30 minutes before etching
4.8	Strip photoresist	Plasma asher 2	O2/N2: 240/70 ml/min, 1000 W, 25 min.	Acetone works OK as well
4.9	Inspection	Optical microscope	Measure etched CMUT cavity side length	
5	**RCA Cleaning**			
5.1	RCA1	RCA 1 bath	10 min	Prepare RCA 1 and RCA 2 before this step. Wash baths with water gun before adding new chemicals. Turn on heater for RCA 1 30 min before this step and turn on heater for RCA 2 when beginning this step.
5.2	Quickdump	Quickdump bath in front of RCA 1	3 min	
5.3	HF	5 % HF bath	30 s	
5.4	Rinse	Water bath in front of HF bath	20 s	
5.5	Bubble rinse	Bubbler in front of BHF bath	3 min	
5.6	RCA2	RCA 2 bath	10 min	
5.7	Quickdump	Quickdump bath in front of RCA 1	3 min	Turn off heater for RCA 1 and RCA 2
5.8	Spin dry	Spin dryer at RCA bench		

Step	Process	Equipment	Recipe	Comments
6	**Wafer bonding**			**Figure c**
6.1	Fusion bonding	EVG NIL	Recipe: CMUT ($50\,^{\circ}\mathrm{C}$, $1500\,\mathrm{N}$, bond time: 5 min, pressure: 0.01 mbar)	Transport wafers in dedicated box from RCA. Minimize ambient exposure and handling time. Use cleaned tweezers.
6.2	Inspection	Infrared camera	Inspect for pre-anneal voids	
6.3	Annealing	Anneal-bond	Recipe: ann1110, Time 1h 10min	
6.4	Inspection	Infrared camera	Inspect for post-anneal voids	
7	**Remove handle/BOX**			**Figure d**
7.1	Oxide etch	BHF	5 min (80 nm/min)	Only if top wafer is oxidized. Cover bottom wafer with blue tape. Dip wafers in water first to fill out potential voids, and blow dry before dipping into BHF. Oxide is removed when surface is water repellant.
7.2	Silicon etch	ASE	Recipe: cmutaway, Time: 1h 25m	
7.3	Oxide etch	BHF	14 min (80 nm/min)	Only if top wafer is oxidized. Cover bottom wafer with blue tape. Dip wafers in water first to fill out potential voids, and blow dry before dipping into BHF. Oxide is removed when surface is water repellant.
7.4	Rinse/dry	Wet bench/Spin dryer	5 min. in DI water, spin dry	

Step	Process	Equipment	Recipe	Comments
8	**RCA Cleaning**			
8.1	RCA1	RCA 1 bath	10 min	Prepare RCA 1 and RCA 2 before this step. Wash baths with water gun before adding new chemicals. Turn on heater for RCA 1 30 min before this step and turn on heater for RCA 2 when beginning this step.
8.2	Quickdump	Quickdump bath in front of RCA 1	3 min	
8.3	HF	5 % HF bath	30 s	
8.4	Rinse	Water bath in front of HF bath	20 s	
8.5	Bubble rinse	Bubbler in front of BHF bath	3 min	
8.6	RCA2	RCA 2 bath	10 min	
8.7	Quickdump	Quickdump bath in front of RCA 1	3 min	Turn off heater for RCA 1 and RCA 2
8.8	HF	5 % HF bath	30 s	
8.9	Rinse	Water bath in front of HF bath	20 s	
8.10	Rinse 2	Bubbler in front of BHF bath	5 min	
8.11	Spin dry	Spin dryer at RCA bench		

Step	Process	Equipment	Recipe	Comments
9	**Etch access to alignment marks**			
9.1	Spin on photoresist	SSE spinner	Recipe: 2,2um 4inch. Resist: AZ5214e. Baked for 90s@$90\,^{\circ}\mathrm{C}$	Or use manual spinner set to 2000 rpm (appr. 2.2 um). Heat on hot plate @ $90\,^{\circ}\mathrm{C}$ for 90 seconds. No alufoil on the hot plate!!
9.2	Exposure	KS Aligner	9 s @ 7 mW/cm2, hard contact	Mask: Alignment mark open (e.g. page 189). Rough alignment to wafer.
9.3	Development	Developer bath	70 s in AZ351 developer	
9.4	Rinse/dry	Wet bench/Spin dryer	5 min. in DI water, spin dry	
9.6	Silicon etch	DRIE Pegasus	Recipe: users/prototyping/CMUT/tlehr/-SOI_membrane_2um	Visually check color to confirm that the oxide has been reached.
9.9	Strip photoresist	Plasma asher 2	O2/N2: 240/70 ml/min, 1000 W, 25 min.	
10	**Etch access to bottom electrode**			**Figure e**
10.1	Spin on photoresist	SSE spinner	Recipe: 2,2um 4inch. Resist: AZ5214e. Baked for 90s@$90\,^{\circ}\mathrm{C}$	Or use manual spinner set to 2000 rpm (appr. 2.2 um). Heat on hot plate @ $90\,^{\circ}\mathrm{C}$ for 90 seconds. No alufoil on the hot plate!!
10.2	Exposure	KS Aligner	9 s @ 7 mW/cm2, hard contact	Mask: Access to bottom electrode (e.g. page 190). Align to Cavity mask.
10.3	Development	Developer bath	70 s in AZ351 developer	
10.4	Rinse/dry	Wet bench/Spin dryer	5 min. in DI water, spin dry	
10.5	Inspection	Optical microscope	Check for errors in lithography	
10.6	Silicon etch	DRIE Pegasus	Recipe: users/prototyping/CMUT/tlehr/-SOI_membrane_2um	Visually check color to confirm that the oxide has been reached.
10.7	Cover alignment marks	Manual spinner	2000 rpm, bake @ $90\,^{\circ}\mathrm{C}$ for 90 seconds on hot plate	Put a drop of resist on each mark before spinning. No alufoil on the hot plate!!
10.8	Oxide etch	AOE	Recipe: m_res_ny, Time: 2+2 min (230 nm/min)	Let AOE cool to 0-$1\,^{\circ}\mathrm{C}$ before etching. Visually check color in openings after etch to confirm that the silicon has been reached
10.9	Strip photoresist	Plasma asher 2	O2/N2: 240/70 ml/min, 1000 W, 25 min.	

Step	Process	Equipment	Recipe	Comments
11	**Metallization of top electrode**			**Figure g**
11.1	Deposit Al	Alcatel	200 nm	Al is deposited over the whole wafer
11.2	Spin on photoresist	SSE spinner	Recipe: 2,2um 4inch. Resist: AZ5214e. Baked for 90s@$90\,^{\circ}\mathrm{C}$	Or use manual spinner set to 2000 rpm (appr. 2.2 um). Heat on hot plate @ $90\,^{\circ}\mathrm{C}$ for 90 seconds. No alufoil on the hot plate!!
11.3	Exposure	KS Aligner	9 s @ 7 mW/cm2, hard contact	Top electrodes (e.g. page 191). Align to Cavity mask
11.4	Development	Developer bath	70 s in AZ351 developer	Maybe slightly overdevelop to ensure good wet Al etch
11.5	Rinse/dry	Wet bench/Spin dryer	5 min. in DI water, spin dry	
11.6	Inspection	Optical microscope	Check for errors in lithography	Look for potential shorts between elements
11.6	Al etch	Aluminium etch 1	H2O:H3PO4 1:2, $50\,^{\circ}\mathrm{C}$. (100 nm/min)	Stir before use. It can be clearly seen when the etch is done through visual inspection
11.7	Rinse/dry	Wet bench/Spin dryer	5 min. in DI water, spin dry	
11.8	Si etch	DRIE Pegasus	Recipe: SOI, Time: 30 seconds (Etch rate: $10\,\mu\mathrm{m}$/min)	Visually check color to confirm that the oxide has been reached
11.9	Strip photoresist	Plasma asher 1	O2/N2: 240/70 ml/min, 1000 W, 25 min.	

Step	Process	Equipment	Recipe	Comments
12	**Protective resist layer**			
12.1	Spin on photoresist	SSE spinner	Recipe: AZ4562_4inch_10um	Optional step, but if left out, saw will leave considerable amount of dust, which can potentially short the device.
13	**Dicing**			
13.1	Dice out arrays	Saw	Set to program 8, then use semiautomatic cut. Align wafer with the x/y buttons. Press start/stop two times in a row to get a single cut.	
13.2	Remove resist	Fumehood outside cleanroom	Acetone bath, IPA bath/water bath, air gun	Place individual arrays in acetone bath until all resist is gone (leave it for a few minutes but make sure arrays are covered with acetone). Then, transfer arrays to a water bath or IPA bath to prevent the acetone from drying on the arrays. Finally, the arrays are dried with an air gun.

PROCESS B

Row-Column SiO_2-SiO_2 Process

Used for: Fabrication of 2-D row-column CMUT arrays.

Period used: April 2013 – February 2014.

Description: This process was developed in 2013 as a slight modification of the 1-D process described in process A. The difference between the two is that the cavities are made on the bottom wafer, which is a SOI wafer. This enables bottom electrodes to be etched into the device layer of this SOI wafer. The insulation oxide is grown on the top SOI wafer, and SiO_2-SiO_2 fusion bonding is used to join the two wafers. The cavities are not made on the top wafer as in process A, since this would require aligning during fusion bonding. The trade-off is that there is oxide on the CMUT plate. The process steps are illustrated below. The vertical line separates top electrodes (left) and bottom electrodes (right). The process is described for use with mask set B, but it can be used for the other mask sets as well.

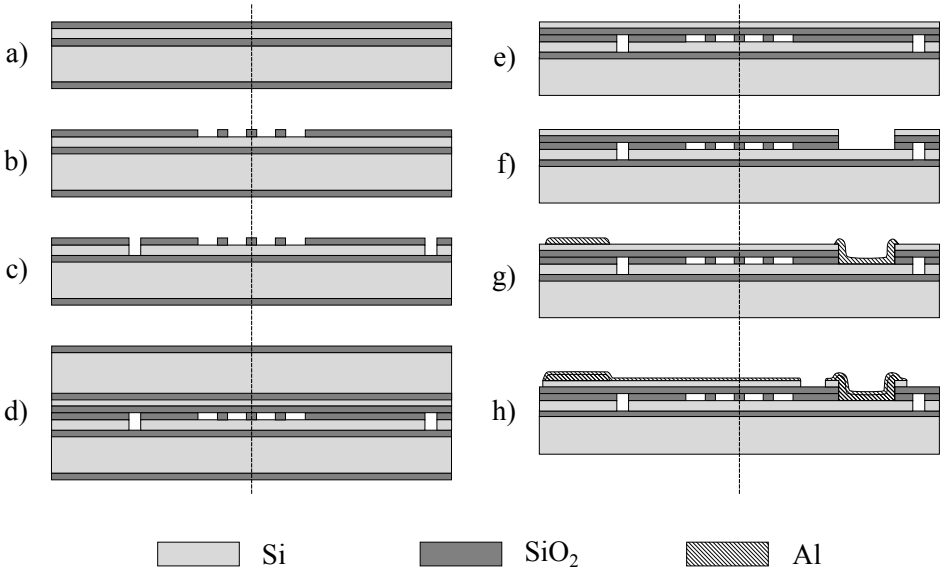

Step	Process	Equipment	Recipe	Comments
1	**RCA Cleaning**			
1.1	RCA1	RCA 1 bath	10 min	Prepare RCA 1 and RCA 2 before this step. Wash baths with water gun before adding new chemicals. Turn on heater for RCA 1 30 min before this step and turn on heater for RCA 2 when beginning this step.
1.2	Quickdump	Quickdump bath in front of RCA 1	3 min	
1.3	HF	5 % HF bath	30 s	
1.4	Rinse	Water bath in front of HF bath	20 s	
1.5	Bubble rinse	Bubbler in front of BHF bath	3 min	
1.6	RCA2	RCA 2 bath	10 min	
1.7	Quickdump	Quickdump bath in front of RCA 1	3 min	Turn off heater for RCA 1 and RCA 2
1.8	HF	5 % HF bath	30 s	
1.9	Rinse	Water bath in front of HF bath	20 s	
1.10	Rinse 2	Bubbler in front of BHF bath	5 min	
1.11	Spin dry	Spin dryer at RCA bench		
2	**Grow oxide (top wafer)**			
2.1	Thermal oxidation	Furnace: Boron drive-in	Recipe: dry1050, Time: 8h 35min, 20 min anneal	Expected thickness from logbook: 300 nm
2.2	Inspection	Filmtek	Measure oxide thickness, 5 points	Measured: 296±1.2 nm
3	**Grow oxide (bottom wafer)**			**Figure a**
3.1	Thermal oxidation	Furnace: Boron drive-in	Recipe: dry1100, Time: 8h 55min, 20 min anneal	Expected thickness from logbook: 400 nm
3.2	Inspection	Filmtek	Measure oxide thickness, 5 points	Measured: 413±2 nm

Step	Process	Equipment	Recipe	Comments
4	**Create CMUT cavities**			**Figure b**
4.1	Adhesion promotion	HMDS oven	Recipe 4	ca. 30 minutes
4.2	Spin on photoresist	SSE spinner	Recipe: 1,5um 4inch. Resist: AZ5214e. Baked for 90s@$90\,^{\circ}\mathrm{C}$	Or use manual spinner set to 4500 rpm (appr. 1.5 um). Heat on hot plate @ $90\,^{\circ}\mathrm{C}$ for 60 seconds. No alufoil on the hot plate!!
4.3	Exposure	KS Aligner	5 s @ 7 mW/cm2, hard contact	Mask: Cavities (e.g. page 195). Rotate aligner to zero and set both wheels to 10 before exposing.
4.4	Development	Developer bath	60 s in AZ351 developer	
4.5	Rinse/dry	Wet bench/Spin dryer	5 min. in DI water, spin dry	
4.6	Inspection	Optical microscope	Check for errors in lithography	Errors with MISSING resist are most severe!
4.7	Oxide etch	AOE	Recipe: m_res_ny, Time: 2 min.	Let AOE cool to 0-$1\,^{\circ}\mathrm{C}$ for roughly 20-30 minutes before etching
4.8	Strip photoresist	Plasma asher 2	O2/N2: 240/70 ml/min, 1000 W, 25 min.	Acetone works OK as well
4.9	Inspection	Optical microscope	Measure etched CMUT cavity side length	
5	**Create trenches for bottom electrode**			**Figure c**
5.1	Adhesion promotion	HMDS oven	Recipe 4	ca. 30 minutes
5.2	Spin on photoresist	SSE spinner	Recipe: 2,2um 4inch. Resist: AZ5214e. Baked for 90s@90 degC	Or use manual spinner set to 2000 rpm (appr. 2.2 um). Heat on hot plate @ $90\,^{\circ}\mathrm{C}$ for 90 seconds. No alufoil on the hot plate!!
5.3	Exposure	KS Aligner	9 s @ 7 mW/cm2, hard contact	Mask: Bottom electrode (e.g. page 196). Align to Cavity mask
5.4	Development	Developer bath	70 s in AZ351 developer	
5.5	Rinse/dry	Wet bench/Spin dryer	5 min. in DI water, spin dry	
5.6	Inspection	Optical microscope	Check for errors in lithography	Errors with resist REMNANTS leads to shorts!
5.7	Oxide etch	AOE	Recipe: m_res_ny, Time: 2 min.	Let AOE cool to 0-$1\,^{\circ}\mathrm{C}$ for roughly 20-30 minutes before etching
5.8	Silicon etch	DRIE Pegasus	Recipe: users/prototyping/CMUT/tlehr/20um_SOIetch	Etch recipe is a 3 min, 40 s standard SOI etch. Visually check color in openings after etch to confirm that the oxide has been reached
5.9	Strip photoresist	Plasma asher 2	O2/N2: 240/70 ml/min, 1000 W, 25 min.	

Step	Process	Equipment	Recipe	Comments
6	**RCA Cleaning**			
6.1	RCA1	RCA 1 bath	10 min	Prepare RCA 1 and RCA 2 before this step. Wash baths with water gun before adding new chemicals. Turn on heater for RCA 1 30 min before this step and turn on heater for RCA 2 when beginning this step.
6.2	Quickdump	Quickdump bath in front of RCA 1	3 min	
6.3	HF	5 % HF bath	30 s	
6.4	Rinse	Water bath in front of HF bath	20 s	
6.5	Bubble rinse	Bubbler in front of BHF bath	3 min	
6.6	RCA2	RCA 2 bath	10 min	
6.7	Quickdump	Quickdump bath in front of RCA 1	3 min	Turn off heater for RCA 1 and RCA 2
6.8	Spin dry	Spin dryer at RCA bench		
7	**Wafer bonding**			**Figure d**
7.1	Fusion bonding	EVG NIL	Recipe: CMUT ($50\,^{\circ}\mathrm{C}$, $1500\,\mathrm{N}$, bond time: 5 min, pressure: 0.01 mbar)	Transport wafers in dedicated box from RCA. Minimize ambient exposure and handling time. Use cleaned tweezers.
7.2	Inspection	Infrared camera	Inspect for pre-anneal voids	
7.3	Annealing	Anneal-bond	Recipe: ann1110, Time 1h 10min	
7.4	Inspection	Infrared camera	Inspect for post-anneal voids	
8	**Remove handle/BOX**			**Figure e**
8.1	Oxide etch	BHF	5 min (80 nm/min)	Only if top wafer is oxidized. Cover bottom wafer with blue tape. Dip wafers in water first to fill out potential voids, and blow dry before dipping into BHF. Oxide is removed when surface is water repellant.
8.2	Silicon etch	ASE	Recipe: cmutaway, Time: 1h 25m	
8.3	Oxide etch	BHF	14 min (80 nm/min)	Only if top wafer is oxidized. Cover bottom wafer with blue tape. Dip wafers in water first to fill out potential voids, and blow dry before dipping into BHF. Oxide is removed when surface is water repellant.
8.4	Rinse/dry	Wet bench/Spin dryer	5 min. in DI water, spin dry	

Step	Process	Equipment	Recipe	Comments
9	**RCA Cleaning**			
9.1	RCA1	RCA 1 bath	10 min	Prepare RCA 1 and RCA 2 before this step. Wash baths with water gun before adding new chemicals. Turn on heater for RCA 1 30 min before this step and turn on heater for RCA 2 when beginning this step.
9.2	Quickdump	Quickdump bath in front of RCA 1	3 min	
9.3	HF	5 % HF bath	30 s	
9.4	Rinse	Water bath in front of HF bath	20 s	
9.5	Bubble rinse	Bubbler in front of BHF bath	3 min	
9.6	RCA2	RCA 2 bath	10 min	
9.7	Quickdump	Quickdump bath in front of RCA 1	3 min	Turn off heater for RCA 1 and RCA 2
9.8	HF	5 % HF bath	30 s	
9.9	Rinse	Water bath in front of HF bath	20 s	
9.10	Rinse 2	Bubbler in front of BHF bath	5 min	
9.11	Spin dry	Spin dryer at RCA bench		
10	**Etch access to bottom electrode**			**Figure f**
10.1	Spin on photoresist	SSE spinner	Recipe: 2,2um 4inch. Resist: AZ5214e. Baked for 90s@$90\,^{\circ}\mathrm{C}$	Or use manual spinner set to 2000 rpm (appr. 2.2 um). Heat on hot plate @ $90\,^{\circ}\mathrm{C}$ for 90 seconds. No alufoil on the hot plate!!
10.2	Exposure	KS Aligner	9 s @ 7 mW/cm2, hard contact	Mask: Access to bottom electrode (e.g. page 197). Align to Cavity mask through silicon plate
10.3	Development	Developer bath	70 s in AZ351 developer	
10.4	Rinse/dry	Wet bench/Spin dryer	5 min. in DI water, spin dry	
10.5	Inspection	Optical microscope	Check for errors in lithography	
10.6	Silicon etch	DRIE Pegasus	Recipe: users/prototyping/CMUT/tlehr/-SOI_membrane_2um	Visually check color to confirm that the oxide has been reached.
10.7	Cover alignment marks	Manual spinner	2000 rpm, bake @ $90\,^{\circ}\mathrm{C}$ for 90 seconds on hot plate	Put a drop of resist on each mark before spinning. No alufoil on the hot plate!!
10.8	Oxide etch	AOE	Recipe: m_res_ny, Time: 2+2 min (230 nm/min)	Let AOE cool to 0-$1\,^{\circ}\mathrm{C}$ before etching. Visually check color in openings after etch to confirm that the silicon has been reached
10.9	Strip photoresist	Plasma asher 2	O2/N2: 240/70 ml/min, 1000 W, 25 min.	

Step	Process	Equipment	Recipe	Comments
11	**Metallization of wire bond pads**			**Figure g**
11.1	Deposit Al	Alcatel	800 nm	Al is deposited over the whole wafer
11.2	Spin on photoresist	SSE spinner	Recipe: 2,2um 4inch. Resist: AZ5214e. Baked for 90s@$90\,^{\circ}\mathrm{C}$	Or use manual spinner set to 2000 rpm (appr. 2.2 um). Heat on hot plate @ $90\,^{\circ}\mathrm{C}$ for 90 seconds. No alufoil on the hot plate!!
11.3	Exposure	KS Aligner	9 s @ 7 mW/cm2, hard contact	Contact pads (e.g. page 198). Align to Cavity mask
11.4	Development	Developer bath	70 s in AZ351 developer	Maybe slightly overdevelop to ensure good wet Al etch
11.5	Rinse/dry	Wet bench/Spin dryer	5 min. in DI water, spin dry	
11.6	Al etch	Aluminium etch 1	H2O:H3PO4 1:2, $50\,^{\circ}\mathrm{C}$. (100 nm/min)	Stir before use. It can be clearly seen when the etch is done through visual inspection
11.7	Rinse/dry	Wet bench/Spin dryer	5 min. in DI water, spin dry	
11.8	Strip photoresist	Plasma asher 1	O2/N2: 240/70 ml/min, 1000 W, 25 min.	
12	**Metallization of top electrode**			**Figure h**
12.1	Deposit Al	Alcatel	200 nm	Al is deposited over the whole wafer
12.2	Spin on photoresist	SSE spinner	Recipe: 2,2um 4inch. Resist: AZ5214e. Baked for 90s@$90\,^{\circ}\mathrm{C}$	Or use manual spinner set to 2000 rpm (appr. 2.2 um). Heat on hot plate @ $90\,^{\circ}\mathrm{C}$ for 90 seconds. No alufoil on the hot plate!!
12.3	Exposure	KS Aligner	9 s @ 7 mW/cm2, hard contact	Top electrodes (e.g. page 199). Align to Cavity mask
12.4	Development	Developer bath	70 s in AZ351 developer	Maybe slightly overdevelop to ensure good wet Al etch
12.5	Rinse/dry	Wet bench/Spin dryer	5 min. in DI water, spin dry	
12.6	Inspection	Optical microscope	Check for errors in lithography	Look for potential shorts between elements
12.6	Al etch	Aluminium etch 1	H2O:H3PO4 1:2, $50\,^{\circ}\mathrm{C}$. (100 nm/min)	Stir before use. It can be clearly seen when the etch is done through visual inspection
12.7	Rinse/dry	Wet bench/Spin dryer	5 min. in DI water, spin dry	
12.8	Si etch	DRIE Pegasus	Recipe: SOI, Time: 30 seconds (Etch rate: $10\,\mu\mathrm{m}$/min)	Visually check color to confirm that the oxide has been reached
12.9	Strip photoresist	Plasma asher 1	O2/N2: 240/70 ml/min, 1000 W, 25 min.	

Step	Process	Equipment	Recipe	Comments
13	**Protective resist layer**			
13.1	Spin on photoresist	SSE spinner	Recipe: AZ4562_4inch_10um	Optional step, but if left out, saw will leave considerable amount of dust, which can potentially short the device.
14	**Dicing**			
14.1	Dice out arrays	Saw	Set to program 8, then use semiautomatic cut. Align wafer with the x/y buttons. Press start/stop two times in a row to get a single cut.	
14.2	Remove resist	Fumehood outside cleanroom	Acetone bath, IPA bath/water bath, air gun	Place individual arrays in acetone bath until all resist is gone (leave it for a few minutes but make sure arrays are covered with acetone). Then, transfer arrays to a water bath or IPA bath to prevent the acetone from drying on the arrays. Finally, the arrays are dried with an air gun.

PROCESS C

Row-Column LOCOS Process

Used for: Fabrication of 2-D row-column CMUT arrays.

Period used: September 2014 – current date.

Description: This process was developed late 2014/early 2015. It was developed together with Mathias Engholm during his master project. The main purpose of the process is to use LOCOS oxidation to create the CMUT cavities. As opposed to process B, this ensures that no oxide is needed on the CMUT plate. Also, the bottom electrodes are electrically insulated during the LOCOS oxidation. The last contact pad deposition step in process B is omitted, since the thick bonding pad is not needed. In general, a number of process steps have been optimized since process B.

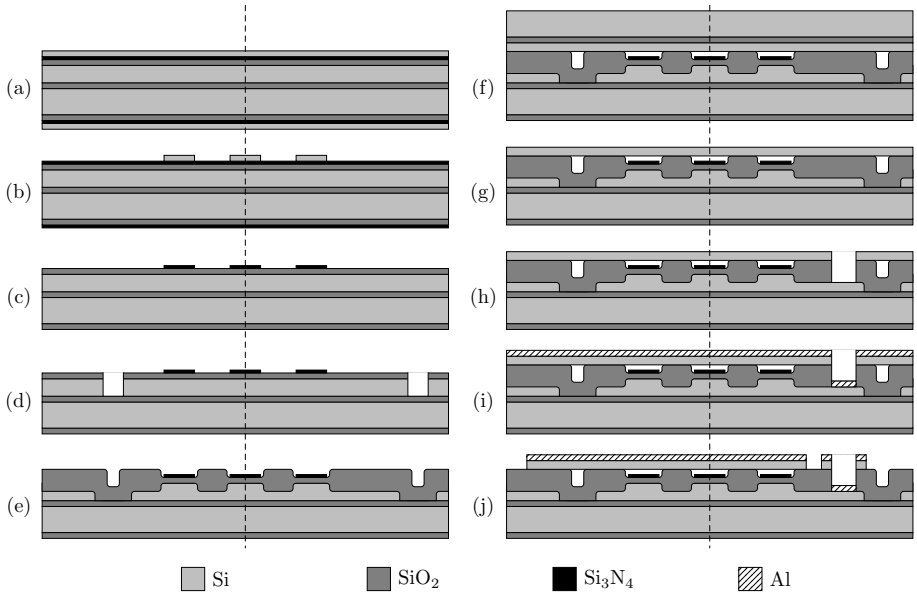

Step	Process	Equipment	Recipe	Comments
1	**RCA Cleaning**			
1.1	RCA1	RCA 1 bath	10 min	Prepare RCA 1 and RCA 2 before this step. Wash baths with water gun before adding new chemicals. Turn on heater for RCA 1 30 min before this step and turn on heater for RCA 2 when beginning this step.
1.2	Quickdump	Quickdump bath in front of RCA 1	3 min	
1.3	HF	5 % HF bath	30 s	
1.4	Rinse	Water bath in front of HF bath	20 s	
1.5	Bubble rinse	Bubbler in front of BHF bath	3 min	
1.6	RCA2	RCA 2 bath	10 min	
1.7	Quickdump	Quickdump bath in front of RCA 1	3 min	Turn off heater for RCA 1 and RCA 2
1.8	HF	5 % HF bath	30 s	
1.9	Rinse	Water bath in front of HF bath	20 s	
1.10	Rinse 2	Bubbler in front of BHF bath	5 min	
1.11	Spin dry	Spin dryer at RCA bench		
2	**Grow oxide**			
2.1	Thermal oxidation	Furnace: Phosphorus drive-in	Recipe: dry1100, Time: 8h 45min, 20 min anneal	Expected thickness from logbook: 400 nm
2.2	Inspection	Filmtek	Measure oxide thickness, 5 points	
3	**Nitride deposition**			
3.1	Si3N4 deposition	Furnace: Nitride	Recipe: 4nitdan, Time: 22 min	Expected thickness from logbook: 55 nm
4	**Polysilicon deposition**			**Figure a**
4.1	Polysilicon deposition	Furnace: Polysilicon	Recipe: Poly, Time: 13 min	Expected thickness from logbook: 100 nm

Step	Process	Equipment	Recipe	Comments
4	**Define polysilicon etch mask**			**Figure b**
4.1	Spin on photoresist	Spin track	$1.5\,\mu m$ with HMDS (Mir 701 positive resist)	
4.2	Exposure	KS Aligner	23 s @ 7 mW/cm2, hard contact	Mask: Cavity (e.g. page 203). Rotate aligner to zero and set both wheels to 10 before exposing.
4.3	Development	TMAH UV developer	PEB 110C 60s + 60s puddle develop	
4.4	Inspection	Optical microscope	Check for errors in lithography	Errors with resist REMNANTS are most severe!
4.5	Polysilicon etch	ASE or DRIE Pegasus	ASE: 8 seconds using a continuous deep etch process (The same as for removing the handle), Pegasus: 1-2 cycles of SOI recipe	
4.6	Inspection	Optical microscope	Check that polysilicon is properly removed	
4.7	Strip photoresist	Plasma asher 2	O2/N2: 240/70 ml/min, 1000 W, 25 min.	
4.8	Spin on photoresist	Spin track	$1.5\,\mu m$ with HMDS (Mir 701 positive resist)	
4.9	Polysilicon etch	Wet poly etch	Strip PolySi of backside for 2 min. Frontside is protected by resist	
4.10	Strip photoresist	Plasma asher 2	O2/N2: 240/70 ml/min, 1000 W, 25 min.	
5	**Nitride etch**			**Figure c**
5.1	Spin on photoresist	Spin track	$1.5\,\mu m$ with HMDS (Mir 701 positive resist)	
5.2	Wafer clean	7-up		Clean wafers after wet nitride etch due to possible contamination by potassium ions from people stripping nitride after KOH
5.3	Inspection	Optical microscope	Check that nitride is properly removed	
5.4	Strip polysilicon mask	ASE or DRIE Pegasus	ASE: 8 seconds using a continuous deep etch process (The same as for removing the handle), Pegasus: 1-2 cycles of SOI recipe	

Step	Process	Equipment	Recipe	Comments
6	**Create trenches for bottom electrode**			**Figure d**
6.1	Spin on photoresist	Spin track	$1.5\,\mu m$ with HMDS (Mir 701 positive resist)	
6.2	Exposure	KS Aligner	23 s @ 7 mW/cm2, hard contact	Mask: Bottom electrodes (e.g. page 204). Align to cavity mask.
6.3	Development	TMAH UV developer	PEB 110C 60s + 60s puddle develop	
6.4	Inspection	Optical microscope	Check for errors in lithography	Errors with resist REMNANTS are most severe!
6.5	Oxide etch	AOE	SiO2_res, Time: 2x1.5 min, Temp: $0\,^{\circ}C$	Wait 30 min for temp to stabilize before etch. Etch wafer 1, then 2, then 1, then 2, then O2 clean chamber for a couple of min.
6.6	Inspection	Optical microscope	Check that oxide is removed in the trenches	
6.7	Silicon etch	DRIE Pegasus	SOI recipe, Time: 4 min, Temp: $20\,^{\circ}C$	
6.8	Inspection	Optical microscope	Check that the silicon is removed in the trenches	
6.9	Strip photoresist	Plasma asher 2	O2/N2: 240/70 ml/min, 1000 W, 45 min.	
7	**LOCOS oxidation**			**Figure e**
7.1	RCA1	RCA 1 bath	10 min	Prepare RCA 1 and RCA 2 before this step. Wash baths with water gun before adding new chemicals. Turn on heater for RCA 1 30 min before this step and turn on heater for RCA 2 when beginning this step.
7.2	Quickdump	Quickdump bath in front of RCA 1	3 min	
7.3	HF	5 % HF bath	15 s	Note: this is half of the usual time!
7.4	Rinse	Water bath in front of HF bath	20 s	
7.5	Bubble rinse	Bubbler in front of BHF bath	3 min	
7.6	RCA2	RCA 2 bath	10 min	
7.7	Quickdump	Quickdump bath in front of RCA 1	3 min	Turn off heater for RCA 1 and RCA 2
7.8	Spin dry	Spin dryer at RCA bench		
7.9	Thermal oxidation	Furnace: Phosphorus drive-in	Recipe: wet1100, Time: 228 min, 20 min anneal	Expected thickness from logbook: 1356 nm
7.10	Inspection	Filmtek	Measure oxide thickness, 5 points	

Step	Process	Equipment	Recipe	Comments
8	**RCA Cleaning**			
8.1	RCA1	RCA 1 bath	10 min	Prepare RCA 1 and RCA 2 before this step. Wash baths with water gun before adding new chemicals. Turn on heater for RCA 1 30 min before this step and turn on heater for RCA 2 when beginning this step.
8.2	Quickdump	Quickdump bath in front of RCA 1	3 min	
8.3	HF	5 % HF bath	15 s	Note: this is half of the usual time!
8.4	Rinse	Water bath in front of HF bath	20 s	
8.5	Bubble rinse	Bubbler in front of BHF bath	3 min	
8.6	RCA2	RCA 2 bath	10 min	
8.7	Quickdump	Quickdump bath in front of RCA 1	3 min	Turn off heater for RCA 1 and RCA 2
8.8	Spin dry	Spin dryer at RCA bench		
9	**Wafer bonding**			**Figure f**
9.1	Fusion bonding	EVG NIL	Recipe: CMUT ($50\,^{\circ}\mathrm{C}$, $1500\,\mathrm{N}$, bond time: 5 min, pressure: 0.01 mbar)	Transport wafers in dedicated box from RCA. Minimize ambient exposure and handling time. Use cleaned tweezers. Optional: bond support wafer to back of bottom wafer in the same step.
9.2	Inspection	Infrared camera	Inspect for pre-anneal voids	
9.3	Annealing	Anneal-bond	Recipe: ann1110, Time 1h 10min	
9.4	Inspection	Infrared camera	Inspect for post-anneal voids	
10	**Remove handle/BOX**			**Figure g**
10.1	Silicon etch	ASE	Recipe: etchaway, Time: 1h 25m	Stop etch when the handle is removed (visual inspection)
10.2	Oxide etch	BHF	14 min (80 nm/min)	Cover bottom wafer with blue tape. Dip wafers in water first to fill out potential voids, and blow dry before dipping into BHF. Oxide is removed when surface is water repellant.
10.3	Rinse/dry	Wet bench/Spin dryer	5 min. in DI water, spin dry	

Step	Process	Equipment	Recipe	Comments
11	**RCA Cleaning**			
11.1	RCA1	RCA 1 bath	10 min	Prepare RCA 1 and RCA 2 before this step. Wash baths with water gun before adding new chemicals. Turn on heater for RCA 1 30 min before this step and turn on heater for RCA 2 when beginning this step.
11.2	Quickdump	Quickdump bath in front of RCA 1	3 min	
11.3	HF	5 % HF bath	30 s	
11.4	Rinse	Water bath in front of HF bath	20 s	
11.5	Bubble rinse	Bubbler in front of BHF bath	3 min	
11.6	RCA2	RCA 2 bath	10 min	
11.7	Quickdump	Quickdump bath in front of RCA 1	3 min	Turn off heater for RCA 1 and RCA 2
11.8	HF	5 % HF bath	30 s	
11.9	Rinse	Water bath in front of HF bath	20 s	
11.1	Rinse 2	Bubbler in front of BHF bath	5 min	
11.1	Spin dry	Spin dryer at RCA bench		
12	**Etch access to bottom electrode**			**Figure h**
12.1	Spin on photoresist	Spin track	$1.5\,\mu\mathrm{m}$ with HMDS (Mir 701 positive resist)	
12.2	Exposure	KS Aligner	23 s @ 7 mW/cm2, hard contact	Mask: Access to bottom electrode (e.g. page 205). Align to cavity mask through silicon partially transparent plate.
12.3	Development	TMAH UV developer	PEB 110C 60s + 60s puddle develop	
12.4	Inspection	Optical microscope	Check for errors in lithography	Errors with MISSING resist are most severe!
12.5	Silicon etch	DRIE Pegasus	SOI recipe, Time: 40 s, Temp: $20\,^{\circ}\mathrm{C}$	Visually check color to confirm that the oxide has been reached.
12.6	Oxide etch	AOE	Recipe: SiO2_res, Time: 4x2 min	Let AOE cool to 0-$1\,^{\circ}\mathrm{C}$ before etching. Visually check color in openings after etch to confirm that the silicon has been reached. Alignment marks should be automatically transferred to the silicon.
12.7	Strip photoresist	Plasma asher 2	O2/N2: 240/70 ml/min, 1000 W, 45 min.	

Step	Process	Equipment	Recipe	Comments
13	**Metallization**			**Figure i**
13.1	Deposit Ti/Al	Alcatel	Ti thickness: 20nm, Al thickness: 400nm	
14	**Top electrode etch**			**Figure j**
14.1	Spin on photoresist	Spin track	$1.5\,\mu m$ with HMDS (Mir 701 positive resist)	
14.2	Exposure	KS Aligner	23 s @ 7 mW/cm2, hard contact	Mask: Top electrode (e.g. page 206). Align to cavity mask through silicon partially transparent plate.
14.3	Development	TMAH UV developer	PEB 110C 60s + 60s puddle develop	
14.4	Inspection	Optical microscope	Check for errors in lithography	Errors with resist REMNANTS are most severe!
14.5	Ti/Al etch	ICP metal	Al etch, Time: 80 s, Temp: $20\,^{\circ}C$	Visually check that metal is etched through.
14.6	Si etch	DRIE Pegasus	SOI recipe, Time: 40 s, Temp: $20\,^{\circ}C$	Visually check color to confirm that the oxide has been reached
14.7	Strip photoresist	Plasma asher 1	O2/N2: 240/70 ml/min, 1000 W, 45 min.	
15	**Protective resist layer**			
15.1	Spin on photoresist	SSE spinner	Recipe: AZ4562_4inch_10um	Optional step, but if left out, saw will leave considerable amount of dust, which can potentially short the device.
16	**Dicing**			
16.1	Dice out arrays	Saw	Set to program 8, then use semiautomatic cut. Align wafer with the x/y buttons. Press start/stop two times in a row to get a single cut.	
16.2	Remove resist	Fumehood outside cleanroom	Acetone bath, IPA bath/water bath, air gun	Place individual arrays in acetone bath until all resist is gone (leave it for a few minutes but make sure arrays are covered with acetone). Then, transfer arrays to a water bath or IPA bath to prevent the acetone from drying on the arrays. Finally, the arrays are dried with an air gun.

Lithography Masks

MASK SET A

1st Generation Row-Column Masks

Used for: Fabrication of 2-D row-column CMUT arrays with and without Hann apodization having square or circular CMUT cells.

Array sizes (number of arrays): 6+6 (68), 16+16 (56), and 32+32 (12).

Test structures: Exposure marks. Test elements with 1-9 cells, square and circular.

Description: This mask set was used for the first generation of functioning row-column arrays. It features three different array sizes: 6+6 elements ($4\,\mathrm{mm}\times4\,\mathrm{mm}$), 16+16 elements ($7\,\mathrm{mm}\times7\,\mathrm{mm}$), and 32+32 elements ($12\,\mathrm{mm}\times12\,\mathrm{mm}$). Each array size exists in four categories: With square and circular CMUT cells, both types existing with and without integrated Hann apodization. For the 6+6 arrays, there are 17 arrays in each of the four categories. For the 16+16 and 32+32, the numbers are 14 and 3, respectively. The mask set was used in papers A, B, E, F, G, and I.

The following page shows a wafer-scale overview of all masks on top of each other. The subsequent pages show a selection of the different structures in each mask. Mask 6 is identical to mask 5, except that the electrodes are shorted. By omitting mask 2 in the fabrication, this enables the fabrication of arrays with one common bottom electrode/top electrode. Mask 3 is for etching away the bonded silicon plate on top of the alignment mark, such that accurate alignment can be performed with the subsequent masks.

Parameter	Value	Unit
Array		
Element pitch	300	µm
Element width	288	µm
CMUT cell		
Cell side length (square)	65	µm
Cell diameter (circular)	72	µm
Distance between circular cells	20	µm
Distance between square cells	25	µm
Max. number of cells along element width	3	-

A.1 Mask Overview

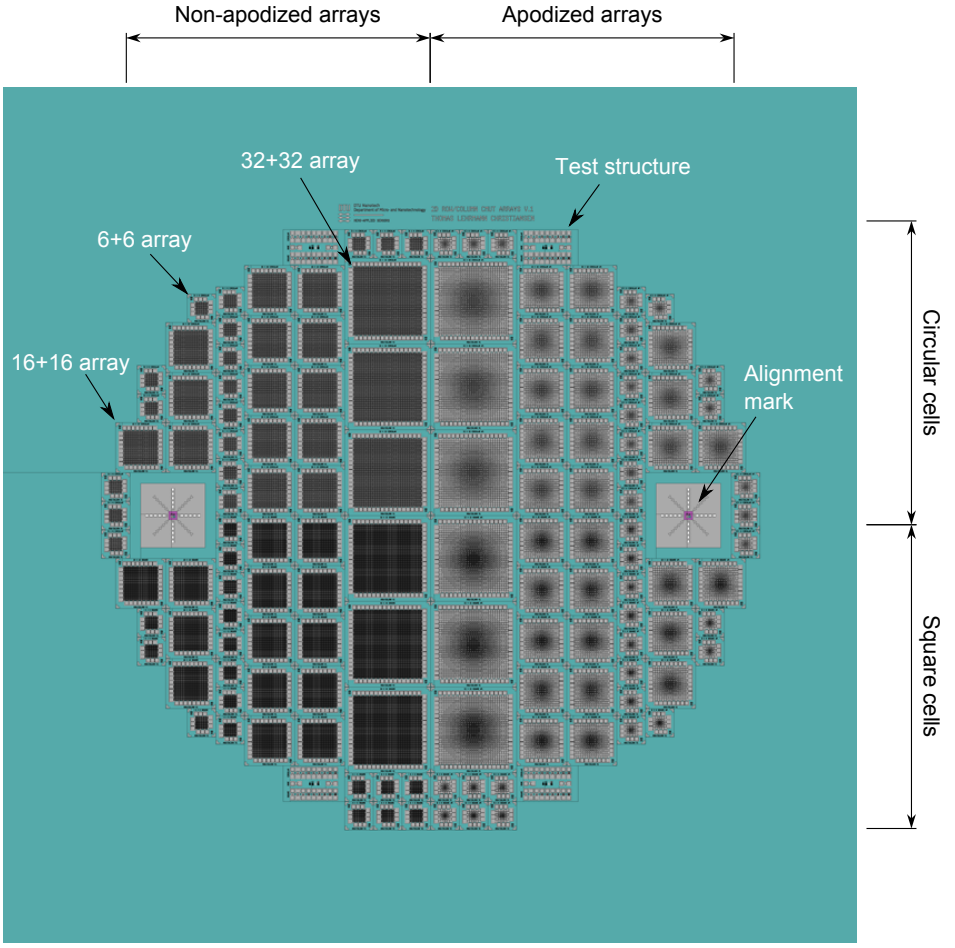

A.2 Mask 1: Cavities

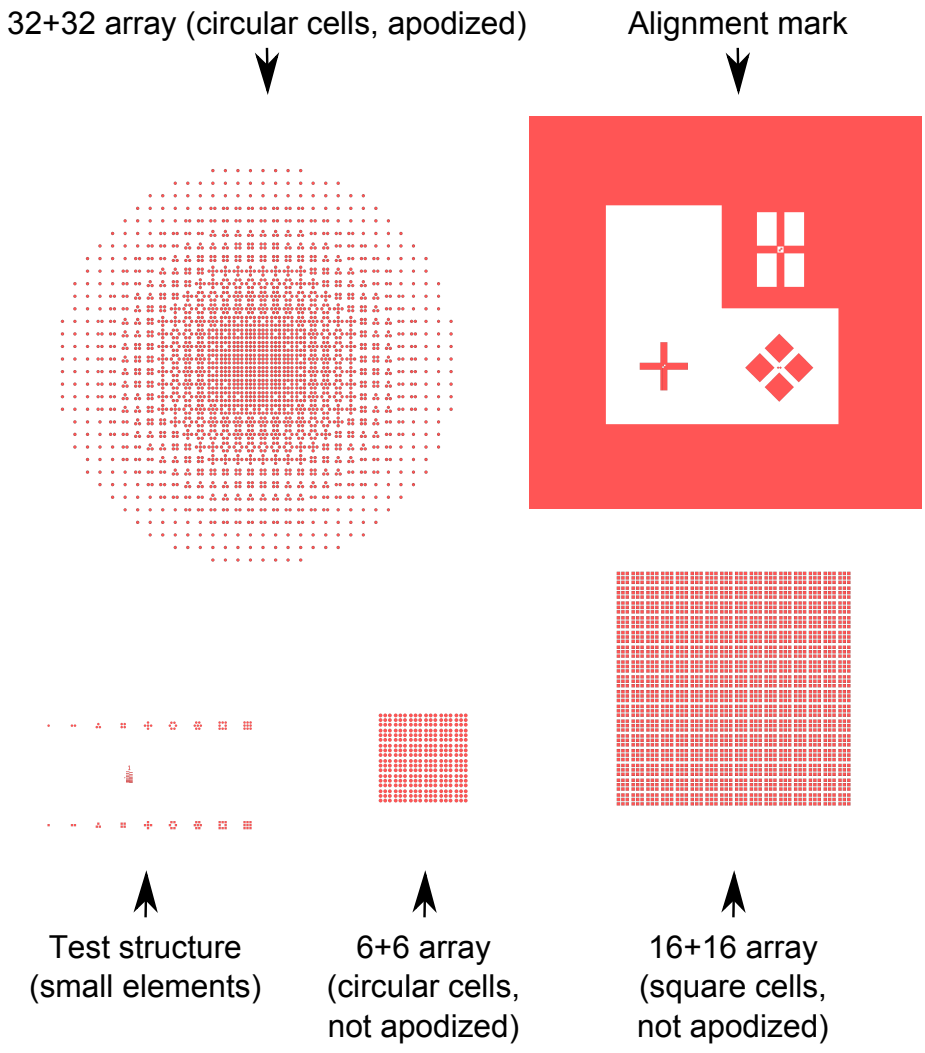

A.3 Mask 2: Bottom Electrodes

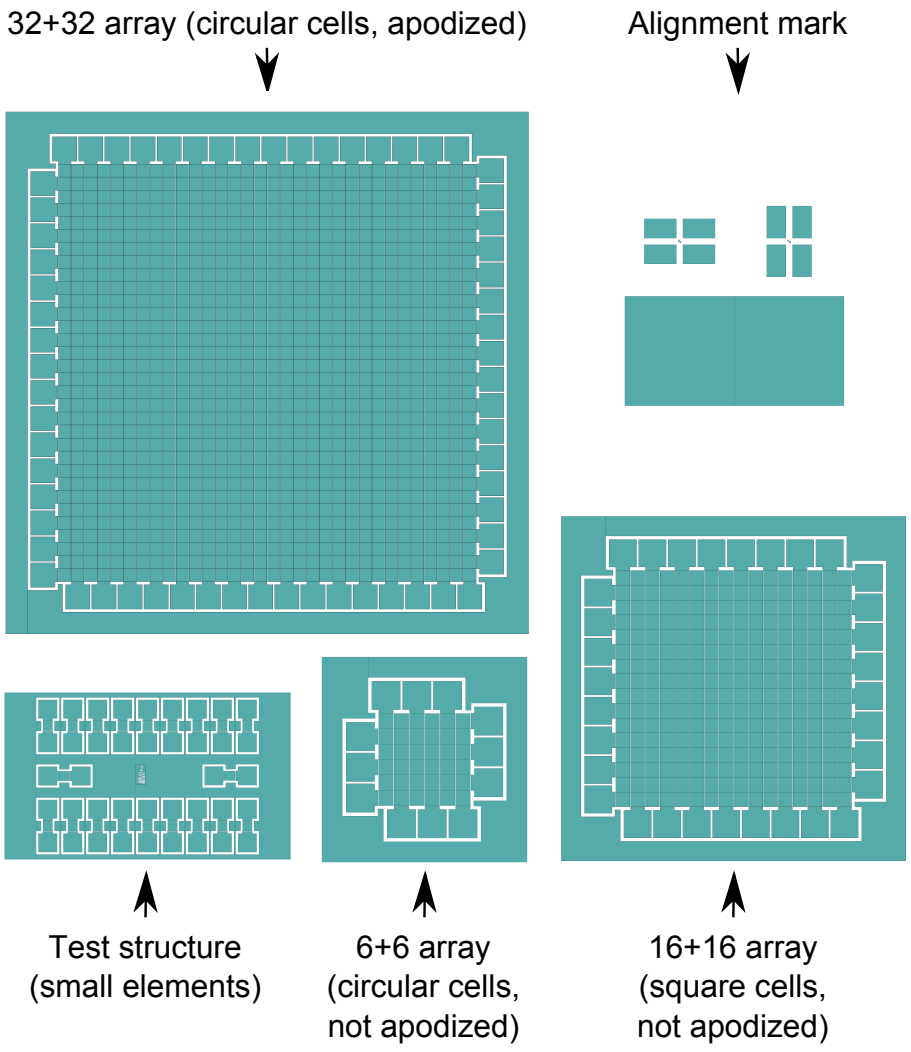

Objects are not to scale

A.4 Mask 3: Open to Alignment Marks

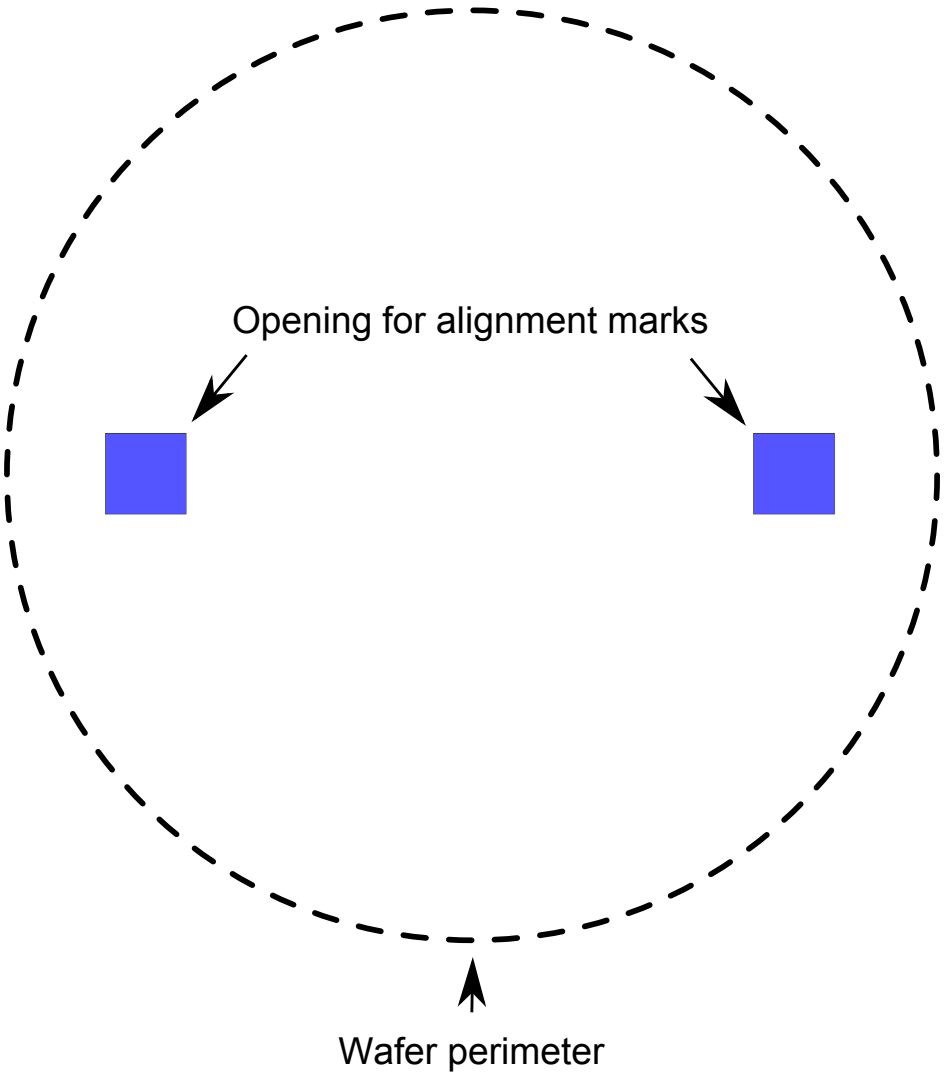

A.5 Mask 4: Access to Bottom Electrode

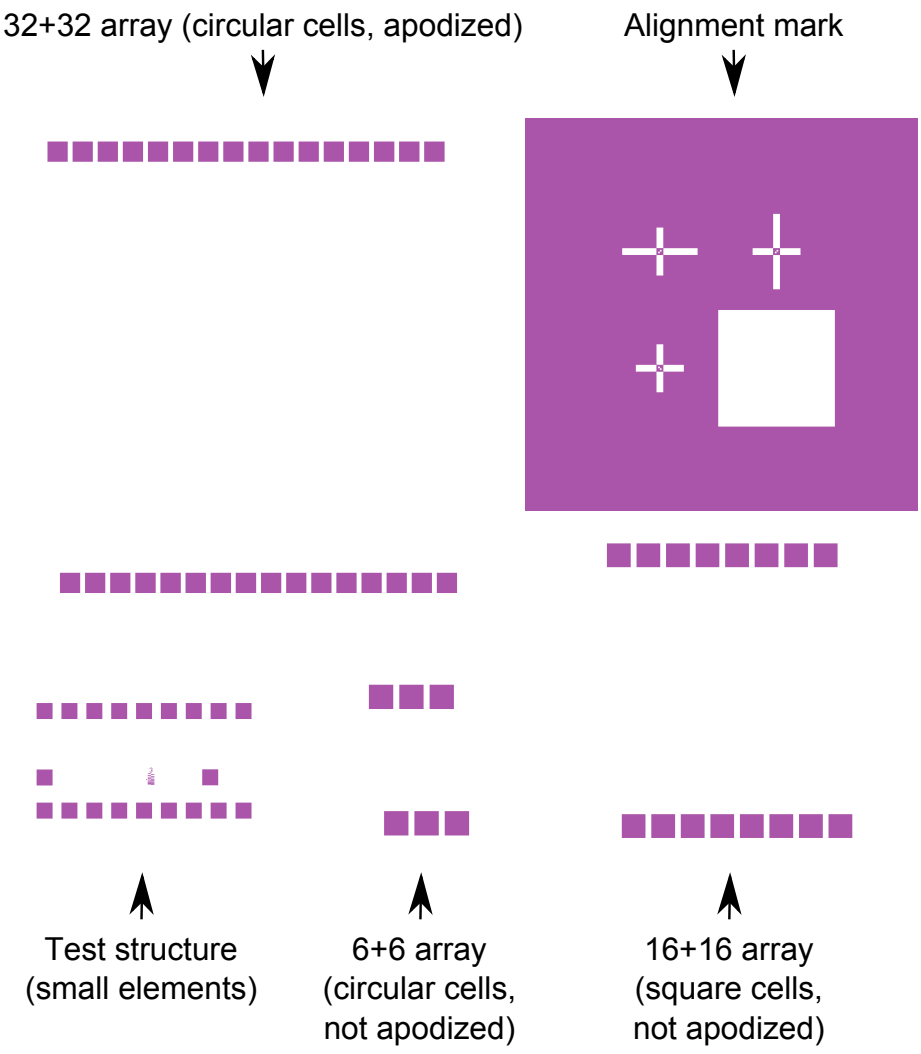

A.6 Mask 5: Top Electrodes

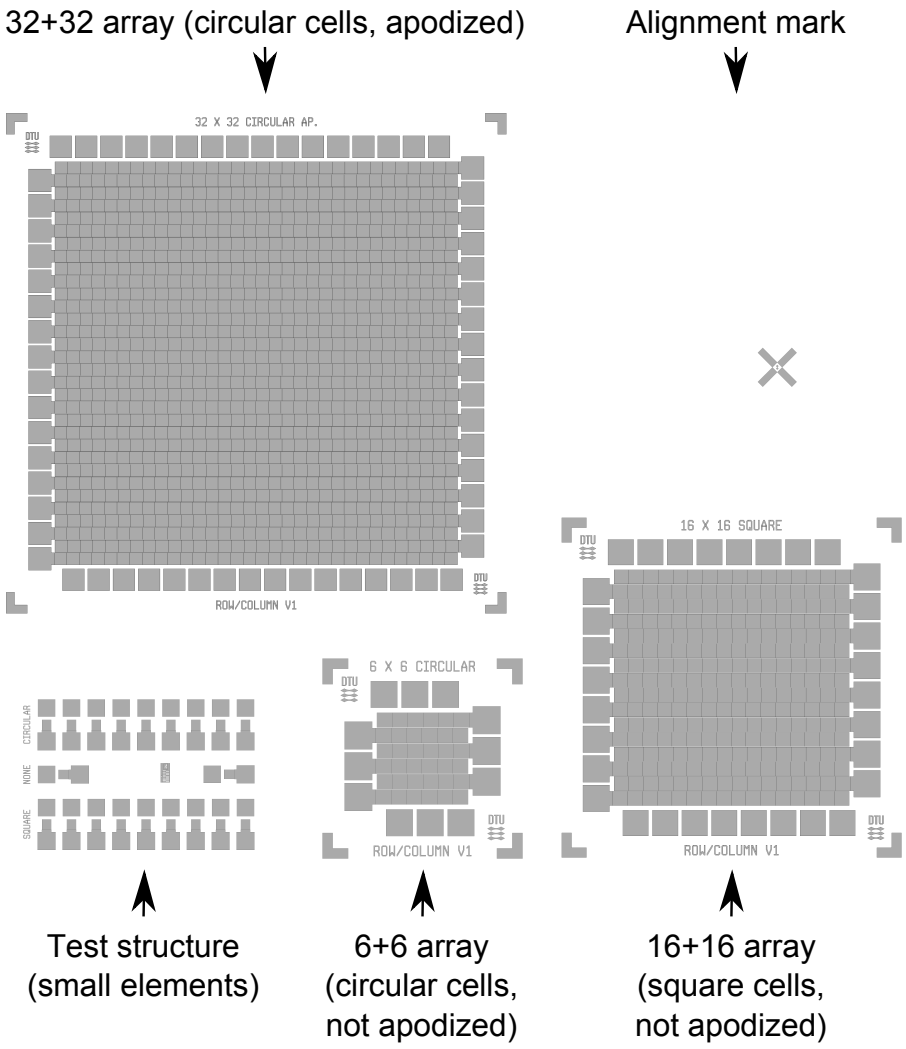

Objects are not to scale

A.7 Mask 6: Top Electrodes (Short Circuit)

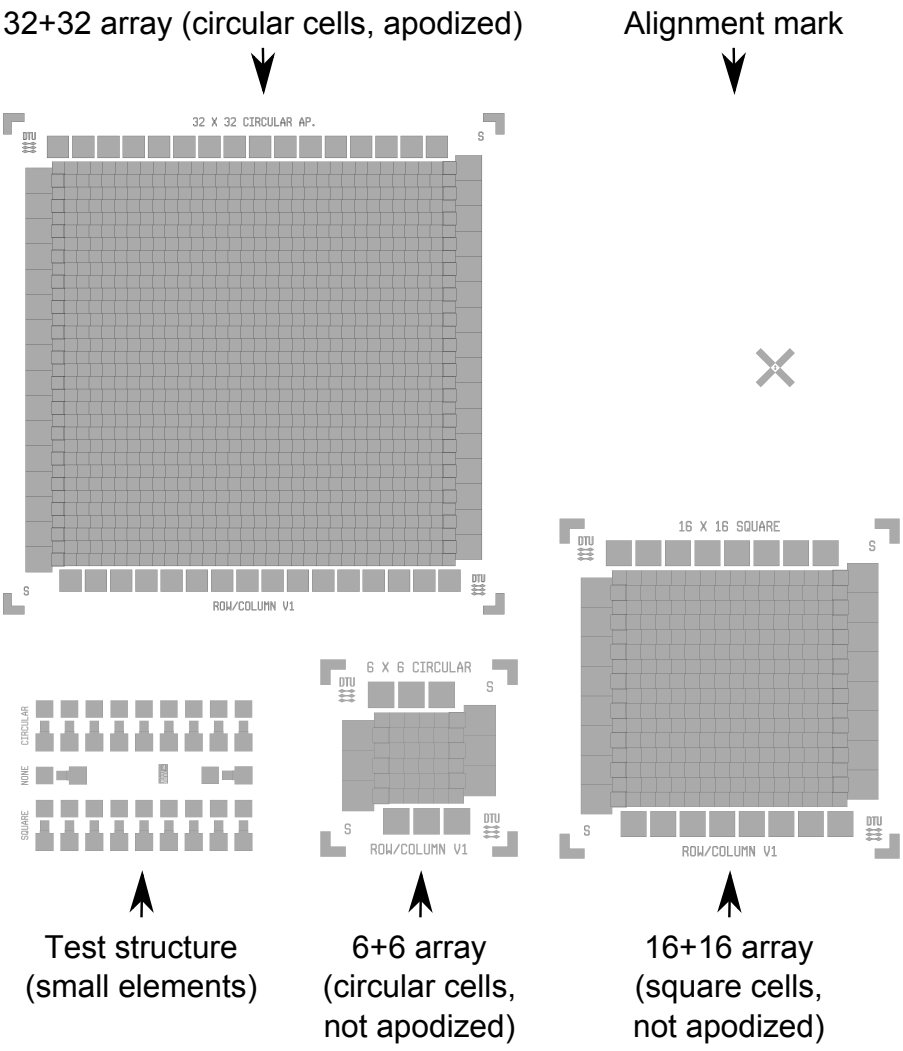

Objects are not to scale

MASK SET B

2nd Generation Row-Column Masks

Used for: Fabrication of 2-D row-column CMUT arrays with roll-off apodization.

Array sizes (number of arrays): 62+62 and 4 apodization elements (6).

Test structures: Exposure marks. Oxide breakdown test element with electrodes in different sizes. Test elements with 1-16 cells. Test elements with the same size as the actual line elements: With apodization, without apodization, and without cavities.

Description: This mask set was used for the second generation of functioning row-column arrays. These arrays have the roll-off apodization. It features six arrays with 62+62 elements and four apodization region electrodes. The total size of an array is $26.3\,\mathrm{mm} \times 26.3\,\mathrm{mm}$. The mask set was used in papers K and L.

The following pages gives an overview of the mask set by first showing a wafer-scale overview of all masks on top of each other. The subsequent pages show the different structures in each of the five masks. Note that compared to mask set A, the alignment mark opening mask has been removed, since this is now incorporated in mask 3. Also, an extra mask (mask 4) has been added to make contact pads with a different thickness than the top electrode.

Parameter	Value	Unit
Array		
Element pitch	270	µm
Element width	265	µm
CMUT cell		
Cell side length (square)	60	µm
Distance between cells	5	µm
Max. number of cells along element width	4	-

B.1 Mask Overview

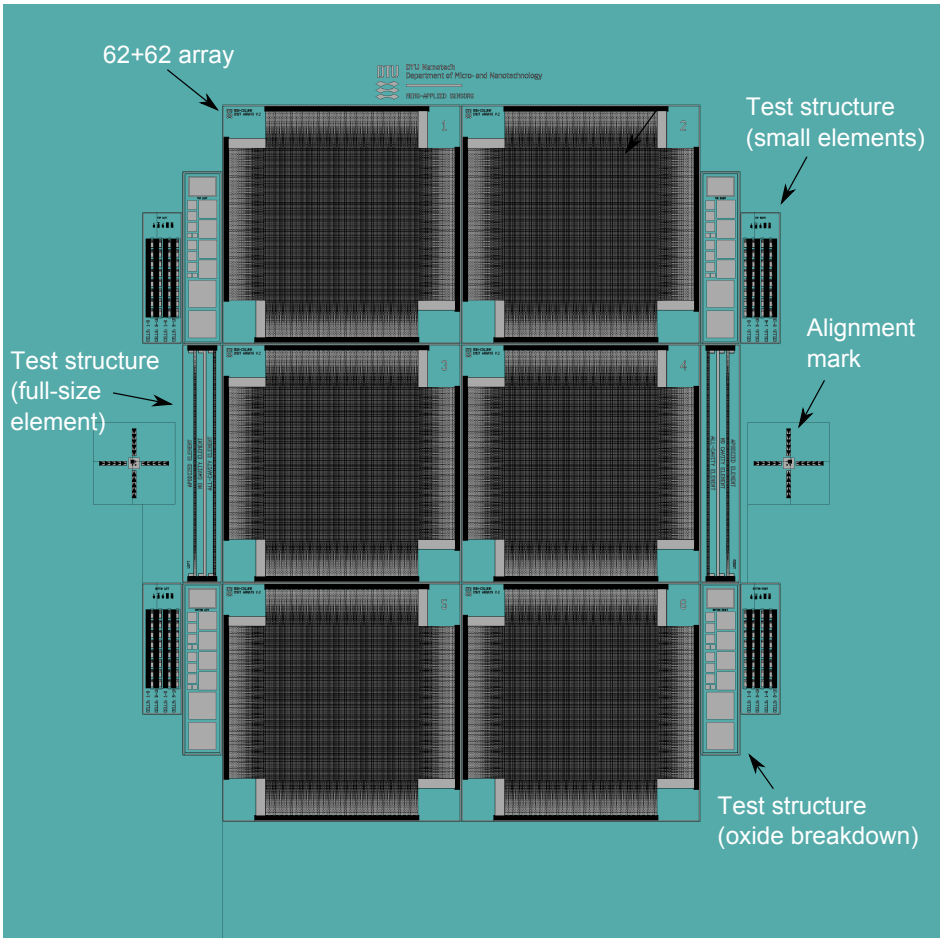

B.2 Mask 1: Cavities

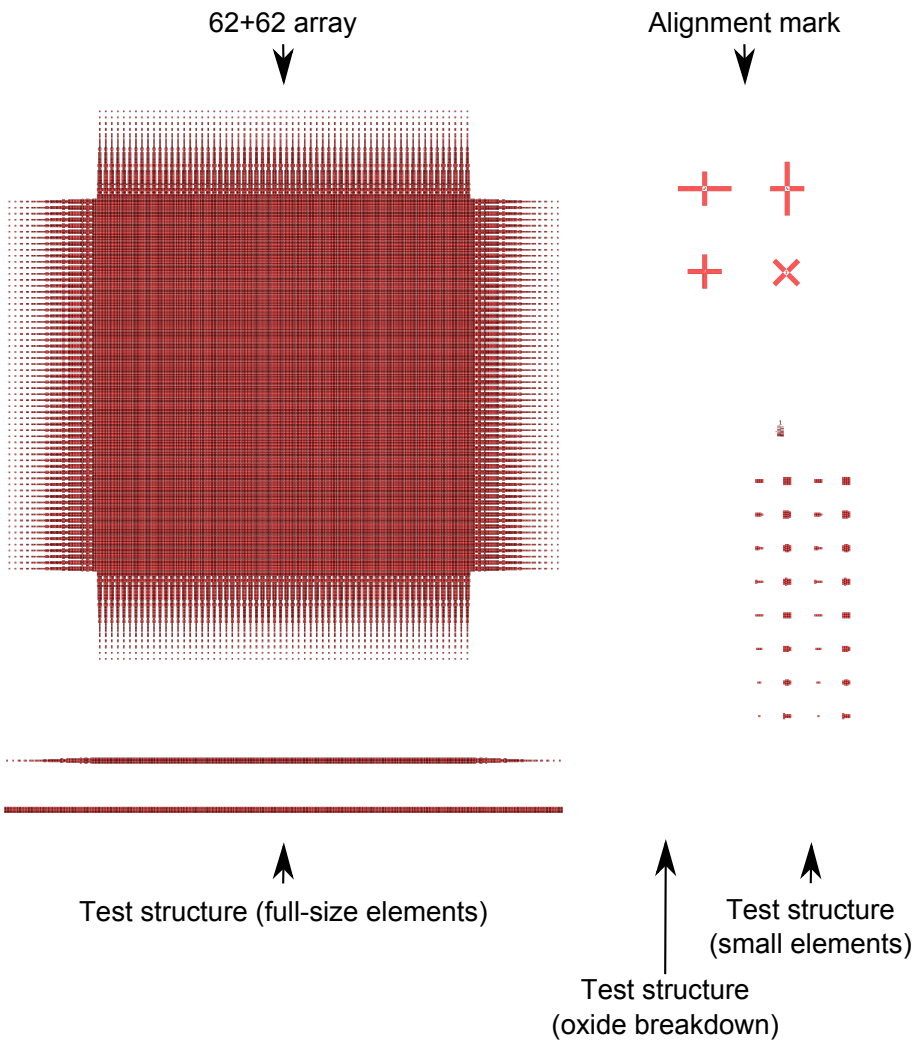

B.3 Mask 2: Bottom Electrodes

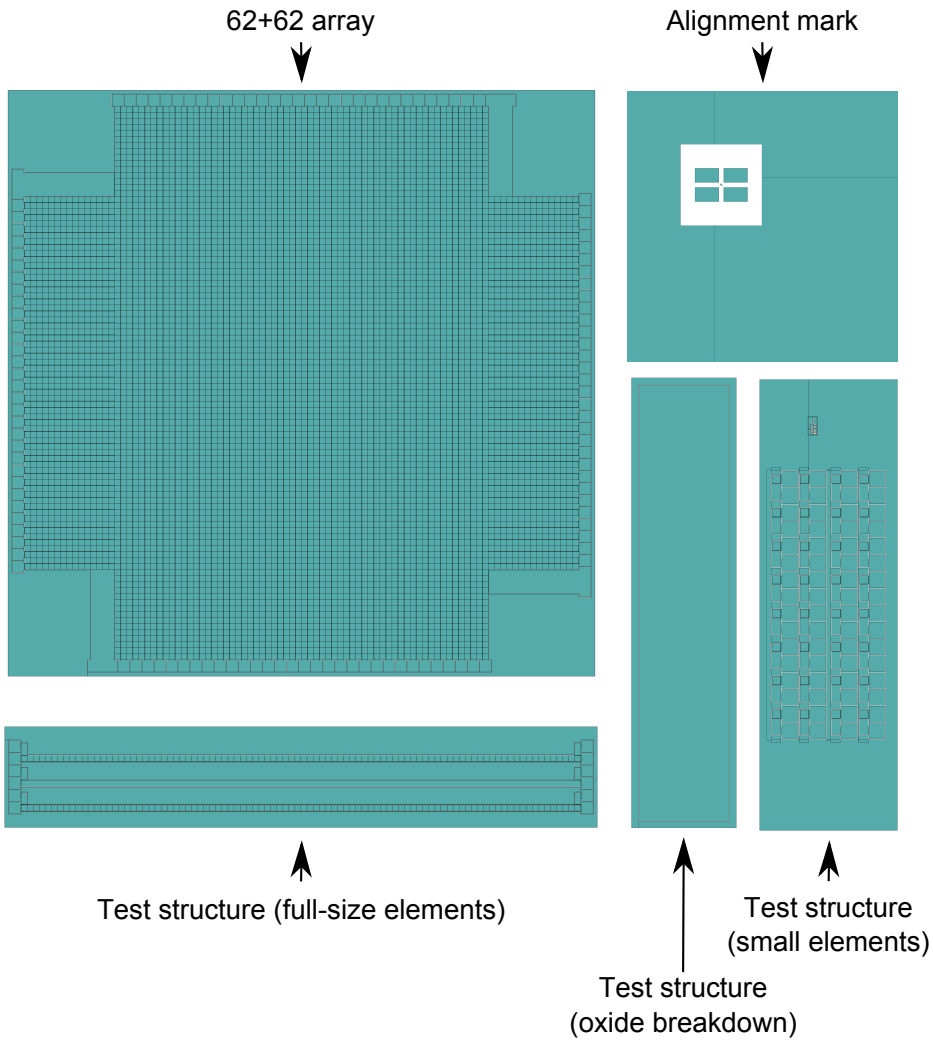

Objects are not to scale

B.4 Mask 3: Access to Bottom Electrode

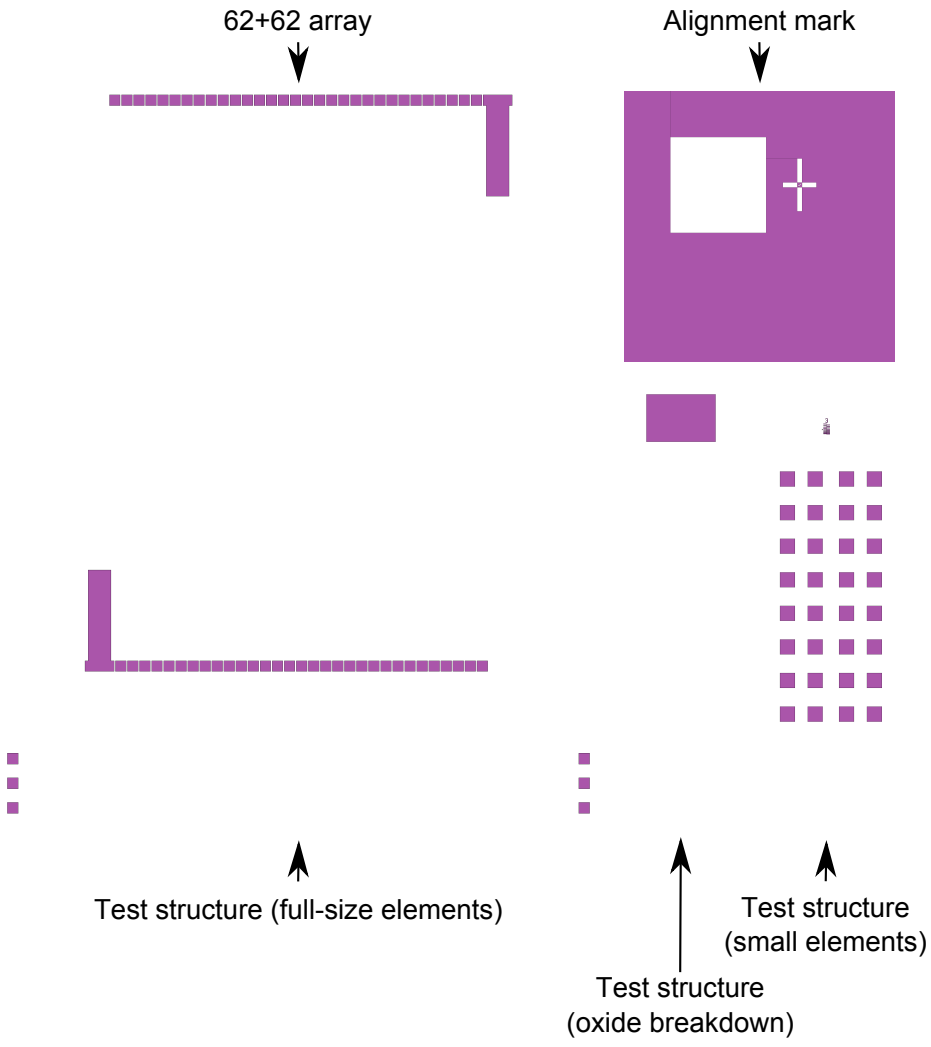

Objects are not to scale

B.5 Mask 4: Contact Pads

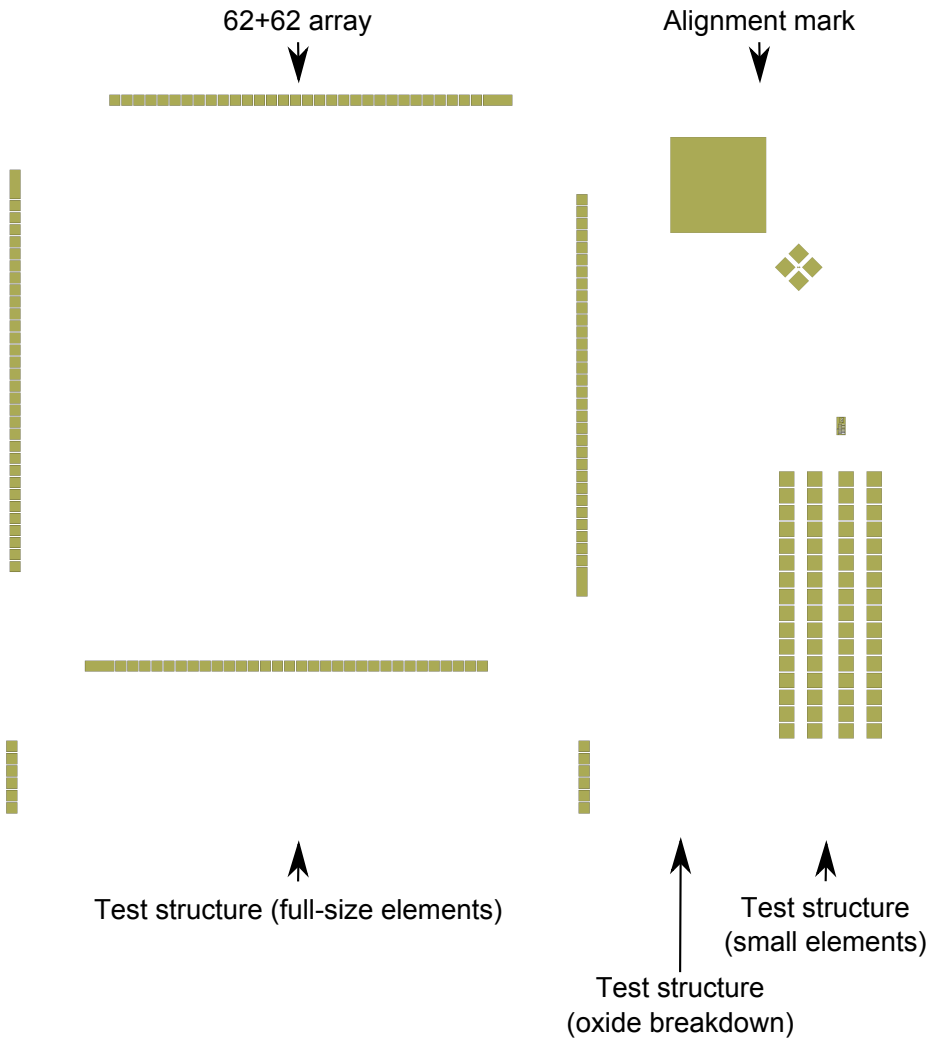

Objects are not to scale

B.6 Mask 5: Top Electrodes

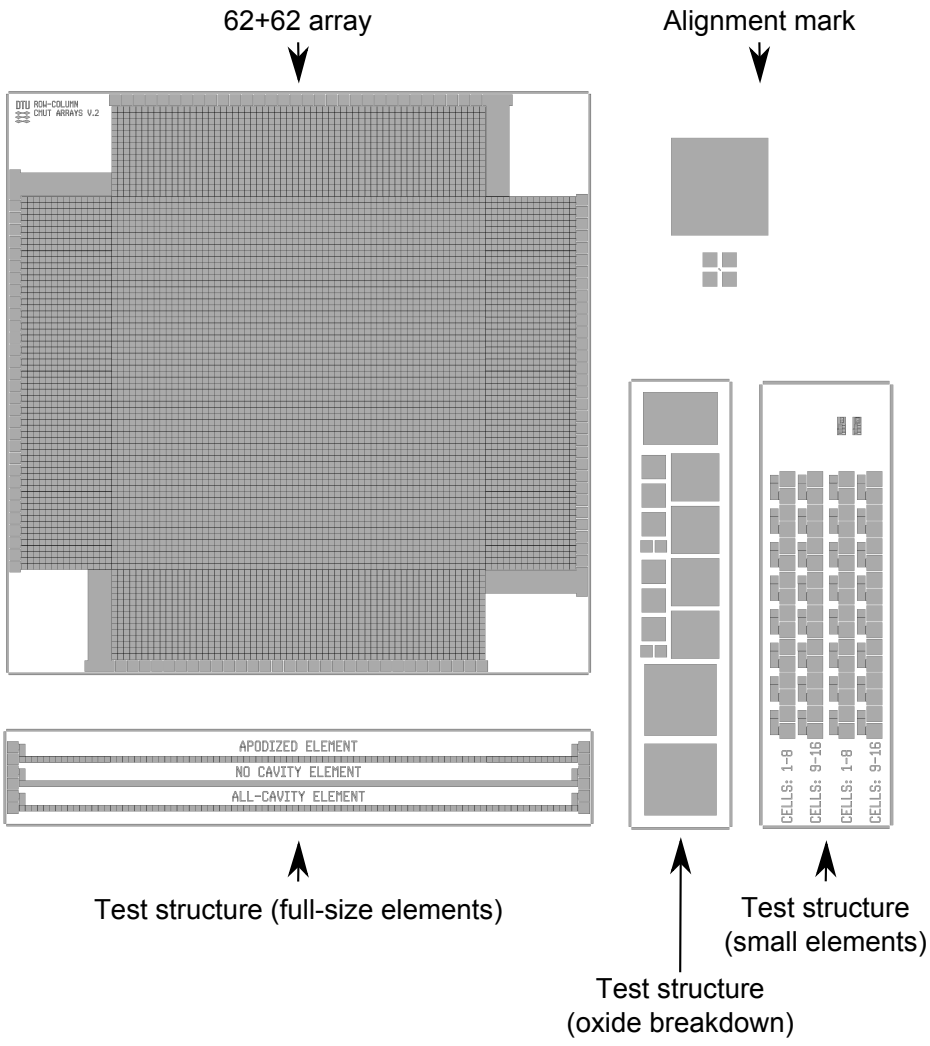

Objects are not to scale

MASK SET C

3rd Generation Row-Column Masks

Used for: LOCOS fabrication of 2-D row-column CMUT arrays with roll-off apodization.

Array sizes (number of arrays): 62+62 and 4 apodization elements (6).

Test structures: Exposure marks. Oxide breakdown test element with electrodes in different sizes. Test elements with 1-16 cells. Test elements with the same size as the actual line elements: With apodization, without apodization, and without cavities. Area with partially covered, partially exposed cavities.

Description: This mask set was used for the third generation of functioning row-column arrays. The mask set is identical to mask set B, but the size of the cavities and the electrode size has been adjusted slightly to accommodate the LOCOS fabrication process. The mask for the contact pads have been removed, since this fabrication process uses only one thickness of the aluminium layer. Furthermore, the alignment marks have been adjusted to improve alignment through the thin silicon membrane. Finally, a new test structure has been added. The mask set features six arrays with 62+62 elements and four apodization region electrodes. The total size of an array is $26.3\,\mathrm{mm} \times 26.3\,\mathrm{mm}$. The mask set was used for fabrication of the row-column probe.

Parameter	Value	Unit
Array		
Element pitch	270	µm
Element width	267.5	µm
CMUT cell		
Cell side length on mask (square)	56	µm
Distance between cells on mask	7	µm
Max. number of cells along element width	4	-

C.1 Mask Overview

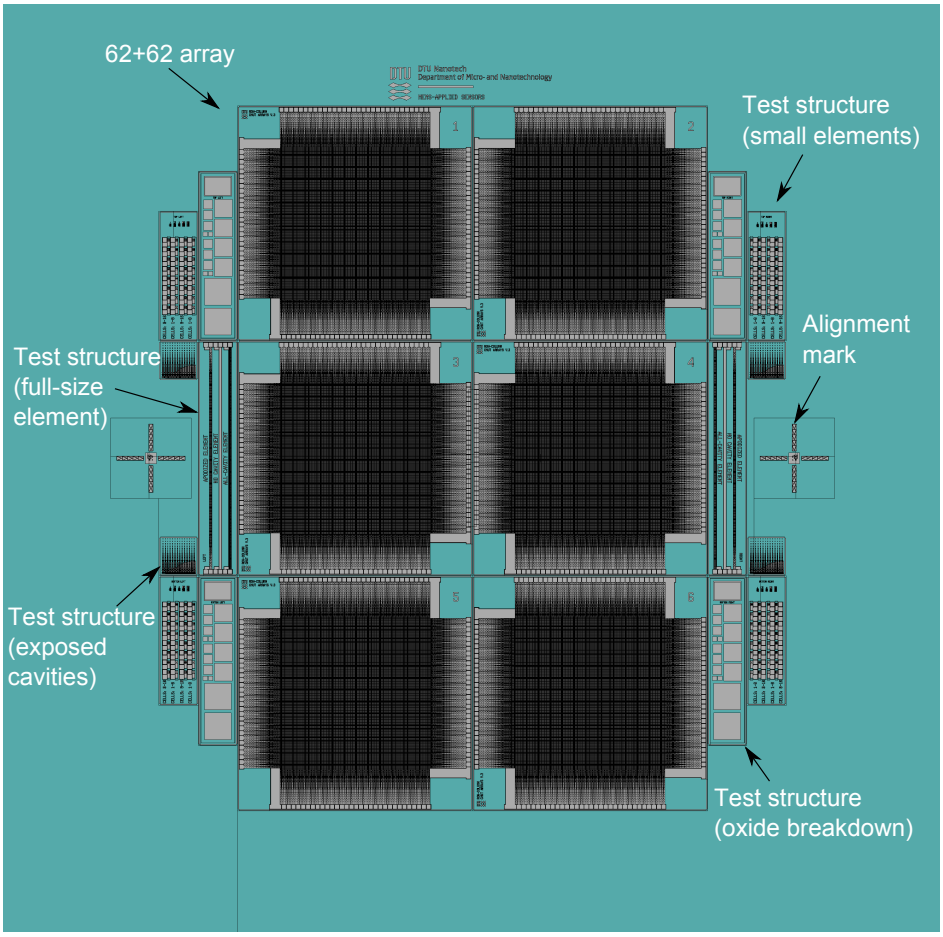

C.2 Mask 1: Cavities

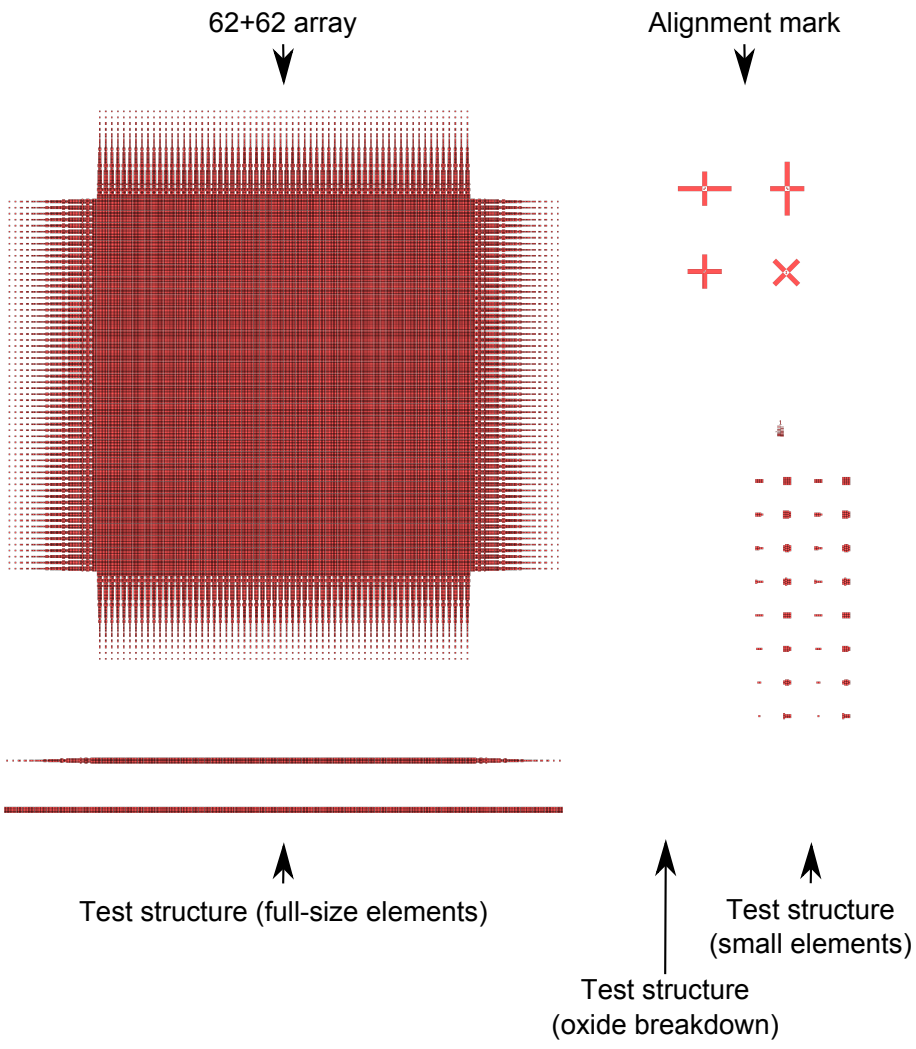

C.3 Mask 2: Bottom Electrodes

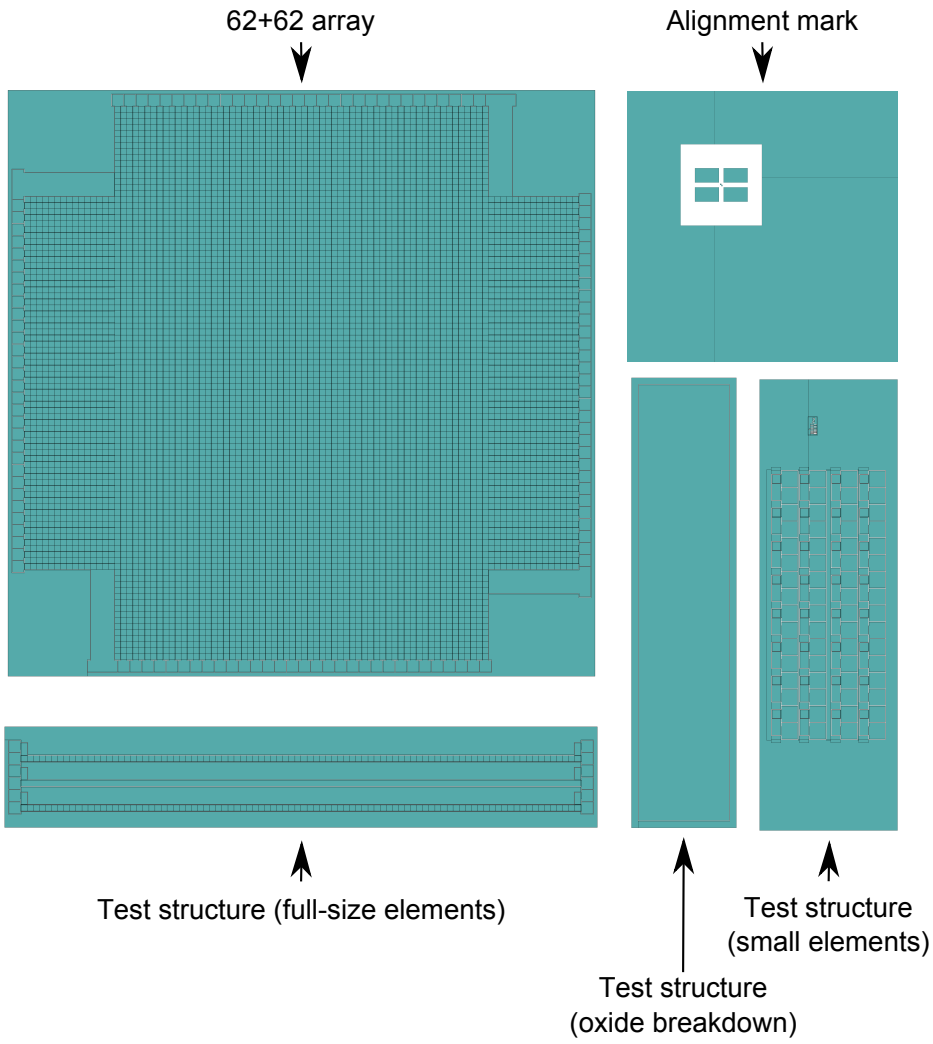

Objects are not to scale

C.4 Mask 3: Access to Bottom Electrode

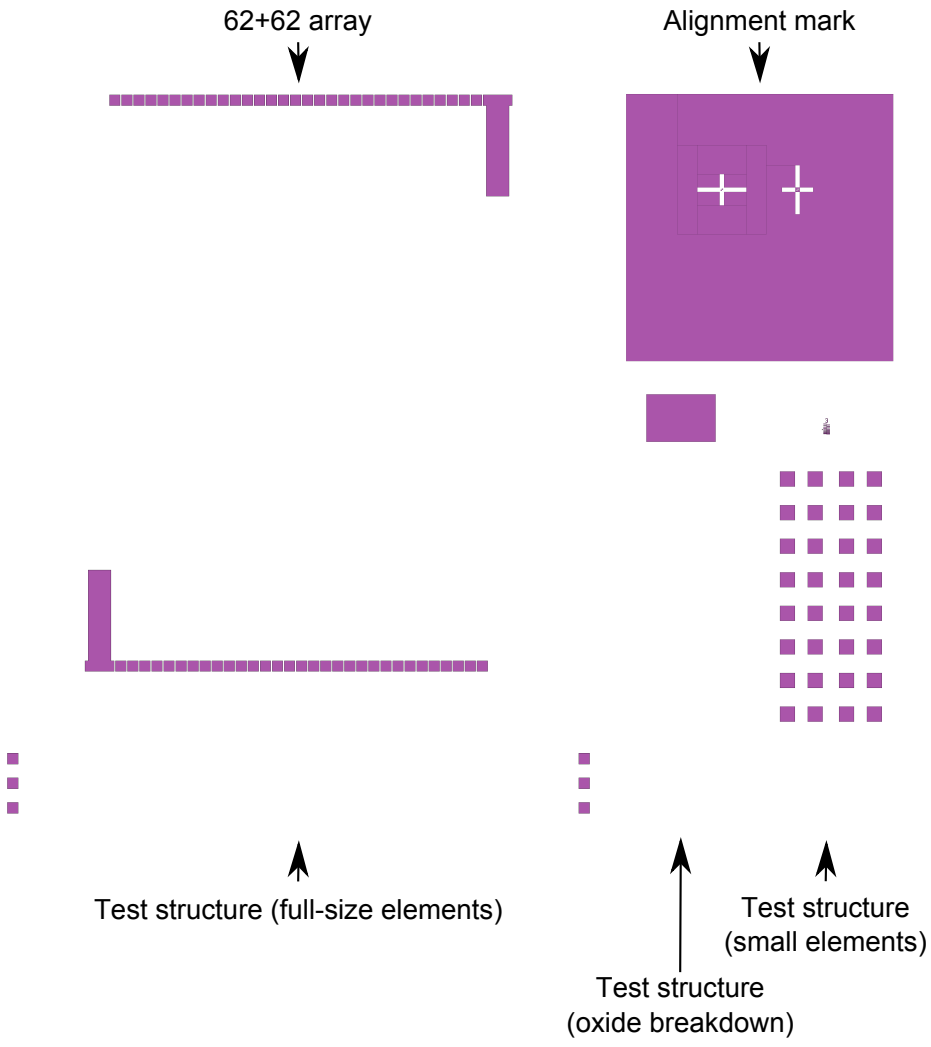

Objects are not to scale

C.5 Mask 4: Top Electrodes

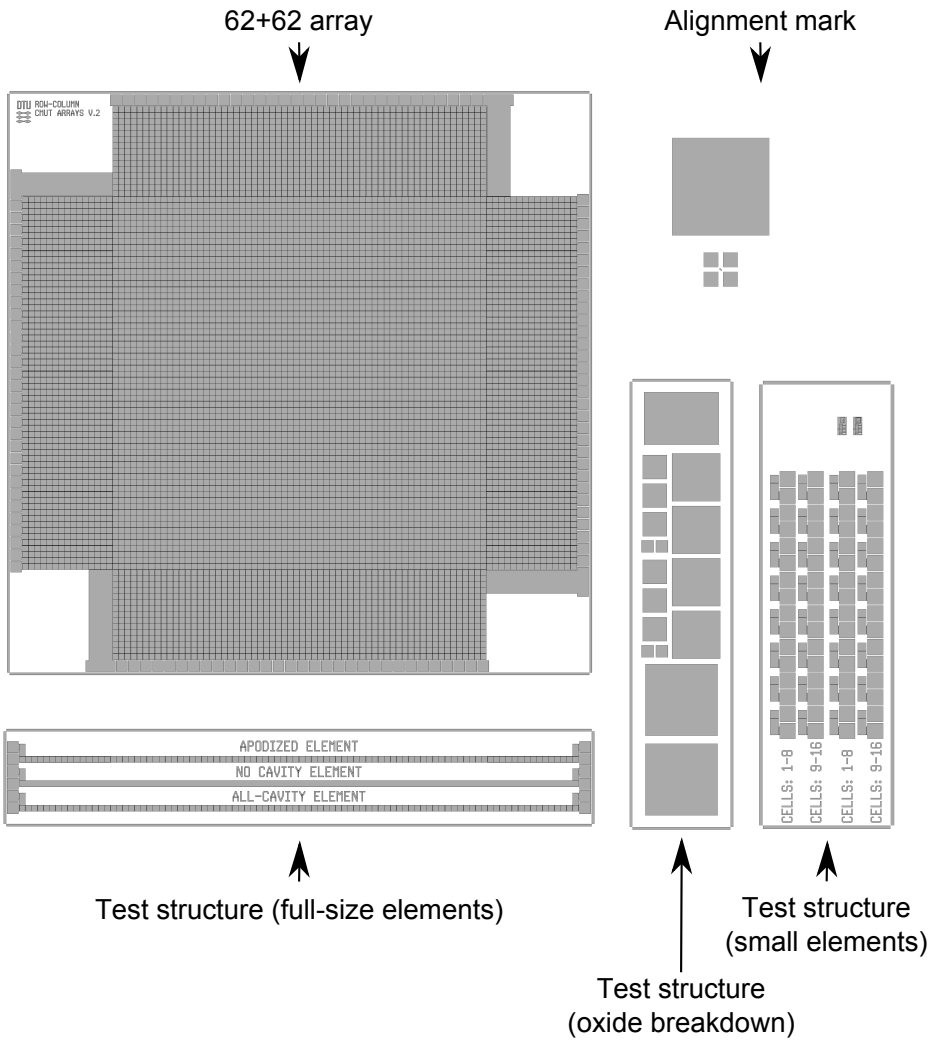

Objects are not to scale

Papers

PAPER A

Modelling of CMUTs with Anisotropic Plates

Authors: Mette Funding la Cour, **Thomas Lehrmann Christiansen**, Jørgen Arendt Jensen, and Erik Vilain Thomsen.

Published in: Proceedings of the IEEE International Ultrasonics Symposium, pp. 588-591, 2012

Abstract

Traditionally, CMUTs are modelled using the isotropic plate equation and this leads to deviations between analytical calculations and FEM simulations. In this paper, the deflection profile and material parameters are calculated using the anisotropic plate equation. It is shown that the anisotropic cal- culations match perfectly with FEM while an isotropic approach causes up to 10% deviations in deflection profile. Furthermore, we show how commonly used analytic modelling methods such as static calculations of the pull-in voltage and dynamic modelling through an equivalent circuit representation can be adjusted to include the correct anisotropic behaviour by using an effective flexural rigidity. The anisotropic caluclations are also compared to experimental data from actual CMUTs showing an error of maximum 3%.

Modelling of CMUTs with Anisotropic Plates

Mette Funding la Cour*†, Thomas Lehrmann Christiansen†, Jørgen Arendt Jensen* and Erik V. Thomsen†
*Center for Fast Ultrasound Imaging, Department of Electrical Engineering, Technical University of Denmark, DK-2800 Kgs. Lyngby, Denmark
†Department of Micro and Nanotechnology, Technical University of Denmark, DK-2800 Kgs. Lyngby, Denmark

***Abstract*—Traditionally, CMUTs are modelled using the isotropic plate equation and this leads to deviations between analytical calculations and FEM simulations. In this paper, the deflection profile and material parameters are calculated using the anisotropic plate equation. It is shown that the anisotropic calculations match perfectly with FEM while an isotropic approach causes up to 10% deviations in deflection profile. Furthermore, we show how commonly used analytic modelling methods such as static calculations of the pull-in voltage and dynamic modelling through an equivalent circuit representation can be adjusted to include the correct anisotropic behaviour by using an effective flexural rigidity. The anisotropic caluclations are also compared to experimental data from actual CMUTs showing an error of maximum 3%.**

I. Introduction

Capacitive micromachined ultrasonic transducers (CMUT) are a promising alternative to piezoelectric transducers and receive considerable attention due to their advantages such as wider bandwidth, higher sensitivity, ease of array fabrication and integration [1], [2]. Analytical and finite element calculations are important for efficient design of CMUTs and much has been put into modelling the behavior of the CMUT using mostly lumped element calculations [1] or finite element modelling [3]. Currently, the analytical approach to modelling the CMUT is based on the isotropic plate equation from which the deflection profile $w(x, y)$ can be obtained.

With the fusion bonding fabrication technology [4], the plate usually consists of crystalline silicon which is an anisotropic material. This leads to differences between analytical deflection profiles calculated with the isotropic plate equation and deflection profiles calculated by finite element programs that uses the correct anisotropic approach.

In this paper, the performance of CMUTs will be analytically calculated using the correct anisotropic approach. Utilising the anisotropic plate equation with fixed boundary conditions, the exact solution for the deflection profile can be obtained. The anisotropic solution is compared to the isotropic solution and FEM simulations. By combining the isotropic and anisotropic deflection profiles an effective flexural rigidity can be found. Using this, the pull in condition is found for a generalised case through energy considerations and the resonance frequency is found by lumped element modelling and compared to measurements. The objective is thus to show that using the anisotropic plate equation gives results matching FEM simulations and to demonstrate how this can easily be implemented into commonly used methods for calculating the performance of CMUTs.

II. The isotropic plate equation

In some cases, the CMUT devices have a thin plate made of an isotropic material, such as silicon nitride, and the static deflection profile, $w(x, y)$, is calculated by solving the isotropic plate equation [5]

$$\frac{\partial^4 w}{\partial x^4} + 2\frac{\partial^4 w}{\partial x^2 \partial y^2} + \frac{\partial^4 w}{\partial y^4} = \frac{p}{D_{\mathrm{i}}} \tag{1}$$

where p is the applied pressure difference across the plate and the flexural rigidity is given by

$$D_{\mathrm{i}} = \frac{E}{12\left(1-\nu^2\right)} h^3 \tag{2}$$

where E is the Young's modulus, ν is the Poisson's ratio, and h is the thickness of the plate. The plate equation is then solved using appropriate boundary conditions.

The plate material, however, is not always isotropic. Crystalline silicon is an anisotropic material with a diamond cubic crystal structure. For plates made on silicon (111) substrates, Young's modulus and Poisson's ratio are constant and the isotropic plate equation can be used. However, for other silicon substrates, such as silicon (001) and silicon (011), Young's modulus and Poisson's ratio are strongly anisotropic, and (1) and (2) are therefore no longer valid.

III. The anisotropic plate equation

The differential equation for the deflection, $w(x, y)$, of a thin, anisotropic plate exposed to a uniform load p is [6]

$$\frac{\partial^4 w}{\partial x^4} + k_1\frac{\partial^4 w}{\partial x^3 \partial y} + k_2\frac{\partial^4 w}{\partial x^2 \partial y^2} + k_3\frac{\partial^4 w}{\partial x \partial y^3} + k_4\frac{\partial^4 w}{\partial y^4} = \frac{p}{D_{\mathrm{h}}} \tag{3}$$

where

$$\begin{gathered} k_1 = \tfrac{4\hat{c}_{16}}{\hat{c}_{11}} \quad k_2 = \tfrac{2(\hat{c}_{12}+2\hat{c}_{66})}{\hat{c}_{11}} \quad k_3 = \tfrac{4\hat{c}_{26}}{\hat{c}_{11}} \\ k_4 = \tfrac{\hat{c}_{22}}{\hat{c}_{11}} \quad D_{\mathrm{h}} = \tfrac{1}{12} h^3 \hat{c}_{11} \end{gathered} \tag{4}$$

and $\hat{c}_{pq}$ are the elements of the reduced stiffness tensor in the plate coordinate system (using the engineering strain convention) given by [6]

$$\hat{c}_{pq} = c'_{pq} - \frac{c'_{p3}c'_{3q}}{c'_{33}} \tag{5}$$

Here, c'_{ij} are the elements of the stiffness tensor in the plate coordinate system.

By aligning the plate coordinate system to the crystallographic coordinate system the expressions in (4) can be

TABLE I
ROOM TEMPERATURE (300K) STIFFNESS COEFFICIENTS FOR CRYSTALLINE SILICON [7].

c_{11}	c_{12}	c_{44}
165.6 GPa	63.9 GPa	79.5 GPa

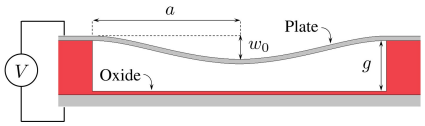

Fig. 1. Cross sectional view of CMUT cell with applied voltage.

expressed through the stiffness coefficients of silicon shown in Table I [7].

For a thin circular plate on a (100) substrate, we obtain

$$k_1 = k_3 = 0 \tag{6}$$

$$k_2 = \frac{2c_{12}}{c_{11}+c_{12}} + \frac{4c_{11}c_{44}}{c_{11}^2 - c_{12}^2} = 2.81 \tag{7}$$

$$k_4 = 1 \tag{8}$$

$$D_\mathrm{h} = \frac{1}{12}\left(c_{11} - \frac{c_{12}^2}{c_{11}}\right)h^3 = 11.75\ \mathrm{GPa}\cdot h^3 \tag{9}$$

The solution to (3) for a circular plate of radius a fixed at the boundary is easily obtained using polar coordinates. The deflection at a point a distance r from the center is given by [5]

$$w(r) = w_0\left(1 - \left(\frac{r}{a}\right)^2\right)^2 \tag{10}$$

This equation is similar to the deflection profile for the isotropic case, however, the center deflections are different

$$w_{0,\mathrm{isotropic}} = \frac{1}{64}\frac{a^4 p}{D_\mathrm{i}} \tag{11}$$

$$w_{0,\mathrm{anisotropic}} = \frac{1}{8\,(3+k_2+3k_4)}\frac{a^4 p}{D_\mathrm{h}} \tag{12}$$

Fig. 1 shows a cross sectional view of a CMUT cell with an applied voltage with parameters shown.

By equating (11) and (12) and isolating D_i it is possible to find an effective flexural rigidity

$$D_\mathrm{eff} = \frac{3+k_2+3k_4}{8}D_\mathrm{h} \tag{13}$$

This can be used to change from the isotropic equation to the anisotropic equation in commonly used analytical models of CMUTs. Examples of this will be shown in the following sections.

Fig. 2 shows the normalised deflection profiles, using (10) to (12), of a CMUT exposed to a pressure difference. Using Young's modulus and Poisson's ratio along the [100] direction (E_{100}=130 GPa, ν_{100}=0.278) gives the solid green curve and using Young's modulus and Poisson's ratio along the [110] direction (E_{110}=169 GPa, ν_{110}=0.062) gives the dashed blue curve. The anisotropic solution is shown as a dotted red curve

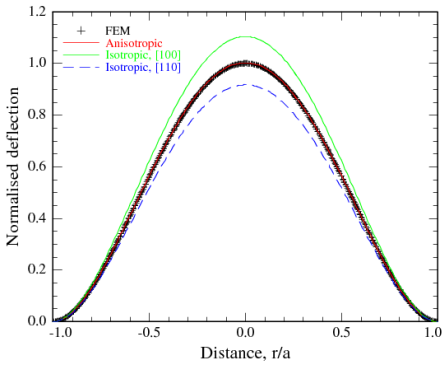

Fig. 2. Normalised deflection profile of a thin circular plate of silicon (001) as calculated by (10), (12), (11) and FEM.The anisotropic profile is on top of the FEM simulations.

and is on top of the FEM simulation shown for comparison. The FEM simulations were performed in COMSOL 4.2a using the full anisotropic stiffness tensor. Excellent agreement between the anisotropic solution and the finite element calculation is seen. The figure also shows that Young's modulus and Poisson's ratio corresponding to [100] or [110] directions leads to errors in the center deflection of around 10%. To reduce this error, it is common practice to use mean values of Young's modulus and Poission's ratio (E_ave=148 GPa, ν_ave=0.177) which decreases the error to around 1.5%. However, using the anisotropic approach gives the exact result. The error between the anisotropic calculation and FEM is less than 0.3%.

IV. ANALYTICAL MODELLING

As mentioned previously, the behavior of CMUTs are in most cases modelled using lumped element analysis or finite element analysis. In the following, an analytical model for CMUTs based on energy and force considerations will be presented. By investigating the energies of the system it is possible to estimate pull-in voltage and distance [8]. This approach also applies when using the anisotropic plate equation and an example will be given in the end of the section.

The total potential energy of the plate, U_t, has three terms

$$U_\mathrm{t} = U_\mathrm{p} + U_\mathrm{e} + U_\mathrm{s} \tag{14}$$

where U_p is the energy associated with pressure, U_e is the electrostatic energy due to the capacitor and U_s is the strain energy stored in the deflected plate. Equation (10) is the solution to the plate equation when a uniform pressure is applied. The electrostatic pressure is not uniform but as observed by [8] it is a very good approximation.

The energy contribution from the pressure difference is calculated as the work performed (i.e. force times length, here pressure times area times length) when deflecting the plate

$$U_\mathrm{p} = -\int_0^a 2\pi p r w dr = -\frac{1}{3}a^2 p\pi w_0 \tag{15}$$

The electrostatic energy for an applied voltage V is given by

$$U_{\mathrm{e}} = -\frac{1}{2} C_{\mathrm{t}} V^2 \tag{16}$$

where the total capacitance C_{t} is given from the capacitance of the plate C_{pl} and of the insulating oxide C_{ox}

The potential energy associated with the plate acting as a spring is given by

$$U_{\mathrm{s}} = \frac{1}{2} D_{\mathrm{eff}} \int_0^a \left(\frac{\partial_r \left(r \partial_r w \right)}{r} \right)^2 2\pi r \, dr = \frac{32 D_{\mathrm{eff}} \pi w_0^2}{3a^2} \tag{17}$$

The flexural rigidity appears in this equation, making it possible to switch between isotropic and anisotropic cases.

By taking the derivative of the total potential energy with respect to the center deflection, the total equivalent force on the center of the plate can be found

$$F_{\mathrm{t}} = -\frac{\partial U_{\mathrm{t}}}{\partial w_0} = \frac{1}{3} a^2 p \pi - \frac{64 D_{\mathrm{eff}} \pi w_0}{3a^2} + \frac{C_0 C_{\mathrm{ox}}^2 \sqrt{g} V^2 \left(\sqrt{g} w_0 + \sqrt{w_0} \left(-g + w_0 \right) \mathrm{ArcTanh} \left[\sqrt{\frac{w_0}{g}} \right] \right)}{4 \left(g - w_0 \right) w_0^2 \left(C_{\mathrm{ox}} + C_0 \sqrt{\frac{g}{w_0}} \mathrm{ArcTanh} \left[\sqrt{\frac{w_0}{g}} \right] \right)^2} \tag{18}$$

where g is the gap distance. The stable position of the plate is found when $F_{\mathrm{t}} = 0$. Thus, this equation can in principle be solved numerically to obtain the center deflection w_0 for a given design (C_0, g, a, D_{eff}) and operating conditions (V and p).

V. Pull in voltage

To simplify the calculation, we normalise by using the following expressions

$$x_{00} = \frac{p a^4}{64 g D_{\mathrm{eff}}}, x_0 = \frac{g}{w_0}, k_{\mathrm{ox}} = \frac{C_0}{C_{\mathrm{ox}}} \quad , V_{\mathrm{A}}^2 = V^2 \frac{3a^2 C_0}{256 D_{\mathrm{eff}} g^2 \pi} \tag{19}$$

x_{00} is the normalised deflection due to the external pressure, x_0 is the normalised center deflection, k_{ox} is the ratio of capacitances at zero voltage and V_{A} is the normalised applied voltage. This way (18) becomes

$$F_{\mathrm{tn}} = -x_0 + x_{00} - \frac{V_{\mathrm{A}}^2 \left(\sqrt{x_0} + \left(-1 + x_0 \right) \mathrm{ArcTanh} \left[\sqrt{x_0} \right] \right)}{\left(-1 + x_0 \right) \sqrt{x_0} \left(\sqrt{x_0} + k_{\mathrm{ox}} \mathrm{ArcTanh} \left[\sqrt{x_0} \right] \right)^2} \tag{20}$$

The pull in voltage V_{PI} and the pull in point x_{PI} of the CMUT cell can be found from the expression of the force as $\partial F_{\mathrm{tn}} / \partial x_0 = 0$ and $F_{\mathrm{tn}} = 0$ apply. By isolating V_{A} in the first equation and substituting this result into the second, x_{PI} can be obtained and then afterwards V_{PI}.

For the special case where both the oxide thickness and the applied pressure is zero, the pull in distance becomes $x_{\mathrm{PI}} = 0.46$. For a parallel plate capacitor, this distance is $x_{\mathrm{PI,parallel}} = 1/3$. With the corrected pull in distance, the pull in voltage becomes

$$V_{\mathrm{PI}} = \sqrt{\frac{89.4459 D_{\mathrm{eff}} g^2}{a^2 C_0}} \tag{21}$$

TABLE II
Pull in Voltages and resonance frequencies for the special case of zero applied pressure and zero oxide thickness.

	V_{PI}	ω_0 (0 V)
Anisotropic	179 V	9.6 MHz
Isotropic [001]	172 V	9.1 MHz
Isotropic [011]	188 V	10.0 MHZ
Isotropic average	179 V	9.5 MHz

To compare calculations using the isotropic and anisotropic approaches, the pull in voltage for the special case (21) is found and shown in Table II. The calculation is performed with $a = 20$ μm, $h = 1$ μm and $g = 0.5$ μm. A difference of more than 10 V is observed so using different parameters for the calculations can make a considerable difference in the expected pull in voltage. Using the average values for Young's modulus and Poisson's ratio gives a result close to the correct anisotropic result.

VI. Resonance frequency

When modelling the dynamic behaviour of transducers, such as CMUTs, it is common practice to set up a lumped parameter equivalent circuit representation [9], [10], [11], [1]. Using the center displacement of the CMUT plate, w_0, and the equivalent charge on the plate, Q, as state variables, the state equations of the system are given by (18) and the three relations $V = Q/C_{\mathrm{t}}$, $i = dQ/dt$ and $v = dw_0/dt$. The system can then be linearized around a bias point $(w_{0,\mathrm{b}}, Q_{\mathrm{b}})$ by using the Jacobian of the system [11], [9], [10]

$$\begin{bmatrix} dV \\ dF_{\mathrm{t}} \end{bmatrix} = \begin{bmatrix} \frac{\partial V}{\partial Q}\Big|_{w_{0,\mathrm{b}}, Q_{\mathrm{b}}} & \frac{\partial V}{\partial w_0}\Big|_{w_{0,\mathrm{b}}, Q_{\mathrm{b}}} \\ \frac{\partial F_{\mathrm{t}}}{\partial Q}\Big|_{w_{0,\mathrm{b}}, Q_{\mathrm{b}}} & \frac{\partial F_{\mathrm{t}}}{\partial w_0}\Big|_{w_{0,\mathrm{b}}, Q_{\mathrm{b}}} \end{bmatrix} \begin{bmatrix} dQ \\ dw_0 \end{bmatrix} \tag{22}$$

The linearized system can then be transformed into the complex frequency domain by Lapace transform. Denoting the matrix in (22) as A, we get the following in the frequency domain

$$\begin{bmatrix} dV \\ dF_{\mathrm{t}} \end{bmatrix} = A \begin{bmatrix} dQ \\ dw_0 \end{bmatrix} = A \begin{bmatrix} \frac{1}{s} di \\ \frac{1}{s} dv \end{bmatrix} = B \begin{bmatrix} di \\ dv \end{bmatrix} \tag{23}$$

The lumped system components, the transformer factor and the coupling coefficient of the transducer can then easily be extracted from the matrix B [11]. The effective mass of the plate is attached to the terminals of the mechanical domain to complete the equivalent circuit as shown in Fig. 3, where k^* is the spring constant including spring softening. The effective mass is found through the relation $m_{\mathrm{eff}} = k_{\mathrm{eff}} / \omega_0^2$, where $k_{\mathrm{eff}} = \partial^2 U_{\mathrm{s}} / \partial w_0^2$ and ω_0 is the fundamental resonance frequency of the plate. The effect on the resonance frequency of using different flexural rigidities is demonstrated in Table II. Note that the velocity of the system in this calculation is

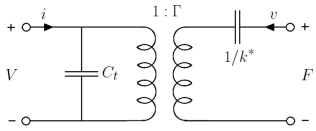

Fig. 3. Equivalent circuit diagram for a CMUT.

the velocity of the center of the plate. For correct coupling to the acoustic domain, a second transformer relation should be added to the equivalent circuit [9], [10]. Only the coupling between the electric and the mechanical domain is shown here for simplicity.

In such an equivalent circuit, the full anisotropic behaviour of the silicon plate is described by simply using the effective flexural rigidity as given in (13). This demonstrates that existing CMUT models can easily be accommodated to include the actual behaviour of single crystalline silicon plates.

VII. Comparison with measurements

To see how well the analytical model describes the behavior of CMUTs, measurements have been performed on fabricated devices. The impedance was measured with a HP 8752A network analyzer for varying bias voltages and the resonance frequency was found from the phase. The measurements were performed on two types of devices, half of them meant for phased array imaging with a frequency of 2.6 MHz ($a = 24.5\ \mu$m, $h = 1.5\ \mu$m, $g = 0.37\ \mu$m and $t_{\text{ox}} = 0.21\ \mu$m) and the others for linear array imaging with a frequency of 5 MHz ($a = 24.5\ \mu$m, $h = 1.77\ \mu$m, $g = 0.29\ \mu$m and $t_{\text{ox}} = 0.21\ \mu$m). Fig. 4 shows the resonance frequency as a function of applied voltage calculated for our two types of devices (red and green curve, circles). The corresponding analytical calculations are shown for comparison (blue and black curves, diamonds). Phased array device has solid curves and linear array device has dashed curves. The model is seen to match well with the measurements. The calculated values for the linear array device (dashed curves) has an average deviation from the measurements of $3\% \pm 0.7$ while for the phased array device (solid curves) it is only $2\% \pm 0.4$. The deviation can be explained by the metal electrode layer on top of the membrane causing a change in effective mass and flexural rigidity which is not included in the analytical calculations.

VIII. Conclusion

We have here demonstrated how wafer bonded CMUTs can be analytically modelled using the full anisotropic properties of single crystalline silicon. Using this approach, the analytic plate deflection profile shows excellent correspondence with FEM calculations. We have used a circular CMUT as an example to show how the anisotropic behaviour is easily incorporated into both static modelling of the pull-in voltage and dynamic equivalent circuit modelling by simply introducing an effective flexural rigidity. Using the anisotropic equivalent

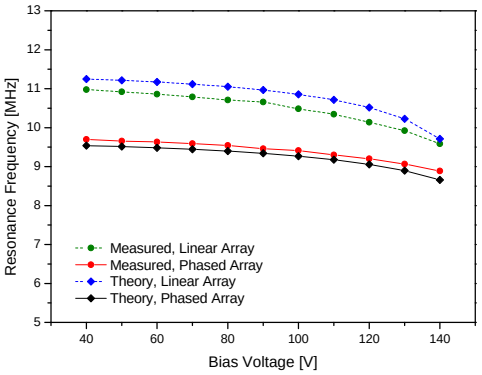

Fig. 4. Resonance frequency vs. applied voltage for measurement on two different devices and corresponding analytical curves.

circuit model, the resonance frequency as a function of bias voltage has been compared to measurements on wafer bonded CMUTs in order to evaluate the accuracy of the model.

References

[1] I. Ladabaum, X. Jin, H. T. Soh, A. Atalar, and B. t. Khuri-Yakub, "Surface micromachined capacitive ultrasonic transducers," *IEEE Transactions on Ultrasonics, Ferroelectrics and Frequency Control*, vol. 45, no. 3, pp. 678–690, May 1998.

[2] O. Oralkan, A. Ergun, J. Johnson, M. Karaman, U. Demirci, K. Kaviani, T. Lee, and B. Khuri-Yakub, "Capacitive micromachined ultrasonic transducers: next-generation arrays for acoustic imaging?" *IEEE Transactions on Ultrasonics, Ferroelectrics and Frequency Control*, vol. 49, no. 11, pp. 1596 –1610, Nov. 2002.

[3] A. Lohfink, P.-C. Eccardt, W. Benecke, and H. Meixner, "Derivation of a 1D CMUT model from FEM results for linear and nonlinear equivalent circuit simulation," in *2003 IEEE Symposium on Ultrasonics*, vol. 1, Oct. 2003, pp. 465 – 468 Vol.1.

[4] Y. Huang, A. Ergun, E. Haeggstrom, M. Badi, and B. Khuri-Yakub, "Fabricating capacitive micromachined ultrasonic transducers with wafer-bonding technology," *Journal of Microelectromechanical Systems*, vol. 12, no. 2, pp. 128 – 137, Apr. 2003.

[5] S. Timoshenko and S. Woinowsky-Krieger, *Theory of Plates and Shells,*, 2nd ed. Mcgraw-Hill College, Jun. 1959.

[6] S. Holgate, "The transverse flexure of perforated aeolotropic plates," *Proceedings of the Royal Society A: Mathematical, Physical and Engineering Sciences*, vol. 185, no. 1000, pp. 50–69, Jan. 1946. [Online]. Available: http://adsabs.harvard.edu/abs/1946RSPSA.185...50H

[7] J. J. Hall, "Electronic effects in the elastic constants of n-type silicon," *Physical Review*, vol. 161, no. 3, pp. 756–761, Sep. 1967. [Online]. Available: http://link.aps.org/doi/10.1103/PhysRev.161.756

[8] H. Koymen, A. Atalar, E. Aydogdu, C. Kocabas, H. Oguz, S. Olcum, A. Ozgurluk, and A. Unlugedik, "An improved lumped element nonlinear circuit model for a circular CMUT cell," *IEEE transactions on ultrasonics, ferroelectrics, and frequency control*, vol. 59, no. 8, pp. 1791–1799, Aug. 2012, PMID: 22899125. [Online]. Available: http://www.ncbi.nlm.nih.gov/pubmed/22899125

[9] H. A. C. Tilmans, "Equivalent circuit representation of electromechanical transducers: I. lumped-parameter systems," *Journal of Micromechanics and Microengineering*, vol. 6, no. 1, pp. 157–176, Mar. 1996. [Online]. Available: http://iopscience.iop.org/0960-1317/6/1/036

[10] ——, "Equivalent circuit representation of electromechanical transducers: II. distributed-parameter systems," *Journal of Micromechanics and Microengineering*, vol. 7, no. 4, pp. 285–309, Dec. 1997. [Online]. Available: http://iopscience.iop.org/0960-1317/7/4/005

[11] S. D. Senturia, *Microsystem Design*. Springer, Nov. 2000.

PAPER B

Modeling and Measurements of CMUTs with Square Anisotropic Plates

Authors: Mette Funding la Cour, **Thomas Lehrmann Christiansen**, Christian Dahl-Petersen, Kasper Reck, Ole Hansen, Jørgen Arendt Jensen, and Erik Vilain Thomsen.

Published in: Proceedings of the IEEE International Ultrasonics Symposium, pp. 2187-2190, 2013

Abstract

The conventional method of modeling CMUTs use the isotropic plate equation to calculate the deflection, leading to deviations from FEM simulations including anisotropic effects of around 10 % in center deflection. In this paper, the deflection is found for square plates using the full anisotropic plate equation and the Galerkin method. Utilizing the symmetry of the silicon crystal, a compact and accurate expression for the deflection can be obtained. The deviation from FEM in center deflection is <0.1 %. The deflection was measured on fabricated CMUTs using a white light interferometer. Fitting the anisotropic calculated deflection to the measurement a deviation of 0.5-1.5 % is seen for the fitted values. Finally it was also measured how the device behaved under increasing bias voltage and it is observed that the model including anisotropic effects is within the uncertainty interval of the measurements.

Modeling and Measurements of CMUTs with Square Anisotropic Plates

Mette Funding la Cour*†, Thomas Lehrmann Christiansen†, Christian Dahl-Petersen†, Kasper Reck†, Ole Hansen†, Jørgen Arendt Jensen* and Erik Vilain Thomsen†

*Center for Fast Ultrasound Imaging, Department of Electrical Engineering, Technical University of Denmark, DK-2800 Kgs. Lyngby, Denmark

†Department of Micro and Nanotechnology, Technical University of Denmark, DK-2800 Kgs. Lyngby, Denmark

***Abstract*—The conventional method of modeling CMUTs use the isotropic plate equation to calculate the deflection, leading to deviations from FEM simulations including anisotropic effects of around 10% in center deflection. In this paper, the deflection is found for square plates using the full anisotropic plate equation and the Galerkin method. Utilizing the symmetry of the silicon crystal, a compact and accurate expression for the deflection can be obtained. The deviation from FEM in center deflection is <0.1%. The deflection was measured on fabricated CMUTs using a white light interferometer. Fitting the anisotropic calculated deflection to the measurement a deviation of 0.5-1.5% is seen for the fitted values. Finally it was also measured how the device behaved under increasing bias voltage and it is observed that the model including anisotropic effects is within the uncertainty interval of the measurements.**

I. Introduction

Precise modeling of capacitive micromachined ultrasonic transducers (CMUT) is important for an efficient design process. The deflection $w(x,y)$ is an important parameter that influences several basic CMUT parameters such as pull-in voltage and capacitance. Most existing analytical approaches use the isotropic plate equation to calculate the deflection [1], [2]. However, when using fusion bonding fabrication technology the plate usually consists of crystalline silicon, which is an anisotropic material. The isotropic approach is then invalidated and this results in deviations in the deflection compared to finite element modeling (FEM) and measurements. Therefore, to get precise modeling of these CMUTs the anisotropy of silicon needs to be taken into account.

For circular plates a simple and exact solution for the deflection exists, but this is not the case for square plates. Existing solutions for the deflection of square plates is based on series expansions with either trigonometric [3] or polynomial basis functions [4]. None of these, however, take the anisotropy of the plate into account.

Previously a model was made for calculating the deflection for an anisotropic plate with circular geometry [5], and in this paper the model is expanded to include square plates as well. The approach used to solve the full anisotropic plate equation is the Galerkin method [6]. Utilizing the symmetry of the silicon crystal, a compact and accurate approximation of the deflection can be obtained. The calculated deflection is compared to the solution for corresponding isotropic cases, a finite element model (FEM) and measurements performed on fabricated devices. Furthermore, the calculated deflection is used to find the stable position of the CMUT plate for a given bias voltage. Equivalent measurements are performed as well and the theory is compared to these.

II. The isotropic plate equation

Conventionally the deflection $w(x,y)$ of a CMUT with a thin plate is modeled using the isotropic plate equation [3]

$$\frac{\partial^4 w}{\partial x^4} + 2\frac{\partial^4 w}{\partial x^2 \partial y^2} + \frac{\partial^4 w}{\partial y^4} = \frac{p}{D_\mathrm{i}}, \tag{1}$$

where p is the applied pressure difference across the plate. The flexural rigidity is given by

$$D_\mathrm{i} = \frac{E}{12\left(1-\nu^2\right)} h^3 \tag{2}$$

with E being Young's modulus, ν being Poisson's ratio, and h being the thickness of the plate. For clamped rectangular and square plates no simple exact solution exists to this equation and approximate methods have to be used. The traditional isotropic approach is based on a series expansion of the deflection and the center deflection for a thin clamped square plate having side length $2L$ is [3]

$$w_{0,\mathrm{isotropic}} = 0.020245 \frac{L^4 p}{D_\mathrm{i}}. \tag{3}$$

However, the plate material is often not isotropic and (1) and (2) are therefore no longer valid. Using the fusion bonding fabrication technique the plate usually consist of silicon which is an anisotropic material with a diamond cubic crystal structure. Having a silicon (001) substrate, which are most often used, Young's modulus and Poisson's ratio are strongly anisotropic, and this leads to inaccurate deflection expressions.

III. Anisotropic plate equation

To be able to take the anisotropy of the plate into account and avoid the inaccuracy from isotropic modeling, the stiffness of the plate needs to be described through the stiffness matrix of the material instead of Young's modulus and Poisson's ratio. The starting point is the relation between stress and strain [7]

$$\boldsymbol{\sigma}^\mathrm{c} = \mathbf{c}^\mathrm{c}\boldsymbol{\varepsilon}^\mathrm{c}, \text{ or } \boldsymbol{\varepsilon}^\mathrm{c} = \mathbf{s}^\mathrm{c}\boldsymbol{\sigma}^\mathrm{c}. \tag{4}$$

Here superscript c denotes the crystallographic coordinate system, so $\mathbf{c}^\mathrm{c}$ is the stiffness matrix and $\mathbf{s}^\mathrm{c} = (\mathbf{c}^\mathrm{c})^{-1}$ the compliance matrix in this coordinate system. Having a thin plate the stresses in the z direction can be ignored and plane

TABLE I. ROOM TEMPERATURE (300K) COMPLIANCE COEFFICIENTS FOR LOW DOPED N-TYPE CRYSTALLINE SILICON [8].

s^c_{11}	s^c_{12}	s^c_{44}
7.69×10^{-12} Pa^{-1}	-2.14×10^{-12} Pa^{-1}	12.58×10^{-12} Pa^{-1}

stress assumed. The relation between strain and stress then becomes

$$\begin{pmatrix}\varepsilon_1\\ \varepsilon_2\\ \varepsilon_6\end{pmatrix}=\begin{pmatrix}s_{11}&s_{12}&s_{16}\\ s_{12}&s_{22}&s_{26}\\ s_{16}&s_{26}&s_{66}\end{pmatrix}\begin{pmatrix}\sigma_1\\ \sigma_2\\ \sigma_6\end{pmatrix}=\mathbf{S}_{\text{eff}}\begin{pmatrix}\sigma_1\\ \sigma_2\\ \sigma_6\end{pmatrix} \quad (5)$$

and we can define an effective stiffness matrix, $\mathbf{C}_{\text{eff}}=(\mathbf{S}_{\text{eff}})^{-1}$. For silicon the effective compliance matrix becomes

$$\mathbf{S}^c_{\text{eff}}=\begin{pmatrix}s^c_{11}&s^c_{12}&0\\ s^c_{12}&s^c_{11}&0\\ 0&0&s^c_{44}\end{pmatrix}. \quad (6)$$

The compliance elements in this matrix are known from measurements and shown in Table I [8]. It is noted that the elements in (6) are known in the crystallographic coordinate system. An equation describing plate deflection on the other hand is valid in the plate coordinate system which is not necessarily the same. To illustrate this further the crystallographic and the plate coordinate systems can be seen in Fig. 1. The solid coordinate system aligned to the $\langle100\rangle$ directions is where the compliance values for silicon are known and the dashed system shows the rotated coordinate system for the plate where the compliance values needs to be calculated. Having silicon as plate material and performing standard cleanroom fabrication, the plate will usually be on a (001) substrate and aligned to the primary wafer flat. Flat alignment is to the $\langle110\rangle$ direction and the plate coordinate system will be rotated $\psi=45^\circ$ and a transformation of the compliance matrix between the two coordinate systems is needed. The resulting effective stiffness matrix for the present case becomes (taking the inverse of the transformed compliance matrix) [9]

$$C^{\text{eff}}_{\text{Si(001),[110]}}=\begin{pmatrix}\frac{1}{s^c_{44}}+\frac{1}{2(s^c_{11}+s^c_{12})}&\frac{1}{2(s^c_{11}+s^c_{12})}-\frac{1}{s^c_{44}}&0\\ \frac{1}{2(s^c_{11}+s^c_{12})}-\frac{1}{s^c_{44}}&\frac{1}{s^c_{44}}+\frac{1}{2(s^c_{11}+s^c_{12})}&0\\ 0&0&\frac{1}{2s^c_{11}-2s^c_{12}}\end{pmatrix}. \quad (7)$$

It is seen that the stiffness matrix now has an orthotropic symmetry.

Now having the effective stiffness matrix the generalized plate equation can be used. This is a differential equation for the deflection, $w(x,y)$, of a thin anisotropic plate exposed to a uniform load p given by [10], [9]

$$\frac{\partial^4 w}{\partial x^4}+k_1\frac{\partial^4 w}{\partial x^3\partial y}+k_2\frac{\partial^4 w}{\partial x^2\partial y^2}+k_3\frac{\partial^4 w}{\partial x\partial y^3}+k_4\frac{\partial^4 w}{\partial y^4}=\frac{p}{D_{\text{a}}}. \quad (8)$$

The plate coefficients k_1-k_4 and the anisotropic flexural rigidity, D_{a}, depend on the elastic constants of the plate material

$$k_1=\frac{4C^{\text{eff}}_{13}}{C^{\text{eff}}_{11}}\quad k_2=\frac{2\left(C^{\text{eff}}_{12}+2C^{\text{eff}}_{33}\right)}{C^{\text{eff}}_{11}}\quad k_3=\frac{4C^{\text{eff}}_{23}}{C^{\text{eff}}_{11}}$$
$$k_4=\frac{C^{\text{eff}}_{22}}{C^{\text{eff}}_{11}}\quad D_{\text{a}}=\tfrac{1}{12}h^3C^{\text{eff}}_{11} \quad (9)$$

where C^{eff}_{pq} are elements in the effective stiffness matrix. Notice that the stiffness of the plate is no longer expressed through Young's modulus and Poisson's ratio but directly through the stiffness values.

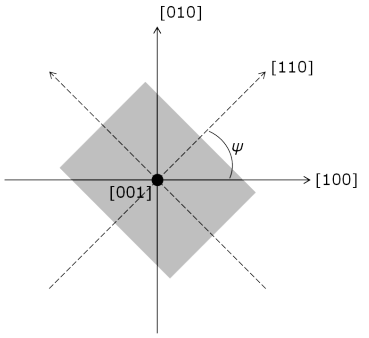

Fig. 1. The two coordinate systems, solid lines are the crystallographic system aligned to the $\langle100\rangle$ direction and the dashed lines the plate system aligned to the $\langle110\rangle$ direction.

TABLE II. SELECTED VALUES FOR THE PLATE COEFFICIENTS AND ANISOTROPIC FLEXURAL RIGIDITY FOR PLATES ON A SILICON (001) SUBSTRATE [9].

Orientation	ψ	k_1	k_2	k_3	k_4	$12D_a/h^3$[GPa]
[100]	0	0	2.8133	0	1	140.96
[110]	$\pi/4$	0	1.3241	0	1	169.62

Using the compliance values for silicon in Table I and inserting the stiffness elements in (7) into (9) it follows that $k_1=k_3=0$ and $k_4=1$. Thus, aligning the plate to the primary flat simplifies the anisotropic plate equation (8) to

$$\frac{\partial^4 w}{\partial x^4}+k_2\frac{\partial^4 w}{\partial x^2\partial y^2}+\frac{\partial^4 w}{\partial y^4}=\frac{p}{D_{\text{a}}}. \quad (10)$$

The same is the case for aligning the plate along the [100] direction where the inverse of (6) is used instead of (7), giving the same values for k_1, k_3 and k_4. For these two special cases the coefficients in the plate equation are summarized in Table II.

IV. SOLVING THE PLATE EQUATION

Having a rectangular or square plate makes analytical deflection calculations complicated and approximate methods must be used to solve the generalized plate equation. With the anisotropic approach the Galerkin method [6] can be used to find approximate expressions for the deflection of a thin anisotropic square plate. In the most common case for CMUTs the plate is fabricated on a silicon (001) substrate and aligned to the [110] direction. For this orthotropic square plate with sidelengths $2L$ the relative deflection is found to [9], [11]

$$\frac{w(x,y)}{w_0}=\left[1-\left(\frac{x}{L}\right)^2\right]^2\left[1-\left(\frac{y}{L}\right)^2\right]^2\times\left[1+\beta\left(\frac{x}{L}\right)^2+\beta\left(\frac{y}{L}\right)^2\right], \quad (11)$$

where the plate parameter is defined as

$$\beta=\frac{182+143k_2}{1432+91k_2}. \quad (12)$$

The center deflection can be written

$$w_{0,\mathrm{Si}(001)} = \frac{77(1432+91k_2)}{256(16220+11k_2(329+13k_2))}\frac{L^4 p}{D_\mathrm{a}}. \quad (13)$$

Eqn. (11)-(13) are also valid when the plate is aligned to the [100] direction on a silicon (001) substrate. Note that the center deflection depends only on the k_2 coefficient. For primary flat alignment it is found by inserting k_2 into (12) that $\beta = 0.23920$. This results in a normalized deflection surface for the plate aligned to the $\langle 110\rangle$ direction given by

$$\left.\frac{w(x,y)}{w_0}\right|_{\mathrm{Si}(001),\langle 110\rangle} = \left[1-(x/L)^2\right]^2\left[1-(y/L)^2\right]^2 \times \left[1+0.239207\left[(x/L)^2+(y/L)^2\right]\right] \quad (14)$$

and the center deflection becomes

$$w_0|_{\mathrm{Si}(001),\langle 110\rangle} = 0.02196\frac{L^4 p}{D_\mathrm{a}}. \quad (15)$$

Comparing (3) and (15) it is seen that they are very similar containing the same parameters but different coefficients and the anisotropic instead of the isotropic flexural rigidity.

Fig. 2 shows the deflection cross section through $y = 0$ of a square plate of silicon (001)

$$w_{y=0} = w_0\left[1-(x/L)^2\right]^2\left[1+\beta(x/L)^2\right]. \quad (16)$$

The deflection calculated with the anisotropic approach uses $k_2 = 1.3241$ in (12) and center deflection (15). This is compared to the isotropic approach using $k_2 = 2$ in (12) and center deflection (3), with Young's modulus and Poisson's ratio in the [100] and [110] directions, and to a finite element (FEM) simulation made using the full anisotropic compliance matrix (compliance coefficients from Table I) in COMSOL. The calculated deflections are normalized to the FEM center deflection. Excellent agreement is shown between the anisotropic curve and FEM with a deviation of less than 0.1 % whereas the isotropic approach leads to deviations in the center deflection of around 10 % for both [100] and [110] directions.

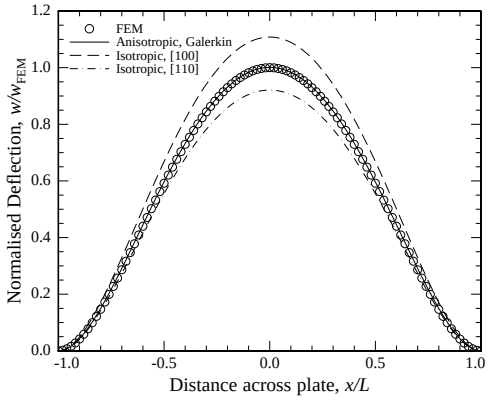

Fig. 2. Normalized deflection cross section ($y = 0$) of a square plate of silicon (001) calculated using both the isotropic approach with Young's modulus and Poisson's ratio in the [100] and [110] directions and the anisotropic approach. The circles represent the deflection calculated by FEM.

V. CMUT APPLICATION

Many important design parameters for CMUTs depend on the deflection of the plate. By using static analysis it is possible to find the stable position of the plate when applying a certain bias voltage. The stable position is easiest expressed through the center deflection and is the position where the strain force balance the electrostatic and pressure forces. The center deflection is found from energy considerations. The total potential energy of the system consists of three terms:

1) Strain energy. Calculated by integrating the strain energy density using (5), (7) and (11) and the result is

$$U_\mathrm{s} = \frac{1}{2}\int_{-h/2}^{h/2}\int_{-L}^{L}\int_{-L}^{L}(\sigma_1\varepsilon_1+\sigma_2\varepsilon_2+\sigma_6\varepsilon_6)\,\mathrm{d}x\mathrm{d}y\mathrm{d}z \quad (17)$$

$$U_{\mathrm{s},\mathrm{Si}(001),[110]} = 3.91172\times 10^{11}\frac{h^3 w_0^2}{L^2}. \quad (18)$$

2) Energy due to applied pressure. This is found from the pressure load on the plate

$$U_\mathrm{p} = -\int_{-L}^{L}\int_{-L}^{L} pw(x,y)\; dxdy \quad (19)$$

$$U_{\mathrm{p},\mathrm{Si}(001),[110]} = -1.216 p w_0 L^2. \quad (20)$$

3) Electrostatic energy. Expressed through the charge Q or applied voltage V, the vacuum permittivity ε_0, gap height g and the total capacitance C_t of the device which for a square plate is found using a Taylor expansion of the integrant with the deflection in (11)

$$U_\mathrm{e} = Q^2/(2C_\mathrm{t}) = \frac{1}{2}V^2 C_\mathrm{t}. \quad (21)$$

$$= \frac{1}{2}V^2\int_{-L}^{L}\int_{-L}^{L}\frac{\varepsilon_0}{g-w(x,y)}dxdy \quad (22)$$

The total force on the system is then found by differentiating the total potential energy with respect to the center deflection. From this the stable center position of the plate can be found for a given applied voltage as the point where the total force is zero.

VI. COMPARISON TO MEASUREMENTS

CMUTs with square silicon plates have been fabricated using fusion bonding. The fabricated devices have a 65x65 μm wide and 2.37 μm thick silicon plate with a gap height of 405 nm and a 198 nm thick insulating oxide at the bottom of the cavity. The deflection was measured with a Sensofar PLu Neox 3D Optical Profiler using white light interferometry.

Fig. 3 shows a measured cross section of the normalized deflection for the fabricated device. It is normalized in both center deflection and distance across the plate to compare the shape of the measured deflection with the calculated deflection. The red curve is a fit made to the measurements using the anisotropic model (16). Both the center deflection and the plate parameter β is fitted. As it is seen in the figure the fitted value for β is 0.243 which matches very well, with a deviation of 1.5%, compared to the calculated value of 0.23920 for this type of plate (silicon (001) substrate aligned to [110] direction). The center deflection found from the fit has a deviation of 0.5% compared to the measurement.

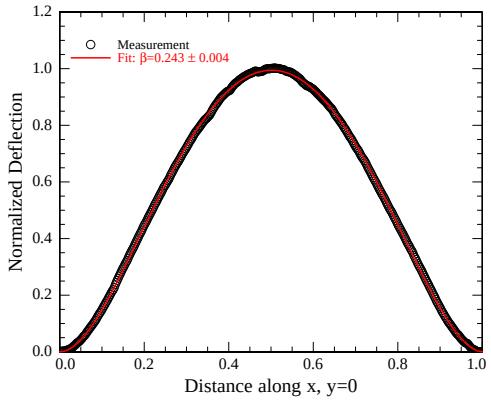

Fig. 3. Normalized deflection cross section from measurement on a fabricated CMUT. The red curve is a fit made with (16).

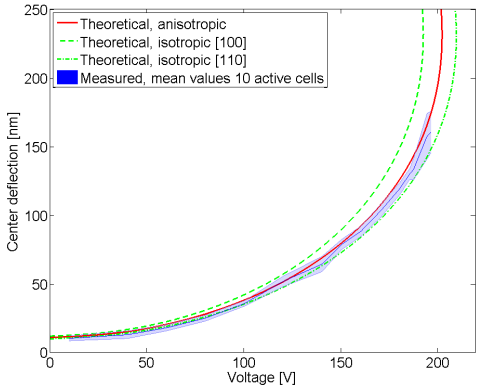

Fig. 4. Measured center deflection for increasing bias voltage together with theoretical curves using anisotropic and isotropic approaches.

Measurements with a DC voltage applied were also performed and the results are shown in Fig. 4. Here it is seen how the center deflection varies with the applied voltage and how it deflects more when approaching the pull-in voltage as expected. The center deflection for the measurements is found as the average of 10 cells. The errorbars corresponds to plus/minus two standard deviations. A theoretical curve made from the stable position analysis described in section V is plotted as well for both anisotropic and isotropic [100] and [110] approaches. The thickness of the plate is adjusted to 2.48, 2.49 and 2.47 μm respectively with the correction found by FEM to take the 200 nm Al layer on top of the Si into account. It is seen that the anisotropic theory matches well with the measurement as it is within the error margin and the isotropic curves show similar behavior as in Fig. 2. Also the pull-in voltage is in good agreement as it was measured to be 206 V, compared to an expected value of 202 V from the anisotropic model.

VII. Conclusion

Using isotropic plate theory to calculate the deflection of anisotropic silicon plates results in deviations from FEM or measurements of up to 10%. The full anisotropic plate equation was solved using the Galerkin method. It is seen that the deflection simplifies by utilizing the symmetry of the silicon crystal and a compact solution is obtained for square CMUT plates on a (001) silicon substrate aligned to the [110] direction. The maximum deviation is less than 0.1% compared to FEM. Furthermore, the deflection was measured on fabricated devices and fitting the anisotropic calculated deflection to the measurement a deviation of 0.5-1.5% is observed in the fitted parameters. The stable position for varying bias voltage was also found using the anisotropic theory and comparing this to measurements it is seen that the theory is within the uncertainty interval of the measurements.

Acknowledgement

This work was financially supported by the Danish National Advanced Technology Foundation (024-2008-3) and (82-2012-4).

References

[1] I. O. Wygant, M. Kupnik, and B. T. Khuri-Yakub, "Analytically calculating membrane displacement and the equivalent circuit model of a circular CMUT cell," in *IEEE Ultrasonics Symposium, 2008. IUS 2008*. IEEE, Nov. 2008, pp. 2111–2114.

[2] A. Lohfink and P.-C. Eccardt, "Linear and nonlinear equivalent circuit modeling of CMUTs," *IEEE Transactions on Ultrasonics, Ferroelectrics and Frequency Control*, vol. 52, no. 12, pp. 2163 –2172, Dec. 2005.

[3] R. L. Taylor and S. Govindjee, "Solution of clamped rectangular plate problems," *Communications in Numerical Methods in Engineering*, vol. 20, no. 10, p. 757765, 2004. [Online]. Available: http://onlinelibrary.wiley.com/doi/10.1002/cnm.652/abstract

[4] M. Rahman, J. Hernandez, and S. Chowdhury, "An improved analytical method to design CMUTs with square diaphragms," *IEEE Transactions on Ultrasonics Ferroelectrics and Frequency Control*, vol. 60, no. 4, pp. 834–845, Apr. 2013, WOS:000317010200020.

[5] M. F. la Cour, T. L. Christiansen, J. A. Jensen, and E. V. Thomsen, "Modelling of CMUTs with anisotropic plates," *Proceedings of IEEE International Ultrasonics Symposium*, pp. 588–591, 2012.

[6] E. Ventsel and T. Krauthammer, *Thin Plates and Shells: Theory: Analysis, and Applications*. Taylor & Francis, Aug. 2001.

[7] R. E. Newnham, *Properties of Materials: Anisotropy, Symmetry, Structure*. Oxford University Press, USA, Jan. 2005.

[8] J. J. Hall, "Electronic effects in the elastic constants of n-type silicon," *Physical Review*, vol. 161, no. 3, pp. 756–761, Sep. 1967. [Online]. Available: http://link.aps.org/doi/10.1103/PhysRev.161.756

[9] E. V. Thomsen, K. Reck, G. Skands, C. Bertelsen, and O. Hansen, "Silicon as an anisotropic mechanical material: Deflection of thin crystalline plates," submitted to Journal of Microelectromechanical Systems.

[10] S. Holgate, "The transverse flexure of perforated aeolotropic plates," *Proceedings of the Royal Society A: Mathematical, Physical and Engineering Sciences*, vol. 185, no. 1000, pp. 50–69, Jan. 1946. [Online]. Available: http://adsabs.harvard.edu/abs/1946RSPSA.185...50H

[11] F. Mbakogu and M. Pavlovi, "Bending of clamped orthotropic rectangular plates: a variational symbolic solution," *Computers & Structures*, vol. 77, no. 2, pp. 117–128, Jun. 2000. [Online]. Available: http://www.sciencedirect.com/science/article/pii/S0045794999002175

PAPER C

Modal Radiation Patterns of Baffled Circular Plates and Membranes

Authors: **Thomas Lehrmann Christiansen**, Ole Hansen, Jørgen Arendt Jensen, and Erik Vilain Thomsen.

Published in: Journal of the Acoustical Society of America, Vol. 135, No. 5, pp. 2523-2533, 2014

Abstract

The far field velocity potential and radiation pattern of baffled circular plates and membranes are found analytically using the full set of modal velocity profiles derived from the corresponding equation of motion. The derivation is valid for a plate or membrane subjected to an external excitation force, which is used as a sound receiver in any medium or as a sound transmitter in a gaseous medium. A general, concise expression is given for the radiation pattern of any mode of the membrane and the plate with arbitrary boundary conditions. Specific solutions are given for the four special cases of a plate with clamped, simply supported, and free edge boundary conditions as well as for the membrane. For all non-axisymmetric modes, the velocity potential along the axis of the radiator is found to be strictly zero. In the long wavelength limit, the radiation pattern of all axisymmetric modes approaches that of a monopole, while the non-axisymmetric modes exhibit multipole behavior. Numerical results are also given, demonstrating the implications of having non-axisymmetric excitation using both a point excitation with varying eccentricity and a homogeneous excitation acting on half of the circular radiator.

Modal radiation patterns of baffled circular plates and membranes

Thomas Lehrmann Christiansen,[a] Ole Hansen,[b] and Erik Vilain Thomsen
Department of Micro- and Nanotechnology, Technical University of Denmark, DK-2800 Kgs. Lyngby, Denmark

Jørgen Arendt Jensen
Center for Fast Ultrasound Imaging, Department of Electrical Engineering, Technical University of Denmark, DK-2800 Kgs. Lyngby, Denmark

(Received 1 September 2013; revised 13 February 2014; accepted 13 March 2014)

The far field velocity potential and radiation pattern of baffled circular plates and membranes are found analytically using the full set of modal velocity profiles derived from the corresponding equation of motion. The derivation is valid for a plate or membrane subjected to an external excitation force, which is used as a sound receiver in any medium or as a sound transmitter in a gaseous medium. A general, concise expression is given for the radiation pattern of any mode of the membrane and the plate with arbitrary boundary conditions. Specific solutions are given for the four special cases of a plate with clamped, simply supported, and free edge boundary conditions as well as for the membrane. For all non-axisymmetric modes, the velocity potential along the axis of the radiator is found to be strictly zero. In the long wavelength limit, the radiation pattern of all axisymmetric modes approaches that of a monopole, while the non-axisymmetric modes exhibit multipole behavior. Numerical results are also given, demonstrating the implications of having non-axisymmetric excitation using both a point excitation with varying eccentricity and a homogeneous excitation acting on half of the circular radiator.

I. INTRODUCTION

The sound field from a circular radiator in an infinite rigid baffle has been subject to intense investigation in the literature. The piston radiator is a textbook example, and numerous treatments of this problem can be found in the literature, with well-known analytical solutions to both the sound field on-axis and in the far field as well as the radiation impedance.[1–4] In the case of circular radiators with non-uniform velocity profiles, the analysis is more involved, and several authors have analyzed this problem using polynomial approximations to represent arbitrary axisymmetric velocity distributions.[5–10] In particular, the specific cases of clamped plates and membranes have often served as important examples of circular radiators with non-uniform velocity distributions. A frequent approach have been to assume velocity profiles of the form $v(\varrho) = v_0[1 - (\varrho/a)^2]^\ell$, where ϱ is the radial coordinate, a the radius of the radiator and v_0 some normalization constant.[5–8,11] Indeed, the static deflection profile of a clamped plate or membrane subject to a static pressure difference is $w(\varrho) = w_0[1 - (\varrho/a)^2]^\ell$, $\ell = 1$ corresponding to the case of a membrane and $\ell = 2$ to the case of a clamped plate.[12] Here, w_0 is the center deflection. However, these profiles are not valid in the dynamic case, since the equation of motion is altered by the addition of an inertial term.[13]

Other authors have applied a more precise approach by using the axisymmetric eigenmodes to find the on-axis sound pressure arising from an elastically supported circular plate,[14] the on-axis sound pressure and radiation pattern of a circular stretched membrane,[15] and the radiation pattern for a circular plate with clamped, simply supported and free boundary conditions.[16] This, however, limits the description to the case of axisymmetric excitation, where only axisymmetric modes are relevant.[15] In the more general case of an arbitrary excitation, the non-axisymmetric modes must be included to provide a complete analysis of the problem. Such a description has become increasingly relevant, as sound sources or receivers with nearly ideal plate or membrane behavior are present in numerous applications, e.g., in microphones, loudspeakers, and ultrasonic transducers utilizing micromachined elements.[17–20] Applications of non-axisymmetric excitation using a multiple-electrode structure have been proposed by You *et al.*, who have utilized non-axisymmetric modes of circular clamped plates to enable physical steering of the transmitted sound and selective off-axis sensitivity in receive mode for high-resolution ultrasonic imaging.[21,22]

Alper and Magrab have presented a comprehensive study of the sound field from a clamped circular plate subjected to fluid loading and arbitrary excitation using Mindlin-Timoshenko plate theory and the wave equation for the acoustic field.[23] While their approach offers means of numerically calculating the general sound field for both thick and thin clamped circular plates subject to non-axisymmetric excitation, the sound field arising from non-axisymmetric modes is, however, not treated and the analysis only covers clamped plates.

[a]Author to whom correspondence should be addressed. Electronic mail: tlehr@nanotech.dtu.dk
[b]Also at: The Center for Individual Nanoparticle Functionality, Technical University of Denmark, DK-2800 Kgs. Lyngby, Denmark

In this paper, it is shown that the far field radiation pattern of baffled plates and membranes with arbitrary boundary conditions can be solved analytically using the full set of modal velocity profiles derived from the time dependent equation of motion using classical plate theory and the Rayleigh integral. Any velocity distribution of the plate or membrane, axisymmetric as well as non-axisymmetric, can then be represented as a series expansion of these modes, although a single term is sufficient if the radiator is operated in the proximity of one of its eigenfrequencies. A single, concise expression for the far field velocity potential valid for any eigenmode of either plates or membranes is derived. The general expression is used to calculate the radiation pattern in the four special cases of a baffled plate with clamped, simply supported, and free boundary conditions, as well as in the case of a baffled membrane. It is shown that, regardless of the boundary conditions, the far field velocity potential for all non-axisymmetric modes of both plates and membranes becomes zero on the axis of the radiator. The long wavelength limit is analyzed in further detail, demonstrating that the sound radiation in all cases of axisymmetric modes will resemble the radiation of a monopole. For the non-axisymmetric modes, the behavior can be described as a multipole radiation. In general, the radiation pattern of the non-axisymmetric modes will exhibit a rejection angle with respect to the axis of the radiator in which the sound radiation is negligible. A simple expression is given for this rejection angle as a function of the mode number. Last, the effect of non-axisymmetric excitation on the far field behavior is investigated through an eigenmode expansion using both point excitations with varying eccentricity and a homogeneous pressure covering half of the radiator in order to emulate a more realistic scenario.

The analysis presented in the following is valid for baffled plates and membranes, where it can be assumed that the effect of reaction forces due to fluid loading is negligible. It thus applies in general to the case where the plate or membrane is used as a receiver, while the assumption only holds for sound transmission in a gaseous medium.

II. THE MODES OF CIRCULAR KIRCHOFF–LOVE PLATES AND MEMBRANES

The governing equation of motion for dynamic Kirchoff–Love plates under uniform biaxial in-plane stress σ and external surface pressure p_{ext} is given by[13,24]

$$\rho_p h \frac{\partial^2}{\partial t^2} w + \nabla^2 D \nabla^2 w - \sigma h \nabla^2 w = p_{\text{ext}}, \tag{1}$$

where w is the plate deflection normal to the plane of the radiator surface and ρ_p is the mass density of the plate of thickness h and flexural rigidity $D = Eh^3/[12(1-\nu^2)]$. Here, E and ν are the Young's modulus and Poisson's ratio of the plate material, respectively. Note that the first term in Eq. (1) accounts for the inertial effects; in the absence of this term, the equation describes the static case, the solution of which has been used by others to approximate the velocity profile.[5–8]

In the case of a stress-free plate, Eq. (1) reduces to

$$\rho_p h \frac{\partial^2}{\partial t^2} w + \nabla^2 D \nabla^2 w = p_{\text{ext}}. \tag{2}$$

Note that the pressure on the radiator p_{ext} is assumed to be a purely external pressure, corresponding to the case where the surface pressure generated by the radiator itself is negligible compared to the pressure exerted on the radiator by external forces. In this case, the system is fully described by its eigenmodes, which for the plate are given by the solution to the homogeneous equivalent of Eq. (2), i.e., for $p_{\text{ext}} = 0$. Any external pressure function can then be included by using the eigenmodes derived in the following as a basis.

Using polar coordinates, it is assumed that the solutions to the equation of motion can be written as time harmonic, separable product functions of the form

$$w(\varrho, \phi, t) = F(\varrho) G(\phi) e^{\mathrm{i}\omega t}. \tag{3}$$

Here, $F(\varrho)$ and $G(\phi)$ are solutions to the resulting set of ordinary differential equations, where ϱ and ϕ are the radial and angular coordinates, respectively. In the time dependent part, $\mathrm{i} = \sqrt{-1}$ is the imaginary unit, ω the angular frequency, and t the time variable. Using this approach, the time independent mode functions of a plate with radius a are given by[24]

$$w_{nm}(\varrho, \phi) = A_{nm}\left[J_n\left(K_{nm}\frac{\varrho}{a}\right) + B_{nm} I_n\left(K_{nm}\frac{\varrho}{a}\right)\right] \times \cos\left[n(\phi + \phi_0)\right], \tag{4}$$

where $J_n(z)$ denotes the Bessel function of the first kind, order n, and $I_n(z)$ denotes the modified Bessel function of the first kind, order n. A_{nm} and B_{nm} are modal constants corresponding to the integer mode numbers n and m. The values of B_{nm} are, together with the values of K_{nm}, dictated by the boundary conditions, while the modal amplitude constants, A_{nm}, are found as the expansion coefficients corresponding to the excitation pressure $p_{\text{ext.}}$ The phase term ϕ_0 is the angular misalignment of the observation point and the mode pattern.

In the case of a stressed membrane, i.e., a sufficiently thin plate with large biaxial in-plane stress $\sigma h \gg D/a^2$, the plate bending term can be ignored, and Eq. (1) reduces to

$$\rho_p h \frac{\partial^2}{\partial t^2} w - \sigma h \nabla^2 w = p_{\text{ext}}. \tag{5}$$

A prerequisite for having a stressed membrane is that the edges are constrained. Employing a zero deflection boundary condition at the rim, the time independent mode functions are given by

$$w_{nm}(\varrho, \phi) = C_{nm} J_n\left(K_{nm}\frac{\varrho}{a}\right)\cos\left[n(\phi + \phi_0)\right], \tag{6}$$

where C_{nm} are modal amplitude constants. Once again, the modal amplitude constants are found as the expansion coefficients corresponding to the excitation pressure p_{ext}. The

values of K_{nm} are dictated by the boundary conditions, and are in this case simply given by the roots of the Bessel function of the first kind, order n.

Note that the mode functions of the membrane are identical to the mode functions of the plate given in Eq. (4), if $B_{nm}=0$. This is exploited in the following section, where a general expression for the far field velocity potential and directivity pattern valid for both plates and membranes is derived. Using this result, the four special cases of plates with clamped, simply supported, and free edges in addition to the case of a membrane are covered afterward.

III. THE FAR FIELD VELOCITY POTENTIAL AND RADIATION PATTERN: GENERAL DERIVATION

The following derivations are carried out using the velocity potential, Φ, defined through the relation $\mathbf{u}=\nabla\Phi$, where $\mathbf{u}$ is the velocity vector. The pressure is readily found from the velocity potential as $p=\rho_a\partial\Phi/\partial t$, where ρ_a is the mass density of the acoustic medium, and the velocity is found from the definition of the velocity potential.[1]

The steady-state velocity potential at any point in the half-space above a radiator in an infinite rigid baffle is given by Rayleigh's integral[25]

$$\Phi=\frac{1}{2\pi}e^{\mathrm{i}\omega t}\int_S u(\varrho,\phi)\frac{e^{-\mathrm{i}kR}}{R}\,\mathrm{d}S, \tag{7}$$

where $k=\omega/c$ is the wavenumber with the speed of sound given by c, and $\mathrm{d}S$ denotes a differential area element. $u(\varrho,\phi)$ is the velocity in polar coordinates of the radiator with radius a. From Fig. 1, it is seen that the distance R to the observation point P from a point located on the radiator at (ϱ,ϕ) is given by $R^2=\varrho^2+r^2-2\varrho r\sin\theta\cos\phi$, where r is the distance to the observation point P from the center of the radiator, θ is the azimuthal angle, and ϕ is the polar angle. In the far field, $r\gg a\geq\varrho$, so that $R\simeq r-\varrho\sin\theta\cos\phi$. In this limit, the velocity potential therefore becomes

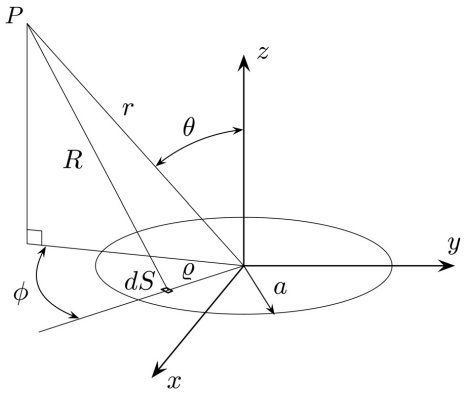

FIG. 1. An illustration of the variables used to determine the velocity potential in the point P originating from a circular source of radius a.

$$\Phi\simeq\frac{1}{2\pi r}e^{\mathrm{i}k(ct-r)}\int_S u(\varrho,\phi)e^{\mathrm{i}k\varrho\sin\theta\cos\phi}\,\mathrm{d}S, \tag{8}$$

where the time-independent velocity eigenmodes are given by

$$u(\varrho,\phi)=\mathrm{i}\omega w(\varrho,\phi). \tag{9}$$

In the general case of a plate, the mode functions are given by Eq. (4). In the case where $B_{nm}=0$, Eq. (4) describes the mode functions of a membrane, and can therefore be used as a general expression for the mode functions of both plates and membranes. The velocity mode functions are then found by inserting this expression into Eq. (9), and the far field velocity potential given by Eq. (8) thus becomes

$$\Phi=\frac{\mathrm{i}\omega e^{\mathrm{i}k(ct-r)}}{2\pi r}A_{nm}\times\int_0^a\left[J_n\left(K_{nm}\frac{\varrho}{a}\right)+B_{nm}I_n\left(K_{nm}\frac{\varrho}{a}\right)\right]\mathcal{I}_1\varrho\,\mathrm{d}\varrho, \tag{10}$$

where $\mathcal{I}_1$ is the integral

$$\mathcal{I}_1=\int_0^{2\pi}\cos\left[n(\phi+\phi_0)\right]e^{\mathrm{i}k\varrho\sin\theta\cos\phi}\,\mathrm{d}\phi. \tag{11}$$

As covered in the Appendix, this integral has the solution

$$\mathcal{I}_1=2\pi\mathrm{i}^n\cos(n\phi_0)J_n(k\varrho\sin\theta). \tag{12}$$

Hence, the velocity potential becomes

$$\Phi=\frac{\mathrm{i}e^{\mathrm{i}k(ct-r)}}{2\pi r}A_{nm}\omega 2\pi\mathrm{i}^n\cos(n\phi_0)\times\int_0^a\left[J_n\left(K_{nm}\frac{\varrho}{a}\right)+B_{nm}I_n\left(K_{nm}\frac{\varrho}{a}\right)\right]\times J_n(k\varrho\sin\theta)\varrho\,\mathrm{d}\varrho. \tag{13}$$

Performing the substitution $\varrho=\xi a$ yields

$$\Phi=\frac{\mathrm{i}e^{\mathrm{i}k(ct-r)}}{2\pi r}A_{nm}\omega 2\pi a^2\mathrm{i}^n\cos(n\phi_0)[\mathcal{I}_2+B_{nm}\mathcal{I}_3], \tag{14}$$

with

$$\mathcal{I}_2=\int_0^1 J_n(K_{nm}\xi)J_n(ka\xi\sin\theta)\xi\,\mathrm{d}\xi \tag{15}$$

and

$$\mathcal{I}_3=\int_0^1 I_n(K_{nm}\xi)J_n(ka\xi\sin\theta)\xi\,\mathrm{d}\xi. \tag{16}$$

The integrals $\mathcal{I}_2$ and $\mathcal{I}_3$ are both standard Bessel integrals with the solutions[27]

$$\mathcal{I}_2=\frac{J_n(K_{nm})J_{n-1}(\eta)\eta-K_{nm}J_{n-1}(K_{nm})J_n(\eta)}{K_{nm}^2-\eta^2} \tag{17}$$

and

$$\mathcal{I}_3 = -\frac{I_n(K_{nm})J_{n-1}(\eta)\eta - K_{nm}I_{n-1}(K_{nm})J_n(\eta)}{K_{nm}^2 + \eta^2}, \tag{18}$$

with $\eta = ka\sin\theta$. Thus, the far field velocity potential for any mode of a plate or membrane is

$$\Phi_{nm} = \frac{ie^{ik(ct-r)}}{2\pi r} A_{nm}\omega 2\pi a^2 R_{nm}(\eta, \phi_0), \tag{19}$$

where

$$R_{nm}(\eta, \phi_0) = \frac{i^n \cos(n\phi_0)}{K_{nm}^4 - \eta^4}\{[\alpha_{nm} + \beta_{nm}\eta^2]J_{n-1}(\eta)\eta - [\gamma_{nm} + \delta_{nm}\eta^2]J_n(\eta)\}. \tag{20}$$

The constants α_{nm}, β_{nm}, γ_{nm}, and δ_{nm} in Eq. (20) are given by

$$\alpha_{nm} = K_{nm}^2[J_n(K_{nm}) - B_{nm}I_n(K_{nm})], \tag{21a}$$

$$\beta_{nm} = J_n(K_{nm}) + B_{nm}I_n(K_{nm}), \tag{21b}$$

$$\gamma_{nm} = K_{nm}^3[J_{n-1}(K_{nm}) - B_{nm}I_{n-1}(K_{nm})], \tag{21c}$$

$$\delta_{nm} = K_{nm}[J_{n-1}(K_{nm}) + B_{nm}I_{n-1}(K_{nm})], \tag{21d}$$

where B_{nm} and K_{nm} are found from the boundary conditions that applies to the specific case of interest.

The factor in front of $R_{nm}(\eta, \phi_0)$ in Eq. (19) is identical to the velocity potential of a monopole of strength $\omega A_{nm} 2\pi a^2$ in an infinite rigid baffle. The magnitude of $R_{nm}(\eta, \phi_0)$ therefore expresses the radiation pattern for any mode of a plate or membrane. From Eq. (20), the modal radiation characteristics common to the plate and the membrane can be deduced. As expected, it is seen that the azimuthal symmetry of the modes is reflected in the radiation pattern, such that only the axisymmetric modes corresponding to $n = 0$ exhibit axisymmetric radiation patterns, since in this case the term $\cos(n\phi_0) = 1$, thus removing the dependency on the azimuthal angle ϕ_0. The resulting expression for $n = 0$ agrees with the result of Shuyu, who considered the special case of purely axisymmetric modes of plates.[16]

Equation (20) furthermore describes all remaining modes, i.e. the non-axisymmetric modes. It is seen that for $\theta = 0$, the velocity potential for all such modes, corresponding to $n \geq 1$, becomes

$$R_{nm}(0, \phi_0) = 0, \quad \theta = 0 \wedge n \geq 1, \tag{22}$$

since $\eta = 0$ for $\theta = 0$. Thus, no sound is radiated along the symmetry axis of the source for all non-axisymmetric modes of both plates and membranes.

This concludes the general analysis of the far field radiation pattern. In the following, the four specific cases of clamped, simply supported, and free edges of the plate, as well as that of a membrane, are considered in detail.

IV. SPECIAL CASES

A. Clamped plate

In the case where the plate is clamped around its circumference at $\varrho = a$, the displacement and slope at the edge is zero. Thus, the displacement given by Eq. (4) and its derivative with respect to the radial coordinate ϱ must disappear at $\varrho = a$, resulting in the equations

$$J_n(K_{nm}) + B_{nm}I_n(K_{nm}) = 0, \tag{23}$$

and

$$[nJ_n(K_{nm}) - K_{nm}J_{n+1}(K_{nm})] + B_{nm}[nI_n(K_{nm}) + K_{nm}I_{n+1}(K_{nm})] = 0. \tag{24}$$

From Eq. (23), it is seen that the modal constant B_{nm} is

$$B_{nm} = -\frac{J_n(K_{nm})}{I_n(K_{nm})}, \tag{25}$$

such that the resulting mode functions for the clamped plate becomes

$$w_{nm}(\varrho, \phi) = A_{nm}\left[J_n\left(K_{nm}\frac{\varrho}{a}\right) - \frac{J_n(K_{nm})}{I_n(K_{nm})}I_n\left(K_{nm}\frac{\varrho}{a}\right)\right] \times \cos[n(\phi + \phi_0)]. \tag{26}$$

From Eqs. (23) and (24), it is seen that the wavenumbers K_{nm} are solutions to the transcendental equation

$$\frac{J_{n+1}(K_{nm})}{I_{n+1}(K_{nm})} + \frac{J_n(K_{nm})}{I_n(K_{nm})} = 0. \tag{27}$$

The values of the constants α_{nm}, β_{nm}, γ_{nm}, and δ_{nm} in Eq. (21) become

$$\alpha_{nm} = 2K_{nm}^2 J_n(K_{nm}), \tag{28a}$$

$$\beta_{nm} = 0, \tag{28b}$$

$$\gamma_{nm} = K_{nm}^3\left[J_{n-1}(K_{nm}) + \frac{J_n(K_{nm})}{I_n(K_{nm})}I_{n-1}(K_{nm})\right], \tag{28c}$$

$$\delta_{nm} = K_{nm}\left[J_{n-1}(K_{nm}) - \frac{J_n(K_{nm})}{I_n(K_{nm})}I_{n-1}(K_{nm})\right]. \tag{28d}$$

B. Simply supported plate

In the case where the plate is simply supported at its circumference at $\varrho = a$, the displacement at the edge is zero, and no bending moment can be supported. Thus, the displacement given by Eq. (4) and the expression $\partial^2 w/\partial\varrho^2 + \nu/\varrho(\partial w/\partial\varrho)$ must disappear at $\varrho = a$, resulting in the equations[24]

$$J_n(K_{nm}) + B_{nm}I_n(K_{nm}) = 0, \tag{29}$$

and

$$[n(n-1)(1-\nu) - K_{nm}^2]J_n(K_{nm}) + K_{nm}(1-\nu)J_{n+1}(K_{nm}) + B_{nm}\{[n(n-1)(1-\nu) + K_{nm}^2]I_n(K_{nm}) - K_{nm}(1-\nu)I_{n+1}(K_{nm})\} = 0. \tag{30}$$

It is readily seen from Eq. (29) that the value of B_{nm} is identical to Eq. (25), such that the mode functions for the simply supported plate is given by the mode functions for the clamped plate in Eq. (26). However, the wavenumber equation is different, and is from Eqs. (29) and (30) seen to be

$$\frac{J_{n+1}(K_{nm})}{J_n(K_{nm})} + \frac{I_{n+1}(K_{nm})}{I_n(K_{nm})} = \frac{2K_{nm}}{1-\nu}. \tag{31}$$

Since the expression for B_{nm} is shared by the two cases of a clamped and a simply supported plate, the expressions for the constants α_{nm}, β_{nm}, γ_{nm}, and δ_{nm} are also identical. Thus, the expressions reported in Eq. (28) also applies to the present case.

C. Plate with free edges

If the plate is free to move at the rim, the bending moment and shear force at $\varrho = a$ must vanish. Hence, the boundary conditions become[26]

$$\begin{aligned}&[n(n-1)(1-\nu) - K_{nm}^2]J_n(K_{nm}) + K_{nm}(1-\nu)J_{n+1}(K_{nm})\\ &+ B_{nm}\{[n(n-1)(1-\nu) + K_{nm}^2]I_n(K_{nm})\\ &- K_{nm}(1-\nu)I_{n+1}(K_{nm})\} = 0\end{aligned} \tag{32}$$

and

$$\begin{aligned}&B_{nm}\{n[-K_{nm}^2 + n(n-1)(1-\nu)]I_n(K_{nm})\\ &+ K_{nm}[n^2(1-\nu) - K_{nm}^2]I_{n+1}(K_{nm})\}\\ &+ n[K_{nm}^2 + n(n-1)(1-\nu)]J_n(K_{nm})\\ &- K_{nm}[n^2(1-\nu) + K_{nm}^2]J_{n+1}(K_{nm}) = 0.\end{aligned} \tag{33}$$

From Eq. (32), the value of B_{nm} can be extracted, resulting in

$$B_{nm} = -\frac{c_1 J_n(K_{nm}) + K_{nm}(1-\nu)J_{n+1}(K_{nm})}{c_2 I_n(K_{nm}) - K_{nm}(1-\nu)I_{n+1}(K_{nm})}, \tag{34}$$

with

$$c_1 = n(n-1)(1-\nu) - K_{nm}^2, \tag{35}$$

and

$$c_2 = n(n-1)(1-\nu) + K_{nm}^2, \tag{36}$$

such that the mode functions are given by

$$\begin{aligned}w_{nm}(\varrho,\phi) = A_{nm}\Bigg[&J_n\left(K_{nm}\frac{\varrho}{a}\right)\\ &- \frac{c_1 J_n(K_{nm}) + K_{nm}(1-\nu)J_{n+1}(K_{nm})}{c_2 I_n(K_{nm}) - K_{nm}(1-\nu)I_{n+1}(K_{nm})}\\ &\times I_n\left(K_{nm}\frac{\varrho}{a}\right)\Bigg]\cos[n(\phi+\phi_0)].\end{aligned} \tag{37}$$

By inserting the value of B_{nm} given in Eq. (34) into Eq. (33), the wavenumber equation for the plate with free edges can be found. Due to its length, it is not given here explicitly. The same is the case for the constants in Eqs. (21), which are likewise found by inserting the value of B_{nm} given in Eq. (34). It should be noted that, as opposed to the two previous cases, the constant β_{nm} does not vanish in the case of a plate with free boundary conditions, thereby resulting in a more complicated expression for the radiation pattern than is seen for plates with constrained edges.

D. Membrane

For the membrane, the mode functions are given by Eq. (6). Using the boundary condition that the displacement at the rim of the membrane should be zero yields

$$J_n(K_{nm}) = 0, \tag{38}$$

i.e., the wavenumbers of the membrane, K_{nm}, are simply given by the zeroes of the Bessel function of the first kind, order n. As covered in Sec. III, the far field velocity potential and radiation pattern given by Eqs. (19) and (20), respectively, are valid for the special case of a membrane, when B_{nm} is equal to zero. With B_{nm} set to zero, and by using the condition in Eq. (38), it is found that the constants in Eq. (21) are simplified significantly:

$$\alpha_{nm} = 0, \tag{39a}$$

$$\beta_{nm} = 0, \tag{39b}$$

$$\gamma_{nm} = K_{nm}^3 J_{n-1}(K_{nm}), \tag{39c}$$

$$\delta_{nm} = K_{nm} J_{n-1}(K_{nm}). \tag{39d}$$

In the case of a membrane, the radiation pattern is thus simply given by

$$R_{nm}(\eta,\phi_0) = \frac{-\mathrm{i}^n K_{nm} J_{n-1}(K_{nm})\cos(n\phi_0)J_n(\eta)}{K_{nm}^2 - \eta^2}. \tag{40}$$

E. Comparison

In Fig. 2, the radiation pattern for the four special cases is plotted for the two modes $(m, n) = (0, 0)$ and $(m, n) = (0, 1)$, both for long wavelengths ($ka = 10^{-5}$) and short wavelengths ($ka = 10$) relative to the radiator dimensions. For the simply supported and the free edge plate, a Poisson ratio of 0.2 has been arbitrarily selected. The radiation pattern is shown for the axisymmetric mode $(m, n) = (0, 0)$ for $\theta = [-90°; 0°]$, while it is shown for the non-axisymmetric mode $(m, n) = (0, 1)$ for $\theta = [0°; 90°]$ and $\phi_0 = 0$. All plots have been normalized to the peak value.

A couple of similarities should be noted. First, it is seen that for $n = 1$, the velocity potential is zero along $\theta = 0$ for both short and long wavelengths, as expected. Second, it is noted that in the case of long wavelengths, corresponding to $ka = 10^{-5}$, the four cases exhibit nearly identical normalized radiation patterns similar to the radiation pattern of a monopole ($n = 0$) and a dipole ($n = 1$). This behavior in the long wavelength limit is analyzed in further depth in the following.

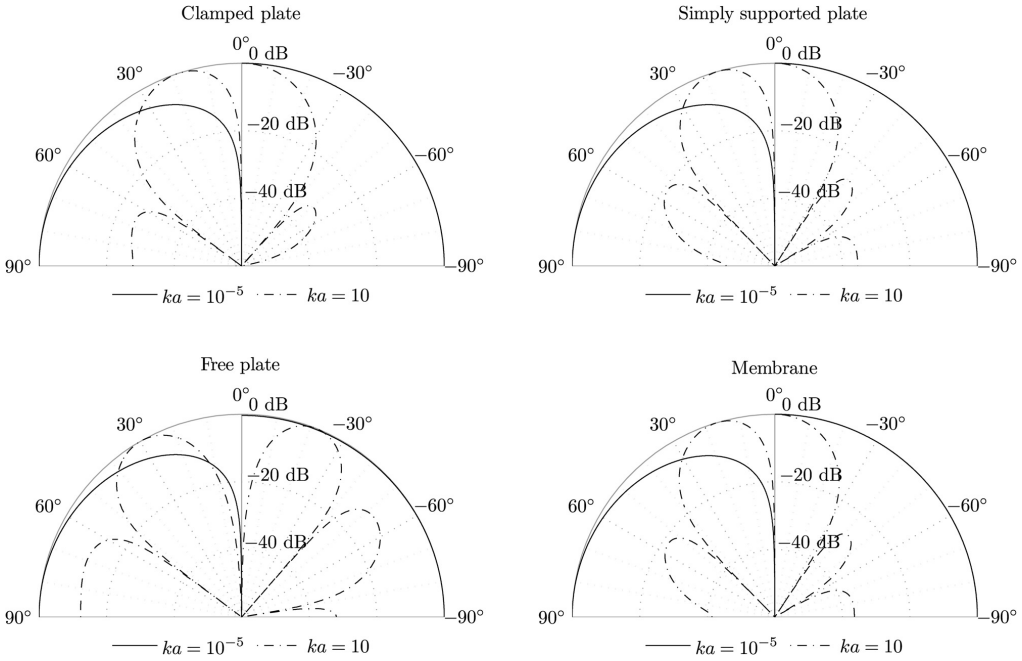

FIG. 2. Plot of the radiation pattern given by the magnitude of Eq. (20) for the three special cases of a plate with clamped, simply supported, and free edges, as well as for the case of a membrane. In all four cases, the two modes $(m, n) = (0, 0)$ and $(m, n) = (0, 1)$ have been plotted at both long wavelengths ($ka = 10^{-5}$) and short wavelengths ($ka = 10$) relative to the radiator dimensions. The radiation pattern for the first axisymmetric mode $(m, n) = (0, 0)$ is shown for $\theta = [-90°; 0°]$, while the radiation pattern for the first non-axisymmetric mode $(m, n) = (0, 1)$ is shown for $\theta = [0°; 90°]$. All plots have been normalized to their peak value.

V. ANALYSIS OF THE LONG WAVELENGTH LIMIT

Although the presented radiation patterns present a full and concise description valid for any mode of a plate or membrane, it is instructive to consider the limit in which the wavelength of the radiated sound is long compared to the dimension of the radiator, i.e., for $ka \to 0$. Apart from providing a basic understanding of the characteristics of the radiated sound, this limit also serves as an important approximation valid in many practical applications.

In Sec. III, it was deduced from the general expression for the radiation pattern in Eq. (20) that the symmetry of the modes is reflected in the radiation pattern, such that only the axisymmetric modes ($n = 0$) exhibit axisymmetric radiation patterns. Furthermore, it was seen that for $\theta = 0$, the velocity potential is strictly zero for all modes with $n \geq 1$, corresponding to the non-axisymmetric modes. In such modes, the plate or membrane is divided into $2n$ regions covering equal azimuthal angles, with neighboring regions vibrating out of phase. Thus, at $\theta = 0$, the velocity potential exactly cancels, resembling the behavior of a multipole.

This behavior is more clearly revealed by considering Eq. (20) in the long wavelength limit $ka \to 0$, corresponding to $\eta \to 0$, where

$$R_{nm}(\eta, \phi_0) \simeq \frac{\mathrm{i}^n \cos(n\phi_0)}{K_{nm}^4 - \eta^4} \left(\frac{\eta}{2}\right)^n \left\{ \frac{2[\alpha_{nm} + \beta_{nm}\eta^2]}{\Gamma(n)} - \frac{[\beta_{nm}\eta^2 + \gamma_{nm}]}{\Gamma(n+1)} \right\}, \quad \eta \to 0. \tag{41}$$

Here, it has been used that

$$J_n(\eta) \to \frac{1}{\Gamma(n+1)} \left(\frac{\eta}{2}\right)^n, \quad \eta \to 0, \tag{42}$$

where Γ denotes the Gamma function.[27] For all axisymmetric modes, corresponding to $n = 0$, it is seen by inspection of Eq. (41) that

$$R_{0m}(\eta, \phi_0) \simeq -\frac{\gamma_{0m}}{K_{0m}^4}, \tag{43}$$

if higher orders of η are neglected. Therefore, for both plates and membranes, regardless of the boundary condition, the radiation pattern is an angle-independent constant, identical to the radiation pattern of a monopole. Note, however, that the values of K_{nm} are dependent on the exact boundary conditions, and hence the amplitude of the monopole radiation will vary accordingly.

For the non-axisymmetric modes with $n = 1$, i.e. with the two halves of the plate or membrane vibrating out of phase, $\Gamma(n) = 1$ and $\Gamma(n + 1) = 1$. Neglecting higher orders of η, the radiation pattern in this case becomes

$$R_{1m}(\eta, \phi_0) \simeq \mathrm{i} \frac{\alpha_{nm} - \gamma_{nm}/2}{K_{nm}^4} \eta \cos\phi_0, \tag{44}$$

hence proportional to $\sin\theta \cos\phi_0$, which is the radiation pattern of a dipole oriented parallel to $\phi_0 = 0$ and perpendicular to $\theta = 0$.

The long wavelength approximation can be written for an arbitrary mode number $n \geq 1$, yielding

$$R_{nm}(\eta, \phi_0) \simeq \mathrm{i}^n \frac{2\alpha_{nm}/(n-1)! - \gamma_{nm}/n!}{K_{nm}^4} \left(\frac{\eta}{2}\right)^n \cos(n\phi_0), \tag{45}$$

where it is used that

$$\Gamma(n+1) = n!, \quad n = 0, 1, 2, ... \tag{46}$$

It is, thus, seen that for $n \geq 1$,

$$R_{nm}(\theta, \phi_0) \propto \sin^n(\theta) \cos(n\phi_0), \tag{47}$$

revealing that the radiation pattern is only strictly zero for $\theta = 0$, i.e., along the symmetry axis of the radiator, but the angle, for which the radiated sound is negligible, increases with increasing mode number n. This fact is illustrated in Fig. 3, where the normalized long wavelength radiation pattern is plotted for $n = 1$, $n = 10$, and $n = 100$. For a given mode number n, the radiated sound is seen to be decreased by a factor of μ relative to the maximum value at an angle of

$$\mu = \sin^n(\theta_\mu) \Longleftrightarrow \theta_\mu = \arcsin(\mu^{1/n}). \tag{48}$$

Any angle numerically smaller than this critical angle will exhibit a sound radiation decreased by more than a factor of μ. Thus, a rejection angle given by $2\theta_\mu$ can be defined for the radiator for $n \geq 1$. This angle is plotted in Fig. 4 for three different values of the reduction μ given in dB.

VI. NON-AXISYMMETRIC EXCITATION RESPONSE

The previous sections have focused on the far field radiation of the individual eigenmodes of plates and membranes. In this section, the implication of having contributions from non-axisymmetric modes during non-axisymmetric excitation is analyzed using two distinct excitations: A delta function representing a point force and an equally distributed pressure covering half of the circular radiator. The former is introduced to investigate the effect of varying eccentricity of the driving force, and the latter represents a more practical example of a non-axisymmetric driving force, which is similar to the one demonstrated by You *et al.*[21,22] All calculations are carried out for the case of a plate with arbitrary

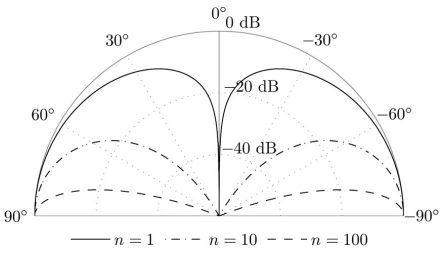

FIG. 3. The normalized long wavelength radiation given by Eq. (47) plotted for the non-axisymmetric modes corresponding to the mode numbers $n = 1$, $n = 10$, and $n = 100$.

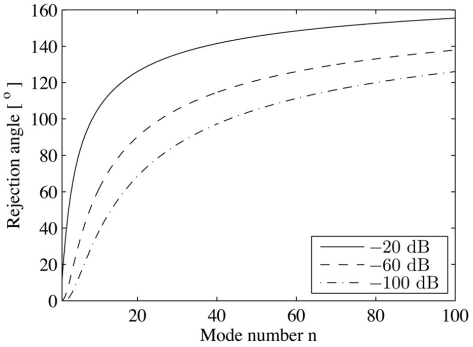

FIG. 4. The rejection angle in the long wavelength limit given by Eq. (48) plotted as a function of mode number $n \geq 1$. The radiated sound is only strictly zero at $\theta = 0$, so the angle is defined as the region in which the signal is decreased more than a specified amount, here given in dB relative to the maximum sound radiation for the given mode.

boundary conditions, but the analysis for the membrane is identical.

A. Displacement transfer function and radiation pattern for an arbitrary positioned harmonic point excitation

Following a method similar to the one used by Mellow *et al.*,[28] the transfer function describing the displacement response to a harmonic delta excitation of unit strength, i.e., the Green's function, may be expressed as an infinite series of eigenmodes:

$$G = \sum_{n=0}^{\infty} \sum_{m=0}^{\infty} A_{nm} \tilde{w}_{nm}(\varrho, \phi), \tag{49}$$

where $\tilde{w}_{nm}(\varrho, \phi)$ are the eigenfunctions given by Eq. (4) normalized by division with the modal amplitude constants A_{nm}. These constants may be found by substituting the Green's function in the wave equation corresponding to a unit point excitation at ϱ_0, ϕ_0, yielding

$$(D\nabla^4 - \rho_p h\omega^2 + \mathrm{i}\omega b)G = \frac{1}{\varrho}\delta(\varrho - \varrho_0)\delta(\phi - \phi_0). \tag{50}$$

Here, δ denotes the Dirac delta function and b is a damping constant for velocity dependent losses. The identity of the Laplace operator can be found using the following property of the undamped eigenfunctions:

$$\nabla^4 \tilde{w}_{nm}(\varrho, \phi) = \frac{\rho_p h \omega_{nm}^2}{D} \tilde{w}_{nm}(\varrho, \phi). \tag{51}$$

Inserting this result in Eq. (50) yields

$$\sum_{n=0}^{\infty} \sum_{m=0}^{\infty} A_{nm} \tilde{w}_{nm}(\varrho, \phi) = \frac{\delta(\varrho - \varrho_0)\delta(\phi - \phi_0)}{\varrho\{\rho_p h(\omega_{nm}^2 - \omega^2) + \mathrm{i}\omega b\}}. \tag{52}$$

The constants A_{nm} may now be found from Eq. (52) by multiplying by the complex conjugate of the eigenfunctions,

$\tilde{w}^*_{nm}(\varrho,\phi)$, integrating over the area of the radiator, and exploiting the orthogonality of the eigenfunctions:

$$A_{nm} = \frac{\tilde{w}^*_{nm}(\varrho_0,\phi_0)}{\{\rho_p h(\omega^2_{nm}-\omega^2)+\mathrm{i}\omega b\}||\tilde{w}_{nm}(\varrho,\phi)||^2}. \tag{53}$$

Here, $||\tilde{w}_{nm}(\varrho,\phi)||^2$ is the norm square given by

$$||\tilde{w}_{nm}(\varrho,\phi)||^2 = \int_0^a\int_0^{2\pi} \tilde{w}_{nm}(\varrho,\phi)\tilde{w}^*_{nm}(\varrho,\phi)\varrho\,\mathrm{d}\varrho\,\mathrm{d}\phi. \tag{54}$$

Using the dispersion relation $\kappa^2 = \rho_p h\omega^2/D$ and that $K=\kappa a$ yields

$$A_{nm} = \frac{a^2\tilde{w}^*_{nm}(\varrho_0,\phi_0)}{D(K^2_{nm}-K^2+\mathrm{i}K_{nm}K/Q)||\tilde{w}_{nm}(\varrho,\phi)||^2}, \tag{55}$$

where $Q=\rho h\omega_{nm}/b=\sqrt{\rho hD}K_{nm}/(ba)$ is the mechanical quality factor. Thus, the displacement transfer function for a harmonic point excitation at ϱ_0, ϕ_0 is

$$G = \sum_{n=0}^{\infty}\sum_{m=0}^{\infty}\frac{a^2\tilde{w}_{nm}(\varrho,\phi)\tilde{w}^*_{nm}(\varrho_0,\phi_0)}{D(K^2_{nm}-K^2+\mathrm{i}K_{nm}K/Q)||\tilde{w}_{nm}(\varrho,\phi)||^2}. \tag{56}$$

The far field radiation pattern is similarly found as an infinite sum of the contribution from each individual eigenmode weighted by the constants A_{nm} given in Eq. (55). Hence, the far field radiation pattern for a point excitation positioned at ϱ_0, ϕ_0 is

$$R = \sum_{n=0}^{\infty}\sum_{m=0}^{\infty}\frac{a^2R_{nm}(\eta,\phi_0)\tilde{w}^*_{nm}(\varrho_0,\phi_0)}{D(K^2_{nm}-K^2+\mathrm{i}K_{nm}K/Q)||\tilde{w}_{nm}(\varrho,\phi)||^2}, \tag{57}$$

where R_{nm} is given by Eq. (20). Note that the radiation pattern becomes a function of the mode shapes, which depends on the boundary conditions on the plate. Furthermore, since $K^2=\rho_p hc^2k^2a^2/D$, the exact radiation pattern will also depend on the dimensions and material properties of the plate as well as the speed of sound in the medium.

In Fig. 5, the on-axis response given by $||R||$ evaluated in $\theta=0$ is plotted as a function of K for the case of a clamped plate excited by a point source at the four different positions illustrated in Fig. 6, corresponding to $(\varrho_0,\phi_0)=(0,0),(a/4,0),(a/2,0)$, and $(3a/2,0)$. The damping is set using a constant quality factor of 100 for all eigenmodes to emulate a realistic scenario, and the plate dimensions and material have been chosen such that $K=ka$. This would correspond to, e.g., a micromachined silicon plate with $a=35\,\mu$m and $h=5\,\mu$m operating in air. In the calculation, the infinite sum in Eq. (57) is approximated by including all eigenmodes with $m=0$, 1, 2 and $n=0$, 1, 2, 3, 4, 5. The wavenumbers corresponding to these modes are listed in Table I, and includes all eigenmodes with wavenumbers below 12. Thus, in the considered range ($K\leq 10$) all contributing eigenmodes are included. As covered in the previous

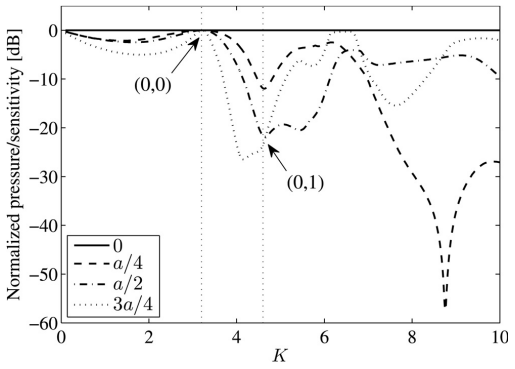

FIG. 5. Plot of the on-axis pressure/sensitivity of a clamped plate for four different positions of the point excitation. For each wavenumber, the pressure/sensitivity has been normalized to the direction having the maximum value. The first axisymmetric and non-axisymmetric modes, respectively, have been indicated in the figure.

analysis, no non-axisymmetric modes will contribute to the on-axis response, since it is strictly zero for these modes. However, they will alter the response for all other angles. To illustrate this, the on-axis response in Fig. 5 is normalized to the maximum value for each wavenumber and position of the point excitation. Figure 5 thereby shows the relative on-axis pressure or sensitivity and thus the effect of the non-axisymmetric modes.

When the point excitation is positioned at the center of the radiator, corresponding to the solid line in Fig. 5, the normalized pressure/sensitivity is 0 dB for all frequencies. Here, no non-axisymmetric modes are excited, resulting in a symmetric radiation pattern with the maximum located on the axis of the radiator. For the three remaining positions of the point excitation, the non-axisymmetric modes will contribute to the radiation pattern, and the maximum pressure/sensitivity is no

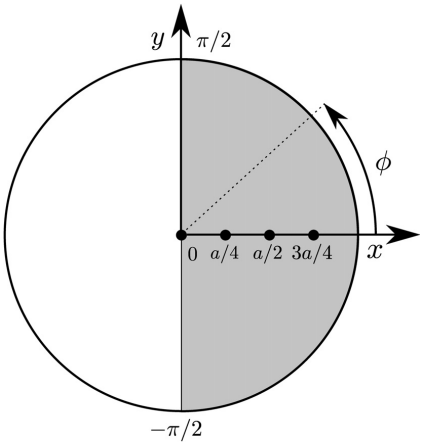

FIG. 6. Illustration of the two types of excitations used to actuate the plate: A point excitation at four different positions and a homogeneous pressure covering half the radiator (shaded region).

TABLE I. Values of K_{nm} for a clamped plate for $m = 0, 1, 2$ and $n = 0, 1, 2, 3, 4, 5$.

m/n	0	1	2	3	4	5
0	3.20	4.61	5.91	7.14	8.35	9.52
1	6.31	7.80	9.20	10.54	11.84	16.48
2	9.44	10.96	12.40	13.80	15.15	19.76

longer located on the axis of the radiator, resulting in dips in the relative on-axis response. Depending on the position of the point excitation, different modes will be accentuated, thereby accounting for the differences in the frequency dependency of the normalized response.

It should be noted that the on-axis response is 0 dB regardless of the position of the point excitation in two special cases: In the low-frequency limit and at the wavenumber corresponding to the first symmetric mode, i.e., the fundamental mode of the clamped plate. The position of this mode (0, 0) and the first non-axisymmetric mode (0, 1) has been indicated in Fig. 5.

B. Radiation pattern of a circular plate with a half-space excitation

The preceding analysis was carried out to emphasize the effect of a point excitation with increasing eccentricity. In practice, however, it is hard to realize such a point excitation. A more practical example would be that of a circular plate or membrane excited by a homogeneous pressure in one half-space of the radiator as illustrated by the shaded area in Fig. 6. This resembles the device proposed by You *et al.*,[21,22] where a micromachined plate is electrostatically actuated by a multi-electrode structure, which is split along the diameter of the radiator in order to allow actuation of non-axisymmetric modes. In this case, the external excitation may be described using the Heaviside step function

$$p_{\text{ext}} = H(\phi + \pi/2) - H(\phi - \pi/2), \tag{58}$$

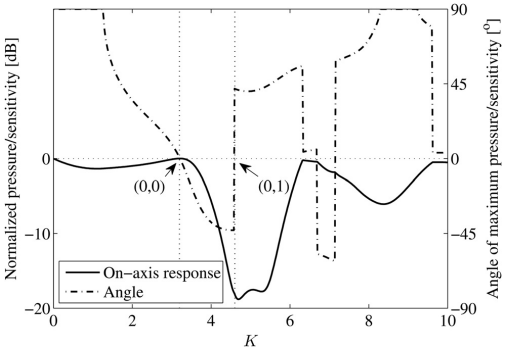

FIG. 7. Plot of the on-axis pressure/sensitivity and azimuthal angle of maximum pressure/sensitivity of a clamped plate excited by a homogeneous pressure covering half of the radiator. For each wavenumber, the on-axis pressure/sensitivity has been normalized to the direction having the maximum value. The first axisymmetric and non-axisymmetric mode, respectively, have been indicated in the figure.

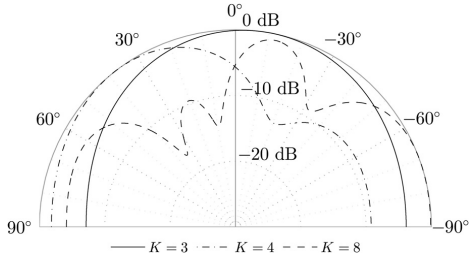

FIG. 8. Plot of the radiation pattern of a clamped plate excited by a homogeneous pressure covering half of the radiator for selected values of K.

denoting a unit pressure in the half-space of the radiator covered by the angle interval $\phi = [-\pi/2; \pi/2]$. Following the procedure used in the previous section yields the mode amplitude constants:

$$A_{nm} = \frac{a^2 \int_0^a \int_{-\pi/2}^{\pi/2} \tilde{w}_{nm}(\varrho, \phi) \tilde{w}^*_{nm}(\varrho, \phi) \varrho \, \mathrm{d}\varrho \, \mathrm{d}\phi}{D(K_{nm}^2 - K^2 + \mathrm{i}K_{nm}K/Q) ||\tilde{w}_{nm}(\varrho, \phi)||^2}. \tag{59}$$

The relative on-axis pressure/sensitivity for a clamped plate excited by a homogeneous pressure covering half of the radiator is plotted in Fig. 7 for wavenumbers $K \leq 10$. In the same plot, the azimuthal angle, θ, of maximum pressure/-sensitivity is given. The plate properties and number of modes included in the calculation are identical to the values utilized in the calculations using a point excitation.

The dips in the relative on-axis response observed for the non-axisymmetric point excitation are also seen for the half-space excitation. The relative on-axis response is close to 0 dB for wave numbers below the fundamental mode (0, 0), and the largest dip in the response appears at the first non-axisymmetric mode (1, 0). The azimuthal angle of maximum pressure/sensitivity is seen to be highly dependent on the wavenumber, and is only strictly zero at the fundamental mode (0, 0). The zero-crossings observed at higher wavenumbers are due to discontinuities.

The resulting radiation patterns for $K = 3, 4, 8$ are plotted in Fig. 8 along the x-direction indicated in Fig. 6. The selected wavenumbers demonstrate the behavior in the vicinity of the fundamental mode, between the fundamental mode and the first non-axisymmetric mode, and for higher order modes. In the vicinity of the fundamental mode, this mode dominates the response, and the radiation pattern resembles the axisymmetric pattern resulting from an axisymmetric excitation. Closer to the first non-axisymmetric mode, the radiation pattern develops a single dip, and the pattern is no longer axisymmetric. At higher wavenumbers, the contribution from the numerous non-axisymmetric modes become prominent, resulting in a complex radiation pattern.

VII. CONCLUSIONS

The modes of clamped and simply supported circular plates and circular membranes were found by solving the time dependent equation of motion corresponding to each

case. For the plate, this was described by the case of a circular disk with no biaxial in-plane stress, while the mode of the membrane was found assuming a thin disk with large biaxial in-plane stress. Using these modes, a concise analytical expression for the far field velocity potential was derived. From this, the radiation pattern for any mode was found, revealing a symmetry relation identical to the radiating mode. Furthermore, it was seen that the velocity potential for the non-axisymmetric modes was zero along the axis of the radiator. This behavior is caused by the regions of the plate or membrane vibrating out of phase for the non-axisymmetric modes.

To further elaborate on this nature of the modal radiation pattern, the long wavelength limit was analyzed, showing that the radiation pattern for all axisymmetric modes of both plates and membranes approaches that of a monopole. For the non-axisymmetric modes, the radiation pattern was seen to exhibit a rejection angle that increased with mode number, in which the sound radiation was negligible. Importantly, this nature of the radiation pattern in the long wavelength limit is shared by both plates and membranes, regardless of the boundary conditions. Hence, for many practical applications, the sound radiation from any plate or membrane may be approximated by the simple reduced expressions given for the long wavelength limit.

The implications of having a non-axisymmetric excitation of a clamped plate was demonstrated using both a point excitation with varying eccentricity and a homogeneous excitation acting on half of the circular radiator. The angle of maximum pressure or sensitivity was seen to be highly dependent on the position and frequency of the excitation, especially for frequencies above the fundamental eigenfrequency of the plate.

ACKNOWLEDGMENTS

This work is supported by the Danish National Advanced Technology Foundation (82-2012-4) and the Danish National Research Foundation's Center for Individual Nanoparticle Functionality (DNRF54).

APPENDIX

The trigonometric relation

$$\cos(n\phi + n\phi_0) = \cos(n\phi)\cos(n\phi_0) - \sin(n\phi)\sin(n\phi_0) \tag{A1}$$

may be used to rewrite Eq. (11) into $\mathcal{I}_1 = \mathcal{I}_{1A} - \mathcal{I}_{1B}$, where

$$\mathcal{I}_{1A} = \cos(n\phi_0)\int_0^{2\pi} \cos(n\phi)e^{\mathrm{i}k\varrho\sin\theta\cos\phi}\,\mathrm{d}\phi \tag{A2}$$

and

$$\mathcal{I}_{1B} = \sin(n\phi_0)\int_0^{2\pi} \sin(n\phi)e^{\mathrm{i}k\varrho\sin\theta\cos\phi}\,\mathrm{d}\phi. \tag{A3}$$

For symmetry reasons, the integral $\mathcal{I}_{1B}$ vanishes. Hence, the azimuthal dependence of the modes could just as well have been defined as $\cos[n(\phi - \phi_0)]$, since the sign in front of the phase term ϕ_0 does not change the result. The integral $\mathcal{I}_{1A}$ can be evaluated by exploiting the similarity to Bessel's integral given by[27]

$$\begin{aligned} J_n(z) &= \frac{\mathrm{i}^{-n}}{\pi}\int_0^{\pi} \cos(n\phi)e^{\mathrm{i}z\cos\phi}\,\mathrm{d}\phi \\ &= \frac{(-\mathrm{i})^{-n}}{\pi}\int_{\pi}^{2\pi} \cos(n\phi)e^{-\mathrm{i}z\cos\phi}\,\mathrm{d}\phi. \end{aligned} \tag{A4}$$

By splitting the integral $\mathcal{I}_{1A}$ into two integrations in the intervals $[0;\,\pi]$ and $[\pi;\,2\pi]$, it follows that

$$\mathcal{I}_1 = 2\pi\mathrm{i}^n\cos(n\phi_0)J_n(k\varrho\sin\theta), \tag{A5}$$

where $J_n(-z) = (-1)^n J_n(z)$ has been used.

[1]P. M. Morse and K. U. Ingard, *Theoretical Acoustics* (McGraw-Hill, New York, 1968), pp. 307–387.
[2]R. L. Pritchard, "Mutual acoustic impedance between radiators in an infinite rigid plane," J. Acoust. Soc. Am. **32**, 730–737 (1960).
[3]T. D. Mast and F. Yu, "Simplified expansions for radiation from a baffled circular piston," J. Acoust. Soc. Am. **118**, 3457–3464 (2005).
[4]L. L. Beranek and T. Mellow, *Acoustics: Sound Fields and Transducers* (Academic Press, Elsevier, Oxford, UK, 2012), pp. 170–174.
[5]D. L. Dekker, R. L. Piziali, and E. Dong, Jr., "Effect of boundary conditions on the ultrasonic-beam characteristics of circular disks," J. Acoust. Soc. Am. **56**, 87–93 (1974).
[6]P. A. Laura, "Directional characteristics of vibrating circular plates and membranes," J. Acoust. Soc. Am. **40**, 1031–1033 (1966).
[7]H. Stenzel, "Über die Berechnung des Schallfeldes von kreisförmigen membranen in starrer wand" ("On the calculation of the sound field of circular membranes in rigid walls"), Ann. Phys. **439**, 303–324 (1949).
[8]D. T. Porter, "Self- and mutual-radiation impedance and beam patterns for flexural disks in a rigid plane," J. Acoust. Soc. Am. **36**, 1154–1161 (1964).
[9]T. Mellow, "On the sound field of a resilient disk in an infinite baffle," J. Acoust. Soc. Am. **120**, 90–101 (2006).
[10]R. M. Aarts and A. J. E. M. Janssen, "Sound radiation quantities arising from a resilient circular radiator," J. Acoust. Soc. Am. **126**, 1776–1787 (2009).
[11]M. Greenspan, "Piston radiator: some extensions of the theory," J. Acoust. Soc. Am. **65**, 608–621 (1979).
[12]S. Timoshenko and S. Woinowsky-Krieger, *Theory of Plates and Shells*, 2nd ed. (McGraw-Hill, New York, 1959), pp. 55–92.
[13]J. A. Pelesko and D. H. Bernstein, *Modeling of MEMS and NEMS* (Chapman & Hall/CRC, London, UK, 2003), p. 36.
[14]H. Suzuki and J. Tichy, "Sound radiation from an elastically supported circular plate," J. Acoust. Soc. Am. **65**, 106–111 (1979).
[15]J. H. Streng, "Sound radiation from circular stretched membranes in free space," J. Audio Eng. Soc. **37**(3), 107–118 (1989).
[16]L. Shuyu, "Acoustic field of flexural circular plates for air-coupled ultrasonic transducers," Acta Acust. **86**, 388–391 (2000).
[17]P. R. Scheeper, A. G. H. van der Donk, W. Olthuis, and P. Bergveld, "A review of silicon microphones," Sens. Actuators, A **44**, 1–11 (1994).
[18]M.-C. Cheng, W.-S. Huang, and S. R.-S. Huang, "A silicon microspeaker for hearing instruments," J. Micromech. Microeng. **14**, 859–866 (2004).
[19]Ö. Oralkan, A. S. Ergun, J. A. Johnson, M. Karaman, U. Demirci, K. Kaviani, T. H. Lee, and B. T. Khuri-Yakub, "Capacitive micromachined ultrasonic transducers: next-generation arrays for acoustic imaging?," IEEE Trans. Ultrason., Ferroelectr., Freq. Control **49**(11), 1596–1610 (2002).
[20]A. S. Savoia, G. Caliano, and M. Pappalardo, "A CMUT probe for medical ultrasonography: From microfabrication to system integration," IEEE Trans. Ultrason., Ferroelectr., Freq. Control **59**(6), 1127–1138 (2012).
[21]W. You, E. Cretu, R. Rohling, and M. Cai, "Tiltable ultrasonic transducers: Concept, beamforming methods and simulation," IEEE Sens. J. **11**(10), 2286–2300 (2011).
[22]W. You, E. Cretu, and R. Rohling, "Super-resolution imaging using multi-electrode CMUTS: Theoretical design and simulation using point targets," IEEE Trans. Ultrason., Ferroelectr., Freq. Control **60**(11), 2295–2309 (2013).

[23]S. Alper and E. B. Magrab, "Radiation from the forced harmonic vibrations of a clamped circular plate in an acoustic fluid," J. Acoust. Soc. Am. **48**, 681–691 (1970).
[24]T. Wah, "Vibration of circular plates," J. Acoust. Soc. Am. **34**, 275–281 (1962).
[25]J. W. S. Rayleigh, *The Theory of Sound* (Dover, New York, 1945), Vol. II, Sec. 278.
[26]L. D. Landau and E. M. Lifshitz, *Theory of Elasticity (Course of Theoretical Physics Vol. 7*), 3rd ed. (Butterworth Heinemann, Oxford, UK, 1986), p. 43.
[27]M. Abramowitz and I. A. Stegun, *Handbook of Mathematical Functions with Formulas, Graphs, and Mathematical Tables* (Dover, New York, 1972), pp. 101–166.
[28]M. Mellow and L. Kärkkäinen, "On the sound field of a shallow spherical shell in an infinite baffle," J. Acoust. Soc. Am. **121**, 3527–3541 (2007).

PAPER D

Dimensional Scaling for Optimized CMUT Operations

Authors: Anders Lei, Søren Elmin Diederichsen, Mette Funding la Cour, Matthias Bo Stuart, **Thomas Lehrmann Christiansen**, Jørgen Arendt Jensen, and Erik Vilain Thomsen.

Published in: Proceedings of the IEEE International Ultrasonics Symposium, pp. 2595-2598, 2014.

Abstract

This work presents a dimensional scaling study using numerical simulations, where gap height and plate thickness of a CMUT cell is varied, while the lateral plate dimension is adjusted to maintain a constant transmit immersion center frequency of 5 MHz. Two cell configurations have been simulated, one with a single square cell and one with an infinite array of square cells. It is shown how the radiation impedance from neighboring cells has a significant impact on the design process. For transmit optimization, both plate dimensions and gap height should be increased. For receive mode, the gap height should be increased while the effect of plate dimensions is ambiguous depending on if the array design is closest to a single cell or infinite array of cells. The findings of the simulations are verified by acoustical measurements on two CMUT arrays with different plate dimensions.

Dimensional Scaling for Optimized CMUT Operations

Anders Lei*, Søren Elmin Diederichsen*, Mette Funding la Cour*†, Matthias Bo Stuart†
Thomas Lehrmann Christiansen*, Jørgen Arendt Jensen† and Erik Vilain Thomsen*
*Department of Micro and Nanotechnology, Technical University of Denmark, DK-2800 Kgs. Lyngby, Denmark
†Center for Fast Ultrasound Imaging, Department of Electrical Engineering, Technical University of Denmark, DK-2800 Kgs. Lyngby, Denmark

***Abstract*—This work presents a dimensional scaling study using numerical simulations, where gap height and plate thickness of a CMUT cell is varied, while the lateral plate dimension is adjusted to maintain a constant transmit immersion center frequency of 5 MHz. Two cell configurations have been simulated, one with a single square cell and one with an infinite array of square cells. It is shown how the radiation impedance from neighboring cells has a significant impact on the design process. For transmit optimization, both plate dimensions and gap height should be increased. For receive mode, the gap height should be increased while the effect of plate dimensions is ambiguous depending on if the array design is closest to a single cell or infinite array of cells. The findings of the simulations are verified by acoustical measurements on two CMUT arrays with different plate dimensions.**

I. Introduction

The potential benefits of utilizing capacitive micromachined ultrasonic transducer (CMUT) arrays in ultrasonic transducers are well discussed in the literature: large bandwidth, ease of fabrication, compatibility with CMOS, design flexibility, etc. All of these properties are nevertheless of secondary concern for imaging purposes, if the CMUT array is not capable of providing the necessary transmit pressure and receive sensitivity. It is therefore essential to understand how the transmit and receive sensitivity scales with the dimensions of the CMUT cell.

In the most basic configuration, there are three adjustable dimensional parameters for a CMUT cell: gap height, plate thickness and side length for a square cell. The two latter parameters determine the mechanical properties of the CMUT and are linked if a fixed resonant frequency of the CMUT cell is desired. The gap height determines the electrical properties of the CMUT, i.e. the capacitance and pull-in voltage; and thereby the required DC biasing and AC excitation voltage. The CMUT will typically be biased and operated at fixed fractions of the pull-in voltage. The result is that for a fixed immersion frequency, only two dimensional parameters can be adjusted independently: gap height and either plate thickness or side length. The aim of this work is to investigate the scaling properties between these parameters.

Numerous lumped element models of CMUTs are presented in the literature with varying degrees of complexity [1], [2]. The conventional advantage of the lumped model is that closed-form expressions can potentially be attained. This provides easy insight in how the performance scales with parameters and direct evaluation of a specific design. To achieve closed-form expressions, several assumptions are required [3]. The radiation impedance, and thus the overall damping of the system, is often assumed to equal the plane-wave radiation impedance. This assumption is valid for situations where the transducer is large relative to the wavelength. The element width of the CMUT array is typically on the order of maximum one wavelength (λ-pitch), and consists of several individual CMUT cells across; the plane wave assumption is hence not suitable for most CMUT designs.

Another way of analyzing the performance of a CMUT is to use numerical simulations such as finite element analysis (FEA) [4], [5]. FEA allows accurate simulation of the CMUT and in particular the medium loading and mutual radiation impedance for multiple cells. The disadvantage of FEA is that the computation time reaches a critical level, if more than just a few CMUT cells are to be analyzed.

This work will utilize two different FEA models to investigate the dimensional scaling: a single CMUT cell with no neighbors, and a CMUT cell in an infinite array of cells with a fixed spacing. Any actual CMUT array design will have characteristics that are in-between these two cell configurations. Since the transducer center frequency is determined by the medical imaging purpose, it is a fundamental requirement for the dimensional scaling analysis that the center frequency of the CMUT in immersion is constant. In this study, the center frequency in transmit is set to 5 MHz. The simulated results will be compared to experimental results from two fabricated CMUT arrays with different designs.

II. Finite Element Analysis

The FEA simulations are performed using the software COMSOL Multiphysics V4.4 (COMSOL AB, Sweden). The FEA model is a full electro-mechanical-acoustical setup with the physics/interfaces *Electromechanics (emi)* and *Pressure Acoustics, Frequency Domain (acpr)*. The first interface models the electro-mechanical interaction and deformation of the CMUT cell. The latter interface models the propagation of acoustic waves in the medium. COMSOL's own internal variables are used for coupling between the two interfaces.

The CMUT cell consists of a 2 µm thick mechanical silicon support representing the fixed bottom plate of the CMUT structure. The suspended top silicon plate of the CMUT with thickness t is separated from the bottom plate by a distance g. The top and bottom plate with a vacuum gap in-between has a side length of a. Both top and bottom plate extend further

2.5 µm outside the vacuum gap representing half the spacing (2.5 µm) to the neighboring cell. The material between the top and bottom plates in this cell spacing is silicon dioxide. To emulate realistic anchoring conditions, the model is only mechanically fixed at the lower boundary of the bottom plate and at the vertical boundary half distance to the neighboring cell.

The square geometry requires a 3D model, but only ¼ of the cell is simulated with symmetry boundaries to minimize the computation. The difference between the two configurations with either a single cell (SC), or an infinite array of cells (IAC) is the medium. A hemisphere medium with a perfectly matched layer (PML) as outer rim is used for SC. The PML layer absorbs all incoming pressure waves, so that no radiated waves are reflected. For IAC, a tube medium is used with the same footprint as the CMUT cell including the cell spacing. The walls of the tube have hard boundary conditions giving full reflections corresponding to the incoming pressure waves from neighboring cells. At the top of the tube, a PML block prevents reflections of waves, which corresponds to an infinite medium.

The essential condition of a constant 5 MHz immersion transmit center frequency required a feedback loop between dimensional parameters and the simulated transmit spectrum. This feedback was achieved by controlling COMSOL through MATLAB (MathWorks, Inc., Natick, MA, USA). A simulation sequence was thus conducted by setting a gap height, plate thickness and side length. The pull-in voltage was determined for this design and fixed fractions of the pull-in voltage were used for the DC and AC voltages, 80% and 50%, respectively. The transmit spectrum was simulated and the center frequency extracted. The feedback loop then changed the plate side length and the simulation sequence was repeated until a transmit center frequency of 5 MHz in immersion was achieved.

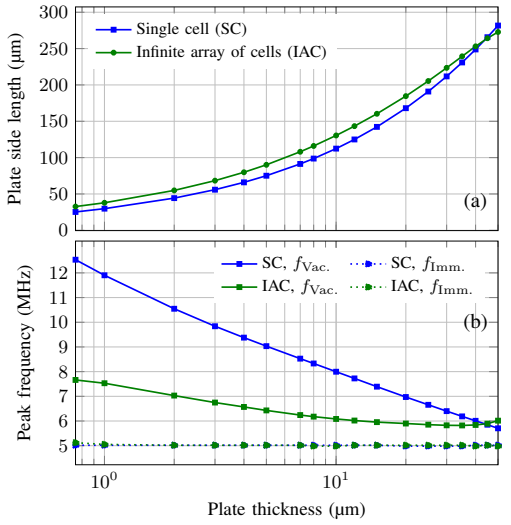

Fig. 1. (a) Plate side length and (b) Vacuum ($f_{\mathrm{Vac.}}$) and immersion ($f_{\mathrm{Imm.}}$) peak frequencies for single and infinite array of cells as function of plate thickness. The feedback loop in the FEA adjust the plate side length to ensure a constant immersion frequency of 5 MHz.

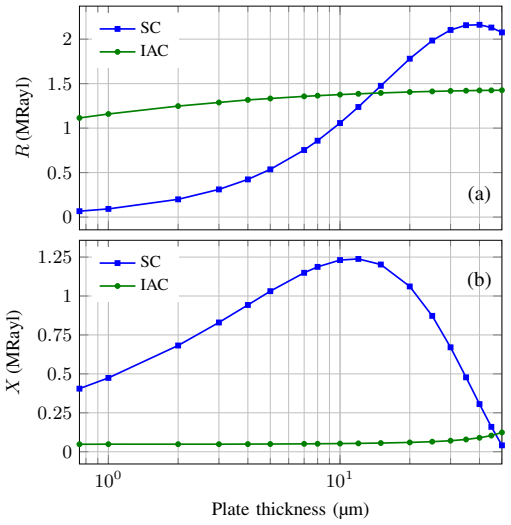

Fig. 2. (a) Real/resistive and (b) imaginary/reactive part of the simulated radiation impedance as function of plate thickness at 5 MHz.

A. FEA Results

The feedback effect of the FEA simulations is seen in Fig. 1(a) where the plate side length is plotted as function of the logarithmic plate thickness. One plate thickness thus results in different plate side lengths depending on SC or IAC configuration. This difference is further emphasized in Fig. 1(b), where the simulated peak frequencies for both vacuum and immersion are plotted. While the feedback loop ensures the required immersion frequency of 5 MHz, the frequency shift from vacuum to immersion differs significantly between the two configurations. The frequency shift between vacuum and immersion is due to the interaction with the medium, and it is thus clear that the impact of the medium is depending on neighboring cells.

The difference in interaction with the medium for the two cell configurations is analyzed in Fig. 2, where the real/resistive (R) and imaginary/reactive (X) parts of the simulated radiation impedance ($Z_{\mathrm{a}} = R + iX$) at 5 MHz are plotted as function of plate thickness. For thick plates with side lengths comparable to or larger than the wavelength ($\lambda \approx 480$ µm), the radiation impedance is expected to approach the plane wave impedance. For a plane wave, the impedance is purely real and equals the characteristic impedance (Z_0) of the medium. Water is used as medium in the simulation with $Z_0 \approx 1.5$ MRayl. With a resistive part close to Z_0 and a small reactive part relative to SC, the impedance for IAC is close to that of a plane wave. The smaller reactive part for IAC compared to SC is what mainly causes the difference in frequency shift from vacuum to immersion between the two configurations in Fig. 1(b). Where the reactive part gives a frequency shift, the resistive part of Z_{a} mainly affects the overall damping of the CMUT.

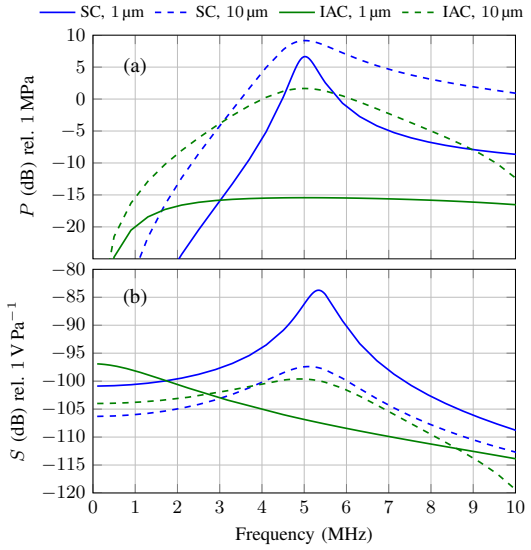

Fig. 3. (a) Transmit and (b) receive sensitivity spectrum for both single and infinite array of cells with 200 nm gap height and plate thicknesses of 1 µm and 10 µm.

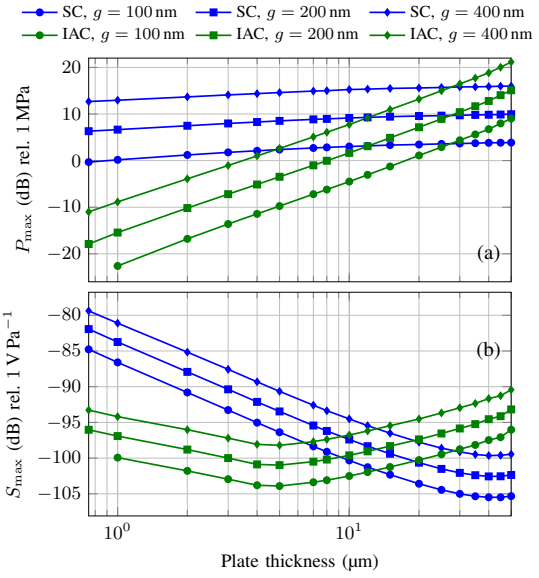

Fig. 4. (a) Peak transmit pressure and (b) peak receive sensitivity for SC and IAC with three different gap heights as function of plate thickness.

This is illustrated in Fig. 3(a) where the simulated average cell surface pressure is plotted as function of frequency for two different plate thicknesses with a gap height of 200 nm. The two solid lines are for a plate thickness of 1 µm. The considerably higher resistive impedance for IAC compared to SC seen in Fig. 2(a), causes a damping effect with lower peak pressure amplitude as consequence. The high medium loading relative to the mechanical impedance for IAC with thin plates causes the CMUT to become over-damped. The transmitted pressure approaches zero for low frequencies since there can exist no static pressure in the medium. The plate deflection however increases for decreasing frequency according to an over-damped oscillator. For a 10 µm thick plate (dashed lines) the mechanical impedance is increased and the difference in resistive impedance between IAC and SC is less (see Fig. 2(a)). The result is that IAC becomes under-damped with a resonance peak, and the difference in pressure amplitude relative to SC is lower.

The receive sensitivity in voltage readout ($\mathrm{d}V/\mathrm{d}P$) for the same CMUT designs as in Fig. 3(a) is seen in Fig. 3(b). The small upwards shift ($\approx$ 0.3 MHz) in center frequency for SC with $t = 1\,\mu\mathrm{m}$ compared to transmit is due to a change in mechanical impedance caused by the difference in force distribution from the electrostatic force in transmit to a uniform incoming pressure distribution in receive. The over-damping for the IAC with thin plate is more clearly seen in the receive sensitivity since it follows the deflection characteristics of an over-damped system. For thicker plates, the IAC becomes under-damped and exhibits a resonance peak around the transmit center frequency.

The full dimensional FEA scaling study is seen in Fig. 4, where the extracted peak surface pressure and peak receive sensitivity, are plotted as function of plate thickness for three different gap heights. The pressure scaling in Fig. 4(a) shows similar tendency for both SC and IAC with increasing pressure for thicker plates and larger gap height. This scaling follows intuition as thicker plates with larger area equals higher mass and more inertia. Increasing the gap height means one can apply a higher voltage and thereby increase the potential energy of the system.

The dimensional scaling of the receive sensitivity is seen in Fig. 4(b). The sensitivity for both SC and IAC is as expected improved for increasing gap height due to higher applicable voltages and hence charge on the plates. For SC, the sensitivity is increasing for decreasing plate thickness. This is expected, since a lower thickness means less mass and therefore lower mechanical impedance. The decreasing sensitivity tendency levels off for thick plates due the maximum in resistive impedance for SC seen in Fig. 2(a). For IAC, the sensitivity is also decreasing with thickness until $\approx 5\,\mu\mathrm{m}$ where it begins to increase. The turning point corresponds to the thickness

TABLE I. SUMMARIZED SCALING TRENDS FROM FIG. 4.

	Single cell		Infinite array of cells	
	TX	RX	TX	RX
Scaling plate thickness (dB) 1 µm → 2 µm	0.8	-4.2	5.3	-1.9
Scaling gap height (dB) 200 nm → 400 nm	6.2	2.8	6.3	3.8

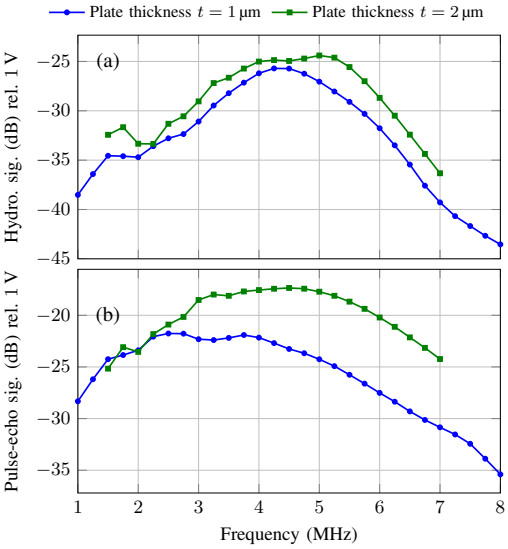

Fig. 5. (a) Hydrophone and (b) pulse-echo measurements for two CMUT arrays with different plate thicknesses.

where the mechanical impedance reaches the critical value that changes the CMUT from under-damped to over-damped. The thickness where the SC and IAC receive scaling lines with same gap height intersect, corresponds to the thickness where the resistive impedance of SC and IAC intersects in Fig. 2(a). A summary of the scaling trends is listed in Table I.

III. Experimental Results

Two different square cell CMUT arrays with plate thicknesses of $1\,\mu m$ and $2\,\mu m$ and plate side lengths of $35\,\mu m$ and $49\,\mu m$, respectively, were fabricated using the process described in [6]. Both arrays have the same element area. The acoustic measurements were carried out using the experimental Synthetic Aperture Real-time Ultrasound System (SARUS) [7] and performed in vegetable oil for electrical insulation of the uncoated device. Hydrophone and pulse-echo measurements were performed at a $10\,mm$ distance from the transducer surface. The hydrophone used was an Optel 5 MHz hydrophone (Optel, Wroclaw, Poland) and the plane reflector a $40\,mm$ thick Polyvinylchlorid plate. A narrowband, 8 periods excitation was used with a frequency step of $250\,kHz$ with the RMS signal taken as the average of 16 center array elements.

TABLE II. Summarized results from hydrophone and pulse-echo spectrum in Fig. 5.

	$t = 1\,\mu m$		$t = 2\,\mu m$	
	TX	TX→RX	TX	TX→RX
Peak values (dB)	-25.7	-21.8	-24.4	-17.4
Center frequency (MHz)	4.43	3.57	4.51	4.41
Fractional bandwidth (%)	70	140	77	108

The measured spectra for the two arrays are seen in Fig. 5 with summarized results in Table II. The difference in peak hydrophone signal amplitude of $1.3\,dB$ between the two arrays is within the expected range of $0.8\,dB$ to $5.3\,dB$ in Table I for SC and IAC, respectively. The pulse-echo center frequency decreases $\approx 0.9\,MHz$ for the $1\,\mu m$ thick plate. This follows the FEA simulations in Fig. 3(b) and Fig. 4(b) where plates with thicknesses less than $\approx 5\,\mu m$ becomes increasingly over-damped due to a lower mechanical impedance. The peak pulse-echo signal amplitude is more than $4\,dB$ higher for the thicker plate due to an increase in the total product of both the transmit and receive sensitivity spectrum. This result is in agreement with the FEA scaling trends in Table I.

IV. Conclusion

A dimensional scaling study using numerical simulations of square CMUT cells with a constant transmit immersion frequency of $5\,MHz$ has been presented. Two cell configurations have been studied: a single cell and an infinite array of cells. Any real CMUT array design will behave within these two extremes. It is demonstrated how the mutual radiation impedance from neighboring cells affects both the transmit and receive sensitivity spectrum. To optimize the transmit sensitivity, the plate size and gap height should be increased. For the receive sensitivity, the gap height should be increased while the scaling on plate size is dependent on the actual CMUT array design. The conclusions from the numerical simulations are validated by acoustical measurements on two fabricated CMUT arrays with plate thicknesses of $1\,\mu m$ and $2\,\mu m$, respectively.

Acknowledgment

This work was financially supported by the Danish National Advanced Technology Foundation (82-2012-4).

References

[1] I. Wygant, M. Kupnik, and B. Khuri-Yakub, "Analytically calculating membrane displacement and the equivalent circuit model of a circular CMUT cell," in *IEEE Ultrasonics Symposium, 2008. IUS 2008*, Nov. 2008, pp. 2111–2114.

[2] H. Koymen, A. Atalar, E. Aydogdu, C. Kocabas, H. Oguz, S. Olcum, A. Ozgurluk, and A. Unlugedik, "An improved lumped element nonlinear circuit model for a circular CMUT cell," *IEEE Transactions on Ultrasonics, Ferroelectrics, and Frequency Control*, vol. 59, no. 8, pp. 1791–1799, Aug. 2012.

[3] I. Wygant, M. Kupnik, and B. Khuri-Yakub, "CMUT design equations for optimizing noise figure and source pressure," in *IEEE Ultrasonics Symposium, 2009. IUS 2009*, 2009.

[4] K. K. Park and B. T. Khuri-Yakub, "Dynamic response of an array of flexural plates in acoustic medium," *The Journal of the Acoustical Society of America*, vol. 132, no. 4, pp. 2292–2303, Oct. 2012.

[5] H. Oguz, A. Atalar, and H. Koymen, "Equivalent circuit-based analysis of CMUT cell dynamics in arrays," *IEEE Transactions on Ultrasonics, Ferroelectrics, and Frequency Control*, vol. 60, no. 5, pp. 1016–1024, May 2013.

[6] M. F. la Cour, M. B. Stuart, M. B. Laursen, S. E. Diederichsen, E. V. Thomsen, and J. A. Jensen, "Investigation of PDMS as coating on CMUTs for imaging," in *IEEE Ultrasonics Symposium, 2014. IUS 2014*, 2014.

[7] J. A. Jensen, H. Holten-Lund, R. Nilsson, M. Hansen, U. Larsen, R. Domsten, B. Tomov, M. Stuart, S. Nikolov, M. Pihl, Y. Du, J. Rasmussen, and M. Rasmussen, "SARUS: A synthetic aperture real-time ultrasound system," *IEEE Transactions on Ultrasonics, Ferroelectrics, and Frequency Control*, vol. 60, no. 9, pp. 1838–1852, Sep. 2013.

PAPER E

Electrostatic and Small-Signal Analysis of CMUTs with Circular and Square Anisotropic Plates

Authors: Mette Funding la Cour, **Thomas Lehrmann Christiansen**, Jørgen Arendt Jensen, and Erik Vilain Thomsen.

Accepted for: IEEE Transactions on Ultrasonics, Ferroelectrics, and Frequency Control, May 2015.

Abstract

Traditionally, Capacitive Micromachined Ultrasonic Transducers (CMUTs) are modeled using the isotropic plate equation and this leads to deviations between analytical calculations and Finite Element Modeling (FEM). In this paper, the deflection is calculated for both circular and square plates using the full anisotropic plate equation. It is shown that the anisotropic calculations match excellently with FEM, while an isotropic approach causes up to $10\,\%$ deviations in deflection. For circular plates an exact solution can be found. For square plates using the Galerkin method, and utilizing the symmetry of the silicon crystal, a compact and accurate expression for the deflection can be obtained. The deviation from FEM in center deflection is $< 0.1\,\%$. The theory of multilayer plates is also applied to the CMUT. The deflection of a square plate was measured on fabricated CMUTs using a white light interferometer. Fitting the plate parameter for the anisotropic calculated deflection to the measurement, a deviation of $0.07\,\%$ is seen. Electrostatic and small-signal dynamic analysis are performed using energy considerations including anisotropy. The stable position, effective spring constant, pull-in distance and pull-in voltage are found for both circular and square anisotropic plates, and the pressure dependence is included by comparing to the corresponding analysis for a parallel plate. Measurements on fabricated devices with both circular and square plates subjected to increasing bias voltage are performed, and it is observed that the models including anisotropic effects are within the uncertainty interval of the measurements. Finally, a lumped element small-signal model for both circular and square anisotropic plates is derived to describe the dynamics of the CMUT.

Electrostatic and Small-Signal Analysis of CMUTs with Circular and Square Anisotropic Plates

Mette Funding la Cour*†, Thomas Lehrmann Christiansen† Jørgen Arendt Jensen* and Erik Vilain Thomsen†
*Center for Fast Ultrasound Imaging, Department of Electrical Engineering, Technical University of Denmark, DK-2800 Kgs. Lyngby, Denmark
†Department of Micro and Nanotechnology, Technical University of Denmark, DK-2800 Kgs. Lyngby, Denmark

***Abstract*—Traditionally, Capacitive Micromachined Ultrasonic Transducers (CMUTs) are modeled using the isotropic plate equation and this leads to deviations between analytical calculations and Finite Element Modeling (FEM). In this paper, the deflection is calculated for both circular and square plates using the full anisotropic plate equation. It is shown that the anisotropic calculations match excellently with FEM, while an isotropic approach causes up to 10 % deviations in deflection. For circular plates an exact solution can be found. For square plates using the Galerkin method, and utilizing the symmetry of the silicon crystal, a compact and accurate expression for the deflection can be obtained. The deviation from FEM in center deflection is < 0.1 %. The theory of multilayer plates is also applied to the CMUT. The deflection of a square plate was measured on fabricated CMUTs using a white light interferometer. Fitting the plate parameter for the anisotropic calculated deflection to the measurement, a deviation of 0.07 % is seen. Electrostatic and small-signal dynamic analysis are performed using energy considerations including anisotropy. The stable position, effective spring constant, pull-in distance and pull-in voltage are found for both circular and square anisotropic plates, and the pressure dependence is included by comparing to the corresponding analysis for a parallel plate. Measurements on fabricated devices with both circular and square plates subjected to increasing bias voltage are performed, and it is observed that the models including anisotropic effects are within the uncertainty interval of the measurements. Finally, a lumped element small-signal model for both circular and square anisotropic plates is derived to describe the dynamics of the CMUT.**

I. Introduction

Precise modeling of capacitive micromachined ultrasonic transducers (CMUT) is important for an efficient design process. A CMUT consists of two plates where one of them is fixed and the other can deflect. The deflection $w(x, y)$ of the movable plate is an important parameter that influences several basic CMUT parameters such as pull-in voltage and capacitance. Most existing analytical approaches use the isotropic plate equation to calculate the deflection [1], [2]. However, when using fusion bonding fabrication technology [3], the plate usually consists of crystalline silicon. Having a silicon (001) substrate, which are most often used, Young's modulus and Poisson's ratio are strongly anisotropic. The isotropic approach is then not correct, and can result in deviations in the deflection compared to finite element modeling (FEM) taking the anisotropy into account. Therefore, to get precise modeling of these CMUTs, the anisotropy of silicon needs to be considered.

The first decade after CMUTs were invented, various analytical models were presented for circular cells [4], [5], [6]. However, these were based on parallel plate approximations for the deflection leading only to estimates of the critical CMUT parameters. Later, the actual deflection of the movable plate clamped at the edges was taken into account [2], [7], [8], and used for calculating pull-in voltage and deriving an equivalent circuit model. The effect from having a non-uniform load on the plate was included in [7] who used superposition and a concentrically loaded plate, and by [9] who used the Galerkin method. The non-uniform load occurs when the bias voltage is increased, as the electrostatic force will be greater where the gap is smaller. This effect gets more distinct when the deflection is larger. However, it is not necessary to include for the typical CMUT case, where the plate never deflect more than half the gap due to pull-in.

All of these models assume a circular plate geometry of the CMUT cells. For circular plates, a simple and exact solution for the deflection exists [10], but this is not the case for square plates. Existing solutions for the deflection of square plates is based on series expansions with either trigonometric [11] or polynomial basis functions [12]. None of these, however, take the anisotropy of the plate into account.

After the fusion bonding fabrication method was applied to CMUTs, the anisotropy of the plate was considered [13]. The anisotropy was not included analytically in the modeling, but FEM was used to estimate a set of material parameters (Young's modulus and Poisson's ratio) to use in the models to get an approximation as close as possible to the correct anisotropic solution.

This paper presents solutions to the full anisotropic plate equation for both circular and square plates used in fusion bonded CMUTs. The models were initially presented in [14] for an anisotropic plate with circular geometry, and this was then modified and expanded to include square plates as well in [15]. For the circular cells, the symmetry reduces the plate equation and an exact solution for the anisotropic case can be obtained similar to the isotropic solution. The approach used to solve the equation for the square plate is the Galerkin method [16]. Utilizing the symmetry of the silicon crystal, a compact and precise approximation of the deflection of a square plate can be obtained for the anisotropic case.

The CMUT plate usually consists of more than one material. The theory of laminar plates is described in [17], [18] and in this paper, the multilayer plate theory including anisotropy

is applied to calculate important parameters for a two layer silicon/metal plate typically used for CMUTs.

Having found the deflection of the CMUT plate, a model for the static and small-signal dynamic behavior of the transducer can be set up. Circular cells have been investigated thoroughly during the years and a full model for this plate geometry has recently been presented [8], whereas the full analysis for the square plate has not been investigated previously. Furthermore, none of the existing models include the anisotropy.

This paper is orginized as follows: The isotropic plate equation and solutions for circular and square plates can be found in Section II. It is followed by a presentation of the anisotropic plate equation in Section III and the symmetry of the silicon crystal is utilized to reduce and solve the problem for both circular and square plates. The calculated deflection is compared to the solution for corresponding isotropic cases and FEM. The theory of multilayered plates are applied to a common CMUT case in Section IV and compared to measurements performed on a fabricated device. Section V considers the energies of a CMUT. These are used in Section VI to find the stable position, effective spring constant, pull-in distance and pull-in voltage. The pressure dependence is also included. Measurements of the stable position are performed on devices with both circular and square plates and the theory is compared to these. Section VII presents the small-signal dynamic model for both circular and square shaped CMUTs.

II. The Isotropic Plate Equation

Conventionally, the deflection $w(x,y)$ of a CMUT with a thin plate is modeled using the isotropic plate equation [11]

$$\frac{\partial^4 w}{\partial x^4} + 2\frac{\partial^4 w}{\partial x^2 \partial y^2} + \frac{\partial^4 w}{\partial y^4} = \frac{p}{D_\mathrm{i}}, \tag{1}$$

where p is the applied pressure difference across the plate and the flexural rigidity is given by

$$D_\mathrm{i} = \frac{E}{12\left(1-\nu^2\right)} h^3, \tag{2}$$

with E being Young's modulus, ν being Poisson's ratio, and h being the thickness of the plate.

For thin clamped circular plates, an exact solution exists. For such a plate with radius a, the center deflection is given by [10]

$$w_{0,\mathrm{iso,circ}} = \frac{1}{64}\frac{a^4 p}{D_\mathrm{i}}. \tag{3}$$

For clamped rectangular and square plates, no simple exact solution exists and approximate methods must be used. The conventional isotropic approach is based on a series expansion of the deflection, and the center deflection for a thin clamped square plate having side length $2L$ is [11]

$$w_{0,\mathrm{iso,sq}} = 0.020245\frac{L^4 p}{D_\mathrm{i}}. \tag{4}$$

Fig. 1 shows a cross sectional view of a CMUT cell with an applied voltage. The device parameters are illustrated for both circular and square plates.

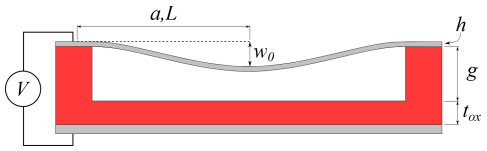

Fig. 1. Cross sectional view of CMUT cell with applied voltage.

TABLE I
Room temperature (300K) compliance coefficients for n-type crystalline silicon measured by [21] for a substrate with low doping level (150 Ω-cm, $\sim 2.8\times10^{13}$ cm^{-3}) and high doping level (3.26 mΩ-cm, $\sim 2.1\times10^{19}$ cm^{-3}).

	Low doping	High doping
s^c_{11}	7.691×10^{-12} Pa^{-1}	7.858×10^{-12} Pa^{-1}
s^c_{12}	-2.1420×10^{-12} Pa^{-1}	-2.2254×10^{-12} Pa^{-1}
s^c_{44}	12.577×10^{-12} Pa^{-1}	12.628×10^{-12} Pa^{-1}

III. The Anisotropic Plate Equation

To take the anisotropy of the plate into account and avoid the inaccuracy from isotropic modeling, the stiffness of the plate must be described through the stiffness matrix of the material instead of Young's modulus and Poisson's ratio. The starting point is the relation between stress, σ, and strain, ϵ, [19]

$$\sigma^\mathrm{c} = \mathbf{c}^\mathrm{c}\epsilon^\mathrm{c}, \text{ or } \epsilon^\mathrm{c} = \mathbf{s}^\mathrm{c}\sigma^\mathrm{c}. \tag{5}$$

Here superscript c denotes the crystallographic coordinate system, so $\mathbf{c}^\mathrm{c}$ is the stiffness matrix and $\mathbf{s}^\mathrm{c} = (\mathbf{c}^\mathrm{c})^{-1}$ the compliance matrix in this coordinate system. Having a thin plate, the stresses in the z direction can be ignored and plane stress assumed. Using the Voigt notation, the relation between strain and stress then becomes [20]

$$\begin{pmatrix}\varepsilon_1\\ \varepsilon_2\\ \varepsilon_6\end{pmatrix} = \begin{pmatrix}s_{11} & s_{12} & s_{16}\\ s_{12} & s_{22} & s_{26}\\ s_{16} & s_{26} & s_{66}\end{pmatrix}\begin{pmatrix}\sigma_1\\ \sigma_2\\ \sigma_6\end{pmatrix} = \mathbf{S}_\mathrm{eff}\begin{pmatrix}\sigma_1\\ \sigma_2\\ \sigma_6\end{pmatrix}, \tag{6}$$

and we can define an effective stiffness matrix from the effective compliance matrix

$$\mathbf{C}_\mathrm{eff} = \left(\mathbf{S}_\mathrm{eff}\right)^{-1}. \tag{7}$$

For silicon, the effective compliance matrix is

$$\mathbf{S}^\mathrm{c}_\mathrm{eff} = \begin{pmatrix}s^\mathrm{c}_{11} & s^\mathrm{c}_{12} & 0\\ s^\mathrm{c}_{12} & s^\mathrm{c}_{11} & 0\\ 0 & 0 & s^\mathrm{c}_{44}\end{pmatrix}. \tag{8}$$

The elements in this matrix are known from measurements and shown in Table I [21]. It is noted that the elements in (8) are known in the crystallographic coordinate system, which is not necessarily the same as the coordinate system of the plate. To illustrate this further, the crystallographic and the plate coordinate systems can be seen in Fig. 2. The solid coordinate

system aligned to the $\langle 100 \rangle$ directions is where the compliance values for silicon are known and the dashed system shows the rotated coordinate system for the plate where the compliance values needs to be calculated. Having silicon as plate material and performing standard cleanroom fabrication, the plate will usually be on a (001) substrate and aligned to the primary wafer flat. Flat alignment is to the $[110]$ direction, so the plate coordinate system will be rotated $\psi = 45°$ with respect to the crystallographic coordinate system. A transformation of the compliance matrix between the two coordinate systems is therefore needed. As it is the stiffness matrix elements that are to be used in the plate equation, the resulting effective stiffness matrix for the present case can be expressed through (7) [20]

$$C^{\text{eff}}_{\text{Si(001),[110]}} = \begin{pmatrix} \frac{1}{s^{\text{c}}_{44}} + \frac{1}{2(s^{\text{c}}_{11}+s^{\text{c}}_{12})} & \frac{1}{2(s^{\text{c}}_{11}+s^{\text{c}}_{12})} - \frac{1}{s^{\text{c}}_{44}} & 0 \\ \frac{1}{2(s^{\text{c}}_{11}+s^{\text{c}}_{12})} - \frac{1}{s^{\text{c}}_{44}} & \frac{1}{s^{\text{c}}_{44}} + \frac{1}{2(s^{\text{c}}_{11}+s^{\text{c}}_{12})} & 0 \\ 0 & 0 & \frac{1}{2s^{\text{c}}_{11}-2s^{\text{c}}_{12}} \end{pmatrix}. \quad (9)$$

It is seen that the stiffness matrix has an orthotropic symmetry.

Having the effective stiffness matrix, the generalized plate equation can be used. This is a differential equation for the deflection, $w(x, y)$, of a thin anisotropic plate exposed to a uniform load p given by [20], [22]

$$\frac{\partial^4 w}{\partial x^4} + k_1 \frac{\partial^4 w}{\partial x^3 \partial y} + k_2 \frac{\partial^4 w}{\partial x^2 \partial y^2} + k_3 \frac{\partial^4 w}{\partial x \partial y^3} + k_4 \frac{\partial^4 w}{\partial y^4} = \frac{p}{D_{\text{a}}}. \quad (10)$$

The plate coefficients k_1-k_4 and the anisotropic flexural rigidity, D_{a}, depend on the elastic constants of the plate material

$$k_1 = \frac{4C^{\text{eff}}_{13}}{C^{\text{eff}}_{11}} \quad k_2 = \frac{2\left(C^{\text{eff}}_{12}+2C^{\text{eff}}_{33}\right)}{C^{\text{eff}}_{11}} \quad k_3 = \frac{4C^{\text{eff}}_{23}}{C^{\text{eff}}_{11}}$$
$$k_4 = \frac{C^{\text{eff}}_{22}}{C^{\text{eff}}_{11}} \quad D_{\text{a}} = \frac{1}{12} h^3 C^{\text{eff}}_{11}, \quad (11)$$

where C^{eff}_{pq} are elements in the effective stiffness matrix (9). Note that the stiffness of the plate is no longer expressed through Young's modulus and Poisson's ratio but directly through the stiffness values.

Using the compliance values for silicon (Table I) and inserting the stiffness elements in (9) into (11), it follows that $k_1 = k_3 = 0$ and $k_4 = 1$. Thus, aligning the plate to the primary flat simplifies the anisotropic plate equation (10) to

$$\frac{\partial^4 w}{\partial x^4} + k_2 \frac{\partial^4 w}{\partial x^2 \partial y^2} + \frac{\partial^4 w}{\partial y^4} = \frac{p}{D_{\text{a}}}. \quad (12)$$

The same is the case for aligning the plate along the [100] direction where the inverse of (8) is used instead of (9), resulting in the same values for k_1, k_3 and k_4. For these two special cases, the coefficients in the plate equation are summarized in Table II for both high and low doping levels of the substrate.

A. Deflection of Circular plates

The solution to (10) for a circular plate of radius a fixed at the boundary is easily obtained using polar coordinates. The deflection at a point a distance r from the center is given by [10]

$$\frac{w(r)}{w_0} = \left(1 - \left(\frac{r}{a}\right)^2\right)^2. \quad (13)$$

This expression is similar to the deflection for the isotropic case, however, the center deflection is different

$$w_{0,\text{circ}} = \frac{1}{8\left(3 + k_2 + 3k_4\right)} \frac{a^4 p}{D_{\text{a}}}. \quad (14)$$

By combining (3) and (14) it is possible to find an effective flexural rigidity

$$D_{\text{eff}} = \frac{3 + k_2 + 3k_4}{8} D_{\text{a}}. \quad (15)$$

This can be used to easily change from the isotropic plate equation to the anisotropic plate equation in already existing analytical models of CMUTs. An example of this will be shown in section VI. Using the plate coefficient values from Table II for a highly doped (001) silicon plate aligned to the $\langle 110 \rangle$ direction, the effective flexural rigidity becomes $D_{\text{eff}} = 0.91551 D_{\text{a}}$.

To compare the anisotropic model with the isotropic approach and FEM simulations, the normalized deflection of a CMUT exposed to a pressure difference is shown in Fig. 3. The FEM simulations were performed in COMSOL Multiphysics version 4.2a using the full anisotropic stiffness tensor and the curves are normalized to the center deflection of this. The isotropic curves are made using (13) and (3) and Young's modulus and Poisson's ratio along the [100] and [110] directions (see Table III) to give the dash and dashdot lines, respectively. The anisotropic solution is made using (13)

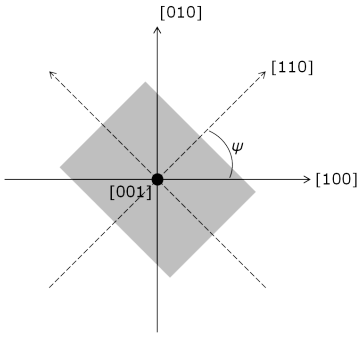

Fig. 2. The two coordinate systems. Solid lines are the crystallographic system aligned to the $\langle 100 \rangle$ direction and the dashed lines the plate system aligned to the $\langle 110 \rangle$ direction.

TABLE III
YOUNG'S MODULUS AND POISSON'S RATIO FOR SILICON (001).

	Young's modulus	Poisson's ratio
[100] direction	130 GPa	0.278
[110] direction	169 GPa	0.062
Mean value	148 GPa	0.177

TABLE II
SELECTED VALUES FOR THE PLATE COEFFICIENTS AND ANISOTROPIC FLEXURAL RIGIDITY FOR PLATES ON A SILICON (001) SUBSTRATE [20]. UPPER VALUES IN BRACKETS ARE FOR LOW DOPING LEVEL AND LOWER VALUES FOR HIGH DOPING LEVEL.

Orientation	ψ	k_1	k_2	k_3	k_4	$12D_a/h^3$[GPa]
[100]	0	0	2.8133 ± 0.0006 2.8559 ± 0.0006	0	1	140.96 ± 0.03 138.35 ± 0.03
[110]	$\pi/4$	0	1.3241 ± 0.0004 1.2949 ± 0.0004	0	1	169.62 ± 0.03 167.96 ± 0.03

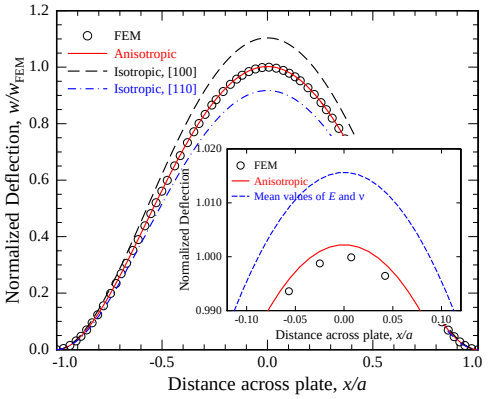

Fig. 3. Normalized deflection cross section ($y = 0$) of a thin circular plate of silicon (001) calculated with (13) using both the isotropic approach (3) with Young's modulus and Poisson's ratio in the [100] and [110] directions and the anisotropic approach (14). The circles represent the deflection calculated by FEM.

and (14) and is shown as a solid curve. This is on top of the FEM simulation (circles). Due to the symmetry of the circular plate, any set of parameters from Table II can be used. Excellent agreement between the anisotropic solution and the finite element calculation is seen with an error of less than 0.3%, which is due to grid size and slightly different boundary conditions. The figure also shows that using Young's modulus and Poisson's ratio corresponding to [100] or [110] directions lead to errors in the center deflection of around 10%. To reduce this error, it is common practice to use mean values of Young's modulus and Poisson's ratio (see Table III) which decreases the error to around 1.5%. As it can be hard to see the solutions with small deviations from the FEM, a zoom in on the center region of the plate is shown in the insert in Fig. 3. Here the reduction in deviation from FEM by using the anisotropic solution compared to the isotropic mean values of Young's modulus and Poisson's ratio is clearly visible. Using the anisotropic approach for a thin circular CMUT plate on a (001) silicon substrate is simple and the result is exact.

B. Deflection of Square Plates

Having a square plate makes analytical deflection calculations complicated and approximate methods must be used to solve the anisotropic plate equation. With the anisotropic approach, the Galerkin method [16] can be used to find approximate expressions for the deflection of a thin anisotropic square plate. As previously stated, in the most common case for CMUTs, the plate is fabricated on a silicon (001) substrate and aligned to the [110] direction. For this orthotropic square plate with sidelengths $2L$, the relative deflection is found to be [20], [23]

$$\frac{w(x,y)}{w_0} = \left[1-\left(\frac{x}{L}\right)^2\right]^2\left[1-\left(\frac{y}{L}\right)^2\right]^2 \times\left[1+\beta\left(\frac{x}{L}\right)^2+\beta\left(\frac{y}{L}\right)^2\right], \tag{16}$$

where the plate parameter β is defined as

$$\beta = \frac{182+143k_2}{1432+91k_2}. \tag{17}$$

The center deflection can be written

$$w_{0,\mathrm{sq,Si(001)}} = \frac{77(1432+91k_2)}{256(16220+11k_2(329+13k_2))}\frac{L^4p}{D_\mathrm{a}}. \tag{18}$$

Equations (16)-(18) are also valid when the plate is aligned to the [100] direction on a silicon (001) substrate. Note that the center deflection depends only on the k_2 coefficient. For primary flat alignment and inserting k_2 from Table II into (17) give $\beta_{\mathrm{low}} = 0.23920$ for the low doing case ($k_2 = 1.3241$) or $\beta_{\mathrm{high}} = 0.23691$ for the high doping case ($k_2 = 1.2949$). For the low doping case, this results in a normalized deflection for the plate aligned to the $\langle 110\rangle$ direction given by

$$\left.\frac{w(x,y)}{w_0}\right|_{\mathrm{sq,Si(001),\langle 110\rangle}} = \left[1-(x/L)^2\right]^2\left[1-(y/L)^2\right]^2 \times\left[1+0.23920\left[(x/L)^2+(y/L)^2\right]\right], \tag{19}$$

and the center deflection becomes

$$w_{0,\mathrm{sq,Si(001),\langle 110\rangle}} = 0.02196\frac{L^4p}{D_\mathrm{a}}. \tag{20}$$

For the high doping case, the factor in front in (20) becomes 0.02204 for the center deflection. Comparing (4) and (20), it is seen that they contain the same parameters but have different coefficients, and that (20) has the anisotropic instead of the isotropic flexural rigidity.

Fig. 4 shows the deflection cross section through $y = 0$ of a square plate of silicon (001) given by the reduced version of (16)

$$w_{y=0,\mathrm{sq}} = w_0\left[1-(x/L)^2\right]^2\left[1+\beta\,(x/L)^2\right]. \tag{21}$$

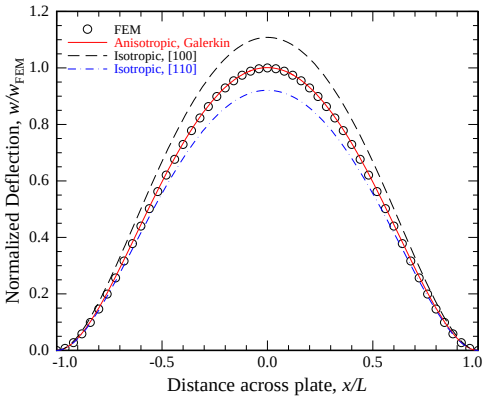

Fig. 4. Normalized deflection cross section ($y = 0$) of a square plate of silicon (001) calculated with (21) using both the isotropic approach (4) with Young's modulus and Poisson's ratio in the [100] and [110] directions and the anisotropic approach (20). The circles represent the deflection calculated by FEM.

The deflection calculated with the anisotropic approach uses $k_2 = 1.3241$ in (17) and center deflection (20) (solid curve). This is compared to the isotropic approach using $k_2 = 2$ in (17) and center deflection (4), with Young's modulus and Poisson's ratio in the [100] and [110] directions (dash and dashdot curves, respectively), and to a finite element (FEM) simulation using the full anisotropic compliance matrix (compliance coefficients from Table I) in COMSOL (circles). The calculated deflections are normalized to the FEM center deflection. Excellent agreement is shown between the anisotropic curve and FEM with a deviation of less than 0.1 % whereas the isotropic approach leads to deviations in the center deflection of around 10 % for both [100] and [110] directions.

IV. Anisotropic Multilayer Plates

The theory for multilayered plates has classically been addressed for both isotropic [17] and anisotropic [18] plates. For CMUTs, the isotropic case for circular plates was included in [1] and for square plates it was included in [12]. Following the method by [17], [18] the anisotropic plate theory for CMUTs can be expanded to also include plates consisting of more than one layer. Starting from equations for the moment and stress resultants, it can be found that the general plate equation including anisotropic effects has the same form as for the single layer plate (10), however, the plate coefficients $k_1 - k_4$ and the plate stiffness D_a will be different to capture effects from having a multilayer plate. The anisotropic multilayer plate theory is in the following applied to a common CMUT case so that it easily can be used in further calculations.

For the CMUT application, the multilayer plate will often consist of two layers with silicon as the main part and a thin aluminum layer on top for contacts. The aluminum is an isotropic material and the silicon is, as seen on (8), an orthotropic material (when aligned to [110] direction on a (001) substrate). For this two-layer plate, the total thickness is called h and the ratio $\alpha = h_\mathrm{Al}/h$ is defined from the thickness of the aluminum, h_Al. When the plate is all silicon $\alpha = 0$ and when the plate is only aluminum $\alpha = 1$. Again utilizing the symmetry of the materials, it can be found that $k_1 = k_3 = 0$ and $k_4 = 1$ so only k_2 and D_a need to be taken into account.

Using the compliance values for highly doped silicon in Table I and Young's modulus of $E = 70$ GPa and Poisson's ratio of $\nu = 0.35$ for aluminum in the expressions for k_2 and the plate stiffness, which has been omitted due to their length, yields

$$D_\mathrm{AlSi} = (13.9963\ \mathrm{GPa} - 22.0458\ \mathrm{GPa} \cdot \alpha)h^3 \tag{22}$$

$$k_{2,\mathrm{AlSi}} = 1.29493 + 1.00464\alpha. \tag{23}$$

Furthermore, it can be found that for a sufficiently thin aluminum layer, $\alpha < 0.2$, a series expansion can be used and simple correction formulas can be derived. This way, the flexural rigidity of the combined aluminum and silicon plate compared to the flexural rigidity of a pure silicon plate with the same total thickness can be expressed as

$$\frac{D_\mathrm{AlSi}}{D_\mathrm{Si}} = 1 - 1.575\alpha. \tag{24}$$

Similarly, for the plate parameter k_2 it is found that

$$\frac{k_{2,\mathrm{AlSi}}}{k_{2,\mathrm{Si}}} = 1 - 0.775822\alpha. \tag{25}$$

Equations (24) and (25) both use the stiffness values for highly doped silicon from Table I.

For a circular plate, the relative center deflection using the same method as above can be found to be

$$\frac{w_{0,\mathrm{AlSi,circ}}}{w_{0,\mathrm{Si,circ}}} = 1 + 1.437\alpha. \tag{26}$$

Doing the same for square plates the relation becomes

$$\frac{w_{0,\mathrm{AlSi,Sq}}}{w_{0,\mathrm{Si,Sq}}} = 1 + 1.445\alpha. \tag{27}$$

The error between the series expansion and the full result for the center deflection is less than 2 % for $\alpha = 0.2$ for both plate geometries. An example of a typical thicknesses of the layers of the CMUT multilayer plate is $\sim$2 μm silicon and $\sim$0.2 μm aluminum. This gives $\alpha = 0.1$ and the error when using the series expansion is less than 0.5 %.

As examples on how the aluminum layer influences the plate parameter, stiffness, and center deflection of the circular and square plates, calculations using single and multilayer plate theory can be seen in Table IV. Here, calculations are made with dimensions identical to the fabricated devices found in Table V. It is seen that including the aluminum layer in the calculations affects k_2 with around 7 %, the stiffness of the plate with around 18 % and the center deflection with around 12 %.

The importance of using the multilayer plate theory can be seen by comparing calculated center deflections using the two layer Si-Al plate and a single layer plate of Si. Using typical values for CMUTs with a 2 µm Si layer and a 0.2 µm Al layer and (27), will result in a difference in center deflection of 13 %.

TABLE IV
EXAMPLES ON k_2, STIFFNESS AND CENTER DEFLECTION WHEN USING SINGLE OR MULTILAYER PLATE THEORY.

	α	k_2	$12D_a/h^3$	w_0
Circ., multi	0.10	1.3954	141.50 GPa	29.4 nm
Circ., Si	-	1.2949	167.96 GPa	25.7 nm
Sq., multi	0.08	1.3753	146.79 GPa	12.5 nm
Sq., Si	-	1.2949	167.96 GPa	11.2 nm

TABLE V
DIMENSIONS OF DEVICES FABRICATED WITH CIRCULAR AND SQUARE PLATES USING WAFER BONDING.

	Circular	Square
Size (a, L)	36 μm	32.5 μm
Plate thickness, Si h_{Si}	1.8 μm	2.3 μm
Al thickness h_{Al}	200 nm	200 nm
Gap height (vacuum) g	(uncertain)	405 nm
Insulation layer t_{ox}	195 nm	198 nm

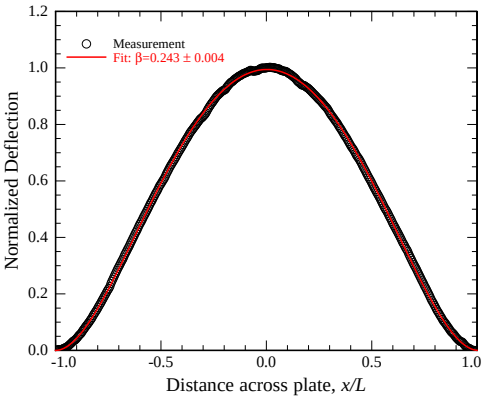

Fig. 5. Normalized deflection cross section ($y = 0$) from measurement on a fabricated CMUT with square plate of silicon (001) aligned to [110]. The red curve is a fit made from (21).

A. Deflection Measurement

To further validate the deflection of the anisotropic multilayer square plate, CMUTs devices have been fabricated using fusion bonding [24]. The dimensions of the fabricated device can be seen in Table V. The deflection was measured with a Sensofar PLu Neox 3D Optical Profiler using white light interferometry. Fig. 5 shows a measured cross section of the normalized deflection for a fabricated device. It is normalized in both center deflection and distance across the plate to compare the shape of the measured deflection with the calculated deflection. The red curve is a fit made to the measurements using the anisotropic model (21). The plate parameter β is fitted to the measurements. As it is seen in the figure, the fitted value for β is 0.243. Using (23) for calculating β for this multilayer plate (2 μm highly doped silicon (001) substrate aligned to [110] direction with 200 nm Al) a deviation of only 0.07 % is obtained.

It should be noted that this theory does not take stress in the layers of the plate and charging effects into account. Stress in the layers and charging can cause deviations, which were, however, not observed in the measurements. Charging will be difficult to predict, as it is dependent on the actual device being used. The charging will affect the deflection of the plate, as it causes deviations in the electric field in the CMUT.

V. ENERGY CONSIDERATIONS

The plate deflection derived in the previous sections can be used to calculate the energy stored in the CMUT. In the following, the total energy will be expressed using lumped parameters, and the governing equations of the CMUT are derived. The subsequent sections will use these to analyze static and small-signal dynamic behavior of the CMUT.

Assuming a loss-less system, the total energy stored in the transducer can be characterized by four terms

$$U_{t,m} = U_s + U_{kin} - U_e - U_p \,. \tag{28}$$

The two first terms are contributed by the internal energy of the plate, which is comprised of the potential energy or strain energy, U_s, as well as the kinetic energy, U_{kin}, due to the plate inertia. U_e is the electrical energy stored in the capacitor formed by the top electrode and the bottom electrode. It is subtracted, since this energy originates from work done *on* the system by the voltage V. The same argument goes for U_p, which is the work done on the system by the external pressure, p.

Using lumped parameters, the total stored energy in the CMUT is

$$U_{t,m} = \frac{1}{2}k_0 w_0^2 + \frac{1}{2}m_0\left(\frac{\partial w_0}{\partial t}\right)^2 - \frac{1}{2}V^2 C(w_0) - p w_0 A_0 \,, \tag{29}$$

where k_0 is the lumped spring constant that comes from the calculation of the strain energy, A_0 is the lumped area of the plates i.e. the area that goes into calculation of the work performed by deflecting the plate due to applied pressure, V is the applied voltage, p the external pressure, C the capacitance of the device and w_0 the center deflection of the plate, which is used as a reference in this work (any deflection could be used as a reference).

The stored energy is seen to be a function of three dependent variables, one for each of the three domains of the transducer: V (electrical), w_0 (mechanical), and p (acoustical). All three dependent variables have time t as the independent variable. The stored energy in the electrical and acoustical domains are found by adjusting the signs to account for the change in the definition of work and internal energy

$$U_{\mathrm{t,e}} = -\frac{1}{2}k_0 w_0^2 - \frac{1}{2}m_0\left(\frac{\partial w_0}{\partial t}\right)^2 + \frac{1}{2}V^2 C(w_0) - pw_0 A_0 \tag{30}$$

$$U_{\mathrm{t,a}} = -\frac{1}{2}k_0 w_0^2 - \frac{1}{2}m_0\left(\frac{\partial w_0}{\partial t}\right)^2 - \frac{1}{2}V^2 C(w_0) + pw_0 A_0 \ . \tag{31}$$

From (29), (30), and (31) it is possible to derive one governing equation for each of the three domains. This is achieved by differentiating the stored energy in each domain with respect to its corresponding variable, yielding the charge Q (electrical), force F (mechanical), and volume displacement W (acoustical)

$$Q = \frac{\partial U_{\mathrm{t,e}}}{\partial V} = VC(w_0) \tag{32}$$

$$F = \frac{\partial U_{\mathrm{t,m}}}{\partial w_0} = k_0 w_0 + m_0\frac{\partial^2 w_0}{\partial t^2} - \frac{1}{2}V^2\frac{\partial}{\partial w_0}C(w_0) - pA_0 \tag{33}$$

$$W = \frac{\partial U_{\mathrm{t,a}}}{\partial p} = w_0 A_0 \ . \tag{34}$$

Eqs. (32)-(34) provide a non-linear description of the transducer behavior. Based on these equations, the following two sections will give a static and a dynamic analysis of a CMUT.

VI. Electrostatic Analysis

By using the solutions found in the previous sections and performing electrostatic analysis, it is possible to find the stable position of the plate, when applying a certain bias voltage. The stable position is the position where the spring force balances the electrostatic and pressure forces. From this the pull-in distance and pull-in voltage can be found. The derivation is initially done using the implicit lumped parameters k_0 and A_0. The explicit values are derived afterwards.

For the static case, the total force on the system, F_{t}, is given by (33) with the second term set to zero

$$F_{\mathrm{t}} = k_0 w_0 - pA_0 - \frac{1}{2}V^2 C'(w_0), \tag{35}$$

where $C'(w_0)$ denotes the capacitance differentiated with respect to w_0. The stable position of the plate can be found for a given applied voltage as the point where the total force is zero, i.e. solving

$$k_0 w_0 = pA_0 + \frac{1}{2}V^2 C'(w_0). \tag{36}$$

The effective spring constant, k_{eff}, can be found by differentiating the total force with respect to the center deflection

$$k_{\mathrm{eff}} = \frac{\partial F_{\mathrm{t}}}{\partial w_0} = k_0 - \frac{1}{2}V^2 C''(w_0). \tag{37}$$

Pull-in occurs when the effective spring constant is zero and the pull-in voltage V_{PI} can be expressed as

$$V_{\mathrm{PI}} = \sqrt{\frac{2k_0}{C''(w_0)}}. \tag{38}$$

Inserting the pull-in voltage (38) into the equation for the stable position (36) the pull-in distance can be found by solving the equation

$$k_0 w_0 = pA_0 + \frac{k_0 C'(w_0)}{C''(w_0)}. \tag{39}$$

The solution can then be inserted into (38) to obtain the pull-in voltage. Finding pull-in distance and voltage is therefore a question of solving the two equations (36) and (39) for the two variables.

In the following, this analysis is shown for both circular and square plates, with the anisotropic effects taken into account, and for a parallel plate capacitor for comparison. A similar analysis has previously been shown by others for isotropic circular plates e.g. [2], [8] and is therefore shown here in compact form with focus on the anisotropy of the plate.

A. Capacitance

An important variable in the electrostatic analysis for CMUTs is the capacitance. The capacitance at zero deflection, C_0, of the plate can for both the circular and square plates be divided into two contributions: The capacitance from the vacuum gap $C_{\mathrm{vac}} = \epsilon_0 A/g$ and the capacitance from the insulation oxide between the electrodes $C_{\mathrm{ox}} = \epsilon_0\epsilon_{\mathrm{ox}}A/t_{\mathrm{ox}}$. A is the area of the plate, g the vacuum gap, ϵ_0 the vacuum permittivity, t_{ox} the thickness of the insulation oxide layer, and ϵ_{ox} the relative permittivity of the oxide. The effect from having both contributions can be collected in an effective gap height

$$g_{\mathrm{eff}} = g + \frac{t_{\mathrm{ox}}}{\epsilon_{\mathrm{ox}}}. \tag{40}$$

The total capacitance at zero deflection can then be written

$$C_0 = \left(\frac{1}{C_{\mathrm{vac}}} + \frac{1}{C_{\mathrm{ox}}}\right)^{-1} = \frac{\epsilon_0 A}{g_{\mathrm{eff}}}. \tag{41}$$

Taking the deflection of the plate into account, the total capacitance of the device is

$$C = \frac{1}{g_{\mathrm{eff}}}\iint \frac{\epsilon_0}{1-\eta f(x,y)}\,\mathrm{d}x\,\mathrm{d}y \tag{42}$$

where $\eta = w_0/g_{\mathrm{eff}}$ is the normalized center deflection and $f(x,y)$ is a function describing the shape of the deflection. For circular plates, this function will be (13), for square plates it is (19), and for the parallel plate $f = 1$.

The total capacitance of a parallel plate capacitor is given by

$$C_{\mathrm{parallel}} = C_0\frac{1}{1-\eta}. \tag{43}$$

For the circular plate, the integral can be solved analytically and the total capacitance becomes [2], [8]

$$C_{\mathrm{circ}} = C_0\sqrt{\frac{1}{\eta}}\,\operatorname{arctanh}\sqrt{\eta}. \tag{44}$$

For the square plate, there is no analytical solution. The integration in (42) can instead be performed numerically. The total capacitance for this plate can be written

$$C_{\mathrm{sq}} = C_0 f_s(\eta). \tag{45}$$

where $f_s(\eta)$ is a function describing the shape of the capacitance curve. Various functions can be used as the shape function, e.g. spline fit to the numerically found solution, a higher order polynomial fit or an interpolation function. A Taylor expansion can also be used, however, at least 8 terms is needed to get sufficient accuracy.

To obtain simpler expressions that can be used for further calculations for the square plate, it is advantageous to look at where the capacitance is used and compare with results for the parallel plate. Inspecting (36)-(39) it is seen that in order to find the stable position, the effective spring constant, the pull-in voltage, and the pull-in distance, the functions $f_s'(\eta)$, $f_s''(\eta)$, $1/f_s''(\eta)$ and $f_s'(\eta)/f_s''(\eta)$ must be used. For the parallel plate, using the normalized capacitance from (43) to obtain the shape function for this plate type, the expressions will have the form

$$f_s(\eta) = \frac{1}{1-\eta}, \quad f_s'(\eta) = \frac{1}{(1-\eta)^2}, \quad f_s''(\eta) = \frac{2}{(1-\eta)^3},$$
$$1/f_s''(\eta) = \frac{1}{2}(1-\eta)^3, \quad f_s'(\eta)/f_s''(\eta) = \frac{1}{2}(1-\eta). \tag{46}$$

All of these expressions for the parallel plate capacitor contain $(1-\eta)$. Changing this to a second order polynomial, $(1 - a\eta - b\eta^2)$, the coefficients a and b can be found for the square plate to match each of the equations in (46) by fitting to the numerically found solution for the capacitance. This way, the following expressions can be used as approximations for the square plate capacitance in the equations in the next sections

$$f_s(\eta) = \frac{1}{1 - 0.296\eta - 0.136\eta^2} \tag{47}$$
$$f_s'(\eta) = \frac{1}{(1.813 - 1.050\eta - 0.299\eta^2)^2} \tag{48}$$
$$f_s''(\eta) = \frac{1}{(1.405 - 0.953\eta - 0.271\eta^2)^3} \tag{49}$$
$$1/f_s''(\eta) = (1.405 - 0.953\eta - 0.271\eta^2)^3 \tag{50}$$
$$f_s'(\eta)/f_s''(\eta) = \frac{1}{1.211 + 0.647\eta + 2.906\eta^2} \tag{51}$$

Using these will result in deviations from the numerical solution of less than 0.05 %, 0.08 %, 0.3 % and 2 %, respectively. Note that the polynomial fits are only valid for relative deflections of 0-0.5, i.e. below pull-in. A plot showing how the polynomials are fitted can be seen in Fig. 6, where the circles show the numerically found solutions for the capacitance and its derivatives and the curves show the fits. Expressions for the derivatives of the circular plate capacitance, (44), can be found in [8].

Fig. 7 shows the total capacitance normalized to the total capacitance with no deflection, C/C_0, versus the relative deflection, η, for all three plate types. For the square plate shape function, the numerically found solution is shown in the plot. It is seen that when normalized, the circular and square plates have similar capacitance responses. For example, at a relative deflection of 0.4 the deviation is 1.4% between the square and circular capacitance, whereas using the parallel plate approximation results in a much larger difference as seen in the figure. For the square plate the polynomial solution from (47) is shown in Fig. 7 as circles.

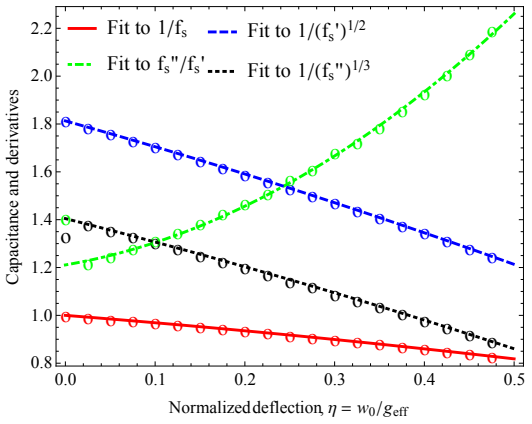

Fig. 6. Capacitance for the square plate and its derivatives. The circles show the numerically found solutions and the curves the second order fits.

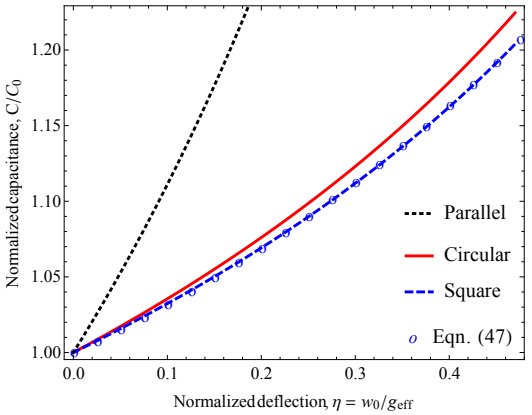

Fig. 7. Normalized total capacitance versus normalized deflection for a circular (44) and a square plate (45). The parallel plate solution (43) shown for comparison. The polynimial solution for the square plate is shown as circles.

B. Lumped Parameter Calculations

The total strain energy is calculated by integrating the strain energy density using (6) and (9). Having a thin plate, we can assume plane stress and the expression becomes

$$U_\mathrm{s} = \frac{1}{2}\iiint (\sigma_1\varepsilon_1 + \sigma_2\varepsilon_2 + \sigma_6\varepsilon_6)\,\mathrm{d}x\,\mathrm{d}y\,\mathrm{d}z, \tag{52}$$

where the strains are given by

$$\epsilon_1 = -z\frac{\partial^2 w(x,y)}{\partial x^2}, \epsilon_2 = -z\frac{\partial^2 w(x,y)}{\partial y^2}, \epsilon_6 = -2z\frac{\partial^2 w(x,y)}{\partial x \partial y}. \tag{53}$$

The energy due to the externally applied pressure is calculated as the work performed (i.e. force times length, here pressure times area times length) when deflecting the plate

$$U_\mathrm{p} = \iint p w(x,y)\,\mathrm{d}x\,\mathrm{d}y. \tag{54}$$

The electrostatic energy is expressed through the charge Q or applied voltage V, the vacuum permittivity ϵ_0, gap height g_{eff} and the total capacitance C of the device

$$\begin{aligned} U_{\text{e}} &= \frac{1}{2}V^2C \\ &= \frac{1}{2}V^2 \iint \frac{\epsilon_0}{g_{\text{eff}} - w(x,y)}\,\mathrm{d}x\,\mathrm{d}y \end{aligned} \tag{55}$$

The capacitance inserted during the second equality in (55) is valid for all plate geometries if the right expression for the deflection is used in each case. It can be seen how the deflection of the plate appears, and therefore the plate geometry and the anisotropy of the plate is included through the deflection.

For a circular plate (52) becomes

$$\begin{aligned} U_{\text{s,circ}} &= \frac{1}{2}\int_{-h/2}^{h/2}\int_0^{2\pi}\int_0^a r\left(\sigma_1\varepsilon_1 + \sigma_2\varepsilon_2 + \sigma_6\varepsilon_6\right)\,\mathrm{d}r\,\mathrm{d}\theta\,\mathrm{d}z \\ &= \frac{h^3\pi w_0^2}{9a^2}\left(3C_{11}^{\text{eff}} + 2C_{12}^{\text{eff}} + 3C_{22}^{\text{eff}} + 4C_{33}^{\text{eff}}\right), \end{aligned} \tag{56}$$

and (54) and (55) become [2]

$$U_{\text{p,circ}} = -\int_0^a 2\pi prw dr = -\frac{1}{3}\pi pa^2w_0 \tag{57}$$

$$U_{\text{e,circ}} = -\frac{1}{2}CV^2 = -\frac{1}{2}V^2C_0\sqrt{\frac{1}{\eta}}\,\operatorname{arctanh}\sqrt{\eta}. \tag{58}$$

Using (11) it can be seen that the strain energy can be written in terms of the effective flexural rigidity

$$U_{\text{s,circ}} = \frac{h^3\pi w_0^2}{9a^2}\left(3 + k_2 + 3k_4\right)\frac{12D_{\text{a}}}{h^3} = \frac{32\pi D_{\text{eff}}w_0^2}{3a^2} \tag{59}$$

By changing the flexural rigidity, it is possible to easily switch between isotropic and anisotropic calculations in (59).

Comparing (59) and (57) with (29), it can be seen that for the circular plate the lumped spring constant and the lumped area are given by

$$k_{0,\text{circ}} = \frac{2\cdot 32D_{\text{eff}}\pi}{3a^2} = \frac{64D_{\text{eff}}\pi}{3a^2} \tag{60}$$

$$A_{0,\text{circ}} = \frac{1}{3}\pi a^2. \tag{61}$$

For the square plate, only the most common case with a highly doped plate on silicon (001) substrate aligned to the $\langle 110\rangle$ direction is considered. Using the deflection from (19), the strain energy for the square plate becomes

$$\begin{aligned} U_{\text{s,sq}} &= \frac{1}{2}\int_{-h/2}^{h/2}\int_{-L}^{L}\int_{-L}^{L}\left(\sigma_1\varepsilon_1 + \sigma_2\varepsilon_2 + \sigma_6\varepsilon_6\right)\,\mathrm{d}x\,\mathrm{d}y\,\mathrm{d}z \\ &= \frac{4096h^3w_0^2}{4729725L^2}\left(\gamma_1C_{11}^{\text{eff}} + 2\gamma_2C_{12}^{\text{eff}} + \gamma_1C_{22}^{\text{eff}} + 4\gamma_2C_{33}^{\text{eff}}\right), \end{aligned} \tag{62}$$

$$\gamma_1 = \left(1001 + 468\beta + 476\beta^2\right), \quad \gamma_2 = 26\left(11 + 2\beta^2\right).$$

Using the value for β_{high}, $\gamma_1 = 1138.5$ and $\gamma_2 = 288.9$. Inserting the plate coefficients from (11) into (62), it can be seen that the strain energy can be written in terms of the plate coefficients and the anisotropic flexural rigidity

$$U_{\text{s,sq}} = \frac{49152}{4729725}\left(\gamma_1 + \gamma_2k_2 + \gamma_1k_4\right)\frac{D_{\text{a}}w_0^2}{L^2}, \tag{63}$$

Using the values from Table II, the strain energy for the square plate of silicon (001) aligned to the $\langle 110\rangle$ direction becomes

$$U_{\text{s,sq,Si(001),[110]}} = \xi_{\text{s}}\frac{h^3w_0^2}{L^2}, \tag{64}$$

where the constant is $\xi_{\text{s}} = 385.637$ GPa.

The energy contribution from applied pressure (54) is for this case given by

$$U_{\text{p,sq}} = -\int_{-L}^{L}\int_{-L}^{L} pw(x,y)\;dxdy \tag{65}$$

$$U_{\text{p,sq,Si(001),[110]}} = -\xi_{\text{p}}pL^2w_0. \tag{66}$$

where $\xi_{\text{p}} = 1.215$.

The electrostatic energy can in this square plate case not be found exact as an approximation is needed for the total capacitance. Using the result from (45) this energy contribution can be expressed as

$$U_{\text{e,sq}} = -\frac{1}{2}V^2C_0f_s(\eta). \tag{67}$$

Comparing (64) and (66) with (29), it is seen that for the square plate the lumped spring constant and the lumped area are given by

$$k_{0,\text{sq}} = \frac{2\cdot\xi_{\text{s}}h^3}{L^2} = \frac{2h^3\xi_{\text{s}}}{L^2} \tag{68}$$

$$A_{0,\text{sq}} = \xi_{\text{p}}L^2. \tag{69}$$

C. Effective Spring Constant

As mentioned earlier, the effective spring constant can be found by performing a differentiation of the total force with respect to the center deflection, see (37). The lumped spring constant can be identified from the strain energy for both circular and square plates, (60) and (68), and for the parallel plate the spring constant is simply just k. All these expressions can be inserted into the effective spring constant (37) to obtain the effective spring constant for each plate type. The effect of spring softening is identified as the second term in (37), and it is seen to depend on the capacitance. Furthermore, it is seen that the spring constant at zero applied voltage is the lumped spring constant.

In Fig. 8, the effective spring constant relative to the spring constant at zero applied voltage k_{eff}/k_0 is shown versus the normalized relative deflection $\eta/\eta_{\text{PI,p0}}$ (lower axis) or normalized voltage (upper axis). The spring softening effect is clearly seen as the effective spring constant becomes smaller when the deflection and bias voltage increases. Again the circular and square plate behave almost identical and the parallel plate approximation differs from the two. Operating at 80% of pull-in, the deviation between square and circular plate results is 0.47% and for the parallel plate it is 12.5%.

D. Stable Position

Using the expressions (57)-(59) for the energies and the equation for the stable position (36), the stable position for

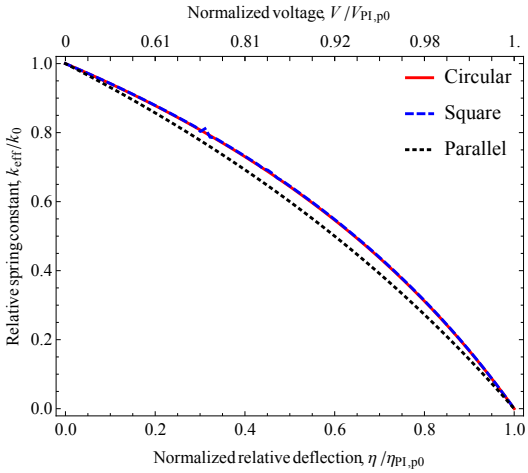

Fig. 8. Normalized effective spring constant versus relative center deflection normalized to the pull-in distance for circular, square and parallel plates.

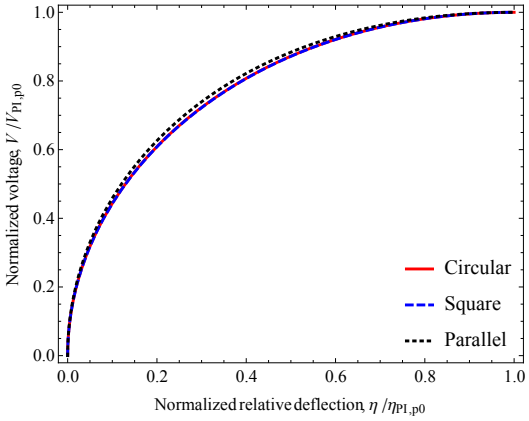

Fig. 9. Stable voltage normalized to pull-in voltage at zero applied pressure versus relative center deflection normalized to the pull-in distance at zero applied pressure for circular (70), square (71) and parallel plates (72).

the circular plate becomes

$$V_{\mathrm{stable,circ}} = \sqrt{\frac{-256 g_{\mathrm{eff}} \eta^{3/2}(-a^4 p\pi/64 + D_{\mathrm{eff}}\pi\eta g_{\mathrm{eff}})(-1+\eta)}{3a^2 C_0\left(-\operatorname{arctanh}\left[\sqrt{\eta}\right] + \eta \operatorname{arctanh}\left[\sqrt{\eta}\right] + \sqrt{\eta}\right)}}. \quad (70)$$

which is found in a similar way as in [2], [8].

A comparison of the stable position found using the anisotropic approach, (70), and measurements on a fabricated device can be found in Section VI-F.

For the square plate, combining the expressions in (64), (66) and (67), the stable position for the highly doped square plate on silicon (001) substrate aligned to the $\langle 110 \rangle$ direction can be found by (36)

$$V_{\mathrm{stable,sq}} = \sqrt{\frac{2 g_{\mathrm{eff}}\left(-L^4 p \xi_{\mathrm{p}} + 2h^3 \eta \xi_{\mathrm{s}} g_{\mathrm{eff}}\right)}{C_0 L^2 f_s'(\eta)}}. \quad (71)$$

For an approximation, (48) can be inserted into (71).

Devices with square plates were also fabricated and a comparison of the stable position found using the anisotropic approaches compared to the measured center deflection can be found in Section VI-F.

Originally, the CMUT was modelled by use of a parallel plate approximation [4], [5]. The parallel plate case is also included here for comparison and in this case, the stable position is

$$V_{\mathrm{stable,parallel}} = \sqrt{\frac{2(-1+\eta)^2 g_{\mathrm{eff}}(-Ap + k\eta g_{\mathrm{eff}})}{C_0}}. \quad (72)$$

Fig. 9 shows the stable position of the plate for varying bias voltages. The bias voltage is normalized to the pull-in voltage at zero applied pressure $V/V_{\mathrm{PI,p0}}$ and the deflection to the pull-in distance at zero applied pressure $\eta/\eta_{\mathrm{PI,p0}}$. It is seen that the circular and square plate give almost identical results, whereas the parallel plate has a slight deviation. At 80 % of pull-in, which is where the CMUT is usually designed to operate, the deviation of the square plate result compared to the circular plate result is only 0.01 %. For the parallel plate the deviation is 0.3 % compared to the circular plate result. It should be noted that the result for the circular plate in Fig. 9 is similar to a previously shown figure in [8].

From the static analysis, it is possible to present a set of general design plots for CMUTs by using adequate normalizations. Hereby, the results for circular, square and parallel plates can be compared. For specific device behavior, the equations for zero applied pressure or voltage can be used to eliminate the normalizations. These expressions are derived in section VI-E.

In general, it is seen from Figs. 8 and 9 that the overall behaviour of the CMUT is well captured by both the more accurate results for the circular and square plates, but also by the parallel plate approximation. The difference lies in the normalizations i.e. the pull-in point calculation, which is different for each case when using the actual shape of the deflection. The anisotropic effects are included through these as well. This means that in practice, the simple expressions can be used to model the CMUTs with good approximations, if the specific de-normalizations are used for each plate type.

E. Pull-in

For the parallel plate, the pull-in distance at zero applied pressure is given by $\eta_{\mathrm{PI,p0,parallel}} = 1/3$. The corresponding pull-in voltage is

$$V_{\mathrm{PI,p0,parallel}} = \sqrt{\frac{8 k g_{\mathrm{eff}}^2}{27 C_0}}. \quad (73)$$

The pressure dependence on the pull-in distance can be found analytically for this plate type and is given by

$$\eta_{\mathrm{PI,parallel}} = 1/3 + 2/3 p_{\mathrm{r}}, \quad (74)$$

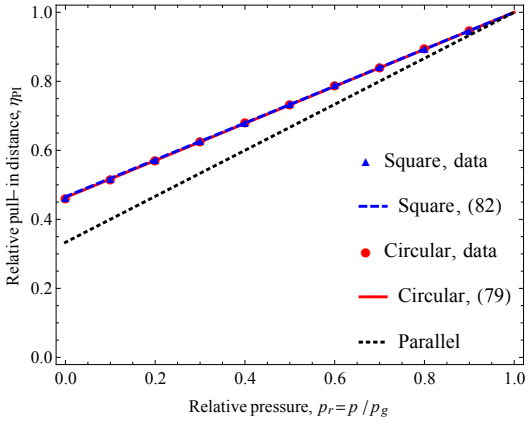

Fig. 10. Pull-in distance versus relative pressure. Circles are the full calculation for circular plates, triangles the full model for square plates, the red solid curve a fit for the circular plate (79), blue dashed curve a fit for the square plate (82) and black dotted the analytical expression for the parallel plate (74).

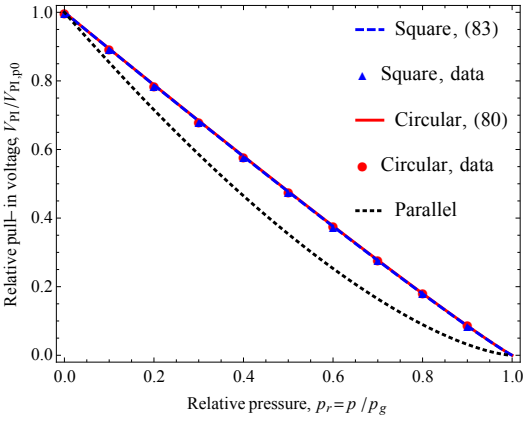

Fig. 11. Pull-in voltage relative to pull-in voltage for zero applied pressure versus relative pressure. Circles are the full calculation for circular plates, triangles the full model for square plates, the red solid curve a fit for the circular plate (80), blue dashed curve a fit for the square plate (83) and black dotted the analytical expression for the parallel plate (76).

where the relative pressure is given by $p_r = pA/(g_{eff}k)$. The relative pressure is the applied pressure normalized to the pressure it takes to deflect the plate the distance of the effective gap, p_g. Fig. 10 shows the linear dependence of the pressure on the pull-in distance, (74), as the black dotted curve. The pressure dependent pull-in voltage can for the parallel plate also be calculated analytically and is given by

$$V_{PI,parallel} = \frac{(-Ap + kg_{eff})^3}{27C_0k^2g_{eff}}. \tag{75}$$

It is seen that the influence of the pressure on the pull-in distance, and thus also the pull-in voltage, is dependent on the geometry of the device. Defining the relative pull-in voltage as $V_{rel} = V_{PI}/V_{PI,p0}$ and using (75) and (73), the relative pull-in voltage for the parallel plate yields

$$V_{rel,parallel} = (1 - p_r)^{(3/2)}. \tag{76}$$

Fig. 11 shows a comparison of the relative voltage versus the relative pressure with a black dotted curve for the parallel plate.

Looking at the circular plate and the special case where the applied pressure is zero, the relative pull-in distance becomes $\eta_{PI,p0,circ} = 0.463$ from (39). With this pull-in distance inserted into (70), the pull in voltage at zero applied pressure for the circular plate becomes

$$V_{PI,p0,circ} = \sqrt{\frac{89.4459D_{eff}g_{eff}^2}{a^2C_0}}. \tag{77}$$

To find the influence of the pressure on the pull-in distance, (39) is evaluated for varying values of the pressure. The result can be seen as red points in Fig. 10. As also observed by [2], [8], the influence of the pressure on the pull-in distance is found to be linear as for the parallel plate. The expression can be found by considering the boundary conditions $\eta_{PI}(0) = \eta_{PI,p0}$ and $\eta_{PI}(1) = 1$. Using these conditions the expression for the pressure dependent relative pull-in distance becomes

$$\eta_{PI} = \eta_{PI,p0} + (1 - \eta_{PI,p0})p_r, \tag{78}$$

where the relative pressure is given by $p_r = p/p_g = pa^4/(64g_{eff}D_{eff})$ for the circular plate. Inserting $\eta_{PI,p0,circ} = 0.463$ for the circular plate yields

$$\eta_{PI,circ} = 0.463 + 0.537p_r. \tag{79}$$

Eqn. (79) is plotted as the red solid curve in Fig. 10. The maximum deviation between the expression and the data points is 0.6 %. Compared to the parallel plate solution the difference in pull-in distance at zero applied pressure is clearly observed. Furthermore, note that (78) also applies for the parallel plate as seen in (74).

To see how the pressure affects the pull-in voltage for the circular plate, the relative pull-in voltage is again considered. For simplicity, the equation for the pressure dependent pull-in voltage is not shown, but it is found from the pull-in distance, (79), inserted into the stable position, (70). The resulting equation is evaluated for varying values of pressure and this is shown as red dots in Fig. 11. It is seen that the pull-in voltage decreases for increasing external pressure as expected, since the plate is deflected due to the applied pressure. To follow the analytical expression obtained for the parallel plate, a fit was made to an expression having the same form as this analytical result $V_{rel} = (1 - p_r)^{(K\cdot 3/2)}$, where K is the fitted parameter. The result from fitting is

$$V_{rel,circ} = (1 - p_r)^{(0.710\cdot 3/2)}, \tag{80}$$

Using this fit a maximum deviation of 3.9 % is obtained relative to calculated points.

To expand this pull-in investigation to square plates as well, the same procedure as for the circular plates is followed. For

the square case, the pull-in distance in the special case of zero applied pressure becomes $\eta_{\mathrm{PI,p0,sq}} = 0.466$ which is very close to the circular plate pull-in distance. The corresponding pull-in voltage is

$$V_{\mathrm{PI,p0,sq}} = \sqrt{\frac{2.95118 g_{\mathrm{eff}}^2 h^3 \xi_{\mathrm{s}}}{C_0 L^2}}. \tag{81}$$

To find the influence of the pressure on the pull-in distance for the square plate it was calculated for different pressures and plotted as triangular points in Fig. 10. As for the two other plate geometries, the influence of the pressure on the pull-in distance is found to be linear and using (78) it can be described as

$$\eta_{\mathrm{PI,sq}} = 0.466 + 0.534 p_{\mathrm{r}}, \tag{82}$$

where the relative pressure for the square plate is given by $p_{\mathrm{r}} = 0.021961 p L^4/(g_{\mathrm{eff}} D_{\mathrm{a}})$. Eqn. (82) is shown as a dashed blue line in Fig. 10. The maximum deviation between the fit and the data points for the square plate is 0.7%.

In Fig. 11, it is seen how the pressure affects the pull-in voltage for the square plate shown as triangular points and a fit with a dashed blue line. The calculation method is the same as for the circular plate, and the same behavior is also observed. A fit of the data points to an expression of the same form as for the parallel plate case yields

$$V_{\mathrm{rel,sq}} = (1 - p_{\mathrm{r}})^{(0.712 \cdot 3/2)}, \tag{83}$$

resulting in a maximum deviation of 1.7%.

F. Stable Position Measurements

To compare the anisotropic approach for modeling CMUTs to measurements for further validation of the theory for both circular and square plates, devices with both plate types were fabricated using a fusion bonding method [24]. The dimensions of the devices can be seen in Table V.

Measurements of the stable position (presented as the deflection in the center of the plate) for increasing bias voltage were performed on the fabricated devices. The deflections were measured as area scans with a Sensofar PLu Neox 3D Optical Profiler using white light interferometry.

Fig. 12 shows the measurements of the circular plate device. It is seen how the center deflection varies with the applied voltage and how the deflection increases when approaching the pull-in voltage as expected. The center deflection for the measurements is found as the average of 10 cells and the gray shaded areas corresponds to plus/minus two standard deviations. For the circular device, there was some uncertainty in the final gap height. Because of this it was not possible to plot the theoretical stable position for a circular plate, (70), together with the measurements. Instead, a fit was made which is shown as the theoretical curve in Fig. 12. From the fit, a gap height of 457 nm was found, and it is seen that the expression captures the behavior of the device excellently. With this gap, the theoretical curve is within the uncertainty interval of the measurements. Also, the pull-in voltage is in good agreement with the experimentally found value, as it was measured to be 140 V, compared to an expected value of 138 V from the anisotropic model (80).

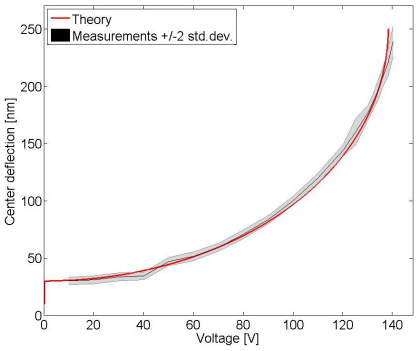

Fig. 12. Measured center deflection for increasing bias voltage together with theoretical curves for a circular plate (70).

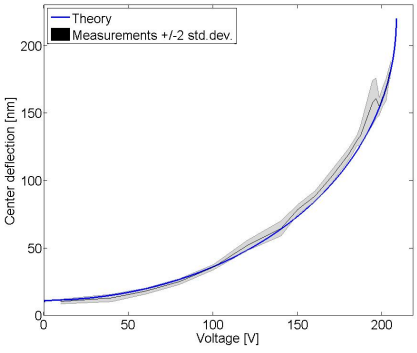

Fig. 13. Measured center deflection for increasing bias voltage together with theoretical curves for a square plate (71).

Measurements with a DC voltage applied were also performed for the square plate and the results are shown in Fig. 13. The center deflection for the measurements is found as the average of 10 cells and the gray shaded areas correspond to plus/minus two standard deviations. The theoretical curve is made from the stable position analysis and is for this case plotted directly as the gap height was known from this fabrication run. It is seen that the anisotropic theory matches well with the measurement as it is within the error margin. Also, the pull-in voltages are in good agreement as it was measured to be 206 V, compared to an expected value of 201 V from the anisotropic model (83).

VII. Small-signal Dynamic Modeling

Assuming that the signals applied to the CMUT are small, a linearized model of the dynamic behaviour for both circular and square anisotropic plates may be derived using well-known methods [25], [26], [27].

Applying the small-signal assumption, (32)-(34) may be linearized around an operating point $(V_{\text{op}}, w_{\text{op}}, p_{\text{op}})$ by differentiating with respect to each of the variables, while the other two are kept constant. This linearization can be expressed in matrix form as

$$\begin{bmatrix} \partial Q \\ \partial F \\ \partial W \end{bmatrix} = \mathbf{A} \begin{bmatrix} \partial V \\ \partial w_0 \\ \partial p \end{bmatrix}, \tag{84}$$

with

$$\begin{aligned} \mathbf{A} &= \begin{bmatrix} \frac{\partial Q}{\partial V} & \frac{\partial Q}{\partial w_0} & \frac{\partial Q}{\partial p} \\ \frac{\partial F}{\partial V} & \frac{\partial F}{\partial w_0} & \frac{\partial F}{\partial p} \\ \frac{\partial W}{\partial V} & \frac{\partial W}{\partial w_0} & \frac{\partial W}{\partial p} \end{bmatrix} \\ &= \begin{bmatrix} C(w_{\text{op}}) & V_{\text{op}} \frac{\partial}{\partial w_0} C(w_{\text{op}}) & 0 \\ -V_{\text{op}} \frac{\partial}{\partial w_0} C(w_{\text{op}}) & k_{\text{eff}} + m_0 \frac{\partial^2}{\partial t^2} & -A_0 \\ 0 & A_0 & 0 \end{bmatrix}. \end{aligned} \tag{85}$$

Since the dynamics of the system are of interest, it is more convenient to use the time derivatives of Q, w_0, and W, which are denoted $\dot{Q} = i$, $\dot{w_0} = v$, and $\dot{W}$. Rewriting yields

$$\begin{bmatrix} \int \partial i \mathrm{d}t \\ \partial F \\ \int \partial \dot{W} \mathrm{d}t \end{bmatrix} = \mathbf{A} \begin{bmatrix} \partial V \\ \int \partial v \mathrm{d}t \\ \partial p \end{bmatrix}. \tag{86}$$

Furthermore, the analysis is simplified by transforming to the frequency domain by a Laplace transform of the linear system in (86)

$$\begin{bmatrix} \partial i/s \\ \partial F \\ \partial \dot{W}/s \end{bmatrix} = \mathfrak{L}\{\mathbf{A}\} \begin{bmatrix} \partial V \\ \partial v/s \\ \partial p \end{bmatrix} \Leftrightarrow \begin{bmatrix} \partial i \\ \partial F \\ \partial \dot{W} \end{bmatrix} = \mathbf{B} \begin{bmatrix} \partial V \\ \partial v \\ \partial p \end{bmatrix}, \tag{87}$$

with

$$\mathbf{B} = \begin{bmatrix} sC(w_{\text{op}}) & V_{\text{op}} \frac{\partial}{\partial w_0} C(w_{\text{op}}) & 0 \\ -V_{\text{op}} \frac{\partial}{\partial w_0} C(w_{\text{op}}) & k_{\text{eff}}/s + s m_0 & -A_0 \\ 0 & A_0 & 0 \end{bmatrix}, \tag{88}$$

where $s = j\omega$ is the complex angular frequency with j being the imaginary unit and ω the angular frequency. From the construction of the matrix elements, it is seen that the first element in the diagonal describes the current i as a function of voltage V, when the velocity and pressure are kept constant. This is equal to the inverse electrical impedance for a blocked mechanical system, $1/Z_{\text{e,b}}$. The second diagonal element relates force F and velocity v for constant voltage and pressure, and it is, thus, the mechanical impedance, $Z_{\text{m,s}}$, for a short circuited electrical system and vacuum in the acoustical system (such that neither voltage nor pressure can be built up). The two first off-diagonal elements relate force F and voltage V as well as the current i and velocity v.

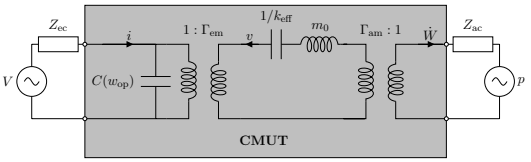

Fig. 14. Equivalent circuit representation of the CMUT and the external circuits. The transducer itself is represented by the circuit in the grey box, while the external electrical and acoustical circuits are represented by their respective Thevenin equivalents.

They, thus, describe the coupling Γ_{em} between the mechanical and electrical domains. The last two off-diagonal elements relate force F and pressure p as well as volume flow $\dot{W}$ and velocity v. These are therefore the coupling terms between the mechanical and acoustical domains, Γ_{am}. Inserting in (88) yields

$$\mathbf{B} = \begin{bmatrix} 1/Z_{\text{e,b}} & \Gamma_{\text{em}} & 0 \\ -\Gamma_{\text{em}} & Z_{\text{m,s}} & -\Gamma_{\text{am}} \\ 0 & \Gamma_{\text{am}} & 0 \end{bmatrix}, \tag{89}$$

Note that there is no acoustical impedance, since the CMUT only interfaces to the acoustical domain, it does not include it. The CMUT also interfaces to the electrical domain, but it includes a capacitive element, hence the electrical impedance. There is no direct coupling between the electrical and acoustical domains, since any interaction is done through the mechanical domain of the plate.

The linear system described by (87) and (89) has the same behavior as the electrical circuit shown in the gray box in Fig. 14, or equivalently, the circuit in the gray box in Fig. 14 is described by (87) and (89). Thus, by deriving the component values in (89), the small-signal dynamic behaviour of the CMUT can be described. Using the results from the previous sections, a small-signal dynamic model can be derived for both circular and square anisotropic CMUTs. In Table VI, the relevant circuit parameters are listed for convenience. These are valid for highly doped (001) silicon plates aligned to the $\langle 110 \rangle$ direction. The capacitance, pull-in voltage and pull-in deflection are evaluated at zero pressure.

VIII. Conclusion

In this paper, it was demonstrated how wafer bonded CMUTs with both circular and square plates can be analytically modelled using the full anisotropic properties of single crystalline silicon. For the circular plate, an exact solution to the plate equation was obtained, and for the square plate, the full anisotropic plate equation was solved using the Galerkin method. In this case, it was seen that the deflection simplifies by utilizing the symmetry of the silicon crystal and a compact solution was obtained for square CMUT plates on a (001) silicon substrate aligned to the [110] direction. Using this approach, the analytic plate deflections showed excellent correspondence with FEM calculations and measurements. Using isotropic plate theory to calculate the deflection of

TABLE VI

STATIC TRANSDUCER PARAMETERS FOR HIGHLY DOPED (001) SILICON PLATES ALIGNED TO THE $\langle 110 \rangle$ DIRECTION. a IS THE RADIUS AND L THE HALF SIDE-LENGTH, h IS THE PLATE THICKNESS, g_{EFF} IS THE EFFECTIVE GAP HEIGHT, w_0 IS THE CENTER DEFLECTION OF THE PLATE, AND ϵ_0 IS THE VACUUM PERMITTIVITY. THE CAPACITANCE, PULL-IN VOLTAGE AND PULL-IN DEFLECTION ARE EVALUATED AT ZERO PRESSURE.

	Circular	Square
Capacitance $C(w_0)$	$C_0\sqrt{\frac{1}{\eta}}\arctan\sqrt{\eta}$	$C_0\frac{1}{1-0.296\eta-0.136\eta^2}$
Lumped mass m_0	$\frac{\pi}{3}\rho h a^2$	$1.215\rho h L^2$
Lumped spring const. k_0	$858.8\,\text{GPa}\cdot\frac{h^3}{a^2}$	$771.3\,\text{GPa}\cdot\frac{h^3}{L^2}$
Turns ratio Γ_{em}	$V_{\text{stable,circ}}C_0\frac{1}{2\eta}\left(\frac{1}{1-\eta}-\sqrt{\frac{1}{\eta}}\arctan\sqrt{\eta}\right)$	$V_{\text{stable,sq}}C_0\frac{1}{\left(1.813-1.050\eta-0.299\eta^2\right)^2}$
Turns ratio Γ_{am}	$\frac{1}{3}\pi a^2$	$1.215L^2$

anisotropic silicon plates, resulted in deviations from FEM or measurements of up to 10 %. Using the anisotropic theory, reduced the deviation from FEM to less than 0.3 % for the circular plate and 0.1 % for the square plate. Fitting the anisotropic calculated deflection for the square plate to the measurement, a deviation of only 0.07 % was observed for the fitted plate parameter. The theory of multilayer plates was also applied to CMUTs, however, only a small difference will be obtained in the deflection for the typical CMUT case.

A full electrostatic analysis including the anisotropic effects was carried out for both circular, square, and parallel plate devices. The analysis was based on energy considerations and the capacitance, effective spring constant, stable position, pull-in distance, and pull-in voltage are all calculated. In the pull-in analysis, the pressure dependence is also included. The circular and square plate devices are seen to behave very similar with a difference of 0.01 % for stable position and 0.47 % for effective spring constant at 80 % of pull-in. Using the parallel plate approximation resulted in deviations of 0.3 % and 12.5 %, respectively, at 80 % of pull-in. The pressure dependence was expressed through linear fits for the pull-in distance with a maximum deviation of 0.6 % for the circular plate and 0.7 % for the square plate. The pressure dependent pull-in voltage was seen to follow an exponentiation expression with maximum deviations of 3.9 % and 1.7 % for the circular and square plate, respectively. Using the capacitance function of the circular plate for the square plate, the maximum deviation was 1.6 %.

Devices with both circular and square plates were fabricated, and the stable position and pull-in voltage measured. Comparing this to to the anisotropic theory, it was seen that the theory is within the uncertainty interval of the measurements in both cases.

Last, a small-signal dynamic model for a CMUT with either circular and square shaped anisotropic plate was presented.

ACKNOWLEDGEMENT

This work was financially supported by the Danish National Advanced Technology Foundation through grants 024-2008-3 and 82-2012-4.

REFERENCES

[1] P. C. Eccardt, P. Wagner, and S. Hansen, "Analytical models for micromachined transducers - an overview," in *Proc. IEEE Ultrason. Symp.*, 2006, pp. 572–581.

[2] I. O. Wygant, M. Kupnik, and B. T. Khuri-Yakub, "Analytically calculating membrane displacement and the equivalent circuit model of a circular CMUT cell," in *Proc. IEEE Ultrason. Symp.*, 2008, pp. 2111–2114.

[3] Y. Huang, A. S. Ergun, E. Hæggström, M. H. Badi, and B. T. Khuri-Yakub, "Fabricating capacitive micromachined ultrasonic transducers with wafer-bonding technology," *J. Microelectromech. Syst*, vol. 12, no. 2, pp. 128–137, 2003.

[4] I. Ladabaum, X. Jin, H. T. Soh, A. Atalar, and B. T. Khuri-Yakub, "Surface micromachined capacitive ultrasonic transducers," *IEEE Trans. Ultrason., Ferroelec., Freq. Contr.*, vol. 45, no. 3, pp. 678–690, 1998.

[5] A. Caronti, G. Caliano, A. Iula, and M. Pappalardo, "An accurate model for capacitive micromachined ultrasonic transducers," *IEEE Trans. Ultrason., Ferroelec., Freq. Contr.*, vol. 49, no. 2, pp. 159–168, feb 2002.

[6] A. Lohfink and P.-C. Eccardt, "Linear and nonlinear equivalent circuit modeling of CMUTs," *IEEE Trans. Ultrason., Ferroelec., Freq. Contr.*, vol. 52, no. 12, pp. 2163–2172, 2005.

[7] A. Nikoozadeh, B. Bayram, G. Yaralioglu, and B. Khuri-Yakub, "Analytical calculation of collapse voltage of CMUT membrane," in *Proc. IEEE Ultrason. Symp.*, vol. 1, 2004, pp. 256–259.

[8] H. Koymen, A. Atalar, E. Aydogdu, C. Kocabas, H. K. Oguz, S. Olcum, A. Ozgurluk, and A. Unlugedik, "An improved lumped element nonlinear circuit model for a circular CMUT cell," *IEEE Trans. Ultrason., Ferroelec., Freq. Contr.*, vol. 59, no. 8, pp. 1791–1799, 2012.

[9] B. Ahmad and R. Pratap, "Elasto-electrostatic analysis of circular microplates used in capacitive micromachined ultrasonic transducers," *IEEE Sensors Journal*, vol. 10, no. 11, pp. 1767–1773, 2010.

[10] S. Timoshenko and S. Woinowsky-Krieger, *Theory of Plates and Shells*, 2nd ed. Mcgraw-Hill College, jun 1959.

[11] R. L. Taylor and S. Govindjee, "Solution of clamped rectangular plate problems," *Communications in Numerical Methods in Engineering*, vol. 20, no. 10, pp. 757–765, 2004.

[12] M. Rahman, J. Hernandez, and S. Chowdhury, "An improved analytical method to design CMUTs with square diaphragms," *IEEE Trans. Ultrason., Ferroelec., Freq. Contr.*, vol. 60, no. 4, pp. 834–845, apr 2013.

[13] G. G. Yaralioglu, B. Bayram, A. Nikoozadeh, and B. T. P. Khuri-Yakub, "Finite element modeling of capacitive micromachined ultrasonic transducers," *Proc. SPIE Med. Imag.*, vol. 5750, pp. 77–86, 2005.

[14] M. F. la Cour, T. L. Christiansen, J. A. Jensen, and E. V. Thomsen, "Modelling of CMUTs with anisotropic plates," in *Proc. IEEE Ultrason. Symp.*, 2012, pp. 588–591.

[15] M. F. la Cour, T. L. Christiansen, C. Dahl-Petersen, K. Reck, O. Hansen, J. A. Jensen, and E. V. Thomsen, "Modeling and measurements of CMUTs with square anisotropic plates," in *Proc. IEEE Ultrason. Symp.*, 2013, pp. 2187–2190.

[16] E. Ventsel and T. Krauthammer, *Thin plates and shells: theory, analysis, and applications*. Dekker, 2001.

[17] K. S. Pister and S. B. Dong, "Elastic bending of layered plates," *Journal of the Engineering Mechanics Division*, vol. 85, no. 4, pp. 1–10, oct 1959.

[18] S. B. Dong, K. S. Pister, and R. L. Taylor, "On the theory of laminated anisotropic shells and plates," *Journal of the Aerospace Sciences*, vol. 29, no. 8, pp. 969–975, aug 1962.

[19] R. E. Newnham, *Properties of Materials: Anisotropy, Symmetry, Structure*. Oxford University Press, USA, jan 2005.

[20] E. V. Thomsen, K. Reck, G. Skands, C. Bertelsen, and O. Hansen, "Silicon as an anisotropic mechanical material: Deflection of thin crystalline plates," *Sensors and Actuators*, p. submitted, 2014.

[21] J. J. Hall, "Electronic effects in the elastic constants of n-type silicon," *Phys. Rev.*, vol. 161, no. 3, pp. 756–761, sep 1967.

[22] S. Holgate, "The transverse flexure of perforated aeolotropic plates," *Proceedings of the Royal Society A: Mathematical, Physical and Engineering Science*, vol. 185, no. 1000, pp. 50–69, jan 1946.

[23] F. Mbakogu and M. Pavlovic, "Bending of clamped orthotropic rectangular plates: a variational symbolic solution," *Computers and Structures*, vol. 77, no. 2, pp. 117–128, jun 2000.

[24] T. L. Christiansen, O. Hansen, M. D. Johnsen, J. N. Lohse, J. A. Jensen, and E. V. Thomsen, "Void-free direct bonding of CMUT arrays with single crystalline plates and pull-in insulation," *Proc. IEEE Ultrason. Symp.*, pp. 1737–1740, 2013.

[25] W. P. Mason, *Electromechanical transducers and wave filters*. D. Van Nostrand Co., New York, 1942.

[26] H. A. C. Tilmans, "Equivalent circuit representation of electromechanical transducers: I. lumped-parameter systems," *J. Microelectromech. S.*, vol. 6, pp. 157–176, 1996.

[27] ——, "Equivalent circuit representation of electromechanical transducers: II. distributed-parameter systems," *J. Microelectromech. S.*, vol. 7, pp. 285–309, 1997.

PAPER F

Void-Free Direct Bonding of CMUT Arrays with Single Crystalline Plates and Pull-In Insulation

Authors: Thomas Lehrmann Christiansen, Ole Hansen, Mathias Dahl Johnsen, Jeppe Nyskjold Lohse, Jørgen Arendt Jensen, and Erik Vilain Thomsen.

Published in: Proceedings of the IEEE International Ultrasonics Symposium, pp. 1737-1740, 2013

Abstract

The implications on direct bonding quality, when using a double oxidation step to fabricate capacitive micromachined ultrasonic transducers (CMUTs), is analyzed. The protrusions along the CMUT cavity edges created during the second oxidation are investigated using simulations, AFM measurements, and a proposed analytical model, which is in good agreement with the simulated results. The results demonstrate protrusion heights in the order of 10 nm to 40 nm, with higher oxidation temperatures giving the highest protrusions. Isotropically wet etched cavities exhibit significantly smaller protrusions than anisotropically plasma etched cavities after the second oxidation. It is demonstrated that the protrusions will prevent good wafer bonding without subsequent polishing or etching steps. A new fabrication process is therefore proposed, allowing protrusion-free bonding surfaces with no alteration of the final structure and no additional fabrication steps compared to the double oxidation process. Two identical CMUT arrays with circular and square cavities having diameter/side lengths of 72 µm/65 µm and a 20 µm interdistance are fabricated with the two processes, demonstrating void-free bonding and 100 % yield from the proposed process compared to poor bonding and 7 % yield using the double oxidation process.

Void-Free Direct Bonding of CMUT Arrays with Single Crystalline Plates and Pull-In Insulation

Thomas Lehrmann Christiansen*,
Ole Hansen*, Mathias Dahl Johnsen*, Jeppe Nyskjold Lohse*, Jørgen Arendt Jensen† and Erik V. Thomsen*
*Department of Micro- and Nanotechnology, Technical University of Denmark, DK-2800 Kgs. Lyngby, Denmark
†Center for Fast Ultrasound Imaging, Department of Electrical Engineering,
Technical University of Denmark, DK-2800 Kgs. Lyngby, Denmark

***Abstract*—The implications on direct bonding quality, when using a double oxidation step to fabricate capacitive micromachined ultrasonic transducers (CMUTs), is analyzed. The protrusions along the CMUT cavity edges created during the second oxidation are investigated using simulations, AFM measurements, and a proposed analytical model, which is in good agreement with the simulated results. The results demonstrate protrusion heights in the order of 10 nm to 40 nm, with higher oxidation temperatures giving the highest protrusions. Isotropically wet etched cavities exhibit significantly smaller protrusions than anisotropically plasma etched cavities after the second oxidation. It is demonstrated that the protrusions will prevent good wafer bonding without subsequent polishing or etching steps. A new fabrication process is therefore proposed, allowing protrusion-free bonding surfaces with no alteration of the final structure and no additional fabrication steps compared to the double oxidation process. Two identical CMUT arrays with circular and square cavities having diameter/side lengths of 72 µm/65 µm and a 20 µm interdistance are fabricated with the two processes, demonstrating void-free bonding and 100 % yield from the proposed process compared to poor bonding and 7 % yield using the double oxidation process.**

I. Introduction

Capacitive micromachined ultrasonic transducers (CMUTs) fabricated using direct wafer bonding offers various advantages such as single crystalline plates with a well-defined thickness and highly predictable mechanical properties. Huang et al. demonstrated a simple fabrication process where the CMUTs are made by etching out cavities in a grown oxide on a silicon wafer. This wafer is bonded to a silicon-on-insulator (SOI) wafer, which after removal of the handle and the buried oxide defines the plate/top electrode [1]. An insulation oxide in the bottom of the cavity is typically grown through a second oxidation after the cavity etch to prevent short circuiting during pull-in and avoid leak currents due to contaminations in the cavities [1], [2]. However, this process creates protrusions at the edge of the cavity as demonstrated in Fig. 1a.

In this paper, the height of the protrusions originating from a double oxidation for various processing parameters is investigated through simulations, analytical estimates, and AFM measurements. It is concluded that, for the investigated processing parameters, the prostrusions are of such a height that direct wafer bonding of a typical CMUT array is impaired or completely prohibited if subsequent etching or grinding steps are not introduced to planarize the bonding surfaces. An alternative simple fabrication approach is therefore proposed, where the cavities are etched in an oxide grown on the SOI wafer. The insulation oxide is then grown on a second wafer, and the two wafers are bonded by SiO_2/SiO_2 direct bonding, see Fig. 1b. Without introducing further processing steps, this provides protrusion-free bonding surfaces and thus optimal conditions for direct bonding. The superiority of the proposed process is demonstrated in practice by fabricating CMUT arrays with typical dimensions using both methods, showing poor bonding results for the non-planarized double oxidation process and void-free bonding results for the proposed process.

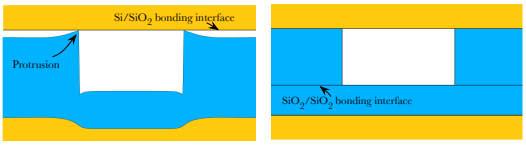

Fig. 1: Cross-sectional views of the CMUT cavities in the two different fabrication approaches. (a) Double oxidation process. (b) The proposed process. Si is orange and SiO_2 is blue.

II. Methods and Materials

A. Protrusion Investigations

The protrusion height was investigated experimentally as a function of processing parameters through two individual oxidations aiming for a 350 nm and a 200 nm oxide layer, respectively. The latter was achieved through various oxidation approaches as described below. The two oxide thicknesses were chosen as they represent realistic values for a typical CMUT design. The first oxidation was performed on six 500 µm single side polished n-type $\langle 100 \rangle$ 4" silicon wafers with a resistivity of 1-10 Ωcm, and the oxide thickness was measured to be 357 ± 1 nm. A lithography step on each wafer was followed by a cavity etch, defining square arrays of circular cavities with a diameter of 72 µm and an interspacing of 20 µm distributed over the entire wafer. In order to investigate the effect of anisotropically and isotropically etched cavities, two different etches were used to etch out cavities in the oxide; on the first three of the wafers, an

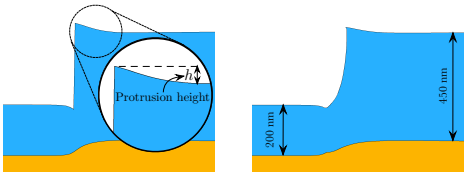

(a) (b)

Fig. 2: Simulated cavity profile after the second oxidation in (a) an anisotropically etched cavity and (b) an isotropically etched cavity. Si is orange and SiO_2 is blue.

anisotropic reactive ion etch was used, while the remaining three were subjected to a buffered hydrogen flouride (HF) wet etch. Reference values of the protrusion height were measured with atomic force microscopy (AFM) on both an isotropically and an anisotropically etched wafer after this step. Subsequently, the wafers were cleaved in two parts, enabling six independent oxidations: Dry and wet oxidations at 950 °C and 1000 °C, and only dry at 1050 °C, and 1100 °C. In all oxidations, both an anisotropically and an isotropically etched wafer were included. Each of these second oxidations aimed for a 200 nm thick oxide in the cavities, and were all within 9 nm of this target. AFM measurements of the protrusion height were then performed on these 12 half wafers. All AFM measurements were made in tapping mode, scanning a 5 µm by 5 µm area covering the cavity edge. The scan direction was towards the cavity to avoid measurement artifacts such as overshooting from the abrupt step at the cavity edge. All heights reported in this study were averaged over three such measurements taken on three different cavities, each being evaluated by averaging over the 5 µm range. The measurement error bars were calculated as 2 sample standard deviations. All dry oxidations were carried out at an ambient pressure of 1 atm, while the wet oxidations were carried out at 0.85 atm as a consequence of the furnace settings.

The simulations were carried out in Athena 5.20.0.R by Silvaco Inc. using the same oxidation parameters in terms of type, final oxide thickness, temperature and pressure as were used in the experiments. A grid size of 1 nm in the vicinity of the oxide cavity edge was used, growing linearly to 500 nm 5 µm from the cavity edge. The simulations were carried out using different models that either includes or excludes stress effects. All simulated results were seen to be identical in the different models, indicating negligible stress effects, and only one set of results is therefore reported in this work.

B. Array Fabrication

For the fabrication of the CMUT arrays, the double oxidation process and the proposed process were carried out on two separate pairs of bonded wafers, one for each process. The main process steps are listed in Table I. As can be seen, the two approaches share the number, order and type of process steps. The only difference is that the respective

TABLE I: A list of the main process steps used in both fabrication approaches. For each step, the wafer on which the process step is carried out in the respective approach is given.

Step	Double oxidation	Proposed process
403 nm oxidation	Standard	SOI
Lithography	Standard	SOI
Cavity etch	Standard	SOI
195 nm oxidation	Standard	Standard
Bonding	Standard/SOI	Standard/SOI
Handle removal	SOI	SOI

process steps were carried out on either a standard, 500 µm single side polished 1-10 Ωcm n-type $\langle 100 \rangle$ 4" silicon wafer or an SOI wafer with the same specifications along with a 2 µm low resistivity device layer and a buried oxide (BOX) layer of 1 µm. The lithography was performed through the same mask for both processes, containing arrays with circular and square cavities having diameter/side lengths of 72 µm/65 µm, respectively. The cavities were separated by 20 µm in regular square lattice arrays with either 324, 2304, or 9216 cavities per array, corresponding to 9 CMUT cells per element in 6×6, 16×16 and 32×32 arrays designed for a nominal resonance frequency in immersion of 3 MHz. The individual arrays were separated by 2.2 mm. The cavity etch was performed in a STI Pegasus reactive ion etcher, and the direct wafer bonding step was carried out at 50 °C, 10^{-3} mbar ambient pressure and 1500 N piston force for 5 minutes. Post-annealing was carried out in an inert nitrogen atmosphere at 1100 °C for 70 minutes [3]. Prior to both oxidations and the bonding step, the wafers were cleaned using a standard RCA cleaning procedure. Before the bonding step, the final HF dip in the RCA cleaning procedure was omitted to avoid oxide removal. After bonding, the bonded wafers were dipped in buffered HF for 10 minutes to remove the oxide from the exposed wafer surfaces, and the SOI handle was subsequently removed in an isotropic 40 minute deep reactive ion etch. After this step, only the 2 µm device layer and the 1 µm BOX layer of the SOI wafer remained, thereby clearly exposing any unbonded regions [4]. As only the bonding step was of interest to this study, the subsequent lithography and top electrode etch steps required to complete the CMUT arrays were not performed.

III. Results and Discussion

A. Protrusion Investigations

In Fig. 3, the measured protrusion heights are shown as a function of temperature. For each temperature, both wet and dry oxidation results are shown for both anisotropically and isotropically etched cavities. No measurements are given for wet oxidations at 1050 °C and 1100 °C as the required oxidation time to reach 200 nm is impractically short. Note that the simulations predict higher protrusions than the measured in most cases, the deviation being 7 nm at the most. Yet, both simulations and measurements agree on the general parameter dependency. It is thus seen that the oxidation temperature only has a minor effect on the protrusion height, with a

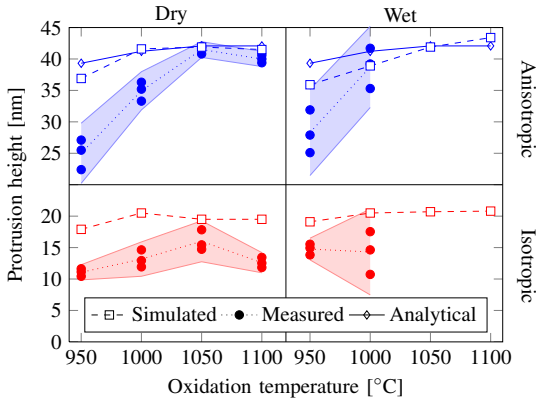

Fig. 3: Simulated, calculated and measured protrusion heights for four independent processing parameters shown as a function of oxidation temperature. The shaded areas denote a confidence interval of two standard deviations.

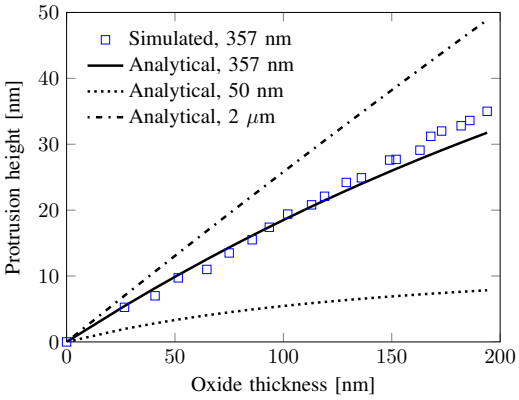

Fig. 4: Protrusion height plotted as a function of the thickness of the second oxide for three different values of the initial oxide thickness. For one of the initial oxide thicknesses, the corresponding simulated values are given.

slightly increasing protrusion height for higher temperatures. The results for the wet and dry oxidation are not significally different, and no conclusions can be made in this case based on the measurements. A much larger effect is seen for the etch type, where the isotropically etched cavities exhibit a significantly smaller protrusion height than the anisotropically etched cavities. For all temperatures, the protrusion height is decreased by almost a factor of two. This can be explained by considering Figs. 2a and 2b, showing the simulation results of both an anisotropically (Fig. 2a) and an isotropically (Fig. 2b) etched cavity after the second oxidation. Since the isotropic etch results in a cavity edge which is retracted slightly from the beginning of the oxide masking, the edge is consequently raised less than the corresponding anisotropic case, where the cavity edge step is more abrupt. This therefore yields smaller protrusions for the isotropically etched cavities.

In the case of anisotropically etched cavities, the protrusion height can be quite accurately estimated using simple analytical considerations. Analytical models of the related LOCOS oxidation are known, but these are based on fitted parameters using nitride diffusion masks and are therefore not directly applicable to the present case [5]. According to the Deal-Grove model, the oxide growth rate is $\mathrm{d}x/\mathrm{d}t = kC/N$, where x is the oxide thickness, k the interface reaction rate constant, N the number of oxidizer molecules incorporated per unit volume of oxide, and C the concentration of oxidizer molecules at the oxide/silicon interface [6]. The interface concentration results from diffusion of the oxidizer from the gas/oxide interface where the oxidizer concentration is assumed contant. Since the oxide thickness varies due to the etched cavity, the interface concentration C is a function of position with well known values far from the cavity edge. At the mask edge, the concentration may be obtained by a full 2-D simulation, but a fair estimate is the average of the two known values $C_{\mathrm{edge}} \simeq (C_{\mathrm{c}} + C_{\mathrm{ox}})/2$, where C_{c} is the concentration in the cavity and C_{ox} the concentration at the oxide far from the cavity. As a result of that simple assumption,

$$\frac{\mathrm{d}x_{\mathrm{edge}}}{\mathrm{d}t} = \frac{1}{2}\left(\frac{\mathrm{d}x_{\mathrm{c}}}{\mathrm{d}t} + \frac{\mathrm{d}x_{\mathrm{ox}}}{\mathrm{d}t}\right) .$$

By subtracting $\mathrm{d}x_{\mathrm{ox}}/\mathrm{d}t$, integrating, and accounting for the volume expansion by a factor of 2.2 of the growing oxide compared to the consumed silicon, the protrusion height becomes

$$h = \frac{2.2-1}{2.2}\frac{1}{2}(\Delta x_{\mathrm{c}} - \Delta x_{\mathrm{ox}}) ,$$

where the grown oxide in the cavity and at the initial oxide, Δx_{c} and Δx_{ox}, are found using the Deal-Grove model for thermal oxidation [6].

The analytical model has been used to predict the protrusion height for the anisotropically etched cavities, and is given in Fig. 3. Only anisotropically etched cavities are considered, as the model assumes an abrupt step. The model shows good agreement with the simulations, confirming that the protrusions arise due to purely geometrical effects resulting in spatially dependent diffusant concentrations. As the study in Fig. 3 is restricted to a fixed oxide thickness, the model has also been used to plot the protrusion height as a function of the second oxide thickness for three different initial oxide thicknesses grown in a dry oxidation at 1000 °C, see Fig. 4. It is seen that the protrusion height increases with both initial oxide thickness and second oxide thickness. For an initial oxide thickness of 357 nm, corresponding to the experimental value, the protrusion height has been simulated, showing excellent agreement over a large range of second oxide thicknesses, thereby confirming the validity of the model.

B. Array Fabrication

In Fig. 5, the result of the double oxidation process (left) and proposed process (right) is shown in split-screen view. It is clearly visible that the 2 µm top plate on most of the arrays to the left have broken off due to poor bonding, resulting in a yield of 7 %. As opposed to this, all arrays are bonded flawlessly for the proposed fabrication process with SiO_2/SiO_2 bonding seen to the right, corresponding to 100 % yield. Martini et al. investigated the crack length of the unbonded region for step heights from 9 nm to 400 nm [7]. For step heights above 55 nm, thin plate theory could be used to predict the crack length. For step heights lower than 55 nm, i.e. in the regime of the protrusion heights seen in this study, dislocation theory was seen to provide a better description, with the crack length L being given by $L = Eh^2/[8\pi\gamma(1-\nu)^2]$. Here, E is the Young's modulus and ν the Poisson ratio of the bonded wafers, while h is the protrusion height and γ is the surface energy of the bonding surfaces. For the anisotropic stiffness properties of the silicon wafers bonded in this study, an average Young's modulus of 148 GPa and a Poisson ratio of 0.177 represent appropriate values. Assuming a representative fracture surface energy of 0.1 J/m^2, a protrusion height of 30 nm would result in a crack length of $\sim$ 80 µm. Even for the smallest measured protrusion height of 11 nm, the crack length would be $\sim$ 10 µm. Two neighboring cavities will therefore need an interdistance well above 20 µm to ensure even a small bonded area between the cavities. In the fabricated arrays, the interdistance was 20 µm, and the fact that the double oxidized wafers did not bond corresponds well to this theoretical prediction. Note that the fracture surface energy used in the calculation corresponds to the typical fracture surface energy before annealing [4]. Annealing will contribute to an increase in fracture surface energy up to a factor of 10 or more by conversion of hydrogen bonds to covalent bonds [4]. However, since completely non-bonded regions between cavities will not close during annealing, the pre-annealing fracture surface energy is the appropriate measure.

The interdistance between cavities in a CMUT array should be kept at a minimum, while still maintaining the required mechanical stiffness, to maximize the fill-factor and hence the highest possible output and sensitivity of the array [8]. Clearly, the double oxidation approach counteracts this. Etching or polishing steps performed prior to the bonding can be used to reduce the protrusions [2], but the issue can be completely bypassed without any additional steps by using the process proposed in this paper, which furthermore contributes with a slightly increased insulation thickness between the electrodes compared to the double oxidation process, see Figs. 1a and 1b. The only requirement is that the reduction of the SOI device layer thickness due to the oxidation is considered in the design.

IV. Conclusion

The protrusions arising from a double oxidation process was investigated using AFM measurements, numerical simulations and a proposed analytical model showing good agreement with simulations, proving that protrusions arise purely due to geometrically dependent diffusion. It was found that the protrusion height increases slightly with temperature, and that the protrusions from isotropically wet etched cavities are significantly smaller than protrusions from anisotropically wet etched cavities. In all cases, it was found that direct wafer bonding would be severely affected by the protrusions for a typical CMUT array using processing parameters in the investigated range. This fact was examplified through fabrication of representative CMUT arrays on a 4" wafer, demonstrating poor bonding equivalent to a 7 % yield. A simple process requiring no additional processing steps was proposed to completely remove the problem of protrusions, and a demonstration of the process revealed void-free wafer bonding resulting in 100 % yield.

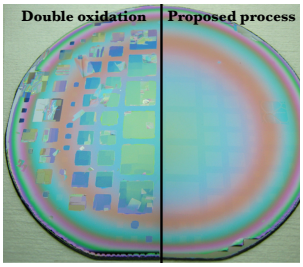

Fig. 5: A split-screen view of the result of the array fabrication using the double oxidation process (left) and the process proposed in this paper (right), showing poor and excellent bonding results, respectively. The color variation is due to variations in BOX layer thickness after the handle removal.

Acknowledgment

This work was financially supported by the Danish National Advanced Technology Foundation (82-2012-4).

References

[1] Y. Huang, A. S. Ergun, E. Hæggström, M. H. Badi, and B. T. Khuri-Yakub, "Fabricating capacitive micromachined ultrasonic transducers with wafer-bonding technology," *J. Microelectromech. S.*, vol. 12, no. 2, pp. 128–137, 2003.

[2] H.-S. Yoon, M.-C. Ho, N. Apte, P. Cristman, S. Vaithilingam, M. Kupnik, K. Butts-Pauly, B. T. Khuri-Yakub, Y. Matsumoto, L. A. Crum, and G. R. ter Haar, "Fabrication of CMUT cells with gold center mass for higher output pressure," in *AIP Conference Proceedings*, pp. 183–188, 2011.

[3] M. Shimbo, K. Furukawa, K. Fukuda, and K. Tanzawa, "Silicon-to-silicon direct bonding method," *Journal of Applied Physics*, vol. 60, no. 8, pp. 2987–2989, 1986.

[4] A. Plossl and G. Kräuter, "Wafer direct bonding: tailoring adhesion between brittle materials," *Materials Science and Engineering: R: Reports*, vol. 25, pp. 1–88, mar 1999.

[5] N. Guillemot, G. Pananakakis, and P. Chenevier, "A new analytical model of the "Bird's beak,"

[6] G. S. May and S. M. Sze, *Fundamentals of semiconductor fabrication*. Wiley, 2004.

[7] T. Martini, S. Hopfe, S. Mack, and U. Gösele, "Wafer bonding across surface steps in the nanometer range," *Sensors and Actuators A: Physical*, vol. 75, pp. 17–23, may 1999.

[8] S. Wong, M. Kupnik, X. Zhuang, D. song Lin, K. Butts-Pauly, and B. Khuri-yakub, "Evaluation of wafer bonded CMUTs with rectangular membranes featuring high fill factor," *IEEE Transactions on Ultrasonics, Ferroelectrics and Frequency Control*, vol. 55, pp. 2053–2065, sep 2008.

PAPER G

Thermal Oxidation of Structured Silicon Dioxide

Authors: **Thomas Lehrmann Christiansen**, Ole Hansen, Jørgen Arendt Jensen, and Erik Vilain Thomsen.

Published in: ECS Journal of Solid State Science and Technology, Vol. 3, No. 5, pp. N63-N68, 2014

Abstract

The topography of thermally oxidized, structured silicon dioxide is investigated through simulations, atomic force microscopy, and a proposed analytical model. A 357 nm thick oxide is structured by removing regions of the oxide in a masked etch with either reactive ion etching or hydrofluoric acid. Subsequent thermal oxidation is performed in both dry and wet ambients in the temperature range 950 °C to 1100 °C growing a 205 ± 12 nm thick oxide in the etched mask windows. Lifting of the original oxide near the edge of the mask in the range 6 nm to 37 nm is seen with increased lifting for increasing processing temperatures. Oxides structured by reactive ion etching are lifted on average a factor of four more than oxides etched in hydrofluoric acid. Both simulations and the analytical model successfully predict the oxide topography qualitatively, showing that the mask lifting phenomenon is governed mainly by diffusion and the geometry of the oxide. Simulations also predict the oxide topography quantitatively, with an average root mean square deviation of 1.2 nm and a maximum deviation of 13 nm (39 %) from the mean of the measured values.

Thermal Oxidation of Structured Silicon Dioxide

Thomas Lehrmann Christiansen,[a,z] Ole Hansen,[a,b] Jørgen Arendt Jensen,[c] and Erik Vilain Thomsen[a]

[a]*Department of Micro- and Nanotechnology, Technical University of Denmark, DK-2800 Kgs. Lyngby, Denmark*
[b]*Center for Individual Nanoparticle Functionality CINF, Technical University of Denmark, DK-2800 Kgs. Lyngby, Denmark*
[c]*Center for Fast Ultrasound Imaging, Department of Electrical Engineering, Technical University of Denmark, DK-2800 Kgs. Lyngby, Denmark*

The topography of thermally oxidized, structured silicon dioxide is investigated through simulations, atomic force microscopy, and a proposed analytical model. A 357 nm thick oxide is structured by removing regions of the oxide in a masked etch with either reactive ion etching or hydrofluoric acid. Subsequent thermal oxidation is performed in both dry and wet ambients in the temperature range 950°C to 1100°C growing a 205 ± 12 nm thick oxide in the etched mask windows. Lifting of the original oxide near the edge of the mask in the range 6 nm to 37 nm is seen with increased lifting for increasing processing temperatures. Oxides structured by reactive ion etching are lifted on average a factor of four more than oxides etched in hydrofluoric acid. Both simulations and the analytical model successfully predict the oxide topography qualitatively, showing that the mask lifting phenomenon is governed mainly by diffusion and the geometry of the oxide. Simulations also predict the oxide topography quantitatively, with an average root mean square deviation of 1.2 nm and a maximum deviation of 13 nm (39%) from the mean of the measured values.

Manuscript submitted December 13, 2013; revised manuscript received February 20, 2014. Published March 5, 2014.

Thermal oxidation of silicon is a well-known and widely used process in the microfabrication of semiconductor devices. Silicon dioxide exhibits excellent electrical and mechanical properties and has a highly predictable growth rate, which has made thermal oxidation an indispensable process in the semiconductor industry.

The growth of silicon dioxide on planar silicon surfaces is well described by the Deal and Grove model, which accurately predicts the growth of silicon dioxides with the exception of very thin oxides (<250 Å) grown in a dry ambient.[1] The latter case was treated by Massoud et al., who introduced an exponentially decaying addition to the growth rate, thereby correcting for the faster initial oxidation rate of thin oxides.[2]

However, for non-planar silicon surfaces, or silicon surfaces with structured thin films, e.g. thin films subjected to a masked etch, the oxidation can no longer be described as a one-dimensional problem in the vicinity of the surface discontinuity. Such situations are frequently encountered, e.g. in the oxidation of silicon surfaces structured by etching and in LOCOS oxidations, where nitride diffusion barriers are exploited to produce selective oxidation of pre-defined regions of the silicon surface. The complex shape of the oxide grown in the vicinity of such nitride masks, known as the bird's beak, has been investigated intensively in the literature due to its widespread use in the fabrication of thick insulation oxides.[3,4,5] Oxidation of structured silicon has also attracted some attention, primarily due to the unwanted artifacts that arise near corners, such as oxide thinning,[6,7,8] rounding or sharpening of convex corners,[9] and oxide protrusions arising from oxidation of 90° silicon corners.[10]

Thermal oxidation of structured silicon dioxide has so far only been studied sparingly in literature.[11] This paper investigates the oxidation of an oxide step, a situation which arises if e.g. a thermally grown oxide is structured by etching and subsequently oxidized a second time in order to grow an oxide in the etched mask windows. The structured oxide acts as a diffusion mask during the second oxidation, and will experience lifting in the vicinity of the mask edge due to 2-D oxidation effects as shown in Fig. 1.[12,13] Such mask lifting can pose a problem if the flatness of the oxide surface is critical, e.g. if direct bonding is involved in subsequent processing steps.[14,15]

In this paper, the topography of the oxide mask is investigated as a function of processing parameters through simulations, measurements, and analytical considerations. The study considers a fixed initial oxide mask thickness of 357 nm, in which mask windows are opened using either reactive ion etching or hydrofluoric acid. For both types of mask windows, a second oxidation is performed, aiming for a 200 nm oxide thickness in the un-masked part of the wafer. By fixing the thickness of the two oxidations, the effect of processing parameters is investigated by carrying out the second oxidation at different oxidation temperatures from 950°C to 1100°C for both wet and dry oxidations.

Good agreement is seen between simulations and measurements, demonstrating increased mask lifting at increasing oxidation temperatures and significantly larger mask lifting for mask windows etched by reactive ion etching compared to those etched using hydrofluoric acid. This trend is confirmed by a proposed analytical model, which demonstrates that the mask lifting is essentially a function of the thicknesses of the oxides far from the oxide step. Stress effects, which are known to have a large influence on the geometry of the bird's beak,[5] are seen to be negligible for the oxide step in the temperature ranges considered in this study.

The structure of the paper is as follows: First, the theory describing the thermal oxidation of an oxide step geometry is covered. The mathematical details of the conformal mapping technique used to solve the problem analytically is presented in the appendix for convenience. This is followed by a description of the experimental setup, including sample preparation and measurement procedure. Subsequently, the approach used in the simulations to emulate the experiments is covered prior to a presentation and discussion of the results.

Theory

The oxide growth in the vicinity of an oxide step can be modeled under the assumption that the oxidation rate is diffusion limited. In the

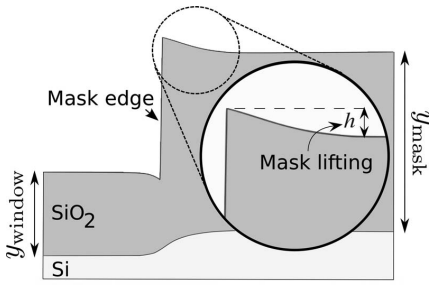

Figure 1. Simulated oxide geometry after thermal oxidation of an oxide step showing the mask lifting near the mask edge.

[z]E-mail: tlehr@nanotech.dtu.dk

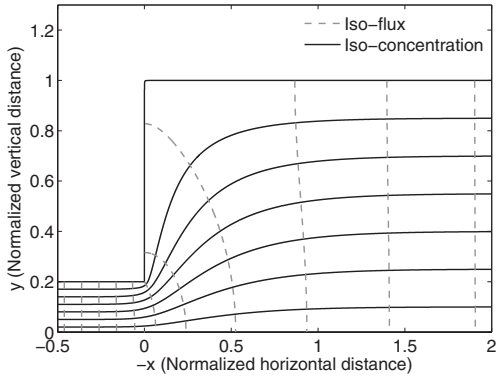

Figure 2. Iso-concentration and iso-flux lines in an oxide step geometry calculated using the conformal mapping approach. The distances are normalized to the thickness of the mask oxide (to the right of the step).

oxide film, the continuity equation governs the transport of the oxidant. For realistic diffusion times $t > y_{ox}^2/(4D)$, where y_{ox} is the thickness of the oxide and D is the diffusivity, the diffusion will be almost stationary, such that the time derivative of the oxidant concentration C becomes

$$\frac{\partial C}{\partial t} = D\nabla^2 C \simeq 0, \qquad [1]$$

where ∇^2 denotes the Laplace operator. Hence, the oxide growth rate can be expressed directly as a function of the flux density normal to the silicon/oxide interface, J,

$$\frac{ds}{dt} = \frac{J}{N}, \qquad [2]$$

where s is the oxide thickness at time t at the silicon/oxide interface, and N is the number of oxidizer molecules incorporated per unit volume of the oxide. Thus, if the normal incident flux density at the interface can be found, the oxide thickness can be calculated by a time integration of Eq. (2).

This can be achieved by use of conformal mapping, covered in detail in the appendix, with which the flux- and concentration distribution in the structured oxide can be calculated. As an example, Fig. 2 shows the iso-concentration and iso-flux contour lines of an oxide step with a thickness ratio of $y_{mask}/y_{window} = 5$, where y_{window} is the thickness of the oxide grown in the mask windows and y_{mask} is the thickness of the oxide mask. The definition of these thicknesses are given in Fig. 1. The flux density at the step, J_0, is in the derivation in the appendix shown to be proportional to the flux density in the mask windows, J_{window},

$$J_0 \simeq 0.83 J_{window}. \qquad [3]$$

The ratio of the oxide grown at the step to the oxide thickness grown in the mask window far from the step, β, thus becomes a constant, since

$$\beta = \frac{\int_0^{t_0} J_0(t)/N dt}{\int_0^{t_0} J_{window}(t)/N dt} = 0.83\frac{\int_0^{t_0} J_{window}(t)/N dt}{\int_0^{t_0} J_{window}(t)/N dt} = 0.83. \qquad [4]$$

The lifting of the mask at the mask edge at time t, denoted h in Fig. 1, may then simply be expressed as

$$h(t) = 0.56\{\beta y_{window}(t) - [y_{mask}(t) - y_{mask}(0)]\}, \qquad [5]$$

where the factor of 0.56 accounts for the volume expansion by a factor of 2.2 of the growing oxide compared to the consumed silicon.[17]

It is seen from Eq. (5) that the mask lifting becomes a function only of the oxide thicknesses far from the step, which may be found using Deal and Grove's model.[1] This states that the thickness of the growing oxide at time t is

$$y_{ox} = \sqrt{\frac{A^2}{4} + B(t+\tau)} - \frac{A}{2}, \qquad [6]$$

where τ is the time shift induced by an already existing oxide. The constants A and B are found via the parabolic and linear rate constants, B and B/A, given by

$$B = B_0 \exp\left(-\frac{E_{a,B}}{k_B T}\right), \qquad [7]$$

$$\frac{B}{A} = \frac{B_0}{A_0} \exp\left(-\frac{E_{a,B/A}}{k_B T}\right), \qquad [8]$$

where k_B is Boltzmann's constant, T is the absolute temperature, $E_{a,B}$ and $E_{a,B/A}$ are activation energies, and B_0 and B_0/A_0 are the parabolic and linear rate constants in the infinite temperature limit. The values relevant for this study are given in Table I.[18,19] The partial pressure, P, of the oxidant during the oxidation influences the parabolic and linear rate constants, such that for a reference pressure of $P_0 = 1$ atm, the pressure dependence is given by [19,20]

$$\frac{B}{A}(P) = \frac{B}{A}\frac{P}{P_0}, \qquad [9]$$

$$B(P) = B\frac{P}{P_0}. \qquad [10]$$

From Eq. (5), the mask lifting's dependency on processing parameters can be deduced. In this study, the initial mask oxide thickness, $y_{mask}(0)$, is kept constant, and the final thickness of the oxide grown in the mask window, y_{window}, is targeted at 200 nm, such that this can be assumed a constant as well. Thus, the only variable is the final mask oxide thickness, with thicker mask oxides yielding smaller mask lifting. The thickness of the oxide can be described by Eq. (6). In the limit of large values of $t + \tau$, where the oxidation time t is dictated by the desired thickness of the oxide in the mask windows, and τ is dictated by the initial mask oxide thickness, Eq. (6) reduces to

$$y_{ox} \simeq \sqrt{B(t+\tau)}, \quad t + \tau \gg 0. \qquad [11]$$

The final oxide mask thickness therefore becomes

$$y_{mask} = \sqrt{y_{window}[y_{window} + A] + y_{mask}(0)[y_{mask}(0) + A]}. \qquad [12]$$

If both y_{window} and $y_{mask}(0)$ are constants, the mask lifting depends only on the constant A, which relates to the oxidant diffusivity D and surface reaction rate k as $A = 2D/k$.[1] In Fig. 3, A has been plotted for both dry and wet oxidations in the temperature range relevant for this study. It is seen that A decreases for increasing temperature, and thus the final mask oxide thickness will decrease for increasing temperature. From Eq. (5), it is seen that this results in an increased mask lifting. This is true for both wet and dry oxidations. However, A decreases more rapidly for increasing temperatures for wet oxidations, indicating that the mask lifting will depend more strongly on temperature for wet oxidations compared to dry oxidations. In addition to this, A will, for a given temperature, be larger for wet oxidations than for dry oxidations, yielding a larger mask lifting for dry oxidations.

Table I. Parameters for the oxidation of Si(100).[18,19]

	B_0 [μ m^{2}min^{-1}]	$E_{a,B}$ [eV]	$\frac{B_0}{A_0}$ [μm min^{-1}]	$E_{a,B/A}$ [eV]
Dry oxidation	12.8667	1.23	6.176×10^4	2.0
Wet oxidation	7.00	0.78	1.755×10^5	2.05

Experimental

Sample preparation.— All samples in this study were made using a total of six 525 ± 25 μm single side polished boron doped (100) 4″

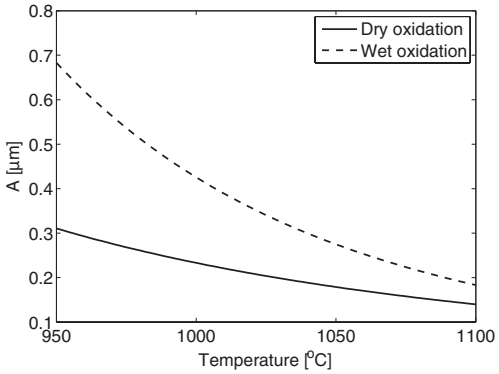

Figure 3. Plot of the constant A as a function of temperature for both dry and wet oxidations.

silicon wafers with a resistivity of 1–10 Ω-cm. To achieve a uniform oxide mask thickness on all samples, the six wafers were oxidized simultaneously using a Tempress horizontal furnace in a dry oxygen ambient at 1100°C, 1 atm, for 6 hours and 40 minutes, yielding an oxide mask thickness of 357 ± 1 nm. The thickness was measured by fitting the reflectance spectrum at zero degrees and 70 degrees angle of incidence. All wafers were then treated with hexamethyldisilazane (HMDS) prior to a lithography step on the polished side of the wafers using a 2.2 µm thick AZ 5214E photoresist and an AZ 351B developer. The photoresist was exposed to UV light for 9 seconds through a chromium/soda-lime glass mask with arrays of squares having a side length of 65 µm. In these squares, the oxide mask windows were opened using an anisotropic reactive ion etch (RIE) for the first three wafers and a buffered hydrofluoric acid (BHF) wet etch for the remaining three. This was done to enable investigation of the influence of the shape of the mask edge. The photoresist was subsequently stripped in an O_2/N_2 RF plasma with gas flows of 240/70 sccm operating at 1000 W for 25 minutes.

Each of the six wafers were then cleaved in half with a diamond scriber, yielding a total of 12 samples that were cleaned using a 10 minute clean in a $NH_4OH{:}H_2O_2{:}H_2O$ (1:1:5) mixture followed by a 10 minute clean in a $HCl{:}H_2O_2{:}H_2O$ (1:1:5) mixture, both heated to 70°C. All samples were subsequently oxidized in a Tempress horizontal furnace using the processing temperatures listed in Table II. Each sample has been assigned a number from 1 to 12, which will be used as identification in the remainder of this paper. All oxidations included a 20 minute post-annealing step in an inert nitrogen atmosphere at the given oxidation temperature. All dry oxidations were performed at 1 atm, while the wet oxidations were performed at 0.8 atm H_2O partial pressure as dictated by the settings of the furnace. The oxidation times for the respective oxidation temperatures were chosen such that a final thickness of roughly 200 nm was achieved in the mask windows. Silicon dummy wafers were included in each oxidation, allowing the actual oxide thickness to be measured, the values of which are listed in Table III. Note that a total of six oxidations

Table II. Table of the processing parameters used for the twelve samples, numbered from 1 to 12.

		Oxidation temp. [°C]			
Mask etch	Ox. type	950	1000	1050	1100
RIE	Dry	1	2	3	4
RIE	Wet	5	6	–	–
BHF	Dry	7	8	9	10
BHF	Wet	11	12	–	–

Table III. Thicknesses of the oxides grown during the second oxidation.

	Oxidation temperature [°C]			
Ox. type	950	1000	1050	1100
Dry	195 nm	210 nm	217 nm	217 nm
Wet	192 nm	204 nm	–	–

were carried out, each containing two samples; one with a RIE etched mask and one with a BHF etched mask. No wet oxidations were performed at 1050°C and 1100°C, as the required oxidation time to reach 200 nm is impractically short (<15 minutes), potentially resulting in a less well-defined and homogeneous oxide.

Measurements.— The oxide mask topography was measured using atomic force microscopy (AFM) using an approach similar to the one used by Sarioglu et al.[10] AFM was chosen over other possible measurement equipment such as scanning electron microscopy and transmission electron microscopy due to the aspect ratio of the investigated features, containing height differences less than 50 nm evolving over a distance in the order of microns. All AFM measurements were made using a Nanoman atomic force microscope operating in tapping mode, scanning a 5 µm by 5 µm area in 512 parallel scan lines covering the mask edge. An example of such a scan is shown in Fig. 4, corresponding to sample no. 3. The scan direction indicated in Fig. 4, was incorporated to avoid measurement artifacts such as overshooting from the abrupt step at the mask edge. Three such scans were performed on each sample to take processing variations into account, resulting in a total of 1536 scan lines per sample. Each scan line was post-processed in MATLAB (MathWorks, Inc., Natick, MA, USA) subject to the following routine:

1 The scan line was leveled by subtracting a linear function with a slope determined from two points on the oxide mask: 1 µm from the mask edge and the point farthest away from the mask edge.
2 The height of the point on the mask farthest away from the mask edge was subtracted from all points on the scan line to set this value to zero.
3 The scan lines were shifted horizontally such that the points with maximum height (corresponding to the mask edge) were aligned.

This routine was carried out to account for drift in the AFM measurements, thereby allowing for comparison of the individual profiles. Each profile measurement reported in this study is the average value

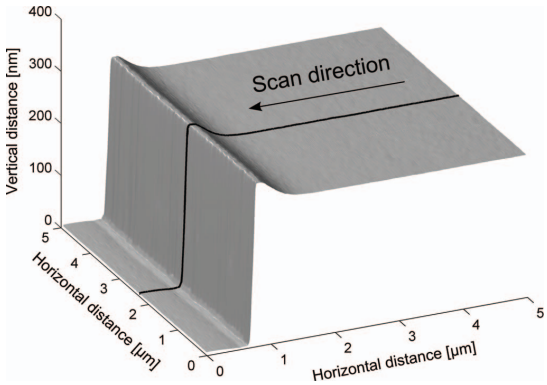

Figure 4. Illustration showing an AFM scan of sample no. 3 with 512 scan lines. A single scan line has been marked in black with an indication of the scan direction incorporated to avoid overshooting artifacts at the oxide mask edge.

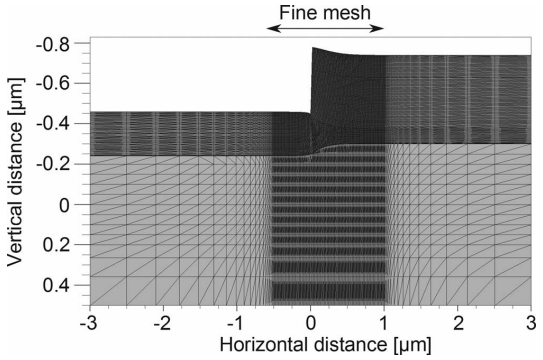

Figure 5. Simulation of the oxidation of sample no. 3 showing the mesh used for all simulations. The mesh is finer in the horizontal direction next to the oxide step where 2-D oxidation effects are prominent.

of these 1536 postprocessed scans. The standard deviation of the j'th measurement point of a profile representing a given sample is found as

$$\sigma(j) = \sqrt{\frac{1}{N-1}\sum_{i=1}^{N}[x_i(j) - \bar{x}(j)]^2}, \qquad [13]$$

where $x_i(j)$ is the average of the j'th measurement point taken over the 512 scan lines of the $N = 3$ measurement sites on each sample, and $\bar{x}(j)$ is the global average of the j'th measurement point taken over all 1536 scan lines from the sample. This standard deviation thus reflects processing variations over the whole sample. The standard deviation within a single measurement containing 512 scan lines was in all cases below 1 nm, corresponding to the roughness of the sample. This small variation is negligible compared to the variation between the three measurement sites and has therefore not been included in the presentation of the data.

Simulations

The simulations were carried out in Athena 5.20.0.R (Silvaco Inc., Santa Clara, CA, USA) using the same oxidation parameters in terms of type, final oxide thickness, temperature, pressure, and annealing as were used in the experiments. The initial structure for the simulations included a region 3 µm to each side of the oxide mask as illustrated in Fig. 5, showing the case of a RIE etched mask after the second oxidation. In the horizontal direction, a mesh size of 10 nm was used in the interval [-0.5 µm, 1 µm], the oxide mask edge being located at $x = 0$. Outside this region, where 2-D oxidation effects are negligible, the mesh size was set to increase linearly to 500 nm at the boundary of the simulation.

The resolution of the mesh created during the oxidation was set to 5 nm. This resolution was found by simulating a dry oxidation at 950°C for 880 minutes using a mesh size of 100 nm, 50 nm, 10 nm, 5 nm, and 1 nm, respectively. The relative change in the final oxide thickness stagnated to a value below 0.5% when changing from 5 nm to 1 nm, hence 5 nm was chosen for giving both sufficient accuracy and computational speed. The simulations were carried out using the "Viscous" model, which includes both viscous flow of the oxide and stress. However, the simulations were also carried out using the "Compress" model that excludes stress, yielding identical results, thereby indicating negligible stress effects.[21] This fact is supported by the work of EerNisse, who demonstrated that thermal oxides grow in stress-free conditions at temperatures above 950–975°C, while large compressive stresses arise during growth for temperatures lower than this.[22]

The RIE etched masks were simulated by a perfect right angle mask etch, while the BHF etched profile was extracted from the actual measured profile. The latter method was not used for the RIE etched masks, as the step was too abrupt to be resolved by the AFM.

Results and Discussion

Fig. 6 shows the measured and simulated profiles of the oxide mask in the vicinity of the mask edge after the second oxidation. Each plot shows the result for a given temperature at either dry or wet oxidation.

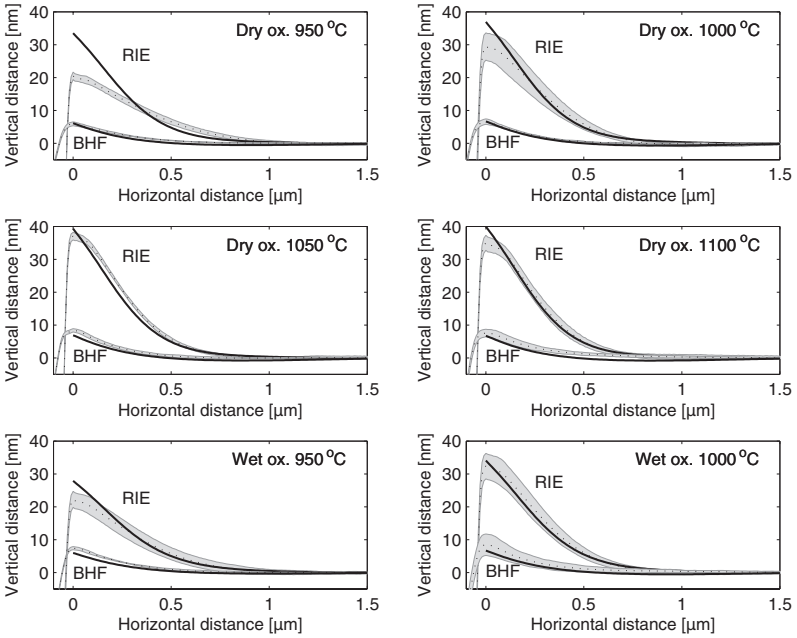

Figure 6. Simulated and measured profiles of the mask surface in the vicinity of the mask edge. The dotted lines indicate the mean of the measurements while the shaded area shows ±2 standard deviations. The solid black lines show the simulated profiles.

Furthermore, the results from both RIE and BHF etched oxide masks are given in each plot.

For the RIE etched oxide masks, the average root mean square (RMS) deviation of the simulated values from the mean of the measured values is 1.6 nm. The simulated values only deviate significantly from the measured in the region just around the mask edge, where the maximum deviation from the mean for the samples 2 through 6 is 7 nm (20%). This discrepancy in the vicinity of the mask edge could be explained by either reflow of the oxide or slight differences between the perfect right angle mask edge assumed in the simulation and the actual profile created by the RIE etch. However, sample 1 is an outlier, since it deviates significantly from the measured values in a much larger region than the remaining samples, up to as much as 13 nm (39%) from the mean. This large deviation cannot be explained by the same factors, since the same RIE etch was used for all the samples 1 through 6, and oxide reflow is expected to be more pronounced for higher temperatures. However, sample 1 was oxidized at 950°C, which is the lower limit of stress-free oxide growth.[22] The pronounced discrepancy could therefore be due to unrelieved stresses in the oxide, which the simulation fails to capture. The discrepancy was still present if stress effects were included in the simulation, but the stress behavior in this limiting case might not be well described by the simulation software.

The results for the samples 7 through 12, corresponding to the samples with BHF etched oxide masks, are in general closer to the measured values than is seen for the samples 1 through 6, with an average RMS deviation between the simulated values and the mean of the measured of 0.8 nm. This is consistent with the fact that the simulation was carried out using the measured profile of the mask after the BHF etch, and thus the simulations are less vulnerable to discrepancies between the simulated and the actual mask profile. The maximum deviation between the simulated profiles and the mean of measured profiles is therefore less than 1.8 nm (26%).

In Fig. 7, the simulated and measured mask lifting at the mask edge has been extracted for each of the six oxidation temperatures and -types. The figure has been divided into four sections, equivalent to the four combinations of wet and dry oxidations, RIE and BHF mask etchings. Furthermore, for the RIE etched masks, the analytical prediction given by Eq. (5) has been plotted along with the measured and simulated values.

It is seen that the analytical prediction in general overestimates both the measured and the simulated mask lifting. The deviation from the measured values is expected, since the simulated values also overestimate these. The reason for the deviation between the analytical and the simulated values can be explained by the fact that the conformal mapping, on which the theory is based, assumes a right angle oxide step and a flat oxide-silicon interface at all times, which is of course a simplifying assumption. Furthermore, the simulated profile considers the top surface of the oxide mask, while the conformal mapping only considers the oxide grown at the silicon/oxide interface, i.e. below the mask. Thus, the geometrical deformation of the mask created during growth is not captured by the theory.

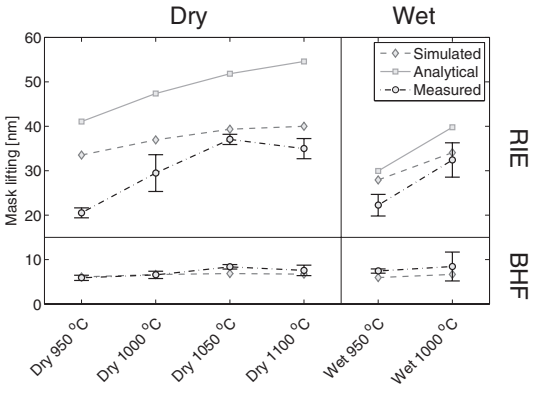

Figure 7. Mask lifting at the mask edge as a function of oxidation temperature and type for oxide mask etched by either RIE or BHF. Both measured, simulated and analytically estimated values are given.

Despite the mentioned discrepancies, both the simulated and the analytically estimated values of the mask lifting successfully capture the qualitative parameter dependency. As was predicted by Eq. (5), and confirmed by both simulations and measurements, the mask lifting increases with oxidation temperature. Note, however, that the temperature dependence seen in Fig. 7 is slightly misleading, since the final oxide thickness outside the mask is not exactly the same for all oxidations. Rather, it increases slightly with temperature, as seen in Table III, leading to an exaggerated temperature dependence.

The analytical estimate and the simulated values both predict that, for equal temperatures, the wet oxidations should yield smaller mask liftings than dry oxidations. Furthermore, they both predict a more pronounced temperature dependency for wet oxidations compared to dry oxidations. However, the measurements do not show significantly different mask liftings for wet and dry oxidations at 950°C and 1000°C, respectively.

In general, the oxidation temperature and oxidation type are seen to have only a minor influence on the mask lifting. As opposed to this, the type of etch used for the oxide mask exhibits a much more pronounced influence. Both simulations and measurements demonstrate significantly smaller mask liftings for BHF etched masks compared to RIE etched masks. For all temperatures, the measured mask lifting is on average a factor of four higher for the RIE etched masks compared to the BHF etched masks. Although the analytical theory does not describe the BHF etched masks' geometry, this effect is to be expected, since the sloped mask edge created by the isotropic BHF etch impedes the oxidant diffusion from the side of the mask.

Conclusions

The topography of thermally oxidized, structured silicon dioxide was investigated through simulations, atomic force microscopy, and a proposed analytical model using conformal mapping. A 357 nm thick oxide was grown and structured by removing regions of the oxide in a masked etch with either reactive ion etching or hydrofluoric acid. Subsequent thermal oxidations were performed in both dry and wet ambient in the temperature range 950°C to 1100°C in order to grow a 205 ± 12 nm thick oxide in the etched mask windows. The original oxide was seen to act as a diffusion mask during the second oxidation, resulting in lifting in the range 6 nm to 37 nm of the masking oxide near the edge of the mask. The mask lifting exhibited a slight oxidation parameter dependency, demonstrating increased lifting for increasing processing temperatures. The etch used to structure the oxide showed a much more pronounced effect on the mask lifting, with the reactive ion etched masks being lifted on average a factor of four more than oxides etched with hydrofluoric acid. Both simulations and the analytical model was able to predict the oxide topography qualitatively. The analytical model was used to derive a simple relationship between the mask lifting and the thicknesses of the oxide far from the mask edge. The simulations predicted the oxide topography quantitatively, with an average RMS deviation of 1.2 nm and a maximum deviation of 13 nm (39%) from the mean of the measured values.

Acknowledgments

The authors thank Mathias Dahl Johnsen and Jeppe Nyskjold Lohse, Technical University of Denmark, for their help with sample preparation. This work was financially supported by the Danish National Advanced Technology Foundation (82-2012-4), and partly supported by the Danish National Research Foundation's Center for Individual Nanoparticle Functionality (DNRF54).

Appendix: Conformal Mapping of the Diffusion Problem

The problem of finding the flux density in an oxide step similar to the structure investigated in this study can be solved through the use of conformal mapping.[16] Let the infinite strip $0 < \mathrm{Im}\, w < 1$ in the complex plane represent a uniform oxide layer. The complex coordinates $w = \Psi + \mathrm{i}\mathcal{C}$ are used to represent the flux, Ψ, and concentration, $\mathcal{C}$, functions of the problem, respectively. The concentration at the top of the oxide at $\mathrm{Im}\, w = 1$ is assumed to be C_0 during the whole oxidation, corresponding to a constant oxidant concentration in the furnace. The concentration at the silicon/oxide interface at $\mathrm{Im}\, w = 0$ is assumed to be negligible and is set to zero. The real concentration is then given by $C = C_0\mathcal{C}$, while the real flux is $\psi = DC_0\Psi$.

The next step is to map the infinite strip on to a geometry similar to an oxide step. Such a geometry can be represented in the complex plane by $0 < \mathrm{Im}\, z < 1 \cap \mathrm{Re}\, z < 0$, and $0 < \mathrm{Im}\, z < 1/\alpha \cap \mathrm{Re}\, z > 0$, where z is a complex value and $\alpha = y_{\mathrm{mask}}/y_{\mathrm{window}}$, where y_{window} is the thickness of the oxide grown in the mask windows and y_{mask} is the thickness of the oxide mask as shown in Fig. 1. The conformal mapping from infinite strip to step geometry is performed in two steps: First, the infinite strip $0 < \mathrm{Im}\, w < 1$ is mapped on the upper half complex plane, ξ, which is accomplished through $\xi = \exp(\pi w)$ and $w = (\ln \xi)/\pi$. The mapping from the the half plane to the step geometry is subsequently accomplished through

$$z = \frac{1}{\pi}\left[\ln\frac{\alpha^2-1}{\alpha^2+1-2\sqrt{\xi-1}\sqrt{\xi-\alpha^2}-2\xi} + \frac{\mathrm{i}}{\alpha}\left(\frac{\pi}{2}+\mathrm{arctanh}\frac{\xi(\alpha^2+1)-2\alpha^2}{2\alpha\sqrt{\xi-1}\sqrt{\xi-\alpha^2}}\right)\right], \qquad \text{[A1]}$$

with poles/zeroes at $\xi = 0$, $\xi = 1$, and $\xi = \alpha^2$ used in a Schwartz-Cristoffel transform.[16] The complex coordinates $z = x + \mathrm{i}y$ represent the position in the oxide normalized to the thickness of the mask oxide, y_{mask}. Fig. 2 shows a plot of Eq. (A1) for $\alpha = 5$, demonstrating iso-flux and iso-concentration contour lines. For convenience, the x-coordinate has been sign-inverted to orient the oxide mask to the right in accordance with the remaining figures in this paper.

The line $\mathrm{Im}\, w = 1$ is mapped on $\mathrm{Im}\, z = 0$, equivalent to the real axis, x, representing the oxide/silicon interface. The concentration at the silicon/oxide interface and at the oxide surface is thus interchanged in this mapping, but this does not affect the result, as it effectively corresponds to shifting the concentration's zero reference. At the silicon/oxide interface, $w = \Psi + \mathrm{i}$, corresponding to $\xi = -\exp(\pi\Psi)$. Inserting this in Eq. (A1) gives an expression for the position along the silicon/oxide interface x as a function of the normalized flux Ψ at the interface.

The parameter that determines the oxide growth is the normalized flux density at the silicon/oxide interface given by $\tilde{J} = d\Psi/dx$. By differentiation, it is seen that

$$\frac{1}{\tilde{J}} = \frac{dx}{d\Psi} = -\sqrt{\frac{1+e^{\pi\Psi}}{\alpha^2+e^{\pi\Psi}}} \Rightarrow -e^{\pi\Psi} = \xi = \frac{\tilde{J}^2-\alpha^2}{\tilde{J}^2-1}. \qquad \text{[A2]}$$

By inserting Eq. (A2) into Eq. (A1), the position at the interface normalized to y_{mask} can be found as a function of normalized flux density $\tilde{J}$:

$$x = \frac{1}{\pi}\ln\left[\frac{\tilde{J}-1}{\tilde{J}+1}\left(\frac{\alpha+\tilde{J}}{\alpha-\tilde{J}}\right)^{1/\alpha}\right]. \qquad \text{[A3]}$$

The thickness of the grown oxide may now, in general, be calculated by finding the normalized flux density from Eq. (A3) and integrating Eq. (2) over time. However, at the edge of the step $x = 0$, Eq. (A3) reduces to

$$\frac{\tilde{J}_0+1}{\tilde{J}_0-1} = \left(\frac{\alpha+\tilde{J}_0}{\alpha-\tilde{J}_0}\right)^{1/\alpha}, \qquad \text{[A4]}$$

where $\tilde{J}_0$ denotes the normalized flux density at the step edge. For $\alpha > 1$, which is always true, Eq. (A4) yields an approximately constant relationship between the normalized flux density at the step edge $\tilde{J}_0$ and the thickness ratio α:

$$\tilde{J}_0 \simeq 0.83\alpha. \qquad \text{[A5]}$$

Hence, the real flux density at the mask edge J_0 becomes

$$J_0 \simeq 0.83\frac{DC_0\alpha}{y_{\mathrm{mask}}} = 0.83\frac{DC_0}{y_{\mathrm{window}}} = 0.83J_{\mathrm{window}}, \qquad \text{[A6]}$$

where the last equality comes from applying Fick's law $J = -D\nabla C$ to the one-dimensional diffusion problem in the mask windows.

References

1. B. E. Deal and A. S. Grove, *J. Appl. Physics*, **36**, 12 (1965).
2. H. Z. Massoud, J. D. Plummer, and E. A. Irene, *J. Electrochem. Soc.*, **132**, 7 (1985).
3. D. Chin, S.-Y. Oh, S.-M. Hu, R. W. Dutton, and J. L. Moll, *IEEE Trans. Electron Devices*, **ED-30**, 7 (1983).
4. T.-C. Wu, W. T. Stacy, and K. N. Ritz, *J. Electrochem. Soc.*, **130**, 7 (1983).
5. N. Guillemot, G. Pananakakis, and P. Chenevier, *IEEE Trans. Electron Devices*, **ED-34**, 5 (1987).
6. D.-B. Kao, J. P. McVittie, W. D. Nix, and K. C. Saraswat, *IEEE Trans. Electron Devices*, **ED-34**, 5 (1987).
7. D.-B. Kao, J. P. McVittie, W. D. Nix, and K. C. Saraswat, *IEEE Trans. Electron Devices*, **ED-35**, 1 (1988).
8. R. B. Marcus and T. T. Sheng, *J. Electrochem. Soc.*, **129**, 6 (1982).
9. K. Yamabe and K. Imai, *IEEE Trans. Electron Devices*, **ED-34**, 8 (1987).
10. A. F. Sarioglu, M. Kupnik, S. Vaithilingam, and B. T. Khuri-Yakub, *J. Electrochem. Soc.*, **159**, 2 (2012).
11. K. K. Park, H. Lee, M. Kupnik, and B. T. Khuri-Yakub, *J. Microelectromech. Syst.*, **20**, 1 (2011).
12. H.-S. Yoon, M.-C. Ho, N. Apte, P. Cristman, S. Vaithilingam, M. Kupnik, K. B. Pauly, and B. T. Khuri-Yakub, *AIP Conf. Proc.*, 183 (2010).
13. T. L. Christiansen, O. Hansen, M. D. Johnsen, J. N. Lohse, J. A. Jensen, and E. V. Thomsen, *Proc. IEEE Ultrason. Symp.*, 1737 (2013).
14. A. Plössl and G. Kräuter, *Materials Science and Engineering*, **R25** (1999).
15. T. Martini, S. Hopfe, S. Mack, and U. Gösele, *Sensors and Actuators A: Physical*, **75** (1999).
16. W. Kaplan, *Introduction to Analytic Functions*, Addison-Wesley, Reading, MA (1966).
17. G. S. May and S. M. Sze, *Fundamentals of Semiconductor Fabrication*, p. 43, John Wiley & Sons, New York (2004).
18. B. E. Deal, *J. Electrochem. Soc.*, **125**, 4 (1978).
19. R. R. Razouk, L. N. Lie, and B. E. Deal, *J. Electrochem. Soc.*, **128**, 10 (1981).
20. L. N. Lie, R. R. Razouk, and B. E. Deal, *J. Electrochem. Soc.*, **129**, 12 (1982).
21. *ATHENA User's manual*, Silvaco, Inc. p. 3–48 (2010).
22. E. P. EerNisse, *Appl. Phys. Lett.*, **35**, 1 (1979).

PAPER H

2-D Row-Column CMUT Arrays with an Open-Grid Support Structure

Authors: Thomas Lehrmann Christiansen, Christian Dahl-Petersen, Jørgen Arendt Jensen, and Erik Vilain Thomsen.

Published in: Proceedings of the IEEE International Ultrasonics Symposium, pp. 1712-1715, 2013

Abstract

Fabrication and characterization of 64+64 2-D row-column addressed CMUT arrays with 250 µm element pitch and 4.4 MHz center frequency in air incorporating a new design approach is presented. The arrays are comprised of two wafer bonded, structured silicon-on-insulator wafers featuring an open-grid support structure on top of the CMUT plates, omitting the need for through wafer vias. A 5 mask process is used to produce 2-D row-column addressed CMUT arrays with 74 nm vacuum gaps, single crystalline silicon plates with optional lithographically defined mass loads, 120 V pull-in voltage, and high voltage insulation up to 310 V.

2-D Row-Column CMUT Arrays with an Open-Grid Support Structure

Thomas Lehrmann Christiansen*, Christian Dahl-Petersen*, Jørgen Arendt Jensen† and Erik V. Thomsen*
*Department of Micro- and Nanotechnology, Technical University of Denmark, DK-2800 Kgs. Lyngby, Denmark
†Center for Fast Ultrasound Imaging, Department of Electrical Engineering,
Technical University of Denmark, DK-2800 Kgs. Lyngby, Denmark

***Abstract*—Fabrication and characterization of $64 + 64$ 2-D row-column addressed CMUT arrays with 250 µm element pitch and 4.4 MHz center frequency in air incorporating a new design approach is presented. The arrays are comprised of two wafer bonded, structured silicon-on-insulator wafers featuring an open-grid support structure on top of the CMUT plates, omitting the need for through wafer vias. A 5 mask process is used to produce 2-D row-column addressed CMUT arrays with 74 nm vacuum gaps, single crystalline silicon plates with optional lithographically defined mass loads, 120 V pull-in voltage, and high voltage insulation up to 310 V.**

I. Introduction

Capacitive micromachined ultrasonic transducers (CMUTs) require high electric field strengths in the order of 10^8 V/m to actuate the movable top plate in transmit operation and to increase its compliance in receive [1]. A prerequisite for achieving such high electric field strengths without using excessively high voltages is to have electrode gap spacings in the order of a couple of hundred nanometers. In the simplest possible CMUT design using direct fusion bonding, the oxide used for both structural support and insulation of the applied voltage has the same thickness as the vacuum gap [2]. As the theoretical dielectric breakdown field strength of silicon dioxide is roughly 10^9 V/m, even a few impurities in the oxide can degrade the breakdown strength enough to cause device failure [3]. Therefore, various designs have been suggested in the literature that seek to combine small vacuum gap spacings and extended structural posts able to withstand high voltages, e.g. through LOCOS oxidation or buried oxides [4], [5]. The latter process offers the highest degree of insulation, since the bottom electrode rests on a buried oxide (BOX) layer, the thickness of which can be chosen independently of the desired vacuum gap size. If such a process is used to fabricate fully populated 2-D arrays, through wafer vias are needed in order to access the bottom electrode [5]. This complicates the fabrication process considerably if the arrays are to be operated in the MHz range, where the via diameter is limited by the pitch of the closely spaced CMUT elements.

The purpose of this paper is to demonstrate a fabrication process primarily intended for row-column addressed 2-D arrays that benefit from the before mentioned insulation advantages of a buried oxide structure without the need for through wafer vias due to the use of an open-grid support structure. Row-column addressing has emerged as a promising addressing scheme for 2-D ultrasonic arrays, and it has been demonstrated theoretically that for three-dimensional imaging, the resolution and contrast of such arrays is comparable to fully addressed 2-D arrays [6], [7]. Prototypes of row-column addressed transducers using both CMUT technology [8], [9], and conventional bulk piezoelectric technology has been demonstrated, in the latter case in an impressive 256×256 size array with corresponding $256 + 256$ connections [10]. This paper exclusively covers the design and fabrication of the proposed structure, which is demonstrated on arrays with $64 + 64$ connections. Preliminary characterization tests are carried out to evaluate the basic performance of the design and to identify its strengths and weaknesses.

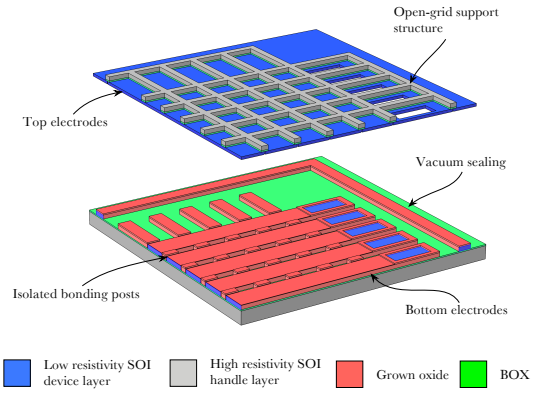

Fig. 1: An illustration of the 2-D row-column array design shown in exploded view with the top and bottom wafer separated at the bonding interface.

II. Design

The design presented in this paper is based on the criterion of having a highly insulating post structure, whilst still allowing for well-controlled vacuum gap sizes in the order of 100-200 nm. As covered in previous work in the literature, such a design can be realized using silicon-on-insulator (SOI) wafers with BOX layers that can support high voltages [5]. A second criterion is that the contact pads to the row- and column elements are accessible from the perimeter of the array. This criterion will allow for wire bonding to

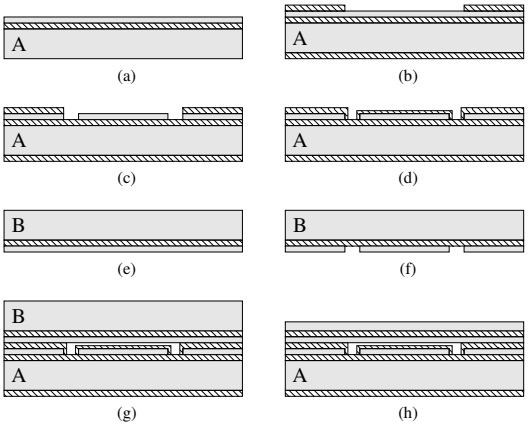

Fig. 2: An illustration of the main steps involved in the fabrication process. Silicon is illustrated in grey while silicon dioxide is shown in a striped pattern.

the front of the device without the need for through wafer vias, thereby simplifying the fabrication process considerably. Through wafer vias can, if desired, still be integrated for e.g. flip chip mounting. Finally, the flexural top plates of the CMUT elements should be made of single crystalline silicon to ensure uniform mechanical properties over large arrays. This dictates a wafer-bonding approach as originally suggested by Huang et. al [2] and used in later processes involving BOX insulation layers [5].

The listed requirements dictates a radical rearrangement of the mechanical structure supporting the flexible CMUT top plates. In Fig. 1, the proposed design is shown in exploded view with the device separated at the bonding interface. The bottom electrodes are resting on a BOX layer and are completely insulated from the top electrodes by either BOX layers or vacuum. Consequently, the isolated posts aligned parallel to the bottom electrodes can only ensure a well-defined gap between the top- and bottom plates. To define the individual CMUT elements, an alternative support structure is therefore needed to supply the mechanical support perpendicular to the bottom electrodes. The approach taken in this paper is to provide this through an open-grid support structure placed *above* the top electrodes, thereby allowing for top- and bottom electrodes insulated by BOX layers and vacuum. As seen in Fig. 1, the device is fabricated using two SOI wafers. Thus, the material for producing the open-grid support is supplied by the highly resistive handle layer and BOX layer of the top SOI wafer, enabling lithographical definition of the frame of the individual elements. The top electrodes are insulated from each other by etching trenches into the top SOI device layer. The vacuum gap between the top- and bottom electrodes is defined by having two accumulated oxide layers on the posts and only one on the bottom electrode as pull-in insulation, thereby ensuring precise control of the gap height. The vacuum is maintained through a vacuum sealing frame that surrounds the entire array.

A couple of important advantages of the open-grid support should be mentioned. First, since it is solely responsible for the definition of the CMUT elements, the bonding of the two wafers essentially only functions as vacuum sealing. All bonding interfaces are furthermore isolated from both top- and bottom electrodes. Thus, the bonding can, if desired, be carried out by alternatives to direct wafer bonding, e.g. eutectic bonding, which do not demand the same cleanliness and low surface roughness. In this paper, the design will be demonstrated using direct wafer bonding. A second major advantage of the open-grid support is the possibility of lithographically defining mass loads on the top plates together with the open-grid support. Additional mass loads can be desirable if high output pressures are wanted or if a more piston-like behavior of the CMUT top plate is needed [11], [12].

III. Fabrication

The main steps of the fabrication process are outlined in Fig. 2. A 4" silicon-on-insulator (SOI) wafer with a 2 µm low resistivity device layer, a 1 µm buried oxide layer (BOX), and a 500 µm high resistivity handle layer (wafer A) is used as the processing substrate for the bottom electrodes, see Fig. 2a. A 168 nm dry thermal oxide is grown and the device layer is patterned in a plasma etch through a lithographically defined resist mask using the silicon device layer as an etch stop as illustrated in Fig. 2b. A second lithography step is used to define a resist mask for a deep reactive ion etch through the device layer, this time with the BOX layer acting as etch stop, see Fig. 2c. The inductively coupled plasma etcher uses a low frequency 380 kHz generator in conjunction with the usual high frequency RF coil to avoid lateral etching or "notching" once the BOX is reached. As illustrated in Fig. 2d, a second 143 nm oxidation step follows, resulting in a total of 217 nm oxide in the post areas already containing oxide, ensuring both electrical insulation of exposed silicon surfaces and insulation of the bottom electrode during pull-in operation. Fig. 3a shows an optical micrograph of the resulting structure after this step. The yellow pads in the bottom of the figure are contact pads to the blue bottom electrodes, which are seen as vertical columns. Every second bottom electrode has a corresponding contact pad in the opposing end of the array. The colors are the actual colors of the different oxide layers, thereby clearly distinguishing the structures. As mentioned, the blue oxide covers the bottom electrodes as a result of the second oxidation. The yellow oxide is a product of both the first and the second oxidation, and will provide the bond surface during the direct wafer bonding step. Note the small rectangular posts in between the bottom electrodes, which will provide support for the crossing top electrodes. Each post is completely isolated on the underlying greenish BOX layer. In the bottom right corner, a part of the vacuum sealing frame illustrated in Fig. 1 is seen.

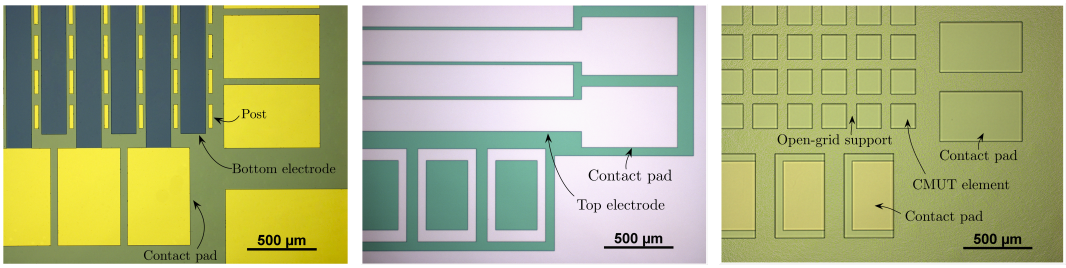

(a) (b) (c)

Fig. 3: Optical micrographs of the fabricated device. The bottom electrodes (a), top electrodes (b), and support grid (c) are all seen in the same corner section of a device, where both the electrodes and the bond pads can be seen. Every second bond pad is located at the opposing side of the array. In order to better visualize the alignment between the three layers, the micrograph of the top electrode (b) has been flipped around a vertical axis.

The top electrodes are etched into the device layer of a second SOI wafer (wafer B) as illustrated in Figs. 2e and 2f, once again using an ICP silicon etcher with a low frequency generator to avoid notching when the BOX layer is reached. The SOI wafer has a highly doped 20 µm device layer, a 1 µm BOX and a 500 µm lightly doped handle layer. Fig. 3b shows an optical micrograph of the result of this processing step. The shown area of the array corresponds to the area shown in Fig. 3a. Note, however, that since the wafer containing the top electrodes is to be bonded to the wafer containing the bottom electrodes, the image in Fig. 3b has been flipped around a vertical axis to better visualize the alignment of the structures. It is seen that the top electrodes are oriented perpendicularly to the bottom electrodes and that access is made to the bottom electrode contact pads through the top electrode device layer.

The two wafers are then cleaned using a standard RCA cleaning procedure, aligned to each other, and bonded at 50 °C for 5 minutes at 1500 N piston force and 10^{-2} mbar ambient pressure as illustrated in Fig. 2g (note that the top electrodes are not visible in this illustration as they are oriented perpendicularly to the bottom electrodes). The bonded wafers are subsequently annealed for 70 minutes at 1100 °C to increase the bonding strength. The handle layer of the SOI wafer containing the top electrodes is then thinned down in KOH at 90 °C, see Fig. 2h, having an etch rate of 1.57 µm/min. The etch rate is stable enough to allow precise thinning of the wafer to a desired thickness with a tolerance of roughly 2-4 µm. Thus, for the desired final handle thickness of 40 µm, a 36 µm thickness was realized in practice. Prior to the bonding, alignment marks had been etched into the handle of the SOI wafer containing the bottom electrodes. This alignment is used as back-to-front alignment in a lithography step on the thinned handle. The resulting resist mask acts as an etch mask in a subsequent ICP silicon etch using the BOX as a stop layer, in which the support structure and optionally mass loads are defined. Fig. 4 shows a SEM micrograph of a device having mass loads incorporated on the CMUT plates. The individual elements are designed for a resonant frequency in air of 7 MHz, dictating an active element side length of 180 µm. The exposed BOX as well as the underlying oxide on the bottom electrode contact pads are etched using an ICP oxide etcher, and the resulting structure after removing the resist mask can be seen in Fig. 3c, in this case with no mass loads. The slight reddish color on seen in the bottom electrode contact pads is due to the partial transparency of the 2 µm device layer. Note that the alignment during bonding is off by roughly 20 µm in the horizontal direction in Fig. 3c due to an issue with the bonding aligner in this direction. However, as this was a known issue, the margins in the design allows for up to 50 µm misalignment during bonding. The metal bond pads needed for wire bonding were not added to this prototype device, as this was not needed for the initial characterizations. Therefore, devices with wire bondings and individual external electrical connections are left for future batches. However, preliminary trials with the needed processing has been carried out, demonstrating the feasibility of patterning a resist over the elevated support structure if two independent resist spin-on steps are used. Alternatively, the metal pads can be incorporated in

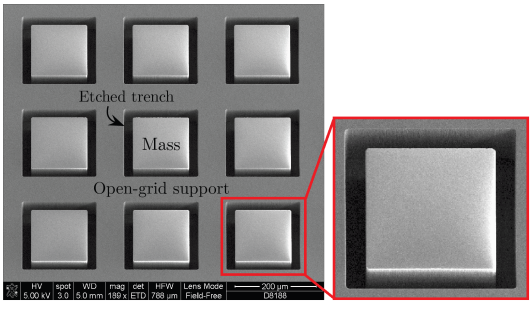

Fig. 4: SEM micrograph showing a detail of a device with lithographically defined and etched mass loads.

the bonding step by using eutectic bonding. As all bonding surfaces are isolated, and since the support grid is responsible for the structural support of the elements, a conductive eutectic bonding can be used with no disadvantage.

IV. Characterization

One of the main requirements of the device is its ability to withstand high voltages. Since all potentials are supported by BOX layers being 1 µm in thickness, the structure should, theoretically, withstand voltages up to 1000 V before breakdown occurs. In order to measure the actual breakdown voltage, a test structure was included on the chip which was identical to the CMUT elements, but with the handle still present on top of the plate. In this way, pull-in was avoided due to the much higher plate stiffness, hence allowing measurement of the breakdown voltage of the post. The measured breakdown voltage on this test structure was 310 V, i.e. considerably lower than the theoretical limit. This either suggests that the BOX oxide quality is poor or that surface currents are able to flow inside the device. The latter could be induced by alteration of the oxide surface during the reactive ion etching, where the ions can lead to trap formation. Despite the relatively low breakdown voltage of the posts compared to the theoretical limit, it is worth noting that this breakdown voltage is much higher than the measured pull-in voltage of the device, being 120 V. Therefore, the functionality of the additionally insulated post structure is verified.

The displacement frequency response of a single CMUT cell of the device for two different DC bias voltages was measured using laser Doppler vibrometry, and is shown in Fig. 5. The element was excited using a 10 V AC chirp signal, covering the frequency range in the vicinity of the resonant frequency in air. The resonant frequency is seen to be 4.4 MHz at a DC bias voltage of 80 V, dropping to just above 4.3 MHz at 110 V DC bias voltage due to the spring softening effect. This resonance frequency is roughly 3 MHz lower than a perfectly clamped rectangular plate of the same dimension as the CMUT element, indicating that the open-grid support structure is, as expected, not ideally rigid.

V. Conclusion

In this work, a new CMUT structure for 2-D row-column addressed arrays was proposed. The introduction of an open-grid support structure on top of the flexural plates enabled highly insulating post structures, the advantage of non-critical bonding, no need for through-wafer vias, and the possibility to integrate mass loads on the plates. The post structures could withstand up to 310 V, being significantly higher than the 120 V pull-in voltage of the device. Despite its demonstrated advantages, the open-grid support might lead to increased cross-coupling, and might have an effect on the acoustic output characteristics. These potential issues will be the subject of future research.

Acknowledgment

This work was financially supported by the Danish National Advanced Technology Foundation (82-2012-4).

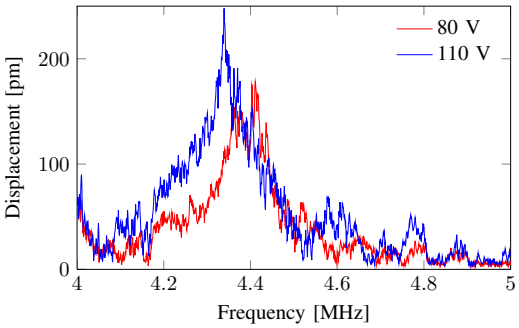

Fig. 5: Measurements of the top plate deflection as a function of frequency in the vicinity of the resonant frequency at two different bias voltages and an AC amplitude of 10 V. The measurements were recorded using laser Doppler vibrometry.

References

[1] O. Oralkan, A. S. Ergun, J. A. Johnson, M. Karaman, U. Demirci, K. Kaviani, T. H. Lee, and B. T. Khuri-Yakub, "Capacitive micromachined ultrasonic transducers: next-generation arrays for acoustic imaging?" *IEEE Trans. Ultrason., Ferroelec., Freq. Contr.*, vol. 49, no. 11, pp. 1596–1610, 2002.

[2] Y. Huang, A. S. Ergun, E. Hæggström, M. H. Badi, and B. T. Khuri-Yakub, "Fabricating capacitive micromachined ultrasonic transducers with wafer-bonding technology," *J. Microelectromech. S.*, vol. 12, no. 2, pp. 128–137, 2003.

[3] G. S. May and S. M. Sze, *Fundamentals of semiconductor fabrication*. Wiley, 2004.

[4] K. K. Park, H. J. Lee, M. Kupnik, O. Oralkan, and B. T. Khuri-Yakub, "Fabricating capacitive micromachined ultrasonic transducers with direct wafer-bonding and locos technology," in *IEEE International Conference on Micro Electro Mechanical Systems*, 2008, pp. 339–342.

[5] M. Kupnik, S. Vaithilingam, K. Torashima, I. Wygant, and B. Khuri-Yakub, "CMUT fabrication based on a thick buried oxide layer," in *Proc. IEEE Ultrason. Symp.*, 2010, pp. 547–550.

[6] C. E. M. Démoré, A. Joyce, K. Wall, and G. Lockwood, "Real-time volume imaging using a crossed electrode array," *IEEE Trans. Ultrason., Ferroelec., Freq. Contr.*, vol. 56, no. 6, pp. 1252–1261, 2009.

[7] M. F. Rasmussen and J. A. Jensen, "3D ultrasound imaging performance of a row-column addressed 2D array transducer: a simulation study," in *Proc. SPIE Med. Imag.*, 2013, pp. 1–11, 86750C.

[8] A. S. Logan, L. L. P. Wong, A. I. H. Chen, and J. T. W. Yeow, "A 32 x 32 element row-column addressed capacitive micromachined ultrasonic transducer," *IEEE Trans. Ultrason., Ferroelec., Freq. Contr.*, vol. 58, no. 6, pp. 1266–1271, jun 2011.

[9] R. Zemp, W. Zheng, and P. Zhang, "Feasibility of top-orthogonal-to-bottom electrode (TOBE) 2D CMUT arrays for low-channel-count 3D imaging," in *Proc. IEEE Ultrason. Symp.*, 2011, pp. 498–502.

[10] C. H. Seo and J. T. Yen, "A 256 x 256 2-D array transducer with row-column addressing for 3-D rectilinear imaging," *IEEE Trans. Ultrason., Ferroelec., Freq. Contr.*, vol. 56, no. 4, pp. 837–847, apr 2009.

[11] Y. Huang, X. Zhuang, E. O. Hæggström, A. S. Ergun, C.-H. Cheng, and B. T. Khuri-Yakub, "Capacitive micromachined ultrasonic transducers with piston-shaped membranes: Fabrication and experimental characterization," *IEEE Trans. Ultrason., Ferroelec., Freq. Contr.*, vol. 56, pp. 136–145, 2009.

[12] H.-S. Yoon, M.-C. Ho, N. Apte, P. Cristman, S. Vaithilingam, M. Kupnik, K. Butts-Pauly, B. T. Khuri-Yakub, Y. Matsumoto, L. A. Crum, and G. R. ter Haar, "Fabrication of CMUT cells with gold center mass for higher output pressure," in *AIP Conference Proceedings*, 2011, pp. 183–188.

PAPER

Row-Column Addressed 2-D CMUT Arrays with Integrated Apodization

Authors: **Thomas Lehrmann Christiansen**, Morten Fischer Rasmussen, Jørgen Arendt Jensen, and Erik Vilain Thomsen.

Published in: Proceedings of the IEEE International Ultrasonics Symposium, pp. 600-603, 2014

Abstract

Experimental results from row-column addressed capacitive micromachined ultrasonic transducers (CMUTs) with integrated apodization are presented. The apodization is applied by varying the density of CMUT cells in the array with the objective of damping the edge waves originating from the element ends. Two row-column addressed 32+32 CMUT arrays are pro- duced using a wafer-bonding technique, one with and one without integrated apodization. Hydrophone measurements of the emitted pressure field from the array with integrated apodization show a reduction in edge wave energy of $8.4\,\mathrm{dB}$ (85 %) compared to the array without integrated apodization. Field II simulations yield a corresponding reduction of $13.0\,\mathrm{dB}$ (95 %). The simulations are able to replicate the measured pressure field, proving the predictability of the technique.

Row-Column Addressed 2-D CMUT Arrays with Integrated Apodization

Thomas Lehrmann Christiansen*, Morten Fischer Rasmussen†, Jørgen Arendt Jensen† and Erik Vilain Thomsen*
*Department of Micro- and Nanotechnology, Technical University of Denmark, DK-2800 Kgs. Lyngby, Denmark
†Center for Fast Ultrasound Imaging, Department of Electrical Engineering,
Technical University of Denmark, DK-2800 Kgs. Lyngby, Denmark

***Abstract*—Experimental results from row-column addressed capacitive micromachined ultrasonic transducers (CMUTs) with integrated apodization are presented. The apodization is applied by varying the density of CMUT cells in the array with the objective of damping the edge waves originating from the element ends. Two row-column addressed $32+32$ CMUT arrays are produced using a wafer-bonding technique, one with and one without integrated apodization. Hydrophone measurements of the emitted pressure field from the array with integrated apodization show a reduction in edge wave energy of 8.4 dB (85 %) compared to the array without integrated apodization. Field II simulations yield a corresponding reduction of 13.0 dB (95 %). The simulations are able to replicate the measured pressure field, proving the predictability of the technique.**

I. Introduction

Row-column addressed arrays for ultrasonic imaging have recently attracted some attention, as they offer volumetric imaging with a greatly reduced number of connections to the array compared to fully wired 2-D matrix probes [1]–[4]. Despite this advantage, such arrays have an inherent drawback: the long elements produce edge waves originating from the abrupt truncation at the element ends. These edge waves generate artefacts in the image in the form of ghost echoes [1], [5]. Due to the row-column addressing scheme, no electronic control is available along the length of the elements. As a consequence, this rules out the option of applying electronic apodization to remove the effect of the truncation. A solution is to integrate the apodization in the transducer array itself, as suggested in recent studies [1], [5]. Several embodiments of the integrated apodization have been suggested, such as attenuating layers [1], variation in the active element area, and bias control of capacitive micromachined ultrasonic transducers (CMUTs) to alter the emitted/received energy [6].

The objective of this paper is to demonstrate the effect of an integrated apodization, based on variation of the effective area, through measurements of the emitted pressure field. Experimental results are presented from two versions of a $32+32$ row-column addressed CMUT array; one without integrated apodization and one with integrated apodization. Simulations in Field II [7], [8] are carried out to compare the measured pressure field with the expected, thereby demonstrating the predictability of the technique.

II. Transducer Design

In this study, two $32+32$ row-column addressed CMUT arrays are produced; one without integrated apodization and one with integrated apodization. The mask layout of the two transducer arrays are depicted in Fig. 1. The two transducers both have a total size of 12 mm×12 mm, a pitch of 300 µm, an element kerf of 12 µm, and a total of 32 row elements and 32 column elements. The aperture size is consequently 9.6 mm×9.6 mm. In the array with no integrated apodization (Fig. 1a), circular CMUT cells are densely distributed over the array, with 3 cells along the width of the elements and 96 cells along their length. The individual cells have a diameter of

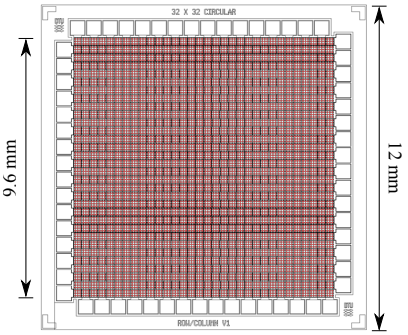

(a)

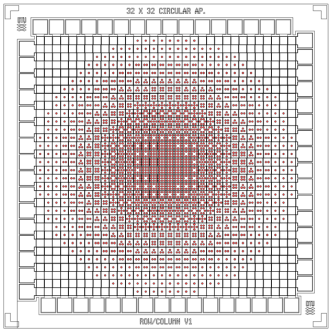

(b)

Figure 1. Mask layout of the row-column addressed $32+32$ CMUT transducers without integrated apodization (a) and with integrated apodization (b). The red circles indicate the individual CMUT cells, which are densely packed in the non-apodized configuration, while the number of cells follows a circular symmetric Hann function in the apodized layout.

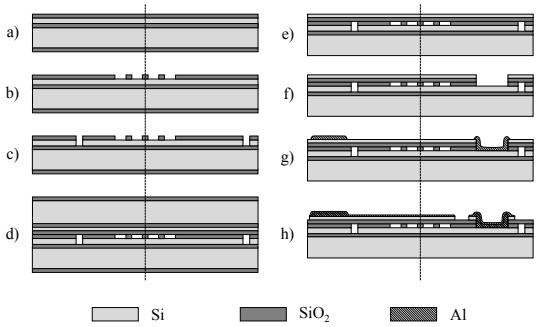

Figure 2. Process flow of the cleanroom fabrication. The line separates the layer composition comprising the top electrodes (to the left of the line) and the bottom electrodes (to the right of the line). The steps are: a) oxidation, b) cavity etch, c) bottom electrode etch, d) wafer bonding, e) handle etch, f) etch access to bottom electrodes, g) deposit and etch wire-bonding pads, and h) deposit and etch top electrodes. A total of five lithography masks are used (in steps b, c, f, g, and h).

72 µm, a plate thickness of 2 µm, and a vacuum gap height and insulation oxide thickness of each 195 nm. Each section of the array, where a row and a column intersects, can accommodate a maximum of 9 CMUT cells. For the array with integrated apodization (Fig. 1b), the number of cells in this square section is varied according to a circularly symmetric Hann function. This effectively alters the active area and consequently the intensity of the emitted/received signal, gradually decreasing it towards the edges of the array to suppress the edge waves.

III. Transducer Fabrication

The arrays were fabricated using cleanroom processing techniques, partly based on previous works described in the literature [9], [10]. The individual process steps are shown in Fig. 2.

The fabrication process utilized two (001) silicon-on-insulator (SOI) wafers, both having a 525 µm thick handle layer with high resistivity (1-10 Ω cm), a 1 µm thick buried oxide layer, and a low resistivity (0.01-0.001 Ω cm) device layer. The device layer on the first SOI wafer was 20 µm thick and was used to create the bottom electrodes (rows). The second SOI wafer had a 1.9 µm thick device layer, which was used for the top electrodes (columns) of the array. These top electrodes also constituted the flexible plate of the CMUTs.

Both SOI wafers were dry oxidized at 1100 °C for 2 hours and 30 minutes to grow a 195 nm thick layer of oxide (Fig. 2a). The CMUT cavities were then defined in the 20 µm SOI wafer using UV lithography and etched using reactive ion etching (RIE), see Fig. 2b. After stripping the photoresist, a second lithography step was used to define the bottom electrodes as shown in Fig. 2c. Two consecutive RIE etches were used to selectively etch first the oxide layer and subsequently the underlying silicon device layer. After stripping the photoresist, the fabrication of the bottom electrodes and the substrate supporting the array was complete.

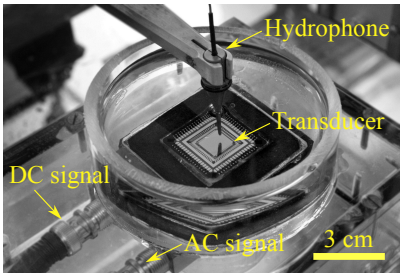

Figure 3. Picture of the experimental setup used to measure the emitted pressure field. The transducer is mounted and wire-bonded on a chip carrier, which is inserted into a chip socket. The transducer array is submerged in rapeseed oil, and a single AC+DC signal is supplied to all the column channels of the array, while the row are grounded.

Both SOI wafers were then cleaned using a standard RCA cleaning procedure [11] and bonded together in vacuum (0.01 mbar) using fusion bonding and a subsequent annealing step (70 min at 1100 °C), see Fig. 2d. The oxide layer covering the back side of both wafers was removed in buffered hydrofluoric acid (BHF), after which the handle layer and buried oxide layer of the top SOI wafer was etched using both RIE and BHF, respectively, as shown in Fig. 2e.

A third lithography step followed by selective RIE in first the silicon layer and subsequently the oxide layer was used to define openings to the bottom electrodes, see Fig. 2f. The thin device layer is partly transparent in the visible spectrum, and alignment to the bottom wafer alignment marks could therefore be performed, thereby omitting the need for alignment during the wafer bonding step.

Fig. 2g shows the wire-bonding pads, which were made by depositing a 800 nm aluminium layer on the entire wafer using electron beam evaporation and structured in a resist masked selective aluminium etch in H_2O: H_3PO_4 (1 : 2) at 50 °C. The top electrodes, or columns, were then finally defined by a step similar to the previous, but this time with a 200 nm aluminium deposition. Before removing the photoresist, the exposed silicon layer was etched using RIE to isolate the individual top electrodes, thereby concluding the fabrication process (Fig. 2h).

IV. Measurement and Simulation Setup

The acoustic field of the two CMUT arrays were measured with a MH28-5 needle hydrophone (Force Technology, Denmark) and a DSO5012A oscilloscope (Agilent Technologies, CA, USA). The measurement setup is shown in Fig. 3. For spatial mapping of the transmit fields, the hydrophone was mounted on the positioner of the intensity measurement system AIMS-3 (Onda Corporation, CA, USA). The hydrophone was positioned 5.3 mm from the array and scanned over the center of each array in lateral steps of 0.1 mm. The transducers were actuated using a 8116A pulse/function generator (Hewlett-Packard Company, CA, USA) with a 15 Vpp 2-cycle 3 MHz pulse through a custom made class B amplifier with a

bandwidth of 8 MHz. The DC bias was 40 V (pull-in: 52 V). All row elements, respectively column elements, were electrically shorted to allow simultaneous actuation of the whole array. All measurements were carried out in rapeseed oil (speed of sound: 1476 m/s) to ensure electrical insulation of the prototype transducers.

In this work, Field II [7], [8] was used for all simulations. Field II was set up to use lines to describe the apertures with each element of the array being divided into square mathematical elements with a side length of $\lambda/4$. In the simulation, the square intersection of each row- and column element, each consisting of four mathematical elements, were given an apodization value of $\{0, \frac{1}{9}, \frac{2}{9}, \frac{1}{3}, \frac{4}{9}, \frac{5}{9}, \frac{2}{3}, \frac{7}{9}, \frac{8}{9}, 1\}$ dependent on whether there were 0, 1, 2, 3, 4, 5, 6, 7, 8, or 9 CMUT cells in the real array within this region. The emission pulse was a 3 MHz 2-cycle Hann weighted pulse.

V. Results

The measured and simulated emitted fields generated by the two arrays are shown in Fig. 4. The result for the array without integrated apodization is shown in Fig. 4a and Fig. 4c (simulation and measurement, respectively), while the result for the array with integrated apodization is shown in Fig. 4b and Fig. 4d. The main wave arrives after 3.6 µs, corresponding to a distance of 5.3 mm. In addition to this, a spherical wave is emitted from the edges of the array. The arrival time of the wave front is the distance travelled divided by the speed of sound. The arrival time of the edge wave at the position of the hydrophone is then

$$t_{\text{edge}} = \sqrt{d^2 + x^2}/c\,, \tag{1}$$

where d is the perpendicular distance from the point being measured and the transducer surface, x is the lateral distance of the point being measured from the edge of the array, and c is the speed of sound. The predicted arrival time of an edge wave originating from the array aperture edge at −4.8 mm has been plotted with a dashed line in both the simulated and measured fields for the array without integrated apodization in Fig. 4a and Fig. 4b, respectively. It is seen that the edge wave is accurately predicted, thereby confirming its origin.

For the array with integrated apodization (Fig. 4b and Fig. 4d), the two edge waves are seen to be significantly damped. The damping in terms of edge wave energy can be quantified by summing the squared pressure values along the curve given by (1) for both arrays. This yields a reduction of edge wave energy of 13.0 dB (95 %) for the simulation and 8.4 dB (85 %) for the measurement. The deviance between the simulation and measurement may be contributed to the transducer ringing present in the measurements due to the lack of a backing material. This will add to the calculated edge wave energy in both cases and thereby reduce the energy ratio.

In Fig. 5a and Fig. 5b, the amplitude of the measured and simulated pressure field is shown for the two arrays. The amplitude is extracted at the arrival of the main wave at time 3.6 µs, and it thereby corresponds to a horizontal cross-section of the plots in Fig. 4. The profiles of the simulated and measured amplitudes are seen to be comparable for both of the arrays. The correspondence is especially relevant for the array with integrated apodization, since it demonstrates that the emitted field, and thereby the apodization, can be accurately predicted.

VI. Conclusions

This paper demonstrated the effect of an integrated apodization in row-column addressed CMUTs. The apodization was applied by varying the density of CMUT cells in the array with the objective of damping the edge waves originating from the element ends, thereby mitigating the problem of ghost echoes in images produced by such arrays. Two row-column addressed $32 + 32$ CMUT arrays were fabricated, one with and one without integrated apodization. Measurements of the emitted pressure field from the array with integrated apodization showed a reduction in edge wave energy of 8.4 dB (85 %) compared to the array without integrated apodization. Simulations in Field II yielded a corresponding reduction of 13.0 dB (95 %). The simulations were able to replicate the measured pressure field, proving the predictability of the technique.

Acknowledgment

This work was financially supported by the Danish National Advanced Technology Foundation (024-2008-3 and 82-2012-4). The authors would like to thank Jens Christian Jensen for producing the mechanical fixtures, and René Gadkjær for assistance with the electronics.

References

[1] C. E. M. Démoré, A. Joyce, K. Wall, and G. Lockwood, "Real-time volume imaging using a crossed electrode array," *IEEE Trans. Ultrason., Ferroelec., Freq. Contr.*, vol. 56, no. 6, pp. 1252–1261, 2009.

[2] C. H. Seo and J. T. Yen, "A 256 x 256 2-D array transducer with row-column addressing for 3-D rectilinear imaging," *IEEE Trans. Ultrason., Ferroelec., Freq. Contr.*, vol. 56, no. 4, pp. 837–847, April 2009.

[3] A. S. Logan, L. L. P. Wong, A. I. H. Chen, and J. T. W. Yeow, "A 32 x 32 element row-column addressed capacitive micromachined ultrasonic transducer," *IEEE Trans. Ultrason., Ferroelec., Freq. Contr.*, vol. 58, no. 6, pp. 1266–1271, June 2011.

[4] A. Sampaleanu, P. Zhang, A. Kshirsagar, W. Moussa, and R. Zemp, "Top-orthogonal-to-bottom-electrode (TOBE) CMUT arrays for 3-D ultrasound imaging." *IEEE Trans. Ultrason., Ferroelec., Freq. Contr.*, vol. 61, no. 2, pp. 266–276, 2014.

[5] M. F. Rasmussen and J. A. Jensen, "3-D ultrasound imaging performance of a row-column addressed 2-D array transducer: A measurement study," in *Proc. IEEE Ultrason. Symp.*, July 2013, pp. 1460–1463.

[6] T. L. Christiansen, M. F. Rasmussen, E. V. Thomsen, and J. A. Jensen, "Ultrasound imaging transducer array with integrated apodization," International Patent PCT/IB2013/002 838, December 19, 2013.

[7] J. A. Jensen and N. B. Svendsen, "Calculation of Pressure Fields from Arbitrarily Shaped, Apodized, and Excited Ultrasound Transducers," *IEEE Trans. Ultrason., Ferroelec., Freq. Contr.*, vol. 39, pp. 262–267, 1992.

[8] J. A. Jensen, "Field: A program for simulating ultrasound systems," *Med. Biol. Eng. Comp.*, vol. 10th Nordic-Baltic Conference on Biomedical Imaging, Vol. 4, Supplement 1, Part 1, pp. 351–353, 1996.

[9] Y. Huang, A. S. Ergun, E. Hæggström, M. H. Badi, and B. T. Khuri-Yakub, "Fabricating capacitive micromachined ultrasonic transducers with wafer-bonding technology," *J. Microelectromech. Syst*, vol. 12, no. 2, pp. 128–137, 2003.

[10] P. Zhang, G. Fitzpatrick, T. Harrison, W. A. Moussa, and R. J. Zemp, "Double-SOI wafer-bonded CMUTs with improved electrical safety and minimal roughness of dielectric and electrode surfaces," *J. Microelectromech. Syst.*, vol. 21, no. 3, pp. 668–680, 2012.

[11] W. Kern, "The evolution of silicon wafer cleaning technology," *J. Electrochem. Soc.*, vol. 137, no. 6, pp. 1887–1892, 1990.

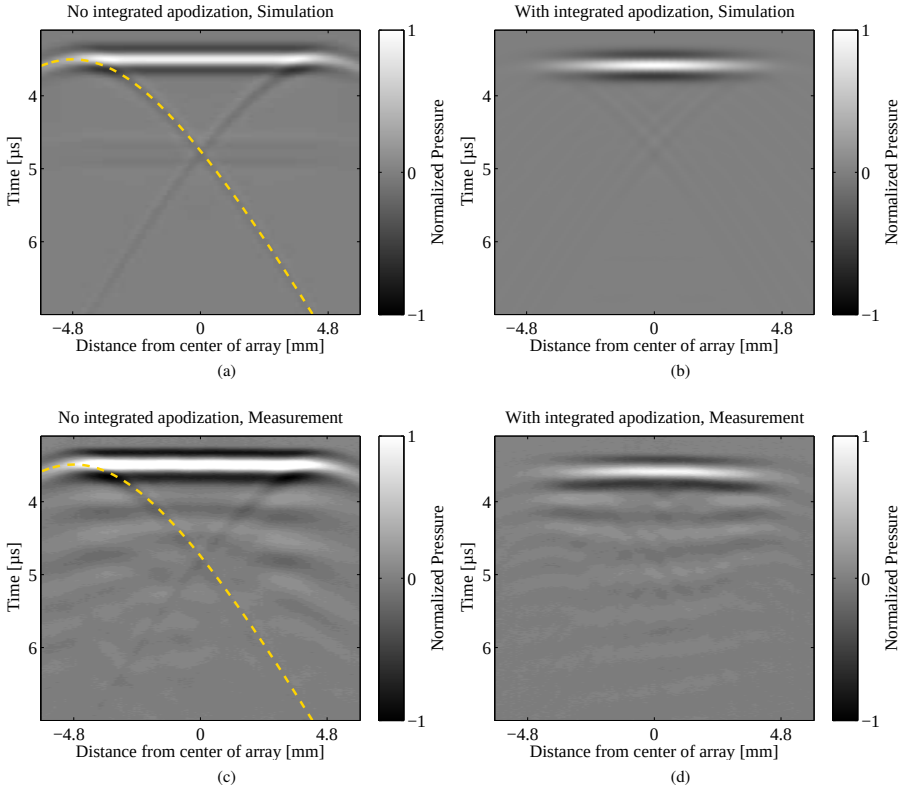

Figure 4. Simulated (a and b) and measured (c and d) pressure field along a line through the center of the array at a depth of 5.3 mm. a and c show the result for the array without integrated apodization, and b and d show the result with integrated Hann apodization. The pressure has been normalized to the maximum pressure of the measurement with no integrated apodization. The extend of the array aperture (from −4.8 mm to 4.8 mm) is marked. Two edge waves are clearly visible for the non-apodized array, and the dashed line show the analytically calculated expected arrival time of the edge wave originating at −4.8 mm. The ripples in the experimental results are due to transducer ringing, and these are therefore not reproduced in the simulations.

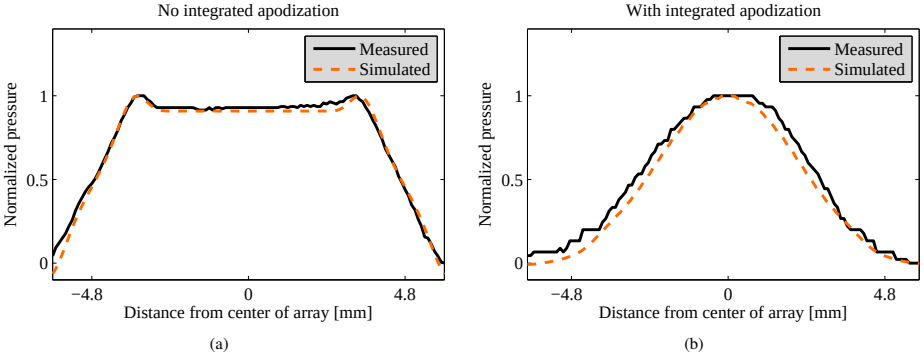

Figure 5. Measured and simulated pressure at a distance of 5.3 mm from the transducer surface at time 3.6 µs. The pressure is measured along a line through the center of the array. The extend of the array aperture (from −4.8 mm to 4.8 mm) is marked. The pressure has been normalized to the maximum pressure to allow comparison of the profile of the emitted field over the array.

PAPER J

3-D Imaging using Row-Column Addressed Arrays with Integrated Apodization – Part I: Apodization Design and Line-element Beamforming

Authors: Morten Fischer Rasmussen, **Thomas Lehrmann Christiansen**, Erik Vilain Thomsen, and Jørgen Arendt Jensen.

Published in: IEEE Transactions on Ultrasonics, Ferroelectrics, and Frequency Control, Vol. 62, No. 5, pp. 947-958 (2015).

Abstract

This paper investigates the effect of transducer-integrated apodization in row-column addressed arrays and presents a beamforming approach specific for such arrays. Row-column addressing 2-D arrays greatly reduces the number of active channels needed to acquire a 3-D volume. A disadvantage of row-column addressed arrays is an apparent ghost effect in the point spread function caused by edge waves. This paper investigates the origin of the edge waves and the effect of introducing an integrated apodization to reduce the ghost echoes. The performance of a $\lambda/2$-pitch $5\,\mathrm{MHz}$ $128 + 128$ row-column addressed array with different apodizations is simulated. A Hann apodization is shown to decrease imaging performance away from the center axis of the array because of a decrease in main lobe amplitude. Instead, a static roll-off apodization region located at the ends of the line elements is proposed. In simulations, the peak ghost echo intensity of a scatterer at $(x, y, z) = (8, 3, 30)$ mm was decreased by $43\,\mathrm{dB}$ by integrating roll-off apodization into the array. The main lobe was unaffected by the apodization. Simulations of a $3\,\mathrm{mm}$-diameter anechoic blood vessel at $30\,\mathrm{mm}$ depth showed that applying the transducer-integrated apodization increased the apparent diameter of the vessel from $2.0\,\mathrm{mm}$ to $2.4\,\mathrm{mm}$,

corresponding to an increase from $67\,\%$ to $80\,\%$ of the true vessel diameter. The line element beamforming approach is shown to be essential for achieving correct time-of-flight calculations, and hence avoid geometrical distortions. In Part II of this work, experimental results from a capacitive micromachined ultrasonic transducer with integrated roll-off apodization are given to validate the effect of integrating apodization into the line elements.

3-D Imaging Using Row–Column-Addressed Arrays With Integrated Apodization—Part I: Apodization Design and Line Element Beamforming

Morten Fischer Rasmussen, Thomas Lehrmann Christiansen, Erik Vilain Thomsen, and Jørgen Arendt Jensen, *Fellow, IEEE*

***Abstract*—This paper investigates the effect of transducer-integrated apodization in row–column-addressed arrays and presents a beamforming approach specific for such arrays. Row–column addressing 2-D arrays greatly reduces the number of active channels needed to acquire a 3-D volume. A disadvantage of row–column-addressed arrays is an apparent ghost effect in the point spread function caused by edge waves. This paper investigates the origin of the edge waves and the effect of introducing an integrated apodization to reduce the ghost echoes. The performance of a $\lambda/2$-pitch 5-MHz 128 + 128 row–column-addressed array with different apodizations is simulated. A Hann apodization is shown to decrease imaging performance away from the center axis of the array because of a decrease in main lobe amplitude. Instead, a static roll-off apodization region located at the ends of the line elements is proposed. In simulations, the peak ghost echo intensity of a scatterer at $(x, y, z) = (8, 3, 30)$ mm was decreased by 43 dB by integrating roll-off apodization into the array. The main lobe was unaffected by the apodization. Simulations of a 3-mm-diameter anechoic blood vessel at 30 mm depth showed that applying the transducer-integrated apodization increased the apparent diameter of the vessel from 2.0 mm to 2.4 mm, corresponding to an increase from 67% to 80% of the true vessel diameter. The line element beamforming approach is shown to be essential for achieving correct time-of-flight calculations, and hence avoid geometrical distortions. In Part II of this work, experimental results from a capacitive micromachined ultrasonic transducer with integrated roll-off apodization are given to validate the effect of integrating apodization into the line elements.**

I. Introduction

For real-time 3-D ultrasonic imaging, 2-D array transducers are needed to achieve real-time scanning of a volume [1], [2]. The number of elements in a fully addressed 2-D array scales with N^2. In 2-D imaging, a 1-D array using more than 100 elements is commonly used. Using a fully addressed 2-D array, this would correspond to an array with more than 10 000 elements. To control the individual elements in the array, a connection must be made to each element. Thereby, any delay or apodization scheme can be applied, offering maximum control and flexibility in the image processing [2]–[4]. However, addressing each element individually results in a vast number of interconnections and offers a great challenge in acquiring and processing the large amount of data. Reducing the number of transducer elements by using sparse arrays has therefore received a great amount of interest in the last couple of decades [5]–[9]. One of the drawbacks of sparse arrays, however, is the lower emitted energy from the reduced number of elements, leading to a lower SNR in the recorded ultrasound image. The sparse arrays also have higher side lobes and can introduce grating lobes in the field.

2-D row–column-addressed arrays have recently attracted some attention [10]–[25]. In a row–column-addressed array, the elements are accessed by their row or column index. Each row and column in the array thereby acts as one large element. This effectively transforms the dense 2-D array into two orthogonal 1-D arrays, as illustrated in Fig. 1. Thereby, the number of elements in a 2-D array is reduced from N^2 to $2N$. The long elements are in this work referred to as row elements and column elements, or simply as line elements.

Considering a fully populated array with $N \times N$ elements, a row–column-addressed array of the same size would contain $N + N$ line elements. The size of one line element is then $1 \times N$, in units of the fully populated array elements. The vibrating surface area, when exciting a single row–column-addressed transducer array channel, is therefore N times as large as the excited area of the fully populated area. A row–column-addressed array therefore emits far more energy per transducer channel than a fully populated array. In [22], the resolution and contrast of row–column-addressed arrays is shown to be better than for fully addressed arrays, when they use the same number of active channels. The row–column-addressed array is a very interesting candidate for real-time 3-D imaging because it both has a large surface area and promises to achieve a high resolution per active channel. Although the row–column addressing scheme greatly reduces the

Manuscript received May 22, 2014; accepted March 19, 2015. This work was financially supported by grant 024-2008-3 and 82-2012-4 from the Danish Advanced Technology Foundation and from BK Medical ApS, Herlev, Denmark.

M. F. Rasmussen and J. A. Jensen are with the Center for Fast Ultrasound Imaging, Department of Electrical Engineering, Technical University of Denmark, Kgs. Lyngby, Denmark (e-mail: research@mofi.dk).

T. L. Christiansen and E. V. Thomsen are with the Department of Micro- and Nanotechnology, Technical University of Denmark, Kgs. Lyngby, Denmark.

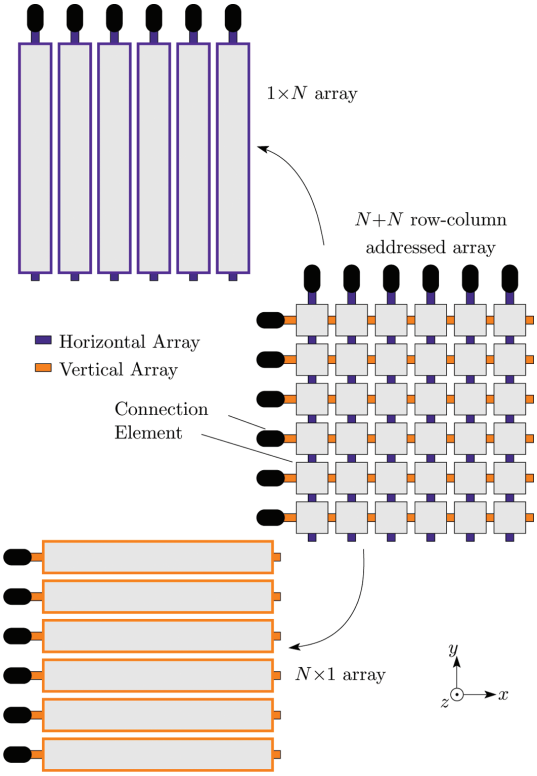

Fig. 1. A row–column-addressed 2-D transducer array can be interpreted as two orthogonal 1-D arrays. To the right is shown a 2-D transducer array, where each transducer element is addressed by its row or column index, effectively creating the two arrays shown to the left.

number of elements and beamformer channels needed to perform real-time 3-D imaging, it has one major disadvantage compared with the fully addressed 2-D arrays: the long row- and column-elements have considerably increased edge effects. As was shown in [22], the edge effect limits the image quality obtainable with 2-D row–column-addressed arrays. This paper demonstrates how these edge effects can be effectively reduced, making row–column-addressed arrays capable of providing a high image quality for real-time 3-D imaging with a low channel count.

The paper is divided into three main sections. The first section describes the edge effects of long, thin line elements, and demonstrates the importance of apodizing the line elements along their length to reduce the edge effects. Subsequently, a transducer-integrated apodization is designed. It is shown that the previously proposed apodization in the literature [19], [22] is not generally applicable for 3-D imaging. Instead, a new apodization scheme is proposed and simulated. Then, it is demonstrated how beamforming can be carried out when both the transmit line elements, the receive line elements, and the focal zone are line segments instead of points. Finally, the effectiveness of the proposed apodization is demonstrated via simulated point spread functions (PSFs) and a simulated anechoic blood vessel surrounded by tissue.

TABLE I. Simulation Parameters.

Parameter name	Notation	Value	Unit
Center frequency	f_0	5.0	MHz
Speed of sound	c	1480	m/s
Wavelength	λ	296	µm
Array pitch—x	d_x	$\lambda/2 = 148$	µm
Array pitch—y	d_y	$\lambda/2 = 148$	µm
Sampling frequency	f_s	120	MHz
Emission pulse	—	2-cycles, Hann-weighted	—

In Part II of this work [26], experimental results from a 62 + 62 element, $\lambda/2$-pitch, 2.77-MHz capacitive micromachined ultrasonic transducer with integrated apodization are given and compared with simulations of an array with identical properties. The array presented in Part II is a prototype, intended to experimentally validate the effect of the integrated apodization. To better illustrate the potential of a larger array, Part I includes simulations of a 128 + 128 element, $\lambda/2$-pitch, 5-MHz row–column-addressed transducer array.

II. Simulation Setup

In this work, Field II pro [27]–[29] is used for all simulations. The simulated receive signals are beamformed using a direct Matlab (The MathWorks Inc., Natick, MA, USA) implementation of the beamformer for row–column-addressed arrays presented in Section V. The transducer arrays used in the simulations are row–column-addressed 128 + 128 element 2-D arrays using the parameters shown in Table I. The orthogonal transmit and receive transducer array pairs are implemented as 1 × 128 and 128 × 1 2-D arrays. Each line element is divided into square mathematical sub-elements with a side length of $\lambda/4$.

III. Edge Effects

Row–column-addressed arrays are quite different acoustically from fully addressed arrays. Because of the row–column addressing, each line element may have a length that is hundreds of times longer than the lengths of the square elements used in a fully addressed array. The long length of the line elements results in prominent edge effects. This section investigates how the line elements of a row–column-addressed array behave and what can be done to decrease the edge effects. The behavior of the line elements is first investigated by analyzing their spatial impulse response.

A. Spatial Impulse Response

In the following, the importance of apodizing the line elements along their length is demonstrated. For this pur-

pose, an approximation to spatial impulse response is derived. The purpose of the derivation is not to introduce a new equation suitable for calculating the impulse response, but to elucidate how the edge effects can be minimized.

The origin of the edge waves can be analyzed by the linear theory of wave propagation. The pressure at a given point $\mathbf{p}$ at the time t has in the literature [30] been shown to be

$$p(\mathbf{p},t) = \rho_0 \frac{\partial}{\partial t} v(t) * h(\mathbf{p},t) \tag{1a}$$

$$= \rho_0 v(t) * \frac{\partial}{\partial t} h(\mathbf{p},t), \tag{1b}$$

where $*$ denotes temporal convolution, ρ_0 is the density of the medium, v is the velocity normal to the transducer surface, and h is the spatial impulse response. It is noted that v is the convolution of the aperture excitation signal and the electro-mechanical impulse response of the aperture. The spatial impulse response $h(\mathbf{p},t)$ is the observed sound field at the point $\mathbf{p}$ when the aperture is excited by a Dirac delta function. The Huygens–Fresnel principle states that the field originating from a sound radiating surface can be calculated by considering all points on the surface as the source of an expanding spherical wave. The field at any point in space is then constructed by superposition of these spherical waves. The acoustic reciprocity theorem states that if the sound source and the sound receiver are interchanged, the received signal remains unchanged. In other words, the spatial impulse response can be determined by letting the point $\mathbf{p}$ be the source of a spherical wavefront and then integrate the wave's intersection with the aperture. This integral is termed the Rayleigh integral [31], [32].

The intersection of the spherical wave and the plane of the aperture makes a circle arc. The spatial impulse response at a certain time t is thereby determined by the length of the arc that intersects the aperture. The radius of the expanding sphere is $R = ct$, where t is time and c is the speed of sound. Determining the arc intersection is reduced to a two-dimensional problem by projecting the point $\mathbf{p}$ onto the transducer plane. Without loss of generality, the aperture is assumed to be flat. In the following, a normal right-handed coordinate system consisting of x, y, and z coordinates is used. The aperture plane is spanned by the x- and y-axes and the z-axis is orthogonal to the aperture plane. If the coordinate of $\mathbf{p}$ is (p_x, p_y, p_z), then the projection of $\mathbf{p}$ onto the xy-plane is $(p_x, p_y, 0)$. The radius of the circle created by the intersection between the aperture and the expanding spherical wave is $\rho(t) = \sqrt{(ct)^2 - p_z^2}$ and the center of the circle is located at (p_x, p_y). The line integral along this expanding arc is the Rayleigh integral in polar coordinates. This is the case shown in the aperture at the top of Fig. 2. The integration is performed along the gray dashed lines. Several authors [33]–[35] have determined the solution to the Rayleigh integral in polar coordinates of an apodized aperture to be

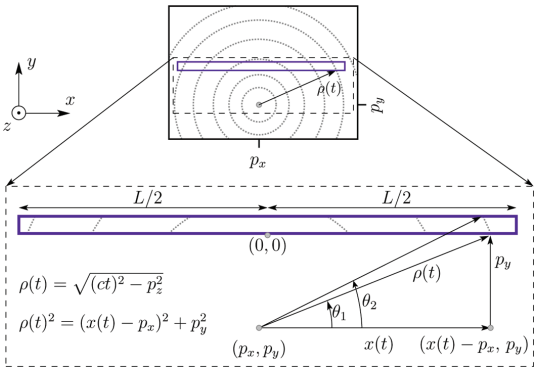

Fig. 2. Spatial impulse response of long, thin line elements. At the top a large aperture is shown with integration paths marked with gray dashed lines. The integration paths are used in (2) to determine the spatial impulse response. Within the large aperture, a thin line element is illustrated. At the bottom, a magnified image of the line element is shown. The expression in (5) approximates the integration paths with vertical lines. The thinner the line element is, the better the approximation.

$$h(\mathbf{p},t) = \begin{cases} \dfrac{c}{2\pi} \displaystyle\int_{\theta_1(t)}^{\theta_2(t)} a(\rho(t),\theta)\mathrm{d}\theta, & \text{if } t \geq \dfrac{p_z}{c} \\ 0, & \text{else,} \end{cases} \tag{2}$$

where a is the apodization function of the aperture in polar coordinates with origin at the projection of $\mathbf{p}$ onto the aperture plane. a is equal to 0 when evaluated outside of the aperture surface. If the apodization function is constant along the integration paths, (2) becomes

$$h(\mathbf{p},t) = \begin{cases} \dfrac{c}{2\pi}(\theta_2(t) - \theta_1(t)) a_\rho(\rho(t)), & \text{if } t \geq \dfrac{p_z}{c} \\ 0, & \text{else.} \end{cases} \tag{3}$$

In the following, the aperture is assumed to be a long, thin, and rectangular line element. The x, y-coordinates are chosen such that the x-axis is oriented along the length of the line element and the origin is placed at the center of the line element length. This is illustrated in Fig. 2.

At the top of Fig. 2, a large aperture is shown where the full integral along the dashed lines must be carried out to find the spatial impulse response. Within the large aperture, a line element is shown. A zoom on the line element is shown at the bottom of the figure. By approximating the integration paths on the line element by a vertical line, the apodization function $a_\rho(\rho)$ from (3) changes dependent variable from the radius ρ to the position x, representing the position along the line element: $a_x(x(t))$. The thinner the line element is, the better is the approximation. From the triangle at the bottom right in Fig. 2, the x-variable as a function of time is determined to:

$$x(t) = p_x \pm \sqrt{\rho(t)^2 - p_x^2} \tag{4a}$$

$$= p_x \pm \sqrt{(ct)^2 - p_z^2 - p_y^2}. \tag{4b}$$

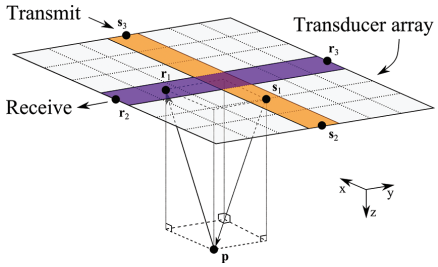

Fig. 3. Illustration of a pulse-echo simulation setup with one line element transmitting and one line element receiving. A scatterer is located at the point $\mathbf{p}$, $\mathbf{s}_1$ is the closest point on the transmit element to $\mathbf{p}$, and $\mathbf{r}_1$ is the closest point on the receive element to $\mathbf{p}$. $\mathbf{s}_2$, $\mathbf{s}_3$ and $\mathbf{r}_2$, $\mathbf{r}_3$ are the edges of the transmit and receive line elements, respectively.

The spatial impulse response then approximately becomes:

$$h(\mathbf{p},t) \approx \begin{cases} \dfrac{c}{2\pi}\left(\theta_2(t)-\theta_1(t)\right) a_x(x(t)), & \text{if } t \geq t_1 \\ 0, & \text{else,} \end{cases} \tag{5}$$

where $t_1 = \sqrt{p_y^2 + p_z^2}/c$ is the earliest time at which the spherical wave arrives at the aperture. For a long, thin line element, the angular element width $(\theta_2(t) - \theta_1(t))$ changes much slower than the apodization function at the edges of the line element, i.e.,

$$\frac{\frac{\mathrm{d}}{\mathrm{d}t}\left(\theta_2(t)-\theta_1(t)\right)}{2\pi} \ll \frac{\mathrm{d}}{\mathrm{d}t} a_x(x(t)) \,. \tag{6}$$

By inserting (5) into (1b), and using (6), the pressure field is seen to be proportional to

$$p(\mathbf{p},t) \propto \begin{cases} v(t) * \dfrac{\mathrm{d}}{\mathrm{d}t} a_x(x(t)), & \text{if } t \geq t_1 \\ 0, & \text{else.} \end{cases} \tag{7}$$

Consider now the transmitting element of the row–column-addressed array shown in Fig. 3. Using the acoustic reciprocity, the pressure at point $\mathbf{p}$ can be found by assuming that $\mathbf{p}$ emits a spherical wavefront that is received by the transmitting line element. The wavefront reaches the closest point on the transmit line element ($\mathbf{s}_1$) at time $t = t_1$. At $t = t_2$, the wavefront first reaches the closest edge at $\mathbf{s}_2$, and at $t = t_3$, the wavefront reaches the furthest edge of the line element at $\mathbf{s}_3$. The apodization of a single line element is usually constant or only slowly varying over the entire element surface. Because the apodization function evaluates to zero outside of the element area, there is a discontinuity at the element edges at $\mathbf{s}_2$ and $\mathbf{s}_3$. The derivative of the aperture function is therefore approximately zero everywhere except at the discontinuities at $\mathbf{s}_1$, $\mathbf{s}_2$, and $\mathbf{s}_3$, where it is the Dirac delta function, δ:

$$\frac{\mathrm{d}}{\mathrm{d}t} a_x(x(t)) \approx \delta(t-t_1) - \delta(t-t_2) - \delta(t-t_3). \tag{8}$$

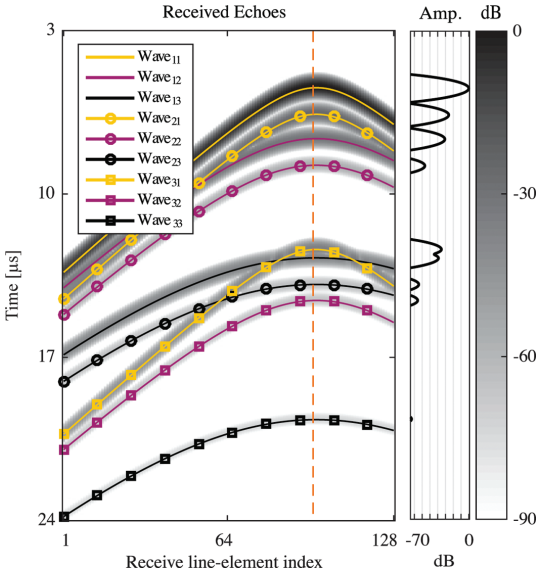

Fig. 4. Nine echoes are received from a single line element emission reflected by a scatter located at $(x, y, z) = (5, 4, 3)$ mm. The gray-scale image is the envelope of the received signals and the overlaid lines are predicted time-of-flights. The predicted time-of-flight is calculated using (9). The amplitudes of the echoes received by a single channel are plotted in the right sub-figure. The strongest ghost echo has an amplitude of -26 dB and the weakest ghost echo approximately -74 dB. That nine echoes are received exactly at the times predicted verifies the assumption that each line element behaves as three discrete elements, as illustrated in Fig. 3.

By inserting (8) into (7), it is seen that the spatial transmit impulse response contains three individual responses. As a result, a single transmit pulse develops three wavefronts that passes the point $\mathbf{p}$. When a scatterer is located at $\mathbf{p}$, there are therefore three reflected waves returning to the line element. Using the same argumentation, the spatial receive impulse response contains also three responses, meaning each wavefront is measured three times. The pulse-echo spatial impulse response is the convolution of the transmit and receive impulse responses and therefore contains up to nine responses. Referring to Fig. 3, the three wavefronts appear to originate from $\mathbf{s}_1$, $\mathbf{s}_2$, and $\mathbf{s}_3$. The receive line element behaves as if it measures at the three discrete points $\mathbf{r}_1$, $\mathbf{r}_2$, and $\mathbf{r}_3$. This analysis considered two out of four edges. The two long edges will also give rise to a response, but for elements with a width in the order of a wavelength, the two extra responses will merge with the $\mathbf{s}_1$ response and are therefore negligible.

That nine echoes are measured from a single scatterer can be tested by a single line element pulse-echo simulation. Fig. 4 shows the signals received by a 128 + 128 element row–column-addressed array from a single scatter located at the point $\mathbf{p} = (5, 4, 3)$ mm, when exciting the center line element with a two-cycle sinusoidal 5 MHz

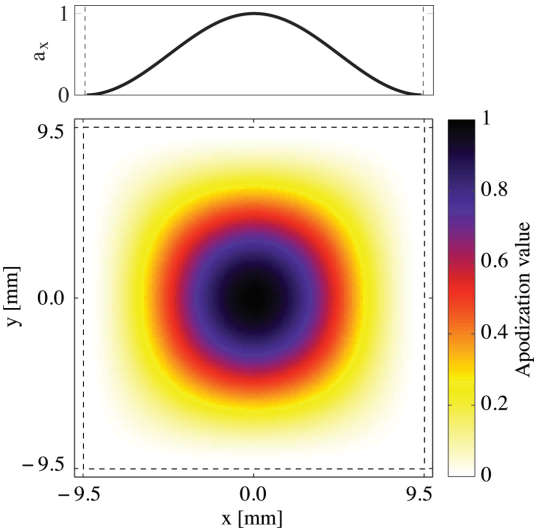

Fig. 5. The row–column-addressed array with a transducer-integrated Hann apodization. The graph at the top shows the Hann apodization of a single line element as a function of the position along the line element. The bottom figure shows the Hann apodization of the full transducer array. The dashed lines mark the edge of the line elements and the row–column-addressed array. The size of the area within the dashed lines is identical to that of the area within the dashed lines in Fig. 6.

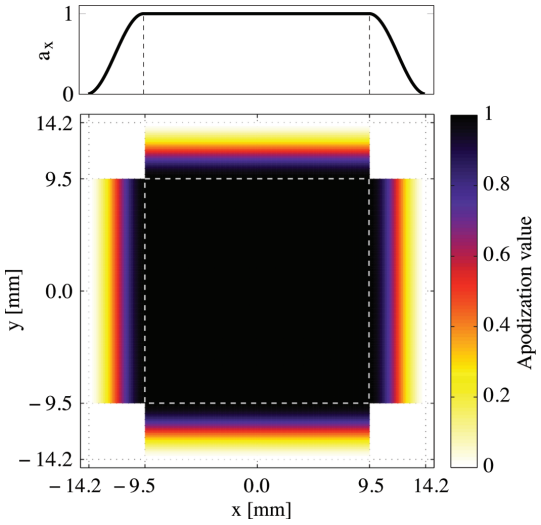

Fig. 6. New integrated-apodization layout where a roll-off region is added to the ends of the line elements. The graph at the top shows the apodization of each line element as a function of the position along the line element. The central region, marked with dashed lines, has an apodization value of one. The size of the area within the dashed lines is identical to that of the area within the dashed lines in Fig. 5.

pulse. As expected, nine echoes are received. Overlaid on the gray level receive echoes are the expected echo arrival time combinations of the three sources and the three receive points of Fig. 3. The echo arrival time, also termed the time-of-flight (ToF), is calculated as

$$\mathrm{ToF}(\mathbf{p}, n, i) = \frac{\|\mathbf{p} - \mathbf{s}_n\| + \|\mathbf{r}_i - \mathbf{p}\|}{c}, \tag{9}$$

where both n and i are indexes between 1 and 3. The wavefronts are named wave_{ni}, where n indicates the $\mathbf{s}$-index and i indicates the $\mathbf{r}$-index. It is seen that the arrival time at each receive line element of all received echoes are perfectly predicted, and the location assumption of the transmitter and receiver of each wavefront, shown in Fig. 3, must therefore be correct.

It is only the first echo, wave_{11}, that can be used for imaging, as the amplitudes of the other ghost echoes are too weak. The amplitude of the most powerful ghost echo is approximately 40 dB lower than the amplitude of the main echo. Even though the ghost echoes cannot be used for imaging, they still degrade the image quality. It is seen from (7) that to reduce the edge waves, and thereby the ghost echoes, the derivative of the apodization function must be kept as small as possible. The apodization function therefore must converge to zero when approaching the line element edges. This cannot be achieved by the usual electronic apodization, because this does not change the line element apodization value along the length of it. Instead, the apodization must be integrated into the transducer array itself, which is the subject of the following sections.

IV. Transducer-Integrated Apodization

Apodizing both the row and column line elements with a Hann function in the entire length of the line elements is very effective at suppressing the ghost echoes [19], [22]. A Hann apodized row–column-addressed array is shown in Fig. 5, where the top graph shows the apodization of a single line element. Because the row and column line elements are overlapping, so are their apodization functions. At each position on the transducer surface, two apodization functions are overlapping, one from a row element and one from a column element. The effective apodization is the multiplication of the two apodization functions. The vertical line elements close to the edges are multiplied by values close to zero by the horizontal apodization function. Similarly, the horizontal line elements at the edges are multiplied by values close to zero by the vertical apodization function. The sensitivity of the edge line elements is therefore highly limited. The only location where this apodization function allows the row–column-addressed array to perform well, is straight down at the center of the array. The output pressure of the Hann-apodized array is in an earlier study shown to be significantly lower than the output pressure of a non-apodized row–column-addressed transducer array [36]. Even if the array angles the trans-

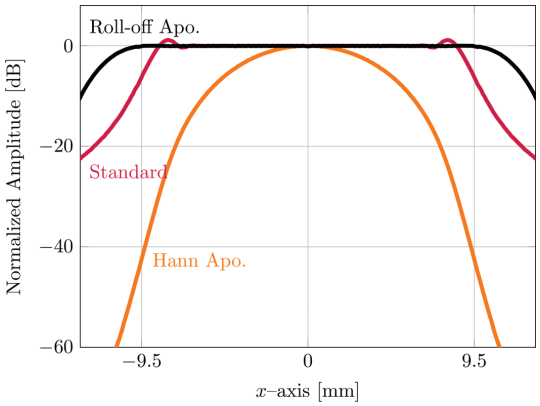

Fig. 7. Maximum received echo intensity from a single scatter at a depth of 10 mm and with its x-coordinate varying from −13 mm to 13 mm. The center line element is sending and all 128 receive elements are receiving. The maximum of all envelope-detected signals is plotted for each scatterer location. The three curves were simulated with three different apertures. The received signal acquired with an integrated Hann-apodized array is seen already to decrease quickly from the center of the array. The signal received with the standard array without any apodization decreases just before the edge of the array, and the roll-off-apodized array maintains the same signal strength until the edge of the array.

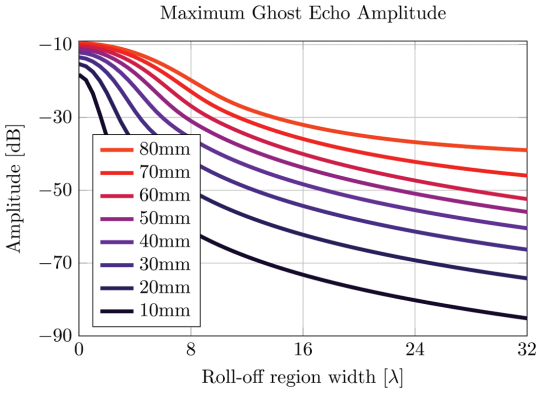

Fig. 8. Maximum ghost-echo intensity of a single scatterer as a function of edge apodization width. The wider the edge, the more the ghost echoes are suppressed. Each curve in the figure corresponds to a given scatterer depth, shown in the legend.

mit beam to the sides, like a phased array transducer, the echoes returning to the transducer surface will be significantly attenuated.

An alternative to the overlapping apodizations is to not apodize the central part of the transducer surface, but instead adding a roll-off region on both sides of all line elements, as shown in Fig. 6. This roll-off region is used for the apodization function to converge smoothly to zero. This way, the central region of the aperture surface has a uniform apodization value of 1, and there is no overlapping of the apodization functions where these are less than 1. At the same time, the discontinuities at the edges have been removed. If the added roll-off region is short, then the derivative of the aperture function will be high, and if the roll-off region is wide, the derivative will be low. From (7), it then follows that a wider roll-off region is better at suppressing the edge waves. Each line element thereby becomes longer, but there are the same number of row- and column-elements in the array. This apodization thereby does not affect the electronics, interconnections, or the data processing.

In Fig. 7, the simulated maximum received main echo as a function of scatterer position is shown. This expresses the array sensitivity as a function of position. The scatterer is placed directly in front of the transmitting line element at a depth of 10 mm. The center line element of the array emits a two-cycled pulse and the received echoes are measured on all receive line elements. The received signal is envelope detected and the maximum value is plotted against the scatterer position. The Hann-apodized array is seen to loose sensitivity very fast. At the edge of the array, the returned main echo is 40 dB weaker than in the center of the array. On the standard array without the integrated apodization, the Fresnel-diffraction of a sharp edge is evident close to the aperture edges at ±9.5 mm [37, p. 145]. The edge-apodized array has a constant sensitivity over entire central aperture, spanning from −9.5 mm to 9.5 mm in both dimensions. Adding roll-off regions to row–column-addressed arrays is therefore proposed as the standard solution.

In Fig. 8, the simulated maximum received ghost echo as a function of roll-off region width is shown. The scatterers are located at depths from 10 mm to 80 mm at the center of the aperture, where the ghost echoes reach their maximum amplitude. As expected, the wider the roll-off region is, the more the ghost echoes are suppressed. The deeper the scatter is located, the narrower is the effective width of the edge aperture, and its ghost-suppressing effect therefore decreases with depth. There is, however, an upper limit on the edge apodization width. A very large footprint results in difficulties getting a good acoustical contact between the aperture and the human body. For the rest of this paper, an edge width of 16λ is chosen as a compromise. 16λ is 1/4 of the original side length of 64λ, yielding a total aperture side length of 28.4 mm. As seen in Fig. 8, for a scatterer located at a depth of 10 mm, this will attenuate the ghost echo from −18 dB to −73 dB, and for a scatterer at 80 mm depth, this will attenuate the ghost echo from −10 dB to −32 dB. This corresponds to a damping of 55 dB and 22 dB, respectively. Importantly, this is without altering the electronics, interconnections, or data processing.

V. Beamforming With Line Sources

With a 1-D transducer array, focusing of the ultrasound wavefronts can be accomplished in the lateral direction.

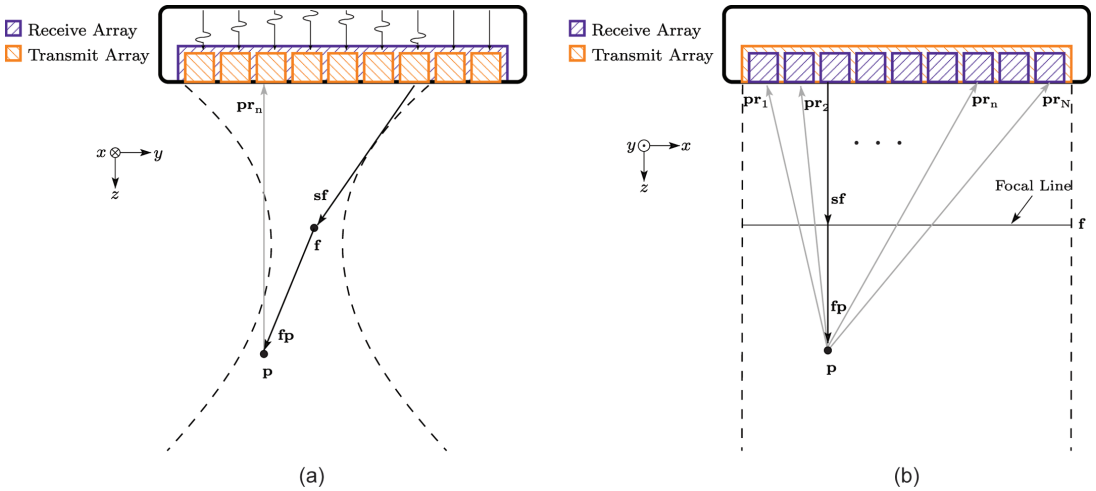

Fig. 9. Time of flight (ToF) illustration of a focused emission. The vector **sf** connects the first source line element that is excited with the focal line **f**. **fp** is the vector from the nearest point on the focal line to the point being beamformed (**p**), and $\mathbf{pr}_i$ is the vector from **p** to the nearest point on the receive line element $\mathbf{r}_i$. In (a) the setup is sliced orthogonal to the transmitting line elements and parallel with the receiving line elements, showing ToF in the y-dimension. In (b) the setup is sliced parallel with the transmitting line elements and orthogonal to the receiving line elements, showing ToF in the x-dimension. In (a) the focal zone **f** looks like a focal point, but in (b) it is seen to be a focal line.

In 2-D ultrasound imaging, the 1-D transmit and receive arrays are both used for focusing in the lateral direction. When focusing the ultrasound wavefronts using a row–column-addressed array, the transmit and receive arrays are orthogonal. This enables focusing of a 3-D volume, but the azimuth and elevation directions are only focused once [10], [18], [19], [22], [24].

Delay-and-sum beamformers usually assume the geometry of the sound sources and receivers to be points. The emitted wavefront of a line element has the shape of a cylindrical surface: it is a plane wave in the plane aligned along the line element and a circular arc in the plane orthogonal to the line element. Assuming the geometry of the line elements to be points is therefore a poor approximation. A better approximation assumes the line elements to be line segments. When an array of line elements is focused, the geometry of the focal zone is also a line segment. Calculating the distances between the line elements and a given point should therefore be calculated as the distance between a line segment and a point.

The vectors **fp** and $\mathbf{pr}_n$, seen in Fig. 9, connect the point **p** to the closest point on, respectively, the focal line **f** and the receiving element $\mathbf{r}_n$. **sf** is the vector from the source line element **s** to the focal line **f**. Because the source elements and the focal line are parallel, determining the distance between them can be solved in the zy-plane.

The time of flight of a wavefront is given by the shortest distance from the source **s** through the focal line **f** to the point being focused **p** and back to the receiving element $\mathbf{r}_n$, divided by the speed of sound. Using the notation from Fig. 9, this can be written as:

$$\mathrm{ToF}_m(\mathbf{p}, n) = \frac{\|\mathbf{sf}\| \pm \|\mathbf{fp}\| + \|\mathbf{pr}_n\|}{c}, \tag{10}$$

where c is the speed of sound in the medium, n is an index from 1 to the number of receive line elements N and m is the emission index. Only one value of ToF_m is calculated per emission. If the point being focused is closer to the transducer array than the focal line, then the case of $-||\mathbf{fp}||$ is used, otherwise $+||\mathbf{fp}||$ is used.

To determine $||\mathbf{fp}||$ and $||\mathbf{pr}_n||$, the distance between a point and line must be calculated. The line segment from point **a** to point **b** is termed **ab**. This is illustrated in Fig. 10. The projection of the point **p** onto the line **ab** is termed l and is determined by the usual equation for projection. l is positive if the projected point is located on the same side of **a** as **b**, and negative if it is located on the other side. By normalizing l with the length of the line segment, $\hat{l}$ takes the values $[0, 1]$ when the projected point is located between **a** and **b**:

$$\hat{l} = \frac{l}{\|\mathbf{ab}\|} = \frac{\mathbf{ap} \cdot \mathbf{ab}}{\|\mathbf{ab}\|^2}. \tag{11}$$

When the projection of **p** onto the line lies between **a** and **b**, i.e., when $\hat{l} \in [0, 1]$, the standard formula for the distance between a line and a point can be used:

$$d = \frac{||\mathbf{ab} \times \mathbf{ap}||}{||\mathbf{ab}||}. \tag{12}$$

When $\hat{l} \notin [0, 1]$, the shortest distance from the line segment to the point is the distance from the closest end of

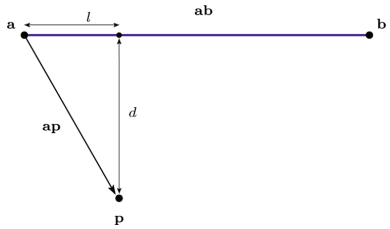

Fig. 10. Projection of the point $\mathbf{p}$ onto the line segment $\mathbf{ab}$. l is the distance from $\mathbf{a}$ to the projected point and d is the shortest distance from $\mathbf{p}$ to $\mathbf{ab}$.

the line segment ($\mathbf{a}$ or $\mathbf{b}$) to the point ($\mathbf{p}$). The following therefore determines the minimum distance between the point $\mathbf{p}$ and the line segment $\mathbf{ab}$:

$$d(\mathbf{ab},\mathbf{p}) = \begin{cases} \dfrac{||\mathbf{ab}\times\mathbf{ap}||}{||\mathbf{ab}||} & \text{if } 0 \le \hat{l} \le 1 \\ ||\mathbf{ap}|| & \text{if } \hat{l} < 0 \\ ||\mathbf{bp}|| & \text{if } \hat{l} > 0. \end{cases} \tag{13}$$

Using (13), the distances $||\mathbf{fp}||$ and $||\mathbf{pr}_n||$ can now be determined as

$$||\mathbf{fp}|| = d(\mathbf{f},\mathbf{p}) \quad \text{and} \quad ||\mathbf{pr}_n|| = d(\mathbf{r}_n,\mathbf{p}). \tag{14}$$

By inserting (14) into (10), we arrive at

$$\mathrm{ToF}_m(\mathbf{p},n) = \frac{||\mathbf{s}_{zy} - \mathbf{f}_{zy}||}{c} + \frac{d(\mathbf{r}_n,\mathbf{p}) \pm d(\mathbf{f},\mathbf{p})}{c}, \tag{15}$$

where $\mathbf{s}_{zy}$ and $\mathbf{f}_{zy}$ are the coordinates in the z-y plane of $\mathbf{s}$ and $\mathbf{f}$, respectively. The focused signal at point $\mathbf{p}$ is calculated by summing all receive signals at the time instances given by (15):

$$s_m(\mathbf{p}) = \sum_{n=1}^{N} a_{\mathrm{elec}}(n)\, y_{m,n}(\mathrm{ToF}_m(\mathbf{p},n)), \tag{16}$$

where N is the number of receive elements, $a_{\mathrm{elec}}(n)$ is the electronic receive apodization, and $y_{m,n}(t)$ is the measured signal from emission m on the receive element n at time t.

A Matlab beamformer that implements (16) was programmed to beamform data from row–column-addressed arrays and produce the point spread functions included in this paper. From (15), only the case in which $||\mathbf{fp}||$ is added is implemented, so that only points further away from the array than the focal line can be beamformed. The beamformer can IQ-beamform 250 000 voxels from a complex data set of 1.5 MiB from 128 receive line elements in approximately 11.4 on a PC with a 3.4-GHz Intel Core i7-3770 CPU (Intel Corp., Santa Clara, CA, USA) and 16 GiB of RAM. The proof-of-concept Matlab implementation of the beamformer can therefore not achieve a frame rate useful for real-time applications, but the frame rate is adequate for research purposes.

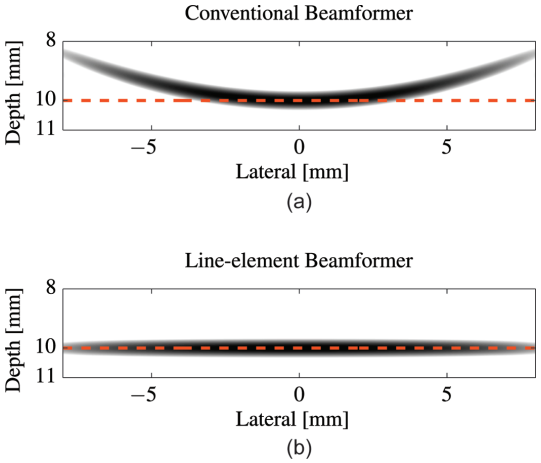

Fig. 11. B-mode images of a wire phantom beamformed (a) with a conventional beamformer and (b) with the proposed line-element beamformer. The dashed lines indicate the location of the wire phantom. The B-mode images are shown with a dynamic range of 40 dB. When using a conventional beamformer, the B-mode is seen to be geometrically distorted.

In Fig. 11, the importance of using a line-element beamformer is shown. In both figures, a wire phantom consisting of point scatterers located at 10 mm depth at the center of the transducer array is imaged. In Fig. 11(b), the line-element beamformer has been used, resulting in a reproduction of the wire with no geometrical distortions. In Fig. 11(a), conventional beamforming assuming point sources/receivers located at the center of the elements has been used. In this case the geometrical distortion of the wire caused by the error in the time-of-flight calculation is apparent, clearly demonstrating the need to take into consideration to the non-infinitesimal size of the sources/receivers.

VI. Image Quality

3-D rectilinear imaging can be achieved directly under the transducer array, marked with dashed lines in Fig. 6. The size of this area can be changed by varying number of transducer elements in the array and the pitch of the elements. The emission sequence can be designed exactly as when performing imaging with a 1-D transducer array.

A. Single-Element Emissions

In this work, a single-element emission sequence is used, leading to the use of 128 emissions for acquiring a full volume. Standard dynamic receive focusing is used to focus the lateral direction (x-dimension) and synthetic transmit focusing is used to dynamically focus the elevation direction (y-dimension) [38]–[41].

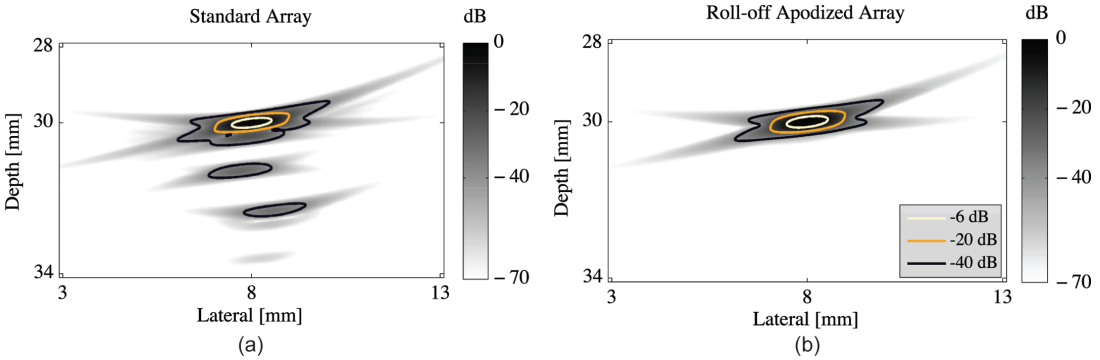

Fig. 12. PSF at $(x, y, z) = (8, 3, 30)$ mm: (a) the PSF of a standard non-apodized transducer array, and (b) the PSF of a transducer array with integrated roll-off apodization. The main responses of the PSFs are practically identical, but the ghost echoes of the roll-off-apodized array are greatly suppressed compared with the non-apodized standard array.

In Fig. 12, the PSF at $(x, y, z) = (8, 3, 30)$ mm, where 9 echoes are measured, is shown for both the standard and roll-off-apodized array. Because several of the ghost echoes arrive with a very short time interval, only 5 of the 8 ghost responses can be distinguished. The main response of the two arrays are almost identical, but the ghost echoes of the roll-off-apodized array are greatly suppressed compared with the non-apodized standard array. The maximum intensity of the PSFs in Fig. 12 is seen in Fig. 13 as a function of depth. The corresponding values for the Hann-apodized array has been added for comparison. The ghost responses seen on the PSF from the standard array are greatly attenuated by both the Hann-apodized array and the roll-off-apodized array. The maximum ghost echo is attenuated by 43 dB for the roll-off-apodized array and by 66.5 dB for the Hann-apodized array. On the other hand, the main response of the Hann-apodized array is seen to be attenuated by 24 dB, which clearly demonstrates the problem with the Hann apodization. As opposed to this, the roll-off-apodized array has preserved the amplitude of the main response. Taking the main response damping into consideration, the maximum ghost echo damping of the Hann-apodized array becomes 42.5 dB.

In Fig. 14, B-mode images of a simulated anechoic blood vessel are shown. The diameter of the blood vessel is 3 mm and both B-mode images were acquired using 128 single-line-element emissions [Fig. 14(a)] with a standard array and [Fig. 14(b)] with a roll-off-apodized array. The blood vessel phantoms used in Figs. 14(a) and 14(b) are identical, but the blood vessel in Fig. 14(a) appears smaller than the blood vessel in Fig. 14(b). The blood vessel diameter in Fig. 14(a) is decreased by the ghost echoes apparent when using the standard array. By determining the mean of the B-mode images in Fig. 14 along the x-dimension, the diameter of the blood vessel can be estimated. Defining the vessel wall as the location where the x-dimension mean crosses -20 dB, the blood vessel diameter is determined to be 2.4 mm and 2.0 mm for the apodized array and the standard array, respectively. This corresponds to 80% and 66.7% of the true vessel diameter, and shows how applying the transducer-integrated apodization increases the detectability of small anechoic objects. The imaging quality is therefore significantly better when the ghost echoes are removed by integrating roll-off apodization into the transducer array.

B. Phased-Array Imaging

The previous imaging examples were made using single-element emissions. To emphasize that the 1-D transmit array can be operated as a standard 1-D array, the following is an example of phased-array imaging. The vertical and horizontal arrays of the row–column-addressed 2-D array can each steer the transmit beam in one direction. In Fig. 15, the relative peak pressure is shown when steer-

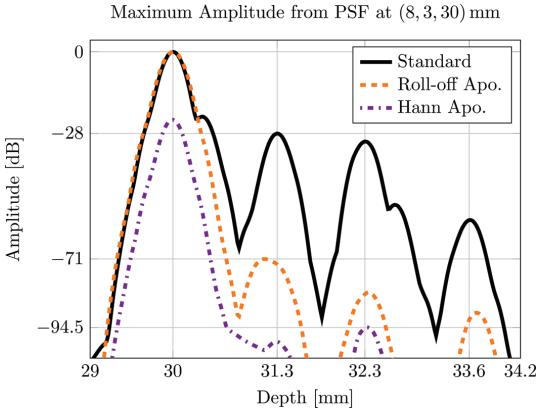

Fig. 13. Maximum intensity of the PSFs at $(x, y, z) = (8, 3, 30)$ mm as a function of depth. The Hann-apodized array is added for comparison. Both the roll-off-apodized array and the Hann-apodized array greatly suppress the ghost echoes, but the maximum intensity of the main response of the Hann-apodized array is 24 dB lower than the other two arrays.

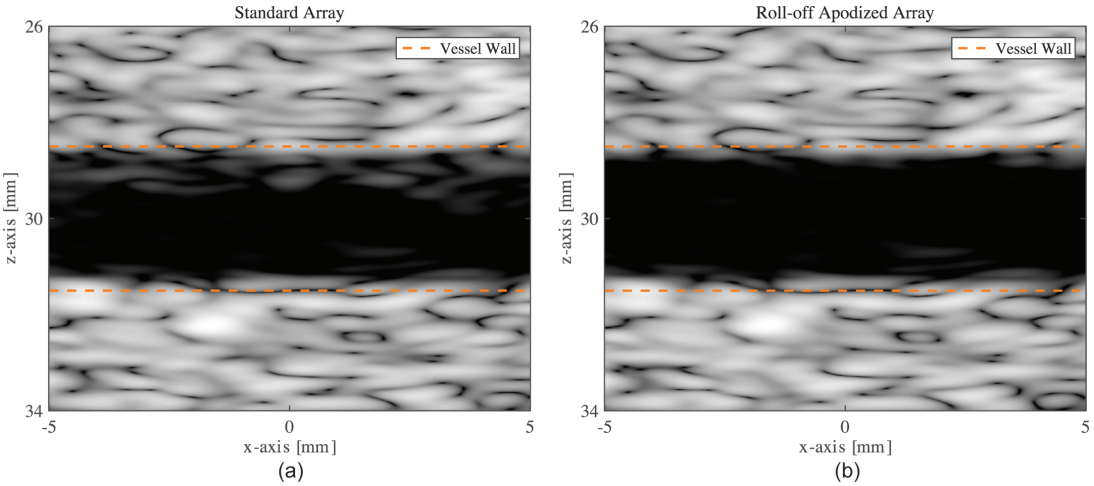

Fig. 14. B-mode images of a slice through the center of an anechoic blood vessel with a diameter of 3 mm located at 30 mm depth; (a) is made with a standard array and (b) with the roll-off-apodized array. The dynamic range is 40 dB for both images. Because of ghost echoes in the PSF for the standard array, the blood vessel in (a) appears to be smaller than the blood vessel in (b).

ing the transmit beam to the sides. For the phased-array transmit beam, all 128 elements were focused at a distance of 80 mm. The transmit beam was varied by ±45° and each voxel in the figure is placed on the focal line for a given emission. 200 emissions were used to create Fig. 15. When the horizontal array is used as a transmit array, it can steer the transmit angle within in the *zx*-plane, and at the same time the vertical array is receiving. When the sequence has completed, the two arrays switch function, and now the vertical array is used as a transmit array. This leads to the energy being distributed as a cross, as seen in Fig. 15. Row–column-addressed arrays are therefore also well suited for cross-plane imaging. Full pyramid volume imaging can be achieved by defocusing the emitted energy using a curved array or an acoustic lens [10], [19]. When the transmit beam is steered to the side, the echoes arrive at the edge of the receive array first. To measure this signal, the roll-off region of the receive line elements must be disabled in that direction. For CMUTs, this can conveniently be achieved by simply removing the bias from the roll-off region. For piezo-element arrays, the roll-off region could be connected with switches to the line elements that then open when needed.

VII. Discussion and Conclusion

The spatial impulse response of thin line elements was shown to be proportional to the derivative of the line element's 1-D apodization function. The ghost echoes, apparent with row–column-addressed arrays, therefore originate from the discontinuity of the apodization function at the edge of the line elements. To minimize the ghost echoes, the derivative of the apodization functions must be minimized.

In the literature, it has previously been proposed to use the Hann apodization to minimize the ghost echoes. In this work, it was shown that using the Hann apodization has the disadvantage of emitting and receiving little energy off-center. Instead, it was proposed to add a transducer-integrated roll-off apodization region to the ends of the line elements. This way, the apodization functions of the horizontal and vertical line elements do not overlap when they differ from the apodization value of 1. The entire central region can thereby emit and receive at full strength. It was shown that a wider roll-off region leads to better ghost echo attenuation. A roll-off region width of

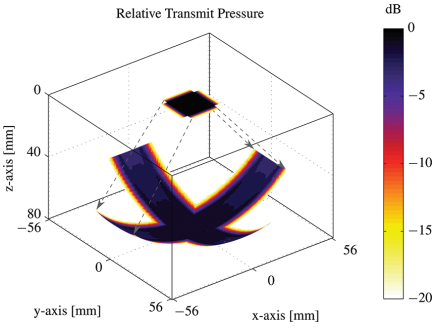

Fig. 15. Peak pressure distribution of a phased row–column-addressed array. The transmit array of the row–column-addressed array is used as a normal 1-D phased array from 2-D ultrasound imaging. Each voxel representing the pressure is located within the focal line. 200 emissions are used for simulating the figure and all 128 elements are excited during each emission. Each emission focuses at a different focal angle, but the focal distance is kept constant. For the pressure field to attain the cross shape shown in the figure, the transmit and receive arrays are interchanged after 100 emissions. This enables beamforming of cross-planes.

16λ was chosen, which led to a ghost echo damping in the PSF at $(x, y, z) = (8, 3, 30)$ mm of 43 dB. This rendered the ghost echoes invisible within the 70 dB dynamic range.

It was shown how data from a row–column-addressed array with a focal line can be delay-and-sum beamformed. The focal line can be located both in front of the array and behind it, and thereby both focused and unfocused emissions can be beamformed. A beamformer that can IQ-beamform 250 000 voxels from one emission in 11.4 s on a standard PC was presented.

Simulations of a 3-mm-diameter anechoic blood vessel at 30 mm depth showed that applying the transducer-integrated apodization increased the apparent diameter of the vessel from 2.0 mm to 2.4 mm. This corresponds to an increase from 67% to 80% of the true vessel diameter, and shows how applying the transducer-integrated apodization increases the detectability of small anechoic objects. The imaging quality is therefore improved when the ghost echoes are removed by integrating roll-off apodization into the transducer array.

In Part II of this work, experimental results from a CMUT array with integrated roll-off apodization are presented to validate the effect of integrating apodization into the line elements.

References

[1] O. T. von Ramm, S. W. Smith, and H. R. Pavy, "High speed ultrasound volumetric imaging system—Part II: Parallel processing and image display," *IEEE Trans. Ultrason. Ferroelectr. Freq. Control*, vol. 38, no. 2, pp. 109–115, 1991.

[2] D. H. Turnbull and F. S. Foster, "Beam steering with pulsed two-dimensional transducer arrays," *IEEE Trans. Ultrason. Ferroelectr. Freq. Control*, vol. 38, no. 4, pp. 320–333, Jul. 1991.

[3] K. E. Thomenius, "Evolution of ultrasound beamformers," in *Proc. IEEE Ultrason. Symp.*, 1996, vol. 2, pp. 1615–1621.

[4] G. R. Lockwood, J. R. Talman, and S. S. Brunke, "Real-time 3-D ultrasound imaging using sparse synthetic aperture beamforming," *IEEE Trans. Ultrason. Ferroelectr. Freq. Control*, vol. 45, no. 4, pp. 980–988, 1998.

[5] R. E. Davidsen, J. A. Jensen, and S. W. Smith, "Two-dimensional random arrays for real time volumetric imaging," *Ultrason. Imaging*, vol. 16, no. 3, pp. 143–163, Jul. 1994.

[6] S. S. Brunke and G. R. Lockwood, "Broad-bandwidth radiation patterns of sparse two-dimensional vernier arrays," *IEEE Trans. Ultrason. Ferroelectr. Freq. Control*, vol. 44, no. 5, pp. 1101–1109, Sep. 1997.

[7] J. T. Yen, J. P. Steinberg, and S. W. Smith, "Sparse 2-D array design for real time rectilinear volumetric imaging," *IEEE Trans. Ultrason. Ferroelectr. Freq. Control*, vol. 47, no. 1, pp. 93–110, Jan. 2000.

[8] A. Austeng and S. Holm, "Sparse 2-D arrays for 3-D phased array imaging—Design methods," *IEEE Trans. Ultrason. Ferroelectr. Freq. Control*, vol. 49, no. 8, pp. 1073–1086, Aug. 2002.

[9] M. Karaman, I. O. Wygant, O. Oralkan, and B. T. Khuri-Yakub, "Minimally redundant 2-D array designs for 3-D medical ultrasound imaging," *IEEE Trans. Med. Imaging*, vol. 28, pp. 1051–1061, Jul. 2009.

[10] C. E. Morton and G. R. Lockwood, "Theoretical assessment of a crossed electrode 2-D array for 3-D imaging," in *Proc. IEEE Ultrason. Symp.*, 2003, pp. 968–971.

[11] N. M. Daher and J. T. Yen, "Rectilinear 3-D ultrasound imaging using synthetic aperture techniques," in *Proc. IEEE Ultrason. Symp.*, 2004, vol. 2, pp. 1270–1273.

[12] N. M. Daher and J. T. Yen, "2-D array for 3-D ultrasound imaging using synthetic aperture techniques," *IEEE Trans. Ultrason. Ferroelectr. Freq. Control*, vol. 53, no. 5, pp. 912–924, 2006.

[13] C. H. Seo and J. T. Yen, "64 × 64 2-D array transducer with row–column addressing," in *Proc. IEEE Ultrason. Symp.*, 2006, vol. 1, pp. 74–77.

[14] C. H. Seo and J. T. Yen, "256 × 256 2-D array transducer with row–column addressing for 3-D imaging," in *Proc. IEEE Ultrason. Symp.*, 2007, pp. 2381–2384.

[15] C. H. Seo and J. T. Yen, "Recent results using a 256 × 256 2-D array transducer for 3-D rectilinear imaging," in *Proc. IEEE Ultrason. Symp.*, 2008, vol. 1–4, pp. 1146–1149.

[16] S. I. Awad and J. T. Yen, "3-D spatial compounding using a row–column array," *Ultrason. Imaging*, vol. 31, no. 2, pp. 120–130, 2009.

[17] A. S. Logan, L. L. P. Wong, and J. T. W. Yeow, "2-D CMUT wafer bonded imaging arrays with a row–column addressing scheme," in *Proc. IEEE Ultrason. Symp.*, 2009, pp. 984–987.

[18] C. H. Seo and J. T. Yen, "A 256 × 256 2-D array transducer with row–column addressing for 3-D rectilinear imaging," *IEEE Trans. Ultrason. Ferroelectr. Freq. Control*, vol. 56, no. 4, pp. 837–847, Apr. 2009.

[19] C. E. M. Démoré, A. Joyce, K. Wall, and G. Lockwood, "Real-time volume imaging using a crossed electrode array," *IEEE Trans. Ultrason. Ferroelectr. Freq. Control*, vol. 56, no. 6, pp. 1252–1261, 2009.

[20] A. S. Logan, L. L. P. Wong, A. I. H. Chen, and J. T. W. Yeow, "A 32 × 32 element row–column addressed capacitive micromachined ultrasonic transducer," *IEEE Trans. Ultrason. Ferroelectr. Freq. Control*, vol. 58, no. 6, pp. 1266–1271, Jun. 2011.

[21] A. I. H. Chen, L. L. Wong, A. S. Logan, and J. T. W. Yeow, "A CMUT-based real-time volumetric ultrasound imaging system with row–column addressing," in *Proc. IEEE Ultrason. Symp.*, 2011, pp. 1755–1758.

[22] M. F. Rasmussen and J. A. Jensen, "3D ultrasound imaging performance of a row–column addressed 2D array transducer: A simulation study," in *Proc. SPIE Med. Imag.*, 2013, art. no. 86750C.

[23] M. F. Rasmussen and J. A. Jensen, "3-D ultrasound imaging performance of a row–column addressed 2-D array transducer: A measurement study," in *Proc. IEEE Ultrason. Symp.*, 2013, pp. 1460–1463.

[24] J. T. Yen, "Beamforming of sound from two-dimensional arrays using spatial matched filters," *J. Acoust. Soc. Am.*, vol. 134, no. 5, pp. 3697–3704, Nov. 2013.

[25] A. Sampaleanu, P. Zhang, A. Kshirsagar, W. Moussa, and R. Zemp, "Top-orthogonal-to-bottom-electrode (TOBE) CMUT arrays for 3-D ultrasound imaging," *IEEE Trans. Ultrason. Ferroelectr. Freq. Control*, vol. 61, no. 2, pp. 266–276, 2014.

[26] T. L. Christiansen, M. F. Rasmussen, J. P. Bagge, L. N. Moesner, J. A. Jensen, and E. V. Thomsen, "3-D imaging using row–column-addressed arrays with integrated apodization—Part II: Transducer fabrication and experimental results," *IEEE Trans. Ultrason. Ferroelectr. Freq. Control*, vol. 62, no. 5, pp. 959–971, 2015.

[27] J. A. Jensen and N. B. Svendsen, "Calculation of pressure fields from arbitrarily shaped, apodized, and excited ultrasound transducers," *IEEE Trans. Ultrason. Ferroelectr. Freq. Control*, vol. 39, no. 2, pp. 262–267, 1992.

[28] J. A. Jensen, "Field: A program for simulating ultrasound systems," *Med. Biol. Eng. Comput.*, vol. 34, suppl. 1, pt. 1, pp. 351–353, 1996.

[29] J. A. Jensen, "A multi-threaded version of Field II," in *Proc. IEEE Ultrason. Symp.*, 2014, pp. 2229–2232.

[30] A. D. Pierce, *Acoustics, An Introduction to Physical Principles and Applications*. New York, NY, USA: Acoustical Society of America, 1989.

[31] P. R. Stepanishen, "Transient radiation from pistons in an infinite planar baffle," *J. Acoust. Soc. Am.*, vol. 49, no. 5B, pp. 1629–1638, 1971.

[32] G. R. Harris, "Review of transient field theory for a baffled planar piston," *J. Acoust. Soc. Am.*, vol. 70, no. 1, pp. 10–20, 1981.

[33] G. R. Harris, "Transient field of a baffled planar piston having an arbitrary vibration amplitude distribution," *J. Acoust. Soc. Am.*, vol. 70, no. 1, pp. 186–204, 1981.

[34] P. R. Stepanishen, "Acoustic transients from planar axisymmetric vibrators using the impulse response approach," *J. Acoust. Soc. Am.*, vol. 70, no. 4, pp. 1176–1181, 1981.

[35] J. Naze Tjøtta and S. Tjøtta, "Nearfield and farfield of pulsed acoustic radiators," *J. Acoust. Soc. Am.*, vol. 71, no. 4, pp. 824–834, 1982.

[36] T. L. Christiansen, M. F. Rasmussen, J. A. Jensen, and E. V. Thomsen, "Row–column addressed 2-D CMUT arrays with integrated apodization," in *Proc. IEEE Ultrason. Symp.*, 2014, pp. 600–603.

[37] P. V. Naik. *Principles of Physics*, 4th ed., Upper Saddle River, NJ, USA: Prentice Hall, 2010.

[38] J. T. Ylitalo and H. Ermert, "Ultrasound synthetic aperture imaging: Monostatic approach," *IEEE Trans. Ultrason. Ferroelectr. Freq. Control*, vol. 41, no. 3, pp. 333–339, 1994.
[39] M. Karaman, P. C. Li, and M. O'Donnell, "Synthetic aperture imaging for small scale systems," *IEEE Trans. Ultrason. Ferroelectr. Freq. Control*, vol. 42, no. 3, pp. 429–442, 1995.
[40] C. H. Frazier and W. D. O'Brien, "Synthetic aperture techniques with a virtual source element," *IEEE Trans. Ultrason. Ferroelectr. Freq. Control*, vol. 45, no. 1, pp. 196–207, 1998.
[41] M. F. Rasmussen and J. A. Jensen, "Comparison of 3-D synthetic aperture phased array ultrasound imaging with parallel beamforming," *IEEE Trans. Ultrason. Ferroelectr. Freq. Control*, vol. 61, no. 10, pp. 1638–1650, 2014.

Morten F. Rasmussen was born in 1981. He received the B.Sc., M.Sc., and Ph.D. degrees in electrical engineering from the Technical University of Denmark (DTU) in 2008, 2011, and 2014, respectively. In 2007, he spent ten months at the Technische Universität Berlin, Berlin, Germany, working on the BeeSat satellite. He is currently a postdoctoral research fellow at Stanford University. His current research interests include 3-D ultrasound imaging, synthetic aperture imaging techniques, and ultrasound neuro-stimulation.

Thomas Lehrmann Christiansen received his B.Sc. and M.Sc. degrees with honors in engineering physics and nanotechnology from the Technical University of Denmark, Kgs. Lyngby, Denmark, in 2010 and 2012, respectively. He is presently pursuing a Ph.D. degree at the Technical University of Denmark, focusing on micromachined ultrasonic transducers for three-dimensional imaging. He received the Oticon award in 2011 and the Danish Engineering Society's award in 2012 for his work on injection-molded microfluidic devices for automated patch-clamping. In 2014, he received the EliteForsk travel grant awarded to twenty selected Ph.D. students by the Danish Ministry of Higher Education and Science.

Erik V. Thomsen is a Professor at DTU Nanotech, the Technical University of Denmark, where he is heading the MEMS Applied Sensors group. He was born in Aarhus in 1964. He received the M.Sc. degree in physics from Odense University, Odense, Denmark, and the Ph.D. degree in electrical engineering from the Technical University of Denmark (DTU), Lyngby, in 1998. His current research and teaching interests include capacitive micromachined ultrasonic transducers, MEMS multisensors, biomedical devices, and small-scale energy systems such as miniature fuel cells and energy harvesting devices. He teaches classes in solid-state electronics, microtechnology, and nano- and microfabrication. Dr. Thomsen received the AEG Electron Prize in 1995 and has also received several teaching awards at DTU.

Jørgen Arendt Jensen earned his M.Sc. degree in electrical engineering in 1985 and his Ph.D. degree in 1989, both from the Technical University of Denmark. He received the Dr.Techn. degree from the same university in 1996. He has published more than 400 journal and conference papers on signal processing and medical ultrasound and the book *Estimation of Blood Velocities Using Ultrasound*, published by Cambridge University Press in 1996. He is also the developer of the Field II simulation program. He has been a visiting scientist at Duke University, Stanford University, and the University of Illinois at Urbana-Champaign. He is currently full professor of biomedical signal processing at the Technical University of Denmark in the Department of Electrical Engineering, and head of the Center for Fast Ultrasound Imaging. He has given courses on blood velocity estimation at both Duke University and the University of Illinois, and teaches biomedical signal processing and medical imaging at the Technical University of Denmark. He has given several short courses on simulation, synthetic aperture imaging, and flow estimation at international scientific conferences. He has received several awards for his research and is an IEEE Fellow. His research is centered on simulation of ultrasound imaging, synthetic aperture imaging, vector blood flow estimation, and construction of ultrasound research systems.

PAPER K

3-D Imaging using Row-Column Addressed Arrays with Integrated Apodization – Part II: Transducer Fabrication and Experimental Results

Authors: **Thomas Lehrmann Christiansen**, Morten Fischer Rasmussen, Jan Peter Bagge, Lars Nordahl Moesner, Jørgen Arendt Jensen, and Erik Vilain Thomsen.

Published in: IEEE Transactions on Ultrasonics, Ferroelectrics, and Frequency Control, Vol. 62, No. 5, pp. 959-971 (2015).

Abstract

This paper demonstrates the fabrication, characterization, and experimental imaging results of a 62+62 element $\lambda/2$-pitch row-column addressed capacitive micromachined ultrasonic transducer (CMUT) array with integrated apodization. A new fabrication process was used to manufacture a $26.3\,\mathrm{mm}$ by $26.3\,\mathrm{mm}$ array using five lithography steps. The array includes an integrated apodization, presented in detail in Part I of this paper, which is designed to reduce the amplitude of the ghost echoes that are otherwise prominent for row-column addressed arrays. Custom front-end electronics was produced with the capability of transmitting and receiving on all elements, and the option of disabling the integrated apodization. The center frequency and $-6\,\mathrm{dB}$ fractional bandwidth of the array elements were $2.77\pm0.26\,\mathrm{MHz}$ and $102\pm10\,\%$, respectively. The surface transmit pressure at 2.5 MHz was $590\pm73\,\mathrm{kPa}$, and the sensitivity was $0.299\pm0.090\,\mu\mathrm{V/Pa}$. The nearest neighbour cross-talk level was $-23.9\pm3.7\,\mathrm{dB}$, while the transmit to receive elements cross-talk level was $-40.2\pm3.5\,\mathrm{dB}$. Imaging of a 0.3 mm diameter steel wire using synthetic transmit focusing with 62 single-element emissions demonstrated an axial and lateral FWHM of $0.71\,\mathrm{mm}$ and $1.79\,\mathrm{mm}$ (F-number: 1.4), respectively, compared to a simulated axial and lateral FWHM of $0.69\,\mathrm{mm}$ and $1.76\,\mathrm{mm}$. The dominant ghost echo was

reduced by $15.8\,\mathrm{dB}$ in measurements using the integrated apodization compared to the disabled configuration. The effect was reproduced in simulations showing a ghost echo reduction of $18.9\,\mathrm{dB}$.

3-D Imaging Using Row–Column-Addressed Arrays With Integrated Apodization—Part II: Transducer Fabrication and Experimental Results

Thomas Lehrmann Christiansen, Morten Fischer Rasmussen, Jan Peter Bagge, Lars Nordahl Moesner, Jørgen Arendt Jensen, and Erik Vilain Thomsen

***Abstract*—This paper demonstrates the fabrication, characterization, and experimental imaging results of a 62+62 element λ/2-pitch row–column-addressed capacitive micromachined ultrasonic transducer (CMUT) array with integrated apodization. A new fabrication process was used to manufacture a 26.3 mm by 26.3 mm array using five lithography steps. The array includes an integrated apodization, presented in detail in Part I of this paper, which is designed to reduce the amplitude of the ghost echoes that are otherwise prominent for row–column-addressed arrays. Custom front-end electronics were produced with the capability of transmitting and receiving on all elements, and the option of disabling the integrated apodization. The center frequency and −6-dB fractional bandwidth of the array elements were 2.77 ± 0.26 MHz and 102 ± 10%, respectively. The surface transmit pressure at 2.5 MHz was 590 ± 73 kPa, and the sensitivity was 0.299 ± 0.090 V/Pa. The nearest neighbor crosstalk level was −23.9 ± 3.7 dB, while the transmit–to–receive-elements crosstalk level was −40.2 ± 3.5 dB. Imaging of a 0.3-mm-diameter steel wire using synthetic transmit focusing with 62 single-element emissions demonstrated axial and lateral FWHMs of 0.71 mm and 1.79 mm (f-number: 1.4), respectively, compared with simulated axial and lateral FWHMs of 0.69 mm and 1.76 mm. The dominant ghost echo was reduced by 15.8 dB in measurements using the integrated apodization compared with the disabled configuration. The effect was reproduced in simulations, showing a ghost echo reduction of 18.9 dB.**

I. Introduction

Recently, row–column-addressed arrays have attracted some attention as they offer real-time volumetric imaging with a greatly reduced number of connections to the array compared with a fully addressed array. Where an $N \times N$ fully addressed array will need N^2 individual connections, a row–column-addressed array only needs $2N$ connections. Numerous techniques have been introduced to reduce the complexity of 2-D matrix arrays, such as sparse arrays [1]–[5] and integrated electronics in the probe handle [6]–[8]. Despite these measures, the dense interconnect requirements, high electrical impedance of the elements, and heating of integrated electronics remain significant challenges for 2-D matrix arrays, which add to their complexity and cost. Therefore, row–column-addressed arrays provide an attractive low-cost alternative to such arrays for real-time volumetric ultrasound imaging.

The concept of volumetric imaging using row–column addressing, where transmit focusing is performed in one dimension and receive focusing is performed in the orthogonal dimension, was first introduced by Morton and Lockwood in 2003 [9], and later expanded by Demoré *et al.* [10]. Different techniques to improve the resolution, sensitivity, or frame rate of row–column-addressed arrays were explored theoretically by Daher *et al.* [11], [12] and Yen [13] using synthetic aperture techniques and spatial matched filters. Recently, Rasmussen and Jensen used a fully addressed 32 × 32 array in a measurement study to compare the imaging performance of a fully addressed array to that of a row–column-addressed array [14]. For the same number of channels used, the row–column-addressed array exhibited superior detail resolution compared with the fully addressed array.

Several groups have presented realizations of row–column-addressed arrays. Yen's group has demonstrated imaging with several versions of row–column-addressed piezo-arrays, starting in 2006, when Seo and Yen [15] presented the first experimental demonstration of a row–column-addressed array. The 64 + 64 elements used in this array was later surpassed by a 256 + 256-element array [16]–[18] by the same authors. More recently, Chen *et al.* [19] and Yen *et al.* [20] have introduced arrays manufactured with a dual-layer structure to simplify the fabrication process. Zemp *et al.* [21] and Sampaleanu *et al.* [22] have performed feasibility studies and recently photoacoustic imaging [23] using capacitive micromachined ultrasonic transducers (CMUTs). Additionally, the Yeow's group has demonstrated both characterization [24] and imaging using 16 + 16-element [25] and 32 + 32-element [26], [27] row–column-addressed CMUT arrays.

Manuscript received October 30, 2014; accepted January 3, 2015. This work was financially supported by grants 024-2008-3 and 82-2012-4 from the Danish National Advanced Technology Foundation and from BK Medical ApS (Herlev, Denmark).

T. L. Christiansen and E. V. Thomsen are with the Department of Micro- and Nanotechnology, Technical University of Denmark, DK-2800 Kgs. Lyngby, Denmark (e-mail: tlehr@nanotech.dtu.dk).

M. F. Rasmussen and J. A. Jensen are with the Center for Fast Ultrasound Imaging, Department of Electrical Engineering, Technical University of Denmark, DK-2800 Kgs. Lyngby, Denmark.

J. P. Bagge and L. N. Moesner are with BK Medical ApS, Analogic Ultrasound Group, DK-2730 Herlev, Denmark.

Despite the promises of row–column addressing, such arrays have an inherent drawback: The long elements produce prominent edge effects, leading to ghost echoes in the beamformed image. The row–column addressing scheme does not allow for electronic control along the length of the elements, and the ghost echoes can therefore not be removed using conventional electronic apodization techniques. This issue was first observed by Demoré *et al.* [10] and later described in further detail by Rasmussen and Jensen [28]. Both authors concluded that a solution to the problem was to integrate the apodization in the transducer array itself, and several embodiments of a transducer-integrated apodization have been suggested [29], [30].

In Part I of this paper [31], an in-depth study of the possibilities of such a transducer-integrated apodization was presented. Simulation studies were used to develop an optimized transducer-integrated apodization that is able to efficiently damp the ghost echoes from row–column-addressed arrays in the entire imaged 3-D volume. Importantly, this was achieved without affecting the main echo regardless of the position of the object being imaged, and without altering the number of channels needed or changing the beamforming in any way. Additionally, beamforming with row–column-addressed arrays using line-element beamforming was presented.

This paper demonstrates the fabrication and characterization of a 62 + 62-element row–column-addressed CMUT array with such an integrated apodization based on the layout presented in [31]. Custom front-end electronics with transmit and receive capability on all channels are made to drive the array. The array is used to perform volumetric imaging of a steel wire twice; once with the apodization enabled and once with the apodization disabled. The purpose is thereby to experimentally demonstrate the effect of an integrated apodization when performing 3-D imaging with row–column-addressed arrays.

The paper is organized as follows: Section II covers the design and fabrication of the CMUT array as well as a description of the front-end electronics. Section III contains a characterization of the array using impedance measurements and acoustical measurements. In Section IV, the imaging results are presented, and Section V concludes the paper.

II. Array Design, Fabrication, and Interconnect Electronics

A. Array Design

The design of the transducer array used in this work can be divided into three main components: Design of the individual CMUT cells to achieve the desired operating frequency and operating voltage, determination of the element size and pitch, and finally design of the layout of the integrated apodization. These three components are addressed in the following.

TABLE I. Transducer Dimensional Parameters.

Parameter	Value	Unit
Array		
Number of elements	62 + 62	—
Number of apodization-region electrodes	4	—
Element pitch	270	μm
Element width	265	μm
Element length	24.84	mm
Length of apodization regions	4.05	mm
Array outer dimensions (square)	26.3	mm
CMUT cell		
Cell side length (square)	60	μm
Distance between cells	5	μm
Plate thickness	1.7	μm
Al electrode thickness	200	nm
Insulation oxide thickness	296	nm
Vacuum gap height	413	nm

A single element of the array consists of multiple individual CMUT cells. The operating frequency of the array is determined by the plate thickness and lateral dimension of the CMUT cells [32]. To obtain a high fill-factor, the geometry of the CMUT cells is designed to be square, and the operating frequency is adjusted such that the cells can be closely fitted in the width of a $\lambda/2$–pitch array element. These considerations resulted in a CMUT cell with a plate thickness of 1.7 μm and a square side length of 60 μm, designed for a center frequency in immersion of 2.74 MHz. The corresponding element pitch for this frequency was 270 μm. The distance between the individual cells and the kerf were set to 5 μm to provide adequate bonding area during the fabrication, as will be covered in Section II-B. All dimensions can be seen in Table I.

The operating voltage of the array is, for fixed CMUT plate dimensions, determined by the gap between the top- and bottom electrodes. The gap consists of a vacuum region and an oxide layer; the latter is used to provide insulation in case of pull-in. The pull-in voltage is here defined as the voltage at which the top plate collapses down to the bottom electrode because the electrostatic forces are larger than the mechanical forces. The desired thickness of the vacuum gap and insulation oxide are 400 nm and 300 nm, respectively, which is designed to give a pull-in voltage of approximately 100 V. The actual gap dimensions, dictated by the fabrication accuracy, are seen in Table I.

A 3-D diagram of the corner portion of the array is given in Fig. 1. The layout of the array, seen in Fig. 2, is based on the findings in Part I [31]. It consists of 62 row elements, 62 column elements, and four apodization-region electrodes. The apodization-region electrodes provide dc bias to the integrated apodization, which is located at both ends of the elements. To the right in Fig. 2, a magnified view of one apodized element end is shown. As seen, it consists of a collection of CMUT cells (red squares), the number of which is reduced toward the outer edge. Such a reduction in the number of CMUT cells will provide a fixed integrated apodization, because the energy transmitted and received by the array scales with the density of

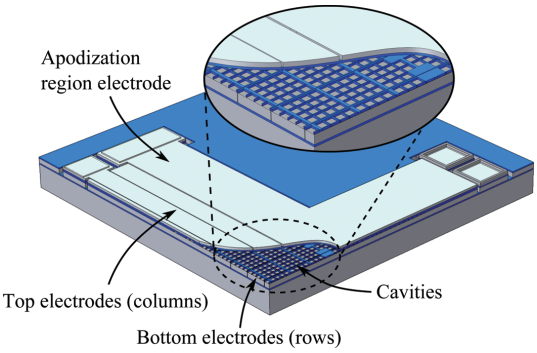

Fig. 1. 3-D illustration of the CMUT row–column-addressed transducer array showing a detail of the upper right corner of the array seen in Fig. 2 (top corner of the mounted array shown in Fig. 4). A section of the top electrodes have been removed to reveal the underlying CMUT cavities. Oxide is blue, silicon is dark gray, and aluminum is light gray. Dimensions are not to scale.

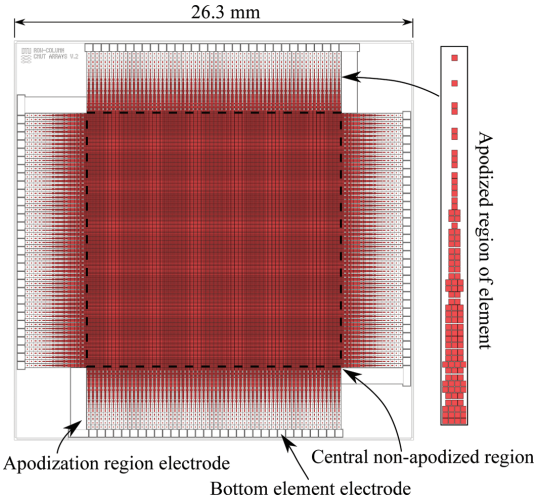

Fig. 2. Array mask layout. The red squares are the individual CMUT cells, which are densely populated in the central region of the array shown within the dashed line. A zoom on the apodized region of one element is seen in the right part of the figure. The four large contact pads provide electrical access to the apodization-region electrodes.

the cells [33]. As in [31], the number of cells follows a Hann function, which in this case is discrete.

The central part of the array, i.e., excluding the apodized element ends, is densely populated with CMUT cells and is thus not apodized in any way. In other words, the part of the array seen within the dashed line in Fig. 2 may be considered a conventional row–column-addressed CMUT transducer array. The apodized regions located outside this central part are responsible for removing the otherwise abrupt truncation of the elements, which is the origin of the ghost echoes produced by row–column-addressed arrays [31]. This configuration allows the array to perform as a conventional row–column-addressed array, regardless of the position of the object being imaged, but with a significant damping of the ghost echoes, as demonstrated in [31].

B. Array Fabrication

The array was fabricated using cleanroom processing techniques, partly based on previous works described in the literature [34], [35]. The individual process steps are shown in Fig. 3.

The fabrication process utilized two silicon-on-insulator (SOI) wafers, both having a 525-µm-thick handle layer with high resistivity (1 to 10 Ω·cm), a 1-µm-thick buried oxide layer, and a low resistivity (0.01 to 0.001 Ω·cm) device layer. The device layer on the first SOI wafer was 20 µm thick and was used to create the bottom electrodes, henceforth defined as the rows. The second SOI wafer had a 1.9-µm-thick device layer, which was used for the top electrode (plate) of the CMUT. These top electrodes are defined as the columns of the row–column-addressed array.

The SOI wafer with 20 µm device layer was dry oxidized at 1050°C for 8 h and 35 min at an oxidant pressure of 100 kPa to grow a 296-nm-thick layer of oxide [Fig. 3(a)]. The CMUT cavities were then defined using conventional UV lithography and etched using reactive ion etching (RIE) as shown in Fig. 3(b). After stripping the photoresist, a second lithography step was used to define the bottom electrodes, or rows, as shown in Fig. 3(c). Two consecutive RIE etches were used to selectively etch first the oxide layer and subsequently the underlying silicon device layer. After stripping the photoresist, the fabrication of the bottom electrodes and the substrate supporting the array was complete.

The second SOI wafer was dry oxidized at 1100°C for 8 h and 55 min at an oxidant pressure of 1 atm to grow a 413-nm-thick layer of oxide, reducing the silicon device layer thickness from 1.9 µm to 1.7 µm. Both SOI wafers were then cleaned using a standard RCA cleaning procedure [36] and bonded together in vacuum (100 Pa) using fusion bonding and a subsequent annealing step (70 min at 1100°C), see Fig. 3(d). The oxide layer covering both wafers was removed in buffered hydrofluoric acid (BHF), after which the handle layer and buried oxide layer of the top SOI wafer were etched using RIE and BHF, respectively, as shown in Fig. 3(e).

A third lithography step followed by selective RIE in first the silicon layer and subsequently the oxide layer was used to define openings to the bottom electrodes, see Fig. 3(f). The thin device layer is partly transparent in the visible spectrum, and alignment to the bottom wafer alignment marks could therefore be performed, thereby omitting the need for alignment during the wafer-bonding step.

Fig. 3(g) shows the wire-bonding pads, which were made by depositing a 800-nm aluminum layer on the entire wafer using electron beam evaporation and structured

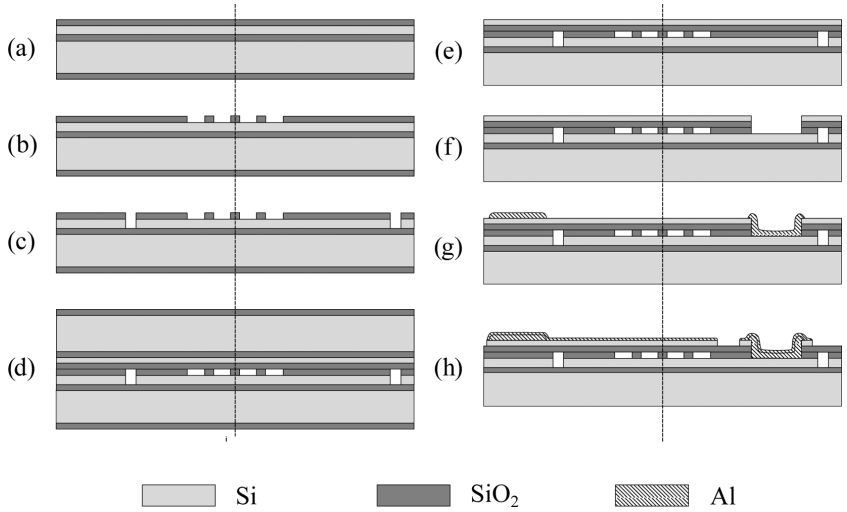

Fig. 3. Process flow of the cleanroom fabrication. The dashed line separates the layer composition comprising the top electrodes (to the left of the line) and the bottom electrodes (to the right of the line), corresponding to a cross-section from left to right in Fig. 1. The steps are: (a) oxidation, (b) cavity etch, (c) bottom electrode etch, (d) wafer bonding, (e) handle etch, (f) etch access to bottom electrodes, (g) deposit and etch wire-bonding pads, and (h) deposit and etch top electrodes. A total of five lithography masks are used [in steps (b), (c), (f), (g), and (h)].

by performing a lithography step followed by a selective aluminum etch in H_2O:H_3PO_4 (1:2) at 50°C. The top electrodes, or columns, were then finally defined by a step similar to the previous one, but this time with a 200-nm aluminum deposition. Before removing the photoresist, the exposed silicon layer was etched using RIE to isolate the individual top electrodes, thereby concluding the fabrication process.

It should be noted that this process only uses five lithography steps, and, wherever possible, the same lithography step is used for multiple etches. Any front-to-back or wafer-to-wafer alignment is omitted to improve the robustness of the process. Also, the oxide-oxide bonding previously presented in [37] was chosen, because it allows for protrusion-free surfaces and thereby very low void density, which is essential for such large arrays.

C. Interconnect Electronics

The fabricated array was mounted on a printed circuit board acting as a carrier board, as shown in Fig. 4. This carrier board contained one lead per channel in the array, having wire-bonding pads in one end and terminating in one of two connectors in the other end (located on the back side of the carrier board shown in Fig. 4). All leads were designed to have equal length to ensure uniformity of the channels. To facilitate this, the orientation of the array was set to 45° relative to the sides of the carrier board. The array was mounted on the carrier board using Namics XS8481–8 epoxy glue (Namics Corp., Niigata, Japan) with no further backing applied. The electrical connection between array and carrier board was made using wire-bonding, and glob-top (dam and fill, Namics G8245-D and G8345–6, Namics Corp.) was applied afterwards to protect and insulate the bonds.

The carrier board was designed to easily connect via the connectors with a second printed circuit board, which acts as an interconnect board (ICB) between the mounted array and the scanner used to send and acquire the data. In this work, the experimental Synthetic Aperture Real-

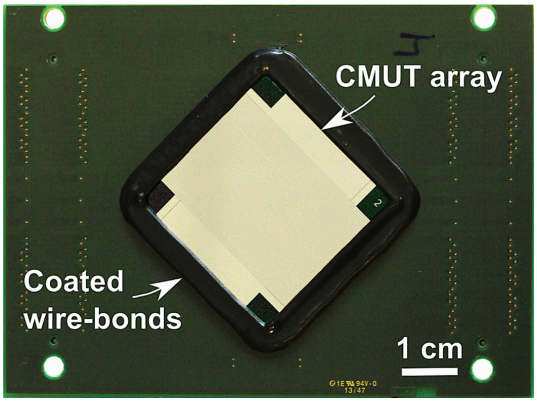

Fig. 4. The row–column-addressed CMUT array mounted and wire-bonded on the carrier board. Two connectors are located on the back side of the carrier board (the vias to the connectors can be seen to the left and right in the picture). The CMUT array is rotated 45° clockwise to ensure that the length of each lead to the connector pins is equal. The top electrodes (columns) can be seen going from the top left to the bottom right of the array.

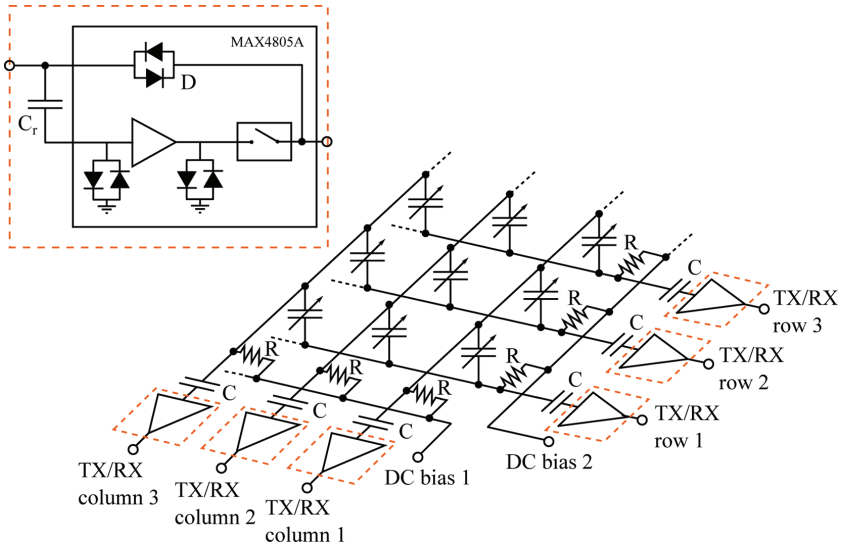

Fig. 5. Diagram of the front-end electronics showing three row channels and column channels. The variable capacitors denote the CMUTs contained in the elements. Every column channel has contact via the CMUTs to all row channels and vice versa. The dc biases are low-pass filtered through a 1-MΩ resistor (R) in conjunction with the CMUT, whereas the ac signals to and from the CMUT via the MAX4805A preamplifier are high-pass filtered using a 10-nF capacitor (C) together with the resistor R before going to the transmitters/receivers. The inset shows a detail of the MAX4805A circuit [39].

time Ultrasound System (SARUS) [38] was used. A total of 192 transmit/receive channels could be interfaced using this ICB, and connection to the scanner was made via a 192 channel coaxial cable (BK Medical, Herlev, Denmark). Every channel was connected to a MAX4805A preamplifier (Maxim Integrated, San Jose, CA, USA), previously demonstrated to work with CMUT arrays [39]. This preamplifier provides a nominal 8.7-dB voltage gain of the receive signals to drive the cable. The MAX4805A contains a built-in switching circuit that can protect the preamplifier during transmit, so that all channels on the ICB could be used for both transmission and reception.

A dc-biasing circuit with two dc bias supplies was made. A diagram of the electronics can be seen in Fig. 5, where the variable capacitors denote the CMUTs contained in the elements. This particular diagram illustrates only the first three rows and columns, respectively. Every element has contact to a single channel on the ICB. DC bias 1 supplies all the column channels, and the row elements passing perpendicularly below them are all held at the voltage potential defined by dc bias 2. The total dc bias seen by the CMUT element thereby becomes the difference between the two dc supplies. The dc bias supply to each element is provided through a 1-MΩ resistor (R), partly acting as a low-pass filter, and partly ensuring that the dc voltage can be maintained in the event of a short circuit of a top and bottom electrode within the CMUT array, or any other dc short of the row or column signals. A 10-nF capacitor (C) is placed in front of the input of the MAX4805A (shown in the inset of Fig. 5) to separate the dc bias from the ground reference of the transmitters and the receive circuit.

If a transmit pulse is sent on a column channel, all the row channels will provide a ground path for the ac signal. This will be established through the rows' 10-nF capacitor (C), then through the transmit-path diodes (D) inside the MAX4805A (see inset of Fig. 5) and finally to the transmit amplifier output of the row channels. It is therefore mandatory that the row channels are in the low-impedance transmit mode to establish this ground reference. No ground is accessible through the receive path because of the high impedance of the 47-pF capacitor, C_r. During reception, the ac voltage generated by the CMUT element is low enough that the diode pair (D) in the transmit path does not provide a path to ground. Therefore, all row channels and column channels will receive and amplify the received signal.

Note that only the 62 + 62 elements are connected to beamformer channels; the four apodization-region electrodes are provided with just a dc bias voltage.

III. Transducer Characterization

The transducer presented in the previous section was characterized both electrically using impedance measurements and acoustically in vegetable oil through hydrophone and pulse–echo measurements. This section describes these measurements, thereby providing an evaluation of the performance of the array.

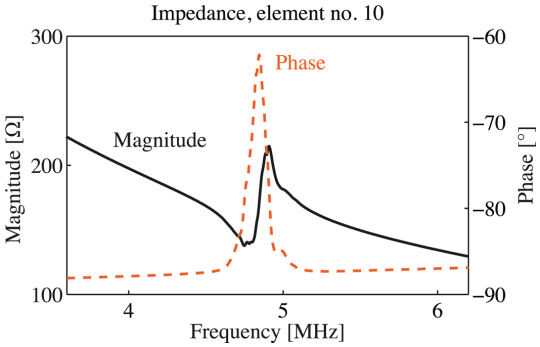

Fig. 6. Impedance magnitude (solid line) and phase (dashed line) for element number 10 acquired at a dc bias of 40 V in the vicinity of the mechanical resonance of the element.

A. Impedance Measurements

The electrical characterization of the transducer array was carried out using an Agilent 4294A impedance analyzer (Hewlett-Packard, Palo Alto, CA, USA). The measurements were performed after mounting the array on the carrier board shown in Fig. 4. Each element of the array was accessed via the pins of the connectors on the carrier board using an Agilent 42941A probe (Hewlett-Packard). When measuring on individual columns, all rows were electrically shorted using a custom-built connector to enable measurement of a whole column at the time. The reverse was true when measuring on individual rows. In all measurements, a 500 mV excitation voltage was used on top of a dc bias of 40 V, which was applied to the array using the built-in dc bias of the impedance analyzer. These values were chosen to acquire adequate signal from the array to locate the resonance peak, while at the same time ensuring negligible frequency shift of the resonance peak resulting from the spring-softening effect.

For every element, a set of three impedance sweeps were performed: one spanning the whole range of the impedance analyzer from 40 Hz to 110 MHz, a second from 1 MHz to 20 MHz, and a final in an interval of ±1 MHz from the detected resonance frequency of the element. From this, the capacitance and resonance frequency in air of each individual element were found. The capacitance was determined at the lowest measured frequency (40 Hz), and the resonance frequency was found as the local minimum in impedance magnitude in the vicinity of the resonance. An example of an impedance sweep showing the resonance of element number 10 is seen in Fig. 6.

The resonance frequency in air and capacitance of each element are shown in Figs. 7(a) and 7(b). Mean and standard deviation over the whole array is given in Table II. The capacitance is seen to be very homogeneous for both the rows and columns with standard deviations of 1.2% and 0.5%, respectively. This is a consequence of the lateral accuracy of the cleanroom processing, which uses UV photolithography for defining the lateral dimensions of the

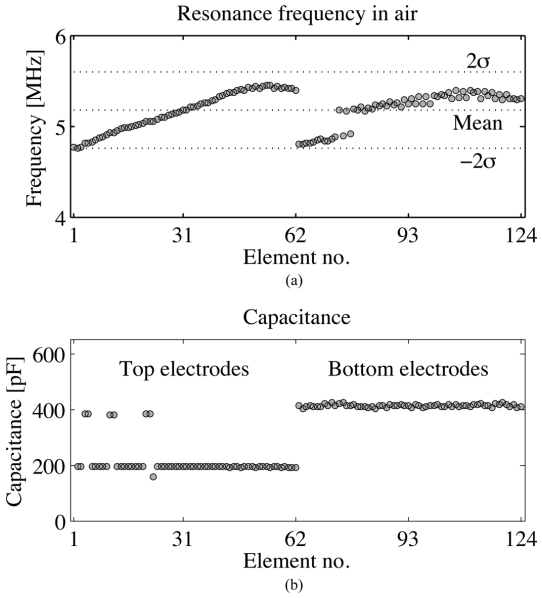

Fig. 7. (a) Resonance frequency in air and (b) capacitance evaluated at 40 Hz versus element number. The resonance frequency is shown with mean and two standard deviations (2σ). Elements 1–62 are top electrode elements and elements 63–124 are bottom electrode elements. The elements 4–5, 11–12, and 21–22 are pair-wise shorted because of fabrication errors, hence the altered capacitance.

array. The rows (bottom electrodes) have a higher capacitance than the columns (top electrodes) because they can couple capacitively to the substrate of the bottom SOI wafer. The apodization-region electrodes have a much higher capacitance than the elements, and their capacitance has therefore only been listed in Table II to better visualize the capacitance of the elements in Fig. 7(b). This higher capacitance is a consequence of the large area of the apodization-region electrodes, as can be seen in Fig. 1. Note also that the column elements 4–5, 11–12, and 21–22 are pair-wise shorted. This is due to fabrication errors in the final aluminum and silicon etch shown in Fig. 3(h). Any particle covering the element kerf on the mask during the lithography step before these etches will result in contact between two top electrodes (columns). This is especially critical for row–column-addressed arrays, where the size of the elements results in an extensive total kerf length. The kerf is only 5 µm, so any particle larger than this will result in a short circuit, as was seen to affect these three different locations of the array.

The resonance frequency in air given in Fig. 7(a) is seen to vary slightly more than the capacitance, the standard deviation being 4%. This is a consequence of the thickness variation of the device layer of the SOI wafer, which is used to define the top electrode that acts as the top vibrating plate of the individual CMUT cells. This thickness is harder to control precisely because the SOI wafer was ordered from external wafer suppliers who promised

TABLE II. Transducer Impedance Characterization Parameters.

Parameter	Mean value	Std.	Unit
Resonance frequency in air	5.18	0.21	MHz
Element capacitance (top)	194	1	pF
Element capacitance (bottom)	413	5	pF
Apodization-region electrode capacitance (top)	2677	105	pF
Apodization-region electrode capacitance (bottom)	4308	14	pF
Pull-in voltage	100	3	V

a thickness tolerance of 300 nm. Because the resonance frequency in air scales linearly with the thickness [32], the observed frequency variation is well within this tolerance limit. Note that the resonance frequency in air is far from the intended center frequency of the array of 2.74 MHz. This is a predictable and well-known effect, because the acoustical loading of air is much lower than the loading from a liquid medium. The resonances reported here therefore only serve as a measure of the functionality and homogeneity of the array.

Finally, the pull-in voltage was measured to determine the operating voltage of the array. To avoid charging of the array elements during pull-in [40], the pull-in voltage was measured on test-elements made on the same wafer as the array. The pull-in voltage was found by performing impedance sweeps while increasing the dc bias voltage sequentially using a Keithley 2400 sourcemeter (Keithley Instruments Inc., Cleveland, OH, USA). The pull-in voltage was then identified as the point where the resonance peak seen in Fig. 6 was abruptly shifted to a higher frequency because of the collapse of the plates. This was done on a total of five test elements, yielding a pull-in voltage of 100 ± 3 V, as reported in Table II. It was chosen to operate the array with a dc bias voltage of 80% of the pull-in voltage and an ac amplitude of 50% of the pull-in voltage. Thus, for all subsequently described measurements, the dc bias voltage was set to 80 V (± 40 V on the two bias supplies), and the ac amplitude to 50 V.

B. Acoustical Measurements

The acoustical characterization of the array was performed with the carrier board mounted on the ICB described in Section II-C. The electronics and the array were then mounted in a poly(methyl methacrylate) (PMMA) box closed using an aluminum lid with a hole, through which there was access to the array. All measurements were performed in rapeseed oil to provide electrical insulation of the exposed electrodes on the array. The speed of sound in the oil was measured to be 1480 m/s, and the damping was 0.3 dB/MHz·cm, which is in agreement with previously reported values for vegetable oil [41]. As mentioned in the previous section, the dc bias voltage was in all measurements set to 80 V, and the amplitude of the ac signal was set to 50 V. The dc bias was provided through a TOE8842 dual dc power supply (Toellner Electronic Instrumente GmbH, Herdecke, Germany) set to ± 40 V, and the ac signals were generated using the experimental ultrasound system SARUS [38], which was also used to record all received signals. The system was set to sample at 70 MHz and to record signals down to a depth of 4 cm. Note that the four apodization-region electrodes are not included in the results presented later because they were not used as actual transmitting/receiving elements during imaging.

First, a reference measurement was made using a 2.5 MHz sinusoidal excitation with 2 and 4 cycles. Here, each individual element was excited one at a time in a tank of oil with no immediate reflecting structures. For each excitation, the signals received by all elements were recorded. This served the dual purpose of determining the crosstalk of the array and providing a noise frame reference that has been subtracted from all subsequent measurements. As listed in Table III, the nearest neighbor crosstalk level was -23.9 ± 3.7 dB. This is in agreement with previously reported values from 1-D CMUT arrays [42]. During imaging, either the rows or columns may be used as transmitters and the other part as receivers. To illustrate the crosstalk between a transmit and a receive event, the average signal on all rows when transmitting with one column at a time was determined. The same was done with the columns when one row at a time was used for transmitting. The resulting transmit-to-receive crosstalk was -40.2 ± 3.5 dB, as given in Table III.

A second setup was established to determine the pulse–echo impulse response of each element. A plane reflector (a 4.1-cm-thick PVC plastic material) was positioned 2.5 cm away from and parallel to the transducer surface. Then,

TABLE III. Transducer Acoustical Characterization Parameters.

Parameter	Mean	Std.	Unit
Center frequency in immersion	2.77	0.26	MHz
−6-dB fractional bandwidth	102	10	%
Transmit pressure peak-to-peak	590	73	kPa
Sensitivity at 2.5 MHz	0.299	0.090	μV/Pa
Nearest neighbor crosstalk level	−23.9	3.7	dB
Transmit to receive elements crosstalk level	−40.2	3.5	dB

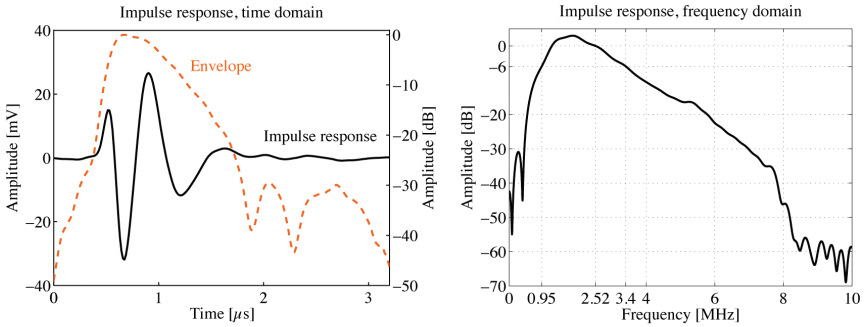

Fig. 8. (a) Pulse–echo impulse response from the center bottom electrode element (no. 96). The solid line (left axis) shows the measured voltage signal and the dashed line (right axis) shows the envelope of the measured signal given in decibels. (b) Frequency domain of the impulse response. The center frequency (2.52 MHz) and the −6-dB bandwidth relative to the center frequency (0.95 to 3.4 MHz) have been indicated.

20 realizations of random Gaussian noise was transmitted on one element at a time and received on the transmitting element. The recorded signal was cross-correlated with the excitation signal for each of the 20 realizations, and the 20 results were averaged to yield the pulse–echo impulse response of the respective element [43]. The higher the number of realizations, the closer one gets to a true white signal, so the number of realizations is a compromise between acquisition/processing time and accuracy. In Fig. 8(a), the impulse response of element number 96 (the center row element) is shown, in this case using 600 realizations of the Gaussian noise, and the corresponding spectrum is shown in Fig. 8(b). Note that the deduced impulse response describes the impulse response of the whole system consisting of transducer, front-end electronics, as well as receivers and transmit amplifiers in the SARUS system. It thereby characterizes the impulse response of the actual imaging setup, which may explain the drop in the spectrum amplitude for higher frequencies.

From the spectrum of the impulse response, the center frequency and bandwidth for each element can be found. The center frequency, f_c, was determined by summing all frequencies from 0 to half the sampling frequency, f_s, weighted by the spectrum amplitude for each frequency, S, and dividing by the sum of the spectrum amplitudes:

$$f_c = \sum_{i=0}^{N/2} [S(if_s/N) \cdot if_s/N] / \sum_{i=0}^{N/2} S(if_s/N). \quad (1)$$

This yielded a center frequency in immersion of 2.77 ± 0.26 MHz. Because the pitch of the array was 270 μm, see Table I, the pitch in units of the wavelength is thereby 0.51, which is very close to the desired pitch of $\lambda/2$. The relative −6-dB bandwidth was determined as the distance in frequency between the −6-dB points in the spectrum relative to the center frequency of the element, yielding a relative bandwidth of 102 ± 10%. The −6-dB bandwidth is illustrated for element number 96 in Fig. 8(b). Fig. 8(a) also shows the envelope of the impulse response in decibels, computed as the log-compressed absolute values of the analytic signal. The −20-dB and −40-dB pulse durations for this element are 1.23 μs and 3.06 μs, respectively, corresponding to 3.1 and 7.7 periods at its center frequency of 2.52 MHz.

A third setup was established to determine the transmit pressure of the elements. An HGL-0400 hydrophone connected to an AC-2010 preamplifier (Onda Corp., Sunnyvale, CA, USA) was placed 7 mm from the transducer surface and scanned over each element using the positioner of the intensity measurement system AIMS-3 (Onda Corp.), while transmitting a 2.5-MHz, 4-cycle sinusoidal signal on the element being measured. The recorded pressure at 7 mm was then compensated to find the pressure at the transducer surface. The compensation was found by a simulation in COMSOL Multiphysics 4.4 (COMSOL AB, Stockholm, Sweden). Here, an element with the same dimensions as the physical elements in the array was set to emit a continuous 2.5 MHz pressure wave, and the pressure magnitude at a distance of 7 mm from the element relative to the pressure magnitude at the element surface was found and used as the compensation factor (9.6). The resulting surface pressure emitted by the elements is seen in Table III to be 590 ± 73 kPa.

Subsequently, the pulse–echo signal from each element against a plane reflector (a 4.1-cm-thick PVC plastic material) set at a distance of 7 mm from and parallel to the transducer surface was measured. Once again, a 2.5-MHz 4-cycle sinusoidal excitation pulse was used. The pressure received by the element was deduced by using the pressure measured with the hydrophone setup at a distance of 7 mm from the transducer surface and compensating for the pressure drop from 7 mm to 14 mm (the return trip to the transducer surface) by using the COMSOL Multiphysics simulation described previously. This yielded a factor of 0.7, which was used to compensate for the pressure drop. Thereby, the sensitivity of each element could be found by dividing the received voltage signal with the incident pressure (0.7 times the measured pressure). The value of 0.299

$\pm$ 0.090 μV/Pa listed in Table III is the signal generated by the transducer itself; i.e., the signal has been reduced to account for the nominal 8.7 dB voltage gain supplied by the preamplifiers.

IV. Imaging

For the imaging experiments, a wire phantom consisting of a steel wire with a diameter of 0.3 mm was used. It was positioned 23 mm away from the transducer array surface and oriented approximately parallel to the rows of the array, but with a 5° to 10° angle with respect to the transducer array surface resulting from alignment inaccuracies. Both the transducer array and the wire phantom were positioned in electrically insulating rapeseed oil, as in the measurements described in the previous section. In the following, the azimuth direction is defined as being parallel to the column elements, and the elevation direction is parallel to the row elements.

To image the 3-D volume, synthetic transmit focusing with single-element emissions was used. The rows were used as transmitters and the columns as receivers. Each row element was excited with a 2-cycle sinusoidal signal, one row element at a time. The acoustical pressure was for each emission recorded on all 62 receive elements. From each measured data set, the entire 3-D volume was beamformed, creating one low-resolution image. Because of the very long elements, a standard delay-and-sum beamformer cannot easily be used to beamform data measured with a row–column-addressed array. Instead, beamforming was performed using a custom-made beamformer presented in the companion paper [31]. By summation of each beamformed low-resolution image, the final 3-D volume was created. A Hann apodization function was used both in transmit and in receive. The pulse repetition frequency was 20 Hz, the sampling rate was 70 MHz, and data were recorded until a depth of 4 cm was reached. The imaging sequence was identical for the transducer array with the integrated apodization regions both enabled and disabled. As with the previous measurements, a 50 V excitation amplitude and an 80 V dc bias were used.

Two imaging sequences were run: One with the apodization enabled, and one with the apodization disabled. In practice, the disabling of the apodization was achieved by modifying the dc bias supply on the front-end electronics, such that the dc bias voltage seen by the apodized regions of the array became zero. The electro-mechanical coupling efficiency of CMUTs is highly dependent on the dc bias [44], and removing the dc bias should therefore make the contribution from the apodized regions of the array negligible. To evaluate this, the pulse–echo sensitivity of the apodized regions before and after removal of the effective dc bias was measured by performing a pulse–echo measurement with each of the four apodization-region electrodes against a plane reflector positioned 7 mm from the transducer surface. The recorded signal with 0 V across the apodization regions was 18 dB lower than the signal with 80 V dc bias, showing that the apodization was considerably suppressed in the 0 V configuration.

The result of the two measurements is seen in Fig. 9(a) (apodization disabled) and Fig. 9(b) (apodization enabled). Both figures show a cross-section of the wire beamformed with 800 $\times$ 800 points and displayed with a dynamic range of 40 dB. Thereby, this is a measure of the line spread function (LSF) of the array, i.e., the array's ability to resolve a line source. In Fig. 9(a), where the integrated apodization is disabled, a ghost echo is clearly visible below the main echo. The maximum amplitude of this ghost echo is -22.6 dB relative to the maximum amplitude of the main echo. The lateral and axial full-widths at half-maximum (FWHM), i.e., the -6-dB resolutions, are 1.79 mm and 0.71 mm, respectively.

Fig. 9(b) shows the result with the integrated apodization enabled, and here the ghost echo is not visible within the 40 dB dynamic range. The amplitude of the signal the same distance from the main echo as the ghost echo in Fig. 9(a) is -38 dB relative to the maximum amplitude of the main echo. Thus, the apodization has reduced the amplitude of the ghost echo by 15.8 dB. The lateral and axial FWHMs here are 1.91 mm and 0.71 mm, respectively. The axial FWHM is therefore unchanged, whereas the lateral FWHM is 12% larger for the apodized measurement. However, this can be attributed to the wire being placed 1 mm further from the center of the array in the apodized measurement because of alignment imperfections. The signal-to-noise ratio (SNR) in the beamformed image was calculated using the method presented in [45, Eq. (9)], yielding an SNR of 46.9 dB.

For comparison, the LSF was simulated in Field II [46], [47] using a row–column-addressed transducer array closely emulating the real transducer array used for the measurements. The exact same imaging sequence and beamforming technique used in the measurements were used in the simulation. The impulse response estimated for element number 96, shown in Fig. 8(a), was used in the simulations. The side length of the square CMUT cells in the physical array are approximately $\lambda/8$. Each element in the simulated transducer array was therefore divided into mathematical elements with a side length of $\lambda/2$ across the element width (i.e., the entire element width) and $\lambda/8$ along the length of the element. Each mathematical element was given an apodization value of $\{0, 1/4, 1/2, 1/3, \text{or } 1\}$ dependent on whether there are 0, 1, 2, 3, or 4 CMUT cells in the real array within the region of each respective mathematical element.

To emulate a wire, 1000 point scatterers were distributed on a line from $(x, y, z) = (-3.3, -2.5, 22.5)$ mm to $(1.3, -2.5, 22.5)$ mm. The point scatterers' amplitudes were weighted by a Hann window along the length of the line. This was done to emulate the effect of a real wire object, which reflects less energy back to the array as the angle to the array is increased. Note that the wire used in the simulation (consisting of point scatterers) does not have the same thickness as the wire used in the measurements (having a diameter of 0.3 mm). Thus, the simula-

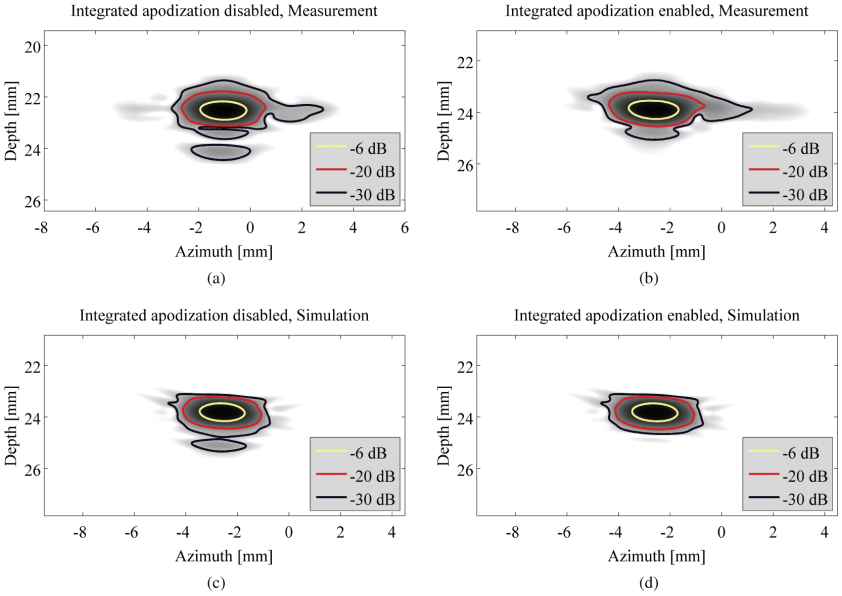

Fig. 9. Measured (a and b) and simulated (c and d) line spread function at a depth of 2.3 cm using a dynamic range of 40 dB. (a) and (c) show the result with the integrated apodization disabled, whereas (b) and (d) show the result with the integrated apodization enabled. The line spread function was acquired using a line of point scatterers in the simulation, whereas a 0.3-mm-diameter steel wire was used for the measurements. The image was beamformed using full synthetic aperture imaging with 62 single element emissions and data received by 62 receive elements for each emission. The azimuth zero-point is positioned at the center of the array.

tion is intended to give a measure of the true LSF, rather than an exact replica of the experimental result.

The result of the simulation is seen in Fig. 9(c) (without integrated apodization) and Fig. 9(d) (with integrated apodization). The lateral and axial FWHMs of the LSF for the simulated array without integrated apodization are 1.74 mm and 0.69 mm, respectively. The corresponding metrics for the LSF of the simulated array with integrated apodization are 1.76 mm and 0.69 mm. Note that, as opposed to the measurements, the wire phantom is placed in exactly the same position in the two simulations (corresponding to the position of the wire during the measurement with the integrated apodization enabled). Therefore, both the axial and lateral FWHMs are practically unchanged between the two. The ghost echo is clearly visible in the simulation of the array without integrated apodization [Fig. 9(c)], whereas the integrated apodization is seen to reduce it significantly [Fig. 9(d)]. The damping of the ghost echo in the simulations is 18.9 dB; a comparison between the experimental and simulated results is seen in Table IV. Note that the measured ghost echo damping is 3.1 dB lower than the simulated damping. This can be attributed to the fact that the response from the simulated wire is not identical to the response from the physical wire as covered previously.

In Fig. 10, a 3-D rendered image of the wire is shown. Note that the signal from the wire dies out as it crosses the borders of the array. This is partly because the transmitting elements are oriented parallel to the wire, and partly because the regions of the wire located outside the array are reflecting the received sound away from the array. The first issue could be addressed by using a phased-array technique, as proposed in Part I [31], whereas the second issue is related to the nature of the wire used, and will not be seen for a structure behaving like a collection of point scatterers. The latter effect also implies that the front of the emitted single-element plane wave is parallel to the element surface once emitted, but the smooth wire

TABLE IV. Imaging Results.

Parameter	Measurement	Simulation	Unit
Lateral FWHM, no apodization	1.79	1.74	mm
Lateral FWHM, with apodization	1.91	1.76	mm
Axial FWHM, no apodization	0.71	0.69	mm
Axial FWHM, with apodization	0.71	0.69	mm
Ghost echo damping	15.8	18.9	dB

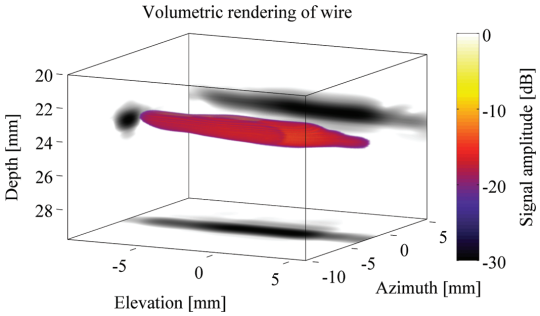

Fig. 10. 3-D beamformed image of the wire shown at a dynamic range of 30 dB. The beamformed image has been projected to the side-walls of the plot in all three dimensions using the same dynamic range. The azimuth and elevation zero-point are positioned at the center of the array.

reflects the wave as a mirror in the direction along the wire. Because the wire is not parallel to the transducer array surface, more energy is received at one end of the transducer array than the other. This is seen in Fig. 10, where the beamformed wire is not symmetric around zero in the elevation direction.

V. Conclusions

In this paper, the first experimental results of a row–column-addressed transducer array with integrated apodization were presented. A 23.6 mm by 23.6 mm 62 + 62 element capacitive micromachined ultrasonic transducer array with a center frequency in immersion of 2.77 MHz and a $\lambda/2$ element pitch was produced using cleanroom techniques in a five-mask fabrication process. The array incorporated an integrated apodization layout as presented in Part I of this paper [31]. The purpose of the integrated apodization was to reduce the ghost echoes that are otherwise prominent for row–column-addressed arrays. Custom front-end electronics were developed to enable transmission and reception on all elements, and the array was characterized using both electrical impedance measurements and acoustical measurements. Thereby, the resonance frequency in air, capacitance, pull-in voltage, impulse response, center frequency, bandwidth, transmit pressure, sensitivity, and crosstalk were determined for all elements. The array was used for volumetric imaging of a 0.3-mm-diameter steel wire placed at a depth of 23 mm, both with the integrated apodization enabled and disabled, the latter by removing the effective dc voltage over the apodized regions of the array. The integrated apodization was seen to reduce the ghost echo by 15.8 dB relative to the measurement with the integrated apodization disabled. Simulations in Field II were performed to mimic the experimental setup. The simulations reproduced the effect seen in the measurements with a ghost echo damping of 18.9 dB.

Acknowledgments

The authors thank BK Medical for producing the interconnect electronics, Daniel Bøjle (DELTA Dansk Elektronik, Lys & Akustik, Hørsholm, Denmark) for wire-bonding and glob-topping of the array, Jens Christian Jensen for producing the mechanical fixtures and boxes used in the experimental setup, and René Gadkjær for providing help with soldering during modifications of the electronics.

References

[1] R. E. Davidsen, J. A. Jensen, and S. W. Smith, "Two-dimensional random arrays for real time volumetric imaging," *Ultrason. Imaging*, vol. 16, no. 3, pp. 143–163, Jul. 1994.

[2] S. S. Brunke and G. R. Lockwood, "Broad-bandwidth radiation patterns of sparse two-dimensional vernier arrays," *IEEE Trans. Ultrason. Ferroelectr. Freq. Control*, vol. 44, no. 5, pp. 1101–1109, 1997.

[3] J. T. Yen, J. P. Steinberg, and S. W. Smith, "Sparse 2-D array design for real time rectilinear volumetric imaging," *IEEE Trans. Ultrason. Ferroelectr. Freq. Control*, vol. 47, no. 1, pp. 93–110, 2000.

[4] A. Austeng and S. Holm, "Sparse 2-D arrays for 3-D phased array imaging—Design methods," *IEEE Trans. Ultrason. Ferroelectr. Freq. Control*, vol. 49, no. 8, pp. 1073–1086, 2002.

[5] M. Karaman, I. O. Wygant, O. Oralkan, and B. T. Khuri-Yakub, "Minimally redundant 2-D array designs for 3-D medical ultrasound imaging," *IEEE Trans. Med. Imaging*, vol. 28, no. 7, pp. 1051–1061, 2009.

[6] B. Savord and R. Solomon, "Fully sampled matrix transducer for real time 3D ultrasonic imaging," in *Proc. IEEE Ultrasonics Symp.*, 2003, vol. 1, pp. 945–953.

[7] T. Halvorsrod, W. Luzi, and T. S. Lande, "A log-domain µbeamformer for medical ultrasound imaging systems," *IEEE Trans. Circuits Syst. I*, vol. 52, no. 12, pp. 2563–2575, 2005.

[8] S. Blaak, Z. Yu, G. C. M. Meijer, C. Prins, C. T. Lancee, J. G. Bosch, and N. de Jong, "Design of a micro-beamformer for a 2D piezoelectric ultrasound transducer," in *Proc. IEEE Ultrasonics Symp.*, 2009, pp. 1338–1341.

[9] C. E. Morton and G. R. Lockwood, "Theoretical assessment of a crossed electrode 2-D array for 3-D imaging," in *Proc. IEEE Ultrasonics Symp.*, 2003, pp. 968–971.

[10] C. E. M. Démoré, A. Joyce, K. Wall, and G. Lockwood, "Real-time volume imaging using a crossed electrode array," *IEEE Trans. Ultrason. Ferroelectr. Freq. Control*, vol. 56, no. 6, pp. 1252–1261, 2009.

[11] N. M. Daher and J. T. Yen, "Rectilinear 3-D ultrasound imaging using synthetic aperture techniques," in *Proc. IEEE Ultrasonics Symp.*, 2004, vol. 2, pp. 1270–1273.

[12] N. M. Daher and J. T. Yen, "2-D array for 3-D ultrasound imaging using synthetic aperture techniques," *IEEE Trans. Ultrason. Ferroelectr. Freq. Control*, vol. 53, no. 5, pp. 912–924, 2006.

[13] J. T. Yen, "Beamforming of sound from two-dimensional arrays using spatial matched filters," *J. Acoust. Soc. Am.*, vol. 134, no. 5, pp. 3697–3704, 2013.

[14] M. F. Rasmussen and J. A. Jensen, "3-D ultrasound imaging performance of a row–column-addressed 2-D array transducer: A measurement study," in *Proc. IEEE Ultrasonics Symp.*, 2013, pp. 1460–1463.

[15] C. H. Seo and J. T. Yen, "64 × 64 2-D array transducer with row–column addressing," in *Proc. IEEE Ultrasonics Symp.*, 2006, vol. 1, pp. 74–77.

[16] C. H. Seo and J. T. Yen, "256 × 256 2-D array transducer with row–column addressing for 3-D imaging," in *Proc. IEEE Ultrasonics Symp.*, 2007, pp. 2381–2384.

[17] C. H. Seo and J. T. Yen, "Recent results using a 256 × 256 2-D array transducer for 3-D rectilinear imaging," in *Proc. IEEE Ultrasonics Symp.*, 2008, vol. 1–4, pp. 1146–1149.

[18] C. H. Seo and J. T. Yen, "A 256 × 256 2-D array transducer with row–column addressing for 3-D rectilinear imaging," *IEEE Trans. Ultrason. Ferroelectr. Freq. Control*, vol. 56, no. 4, pp. 837–847, 2009.

[19] Y. Chen, M. Nguyen, and J. T. Yen, "Real-time rectilinear volumetric acquisition with a 7.5 MHz dual-layer array transducer—Data acquisition and signal processing," in *Proc. IEEE Ultrasonics Symp.*, 2011, pp. 1759–1761.
[20] J. T. Yen, C. H. Seo, S. I. Awad, and J. S. Jeong, "A dual-layer transducer array for 3-D rectilinear imaging," *IEEE Trans. Ultrason. Ferroelectr. Freq. Control*, vol. 56, no. 1, pp. 204–212, 2009.
[21] R. J. Zemp, W. Zheng, and P. Zhang, "Feasibility of top-orthogonal-to-bottom electrode (TOBE) 2D CMUT arrays for low-channel-count 3D imaging," in *Proc. IEEE Ultrasonics Symp.*, 2011, pp. 498–502.
[22] A. Sampaleanu, P. Zhang, A. Kshirsagar, W. Moussa, and R. Zemp, "Top-orthogonal-to-bottom-electrode (TOBE) CMUT arrays for 3-D ultrasound imaging," *IEEE Trans. Ultrason. Ferroelectr. Freq. Control*, vol. 61, no. 2, pp. 266–276, 2014.
[23] R. K. W. Chee, A. Sampaleanu, D. Rishi, and R. J. Zemp, "Top orthogonal to bottom electrode (TOBE) 2-D CMUT arrays for 3-D photoacoustic imaging," *IEEE Trans. Ultrason. Ferroelectr. Freq. Control*, vol. 61, no. 8, pp. 1393–1395, 2014.
[24] A. S. Logan, L. L. P. Wong, and J. T. W. Yeow, "2-D CMUT wafer bonded imaging arrays with a row–column addressing scheme," in *Proc. IEEE Ultrason. Symp.*, 2009, pp. 984–987.
[25] A. I. H. Chen, L. L. Wong, A. S. Logan, and J. T. W. Yeow, "A CMUT-based real-time volumetric ultrasound imaging system with row–column addressing," in *Proc. IEEE Ultrason. Symp.*, 2011, pp. 1755–1758.
[26] A. S. Logan, L. L. P. Wong, A. I. H. Chen, and J. T. W. Yeow, "A 32×32 element row–column-addressed capacitive micromachined ultrasonic transducer," *IEEE Trans. Ultrason. Ferroelectr. Freq. Control*, vol. 58, no. 6, pp. 1266–1271, 2011.
[27] L. L. Wong, A. I. Chen, Z. Li, A. S. Logan, and J. T. Yeow, "A row–column-addressed micromachined ultrasonic transducer array for surface scanning applications," *Ultrasonics*, vol. 54, no. 8, pp. 2072–2080, 2014.
[28] M. F. Rasmussen and J. A. Jensen, "3D ultrasound imaging performance of a row–column-addressed 2D array transducer: A simulation study," in *Proc. SPIE Medical Imaging*, 2013, art. no. 86750C.
[29] T. L. Christiansen, M. F. Rasmussen, E. V. Thomsen, and J. A. Jensen, "Ultrasound imaging transducer array with integrated apodization," in *IEEE Int. Ultrasonics Symp.*, 2014, pp. 600–603.
[30] A. W. Joyce and G. R. Lockwood, "Variably polarized ceramic for passive aperture apodization," in *Proc. IEEE Ultrasonics Symp.*, 2012, pp. 1557–1559.
[31] M. F. Rasmussen, T. L. Christiansen, E. V. Thomsen, and J. A. Jensen, "3-D imaging using row–column-addressed arrays with integrated apodization—Part I: Apodization design and line-element beamforming," *IEEE Trans. Ultrason. Ferroelectr. Freq. Control*, vol. 62, no. 5, pp. 947–958, 2015.
[32] E. Ventsel and T. Krauthammer, *Thin Plates and Shells: Theory, Analysis, and Applications*. New York, NY: Marcel Dekker, 2001.
[33] T. L. Christiansen, M. F. Rasmussen, J. A. Jensen, and E. V. Thomsen, "Row-column addressed 2-D CMUT arrays with integrated apodization," in *Proc. IEEE Ultrasonics Symp.*, 2014, pp. 600–603.
[34] Y. Huang, A. S. Ergun, E. Hæggström, M. H. Badi, and B. T. Khuri-Yakub, "Fabricating capacitive micromachined ultrasonic transducers with wafer-bonding technology," *J. Microelectromech. Syst.*, vol. 12, no. 2, pp. 128–137, 2003.
[35] P. Zhang, G. Fitzpatrick, T. Harrison, W. A. Moussa, and R. J. Zemp, "Double-SOI wafer-bonded CMUTs with improved electrical safety and minimal roughness of dielectric and electrode surfaces," *J. Microelectromech. Syst.*, vol. 21, no. 3, pp. 668–680, 2012.
[36] W. Kern, "The evolution of silicon wafer cleaning technology," *J. Electrochem. Soc.*, vol. 137, no. 6, pp. 1887–1892, 1990.
[37] T. L. Christiansen, O. Hansen, M. D. Johnsen, J. N. Lohse, J. A. Jensen, and E. V. Thomsen, "Void-free direct bonding of CMUT arrays with single crystalline plates and pull-in insulation," *Proc. IEEE Ultrasonics Symp.*, 2013, pp. 1737–1740.
[38] J. A. Jensen, H. Holten-Lund, R. T. Nilsson, M. Hansen, U. D. Larsen, R. P. Domsten, B. G. Tomov, M. B. Stuart, S. I. Nikolov, M. J. Pihl, Y. Du, J. H. Rasmussen, and M. F. Rasmussen, "SARUS: A synthetic aperture real-time ultrasound system," *IEEE Trans. Ultrason. Ferroelectr. Freq. Control*, vol. 60, no. 9, pp. 1838–1852, 2013.
[39] A. S. Savoia, G. Caliano, and M. Pappalardo, "A CMUT probe for medical ultrasonography: From microfabrication to system integration," *IEEE Trans. Ultrason. Ferroelectr. Freq. Control*, vol. 59, no. 6, pp. 1127–1138, 2012.
[40] Y. L. Huang, E. O. Hæggström, X. F. Zhuang, A. S. Ergun, and B. T. Khuri-Yakub, "A solution to the charging problems in capacitive micromachined ultrasonic transducers," *IEEE Trans. Ultrason. Ferroelectr. Freq. Control*, vol. 52, no. 4, pp. 578–580, 2005.
[41] Ö. Oralkan, A. S. Ergun, J. A. Johnson, M. Karaman, U. Demirci, K. Kaviani, T. H. Lee, and B. T. Kuri-Yakub, "Capacitive micromachined ultrasonic transducers: Next-generation arrays for acoustic imaging?" *IEEE Trans. Ultrason. Ferroelectr. Freq. Control*, vol. 49, no. 11, pp. 1596–1610, 2002.
[42] B. Bayram, M. Kupnik, C. G. Yaralioglu, Ö. Oralkan, A. S. Ergun, D.-S. Lin, S. H. Wong, and B. T. Khuri-Yakub, "Finite element modeling and experimental characterization of crosstalk in 1-D CMUT arrays," *IEEE Trans. Ultrason. Ferroelectr. Freq. Control*, vol. 54, no. 2, pp. 418–430, 2007.
[43] M. R. Schroeder, "Integrated-impulse method measuring sound decay without using impulses," *J. Acoust. Soc. Am.*, vol. 66, no. 2, pp. 497–500, 1979.
[44] G. G. Yaralioglu, A. S. Ergun, B. Bayram, E. Hæggström, and B. T. Khuri-Yakub, "Calculation and measurement of electromechanical coupling coefficient of capacitive micromachined ultrasonic transducers," *IEEE Trans. Ultrason. Ferroelectr. Freq. Control*, vol. 50, no. 4, pp. 449–456, 2003.
[45] M. F. Rasmussen and J. A. Jensen, "Comparison of 3-D synthetic aperture phased array ultrasound imaging with parallel beamforming," *IEEE Trans. Ultrason. Ferroelectr. Freq. Control*, vol. 61, no. 10, pp. 1638–1650, 2014.
[46] J. A. Jensen and N. B. Svendsen, "Calculation of pressure fields from arbitrarily shaped, apodized, and excited ultrasound transducers," *IEEE Trans. Ultrason. Ferroelectr. Freq. Control*, vol. 39, no. 2, pp. 262–267, 1992.
[47] J. A. Jensen, "Field: A program for simulating ultrasound systems," *Med. Biol. Eng. Comput.*, vol. 34, suppl. 1, pt. 1, pp. 351–353, 1996.

Thomas Lehrmann Christiansen received his B.Sc. and M.Sc. degrees with honors in engineering physics and nanotechnology from the Technical University of Denmark, Kgs. Lyngby, Denmark, in 2010 and 2012, respectively. He is presently pursuing a Ph.D. degree at the Technical University of Denmark, focusing on micromachined ultrasonic transducers for three-dimensional imaging.

He received the Oticon award in 2011 and the Danish Engineering Society's award in 2012 for his work on injection-molded microfluidic devices for automated patch-clamping. In 2014, he received the EliteForsk travel grant awarded to twenty selected Ph.D. students by the Danish Ministry of Higher Education and Science.

Morten F. Rasmussen was born in 1981. He received the B.Sc., M.Sc., and Ph.D. degree in electrical engineering from the Technical University of Denmark (DTU) in 2008, 2011, and 2014, respectively. In 2007, he spent ten months at the Technische Universität Berlin, Berlin, Germany, working on the BeeSat satellite. He is currently a postdoctoral research fellow at Stanford University. His current research interests include 3-D ultrasound imaging, synthetic aperture imaging techniques, and ultrasound neurostimulation.

Jan P. Bagge was born in 1950. He received a MSc. in electronic engineering in 1975 from the Technical University of Denmark (DTU). From 1976 to 1986, he was working in the Danish Airforce with flight control systems and fire control systems. From 1986 to 1998, he was working at Electronik Centralen with general design tasks, including a switch-mode power supply for the SILEX space project. Since 1998, he has been working for BK-Medical on the design of ultrasound

systems, with a focus area on receiver, transmitter, and low-noise circuits. He holds 2 patents on ultrasound technology.

Lars N. Moesner was born in 1964. He received his M.Sc. degree in electronics engineering from the Technical University of Denmark (DTU) in 1989 and was employed by Brüel & Kjær the same year. He started as a Technical Writer but quickly moved on to the Development Department, writing embedded software in Brüel & Kjær's ultrasound division. He continued as a hardware designer at BK Medical after Analogic Corporation's acquisition, primarily working with digital hardware and FPGA firmware. After a two-year detour to the telecom industry, he was re-employed by BK Medical in 2001 as Hardware Architect and is currently a part of BK Medical's R & D Applications and Technologies (RDAT) group.

Jørgen Arendt Jensen earned his Master of Science degree in electrical engineering in 1985 and his Ph.D. degree in 1989, both from the Technical University of Denmark. He received the Dr.Techn. degree from the same university in 1996. He has published more than 400 journal and conference papers on signal processing and medical ultrasound and the book *Estimation of Blood Velocities Using Ultrasound*, published by Cambridge University Press in 1996.

He is also developer of the Field II simulation program.

He has been a visiting scientist at Duke University, Stanford University, and the University of Illinois at Urbana-Champaign. He is currently a full professor of Biomedical Signal Processing in the Department of Electrical Engineering at the Technical University of Denmark and is head of the Center for Fast Ultrasound Imaging. He has given courses on blood velocity estimation at both Duke University and the University of Illinois and teaches biomedical signal processing and medical imaging at the Technical University of Denmark.

He has given several short courses on simulation, synthetic aperture imaging, and flow estimation at international scientific conferences. He has received several awards for his research and is an IEEE Fellow. His research is centered on simulation of ultrasound imaging, synthetic aperture imaging, vector blood flow estimation, and construction of ultrasound research systems.

Erik V. Thomsen is Professor at DTU Nanotech, the Technical University of Denmark, where he is heading the MEMS Applied Sensors group. He was born in Aarhus in 1964. He received the M.Sc. degree in physics from Odense University, Odense, Denmark, and the Ph.D. degree in electrical engineering from the Technical University of Denmark (DTU), Lyngby, in 1998. His current research and teaching interests include capacitive micromachined ultrasonic transducers, MEMS multisensors, biomedical devices and small-scale energy systems such as miniature fuel cells and energy harvesting devices. He teaches classes in solid-state electronics, microtechnology, and nano- and microfabrication. Dr. Thomsen received the AEG Electron Prize in 1995 and has also received several teaching awards at DTU.

PAPER L

Acoustical cross-talk in row-column addressed 2-D transducer arrays for ultrasound imaging

Authors: **Thomas Lehrmann Christiansen**, Jørgen Arendt Jensen, and Erik Vilain Thomsen.

Submitted to: Journal of the Acoustical Society of America, 2015

Abstract

The acoustical cross-talk in row-column addressed 2-D transducer arrays for volumetric ultrasound imaging is investigated. Experimental results from a 2.7 MHz, $\lambda/2$-pitch capacitive micromachined ultrasonic transducer (CMUT) array with 62 rows and 62 columns are presented and analyzed in the frequency-wavenumber domain. The sources of cross-talk are identified and predicted theoretically. The nearest neighbor cross-talk is -23.9 ± 3.7 dB when the array is used as a 1-D array with the rows functioning as both transmitters and receivers. In the row-column configuration, with the columns transmitting and the rows receiving, the cross-talk is reduced to -40.2 ± 3.5 dB.

Acoustical cross-talk in row-column addressed 2-D transducer arrays for ultrasound imaging

Thomas Lehrmann Christiansen[1] **and Erik Vilain Thomsen**
Department of Micro- and Nanotechnology,
Technical University of Denmark, Building 345E, DK-2800 Kgs. Lyngby, Denmark
tlehr@nanotech.dtu.dk, Erik.V.Thomsen@nanotech.dtu.dk

Jørgen Arendt Jensen
Center for Fast Ultrasound Imaging, Department of Electrical Engineering,
Technical University of Denmark, Building 349, DK-2800 Kgs. Lyngby, Denmark
jaj@elektro.dtu.dk

Running title: Cross-talk in row-column addressed transducer arrays

Abstract

The acoustical cross-talk in row-column addressed 2-D transducer arrays for volumetric ultrasound imaging is investigated. Experimental results from a 2.7 MHz, $\lambda/2$-pitch capacitive micromachined ultrasonic transducer (CMUT) array with 62 rows and 62 columns are presented and analyzed in the frequency-wavenumber domain. The sources of cross-talk are identified and predicted theoretically. The nearest neighbor cross-talk is -23.9 ± 3.7 dB when the array is used as a 1-D array with the rows functioning as both transmitters and receivers. In the row-column configuration, with the columns transmitting and the rows receiving, the cross-talk is reduced to -40.2 ± 3.5 dB.

PACS numbers: 43.38.Hz, 43.35.Pt

[1]Author to whom correspondence should be addressed.

1 Introduction

Row-column addressed 2-D transducer arrays have been shown to provide volumetric ultrasound images utilizing a significantly reduced number of connections to the array compared to 2-D matrix arrays.[1,2] The elements are addressed by their row- and column indices, effectively creating two orthogonal 1-D arrays, where typically the columns are used as transmitters and the rows as receivers or vice versa. However, the acoustical cross-talk in such arrays have so far not been investigated. This paper seeks to address this subject using experimental data from a 2.7 MHz, $\lambda/2$-pitch capacitive micromachined ultrasonic transducer (CMUT) array with 62 rows and 62 columns.

Several studies involving 1-D linear CMUT arrays for medical imaging have revealed significant acoustical cross-talk in such arrays, reporting nearest neighbor cross-talk in the order of -20 dB relative to the emitting element.[3,4] The origin of the cross-talk has been identified as being Lamb waves in the silicon substrate, interface waves, and the longitudinal waves emitted into the medium.[3–5] Of these, the by far most dominating contribution are the interface waves.[4] Using a row-column addressed CMUT array presented in detail in a previous publication,[2] it is here shown that the orthogonal arrangement of transmitter- and receiver elements in the row-column addressing scheme averages out the majority of the cross-talk, which is a previously unknown advantage of such arrays. Similar to previous investigations for 1-D CMUT arrays, the cross-talk is measured by emitting with one element and recording the signal on all receiving elements.[4] This yields data in the temporal-spatial domain, which is subsequently analyzed in the frequency domain using a 2-D Fourier transform of the data.[6]

The cross-talk cancelling effect of the row-column addressing scheme is illustrated through two experiments: In the first experiment, one row is emitting and all rows are receiving as shown in Fig. 1 (left). This mimics the configuration in a 1-D array used for 2-D B-mode imaging. In the second experiment, one column is emitting while all rows are receiving, see Fig. 1 (right). This corresponds to the row-column configuration used for volumetric imaging. It is shown that the 1-D configuration yields results consistent with previous cross-talk investigations with 1-D CMUT arrays,[4] while the row-column configuration exhibits significantly reduced cross-talk levels.

2 Dispersion relations

As briefly covered above, the acoustical cross-talk in a CMUT array is in general comprised of substrate waves, interface waves, and longitudinal waves in the medium. While the first two are dispersive waves, the latter are traveling non-dispersively at the speed of sound c in the medium. The following gives a brief presentation of the dispersion relation for the substrate waves and the interface waves.

The substrate of the CMUT is made from a silicon wafer, and the waves traveling in this may be described by Lamb wave theory. Assuming an idealized case in which the substrate is an isolated silicon plate of thickness d having infinite lateral extent, a pair of characteristic equations describe the dispersion relation of the Lamb waves[7]

$$\frac{\tan(\beta d/2)}{\tan(\alpha d/2)} = -\frac{4\alpha\beta k^2}{(k^2-\beta^2)^2} \tag{1}$$

$$\frac{\tan(\beta d/2)}{\tan(\alpha d/2)} = -\frac{(k^2-\beta^2)^2}{4\alpha\beta k^2}\ . \tag{2}$$

Here, $\alpha^2 = \omega^2/c_L^2 - k^2$ and $\beta^2 = \omega^2/c_T^2 - k^2$ where ω is the angular frequency, and k is the wave number. c_L and c_T are the longitudinal and shear wave velocities, respectively. In this work, the substrate is a (001) silicon wafer having cubic symmetry with stiffness coefficients $c_{11} = 165.64\,\mathrm{GPa}$, $c_{12} = 63.94\,\mathrm{GPa}$, and $c_{44} = 79.51\,\mathrm{GPa}$.[8] The transducer array is aligned to the wafer flat such that a Lamb wave propagating away from the emitting element travels in the [110]-direction. It follows that $c_L = \sqrt{(c_{11} + c_{12} + 2c_{44})/(2\rho)} = 9132\,\mathrm{m/s}$ and $c_T = \sqrt{c_{44}/\rho} = 5842\,\mathrm{m/s}$, where $\rho = 2330\,\mathrm{kg/m^3}$ is the mass density of silicon.[9]

Equation (1) describes the symmetric modes, S_n, whereas Eq. (2) describes the antisymmetric modes, A_n. The zeroth-order modes exist for all frequencies and have been observed in several studies of 1-D CMUT arrays.[3,4] The higher-order modes have lower cut-off frequencies at $f_c = nc_L/(2d)$ and $f_c = nc_T/(2d)$. At these frequencies, the plate resonates with infinite phase velocity and zero group velocity. Ladabaum *et al.* observed significant substrate ringing at the frequencies corresponding to longitudinal-wave resonances along the thickness of the substrate, and demonstrated that these resonances could be moved out of the transducer frequency spectrum by thinning the substrate.[10]

In addition to substrate waves and waves in the medium, evanescent waves may propagate next to the interface between the transducer and the medium. Previous studies have shown that such waves are the most significant contribution to acoustical cross-talk in 1-D CMUT arrays.[3,4] Eccardt *et al.* have provided a simple description of the dispersion relation of these waves in CMUT arrays based on the assumption of a semi-infinite homogeneous fluid interfaced by a semi-infinite solid with a given surface stiffness per area and mass per area.[5] In this framework, the pressure wave propagating in the fluid at the interface is described by $p = \exp(-\gamma z + jkx - j\omega t)$ with $\gamma > 0$ being the decay constant in the z-direction perpendicular to the surface. Denoting the speed of sound in the medium c, the wave number along the surface is given by the relation $k^2 = \gamma^2 + \omega^2/c^2$, which is found by inserting the expression for the pressure in the time-dependent wave equation for the medium, $\partial^2 p/\partial t^2 = c^2 \nabla^2 p$. The impedance of the surface wave is given by $Z_w = j\omega\rho_m/\gamma$,[5] where j is the imaginary unit and ρ_m is the mass density of the medium. A surface with a homogeneous stiffness per area s and mass per area m will have an acoustic impedance given by $Z_i = s/(j\omega) + j\omega m$. The wave travels along this surface when $Z_w = Z_i$, and thus $\gamma = j\omega\rho_m/Z_i$. It therefore follows that the phase velocity of the surface wave is

$$c_{\mathrm{phase}} = \frac{\omega}{k} = \frac{c}{\sqrt{1 - \left(\frac{\rho_m c}{Z_i}\right)^2}}\,, \tag{3}$$

from which the dispersion relation $k = \omega/c_{\mathrm{phase}}$ is readily found. Note that for an infinitely stiff surface, the interface wave propagates non-dispersively at $c_{\mathrm{phase}} = c$.

3 Experimental method

The transducer used in this work is a CMUT array with 62 rows and 62 columns. The elements have a mean center frequency of 2.7 MHz and a pitch of 270 µm. Each element consists of densely packed square CMUT cells with a side length of 60 µm and an inter-distance of 5 µm. Further details can be found in a previous publication.[2]

The transducer array is mounted and wire-bonded on a printed circuit board with each of the 124 channels connected to a research scanner system.[11] In order to drive the

cable to the scanner system, the received signals are amplified though MAX4805A pre-amplifiers (Maxim Integrated, San Jose, CA, USA) providing a nominal 8.7 dB voltage gain. All elements are kept at a constant DC voltage of 80 V. The transducer array is then mounted in a sealed box that allows it to be submerged in vegetable oil containing no reflecting structures. Vegetable oil is used to avoid short circuiting of the array, which does not have a protective coating nor lens.

In the first experiment, only the rows of the array are used in order to mimic a 1-D array. The setup is illustrated in Fig. 1 (left). The outer-most row element is actuated using a 4-cycle AC voltage signal with an amplitude of 50 V on top of the 80 V DC bias. The onset of the AC signal triggers the scanner system, which then records the voltage signal on all the rows for a duration of 54 µs. At a speed of sound in the vegetable oil of 1480 m/s, this corresponds to an imaging depth of 4 cm.

The second experiment is illustrated in Fig. 1 (right). Here, the setup is the same as in the first experiment, except that this time the outer-most column element is actuated. This therefore corresponds to the situation where the array is used in the row-column configuration with transmitting elements oriented orthogonal to receiving elements.

4 Results and discussion

The result of the two experiments are shown in Fig. 2. Both plots are normalized to the maximum value in the 1-D configuration. The black dashed line indicates the end of the transmit pulse and ring-down of the electronics at 2.8 µs which saturates the receivers on all channels. Data recorded earlier than this are therefore not included in the subsequent analysis.

In the data from the 1-D configuration (Fig. 2, left), the emitting element is located to the far left in the figure. High-velocity waves are visible in the upper right corner, but the most dominating waves occur at varying velocities and are seen to experience little damping. Also, reflections from the array edge can be seen. The nearest neighbor cross-talk in the 1-D configuration was found by repeating the measurement sequence with a new emitting row element for each sequence, yielding a mean of −23.9 dB with a standard deviation of −3.7 dB consistent with results in the literature.[3,4] The nearest neighbor cross-talk was calculated by recording the signal from the neighbor to the emitting element and normalizing it to the transmit voltage of the emitting element corrected for the insertion loss of the emitting element.

From the data acquired in the row-column configuration (Fig. 2, right), it is evident that the amplitude of the cross-talk is significantly reduced compared to the 1-D configuration. In the row-column configuration, the concept of nearest neighbor cross-talk does not make sense due to the orthogonal orientation of transmit- and receive elements. Instead, the average of the maximum signal received on each receiving element is used. Repeating the emission sequence for each of the columns and recording on all rows for each emission yields a mean cross-talk of −40.2 dB with a standard deviation of 3.5 dB.

In order to further analyze the data, a 2-D Fourier transform is performed on the data for times greater than 2.8 µs.[6] The data is multiplied with a Hann-window in both dimensions to suppress side-lobes. The resulting plots in the frequency domain are shown in Fig. 3. The maximum spatial frequency corresponds to one-half of the reciprocal pitch of the transducer array (the Nyquist frequency). The maximum temporal frequency is set to 4 MHz since no data is within the dynamic range of the plot above this frequency. The dispersion curves for the interface waves, substrate waves, and longitudinal waves in the

medium have been plotted as well using the theory presented in section 2. Calculation of the Lamb wave dispersion curves was done using the array substrate thickness of 520 µm. Only the zeroth-order modes are visible in the shown frequency range. The dispersion curve for the interface waves was calculated assuming that the whole transducer surface is covered by CMUT cells (i.e. neglecting the 5 µm wide anchoring area between the cells). The surface stiffness per area is then found as the stiffness of a single cell divided by its effective area. For a square cell with a plate thickness of $h = 2\,\mu\text{m}$ and a side-length of $2L = 60\,\mu\text{m}$, the stiffness is $s_{\text{cell}} = 771.3\,\text{GPa}h^3/L^2$ and the effective area is $a_{\text{eff}} = 1.215L^2$.[12] The mass per area of the surface is simply $m = \rho h$.

Note that both substrate waves, interface waves, and waves in the medium are clearly observed for the 1-D configuration (Fig. 3, left). The plot has been normalized to the amplitude of the interface waves, which are by far the most dominating. The non-dispersive waves in the medium are located at or more than 36 dB below the interface waves, while the number is 34 dB for the A_0 Lamb wave. The S_0 Lamb wave is not visible within the displayed dynamic range. The substrate waves and the waves in the medium are most visible in the frequency range defined by the −6 dB bandwidth of the transducer, which has its limits at 0.95 MHz and 3.4 MHz, respectively.[2]

Note that all types of waves are accurately predicted by the theory. The dispersion curve for the interface modes would follow the non-dispersive line at 1480 m/s for an infinitely stiff transducer surface.[5] Since the actual surface is comprised of small areas of solid silicon in addition to the CMUT cells, the calculated dispersion curve expectedly borders the lower part of the interface modes' spectrum.

For the row-column configuration (Fig. 3, right), the cross-talk is seen to be reduced by more than 24 dB. The plot is normalized to the 0 dB-value for the 1-D configuration to illustrate the reduction. The reason for this is the orientation of the receiving elements relative to the emitting elements. As illustrated in Fig. 1 (left), the wave front of the acoustical wave generated by the emitting element in the 1-D configuration will impinge parallel to each of the receiving elements. Thus, the whole element surface vibrates in phase, generating a strong signal. The case for the row-column configuration is seen in Fig. 1 (right). Here, the wave front from the emitting element is oriented perpendicular to the receiving elements. As the element is much longer than the wavelength of the acoustical wave, the signals generated at the actuated parts of the element will average out due to the symmetry of the wave, and ideally no signal is received. In practice, however, the finite length of the elements and the reflections and mode conversions of the waves will contribute with some net cross-talk as observed in the experiment.

5 Conclusion

This paper investigated the acoustical cross-talk in a row-column addressed CMUT array for ultrasound imaging. It was shown that when used as a 1-D array, the array exhibited a cross-talk of -23.9 ± 3.7 dB, consistent with previous results in the literature. The acoustical cross-talk was identified as Lamb waves in the substrate, interface waves, and non-dispersive waves in the medium. When used in the row-column configuration, with columns emitting and rows receiving, the cross-talk was reduced to -40.2 ± 3.5 dB due to the orthogonal orientation of the transmit- and receive elements.

Acknowledgments

The authors would like to thank Morten Fischer Rasmussen for assistance with setting up the experiment. This work is financially supported by the Danish National Advanced Technology Foundation (82-2012-4).

References and links

[1] C. H. Seo and J. T. Yen, "A 256 x 256 2-D array transducer with row-column addressing for 3-D rectilinear imaging," IEEE Trans. Ultrason., Ferroelec., Freq. Contr. **56**, 837–847 (2009).

[2] T. L. Christiansen, M. F. Rasmussen, J. P. Bagge, L. N. Moesner, J. A. Jensen, and E. V. Thomsen, "3-D Imaging using Row-Column Addressed Arrays with Integrated Apodization – Part II: Transducer Fabrication and Experimental Results," IEEE Trans. Ultrason., Ferroelec., Freq. Contr., in press (2015)

[3] X. Jin, Ö. Oralkan, F. L. Degertekin, and B. T. Khuri-Yakub, "Characterization of One-Dimensional Capacitive Micromachined Ultrasonic Immersion Transducer Arrays," IEEE Trans. Ultrason., Ferroelec., Freq. Contr. **48**, 750–760 (2001)

[4] B. Bayram, K. Kupnik, G. G. Yaralioglu, Ö. Oralkan, A. S. Ergun, D.-S. Lin, S. H. Wong, and B. T. Khuri-Yakub, "Finite Element Modeling and Experimental Characterization of Crosstalk in 1-D CMUT Arrays," IEEE Trans. Ultrason., Ferroelec., Freq. Contr., **54**, 418–430 (2007)

[5] P.-C. Eccardt, A. Lohfink, H.-G. von Garssen, "Analysis of Crosstalk between Fluid Coupled CMUT Membranes," Proc. IEEE Ultrason. Symp., 593–596 (2005)

[6] D. Alleyne and P. Cawley, "A two-dimensional Fourier transform method for the measurement of propagating multimode signals," J. Acoust. Soc. Am. **83**, 1159–1168 (1991)

[7] H. Lamb, "On Waves in an Elastic Plate," Proc. Roy. Soc. (London), Ser. A **93**, 114–128 (1917)

[8] J. Hall, "Electronic effects in the elastic constants of n-type silicon," Phys. Rev. **161**, 756–761 (1967)

[9] G. F. Miller and M. J. P. Musgrave, "On the Propagation of Elastic Waves in Aeolotropic Media. III. Media of Cubic Symmetry," Proc. Roy. Soc. (London), Ser. A **236**, 352–383 (1956)

[10] I. Ladabaum, P. Wagner, C. Zanelli, J. Mould, and G. Wojcik, "Silicon Substrate Ringing in Microfabricated Ultrasonic Transducers," Proc. IEEE Ultrason. Symp., 943–946 (2000)

[11] J. A. Jensen, H. Holten-Lund, R. T. Nilsson, M. Hansen, U. D. Larsen, R. P. Domsten, B. G. Tomov, M. B. Stuart, S. I. Nikolov, M. J. Pihl, Y. Du,

J. H. Rasmussen, and M. F. Rasmussen,"SARUS: A synthetic aperture real-time ultrasound system," IEEE Trans. Ultrason., Ferroelec., Freq. Contr. **60**, 1838–1852 (2013).

[12] M. F. la Cour, T. L. Christiansen, J. A. Jensen, and E. V. Thomsen, "Electrostatic and Small-Signal Analysis of CMUTs with Circular and Square Anisotropic Plates," IEEE Trans. Ultrason., Ferroelec., Freq. Contr., in press (2015)

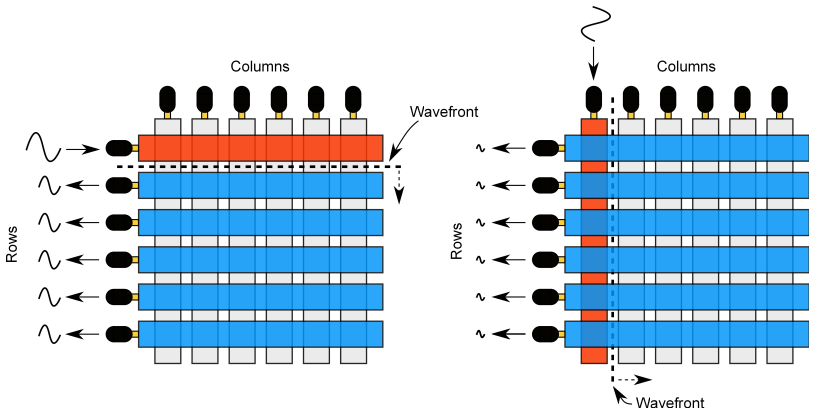

Figure 1: Illustration of the two setups used for measuring the cross-talk. In the case to the left, one row (red) is actuated, and the received signal on all rows (blue) are recorded. This corresponds to a 1-D array configuration. In the case to the right, one column is actuated, and the signals from the rows are recorded. This corresponds to the row-column configuration. The wavefront generated by the actuated element is shown with a black dashed line. The size of the sine-symbols graphically illustrates the magnitude of the signals. (Color online)

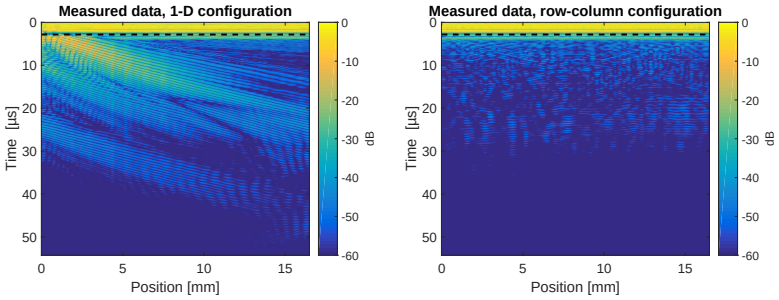

Figure 2: Data acquired using the two setups shown in Fig. 1. Time zero corresponds to the onset of the transmit pulse. The black dashed line indicates the end of the transmit pulse, and only data after this time has been included in the cross-talk analysis. (Color online)

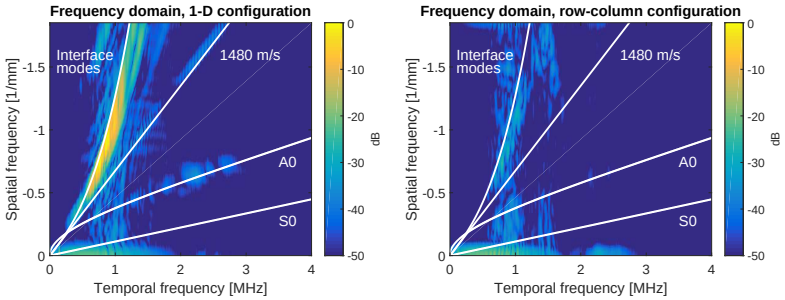

Figure 3: 2-D Fourier transforms of the data shown in Fig. 2. The data has been multiplied with a Hann-window in both the spatial and temporal dimension before the Fourier transform. The theoretically calculated dispersion curves for the interface modes, the waves in the medium, and the substrate Lamb waves are shown as white solid lines. Both plots are normalized to the maximum value in the 1-D configuration. (Color online)

PAPER M

3-D Vector Flow Estimation with Row-Column Addressed Arrays

Authors: S. Holbek, **T. L. Christiansen**, M. F. Rasmussen, M. B. Stuart, E. V. Thomsen, and J. A. Jensen.

Accepted for: IEEE Ultrason. Symp., 2015 (full abstract provided on next page)

Abstract

For real-time ultrasonic 3-D volumetric imaging and velocity estimation a 2-D array transducer is needed. The complexity associated with fabricating 2-D matrix arrays with a large number of channels have led to the development of row-column (RC) addressed transducer arrays. The number of individual connections to the array is thereby reduced from N^2 to $2N$. So far, only the imaging properties of such arrays have been investigated. It is here demonstrated that RC arrays can also be used to estimate 3-D vector flow using the Transverse Oscillation (TO) method.

Submission ID: 385
Subject Classification: MBF Blood Flow Measurement
Presentation Preference: Oral
Student Paper: Yes **Participate in the Student Paper Competition:** Yes
Invited Speaker: No
Keywords: Row-Column, Transverse Oscillation, 3-D Vector Flow

3-D Vector Flow Estimation with Row-Column Addressed Arrays

Simon Holbek[1], Thomas Lehrmann Christiansen[2], Morten Fischer Rasmussen[1], Matthias Bo Stuart[1], Erik Vilain Thomsen[2], Jørgen Arendt Jensen[1]
[1]*Department of Electrical Engineering, Technical University of Denmark, Lyngby, Denmark,* [2]*Department of Micro- and Nanotechnology, Technical University of Denmark, Lyngby, Denmark*

Background, Motivation and Objective

For real-time ultrasonic 3-D volumetric imaging and velocity estimation a 2-D array transducer is needed. The complexity associated with fabricating 2-D matrix arrays with a large number of channels have led to the development of row-column (RC) addressed transducer arrays. The number of individual connections to the array is thereby reduced from N^2 to 2N. So far, only the imaging properties of such arrays have been investigated. It is here demonstrated that RC arrays can also be used to estimate 3-D vector flow using the Transverse Oscillation (TO) method.

Statement of Contribution/Methods

A 3 MHz, λ/2 pitch 2-D array with 64 rows and 64 columns was simulated in Field II. Velocities were estimated from a simulated cylendrical blood vessel (Ø = 12 mm) located at 3 cm depth with parabolic flow, a peak velocity of 1 m/s and a 90 degree beam-to-flow angle. To obtain RF data for estimation of all three velocity components, the emission sequence was alternating between emitting on the rows and recieving on the columns and vice versa. At a PRF of 3.2 kHz, 2x32 focused emissions were emitted one line at a time to sweep across 11 different directions within a plane perpendicular to the vessel, see Fig 1. Beamformation was performed with an in-house-developed RC-beamformer, and velocities were estimated by using the TO method. Estimates from 10 frames were scan converted, interpolated, and averaged to get the mean 3-D vector flow estimate.

Results/Discussion

A colormap of the estimated 3-D vector flow is seen in Fig. 2. Projections of the mean velocity component along the flow direction (v_x) are illustrated as shadowed areas, the standard deviations as dashed lines and the expected values as red lines. On the right side the velocity profile for a line through the center of the vessel in the *z*-direction is shown, and the left side shows the corresponding velocity profile in the *y*-direction. Relative mean bias for the velocities through the center of the vessel in the z-direction was (-8.6%, -0.6%, -0.1%) for (v_x, v_y, v_z) respectively. Peak velocity found from the 3-D vector flow image was 1.02 m/s which was 2% higher than expected. The results shows for the first time, that 3-D vector flow can be estimated with RC-arrays, despite their reduced number of channels.

Simulation Setup

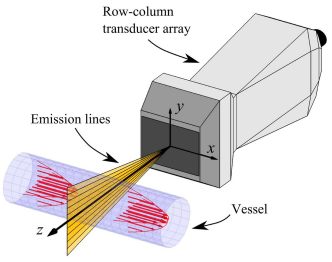

Fig. 1

3-D Vector Flow

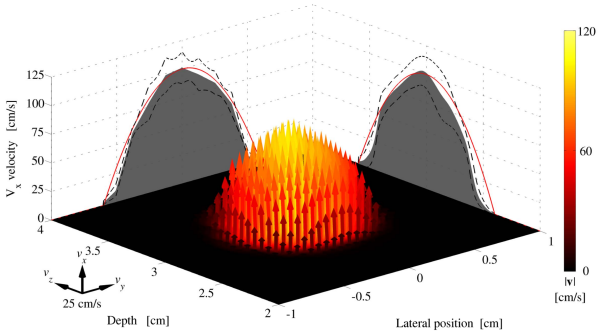

Fig. 2

PAPER N

A Row-Column Addressed CMUT Probe with Integrated Electronics for Volumetric Imaging

Authors: **Thomas Lehrmann Christiansen**, Mathias Engholm, Christopher Beers, Michael Berkheimer, Lars Nordahl Moesner, Jan Peter Bagge, Matthias Bo Stuart, Anders Lei, Søren Elmin Diederichsen, Jørgen Arendt Jensen, Erik Vilain Thomsen

Accepted for: IEEE Ultrason. Symp., 2015 (full abstract provided on next page)

Abstract

The number of transmit and receive channels needed to perform real-time 3-D ultrasonic imaging can be greatly reduced if row-column addressed 2-D transducer arrays are used. So far, a fully assembled hand-held row-column probe for volumetric imaging has not been demonstrated. This contribution presents results from the development of such a probe. The probe is designed to be used on a commercial bk3000 scanner from BK Medical (Herlev, Denmark).

Submission ID: 136
Subject Classification: TMU Micromachined Ultrasonic Transducers
Presentation Preference: Oral
Student Paper: Yes **Participate in the Student Paper Competition:** Yes
Invited Speaker: No
Keywords: Row-column, CMUT, Ultrasound probe

A Row-Column Addressed CMUT Probe with Integrated Electronics for Volumetric Imaging

Thomas Lehrmann Christiansen[1], **Mathias Engholm[1]**, Christopher Beers[2], Michael Berkheimer[2], Lars Nordahl Moesner[3], Jan Peter Bagge[3], Matthias Bo Stuart[4], Anders Lei[1], Søren Elmin Diederichsen[1], Jørgen Arendt Jensen[4], Erik Vilain Thomsen[1]
[1]Department of Micro- and Nanotechnology, Technical University of Denmark, Kgs. Lyngby, Denmark, [2]Sound Technology, State College, PA, USA, [3]BK Medical, Herlev, Denmark, [4]Center for Fast Ultrasound Imaging, Department of Electrical Engineering, Technical University of Denmark, Kgs. Lyngby, Denmark

Background, Motivation and Objective

The number of transmit and receive channels needed to perform real-time 3-D ultrasound imaging can be greatly reduced if row-column addressed 2-D transducer arrays are used. So far, a fully assembled hand-held row-column probe for volumetric imaging has not been demonstrated.

This work presents results from the development of such a probe. The probe is designed to be used on a commercial bk3000 scanner from BK Medical (Herlev, Denmark).

Statement of Contribution/Methods

A 3 MHz, λ/2-pitch 62+62 channel row-column addressed 2-D capacitive micromachined ultrasonic transducer (CMUT) array with a footprint of 26 mm x 26 mm is fabricated using a LOCOS (LOCal Oxidation of Silicon) process with 4 lithography steps. The array employs integrated apodization to avoid ghost echoes in the image. It is mounted and wire-bonded on a flexible printed circuit board (PCB), which is connected to two rigid PCBs with pre-amplifiers for driving the cable to the scanner. The array and PCBs are encapsulated in a 3-D printed handle, and a grounded shielding layer and silicone coating is applied to the front-side of the array for physical and electrical isolation. The handle is assembled together with a 128-channel coaxial cable that connects it to the ultrasound scanner, which supplies the probe with a 190 V DC bias voltage and an AC excitation voltage of 150 V_{pp}. The electronics are designed to allow all elements to be used interchangeably as either transmitters or receivers.

Results/Discussion

The image shows the probe components before assembly. The array is seen on the flexible PCB, which connects to the in-handle electronics PCBs driving the cable to the scanner. The probe handle itself is composed of three parts. The square acoustic window for the transducer array is seen in the nose piece, which is to be sealed off with a grounded shielding layer and a silicone coating. The shielding layer is measured to give a noise performance equivalent to a commercial 8812 transducer (BK Medical, Herlev, Denmark). The array elements are measured prior to mounting and exhibit stable performance with no significant change in resonance frequency or coupling coefficient over 10 hours of continuous use.

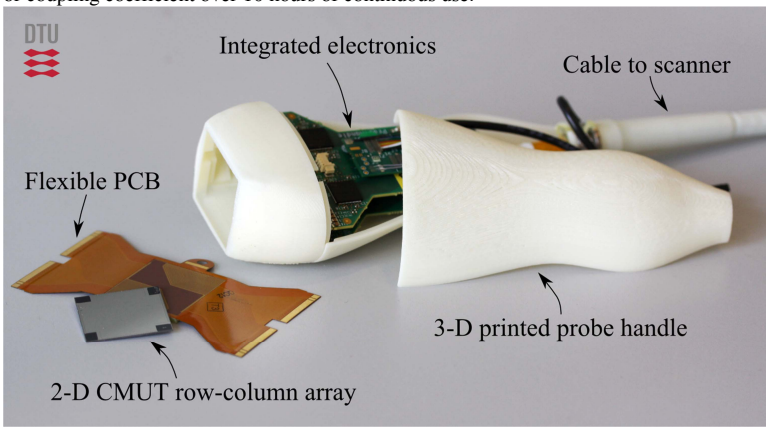

Patent Applications

PATENT APPLICATION A

Ultrasound Imaging Transducer Array with Integrated Apodization

Authors: Thomas Lehrmann Christiansen, Morten Fischer Rasmussen, Erik Vilain Thomsen, and Jørgen Arendt Jensen.

Filed on: December 19, 2013.
International patent number: PCT/IB2013/002838.
Analogic patent number: ANA1219-WO (BKM-10-7578-PCT).

Abstract

A transducer array (802) includes at least one 1D array of transducing elements (804). The at least one 1D array of transducing elements includes a plurality of transducing elements (904). A first of the plurality of transducing elements has a first apodization and a second of the plurality of transducing elements has a second apodization. The first apodization and the second apodization are different. The transducer array further includes at least one electrically conductive element (910) in electrical communication with each of the plurality of transducing elements. The transducer array further includes at least one electrical contact (906) in electrical communication with the at least one electrically conductive element. The at least one electrical contact concurrently addresses the plurality of transducing elements through the at least one electrically conductive element.

ULTRASOUND IMAGING TRANSDUCER ARRAY WITH INTEGRATED APODIZATION

TECHNICAL FIELD

The following generally relates to a transducer array and more particularly to an ultrasound imaging transducer array with integrated apodization.

BACKGROUND

Ultrasound imaging has been used to determine information about the interior characteristics of an object or a subject. Generally, an ultrasound imaging system includes a transducer array and components for at least generating and transmitting ultrasound waves, receiving echoes or reflected waves, processing the received signal, generating images, and displaying the images. The transducer array may include a one-dimensional (1D) array of elements or a two-dimensional (2D) transducer array of elements.

For three dimensional (3D) imaging with a 2D transducer array, the elements can be addressed element-wise where each element is individually addressed. Alternatively, the elements can be addressed group-wise, e.g., using row-column addressing. In a configuration in which each element is individually addressed, an NxN array of elements would require NxN (or N^2) electrical connections and channels to fully address the array. With row-column addressing, an NxN array of elements can be operated using 2N electrical connections and channels to fully address the array.

As such, the row-column addressing approach can simplify fabrication of the transducer array, for example, due to the reduced number of electrical interconnects to the transducer array (e.g., from NxN to 2N). Furthermore, the data bandwidth requirements are also reduced. Unfortunately, the row-column addressing approach may introduce ghost artifact in the images, for example, because of the significant element height, the lack of an acoustic lens, and the lack of electronic control along the length of the row/column elements.

A non-limiting example of row-column addressing of a 2D transducer array 100 is shown in Figures 1 and 2. In Figure 1, each 1D array 102, 104, and 106 of elements (three elements in the illustrated embodiment) in a first direction (y in the illustrated embodiment)

respectively is excited with a single pulse 108, 110, and 112 in transmit. In Figure 2, a single signal 202, 204, and 206 respectively is produced for each 1D array 208, 210, and 212 of elements (three elements in the illustrated embodiment) in a second different direction (x in the illustrated embodiment, where x is transverse to y) in receive.

Figures 3, 4, 5, 6, and 7 provide an example of ghost artifact originating during both receive and transmit in connection with the 1D arrays 208-212 of Figure 2. For sake of brevity, this example is described with respect to the array 208 in receive. However, the same edge effect arises in transmit due to the receive/transmit reciprocity of the sound field. In Figure 3, when an emitted waveform is reflected by a point scatterer 304, the reflected wave will have the shape of a sphere 300. At a first time 306 thereafter, the reflected spherical wave 300 intersects only a first subset 308 of elements of the array 208 of the 1D array. Figure 4 shows the response 402 of the 1D array and the corresponding output signal 404, which is a sum of the measured signals, which are approximately in phase, producing a strong output signal.

Returning to Figure 3, subsequently, at time 310, the reflected wave 300 intersects with a second subset 312 of elements of the array 208. Where the amplitude of the transmit waveform is symmetric around zero, which it typically is in at least medical ultrasound, the integration of the output is close to zero. Figure 5 shows the response 502 of the array 208 and the corresponding output signal 504 at time 310. Returning to Figure 3, subsequently, at time 314, the reflected wave crosses edges 316. Figure 6 shows the response 602 of the array 208 and the corresponding output signal 604 at time 314.

From the above, during receive, a point scatterer will receive three pressure waves: one main wave and one from each edge of the 1D array. Each of these three waves is reflected and each generates three signals during receive: One main, and one at each edge of the 1D array. Thus, a total of nine signals are generated from one point scatterer. However, only one of these is of interest (the main echo, i.e. the shortest distance from the array to the point scatterer). The remaining eight echoes are artifacts that, in general, are seen as ghosts (three pairs and two single).

Where the point scatterer is located directly above the center of the 1D array (the scenario shown in FIGURE 3), the number of ghosts collapses to two (each containing four of

the eight artifacts). This is shown in Figure 7, which shows a main wave 702, and two ghost waves 704 and 706. In the example shown in Figure 3-7, row-column addressing results in a main lobe at the center at 0 dB, and, beneath it, two ghosts as a result of edge effects on the long row and column elements. Unfortunately, the ghosts introduce artifact, degrading image quality.

SUMMARY

Aspects of the application address the above matters, and others.

In one aspect, a transducer array includes at least one 1D array of transducing elements. The at least one 1D array of transducing elements includes a plurality of transducing elements. A first of the plurality of transducing elements has a first apodization and a second of the plurality of transducing elements has a second apodization. The first apodization and the second apodization are different. The transducer array further includes at least one electrically conductive element in electrical communication with each of the plurality of transducing elements. The transducer array further includes at least one electrical contact in electrical communication with the at least one electrically conductive element. The at least one electrical contact concurrently addresses the plurality of transducing elements through the at least one electrically conductive element.

In another aspect, a method includes transmitting an ultrasound waveform with a transducer array that includes apodization that is integrated into physical elements of the transducer array. The method further includes receiving a reflected wave with the transducer array. The method further includes processing the received reflected wave to generate at least one image.

In another aspect, an ultrasound imaging system includes a transducer array with an array-wise addressable array of elements that includes at least two elements with a different apodization. The apodization is one of a fixed area controlled apodization, a dynamic area controlled apodization, a fixed bias controlled apodization, or a dynamic bias controlled apodization. The ultrasound imaging system further includes transmit circuitry that conveys an excitation pulse to the transducer array. The ultrasound imaging system further includes receive circuitry that receives a signal indicative of an ultrasound echo from the transducer

array. The ultrasound imaging system further includes a beamformer that processes the received signal, generating ultrasound image data.

Those skilled in the art will recognize still other aspects of the present application upon reading and understanding the attached description.

BRIEF DESCRIPTION OF THE DRAWINGS

The application is illustrated by way of example and not limited by the figures of the accompanying drawings, in which like references indicate similar elements and in which:

Figure 1 schematically illustrates prior art row or column addressing for transmit or receive in connection with a 2D transducer array;

Figure 2 schematically illustrates prior art column or row addressing for receive or transmit in connection with a 2D transducer array;

Figure 3 schematically illustrates prior art interaction of a wave reflected by a point scatterer with a 1D array of a 2D transducer array at three different points in time;

Figure 4 graphically illustrates a prior art response and output of the 1D array of Figure 3 at a first of the three points in time;

Figure 5 graphically illustrates a prior art response and output of the 1D array of Figure 3 at a second of the three points in time;

Figure 6 graphically illustrates a prior art response and output of the 1D array of Figure 3 at a third of the three points in time;

Figure 7 graphically illustrates a main lobe and ghost lobes in connection with the prior art row-column addressing of Figures 1-6;

Figure 8 schematically illustrates an example ultrasound imaging system with a transducer array with integrated apodization;

Figure 9 schematically illustrates an example of fixed area controlled apodization in connection with rectangular piezoelectric elements;

Figure 10 schematically illustrates an example of fixed area controlled apodization in connection with rectangular and triangular piezoelectric elements;

Figure 11 schematically illustrates an example of dynamic area controlled apodization in connection with a piezoelectric 2D transducer array;

Figure 12 schematically illustrates an example of a CMUT 2D transducer array.

Figure 13 schematically illustrates an example of fixed area controlled apodization in connection with a CMUT 2D transducer array;

Figure 14 schematically illustrates an example of dynamic area controlled apodization in connection with a CMUT 2D transducer array;

Figure 15 schematically illustrates an example of bias controlled apodization in connection with a CMUT 2D transducer array;

Figure 16 schematically illustrates an example of area apodization with nine apodization levels that are set as a rotationally symmetric 2D Hann window;

Figure 17 schematically illustrates an example mask layout for the apodization of Figure 16;

Figure 18 illustrates an example of integrated fixed area apodization enabling homogeneous rectilinear imaging with optional beam steering;

Figure 19 graphically illustrates a main lobe in connection with the row-column addressing of Figures 8 and 17;

Figure 20 illustrates a method in accordance with the embodiments discussed herein; and

Figure 21 illustrates an example mask layout for a CMUT using the apodization described in connection with Figure 18.

DETAILED DESCRIPTION

Figure 8 schematically illustrates an example ultrasound imaging system 800.

The ultrasound imaging system 800 includes a transducer array 802 that includes at least one 1D array of transducing elements 804. The at least one 1D array of transducing elements 804 is configured to transmit ultrasound signals when in transmit mode and receive echoes, reflected waveforms, etc. when in receive mode. In one non-limiting instance, the at least one 1D array of transducing elements 804 includes a 2D array of two or more 1D arrays. An example 2D array includes a 16x16 array, a 32x32 array, a 64x64 array, a larger array, or a smaller array. In another embodiment, the at least one 1D array of transducer elements 804 includes a non-square array such as rectangular, circular array, and/or other shaped arrays. In

yet another instance, the array of transducing elements 804 includes only a single 1D array of transducing elements.

As described in greater detail below, the at least one 1D array of transducer elements 804 includes integrated apodization, or apodization that is integrated in and part of the physical transducing elements themselves. In one instance, the integrated apodization, e.g., weights end or peripheral regions of each 1D array of transducing elements lower than other regions (e.g., more central regions) of the at least one 1D array of transducer elements 804. This may reduce or mitigate the artifacts such as the ghost artifacts such as from the edges of a transducer array as discussed in connection with Figures 3-7 and/or other artifacts. Examples of such apodization include, but are not limited to, area (fixed and dynamic) and/or voltage bias (fixed and dynamic) controlled apodization. These approaches can be used with different types of transducing elements such as piezoelectric, capacitive micro machined ultrasonic transducer (CMUT), and/or other transducing elements.

Transmit circuitry 806 generates pulses that excite a predetermined set of addressed 1D arrays of the at least one 1D array of transducer elements 804 to emit one or more ultrasound beams or waves into a scan field of view. Receive circuitry 808 receives echoes or reflected waves, which are generated in response to the transmitted ultrasound beam or wave interacting with (stationary and/or flowing) structure in the scan field of view, from a predetermined set of addressed arrays of the at least one 1D array of transducer elements 804. A switch 810 switches between the transmit circuitry 806 and the receive circuitry 808, depending on whether the transducer array 802 is being operated in transmit or receive mode. In transmit mode, the switch 810 electrically connects the transmit circuitry 806 to the at least one 1D array of transducer elements 804. In receive mode, the switch 810 electrically connects the receive circuitry 808 to the at least one 1D array of transducer elements 804.

A beamformer 812 processes the received echoes, for example, by applying time delays and weights, summing, and/or otherwise processing the received echoes. In one non-limiting instance, the beamformer 812 includes a single sub-beamformer for each of the at least one 1D array of transducer elements 804. In another instance, more than a single sub-beamformer can be used with a 1D array and/or a single sub-beamformer can be used two more of the 1D arrays. A scan converter 814 scan converts the beamformed data, converting

the beamformed data (e.g., images) into the coordinate system of a display 816, which visually displays the data. In one instance, the data is visually displayed in an interactive graphical user interface (GUI), which allows the user to selectively rotate, scale, and/or manipulate the displayed data through a mouse, a keyboard, touch-screen controls, etc.

A controller 818 controls one or more of the components of the system 800 such as at least one of the transmit circuitry 806 or receive circuitry 806, the switch 810 based on whether the at least one 1D array of transducer elements 804 is transmitting or receiving, etc. Such control can be based on available modes of operation (e.g., B-mode, C-mode, Doppler, etc.) of the system 800. A user interface 820 includes include one or more input devices (e.g., a button, a knob, a slider, a touch pad, etc.) and/or one or more output devices (e.g., a display screen, lights, a speaker, etc.). A particular mode, scanning, and/or other function can be activated by one or more signals indicative of input from the user interface 820. The user interface 820 can also be used to set and/or change parameters such as imaging parameters, processing parameters, display parameters, etc.

In one instance, the transducer array 802 is part of a probe and the transmit circuitry 806, the receive circuitry 808, the switch 810, the beamformer 812, the scan converter 814, the controller 818, the user interface 820, and the display 816 are part of a console. Communication there between can be through a wired (e.g., a cable and electro-mechanical interfaces) and/or wireless communication channel. In this instance, console can be similar to a portable computer such as a laptop, a notebook, etc., with additional hardware and/or software for ultrasound imaging. The console can be docked to a docketing station and used.

Alternatively, the console can be part (fixed or removable) of a mobile or portable cart system with wheels, casters, rollers, or the like, which can be moved around. In this instance, the display 816 may be separate from the console and connected thereto through a wired and/or wireless communication channel. Where the cart includes a docking interface, the laptop or notebook computer type console can be interfaced with the cart and used. An example of a cart system where the console can be selectively installed and removed is described in US publication 2011/0118562 A1, entitled “Portable ultrasound scanner,” and filed on November 17, 2009, which is incorporated herein in its entirety by reference.

Alternatively, the transducer 802, the transmit circuitry 806, the receive circuitry 808, the switch 810, the beamformer 812, the scan converter 814, the controller 818, the user interface 820, and the display 816 are all housed and enclosed within a hand-held ultrasound apparatus, with a housing that mechanically supports and/or shields the components within. In this instance, the transducer 802 and/or display 816 are also part of the housing, being structurally integrated or part of a surface or end of the hand-held ultrasound apparatus. An example of a hand-held device is described in US patent 7,699,776, entitled "Intuitive Ultrasonic Imaging System and Related Method Thereof," and filed on March 6, 2003, which is incorporated herein in its entirety by reference.

As briefly discussed above, the at least one 1D array of transducer elements 804 includes integrated apodization, including, but not limited to, fixed area controlled apodization, dynamic area controlled apodization, fixed bias controlled apodization, and dynamic bias controlled apodization. Non-limiting examples of each of these are discussed below.

Figures 9, 10, and 11 show examples of area controlled apodization where the transducer array 802 includes a piezoelectric transducer array. Figure 9 illustrates fixed area controlled apodization where the elements include rectangular elements. Figure 10 illustrates fixed area controlled apodization where the elements include rectangular and non-rectangular elements. Figure 11 illustrates dynamic area controlled apodization. Generally, area-controlled apodization refers to apodization that is based on a physical area of a transducing surface of each element of each of the at least one 1D array of transducer elements 804. With area controller apodization, the transmit pressure and the signal generated during receive for each transducing element scale with the physical surface area of the transducing element.

For sake of clarity and explanatory purposes, a first direction 900 of the array 802 is referred to herein as a row, and a second direction 902 of the array 802 is referred to herein as a column, and the first direction is considered the transmit direction, and the second direction is considered the receive direction. However, the directions 900 and 902 respectively can alternatively refer to the column and the row and/or receive and transmit. In general, the first direction 900 and the second direction 902 are different directions, approximately

perpendicular, as shown in Figure 9, or otherwise angularly offset. Furthermore, transmit and/or receive can be performed in more than one direction.

Initially referring to Figure 9, the transducer array 802 includes NxM transducing elements 904 (or elements $904_{1,1}$, …, $904_{N,M}$, where N and M are positive integers). In one instance, N = M. In another instance, N ≠ M. The transducer array 802 further includes N electrical contacts 906_1, …, 906_N, and M electrical contacts 908_1, …, 908_M.

The array 902 further includes an electrically conductive element 910_1 that electrically connects the electrical contact 906_1 to each of the elements $904_{1,1}$, …, $904_{1,M}$, forming a row line element 912_1. Likewise, electrically conductive elements 910_2, 910_3, 910_4, ….910_N, respectively electrically connect the electrical contacts 906_2, 906_3, 906_4, ….906_N to the elements $904_{2,1}$, …, $904_{2,M}$, $904_{3,1}$, …, $904_{3,M}$, $904_{4,1}$, …, $904_{4,M}$, … $904_{N,1}$, …, $904_{N,M}$, forming row line elements 912_2, 912_3, 912_4, …, 912_N.

Each of the row line element 912_1, 912_2, 912_3, 912_4, …, 912_N is addressed via the corresponding electrically conductive element 906_1, 906_2, 906_3, 906_4, ….906_N. For example, an excitation signal at the electrically conductive element 906_1 excites the entire row line element 912_1, or the elements $904_{1,1}$, …, $904_{1,M}$, …, an excitation signal at the electrically conductive element 906_N excites the entire row line element 912_N, or the elements $904_{N,1}$, …, $904_{N,M}$. In another example, receiving a signal from the electrically conductive element 906_1 receives signals from the entire row line element 912_1, or the elements $904_{1,1}$, …, $904_{1,M}$, …, receiving a signal from the electrically conductive element 906_N receives signals from the entire row line element 912_N, or the elements $904_{N,1}$, …, $904_{N,M}$.

The array 902 further includes an electrically conductive element 914_1 that electrically connects the electrical contact 908_1 to each of the elements $904_{1,1}$, …, $904_{N,1}$, forming a column line element 916_1. Likewise, electrically conductive elements 914_2, 914_3, 914_4, ….914_M, respectively electrically connect the electrical contacts 908_2, 908_3, 908_4, ….908_N to the elements $904_{2,1}$, …, $904_{2,M}$, $904_{3,1}$, …, $904_{3,M}$, $904_{4,1}$, …, $904_{4,M}$, … $904_{N,1}$, …, $904_{N,M}$, forming column line elements 916_2, 916_3, 916_4, …, 916_N.

Each of the column line element 916_1, 916_2, 916_3, 916_4, …, 916_M is addressed via the corresponding electrically conductive element 908_1, 908_2, 908_3, 908_4, ….908_M. For example, an excitation signal at the electrically conductive element 908_1 excites the entire column line

element 916_1, or the elements $904_{1,1}$, …, $904_{N,1}$, …, an excitation signal at the electrically conductive element 908_M excites the entire column line element 916_M, or the elements $904_{1,M}$, …, $904_{N,M}$. In another example, receiving a signal from the electrically conductive element 908_1 reads signal from the entire column line element 916_1, or the elements $904_{1,1}$, …, $904_{N,1}$, …, receiving a signal from the electrically conductive element 908_M reads signals from the entire column line element 916_M, or the elements $904_{1,M}$, …, $904_{N,M}$.

A first group 918 of elements at a central region of the array 802 each have a first area A_1 (W_1*L_1). A second group 920 of sub-elements (which excludes the first group 918) disposed along a perimeter or periphery of the array 802 each have a second area A_2 (W_2*L_2). A third group of sub-elements 922 disposed at the corners of the array 802 each have a third area A_3 (W_3*L_3). However, this configuration is not limiting. For example, in another embodiment, there may be more or less groups and/or different groups. Furthermore, in Figure 9, the elements for all three of the groups 918, 920 and 922 is rectangular or square, and, in another embodiment, at least one of the sub-elements is otherwise shaped, such as circular, elliptical, triangular, hexagonal, etc.

In the illustrated embodiment, $W_1 > W_2 \approx W_3$ and $L_1 \approx L_2 > L_3$, However, this configuration is not limiting. Generally, the width (W) and length (L) of each element is such that $A_1 > A_2 >, A_3$. The pressure output (the transmitted pressure), transmitted in response to an excitation signal (e.g., a voltage pulse) of an element with an area A (or W*L) is P. As such, the pressure output, due to excitation signal, of the elements of the first group 918, which have an area A_1, is P_1. The pressure output, due to excitation signal, of the elements of the second group 920, which have an area A_2, is P_2, where $P_2 = \alpha P_1$, where $\alpha = A_2/A_1$. The pressure output, due to excitation signal, of the elements of the third group, which have an area A_3, is P_3, where $P_3 = \beta P_1$, where $\beta = A_3/A_1$.

The signal output, generated by an element in response to an incident acoustical wave impinging thereon, for an element with an area A is S. As such, the signal output, due to an impinging acoustical wave, of the elements of the first group 918, which have an area A_1, is S_1. The signal output, due to an impinging acoustical wave, of the elements of the second group 920, which have an area A_2, is S_2, where $S_2 = \alpha S_1$, where $\alpha = A_2/A_1$. The signal output,

due to an impinging acoustical wave, of the elements of the third group 922, which have an area A_3, is S_3, where $S_3 = \beta S_1$, where $\beta = A_3/A_1$.

With this configuration, the transmit pressure and/or the signal generated during transmit and receive scale with the transducing area of each element. In the illustrated embodiment, the scaling scales down the transmit pressure and the signal generated during receive going from the first group 918, to the second group 920, to the third group 922 of elements. Thus, a particular row line element or column line element includes fixed discrete area controlled apodization. Such apodization effectively down weights the output pressure transmitted by (during transmit) and the electrical signal generated by (during receive) at the ends of each row and/or column line element, mitigating or reducing ghost artifact introduced by the edge elements.

The configuration shown in Figure 9, can be formed by through dicing, screen-printing (where the layout of each cell is defined by a mask), and/or other approach. Dicing is well suited for creating the rectangular sub-elements shown in Figure 9. As the resonance frequency of piezo-elements is given by the height, the area can be freely adjusted without altering the operating frequency of each sub-element. This configuration allows for varying the transmitted/received signal of a single line element. For transmit, the amplitude of the excitation pulses need not be varied, so a fixed excitation pulse waveform at a single amplitude can be used. Only phase control is required to allow focusing and steering of the beam.

Figure 10 schematically illustrates a variation of the transducer array 802 in Figure 9 in which the geometry of the second group 920 of elements is not rectangular, and the apodization linearly scales (rather than discretely scales) the output pressure transmitted by (during transmit) and the electrical signal generated by (during receive) of the elements of the periphery. This is achieved in this example through a triangular geometry of the second group 920 of elements in which the apodization decreases in a direction towards the periphery. Again, other geometries, such as hexagonal, irregular, circular, etc. are also contemplated herein. Screen-printing is well suited for such shapes. The configuration of Figure 10 also does not include the third group 922, or corner elements $904_{1,1}$, $904_{N,1}$, $904_{1,M}$, and $904_{N,M}$. In another variation, the apodization can scale in a non-linear manner, for

example, where the geometry of the outer sub-elements in a non-linear. Furthermore, the first group 916 can also have non-linear geometries.

Figure 11 shows an example of dynamic area controlled apodization for a single one of the elements 904 of the transducer array 802. In Figure 11, the single element 904 includes a 3x3 arrangement of piezo sub-elements 1102, including a first row 1104_1 of sub-elements 1102, a second row 1104_2 of sub-elements 1102, and a third row 1104_3 of sub-elements 1102, each row including three sub-elements 1102, and a first column 1106_1 of sub-elements 1102, a second column 1106_2 of sub-elements 1102, and a third column 1106_3 of sub-elements 1102, each column including three sub-elements 1102.

A row electrode 1108 is in electrical communication with the sub-elements 1102 of the second row 1104_2. A first plurality of switches 1110 and 1112 respectively selectively electrically connect the sub-elements 1102 of the first row 1104_1 and the sub-elements 1102 of the third row 1104_3 to the row electrode 1108. As such, the area of the illustrated element 904 can be dynamically changed, row-wise, between three different discrete area levels. The levels include: only the second row 1104_2; the second row 1104_2 and either the first row 1104_1 or the third row 1104_3, and all three rows.

A column electrode 1114 is in electrical communication with the sub-elements 1102 of the second column 1106_2. A second plurality of switches 1116 and 1118 respectively selectively electrically connect the sub-elements 1102 of the first column 1106_1 and the sub-elements 1102 of the third column 1106_3 to the column electrode 1114. As such, the area of the illustrated element 904 can be dynamically changed, column-wise, between three different discrete area levels. The levels include: only the second row 1106_2; the second row 1106_2 and either the first row 1106_1 or the third row 1106_3, and all three rows.

Combining the switching of the rows and columns, the area of the illustrated element 904 can be dynamically changed between nine different discrete area levels. This includes only the central sub-elements 1102 up to all of the sub-elements 1102.

Generally, if the number of enabled switches in row i is denoted k_i and the number of enabled switches in column j is denoted k_j, the area apodization A of element (i; j) is A(i; j) = k_i x kj. Any separable 2-D function can be implemented as an apodization function. The number of switches per row or column for k x k cells per element can in principle be reduced

to 2k - 2, as this – together with the possibility of not reading out the signal from a row or column – allows any number of cells in a given element to be active.

Figures 12, 13, and 14 shows examples of area controlled apodization where the transducer array 802 includes a CMUT transducer array. Figure 12 shows a sub-portion of a CMUT transducer array 802. Figure 13 shows an example of fixed area controlled apodization. Figure 14 shows an example of dynamic area controlled apodization.

In Figure 12, the sub-portion of the transducer array 802 includes two line elements 1202 and 1204 in one direction 1206 and four line elements 1208, 1210, 1212 and 1214 in a different direction 1216. An element 904 includes XxY cells 1218, where X and Y are positive integers, and $X = Y$ or $X \neq Y$. Different elements 904 may have the same or a different number of cells 1218.

In Figure 13, $X = Y = 5$, arranged as a 5x5 matrix, or 25 elements 904. For sake of clarity and explanatory purposes, only reference numerals for a single element 904 and a single cell 1218 of the element 904 are provided. For the other components, the description of Figure 9 can be referenced. In Figure 13, the transducing area of each element 904 is fixed by the number of cells 1218 which populate the element 904. That is, an element 904 with twice the number of cells 1218 as another element 904 will have twice the transducing area as the other element 904.

By way of example, for the row line element 912_1, element 1,1 includes a single cell 1218, element 1,2 includes two cells 1218, the element 1,3 includes three cells 1218, element 1,4 includes two cells 1218, and element 1,5 includes one cell 1218. As such, the elements 1,2 and 1,3 have twice the transducing area as the elements 1,1 and 1,4, and the element 1,3 has three times the transducing area as the elements 1,1 and 1,4. In this embodiment, a similar pattern is followed for the column line element 916_1. That is, the element 1,1 includes a single cell 1218, element 2,1 includes two cells 1218, element 3,1 includes three cells 1218, element 4,1 includes two cells 1218, and element 5,1 includes one cell 1218.

As shown in the illustrated embodiment, the center element 3,3 includes nine cells 1218. The elements (element 3,2; element 2,3; element 4,3; element 3,4) adjacent to the center element 3,3 each include five cells 1218. The elements (element 2,2; element 4,2; element 2,4; element 4,4) at the corners of the element 3,3 each include four cells 1218. The

elements along the periphery and at the corners include less than four cells 1218. With this configuration, the apodization rolls off from the center element 3,3 to the edge elements as a function of a distance from the center element 3,3 to each of the other elements 904. Again, this has the effect of down waiting the edge sub-elements, mitigating ghost artifact introduced thereby. The geometry of each element 904 can be the same or different.

Generally, a size of each cell 1218 is determined by the desired fundamental resonant frequency of the transducer array 802. The active or transducing area of an element 904 is adjusted by varying the number of cells 1218 per element 904. With the geometry in Figure 13, the element 3,3 has nine (9) discrete apodization levels, and the other elements 907 have less than nine discrete apodization levels, or a number of discrete apodization levels determined by the number of cells 1218. A given transducer element 904 pitch and cell 1218 pitch defines a maximum number of cells per element 904, and the apodization profile is discretized into a number of levels equal to the maximum number of cells per element 904.

Figure 14 shows an example of dynamic area controlled apodization. In Figure 14, a single element 904 includes a 3x3 arrangement of CMUT cells 1218, including a first row 1402_1 of CMUT cells 1218, a second row 1402_2 of CMUT cells 1218, and a third row 1402_3 of CMUT cells 1218, each row including three CMUT cells 1218, and a first column 1404_1 of CMUT cells 1218, a second column 1404_2 of CMUT cells 1218, and a third column 1404_3 of CMUT cells 1218, each column including three CMUT cells 1218.

A row electrode 1406 is in electrical communication with the cells of the second row 1402_2. A first plurality of switches 1408 and 1410 respectively selectively electrically connect the cells of the first row 1402_1 and the cells of the third row 1402_3 to the row electrode 1406. As such, the area of the illustrated element 904 can be dynamically changed, row-wise, between three different discrete area levels. The levels include: only the second row 1402_2; the second row 1402_2 and either the first row 1402_1 or the third row 1102_3, and all three rows.

A column electrode 1416 is in electrical communication with the cells of the second column 1404_2. A second plurality of switches 1412 and 1414 respectively selectively electrically connect the cells of the first column 1404_1 and the cells of the third column 1404_3 to the column electrode 1416. As such, the area of the illustrated element 904 can be

dynamically changed, column-wise, between three different discrete area levels. The levels include: only the second row 1404_2; the second row 1404_2 and either the first row 1404_1 or the third row 1404_3, and all three rows.

Combining the switching of the rows and columns, the area of the illustrated element 904 can be dynamically changed between nine different discrete area levels. This includes only the central CMUT cell 1218 up to all of the CMUT cells 1218. Similar to the piezoelectric element 904 of Figure 11, if the number of enabled switches in row i is denoted k_i and the number of enabled switches in column j is denoted k_j, the area apodization A of element (i; j) is $A(i; j) = k_i \times kj$. As with fixed area-controlled apodization, dynamic area controlled apodization of row-column addressed arrays offers 2N transmit and receive connections to an N x N transducer array since the switches can be operated from a pre-programmed independent circuit.

Figure 15 shows an example of bias controlled apodization in connection with a CMUT transducer array 802. For sake of clarity and explanatory purposes, this example includes a 6x6 array. However, it is to be understood that smaller and larger arrays, and non-square arrays are also contemplated herein. It is also to be understood that the illustrated voltage levels are also provided for explanatory purposes and are not limiting; other voltage levels are contemplated herein.

The transducer array 802 includes the electrical contacts 906_1, …, 906_6, each electrically connected to a plurality of the elements 904 via the electrically conductive elements 910_1, …, 910_6, forming the row line elements 912_1, …, 912_6. The array 802 further includes the electrical contacts 908_1, …, 908_6, each electrically connected to a plurality of elements 904 via the electrically conductive elements 914_1, …, 914_6, forming the column line elements 916_1, …, 916_6.

In this example, the transducer array 802 further includes a first set of direct current (DC) voltage sources 1502_1, …, 1502_6, and a second set of DC voltage sources 1504_1, …, 1504_6. The first set of DC voltage sources 1502_1, …, 1502_6 respectively are electrically connected to the electrical contacts 906_1, …, 906_6, and the second set of DC voltage sources 1504_1, …, 1504_6 respectively are electrically connected to the electrical contacts 908_1, …, 908_6.

The DC voltages generate a map of voltage differences over the sub-elements of the array 802. In general, if the DC bias voltage applied to the i'th row is denoted r(i) and the DC bias voltage applied to the j'th column is denoted c(j), then the bias voltage of element (i; j) is given by $V_{DC}(i; j) = |r(i) - c(j)|$. As the apodization of the individual sub-elements in terms of power scaling is a function of only $V_{DC}(i; j)$ for a given operating frequency, DC bias control allows application of any apodization profile over the entire 2D array that can be described as the sum of two arbitrary discrete 1D functions.

Since the number apodization levels are not limited by the number of cells per sub-element, the DC bias voltage can take any level. Bias-controlled apodization can be implemented as either a fixed or a dynamic apodization. In the first case, a simple voltage divider circuit can be implemented next to the transducer, and the apodization profile is fixed, but the apodization levels are continuous. For dynamic DC bias, a slightly more complicated electronic circuit has to be designed; however, usually only a small number of predefined apodization profiles are needed, so these could be pre-programmed and switched between by an external IC.

With dynamic DC bias voltage control apodization, time gain compensation can be directly integrated into the transducer array 802. By ramping up the DC bias voltage during receive, the signals from the transducer array 802 are effectively time gain compensated, and only a weaker subsequent time dependent amplification of the signals are needed.

Figures 16 and 17 illustrate an example of integrated fixed area apodization for the symmetry axis normal to the array 802. In this instance, the suppression of ghost echoes from a point scatterer located on the symmetry axis normal to the transducer is achieved by applying a rotationally symmetric apodization profile to the transducer. For a CMUT array with 9 cells per sub-element, there are nine (9) apodization levels. A discretized version of a 2D Hann window with 9 levels on a 32x32 array is shown in Figure 16, and the corresponding mask layout for the CMUT array is shown in Figure, 17. Other suitable windows include, but are not limited to, a Hamming, a linear, a Gaussian, and/or other discrete and/or continuous windows.

For point scatterers located away from the symmetry axis normal to the transducer, the main echo will be damped, as the active area of the sub-elements directly beneath it is

reduced. Consequently, the resulting image will have a decreasing signal-to-noise ratio (SNR) as a function of the point scatterer's distance from the symmetry axis. In order to address this issue, a second layout is proposed.

Figure 18 illustrates an example of apodization enabling homogeneous rectilinear imaging with optional beam steering. Using fixed area apodization as an example, the layout in Figure 18 consists of a 2-D row-column addressed array 1800 with all elements having the same (maximum) active area. On each end of the line elements, an apodization element 1802 is attached in which the active area is gradually decreased from a full active area next to the line element to zero active area at the opposing end (the edge of the entire array). With this approach, all point scatterers imaged using rectilinear imaging will experience the same apodization and exhibit the same SNR. In general, the layout in Figure 18 can be used in connection with area apodization (e.g., the example of Figure 21), bias apodization, damping material, and/or apodization. Damping materials are discussed in Demore et al., "Real-Time Volume Imaging Using a Crossed Electrode Array," IEEE Transactions on Ultrasonics, Ferroelectrics, and Frequency Control, vol. 56, no. 6, June 2009.

Beam steering can be employed through a modification: If the apodization elements located in the direction of the beam steering are turned off, the main echo from a point scatterer located will reach the non-apodized part of the line elements first, hence resulting in a full amplitude response. The transmitted/received signal from CMUTs is negligible if no DC bias is applied. By providing four separate DC bias supplies to the apodization elements located on the four sides of the array (or providing four switches, using floating ground, etc.), the apodization elements can be turned on and off in these four groups.

Figure 21 illustrates an example mask layout 2100. In contrast to the embodiment discussed in connection with Figures 16 and 17, in which the array includes a rotationally symmetric apodization profile, this layout is not rotationally symmetric to the axis normal to the array 802. Rather, a same apodization pattern is employed apodization elements which are located only at the end of each 1D array.

In the illustrated example, each of the 1D arrays is a line element that includes a first end, a second end and a middle region there between, and apodization is only at the first and second end regions of each of the 1D arrays, and not at the middle region of each of the 1D

arrays. The illustrated mask layout 2100 includes column contacts 2102 and row contacts 2104.

The mask layout 2100 further includes a first group 2106 of column apodization elements and a second group 2108 of column apodization elements. The mask layout 2100 further includes a third group 2110 of row apodization elements and a fourth group 2112 of row apodization elements. As shown, the first, second, third and fourth groups 2106, 2108, 2110, and 2112 of apodization elements are located only at the first and second ends of each 1D array, and not at the middle region of the 1D arrays.

The mask layout 2100 further includes first row contacts 2114 to apodization elements in the first group 2106, and second row contacts 2116 to apodization elements in the second group 2108. The mask layout 2100 further includes third column contacts 2118 to apodization elements in the third group 2110, and fourth column contacts 2120 to apodization elements in the fourth group 2112.

The mask layout 2100 further includes a non-apodized region 2122, which corresponds to only the middle regions of the 1D arrays, and not the first and second ends of the 1D arrays. In this example, the non-apodized region 2122 is a rectangular region about a center of the array, in a central region within the boundary of the first, second, third and fourth groups 2106, 2108, 2110, and 2112 of the apodization elements.

The mask layout 2100 is shown inside of a chip border 2124. Corner regions 2126 do not include any elements. The corner regions 2126 are rectangular shaped. One side of each corner regions 2126 is adjacent to apodized rows elements. Another side of each corner regions 2126 is adjacent to apodized column elements. The two sides intersect at a corner at which the corresponding corner region 2126 is adjacent to the non-apodized region 2122.

Figure 19 graphically illustrates the output of the transducer array 208 in connection with the row-column addressing of described herein, for example, in connection with Figures 8-18. From Figure 19, the output includes only a main lobe 1900 (and no ghost lobes). For comparative purposes, Figure 7 graphically illustrates the row-column addressing of discussed in connection with Figures 1 and 2. In Figure 7, the output includes a main lobe 702 as well as ghost lobes 704 and 706.

In the above, the focus has been on 2-D transducer arrays utilizing row-column addressing. However, as 2-D row-column addressed arrays are essentially two 1-D arrays orthogonal to each other, the described apodization techniques and time gain compensation can also be applied to 1-D arrays. For low-end ultrasound scanners that do not incorporate the extra electronics needed to apply transmit apodization, a static apodization can be implemented directly in the transducer using these techniques.

Another possible use of these techniques is to improve the out-of-plane performance by apodizing 1-D arrays in the out-of-plane direction. This out-of-plane apodization could either be fixed or dynamic. If the apodization is fixed, it would not influence how the ultrasound scanner uses the transducer nor would it lead to extra connections. Fixed area-controlled apodization can be incorporated in both CMUTs and piezoelectric transducers. In 1-D piezoelectric arrays the fixed area apodization can be changed by e.g. widening the dicing trenches in the crystal.

Figure 20 illustrates an example method.

It is to be understood that the following acts are provided for explanatory purposes and are not limiting. As such, one or more of the acts may be omitted, one or more acts may be added, one or more acts may occur in a different order (including simultaneously with another act), etc.

At 2002, a transmit mode signal is received, placing a transducer array that includes at least one 1D array of transducing elements with integrated apodization in transmit mode.

At 2004, optionally, where the apodization is dynamic, a transmit apodization pattern signal is received setting the transmit apodization pattern.

At 2006, an excitation signal is received by the transducer array.

At 2008, the at least one 1D array of transducing elements transmits an ultrasound wave in response to receiving the excitation signal.

At 2010, a receive mode signal is received placing the transducer array in receive mode.

At 2012, optionally, where the apodization is dynamic, a receive apodization pattern signal is received setting the receive apodization pattern.

At 2014, a reflected wave, generated in response to an interaction of the transmitted ultrasound wave with structure, is received by the at least one 1D array of transducing elements or another the at least one 1D array of transducing elements.

At 2016, the at least one 1D array of transducing elements receiving the reflected wave generates a signal indicative thereof.

At 2018, the generate signal is processed and at least image is generated based thereon.

The methods described herein may be implemented via one or more computer processors (e.g., a micro-processor, a central processing unit (cpu), etc.) executing one or more computer readable instructions encoded or embodied on computer readable storage medium (which excludes transitory medium) such as physical memory which causes the one or more processors to carry out the various acts and/or other functions and/or acts. Additionally or alternatively, the one or more processors can execute instructions carried by transitory medium such as a signal or carrier wave.

The application has been described with reference to various embodiments. Modifications and alterations will occur to others upon reading the application. It is intended that the invention be construed as including all such modifications and alterations, including insofar as they come within the scope of the appended claims and the equivalents thereof.

CLAIMS

What is claimed is:

1. A transducer array (802), comprising:

at least one 1D array of transducing elements (804), the at least one 1D array of transducing elements, including:

a plurality of transducing elements (904), wherein a first of the plurality of transducing elements has a first apodization and a second of the plurality of transducing elements has a second apodization, and the first apodization and the second apodization are different;

at least one electrically conductive element (910) in electrical communication with each of the plurality of transducing elements; and

at least one electrical contact (906) in electrical communication with the at least one electrically conductive element,

wherein the at least one electrical contact concurrently addresses the plurality of transducing elements through the at least one electrically conductive element.

2. The transducer array claim 1, further comprising:

a plurality of the 1D array of transducing elements, physically arranged with respect to each other in a 2D array, wherein each of the plurality of 1D array of transducing elements is independently addressable.

3. The transducer array of claim 2, wherein one of the plurality of the 1D array of transducing elements is addressable to transmit ultrasound energy, and a second of the plurality of the 1D array of transducing elements is addressable to receive reflected ultrasound waves.

4. The transducer array of any of claims 2 to 3, wherein each of the plurality of the 1D array of transducing elements includes a first end, a second end and a middle region there between, each of the plurality of the 1D array of transducing elements has a same apodization

pattern, and the apodization of each of the plurality of the 1D array of transducing elements is only at the first and second ends, and not at the middle region.

5. The transducer array of claim 1, wherein the first of the plurality of transducing elements has a first transducing surface area and the second of the plurality of transducing elements has a second transducing surface area, and a first value of the first transducing surface area and a second value of the second transducing surface area are different.

6. The transducer array of claim 5, wherein the first apodization is proportional to the first value and the second apodization is proportional to the second value.

7. The transducer array of any of claims 5 to 6, wherein the first of the plurality of transducing elements has a first geometric surface area and the second of the plurality of transducing elements has a second geometric surface area, and the first geometric surface area and the first transducing surface area are approximately the same and the second geometric surface area and the second transducing surface area are approximately the same.

8. The transducer array of any of claims 2 to 4, wherein the first value is a fixed single value and the second value is a fixed single value.

9. The transducer array of any of claims 2 to 3, wherein at least one of the plurality of transducing elements includes a plurality of sub-elements (1102), each of the plurality of sub-elements having a transducing surface area, and a value of a transducing surface area of the at least one of the plurality of transducing elements is a summation of the transducing surface areas of each of the plurality of sub-elements.

10. The transducer array of claim 9, wherein at least one of the first value or the second value is dynamically changeable between at least two different values.

11. The transducer array of claim 10, further comprising:

a switch (1110, 1112, 1116, 1118) that electrically connects and disconnects at least one of the plurality of sub-elements with the other of the plurality of sub-elements, wherein the value of the transducing surface area of the at least one of the plurality of transducing elements is a summation of the transducing surface areas of each of the electrically connected plurality of sub-elements.

12. The transducer array of claim 11, wherein the value of the transducing surface area of the at least one of the plurality of transducing elements does not include a transducing surface area of a sub-element not electrically connected to the plurality of sub-elements.

13. The transducer array of any of claims 1 to 12, wherein the plurality of transducing elements includes piezoelectric transducing elements.

14. The transducer array of any of claims 5 to 6, wherein a transducing element of at least one of the first or second of the plurality of transducing elements includes a first number of transducing cells, each of the transducing cells having a transducing area, and at least one of the first or second values is a summation of the areas of the transducing cells.

15. The transducer array of claim 14, wherein the at least one of the first or second values is a fixed single value.

16. The transducer array of claim 14, wherein the at least one of the first or second values is a fixed single value is dynamically changeable between at least two different values.

17. The transducer array of claim 16, further comprising:

a switch (1408, 1410, 1412, 1414) that electrically connects and disconnects at least one of the transducing cells with the other of the transducing cells, wherein the first or second value is a summation of the transducing surface areas of each of the electrically connected transducing cells.

18. The transducer array of any of claims 14 to 16, wherein the plurality of transducing elements includes capacitive micro machined ultrasonic transducer transducing elements.

19. The transducer array of any of claims 5 to 18, wherein at least one of the first transducing surface area or the second transducing surface area is dynamically variable and performs time gain compensation.

20. The transducer array of claim 1, further comprising:

a first voltage source (1500) that applies a first bias voltage to the first of the plurality of transducing elements, wherein a first value of the first bias voltage provides the first apodization; and

a second voltage source (1500) that applies a second bias voltage to the second of the plurality of transducing elements, wherein a second value of the second bias voltage provides the second apodization,

wherein the first and second values are different values.

21. The transducer array of claim 20, wherein the first and second voltage sources have fixed voltages, and the first value is a fixed single value and the second value is a fixed single value.

22. The transducer array of claim 20, wherein the first and second voltage sources have variable voltages, and at least one of the first value or the second value is switchable between two different values.

23. The transducer array of any of claims 20 to 22, wherein the plurality of transducing elements includes capacitive micro machined ultrasonic transducer transducing elements.

24. The transducer array of any of claims 20 to 23, wherein at least one of the first and second values of the first and second bias voltages includes a time-gain compensation voltage.

25. The transducer array of any of claims 1 to 24, wherein the at least one 1D array of transducing elements includes a central region and at least one end region, the first apodization is less than the second apodization, and the first of the plurality of transducing elements is disposed at the central region and the second of the plurality of transducing elements is disposed at the at least one end region.

26. A method, comprising:

transmitting an ultrasound waveform with a transducer array that includes apodization that is integrated into physical elements of the transducer array;

receiving a reflected wave with the transducer array; and

processing the received reflected wave to generate at least one image.

27. The method of claim 26, further comprising:

using a different apodization, for the same transducer array, for transmit and receive operations.

28. The method of any of claims 26 to 27, further comprising:

changing the apodization, of the same transducer array, for transmit and receive operations.

29. The method of any of claims 26 to 28, further comprising:

controlling a transducing area to control the apodization.

30. The method of any of claims 26 to 29, further comprising:

controlling a voltage bias applied to each element to control the apodization.

31. An ultrasound imaging system (800), comprising:

a transducer array (802) with an array-wise addressable array of elements that includes at least two elements with a different apodization, wherein the apodization is one of a fixed

area controlled apodization, a dynamic area controlled apodization, a fixed bias controlled apodization or a dynamic bias controlled apodization;

transmit circuitry (806) that conveys an excitation pulse to the transducer array;

receive circuitry (808) that receives a signal indicative of an ultrasound echo from the transducer array; and

a beamformer (812) that processes the received signal, generating ultrasound image data.

32. The ultrasound imaging system of claim 31, wherein the transducer array includes a 2D array of transducing elements, and the apodization of the 2D array is not rotationally symmetric.

ABSTRACT

A transducer array (802) includes at least one 1D array of transducing elements (804). The at least one 1D array of transducing elements includes a plurality of transducing elements (904). A first of the plurality of transducing elements has a first apodization and a second of the plurality of transducing elements has a second apodization. The first apodization and the second apodization are different. The transducer array further includes at least one electrically conductive element (910) in electrical communication with each of the plurality of transducing elements. The transducer array further includes at least one electrical contact (906) in electrical communication with the at least one electrically conductive element. The at least one electrical contact concurrently addresses the plurality of transducing elements through the at least one electrically conductive element.

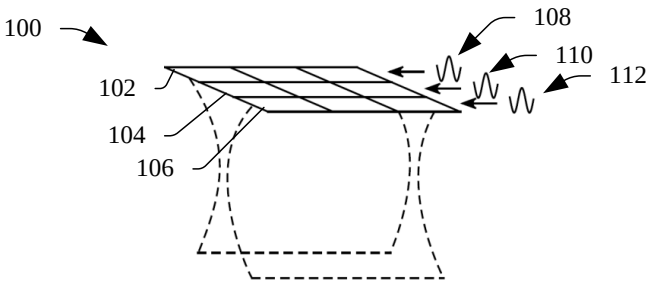

FIGURE 1
(PRIOR ART)

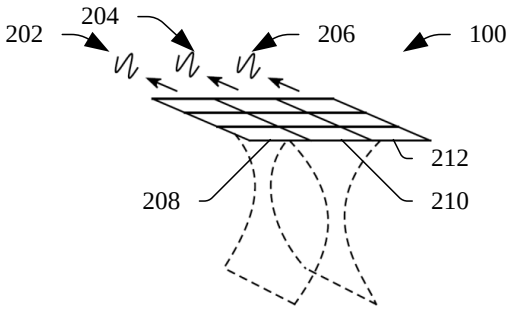

FIGURE 2
(PRIOR ART)

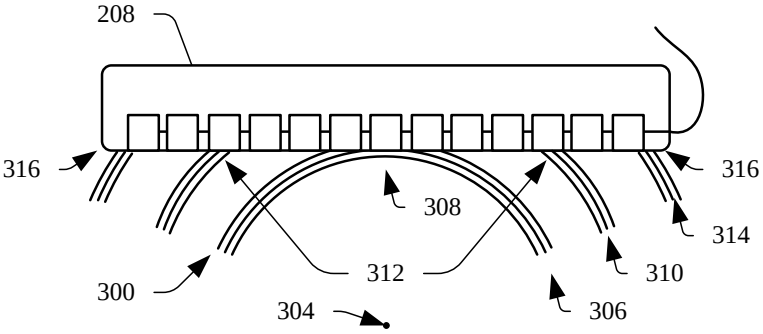

FIGURE 3
(PRIOR ART)

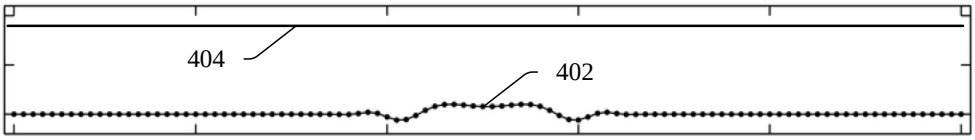

FIGURE 4
(PRIOR ART)

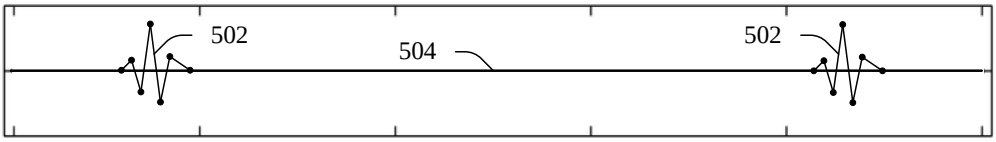

FIGURE 5
(PRIOR ART)

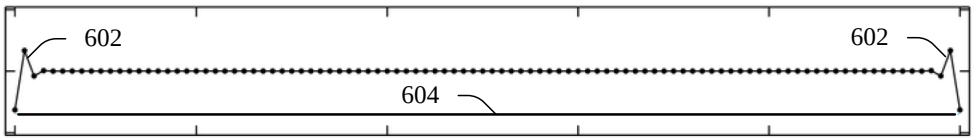

FIGURE 6
(PRIOR ART)

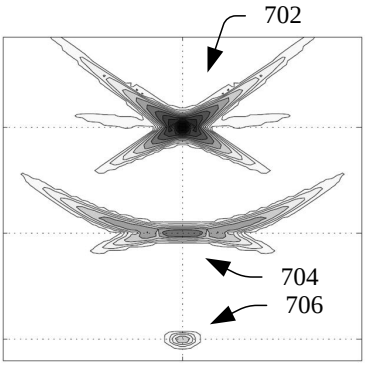

FIGURE 7
(PRIOR ART)

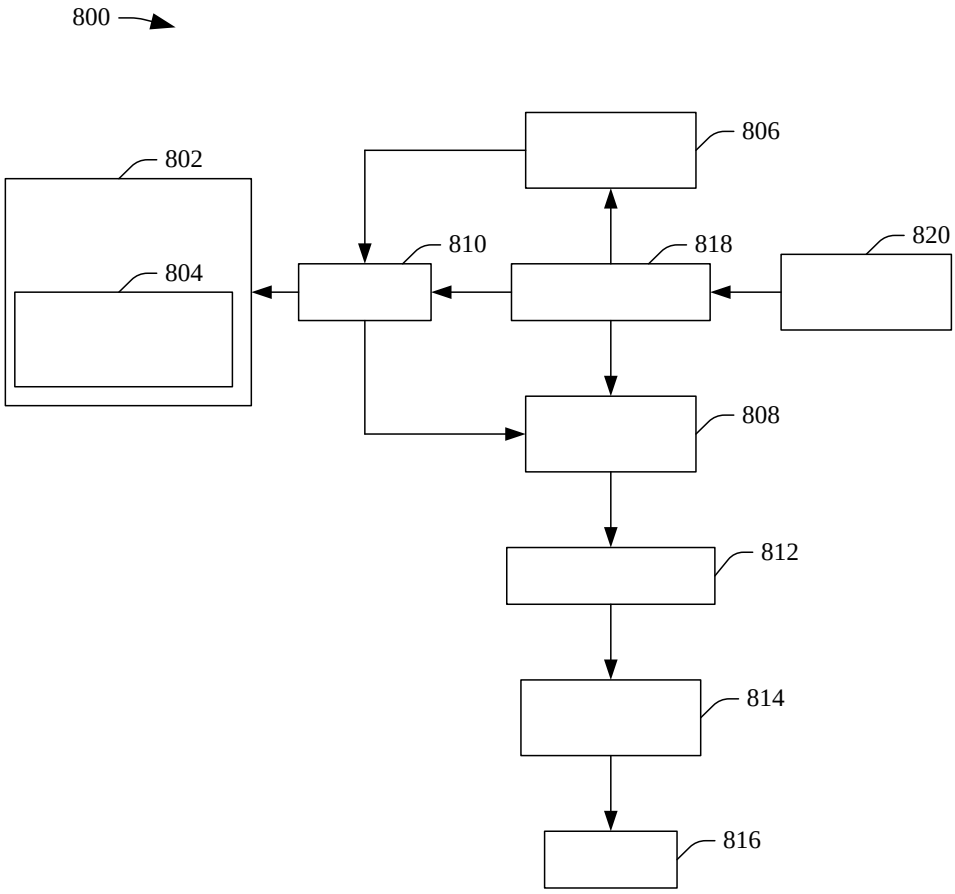

FIGURE 8

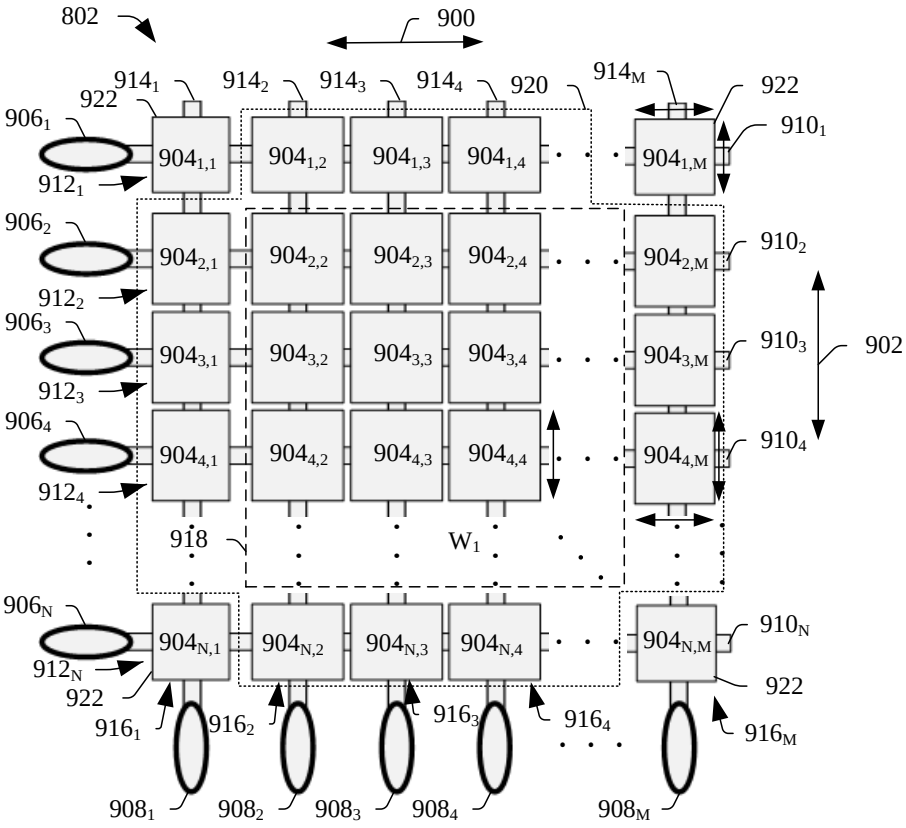
802
900
914$_1$
914$_2$
914$_3$
914$_4$
920
914$_M$
922
922
906$_1$
910$_1$
912$_1$
904$_{1,1}$
904$_{1,2}$
904$_{1,3}$
904$_{1,4}$
904$_{1,M}$
906$_2$
910$_2$
912$_2$
904$_{2,1}$
904$_{2,2}$
904$_{2,3}$
904$_{2,4}$
904$_{2,M}$
906$_3$
910$_3$
902
912$_3$
904$_{3,1}$
904$_{3,2}$
904$_{3,3}$
904$_{3,4}$
904$_{3,M}$
906$_4$
910$_4$
912$_4$
904$_{4,1}$
904$_{4,2}$
904$_{4,3}$
904$_{4,4}$
904$_{4,M}$
918
W$_1$
906$_N$
910$_N$
912$_N$
904$_{N,1}$
904$_{N,2}$
904$_{N,3}$
904$_{N,4}$
904$_{N,M}$
922
916$_1$
916$_2$
916$_3$
916$_4$
916$_M$
908$_1$
908$_2$
908$_3$
908$_4$
908$_M$

FIGURE 9

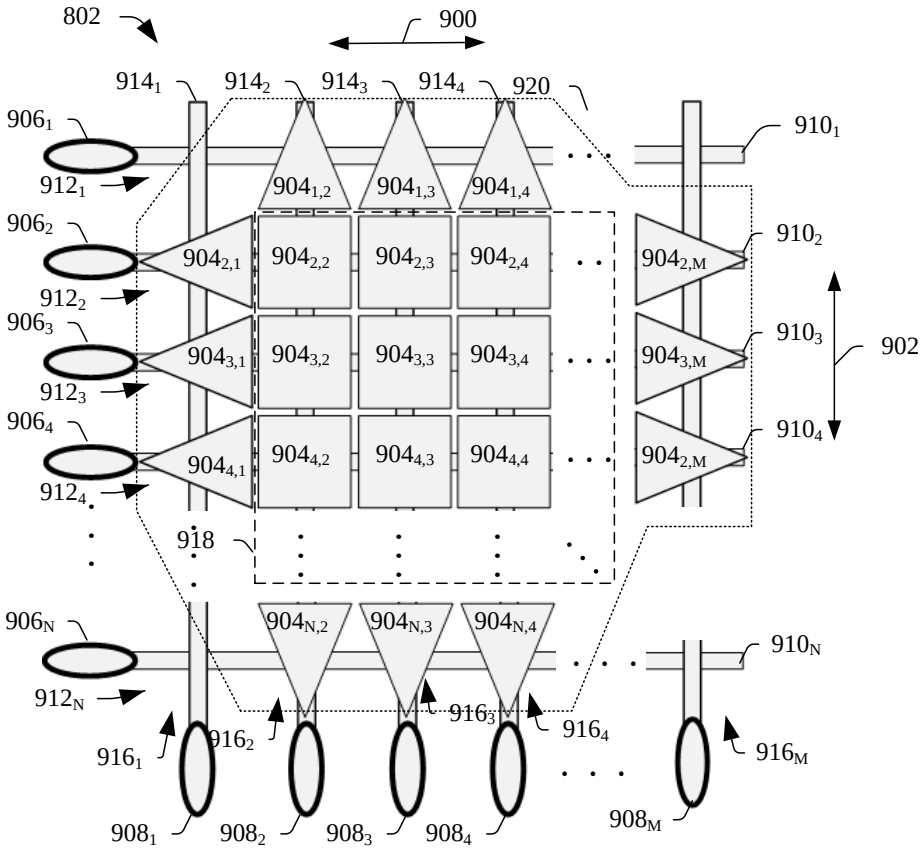
802
900
914$_1$
914$_2$
914$_3$
914$_4$
920
906$_1$
912$_1$
910$_1$
904$_{1,2}$
904$_{1,3}$
904$_{1,4}$
906$_2$
912$_2$
904$_{2,1}$
904$_{2,2}$
904$_{2,3}$
904$_{2,4}$
904$_{2,M}$
910$_2$
906$_3$
912$_3$
904$_{3,1}$
904$_{3,2}$
904$_{3,3}$
904$_{3,4}$
904$_{3,M}$
910$_3$
902
906$_4$
912$_4$
904$_{4,1}$
904$_{4,2}$
904$_{4,3}$
904$_{4,4}$
904$_{2,M}$
910$_4$
918
906$_N$
912$_N$
904$_{N,2}$
904$_{N,3}$
904$_{N,4}$
910$_N$
916$_1$
916$_2$
916$_3$
916$_4$
916$_M$
908$_1$
908$_2$
908$_3$
908$_4$
908$_M$

FIGURE 10

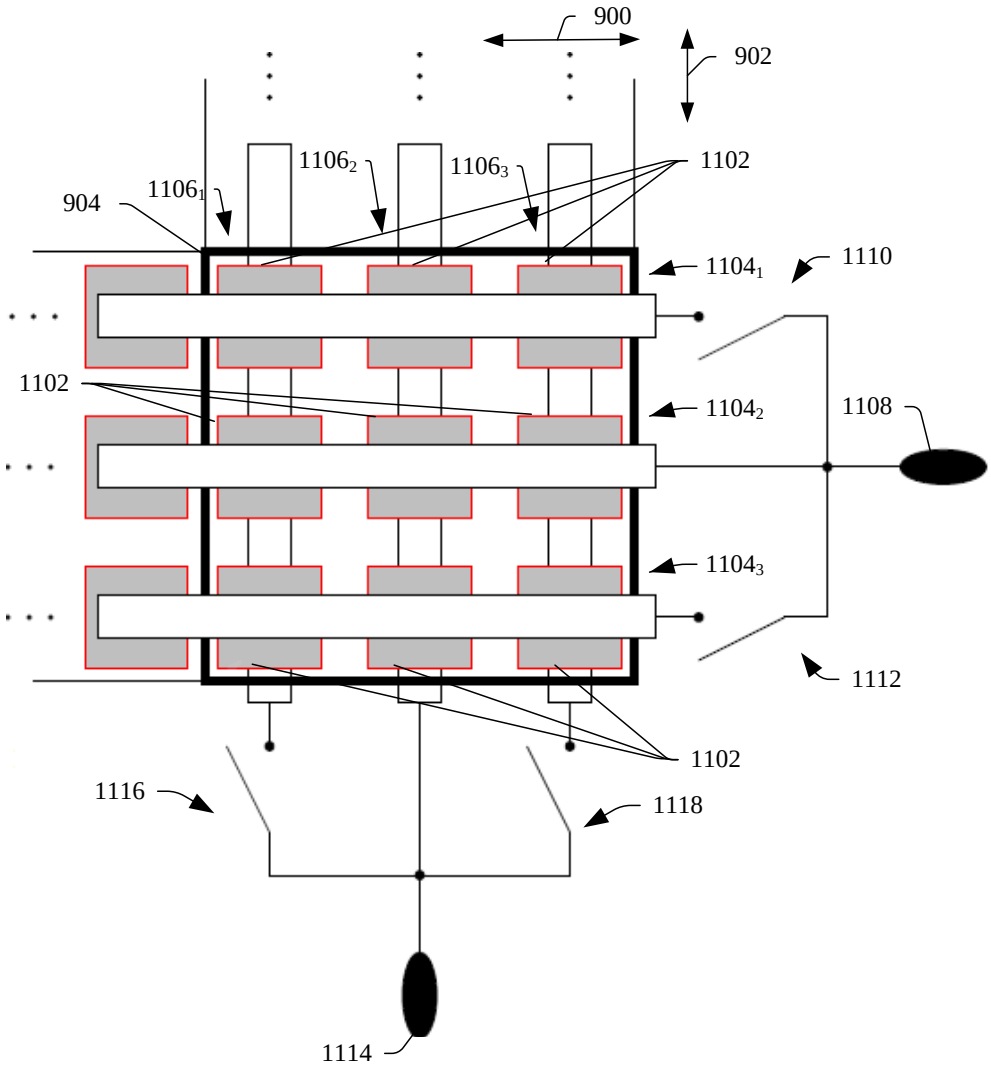
900
902
1106$_2$
1106$_3$
1102
1106$_1$
904
1104$_1$
1110
1102
1104$_2$
1108
1104$_3$
1112
1102
1116
1118
1114

FIGURE 11

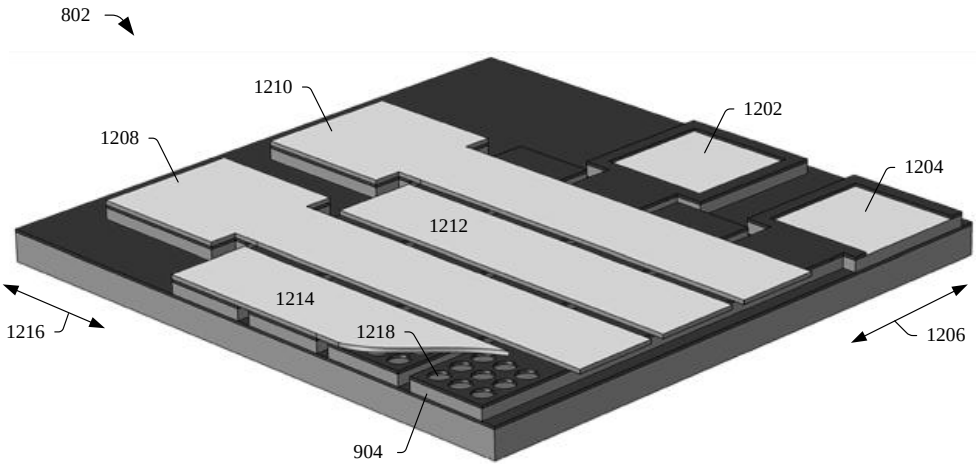

FIGURE 12

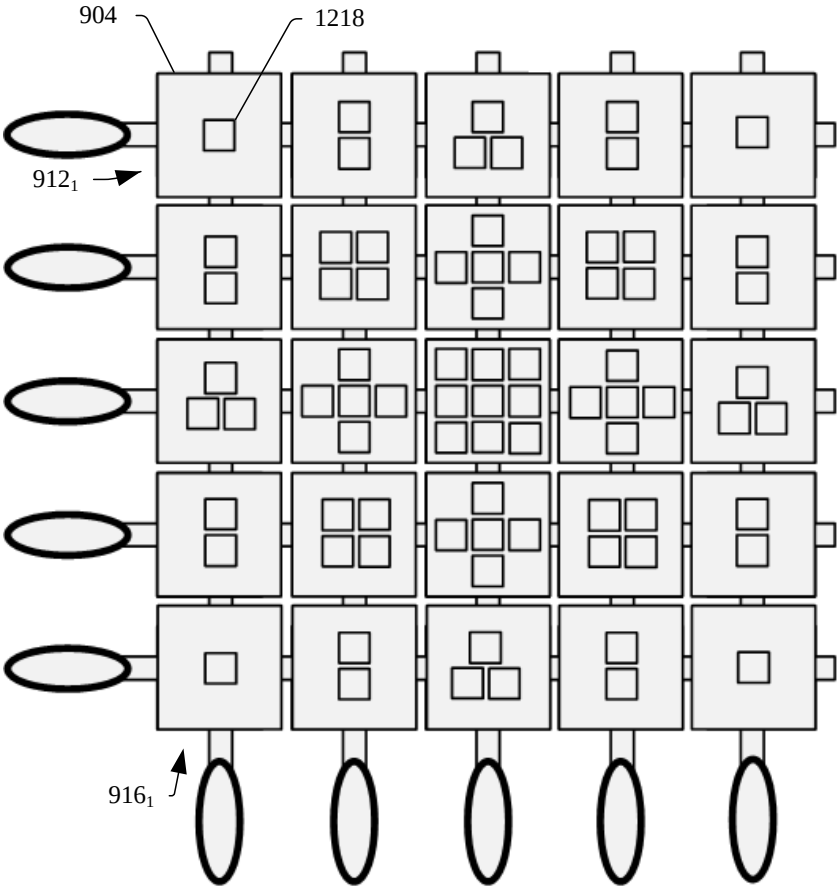

FIGURE 13

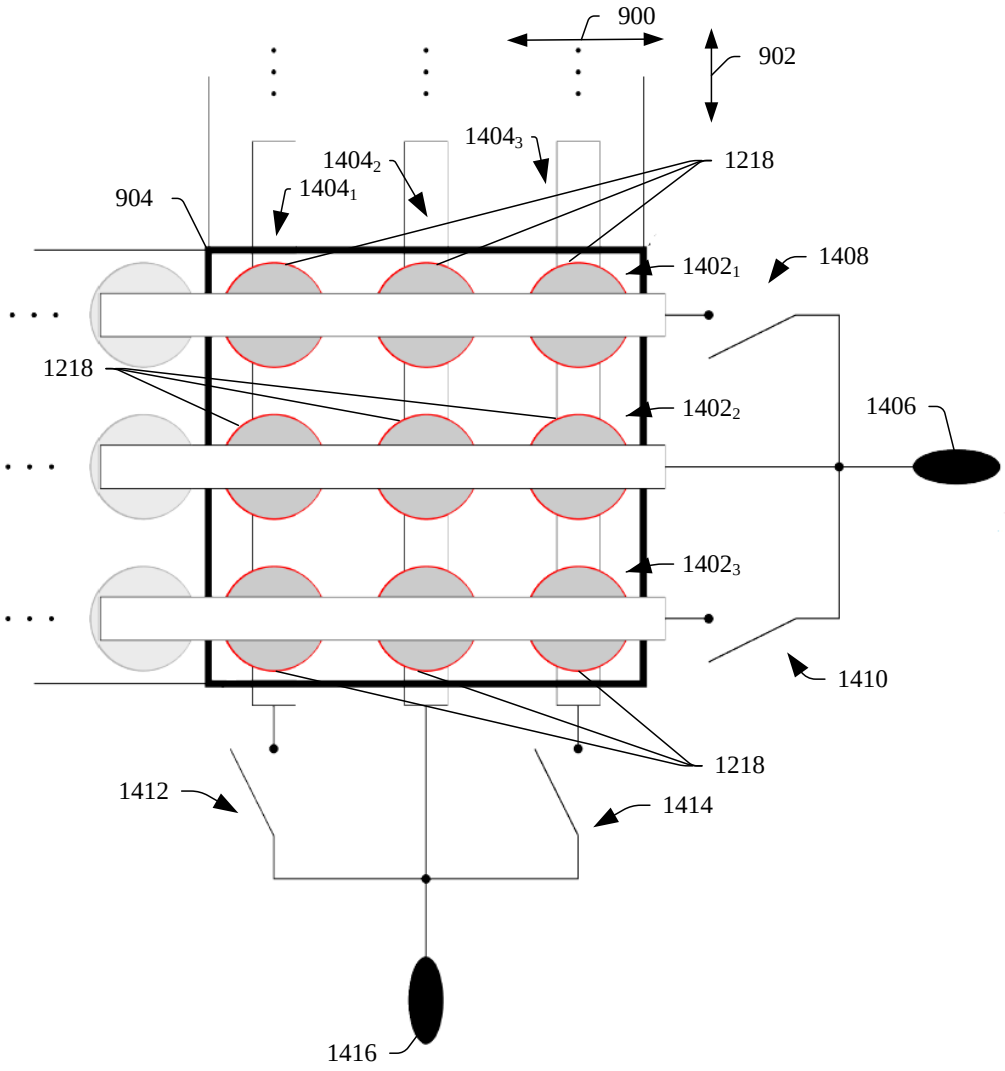
900
902
1404$_3$
1404$_2$
1404$_1$
1218
904
1402$_1$
1408
1218
1402$_2$
1406
1402$_3$
1410
1218
1412
1414
1416

FIGURE 14

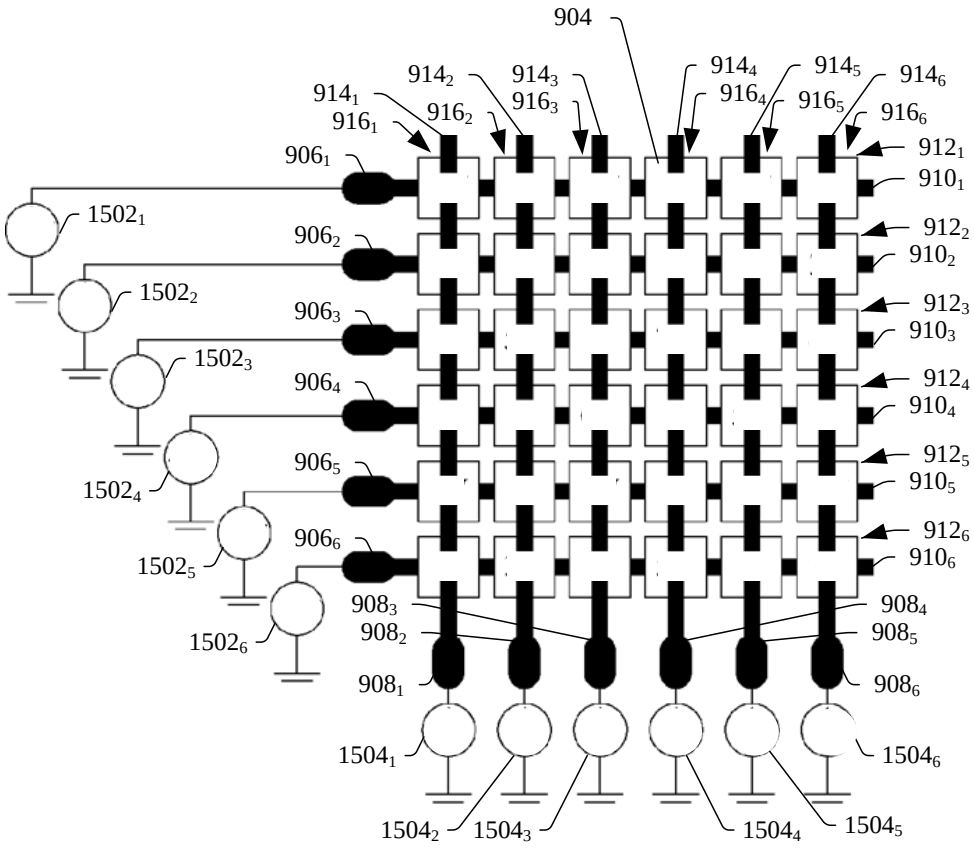
904
914$_1$
914$_2$
914$_3$
914$_4$
914$_5$
914$_6$
916$_1$
916$_2$
916$_3$
916$_4$
916$_5$
916$_6$
906$_1$
906$_2$
906$_3$
906$_4$
906$_5$
906$_6$
912$_1$
912$_2$
912$_3$
912$_4$
912$_5$
912$_6$
910$_1$
910$_2$
910$_3$
910$_4$
910$_5$
910$_6$
1502$_1$
1502$_2$
1502$_3$
1502$_4$
1502$_5$
1502$_6$
908$_1$
908$_2$
908$_3$
908$_4$
908$_5$
908$_6$
1504$_1$
1504$_2$
1504$_3$
1504$_4$
1504$_5$
1504$_6$

FIGURE 15

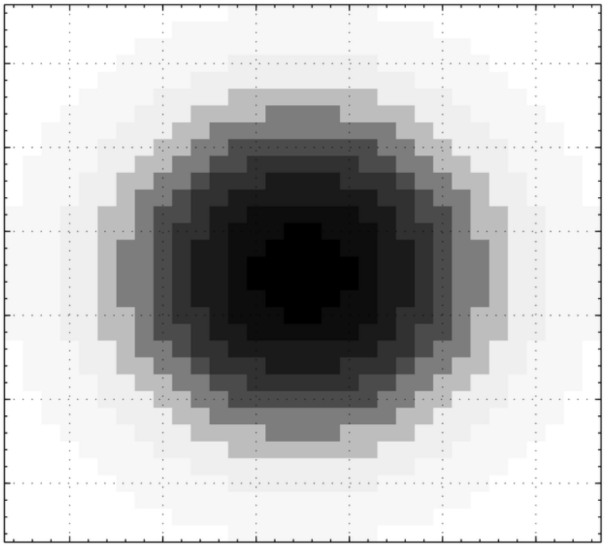

FIGURE 16

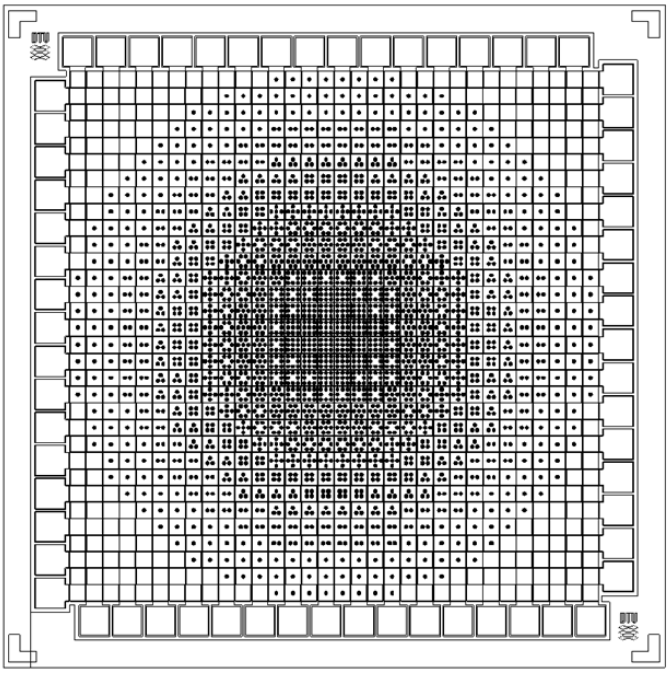

FIGURE 17

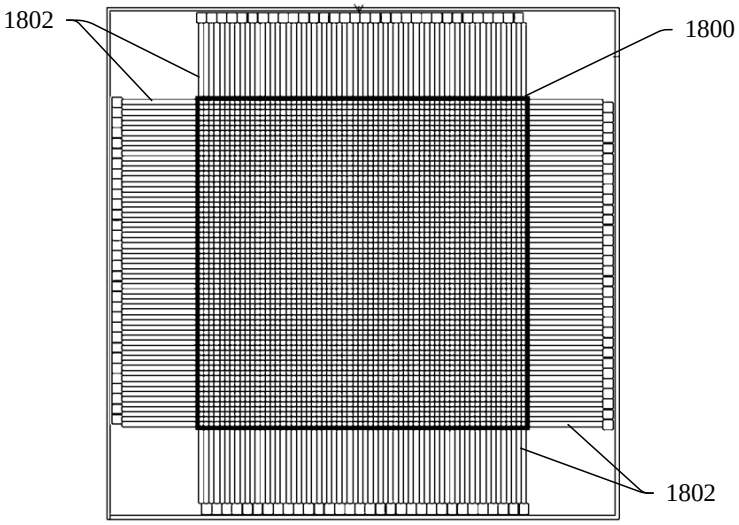

FIGURE 18

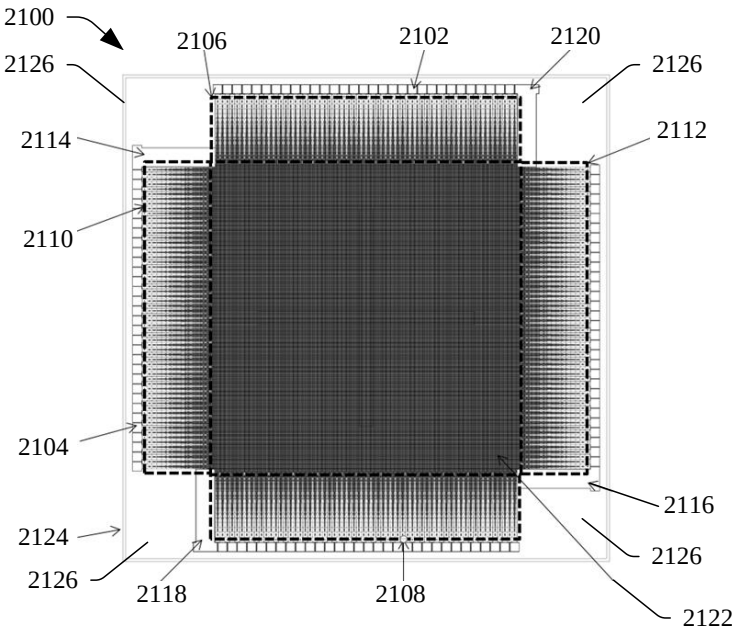

FIGURE 21

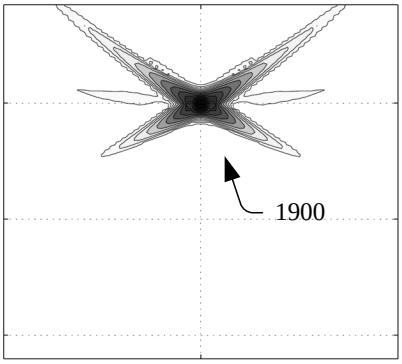

FIGURE 19

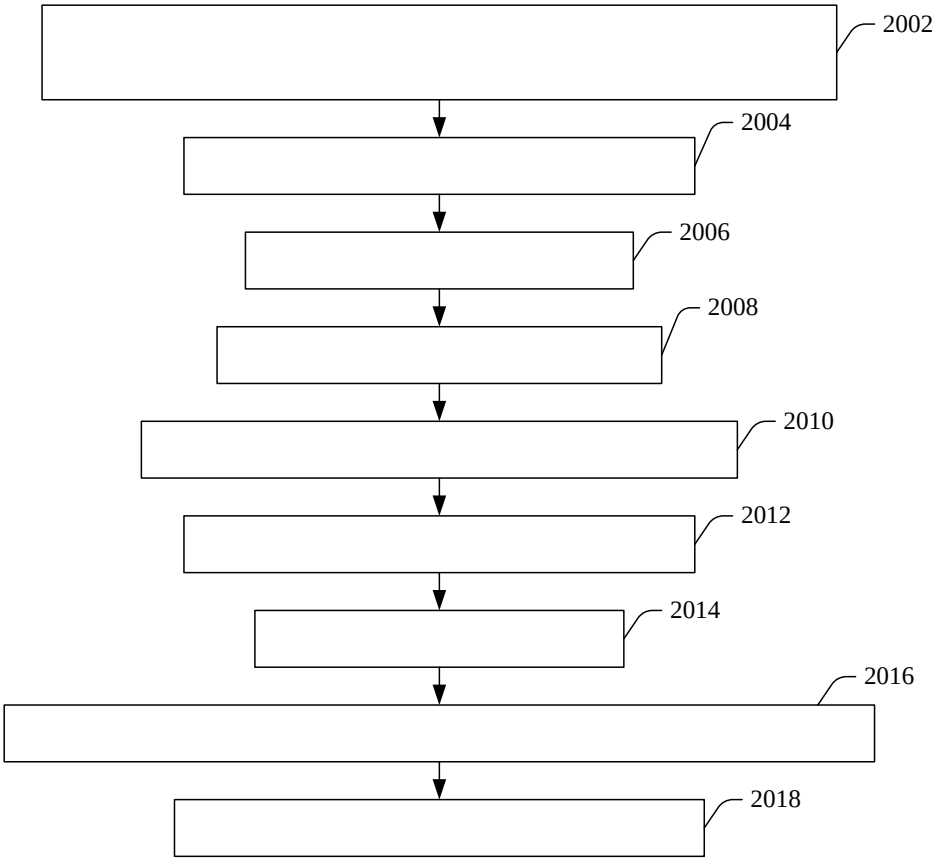

FIGURE 20

PATENT APPLICATION B

3-D Flow Estimation using Row-Column Addressed Transducer Arrays

Authors: Thomas Lehrmann Christiansen, Simon Holbek, Morten Fischer Rasmussen, Erik Vilain Thomsen, and Jørgen Arendt Jensen.

Filed on: January 19, 2015.
US application number: 14/599,857.

Abstract

An ultrasound system includes a 2-D transducer array and a velocity processor. The 2-D transducer array includes a first 1-D array of one or more rows of transducing elements configured to produce first ultrasound data. The 2-D transducer array further includes a second 1-D array of one or more columns of transducing elements configured to produce second ultrasound data. The first and second 1-D arrays are configured for row-column addressing. The velocity processor processes the first and the second ultrasound data, producing 3-D vector flow data. The 3-D vector flow data includes an axial component, a first lateral component transverse to the axial component, and a second lateral component transverse to the axial component and the first lateral component.

3-D FLOW ESTIMATION USING ROW-COLUMN ADDRESSED TRANSDUCER ARRAYS

TECHNICAL FIELD

The following generally relates to ultrasound imaging and more particularly to 3-D flow estimation using row-column addressed transducer arrays.

BACKGROUND

For ultrasound velocity estimation, the oscillation of the pulsed ultrasound field has been used to estimate the axial velocity component of the structure of interest. The axial component is the component of the velocity vector in the direction of propagation of ultrasound energy from the ultrasound transducer array. Several methods have been proposed in the literature to estimate the lateral components of the velocity vector (perpendicular to the axial component). For 2-D imaging using 1-D transducer arrays, these include speckle tracking, directional beamforming, and transverse oscillation (TO). In directional beamforming, the received signals are focused along the flow direction for a given depth. The signals for two emissions are then cross-correlated, and the shift between them is found. This is a shift in spatial position of the scatterers, and dividing by the time between emissions, thus, directly gives the velocity magnitude. The angle between the emitted beam and the flow direction must be known before the beamformation can be done. The angle could, e.g., be found from the B-mode image as in conventional spectral velocity estimation.

For 2-D velocity vector estimation using the TO approach, an oscillation oriented transverse to that of the ultrasound pulse is introduced in the ultrasound field by applying the same transmit beam as used in conventional axial velocity estimation and adjusting the apodization of the receive aperture in such a way that the whole aperture resembles two point sources. Two point sources separated in space will give rise to two interfering fields , which creates the transverse oscillation. Using the Fraunhofer approximation, the relation between the lateral spatial wavelength and the apodization function is $\lambda_x = 2\lambda_z z_0/d$, where d is the distance between the two peaks in the apodization function, z_0 is a depth, and λ_z is the axial wavelength. In axial velocity estimation, a Hilbert transform is performed to yield two 90°

phase shifted signals; the in-phase signal and the quadrature signal. This enables the direction of the flow to be determined. The 90° phase shift in the transverse direction can be accomplished by having two parallel beamformers in receive. The two receive beams are steered, so that the transverse distance between each beam is $\lambda_x/4$, which corresponds to a 90° phase shift in space. Along with these two TO lines, a center line can be beamformed by a third beamformer for conventional axial velocity estimation.

For 3-D velocity vector estimation using the TO approach, 2-D transducer arrays are used to generate the TO field in both lateral dimensions allowing estimation of the velocity vector components in all three dimensions. 3-D velocity vector estimation using multiple crossed-beam ultrasound Doppler velocimetry and speckle tracking have also been proposed in the literature. There is an unresolved need for other approaches to 3-D velocity vector estimation that are applicable to arrays with a reduced number of connections, such as row-column addressed arrays.

SUMMARY

Aspects of the application address the above matters, and others.

In one aspect, an ultrasound system includes a 2-D transducer array and a velocity processor. The 2-D transducer array includes a first 1-D array of one or more rows of transducing elements configured to produce first ultrasound data. The 2-D transducer array further includes a second 1-D array of one or more columns of transducing elements configured to produce second ultrasound data. The first and second 1-D arrays are configured for row-column addressing. The velocity processor processes the first and the second ultrasound data, producing 3-D vector flow data. The 3-D vector flow data includes an axial component, a first lateral component transverse to the axial component, and a second lateral component transverse to the axial component and the first lateral component.

In another aspect, a method includes employing row-column addressing with an orthogonally disposed 1-D arrays of a 2-D transducer array to produce data for determining 3-D velocity components. The method further includes processing, with a velocity processor, the data to produce the 3-D velocity components, which includes at least two lateral

components, one transverse to the axial component and the other transverse to the axial component and the one lateral component.

In another aspect, an ultrasound imaging system includes a pair of 1-D arrays oriented orthogonal to each other and row-column addressed. The ultrasound imaging system further includes processing components that process an output of the pair of 1-D arrays to estimate an axial and two lateral components using 2-D velocity vector estimator.

Those skilled in the art will recognize still other aspects of the present application upon reading and understanding the attached description.

BRIEF DESCRIPTION OF THE DRAWINGS

The application is illustrated by way of example and not limited by the figures of the accompanying drawings, in which like references indicate similar elements and in which:

Figure 1 schematically illustrates an example ultrasound imaging system with a 2-D transducer array of row-addressed orthogonal 1-D arrays;

Figure 2 schematically illustrates an example of the 2-D transducer array;

Figure 3 illustrates an example method for determining 3-D vector velocity component utilizing the 2-D transducer array of row-addressed orthogonal 1-D arrays;

Figures 4 and 5 schematically illustrate transmit along rows (or columns) and receive by both rows and columns;

Figure 6 schematically illustrates an example beamformer and velocity processor;

Figure 7 schematically illustrates a variation of the beamformer of Figure 6;

Figures 8, 9, 10 and 11 schematically illustrate transmit along rows (or columns) and receive along columns (or rows), and subsequent transmit along columns (or rows) and receive along rows (or columns);

Figures 12 and 13 schematically illustrate other variations of the beamformer of Figure 6;

Figure 14 shows an example of the two angles used for a velocity estimator using directional beamforming; and

Figure 15, 16 and 17 illustrate an example in which the 2-D array 102 includes a physical lens for fixed elevation focus.

DETAILED DESCRIPTION

The following describes an approach to estimate the axial component and both lateral components of the 3-D velocity vector with ultrasound imaging data acquired through row-column addressing of two orthogonally oriented 1-D transducer arrays.

Figure 1 schematically illustrates an example ultrasound imaging system 100. The ultrasound imaging system 100 includes a 2-D transducer array 102 with at least two one-dimensional (1-D) arrays 104 of transducing elements orthogonally arranged with respect to each other. An example of the 2-D array 102 includes N rows (or columns) and M columns (or rows) of transducing elements, where N and M are positive integers and $N = M$ or $N \neq M$. The 2-D array 102 may include a 16x16, 32x32, 32x16, 64x64, larger or smaller array, a non-square/rectangular array, and/or other 2-D array. Figure 2 illustrates an example of the 2-D transducer array 102.

Briefly turning to Figure 2, the example 2-D transducer array 102 is 6x6 transducer array (N=M=6). The 2-D array 102 includes a plurality of rows 204_1, 204_2, 204_3, 204_4, 204_5, and 204_6, collectively referred to herein as rows 204. The 2-D array 102 also includes a plurality of columns 206_1, 206_2, 206_3, 206_4, 206_5, and 206_6, collectively referred to herein as columns 206. The rows 204 and columns 206 provide individual elements $208_{1,1}$, …, $208_{1,6}$, … $208_{6,1}$, … $208_{6,6}$, collectively referred to herein as elements 208. The individual rows 204 and columns 206 are addressable (individually or in groups) respectively through contacts 210_1, 210_2, 210_3, 210_4, 210_5, and 210_6, and 212_1, 212_2, 212_3, 212_4, 212_5, and 212_6, collectively referred to as row contacts 210 and column contacts 212.

Returning to Figure 1, multiple different types of row-column addressed array configurations are contemplated herein. One type includes a conventional row-column addressed 2-D array. This may allow volumetric imaging and estimation of all three velocity vector components in a volume. Another type includes a row-column addressed 2-D array with a physical or electronic elevation lens. This may offer two-way focused B- mode imaging and estimation of the two velocity vectors in the plane of the B-mode image in addition to the out-of-plane velocity vector. This transducer array may include a dynamic receive capability in elevation to improve B-mode image resolution.

The transducing elements may include piezoelectric, capacitive micromachined ultrasonic transducer (CMUT), and/or other transducing elements. Furthermore, the transducing elements may include integrated apodization, which may be identical or different for the individual elements. An example of integrated apodization is described in international patent application serial number PCT/IB2013/002838, entitled "Ultrasound Imaging Transducer Array with Integrated Apodization," and filed December 19, 2013, the entirety of which is incorporated herein by reference. Furthermore, the 2-D array 102 may have a flat or a curved surface. Furthermore, the 2-D array 102 may include one or more lenses.

Transmit circuitry 106 generates pulses that excite a predetermined set of addressed 1D arrays of the 2-D array 102 to emit one or more ultrasound beams or waves into a scan field of view. Receive circuitry 108 receives echoes or reflected waves, which are generated in response to the transmitted ultrasound beam or wave interacting with (stationary and/or flowing) structure in the scan field of view, from a predetermined set of addressed arrays of the 2-D array 102. A controller 110 controls the transmit circuitry 106 and/or the receive circuitry 108 based on a mode of operation. An example of suitable control includes row-column addressing, as well as individual element addressing.

A beamformer 112 processes the echoes, for example, by applying time delays, weighting on the channels, summing, and/or otherwise beamforming received echoes. The beamformer 112 includes a plurality of beamformers (e.g., 2, 3, 4, 5, etc.) that process the echoes and produce data for determining the 3-D velocity components. As described in greater detail below, in one instance the beamformers simultaneously process the echoes, and, in another instance, the beamformers sequentially process the echoes. The illustrated beamformer 112 also produces data for generating images in A-mode, B-mode, Doppler, and/or other ultrasound imaging modes.

A velocity processor 114 processes the beamformed data to determine the 3-D velocity components. The velocity processor 114 employs on one or more algorithms from an algorithm bank 116. A suitable algorithm includes a 2-D velocity vector estimator such as a speckle tracking, crossed-beam ultrasound Doppler velocimetry, directional beamforming, transverse oscillation (TO), and/or other estimator. An image processor 118 also processes

the beamformed data. For B-mode, this includes generating a sequence of focused, coherent echo samples along focused scanlines of a scanplane. The image processor 118 may also be configured to process the scanlines to lower speckle and/or improve specular reflector delineation via spatial compounding, apply filtering such as FIR and/or IIR, etc.

A scan converter 120 scan converts the output of the image processor 118 and generates data for display, for example, by converting the data to the coordinate system of the display. The scan converter 120 can be configured to employ analog and/or digital scan converting techniques. A rendering engine 122 visually presents one or more images and/or velocity information via a display monitor 124. Such presentation can be in an interactive graphical user interface (GUI), which allows the user to selectively rotate, scale, and/or manipulate the displayed data. Such interaction can be through a mouse or the like, and/or a keyboard or the like, and/or other approach for interacting with the GUI.

A user interface 126 includes one or more input devices (e.g., a button, a knob, a slider, a touch pad, etc.) and/or one or more output devices (e.g., a display screen, lights, a speaker, etc.). A particular mode, scanning, and/or other function can be activated by one or more signals indicative of input from the user interface 126. For example, where the algorithm bank 116 include more than one 2-D velocity vector estimators the user interface 126 can be used to select one through a user input. The user interface 126 can also be used to set and/or change parameters such as imaging parameters, processing parameters, display parameters, etc.

The beamformer 112, the velocity processor 114 and/or the image processor 118 can be implemented via a processor (e.g., a microprocessor, a CPU, a GPU, etc.) executing one or more computer readable instructions encoded or embedded on non-transitory computer readable storage medium such as physical memory. Such a processor can be part of the system 100 and/or a computing device remote from the system 100. Additionally or alternatively, the processor can execute at least one computer readable instructions carried by a carrier wave, a signal, or other transitory medium.

In one instance, the transducer array 102 is part of a probe and the transmit circuitry 106, the receive circuitry 108, the beamformer 112, the controller 110, the velocity processor 114, the image processor 118, the scan converter 120, the rendering engine 122, the user

interface 126, and the display 124 are part of a separate console. Communication there between can be through a wired (e.g., a cable and electro-mechanical interfaces) and/or wireless communication channel. In this instance, console can be similar to a portable computer such as a laptop, a notebook, etc., with additional hardware and/or software for ultrasound imaging. The console can be docked to a docketing station and used.

Alternatively, the console can be part (fixed or removable) of a mobile or portable cart system with wheels, casters, rollers, or the like, which can be moved around. In this instance, the display 124 may be separate from the console and connected thereto through a wired and/or wireless communication channel. Where the cart includes a docking interface, the laptop or notebook computer type console can be interfaced with the cart and used. An example of a cart system where the console can be selectively installed and removed is described in US publication 2011/0118562 A1, entitled "Portable ultrasound scanner," and filed on November 17, 2009, which is incorporated herein in its entirety by reference.

Alternatively, the transducer array 102, the transmit circuitry 106, the receive circuitry 108, the beamformer 112, the controller 110, the velocity processor 114, the image processor 118, the scan converter 120, the rendering engine 122, the user interface 126, and the display 124 are housed within a hand-held ultrasound apparatus, where the housing mechanically supports and/or encloses the components therein. In this instance, the transducer array 102 and/or the display 124 can be part of the housing, being structurally integrated or part of a surface or end of the hand-held ultrasound apparatus. An example of a hand-held device is described in US 7,699,776, entitled "Intuitive Ultrasonic Imaging System and Related Method Thereof," and filed on March 6, 2003, which is incorporated herein in its entirety by reference.

Figure 3 illustrates a method for 3-D flow estimation using row-column addressed arrays.

At 302, either the rows or the columns (or both sequentially) are used as transmit elements. Any apodization and phase delay can be applied to the transmit elements, and any number of transmit elements can be used simultaneously. Furthermore, any emission technique may be used, e.g. focused emission, plane wave emission, single element emission, synthetic transmit aperture, etc.

An example of transmit along a subset of the rows or the columns 402 of the 2-D transducer array 102 is shown in Figure 4. In Figure 4, the example transmit produces a focused sound wave 404 in one line of direction.

Returning to Figure 3, at 304, echoes are subsequently received by the rows and the columns. An example of this is shown in Figure 5, which shows both rows 502 (or columns) and columns 504 (or rows) of the 2-D transducer array 102 respectively receive echoes 506 and 508.

Returning to Figure 3, at 306, the echoes are processed to determine the 3-D velocity components. Depending on the velocity estimator, any subset of the received signals may be used. For example, in one instance, only the signals received by the rows are used. Furthermore, any apodization and phase delay may be applied to the receiving elements. The full 3-D velocity estimation may be performed using a single or several of such transmit-receive events, which may be combined in the estimation.

In one embodiment, the controller 110 controls the transmit circuitry 106 so that either the rows or the columns emit ultrasound, and the velocity processor 114 estimates velocity by synthesizing TO fields in receive for both the rows and columns, respectively. The sequence may be repeated with the same or different transmit setup. This embodiment may be realized with a total of five beamformers 602, 604, 606, 608 and 610, as shown in Figure 6, each beamforming a line. The velocity processor 114 includes a transverse velocity processor 612, a transverse velocity processor 614, and an axial velocity processor 616.

The received signals from the rows 612 are processed by beamformers 602 and 604, which are configured to produce data, which the transverse velocity processor 612 processes to determine the velocity component perpendicular to the rows. The received signals from the columns 614 are processed by beamformers 608 and 610, which are configured to produce data, which the transverse velocity processor 614 processes to determine the velocity component perpendicular to the columns. Example approaches for each of the two sets of beamformers are described in Jensen et al., “A new method for estimation of velocity vectors,” IEEE Trans. Ultrason., Ferroelec., Freq. Contr., vol. 45, pp. 837–851, 1998, Jensen, “A New Estimator for Vector Velocity Estimation”, IEEE Trans. Ultrason., Ferroelec., Freq. Contr., vol. 48, pp. 886-894, 2001, and Udesen et al., “Investigation of Transverse Oscillation

Method," IEEE Trans. Ultrason., Ferroelec., Freq. Contr., vol. 53, pp. 959–971, 2006, and international application publication WO/2000/068678, entitled "Estimation of Vector Velocity," and filed November 16, 2000, the entirety of which is incorporated herein by reference.

The beamformer 606 is configured to produce data, which the axial velocity processor 616 processes to determine the axial velocity component. In one instance, the beamformer 606 processes the signals received by the rows 612. In another instance, the beamformer 606 processes the signals received by the columns 614. In yet another instance, the beamformer 606 processes both the signals received by the rows 612 and the signals received by columns 614. In a variation, the beamformer 606 is omitted, and data from beamformers 602 and 604 and/or the beamformers 608 and 610 are feed to the axial velocity processor 616, as shown in Figure 7, which processes the signals to determine the axial velocity component.

In a variation, columns 802 (or rows 804) emit ultrasound (Figure 8), and the TO field is synthesized in receive using the rows 804 (or the columns 802) (Figure 9). This allows estimation of the velocity component perpendicular to the rows (or columns). Subsequently, the rows 804 (or the columns 802) emit ultrasound (Figure 10), and the TO field is synthesized in receive using the columns 802 (or the rows 804) (Figure 11). This allows estimation of the velocity component perpendicular to the columns (or rows). The axial velocity component may be estimated using data from either of the two transmit-receive events. The signal processing may be done as shown in Figure 6.

Alternatively, the signal processing may be done as shown in Figure 12. Figure 12 is substantially similar to Figure 6 except that the two of beamformers feeding one the transverse velocity processors are omitted. In this example, the beamformer 602 and 604, are omitted. In another example, the beamformers 608 and 610, are omitted. This can be implemented because the two transverse components of the velocity vector are estimated in two separate transmit-receive events. Hence, the same set of beamformers may be used. In a variation, the axial beamformer 606 is also omitted (Figure 13), and data from beamformers 602 and 604 and/or beamformer 608 and 610 (as shown) is used to feed the axial velocity processor 614.

In another embodiment, either the rows or columns emit ultrasound, and the velocity estimation is subsequently done by performing directional beamforming in receive for both the rows and columns, respectively. The sequence may be repeated with the same or different transmit setup. In another embodiment, the rows emit ultrasound, and the velocity estimation is done by performing directional beamforming in receive for the columns. This is used to estimate the velocity component perpendicular to the columns. Subsequently, the columns emit ultrasound, and the velocity estimation is done by performing directional beamforming in receive for the rows. This is used to estimate the velocity component perpendicular to the rows. In both embodiments using directional beamforming, two angles must be predetermined.

As shown in Figure 14, this includes a first angle (a1) 1402 between a surface 1404 of the transducer array 102 and a first projected direction of flow 1412, which is a direction of flow 1406 projected on a plane 1408 parallel to columns 1410. This also includes a second angle (a2) 1414 between the transducer surface 1404 and a second projected direction of flow 1420, which is the direction of flow 1406 projected on a plane 1416 parallel to columns 1418. These angles are used to determine the line to be produced using the received data. They may be estimated e.g. from the volumetric image generated by the transducer array. Alternatively, they may be found using the TO approach and/or the methods approach disclosed in Jensen et al., "Estimation of velocity vectors in synthetic aperture ultrasound imaging." IEEE Trans. Ultrason., Ferroelec., Freq. Contr., vol. 25, pp. 1637–1644, 2006, Kortbek et al., "Estimation of velocity vector angles using the directional cross-correlation method," IEEE Trans. Ultrason., Ferroelec., Freq. Contr., vol. 53, pp. 2036–2049, 2006, and/or other approach.

Figure 15, 16 and 17 illustrate an example in which the 2-D array 102 includes a physical lens 1502 giving fixed elevation focus. A conventional row-column addressed array using delay-and-sum beamforming can only achieve one-way focusing in each dimension. The elevation lens 1502 can be of any suitable material and can focus in any desired depth. Alternatively, an electronic lens could be used. An example of an electronic lens is described in Daft et al., "Elevation beam profile control with bias polarity patterns applied to microfabricated ultrasound transducers," in Proc. IEEE Ultrason. Symp., vol. 2, 2003, pp.

1578–1581. In such a lens configuration, the row-column array essentially functions as a conventional 1-D array.

From Figure 15, in the illustrated example rows 1504 oriented in the *x*-direction are used for transmitting. Electronic transmit focusing can then be performed in the *y*-direction, while the lens provides transmit focusing in the *x*-direction. A B-mode image can be acquired using the rows as receivers, in which case the array functions exactly like a 1-D array with elevation focus. The array may be used for estimating the 3-D velocity vector in the plane defined by the elevation lens. This is done by processing the data received on the rows and columns using an estimator discussed herein and/or other estimator for the conventional row-column addressed array.

The velocity vector component in the *y*-direction is estimated using received data from the rows 1504 (Figure 16) and the velocity vector component in the *x*-direction is estimated using received data from columns 1702 (Figure 17). The *z*-component may be estimated using received data from either the rows or the columns, e.g., as shown in Figure 6. As such, by installing the lens 1502 on the row-column array, a two-way focused B-mode image with full 3-D velocity vector information in the plane of the B-mode image is achieved. This can be used for finding e.g. flow rate, direction of flow, peak velocities, etc., without sacrificing frame-rate nor B-mode image quality. A clinician will experience the same performance as when using a 1-D transducer for B-mode imaging in conjunction with 2-D velocity vector imaging, but with the addition of out-of plane velocity estimation.

The application has been described with reference to various embodiments. Modifications and alterations will occur to others upon reading the application. It is intended that the invention be construed as including all such modifications and alterations, including insofar as they come within the scope of the appended claims and the equivalents thereof.

CLAIMS

What is claimed is:

1. An ultrasound system, comprising:

a 2-D transducer array, including:

a first 1-D array of one or more rows of transducing elements configured to produce first ultrasound data; and

a second 1-D array of one or more columns of transducing elements (208) configured to produce second ultrasound data,

wherein the first and second 1-D arrays are configured for row-column addressing; and

a velocity processor that processes the first and the second ultrasound data, producing 3-D vector flow data, including: an axial component, a first lateral component transverse to the axial component, and a second lateral component transverse to the axial component and the first lateral component.

2. The ultrasound system of claim 1, further comprising:

an algorithm bank that includes at least one algorithm from a group consisting of speckle tracking, crossed-beam ultrasound Doppler velocimetry, directional beamforming and transverse oscillation,

wherein the velocity processor employs the at least one algorithm to process the first and the second ultrasound data to produce the 3-D vector flow data.

3. The ultrasound system of claim 1, further comprising:

transmit circuitry;

receive circuitry; and

a controller that controls the transmit and receive circuitry to transmit using one of the first or second 1-D arrays and receive simultaneously from both of the first and second 1-D arrays.

4. The ultrasound system of claim 3, further comprising:

first and second beamformer that process signals from one of the first or second 1-D arrays and produce first beamformed data;

a first velocity processor that processes the first beamformed data, producing the velocity component perpendicular to the first or second 1-D array;

third and fourth beamformer that process signals from the other of the first or second 1-D arrays and produce second beamformed data; and

a second velocity processor that processes the second beamformed data, producing the velocity component perpendicular to the other of the first or second 1-D array.

5. The ultrasound system of claim 4, further comprising:

a fifth beamformer that process at least one of the signal from the first or the second 1-D array and produces third beamformed data; and

a third velocity processor that processes the third beamformed data, producing the axial component.

6. The ultrasound system of claim 4, further comprising:

a third velocity processor that processes at least one of first beamformed data or the second beamformed data, producing the axial component.

7. The ultrasound system of claim 1, further comprising:

transmit circuitry;

receive circuitry; and

a controller that controls the receive and transmit circuitry to transmit using one of the first or second 1-D arrays and receive using the other of the first or second 1-D arrays and subsequently to transmit using the other of the first or second 1-D arrays and receive using the one of the first or second 1-D arrays,

wherein the velocity processor processes data from at least one of transmit-receive sequences to estimate the lateral velocity components.

8. The ultrasound system of claim 7, further comprising:

first and second beamformer that process signals from one of the first or second 1-D arrays and produce first beamformed data;

a first velocity processor that processes the first beamformed data, producing the velocity component perpendicular to the first or second 1-D array;

third and fourth beamformer that process signals from the other of the first or second 1-D arrays and produce second beamformed data; and

a second velocity processor that processes the second beamformed data, producing the velocity component perpendicular to the other of the first or second 1-D array.

9. The ultrasound system of claim 8, further comprising:

a fifth beamformer that process at least one of the signal from the first or the second 1-D array and produces third beamformed data; and

a third velocity processor that processes the third beamformed data, producing the axial component.

10. The ultrasound system of claim 8, further comprising:

a third velocity processor that processes at least one of first beamformed data or the second beamformed data, producing the axial component.

11. The ultrasound system of claim 7, further comprising:

a first pair of beamformers that processes signals from one of the first or second 1-D arrays and produces first or second beamformed data;

a first velocity processor that processes the first beamformed data, producing the two lateral velocity components.

12. The ultrasound system of claim 11, further comprising:

an axial velocity beamformer that process at least one of the signal from the first or the second 1-D array and produces third beamformed data; and

a third velocity processor that processes the third beamformed data, producing the axial component.

13. The ultrasound system of claims 11, further comprising:

a third velocity processor that processes at least one of first beamformed data or the second beamformed data, producing the axial component.

14. The ultrasound system of claim 1, wherein the velocity processor employs transverse oscillation to produce the first and second lateral components.

15. The ultrasound system of claim 1, wherein the velocity processor employs directional beamforming to produce the first and second lateral components.

16. The ultrasound system of claim 1, further comprising:

an acoustical elevation lens affixed to the first and second 1-D arrays.

17. The ultrasound system claim 16, wherein the 2-D array is configured for two way focused B-Mode imaging, and the velocity processor estimates two velocity vectors in a plane of a B-mode image and a velocity vector out of the plane of the B-mode image.

18. A method, comprising:

employing row-column addressing with a orthogonally disposed 1-D arrays of a 2-D transducer array to produce data for determining 3-D velocity components; and

processing, with a velocity processor, the data to produce the 3-D velocity components, which includes at least two lateral components, one transverse to the axial component and the other transverse to the axial component and the one lateral component.

19. The method of claim 18, wherein the velocity processor employs at least one of speckle tracking, crossed-beam ultrasound Doppler velocimetry, directional beamforming and transverse oscillation to produce the 3-D velocity components.

20. The method of claim 19, further comprising:

transmitting ultrasound with only one of the orthogonally disposed 1-D arrays;

receiving echoes concurrently with the orthogonally disposed 1-D arrays; and

processing the received echoes to produce at least the two lateral components.

21. The method of claim 19, further comprising:

transmitting ultrasound with only one of the orthogonally disposed 1-D arrays and receiving echoes with only the other of the orthogonally disposed 1-D arrays; and

processing the received echoes to produce at least the two lateral components.

22. The method of claim 21, further comprising:

transmitting ultrasound with only the other of the orthogonally disposed 1-D arrays and receiving echoes with only the one of the orthogonally disposed 1-D arrays; and

processing the echoes received by the one and the other one of the 1-D arrays to produce at least the two lateral components.

23. The method of claim 18, further comprising:

applying apodization for the transmitting.

24. The method of claim 23, wherein the apodization is integrated into transducer elements of the 1-D arrays.

25. The method of claim 18, further comprising:

applying a phase delay for the transmitting.

26. The method of claim 18, further comprising:

utilizing at least one of focused emission, plane wave emission, single element emission, or synthetic transmit aperture for transmitting.

27. The method of claim 18, further comprising:
providing one-way focusing in both lateral directions.

28. The method of claim 18, further comprising:
employing a lens having a fixed elevation focus with the orthogonally disposed 1-D arrays.

29. The method of claim 28, wherein the lens is a physical lens.

30. The method of claim 29, wherein the lens is an electronic lens.

31. The method of claim 28, further comprising:
providing two-way focusing in a plane of the orthogonally disposed 1-D arrays.

32. An ultrasound imaging system, comprising:
a pair of 1-D arrays oriented orthogonal to each other and row-column addressed; and
processing components that process an output of the pair of 1-D arrays to estimate an axial and two lateral components using 2-D velocity vector estimator.

ABSTRACT

An ultrasound system includes a 2-D transducer array and a velocity processor. The 2-D transducer array includes a first 1-D array of one or more rows of transducing elements configured to produce first ultrasound data. The 2-D transducer array further includes a second 1-D array of one or more columns of transducing elements configured to produce second ultrasound data. The first and second 1-D arrays are configured for row-column addressing. The velocity processor processes the first and the second ultrasound data, producing 3-D vector flow data. The 3-D vector flow data includes an axial component, a first lateral component transverse to the axial component, and a second lateral component transverse to the axial component and the first lateral component.

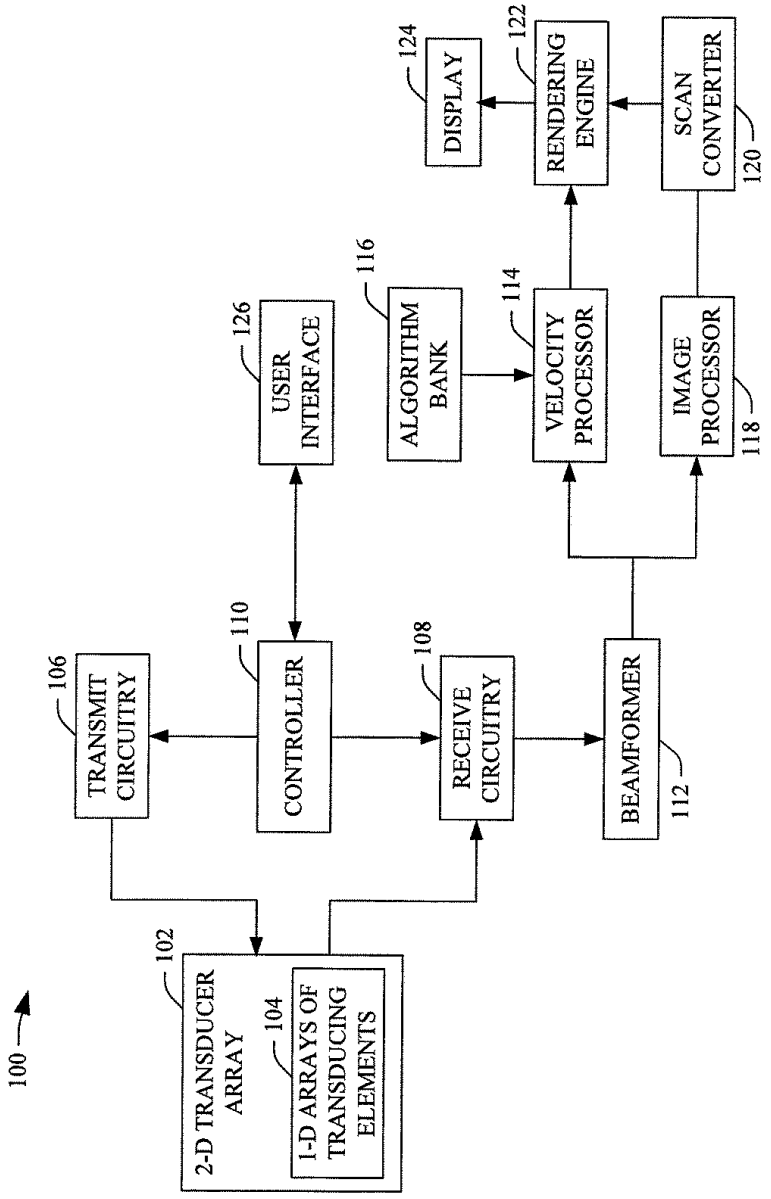
100
2-D TRANSDUCER ARRAY
102
1-D ARRAYS OF TRANSDUCING ELEMENTS
104
TRANSMIT CIRCUITRY
106
CONTROLLER
110
RECEIVE CIRCUITRY
108
BEAMFORMER
112
USER INTERFACE
126
ALGORITHM BANK
116
VELOCITY PROCESSOR
114
IMAGE PROCESSOR
118
SCAN CONVERTER
120
RENDERING ENGINE
122
DISPLAY
124

FIGURE 1

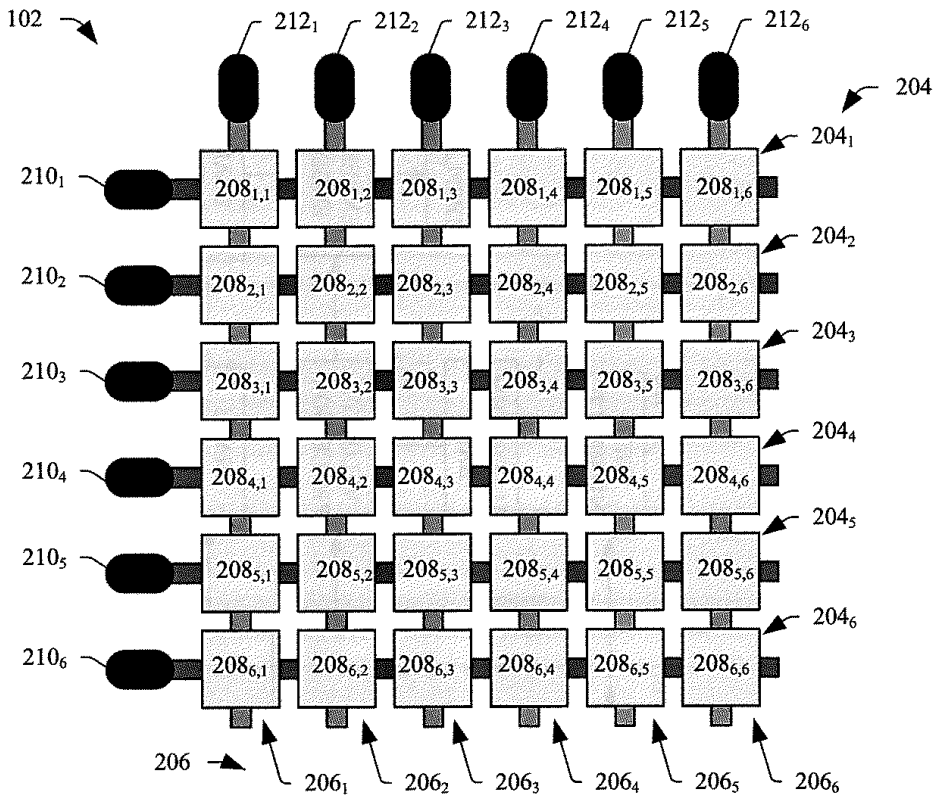

FIGURE 2

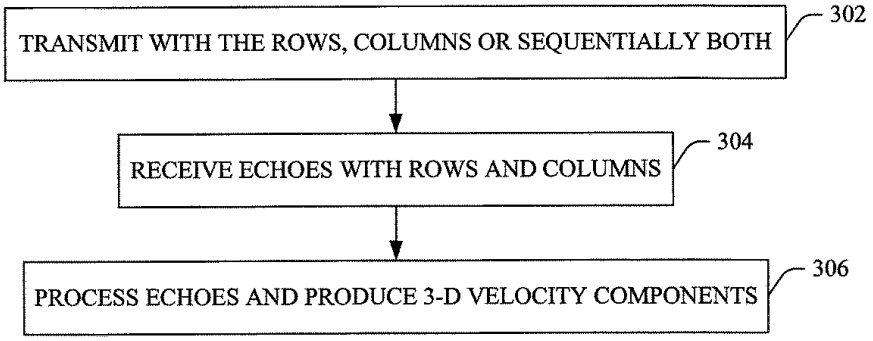

FIGURE 3

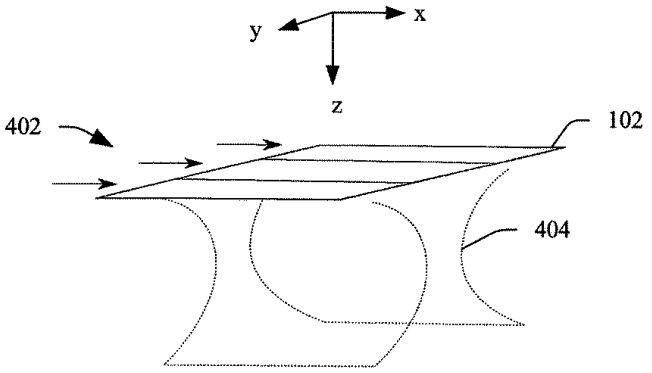

FIGURE 4

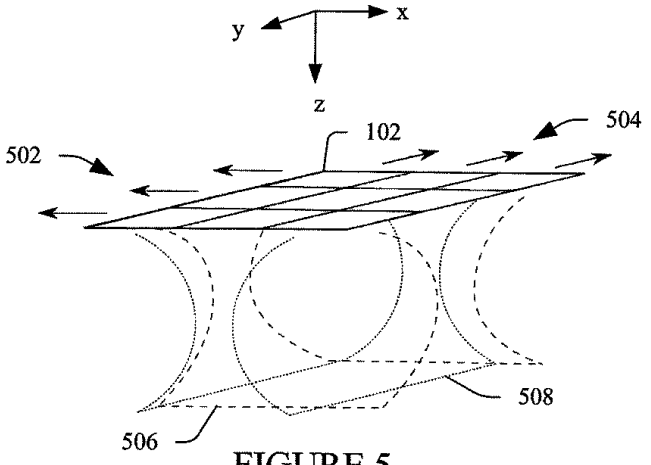

FIGURE 5

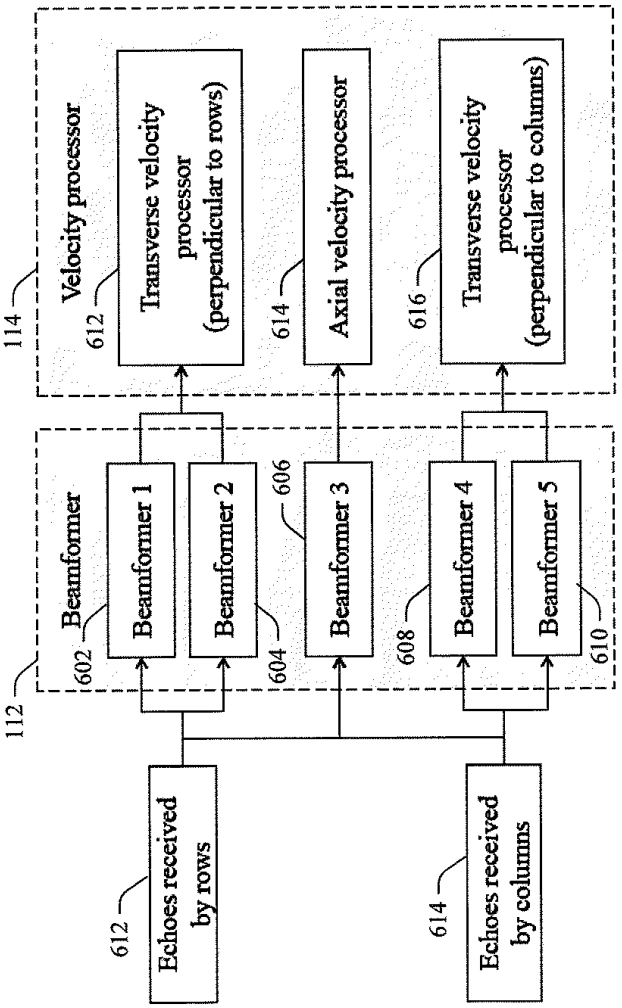
112
Beamformer
602
Beamformer 1
Beamformer 2
604
606
Beamformer 3
608
Beamformer 4
Beamformer 5
610
612
Echoes received by rows
614
Echoes received by columns
114
Velocity processor
612
Transverse velocity processor (perpendicular to rows)
614
Axial velocity processor
616
Transverse velocity processor (perpendicular to columns)

FIGURE 6

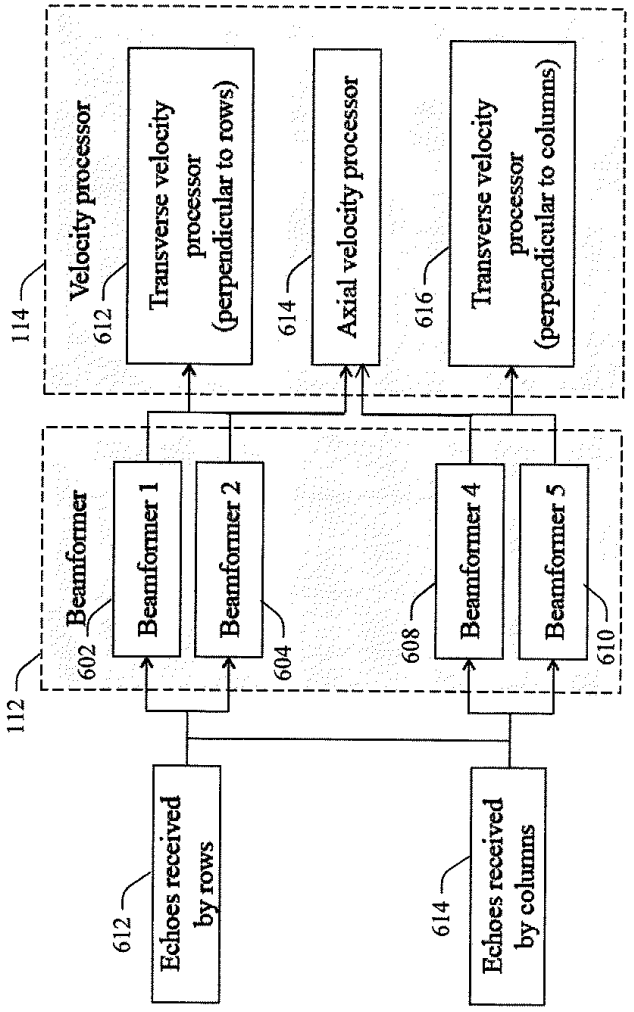
Echoes received by rows
612
Echoes received by columns
614
112
Beamformer
602
Beamformer 1
Beamformer 2
604
608
Beamformer 4
Beamformer 5
610
114
Velocity processor
612
Transverse velocity processor (perpendicular to rows)
614
Axial velocity processor
616
Transverse velocity processor (perpendicular to columns)

FIGURE 7

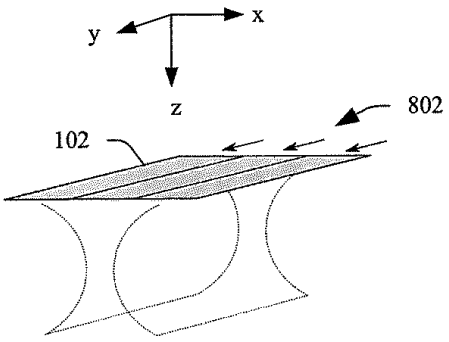

FIGURE 8

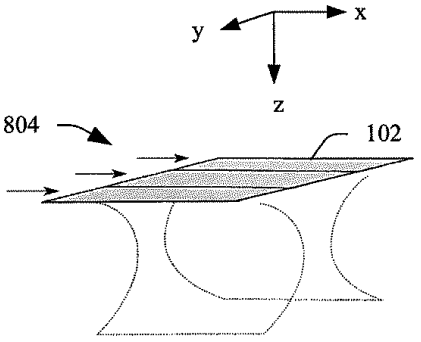

FIGURE 10

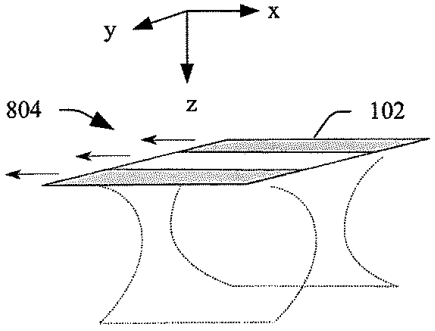

FIGURE 9

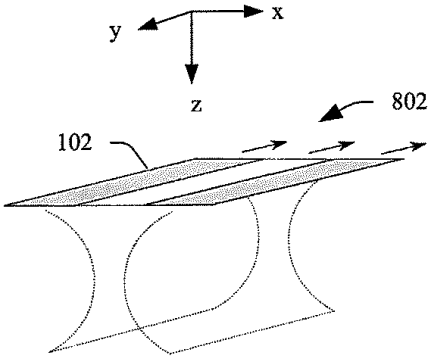

FIGURE 11

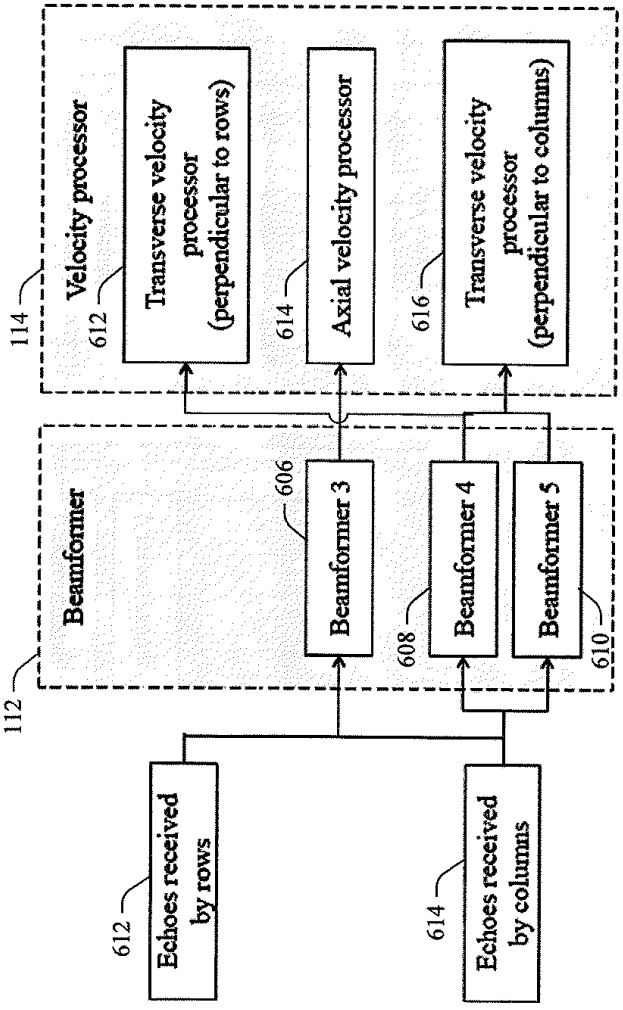
Velocity processor
114
Transverse velocity processor (perpendicular to rows)
612
Axial velocity processor
614
Transverse velocity processor (perpendicular to columns)
616
Beamformer
112
Beamformer 3
606
Beamformer 4
608
Beamformer 5
610
Echoes received by rows
612
Echoes received by columns
614

FIGURE 12

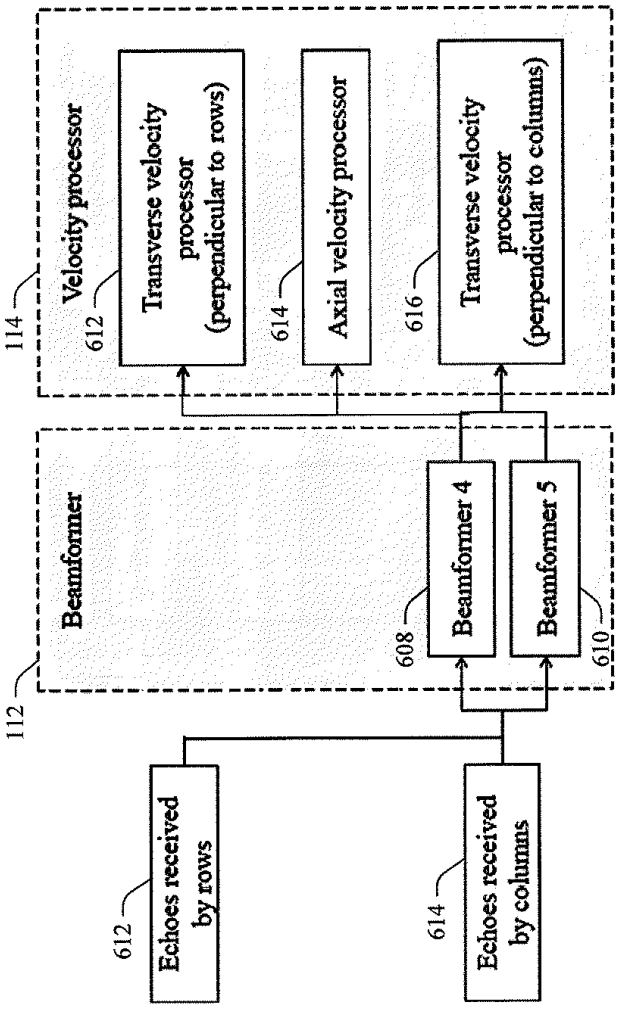
Echoes received by rows
612
Echoes received by columns
614
112
Beamformer
Beamformer 4
608
Beamformer 5
610
114
Velocity processor
Transverse velocity processor (perpendicular to rows)
612
Axial velocity processor
614
Transverse velocity processor (perpendicular to columns)
616

FIGURE 13

Transducer
Column connections
1410
Row connections
1418
Direction of flow
1406
1408
1416
1412
1420
1402
1414
1404
102
a_1
a_2

FIGURE 14

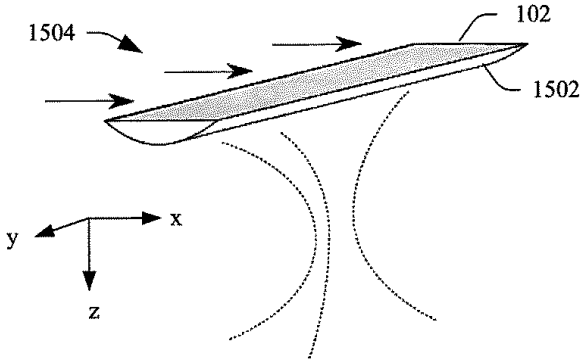

FIGURE 15

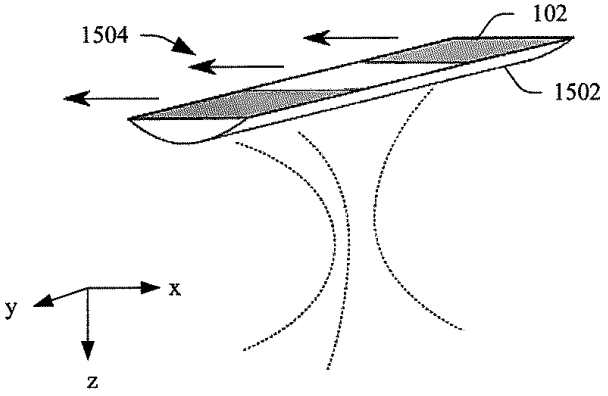

FIGURE 16

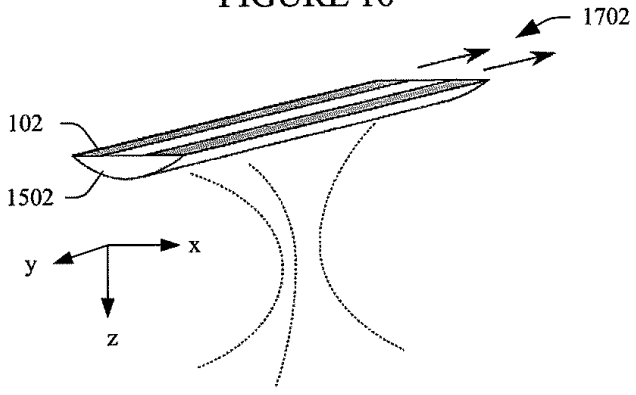

FIGURE 17